Crystallography Reports, Vol. 48, No. 5, 2003, pp. 717–720. Translated from Kristallografiya, Vol. 48, No. 5, 2003, pp. 775–778.

CRYSTAL CHEMISTRY

Dedicated to the 60th Anniversary of the Shubnikov Institute of Crystallography of the Russian Academy of Sciences

Ikranite: Composition and Structure of a New Mineral of the Eudialyte Group

R. K. Rastsvetaeva* and N. V. Chukanov**

** Shubnikov Institute of Crystallography, Russian Academy of Sciences, Leninskiĭ pr. 59, Moscow, 119333 Russia*

e-mail: rast@ns.crys.ras.ru

*** Institute of Problems of Chemical Physics in Chernogolovka, Russian Academy of Sciences, Chernogolovka, Moscow oblast, 142432 Russia*

Received March 14, 2003

Abstract—The crystal structure of a new mineral, ikranite, of the eudialyte group discovered in the Lovozero massif (the Kola Peninsula) was established by X-ray diffraction analysis. The crystals belong to the trigonal system and have the unit-cell parameters $a = 14.167(2)$ Å, $c = 30.081(2)$ Å, $V = 5228.5$ Å^3, sp. gr. $R3m$. Ikranite is the first purely ring mineral of the eudialyte group (other minerals of this group contain ring platforms of either tetrahedral or mixed types). It is also the first representative of the eudialyte group where Fe^{3+} prevail over Fe^{2+} ions. *© 2003 MAIK "Nauka/Interperiodica".*

A new mineral, ikranite, is named after the Shubnikov Institute of Crystallography of the Russian Academy of Sciences.[1] This mineral belongs to the eudialyte family, which includes ring zircono- and titanosilicates of the trigonal symmetry ($R3m$, $R\bar{3}m$, and $R3$). The concept of the composition and atomic structure of eudialyte gradually changed with the accumulation of the information beginning with the first structural studies published in 1971 [1, 2]. One of these structures was established at the Shubnikov Institute of Crystallography of the Russian Academy of Sciences. At present, the variable complex chemical composition of the minerals of the eudialyte group is described by the following general formula proposed by the Commission on New Minerals and Mineral Names of the International Mineralogical Association (CNMMN IMA): $[A(1)A(2)A(3)A(4)A(5)]_3[M(1)M(1)']_3[M(2)M(2a)M(2b)]_{3–6}[M(3)M(4)]Z_3[Si_{24}O_{72}] \cdot OH_{2–6}X_{2–4}$, where A = Na, K, Sr, *REE*, Ba, Mn, H_3O; $M(1)$ and $M(1)'$ = Ca, Mn, *REE*, Na, Fe; $M(2)$ = Fe, Na, Zr, Ta; $M(2a)$ and $M(2b)$ = Mn, Zr, Ti, Na, K, Ba, H_3O; $M(3)$ and $M(4)$ = Si, Nb, Ti, W, Na; Z = Zr, Ti; and X = H_2O, Cl, F, CO_3, SO_4, SiO_4. The letters correspond not only to a set of elements but also to particular structural positions. According to the nomenclature developed by the CNMMN IMA, new mineral species in the eudialyte family are singled out based on the variations in the chemical composition in a number of key positions, among which are both $A(1)$–$A(7)$ and $M(2)$–$M(4)$ extraframework positions and some framework positions, such as $M(1)$ and Z. Several minerals of the eudialyte group were discovered with the participation of researchers from the Institute of Crystallography. These are alluaivite [3], in which Ti in the Z framework position is replaced by Zr; feklichevite [4], in which Na in the $A(4)$ position is replaced by Ca; and raslakite [5], in which Ca in the $M(1)'$ position of the six-membered ring is orderly replaced by Fe.

In the present study, we established the structure of ikranite, a new representative of this mineralogical and crystallochemical family. The preliminary data on the ikranite structure, corresponding to the anisotropical refinement up to $R = 3.7\%$, were published earlier [6]. Here, we report the results of the repeated refinement of several framework positions and characterize the mineral and its structure in more detail consistent with the modern concept of minerals of the eudialyte group.

Ikranite was discovered in the aegirine zone of agpaitic pegmatites from Mount Karnasurt in the northern region of the Lovozero alkaline massif (the Kola Peninsula) in the form of 1-cm-large transparent grains with the color varying from yellow to brown-yellow. This mineral occurs in association with microcline, lorenzenite, nepheline, lamprophyllite, murmanite, and arfvedsonite as well as with tetranatrolite and halloysite formed at a later stage. Ikranite differs from other representatives of the eudialyte group in its physical prop-

[1] This name was approved by the Commission on New Minerals and Mineral Names of the International Mineralogical Association on March 3, 2003.

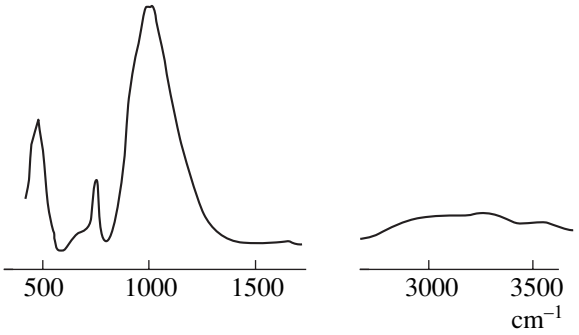

Fig. 1. IR spectrum of ikranite.

erties and some compositional characteristics, in particular, by the presence of trivalent iron and deficit of sodium.

The parameters of the trigonal unit cell are: a = 14.167(2) Å, c = 30.081(2) Å, V = 5228.5 Å^3, sp. gr. $R3m$. According to the results of microprobe analysis, the empirical formula of ikranite (for 24 Si atoms) can be written as $Na_{7.56}(H_3O)_{6.64}K_{0.27}Ca_{3.31}Sr_{0.46}Ce_{0.27}La_{0.11} \cdot Nd_{0.03}Mn^{2+}_{1.41}Fe^{2+}_{0.16}Fe^{3+}_{1.77}Zr_{3.33}Ti_{0.14}Nb_{0.06}Si_{24}O_{72}Cl_{0.74} \cdot 2.64H_2O$.

The ikranite crystals are optically positive with n_o = 1.612(1) and n_e = 1.615(2) and often show a weak anomalous biaxiality. The densities measured by balancing mineral grains in heavy liquids and calculated from the empirical formula are 2.82(1) and 2.83 g/cm^3, respectively. Ikranite was also studied by Mössbauer spectroscopy on a YaGRS-4 spectrometer in a mode of permanent acceleration using a ^{57}Co source in a rhodium matrix (analyst V.V. Korovushkin, All-Russia Research Institute of Synthesis of Mineral Raw Materials). According to the results of Mössbauer spectroscopy, 84.56% of iron in ikranite is in the trivalent state, which is in good agreement with the chemical-analysis data. The presence of two close doublets of Fe^{3+} ions in the Mössbauer spectrum seems to be indicative of weak splitting of the Fe^{3+} position.

The IR spectrum of ikranite (Fig. 1) has broad bands in the frequency range from 3000 to 3300 cm^{-1} (corresponding to vibrational frequencies $\nu_3(E)$ and $\nu_1(A_1)$ of the H_3O^+ groups) and an intense band at 473 cm^{-1} (attributed to vibrations of an $[Fe^{3+}O_6]$ octahedron) absent in the spectra of other minerals of the eudialyte group. Main stretching vibrations of the tetrahedral rings are observed as an intense band at 1000 cm^{-1}, whereas the band due to additional SiO_4 tetrahedra is rather weak (the spectrum shows only the shoulder at 930 cm^{-1}). Therefore, the IR spectrum of ikranite differs radically from the spectra of other minerals of the eudialyte group and can serve as a reliable diagnostic characteristic. Apparently, the replacement of $^{[4]}Fe^{2+}$ by $^{[6]}Fe^{3+}$ is responsible for the change from lilac-red color (eudialyte) to brown-yellow color (ikranite).

A total of 631 X-ray diffraction reflections were collected from a 0.4 × 0.4 × 0.15-mm single crystal on a KM-4 diffractometer (MoK_α radiation, graphite monochromator, $\sin\theta/\lambda < 0.481$). All the computations were made using the AREN program package [7].

The atomic coordinates, equivalent thermal parameters, and occupancies of the positions are listed in Table 1. Since the positions of silicon atoms of the tetrahedral rings and positions of the framework O atoms were published in [6], these data are omitted from

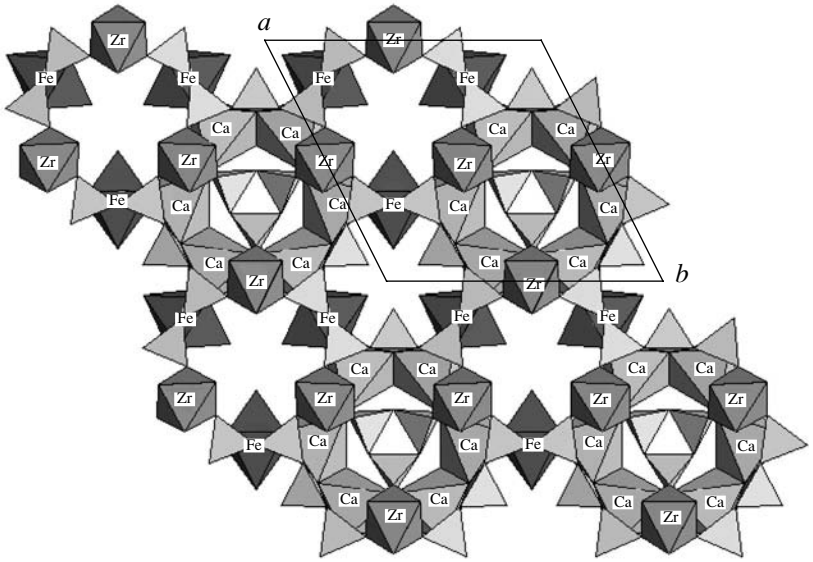

Fig. 2. Framework of the ikranite structure projected onto the (001) plane.

Table 1. Coordinates, occupancies of the key positions, and equivalent thermal parameters of the atoms in the ikranite structure

Position	*x*/*a*	*y*/*b*	*z*/*c*	B_{eq}, Å^2	*Q*	*q*
Zr	0.3332(1)	0.1666(1)	0.1669(1)	1.86(8)	9	1
M(1)	0.2626(1)	0.0012(2)	0.0004(1)	2.21(6)	18	1
M(2*a*)	0.4907(3)	0.5094(2)	0.0016(2)	4.6(1)	9	0.70(1)
M(2*b*)	0.5324(9)	0.4676(9)	–0.003(1)	9.3(7)	9	0.30(2)
M(3*a*)	0.3334	0.6667	0.0306(6)	1.9(5)	3	0.15(1)
M(3*b*)	0.3334	0.6667	0.0859(8)	1.7(7)	3	0.30(2)
M(4*a*)	0.3334	0.6667	0.2271(4)	2.2(3)	3	0.15(1)
M(4*b*)	0.3334	0.6667	0.2875(2)	2.8(3)	3	0.30(2)
A(1*a*)	0.1110(3)	0.2220(5)	0.1528(3)	2.2(2)	9	0.66(1)
A(1*b*)	0.0808(6)	0.1616(9)	0.1663(5)	3(1)	9	0.34(5)
A(2*a*)	0.5681(2)	0.4319(2)	0.1730(2)	1.3(2)	9	0.70(1)
A(2*b*)	0.5450(8)	0.4550(8)	0.1789(7)	2.6(5)	9	0.30(1)
A(3*a*)	0.4648(6)	0.2324(4)	0.0484(2)	1.4(1)	9	0.82(2)
A(3*b*)	0.492(4)	0.246(2)	0.035(2)	1.2(3)*	9	0.18(2)
A(4*a*)	0.2359(4)	0.4718(3)	–0.0459(2)	2.5(2)	9	0.80(2)
A(4*b*)	0.266(3)	0.533(2)	–0.054(1)	1.9(5)*	9	0.20(1)
A(5*a*)	0.391(1)	0.609(1)	0.159(1)	4(1)	9	0.23(4)
A(5*b*)	0.185(1)	0.593(1)	0.164(1)	4(1)	9	0.45(4)
OH(1)	0.3334	0.6667	0.137(3)	7(1)	3	0.30(2)
OH(2)	0.391(1)	0.609(1)	0.159(1)	4(1)	9	0.23(4)
OH(3)	0.259(1)	0.518(2)	0.3307(7)	6.5(5)	9	0.70(5)
OH(4)	0.420(1)	0.580(1)	–0.001(1)	7.1(5)	9	0.70(4)
Cl	0.3334	0.6667	0.150(1)	5.3(9)	3	0.26(2)
H_2O(1*a*)	0	0	0.2250(9)	1.5(4)	3	0.7(1)
H_2O(1*b*)	0	0	0.199(2)	1.4(3)	3	0.3(1)
H_2O(2)	0.6667	0.3334	0.0999(6)	2.5(6)	3	1

Note: The composition of the *M*(1) position is $Ca_{3.3}Mn_{1.4}REE_{0.5}Na_{0.45}Sr_{0.35}$.
* Isotropic thermal parameters.

Table 1. Only the interatomic distances for the extraframework atoms are listed in Table 2.

Like the motifs of other minerals of the eudialyte group, the structural motif of ikranite (Fig. 2) can be described as a loose framework consisting of $[Si_3O_9]$ three-membered rings and $[Si_9O_{27}]$ nine-membered rings linked by the Zn(Ti) octahedra and $[CaO_6]$ six-membered rings. The mixed framework is built by cationic layers alternating along the *c* axis in the Si–Ca–Si–Zr… order. In the *R* lattice, this four-layers fragment is repeated three times along the threefold axis and, thus, gives rise to the formation of a structure consisting of 12 layers with the *c* parameter equal to ~30 Å. The cavities of the framework are occupied by cations in different valence states with various ionic radii, additional anions, anionic groups, and water molecules. Analysis of the key positions revealed the individual characteristic features of ikranite, some of which being predicted from its IR spectrum.

The main feature of the ikranite structure (Fig. 2) is the location of the predominantly vacant *M*(3) and *M*(4) cation positions on a threefold axis in the central region of the nine-membered silicon–oxygen rings $[Si_9O_{27}]$. These rings are generally occupied by either additional Si tetrahedra or octahedra of highly charged cations. Two statistically distributed *M*(4*a*) and *M*(4*b*) octahedra in different orientations are located in the central region of one of these rings. The *M*(4*a*) octahedron is occupied by Zr, whereas the *M*(4*b*) octahedron is occupied by Zr, Nb, or Ti. The distance between the centers of these octahedra is 1.81(1) Å. The central region of the second nine-membered ring also includes two statistically occupied cation positions denoted as *M*(3*b*) and *M*(3*a*). The *M*(3*b*) position is occupied by Si. The *M*(3*a*) position, which has a composition similar to that of the *M*(4*b*) position, is located at a distance of 1.66(3) Å from the *M*(3*b*) position (Table 2). The occupancies of all four positions are very low, and, hence, the central

Table 2. Characteristics of the coordination polyhedra of extraframework cations

Position	Composition ($Z = 1$)	Coordination number	Ranges of cation–anion distances	Average cation–anion distance
M(2*a*)	$6.3Fe^{3+}$	6	1.74(1)–2.52(1)	2.15
M(2*b*)	2.7Na	5	2.20(3)–2.38(2)	2.29
M(3*a*)	0.24Zr + 0.09Nb + 0.09Ti	6	1.92(1)–2.32(1)	2.12
M(3*b*)	0.9Si	4	1.51(4)–1.56(1)	1.55
M(4*a*)	0.45Zr	6	1.71(1)–2.48(4)	2.07
M(4*b*)	0.5Zr + 0.21Nb + 0.21Ti	6	1.82(1)–2.08(2)	1.95
A(1*a*)	$4.45Na + 1.49H_3O$	9	2.57(1)–3.05(2)	2.68
A(1*b*)	$3.06H_3O$	7	2.49(1)–2.85(1)	2.61
A(2*a*)	6.3Na	9	2.43(1)–3.00(1)	2.68
A(2*b*)	2.7Na	8	2.50(1)–2.85(1)	2.63
A(3*a*)	$5.54Na + 1.85H_3O$	9	2.48(1)–3.00(1)	2.74
A(3*b*)	$1.62H_3O$	9	2.60(5)–3.33(5)	2.99
A(4*a*)	5.85Na + 0.9K + 0.45Sr	9	2.51(1)–3.08(1)	2.77
A(4*b*)	$1.8H_3O$	8	2.51(3)–3.26(3)	2.88
A(5*a*)	$0.63H_3O + 1.35(OH)$	7	2.63(5)–2.80(5)	2.7
A(5*b*)	$4.15H_3O$	9	2.48(6)–3.28(1)	2.9

regions of both silicon–oxygen rings are less than half-occupied. Such a degree of decationization of this set of positions is atypical of the known representatives of the eudialyte family.

Since the Ca content in ikranite is low, the octahedra of the six-membered ring are isomorphically occupied by the Ca cations and other elements, and the composition of the position can be written as $Ca_{3.3}Mn_{1.4}REE_{0.5}Na_{0.45}Sr_{0.35}$. One of the governing key positions is linked to a planar square formed by neighboring six-membered rings consisting of the Ca octahedra. Two statistically occupied positions were revealed in ikranite. The *M*(2*b*) position corresponds to a classical five-membered polyhedron. However, it is occupied by Na, whereas the most traditional cation for this position is Fe. The *M*(2*a*) position corresponds to a strongly distorted Fe^{3+} octahedron.

Ikranite is a water-rich mineral. In addition to the OH groups, which complete the framework polyhedra of the structure, three statistically occupied H_2O positions are located on the threefold axis. In ikranite, the cavity between the rings, usually occupied by Na, is filled with hydroxy groups.

One of the characteristic features of the ikranite composition is oxonium occupying the Na position. The ikranite structure has eight positions statistically occupied either by Na or H_3O and mixed positions occupied by both oxonium groups and Na atoms.

Taking into account the structural data, the following generalized formula of ikranite reflects the individual features of the new mineral: $(Na,H_3O)_{15} \cdot (Ca,Mn,REE)_6Fe_2^{3+}Zr_3(\square,Zr)(\square,Si)Si_{24}O_{66}(O,OH)_6Cl \cdot nH_2O$ (n = 2–3). In particular, this formula shows that ikranite is a ring representative of the eudialyte group, whereas other minerals of this group contain either tetrahedral or mixed-ring platforms. In addition, ikranite is the first representative of the eudialyte group where Fe^{3+} ions were proven to prevail over Fe^{2+} ones.

ACKNOWLEDGMENTS

This study was supported by the Russian Foundation for Basic Research, project no. 02-05-64080.

REFERENCES

1. V. M. Golyshev, V. I. Simonov, and N. V. Belov, Kristallografiya **16** (1), 70 (1971) [Sov. Phys. Crystallogr. **16**, 56 (1971)].
2. G. Guiseppetti, F. Mazzi, and C. Tadini, TMPM Tschermaks Mineral. Petrogr. Mitt. **16**, 105 (1971).
3. R. K. Rastsvetaeva, A. P. Khomyakov, V. I. Andrianov, and A. I. Gusev, Dokl. Akad. Nauk SSSR **312** (6), 1379 (1990) [Sov. Phys. Dokl. **35**, 492 (1990)].
4. R. K. Rastsvetaeva, I. A. Ekimenkova, and I. V. Pekov, Dokl. Akad. Nauk **368** (5), 636 (1999).
5. I. A. Ekimenkova, R. K. Rastsvetaeva, and N. V. Chukanov, Dokl. Akad. Nauk **374** (3), 352 (2000).
6. I. A. Ekimenkova, R. K. Rastsvetaeva, and N. V. Chukanov, Dokl. Akad. Nauk **371** (5), 625 (2000).
7. V. I. Andrianov, Kristallografiya **32** (1), 228 (1987) [Sov. Phys. Crystallogr. **32**, 130 (1987)].

Translated by T. Safonova

Crystallography Reports, Vol. 48, No. 5, 2003, pp. 721–727. Translated from Kristallografiya, Vol. 48, No. 5, 2003, pp. 779–785.

CRYSTAL CHEMISTRY

Dedicated to the 60th Anniversary of the Shubnikov Institute of Crystallography of the Russian Academy of Sciences

Incommensurately Modulated Structure of Isotropic Lazurite as a Product of Twinning of Two-Dimensionally Modulated Domains

N. B. Bolotina*, R. K. Rastsvetaeva*, A. N. Sapozhnikov, A. A. Kashaev***, A. Shönleber****, and G. Chapuis******

** Shubnikov Institute of Crystallography, Russian Academy of Sciences, Leninskiĭ pr. 59, Moscow, 119333 Russia*

e-mail: rast@ns.crys.ras.ru

*** Vinogradov Institute of Geochemistry, Siberian Division, Russian Academy of Sciences, ul. Favorskogo 1a, Irkutsk, 664033 Russia*

**** Irkutsk Institute for Engineers of Railway Transport, ul. Chernyshevskogo 15, Irkutsk, 664074 Russia*

***** Institute of Crystallography, University of Lausanne, BSP, Lausanne, 1015 Switzerland*

Received October 28, 2002

Abstract—The incommensurately modulated structure of isotropic lazurite (the Baikal region) was established for the first time. The structure was solved within a pseudocubic unit cell with the parameter $a = 9.077(1)$ Å and the (3 + 2)-dimensional superspace group $Pnn2(\gamma\gamma0, \gamma{-}\gamma0)$ based on a twin model consisting of three two-dimensionally modulated orthorhombic components related by a threefold axis along the [111] direction. The structure was refined with isotropic thermal parameters to $wR_0 = 1.98\%$ and $wR_1 = 7.5\%$ using 257 main reflections and 2392 first-order satellite reflections, respectively. *© 2003 MAIK "Nauka/Interperiodica".*

INTRODUCTION

Lazurite belongs to the sodalite group of minerals with the general formula $(Na,Ca,K)_8(AlSiO_4)_6(SO_4,S,OH,Cl)_2$ and a cubic unit cell with the parameter $a \sim 9$ Å. Not only various sodalites but (often) also various samples of the same mineral species differ in the composition and details of structure ordering of framework ions. X-ray diffraction patterns of many sodalites have additional reflections indicative of distortions of the basic cubic structure. For example, the structures of triclinic [1] and orthorhombic [2] lazurites have orthorhombic superstructures (as regards their metrics) with the unit-cell parameters $a = na_{cub}\sqrt{2}$ (where n is an integer), $b = a_{cub}\sqrt{2}$, and $c = a_{cub}$.

Attempts to study lazurites with modulated structures have been repeatedly made. For example, Hassan [3] studied cubic lazurite from Afghanistan by transmission electron microscopy (TEM) and differential thermal analysis (DTA-TG). The X-ray diffraction pattern of this sample had satellite reflections oriented along several noncoplanar directions. Hassan concluded that the sample had domains with different character of ordering of the $[Na_3CaSO_3]^{3+}$ and $[Na_3CaS]^{3+}$ clusters, with each type of domain giving rise to satellite reflections of a different type. Cubic lazurite from the Southern Baikal region (Russia) consisting of structurally ordered and disordered domains was studied by TEM [4]. Later, the same authors revealed structural modulations along several equivalent directions in optically isotropic lazurite from the Baikal region [5]. Sapozhnikov and coworkers [6] observed gradual changes in the satellite component of the X-ray diffraction pattern from cubic lazurite from the Baikal region after its prolonged annealing ($t = 550$°C). During the first three days of the experiment, the $\{hkl110\}$ satellite reflections with the incommensurability parameter $\gamma \simeq 0.217$ coexisted with satellites which had the same indices but different parameter $\gamma \simeq 0.147$. During the first ten days, the intensities of the former satellite reflections gradually decreased, whereas the intensities of the latter satellites increased. Then, the intensities of satellites of the second type started decreasing until the complete disappearance of all the satellites after two-month annealing. Apparently, for some time, domains characterized by different periods of incommensurate structural modulation coexisted in the sample.

1063-7745/03/4805-0721$24.00

Table 1. Main and satellite reflections from lazurite from the Baikal region (intensities are averaged within the X-ray diffraction class *m*3)

Reflection indices	Number of measured reflections	Number of reflections after averaging	k_{int}, %	$R_{e.s.d}$, %
*hkl*000	3688	309	3.10	0.21
*hkl*110	30219	2644	5.63	2.23
*hkl*200	6830	1056	9.49	8.46
*hkl*211	22999	3628	9.82	11.62
*hkl*222	2659	740	13.03	18.32
*hkl*220	8764	1617	14.54	14.11
*hkl*422	8656	2882	26.43	17.03
*hkl*332	8852	3370	26.96	17.95
*hkl*321	27087	7297	28.18	14.93
*hkl*433	11165	3765	31.92	17.76
*hkl*411	34613	4851	42.81	4.09
*hkl*310	27604	4762	48.49	4.77
*hkl*444	13238	1659	51.32	4.73
*hkl*400	14534	1634	74.20	0.65
Σ	220908	40214		

Earlier, we established the average structure of cubic isotropic lazurite [7] with the unit-cell parameter a_{cub} = 9.077(1) Å based on the strongest reflections (called main reflections), sp. gr. *P*23. This structure served as a basis for the further refinement of the modulation parameters with the use of satellite reflections. The results of this refinement can be found elsewhere [8]. However, taking into account the pioneering character of this study, we describe this refinement in more detail and draw some new conclusions about the nature of atomic modulations in isotropic lazurite.

EXPERIMENTAL

The X-ray diffraction data (Mo radiation) were collected on an Oxford Xcalibur four-circle diffractometer equipped with a CCD detector at the University of Lausanne (Switzerland). These data were processed with the use of the CrysAlisRED [9] and NADA [10] programs to obtain a set of integrated intensities with six-digit indices (Table 1). All the satellites were given integer *hklmnp* indices in the basis consisting of six vectors—**a***, **b***, **c***, γ**a***, γ**b***, γ**c***, where **a***, **b***, and **c*** are the basis vectors of the reciprocal cubic lattice and γ = 0.2154(1) ≃ 3/14. Of all the satellite reflections, those oriented along the [110] diagonals of the reciprocal cubic lattice and located at distances $\gamma \mathbf{a}^*_{cub}\sqrt{2}$ from the main reflections were much more intense. In addition to the {*hkl*110} satellite reflections, the X-ray diffraction pattern also had numerous much weaker {*hkl*211} satellite reflections and other higher-order satellites, which are listed in Table 1. The R_{int} factor of averaging of all the reflections with the indices |*m*|, |*n*|, |*p*| < 3 within the cubic X-ray diffraction class *m*3 is substantially lower than that of averaging of higher-order reflections (Table 1). The choice of the superspace symmetry group of the modulated crystal presented some difficulties associated with the determination of the basis of modulation vectors [11] which should satisfy certain requirements, i.e., it should be linearly independent, completed (closed with respect to the symmetry group), and meet the minimum necessary requirements for integer indexing of satellites. Assuming the cubic symmetry of the three-dimensionally modulated structure, only the aforementioned triad of the vectors γ**a***, γ**b***, and γ**c*** meets these requirements. Six vectors chosen along the ⟨110⟩ directions of the reciprocal cubic lattice are linearly dependent and redundant for indexing, and any set of three such vectors, although independent, are not closed with respect to the cubic symmetry. In the γ**a***, γ**b***, γ**c*** basis, there are no first-order {*hkl*100} satellite reflections on edges of the cube, whereas the strong {*hkl*110} satellites should formally be considered as a result of the superposition of the basis waves. In this basis, all the reflections, including the main ones, satisfy the condition of reflection existence $m + n + p = 2N$. In other words, any group of the (3 + 3)-dimensional cubic symmetry should be supplemented with the translation (0, 0, 0, 1/2, 1/2, 1/2) not changing the atomic positions in the three-dimensional space. Therefore, according to Petricek and Coppens [11], the displacements of all the atoms should obey the constraint $\mathbf{u}(t) = \mathbf{u}(t + 1/2)$ (1), where $\mathbf{u}(t)$ is the vector function determining the displacement of the atom **r** from the site $\mathbf{r}_0(x, y, z)$ of the basic lattice: $\mathbf{r} = \mathbf{r}_0 + \mathbf{u}$; $\mathbf{u} = \mathbf{u}(t) = (u_x(t), u_y(t), u_z(t))$. The periodic shifts of the atomic coordinates are given by the sums of the sinusoidal functions $\mathbf{u}(t) = \Sigma A_i \sin[2\pi(\mathbf{q}_i\mathbf{r} + \varphi_{0i} + t)]$, where *i* is the number of the harmonic, φ_{0i} is the initial phase, $0 \le t \le 1$ is the shift phase, and condition (1) reduces to the requirement that $A_i = 0$ for all the atoms. Hence, assuming the three-dimensionally modulated cubic structure for lazurite, we came to the conclusion that no modulations are possible at all. Hence, it should be admitted that the true symmetry of this lazurite is lower than cubic, and the symmetry of the diffraction pattern is explained by twinning by the elements of cubic symmetry. The hypothesis that it is twinning that is responsible for the appearance of satellites along the [110] direction in cubic hauyne was also put forward in [12], where the domain twinning with an orthorhombic superstructure was discussed. In the structure considered in the present study, there are no obvious reasons for the rotation by 45° and the transformation into the orthorhombic superstructure, because none of the main reflections violates the symmetry of the sodalite cubic lattice. The preliminarily taken X-ray diffraction patterns recorded on photographic films showed weak

$\{h + 1/2, k + 1/2, l\}$ reflections. Subsequent measurements on a diffractometer showed that these are satellite reflections $\{h + 0.430, k + 0.430, l\} = \{hkl220\}$ surrounding the vacant centers of the faces of the reciprocal cubic lattice.

At the next stage of the study, we selected a twin model within the cubic unit cell. First, we tested a model consisting of trigonal three-dimensionally modulated components along the symmetrically equivalent [110] directions, which were twinned by twofold axes. However, the refinement of the average structure gave unsatisfactory results. Since the model of twinning by fourfold axes was hardly probable because of a large number (up to 64) of possible twin components and their combinations, we selected the simplest twin model consisting of three orthorhombic components related by the threefold axis along the [111] direction, which allowed us to pass to a modulated structure.

We assumed that each orthorhombic component of a twin is characterized by a two-dimensional modulation along two mutually perpendicular [110] and $[1\bar{1}0]$ directions in the *xy* plane with the wavevectors $\mathbf{q}_1 = \gamma\mathbf{a}^* + \gamma\mathbf{b}^*$ and $\mathbf{q}_2 = \gamma\mathbf{a}^* - \gamma\mathbf{b}^*$, respectively. In the basis of five coordinate vectors $\mathbf{a}^*$, $\mathbf{b}^*$, $\mathbf{c}^*$, $\mathbf{q}_1$, and $\mathbf{q}_2$, the satellites located on the face diagonals of the reciprocal cubic lattice were given five-digit *hklm*0 and *hkl*0*m* indices (each reflection was indexed in the coordinate system of its own twin component). A complex X-ray diffraction pattern containing numerous satellites also has reflections from different-type domains. However, we used in our calculations only the main reflections and the most representative group of the first-order satellites with the index $m = \pm 1$ located along the diagonals, because, judging from the intensities of the latter reflections, the domains responsible for the appearance of these satellites comprise the greatest portion of the specimen. The transition to the three-dimensionally modulated orthorhombic structure (by adding the basis vector $\mathbf{q}_3 = 2\gamma\mathbf{c}^*$ and performing indexing based on a unified data set of all the satellites observed) with the invocation of the $\{hkl200\}$ satellites from Table 1 gave worse results discussed below. The probable explanation is that satellites along the $\mathbf{q}_3$ direction can be generated by both an independent modulation along this direction and by the superposition of modulation waves from another twin component, which results in an uncertainty in selection of the parameters of the third harmonic.

Analysis of the systematic extinctions made it possible to distinguish the symmetry groups *P*222 (no extinctions at all) and *Pnn*2 (0*kl*: $k + l \neq 2N$; *h*0*l*: $l + h \neq 2N$; *hk*0: no extinctions; *h*00: $h \neq 2N$; 0*k*0: $k \neq 2N$; 00*l*: $l \neq 2N$). The absence of extinctions in one of the reflection sets with two non-zero indices in the sp. gr. *Pnn*2 results in the absence of extinctions for all such sets in the pattern from the twin. Of all the reflections with one non-zero index, only the 003 reflection (weak as compared to the even axial reflections) and a few other weak satellites violate the symmetry *Pnn*2. For the lazurite structure, the main difference between the sp. grs. *P*222 and *Pnn*2 reduces to the fact that the sulfur positions at the vertices and centers of cubes in the sp. gr. *Pnn*2 are equivalent and have a degree of freedom along the *z* axis, whereas these positions in the sp. gr. *P*222 are nonequivalent and are fixed along the *z* axis. In addition, the sp. gr. *Pnn*2 is more consistent with the wavevectors in one "special face" (perpendicular to the twofold axis) and their absence in two other faces.

Correspondingly, we chose the group $Pnn2(\gamma\gamma0, \gamma\text{–}\gamma0)$ of the (3 + 2)-dimensional symmetry in the (3 + 2)-dimensional space. The modulation shifts of the structure parameters were set by the sum of two harmonics with the wavevectors $\mathbf{q}_1$ and $\mathbf{q}_2$, whose amplitudes and phases were refined by the least-squares method simultaneously with the parameters of the basic structure using the JANA program [13]. Taking into account the cubic symmetry of the X-ray diffraction pattern, the volumes of the twin components were fixed as equal, and the structural computations were performed based on the reflections averaged within the X-ray diffraction class *m*3. Since the main reflections contain the contributions from all the domains, different scale factors (S_0 and S_1) were used for the main and satellite reflections. The refined scale factors were related as $S_0/S_1 = 1.254$.

The modulated structure was solved with the isotropic thermal parameters because of the correlations between the anisotropic thermal parameters and modulation parameters. The final *R* factors were $wR_0 = 1.98\%$ and $wR_1 = 7.50\%$ for 257 main reflections and 2392 satellites, respectively, rejected based on the condition $|F_{calc} - F_{obs}| < 50\sigma(F_{obs})$. The refined parameters of the basic structure are given in Table 2. At the final stage of the refinement, all the attempts to complicate the model by supplementing the set of twin elements with other threefold axes failed.

RESULTS AND DISCUSSION

One of the six-membered rings forming the structure framework is shown in Fig. 1. The modulations of the atomic coordinates of the framework are presented in Figs. 2a–2c as functions of the phase *t* of the first harmonic with the wavevector $\mathbf{q}_1$, whereas the second harmonic with the wavevector $\mathbf{q}_2$ had the phase fixed at $u = 0$. The shifts of the atomic coordinates (Å) from the positions in the basic-lattice nodes were the values of the aforementioned functions. Using the *z* coordinate, we modulated in phase all the symmetrically independent framework atoms with equal amplitudes, except for the O(1) and O(4) atoms. The modulations with respect to the *x* and *y* coordinates are out of phase and have weaker amplitudes. However, the *x* coordinate of the pair of the O(3) and O(6) atoms and the *y* coordinate of the pair of the O(2) and O(5) atoms are modulated in phase to a much greater extent than the remaining atoms. In addition, the O(6), O(5), and O(1) atoms are

Table 2. Occupancies (*P*), coordinates ($\times 10^4$), and isotropic thermal parameters of the atoms ($\times 10^4$) in the basic structure of lazurite described by the sp. gr. *Pnn*2($\gamma\gamma$0, γ–γ0)

Atom	Position	*P*	*x*	*y*	*z*	U_{iso}
T(1)	2	0.5/0.5	0	5000	2500*	246(11)
T(2)	2	0.5/0.5	5000	0	2518(4)	259(11)
T(3)	4	0.5/0.5	2514(2)	4993(5)	–9(6)	270(6)
T(4)	4	0.5/0.5	4993(4)	2512(2)	6(6)	231(6)
O(1)	4	1	3475(9)	3569(8)	–245(14)	382(28)
O(2)	4	1	3482(11)	–115(16)	3569(10)	635(30)
O(3)	4	1	–106(10)	3485(8)	3460(8)	263(20)
O(4)	4	1	1479(8)	1456(8)	5016(16)	399(26)
O(5)	4	1	1469(7)	5176(9)	1513(7)	161(16)
O(6)	4	1	5097(8)	1411(9)	1421(9)	228(20)
Na(1)	4	0.35	1922(17)	2111(15)	2014(17)	205(37)
Na(2)	4	0.33	2564(13)	2569(13)	2565(16)	38(25)
Na(3)	4	0.37	3132(11)	3234(11)	3239(13)	113(19)
Na(4)	4	0.30	6823(17)	7079(17)	7177(20)	190(45)
(Na, Ca)(5)	4	0.236/0.154	7483(15)	7359(15)	7293(19)	97(24)
Ca	4	0.23	7810(14)	7882(13)	7985(12)	10*
S(1)	2	0.42	0	0	308(10)	292(27)
O(7)	4	0.42	1220(32)	1269(20)	1498(19)	10*
O(8)	4	0.42	4632(48)	3784(39)	6318(22)	10*
S(2)	2	0.157	0	0	2979(32)	10*
S(3)	2	0.153	0	0	6565(64)	10*
S(4)	4	0.110	2453(52)	15(40)	589(41)	10*
S(5)	4	0.121	485(31)	2387(34)	–279(33)	10*

* The parameter was not refined.

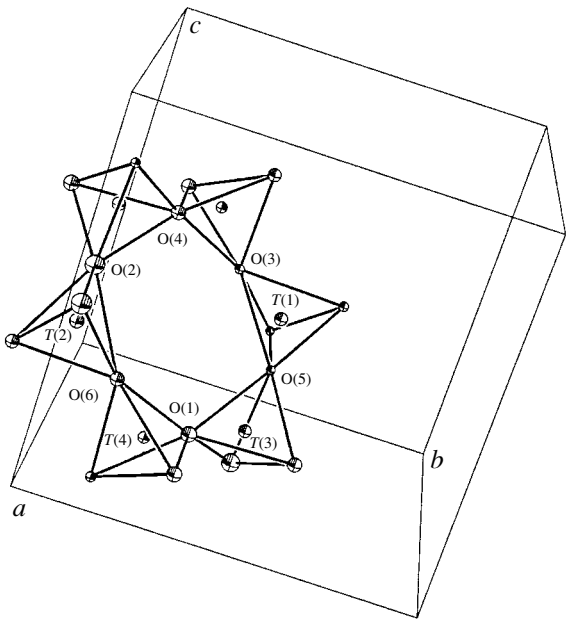

Fig. 1. Six-membered tetrahedral ring, a fragment of the lazurite framework.

modulated in phase as regards the *x*, *y*, and *z* coordinates, respectively. The same is true for the O(3), O(2), and O(4) triad, with the difference in phases between the two triads being small. Taking into account that each oxygen atom occupies a vertex shared by two adjacent (Al,Si)O_4 tetrahedra, the modulation of the framework consists primarily in mutual rotations of the tetrahedra resulting in the change of the configuration of the intraframework cavity bounded by the O(1)–O(6) six-membered ring. Hence, plots of modulations of the *T*–O distances show that the orientation of the tetrahedra (and not their sizes) is modulated, i.e., the distribution of Al and Si over the *T* tetrahedra remains disordered.

One of the two independent Na (Ca) cations occupies the center of the six-membered ring composed by the tetrahedra (Fig. 1), whereas the other cation is located in the center of the adjacent ring at an average distance $0.5a_{cub}\sqrt{3}$ from the first cation on the same [111] diagonal. Each position of large cations in the average structure is split into three subpositions, which are present in the modulated structure as well. The

Na(1), Na(2), and Na(3) subpositions correspond to the first type of cations. The Na(4), (Na,Ca)(5), and Ca subpositions are occupied by cations of the second type. The refined total occupancy of the Na(1)–Na(3) subpositions is slightly higher than unity, apparently due to the fact that calcium atoms replace sodium atoms in small amounts. Almost all the calcium cations are located in the mixed (N,Ca)(5) position and the calcium position on the other half of the body diagonal. As can be seen from Fig. 2d, the modulations of the *z* coordinates of the cations correlate rather well in phase with each other. The modulations of the *z* coordinates of the cations in the Na(1)–Na(3) positions correlate in phase not only with each other but also with the modulations of the *z* coordinates of the atoms of the nearest six-membered ring. As can be seen from Table 3, the basic (unmodulated) Na(Ca)–O distances in two adjacent six-membered rings on the [111] diagonal are substantially different. In the rings, whose centers are occupied by only sodium cations, the average distance is approximately by 0.3 Å longer than that in the rings involving calcium cations.

Therefore, well-matched and strong modulations of the framework atoms of isotropic lazurite are observed along the direction normal to the propagation plane of modulation waves. The same characteristic feature was observed earlier in triclinic and orthorhombic lazurites [1, 2].

The choice of the modulation parameters (and, sometimes, average parameters) for sulfur atoms and sulfate-containing groups presents a serious problem. The most pronounced difference between the results of our study and the data obtained earlier is that we established new structural positions of sulfur atoms of sulfide. It is known that chemical analyses of lazurites calculated with respect to the typical formula of sodalite minerals gave an excess of anions, with the sulfur sulfide atoms being redundant in terms of electrostatic balance. There is no consensus of opinion among researchers about the positions occupied by sulfur atoms of sulfide in the structures of minerals. Some researchers believe that these sulfur atoms partially replace oxygen atoms of the framework, whereas some other researchers assume that these atoms are either located in sodalite cavities as polysulfide anions or are completely

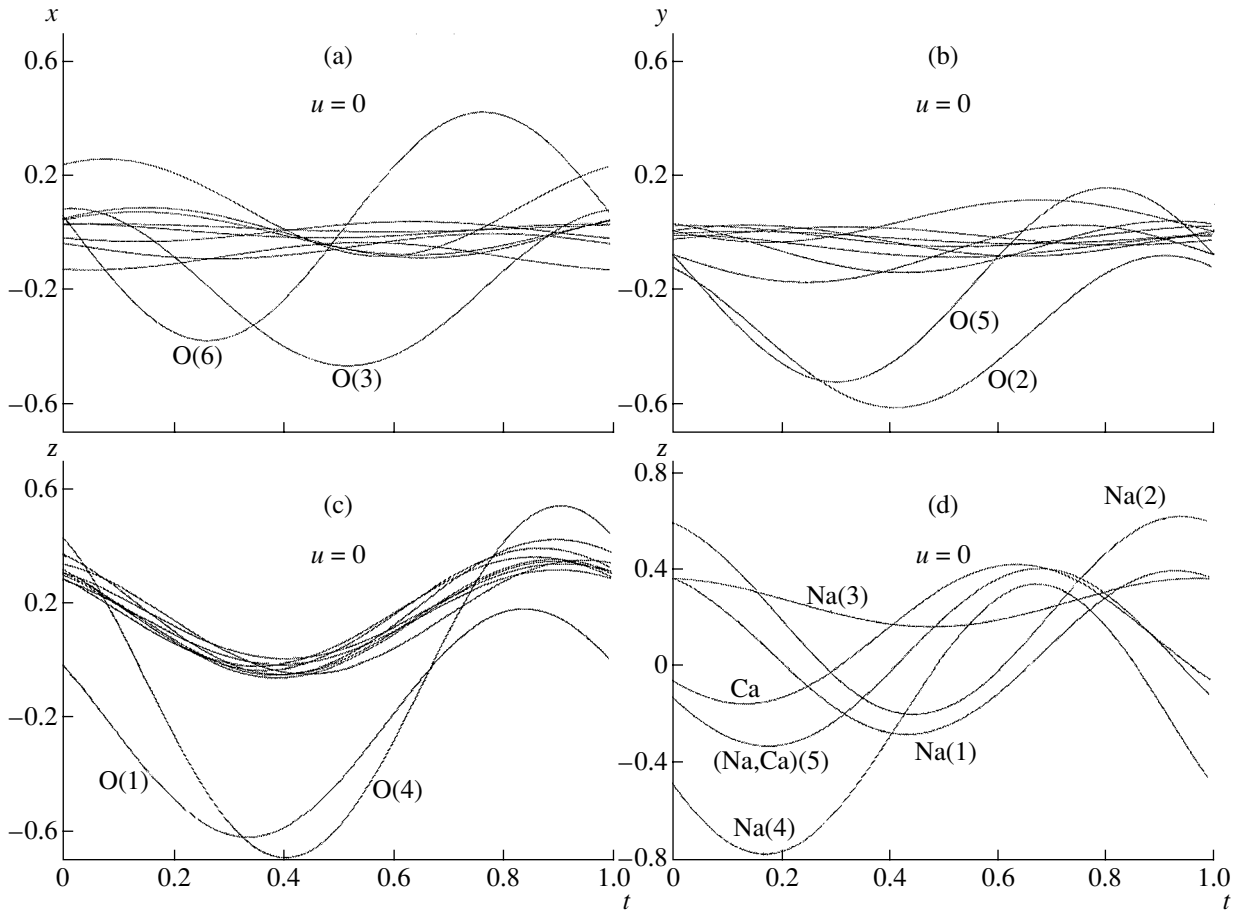

Fig. 2. (a–c) Modulation shifts (Å) of the *x, y, z* atomic coordinates of the Al,Si–O framework versus the phase *t* of the wave with the vector $\mathbf{q}_1$. (d) Modulation shifts of the *z* coordinates of the independent Na, Ca cations with the vector $\mathbf{q}_2$ in the phase $u = 0$.

Table 3. Basic interatomic distances

(Al,Si) tetrahedra			
T(1)–O(3)	1.631(7) × 2	*T*(2)–O(2)	1.679(10) × 2
O(5)	1.614(7) × 2	O(6)	1.624(8) × 2
	⟨1.623⟩		⟨1.651⟩
T(3)–O(1)	1.574(9)	*T*(4)–O(1)	1.695(9)
O(2)	1.579(11)	O(3)	1.672(9)
O(4)	1.612(8)	O(4)	1.642(8)
O(5)	1.684(8)	O(6)	1.631(9)
	⟨1.612⟩		⟨1.660⟩

(Na,Ca) polyhedra					
Na(1)–O(1)	2.82(2)	Na(2)–O(1)	2.83(2)	Na(3)–O(1)	3.19(2)
O(2)	2.84(2)	O(2)	2.73(2)	O(2)	3.07(2)
O(3)	2.58(2)	O(3)	2.69(2)	O(3)	2.95(1)
O(4)	2.82(2)	O(4)	2.63(2)	O(4)	2.73(2)
O(5)	2.85(2)	O(5)	2.74(2)	O(5)	2.80(1)
O(6)	3.00(2)	O(6)	2.73(2)	O(6)	2.94(1)
O(8)	2.32(4)	O(7)	1.96(3)	O(8)	3.15(3)
S(2)	2.74(2)	O(8)	3.14(4)	S(3)	2.78(3)
S(4)	2.35(4)	S(4)	2.93(4)	S(4)	2.73(4)
S(5)	2.47(3)			S(5)	2.59(3)
Na(4)–O(1)	2.43(2)	(Na,Ca)(5)–O(1)	2.54(2)	Ca–O(1)	2.38(2)
O(2)	2.65(2)	O(2)	2.51(2)	O(2)	2.64(2)
O(3)	2.33(2)	O(3)	2.61(2)	O(3)	2.55(1)
O(4)	2.83(2)	O(4)	2.51(2)	O(4)	2.84(2)
O(5)	2.58(2)	O(5)	2.52(2)	O(5)	2.53(1)
O(6)	2.94(2)	O(6)	2.49(2)	O(6)	2.72(1)
O(7)	2.92(3)	O(8)	2.36(4)	O(8)	3.08(4)
O(7)	3.15(2)	S(2)	3.17(1)	S(2)	3.05(3)
S(2)	2.61(2)	S(4)	2.65(4)	S(4)	3.05(4)
S(4)	2.45(4)	S(5)	2.88(3)	S(5)	2.22(3)
S(5)	3.07(3)				

absent. Hassan in his studies of cubic lazurites from Afghanistan and Baffin Island (see, for example, [3]) never mentioned the sulfur positions on the unit-cell edges and discussed the positions of sulfur atoms of sulfate and sulfide only at the vertices and center of the cube. However, the S(2)–S(5) positions on the edges in the lazurite specimen from the Baikal region are quite distinct. On the contrary, the oxygen atoms located on the [111] diagonals, which along with the S(1) atoms should form the SO_4^{2-} sulfate groups, are poorly localized in the modulated structure, although S(1) atoms are readily localized. As a result, the occupancies of the O(7) and O(8) positions were not refined—they were specified based on the refined occupancy of the S(1) position. The positions of the oxygen atoms surrounding the sulfur atom differ from those in the average structure [7].

Microprobe chemical analysis revealed a substantially higher oxygen content than was established for the O(7) and O(8) positions. Thus, according to the results of chemical analysis, the mineral contains 1.73 SO_4^{2-} groups (with respect to the formula unit) instead of 0.84 SO_4^{2-} groups determined by X-ray diffraction analysis. It can be assumed that the S(2)–S(5) positions are partially occupied by oxygen atoms of the sulfate groups. The refined total occupancy of the S(2)–S(5) positions on the edges is 1.54 atoms per unit cell rather than the value 0.9 determined for analogous positions in [7].

CONCLUSIONS

Lazurites are minerals with variable composition and defect structures. They are characterized by a diversity of incommensurate and commensurate structure modulations. Commensurately modulated structures can be described in terms of a classical crystal, whereas incommensurately modulated structures are aperiodic. The nature of modulations in cubic lazurite is still poorly understood. Hassan believed that these modulations are associated with the difference in the size of the $[Na_3CaSO_4]^{3+}$ and $[Na_3CaS]^{3+}$ clusters. However, this brings up the question of why the modulations in different domains of the sample occur along different directions but have the same incommensurability parameter γ with respect to a_{cub}. It is reasonable to assume that the modulation period is determined by the framework the same in all domains, whereas the gradient of modulation displacements, i.e., the wave direction, in different domains is determined by the character of ordering of the framework ions in the corresponding fragment of the sample. With due regard for the results of the geochemical studies, our data confirm the assumption that modulations of the lazurite structure result primarily from the simultaneous presence in the structure of different sulfate and sulfide complexes in different ratios. Sulfur atoms serving as centers of formation of intraframework clusters are very sensitive to the variations in the external conditions. The variations of the oxidation state of sulfur and the related transformations, rearrangements, and ordering of clusters upon recrystallization of lazurite give rise to the changes in the satellite components of X-ray diffraction patterns from different parts of the mineral.

ACKNOWLEDGMENTS

We are grateful to Prof. V.I. Simonov for continuous interest in our work and valuable advice.

This study was supported by the Russian Foundation for Basic Research (project nos. 01-05-64604, 00-02-16636, and 02-05-64080) and the Russian Federation Government Program for Support of Leading Scientific Schools (project no. 00-15-96633).

REFERENCES

1. V. G. Evsyunin, R. K. Rastsvetaeva, A. N. Sapozhnikov, and A. A. Kashaev, Kristallografiya **43** (6), 1057 (1998) [Crystallogr. Rep. **43**, 999 (1998)].
2. V. G. Evsyunin, A. N. Sapozhnikov, A. A. Kashaev, and R. K. Rastsvetaeva, Kristallografiya **42** (6), 1014 (1997) [Crystallogr. Rep. **42**, 938 (1997)].
3. I. Hassan, Am. Mineral. **85**, 1383 (2000).
4. Luo Gu-Feng, Zhao Ming, Ge Xiao-Yue, and Zhang Fu-Sheng, Gaoxiao Dizhi Xuebao (China), No. 6 (2), 132 (2000).
5. Ge Xiaoyue, Luo Gufeng, Zhao Ming, *et al.*, Kuangwu Xuebao (China), No. 19 (4), 385 (1999).
6. A. N. Sapozhnikov, V. L. Tauson, and L. N. Matveeva, Zap. Vses. Mineral. O–va, No. 130 (2), 121 (2001).
7. R. K. Rastsvetaeva, N. B. Bolotina, A. N. Sapozhnikov, *et al.*, Kristallografiya **47** (3), 449 (2002) [Crystallogr. Rep. **47**, 404 (2002)].
8. N. B. Bolotina, R. K. Rastsvetaeva, A. N. Sapozhnikov, *et al.*, Kristallografiya **48** (1), 14 (2003) [Crystallogr. Rep. **48**, 8 (2003)].
9. *CrysAlis Software System. Version 1.164 and 1.166* (Oxford Diffraction, Oxford, England, 2001).
10. A. Schönleber, M. Meyer, and G. Chapuis, J. Appl. Crystallogr. **34**, 777 (2001).
11. V. Petricek and P. Coppens, Acta Crystallogr., Sect. A: Found. Crystallogr. **44**, 235 (1988).
12. H. Xu and D. R. Veblen, Am. Mineral., No. 80, 87 (1995).
13. V. Petricek and M. Dusek, *JANA2000. Structure Determination Software Programs* (Inst. of Physics, Praha, 2000).

Translated by T. Safonova

Crystallography Reports, Vol. 48, No. 5, 2003, pp. 728–743. Translated from Kristallografiya, Vol. 48, No. 5, 2003, pp. 786–801.

DIFFRACTION AND SCATTERING OF IONIZING RADIATION

Dedicated to the 60th Anniversary of the Shubnikov Institute of Crystallography of the Russian Academy of Sciences

Structural Characterization of Quantum-Well Layers by Double-Crystal X-ray Diffractometry

A. M. Afanas'ev* and R. M. Imamov**

** Institute of Physics and Technology, Russian Academy of Sciences, Nakhimovskiĭ pr. 36, Moscow, 119218 Russia*

*** Shubnikov Institute of Crystallography, Russian Academy of Sciences, Leninskiĭ pr. 59, Moscow, 119333 Russia*

e-mail: Imamov@ns.crys.ras.ru

Received April 1, 2003

Abstract—It is demonstrated that double-crystal X-ray diffractometry, which has been known for more than 50 years, is a powerful tool for the characterization of modern materials used in microelectronics and nanoelectronics that makes it possible to thoroughly investigate very thin layers and interfaces of nanometer sizes in complex heterostructures. The physical and mathematical principles of this method are analyzed, and the most prominent examples of its application are given. It is established that, in a number of cases, quantum-layer displacements as small as several hundredths of a nanometer can be reliably determined in heterostructures.

1. INTRODUCTION

Low-dimensional semiconductor quantum-well structures have attracted the particular attention of researchers. This can be explained by the interesting and important physical phenomena associated with two-dimensional confinement of an electron gas in deep and narrow quantum wells. Moreover, commercial interest in these objects has also stimulated extensive investigations into the properties of quantum-well structures. At present, much progress has been achieved in the technology of growing heterostructures with ultrathin layers (quantum wells, quantum wires, and quantum dots). However, in order to gain a more detailed knowledge of the physics of such systems and their technical applications, it is necessary to thoroughly investigate the structure and different characteristics of materials with a high resolution up to individual monolayers [1–3]. Information on the structure of these systems and the degree of perfection of individual layers and interfaces has been obtained by different methods, such as photoluminescence and high-resolution electron and scanning probe microscopies. Although X-ray diffraction methods are also widely used for these purposes [4–18], their capabilities and implications in solving the above problems have not been conclusively established. In our opinion, the potentialities of X-ray diffraction methods for the structural characterization of extremely thin layers are very high. The aim of the present work is to demonstrate these potentialities on the basis of the investigations performed at the Shubnikov Institute of Crystallography, Russian Academy of Sciences.

2. PHYSICAL PRINCIPLES OF THE X-RAY DIFFRACTION METHOD

X-ray diffraction scattering by crystals is associated with the interference of beams reflected from different planes of a crystal lattice. The amplitudes of waves reflected from different planes add up at specific angles of incidence $\theta = \theta_B$, whereas the total suppression of scattered beams—destructive interference—occurs at other angles θ. The angle θ_B corresponding to strong diffraction reflection can be found from simple geometric considerations and is determined by the Bragg–Wulf formula

$$2d_{hkl}\sin\theta_B = n\lambda, \quad (1)$$

where d_{hkl} is the interplanar distance, λ is the wavelength of incident radiation, and n is the order of reflection. This formula relating the directions of propagation of scattered beams to interplanar distances in the crystal lattice underlies X-ray structure analysis and plays an extremely important role in many fields of science and engineering, such as physical materials science, and in the study of inorganic and organic materials, biological structures, etc.

1063-7745/03/4805-0728$24.00 © 2003 MAIK "Nauka/Interperiodica"

Theoretical investigations carried out in the early 20th century [19] gave a deep insight into the physics of X-ray diffraction. The dynamic theory of X-ray diffraction was developed, which made it possible to predict a number of new physical effects. (i) A strong diffraction scattering with a reflection coefficient close to unity is observed not only when condition (1) is rigorously satisfied but also in a certain finite angle range $|\theta - \theta_B| \le \theta$, where θ_0 is the so-called half-width of the Darwin table (Fig. 1). (ii) Outside the Darwin table, the reflection coefficient $P_R(\theta)$ also does not become zero and, at $|\theta - \theta_B| \gg \theta_0$, decreases according to the law

$$P_R(\theta) \approx \frac{4\theta_0^2}{(\theta - \theta_B)^2}. \quad (2)$$

Subsequently, the former effect was theoretically examined in detail and was carefully verified in experiments, whereas, until very recently, little attention was given to the occurrence of extended wings. However, as will be shown below, the understanding of the physical factors responsible for their formation offers strong possibilities of analyzing multilayer structures.

The physical origin of extended wings in a rocking curve (Fig. 2) is the occurrence of an abrupt crystal–vacuum interface. As was demonstrated in [4–6], this interface can be eliminated by gradually modifying the crystal structure in a thin surface layer. In this case, the diffraction reflection intensity can be considerably reduced on the wings of the rocking curve and remain virtually unchanged in the central part of the curve in the range of the Darwin table. On the other hand, in [4–6], it was shown that this phenomenon can be efficiently used for examining the structural perfection of ultrathin surface layers. Figure 2a depicts the diffraction reflection curves over a relatively wide range of angles θ up to approximately 600″ for germanium disks subjected to different surface treatments. It can be seen from Fig. 2a that, for a germanium crystal after deep polishing chemical etching, the reflection coefficient is well approximated by relationship (2) and the reduced intensity

$$I(\theta) = (\theta - \theta_B)^2 P_R(\theta) \quad (3)$$

is described by a linear dependence.

For a crystal with a usual superfinish polishing, the reduced intensity $I(\theta)$ strongly decreases away from the Darwin table. The inclusion of a defect surface layer only 10 nm thick makes it possible to describe the experimental curve to sufficient accuracy. Subsequently, similar measurements were performed over a wider angle range up to 6000″ [6]. The experimental results are presented in Fig. 2b. These results uniquely indicate that the surface of a crystal subjected to deep polishing chemical etching also involves a defect layer but with a substantially smaller thickness (less than 1 nm).

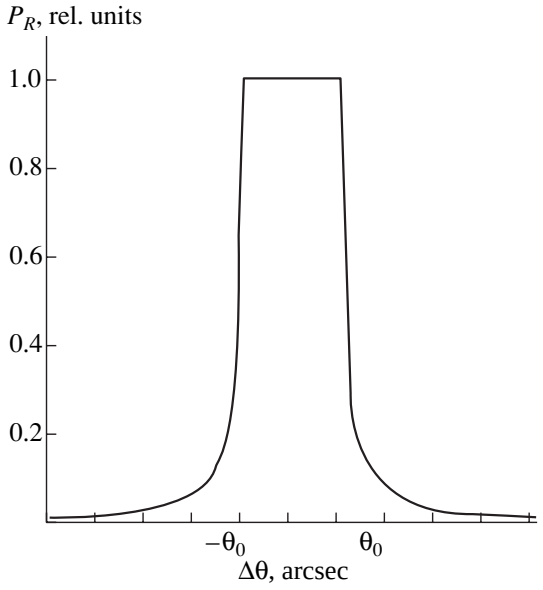

Fig. 1. Diffraction reflection curve with a Darwin table.

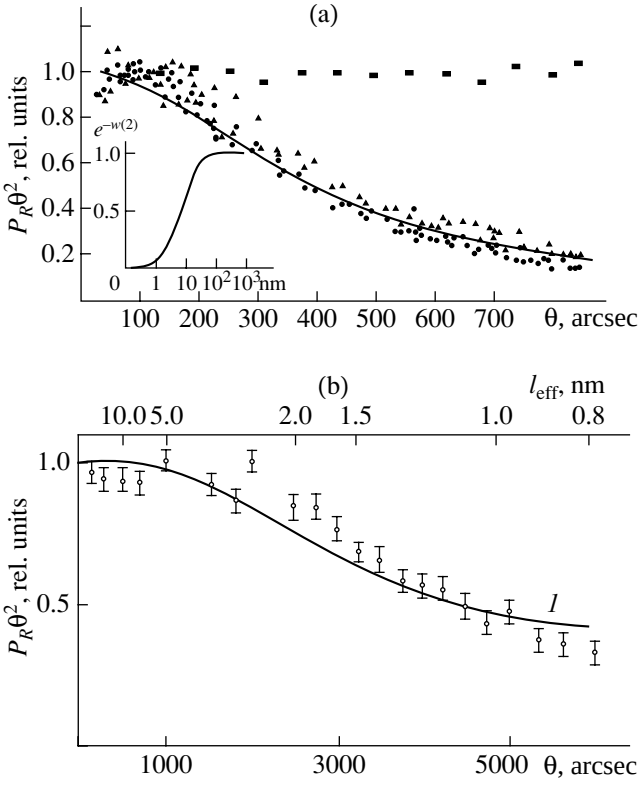

Fig. 2. Dependences of $\theta^2 \times P_R(\theta)$ on θ for (a) perfect (rectangles) and defect (circles and triangles) Ge crystals and (b) defect Ge crystal over a wider range of rotation angles of crystals. The solid line represents the theoretical curve for the Debye–Waller factor, which is shown in the inset in panel (a). The upper scale in panel (b) refers to the depth of the analyzed layer.

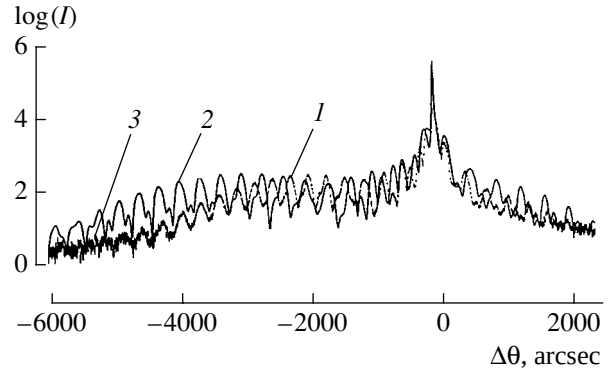

Fig. 3. (*1*) Experimental and (*2*, *3*) theoretical diffraction reflection curves for a GaAs–$In_xGa_{1-x}As$ multilayer system. The theoretical curves are calculated for (*2*) the independent variation in all layer parameters in the system and (*3*) the model with diffuse interfaces.

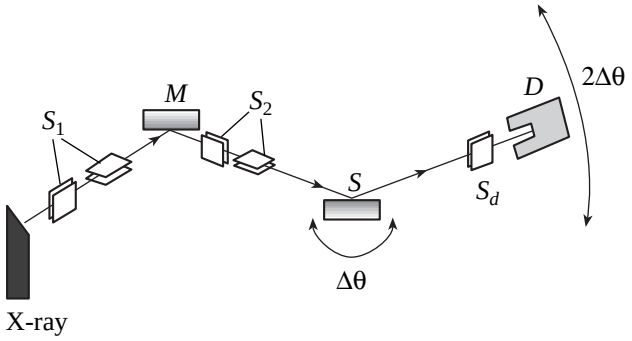

Fig. 4. Schematic drawing of the double-beam X-ray diffractometer. Designations: *M* is the monochromator unit, *D* is the detector, *S* is the sample, S_1 and S_2 represent a system of slits of the monochromator unit, and S_d is the slit ahead of the detector.

These results allowed us to propose a qualitatively new experimental method—the so-called asymptotic Bragg diffraction technique, which is based on measurements of the rocking curve not in the central part but away from the Darwin table up to angles that are thousands of times larger than the width of this table. More recently, this technique was applied to investigate the surface structure of InSb and permitted us to reliably reveal the existence of three defect layers [13].

It is reasonable to assume that, in heterosystems, boundaries located in the bulk of a crystal should also manifest themselves in the diffraction reflection curves. According to the experimental data [20–25], diffraction reflection curves for multilayer systems in a large number of cases have a pronounced interference structure.

Similar diffraction reflection curves have been usually interpreted in the framework of the interference of X-ray beams scattered from layers, and the interference itself is treated as a fact that indicates a high quality of a grown structure. However, a more consistent theoretical analysis demonstrates that the formation of the interference structure as a whole and, especially, on the wings of diffraction reflection curves at $|\Delta\theta| \gg \theta_0$ is primarily determined by the characteristics of interfaces. Figure 3 shows the experimental curve (curve *1*) and the theoretical curves. Curve *2* corresponds to a model with absolutely abrupt interfaces. It can be seen from Fig. 3 that this model does not describe the experimental curve. The introduction of diffuse interfaces leads to the excellent agreement between the theoretical (curve *3*) and experimental data and, hence, enables us to obtain a large amount of information on the structure of interfaces and parameters of quantum-well layers (see Section 5). At present, the existing possibilities of investigating heterostructures with ultrathin layers of subnanometer sizes surpass all expectations. As will be seen from the examples given in Section 5, this technique makes it possible to reliably determine individual-layer displacements as small as several hundredths of a nanometer.

3. EXPERIMENTAL SETUP AND TECHNIQUE

A double-crystal X-ray diffractometer is schematically depicted in Fig. 4. X rays from a source are preliminarily collimated with a system of slits S_1 and are incident on a crystal monochromator. After reflection, a beam of X rays with wavelengths within the width of a characteristic line is separated. The beam thus formed passes through a system of slits S_2 and is incident on crystal *S* under investigation. The intensity of reflected radiation $I_h(\Delta\theta)$ is measured using detector *D* as a function of the rotation angle $\Delta\theta$ of the crystal with respect to the incident beam.

The experimental scheme shown in Fig. 4 differs little from the corresponding schemes used in the 1950s, even though the purposes of the experiments differ radically. Investigations of multilayer structures require the performance of measurements over a wide angle range that exceeds the width of the initial Bragg peak by many orders of magnitude. The wider the range of measured angles $\Delta\theta$, the larger the amount of information that can be obtained from analysis of the measured curves. At large rotation angles, the reflection intensity sharply decreases (by a factor of 10^6–10^7) and becomes comparable to the intensity of different scatterings of nondiffraction origin, for example, thermal diffuse scattering. In this respect, an important problem is the suppression of the diffuse background. In principle, this problem can easily be solved using a triple-crystal X-ray diffractometer. In this case, the third analyzing crystal is placed between the studied crystal and the detector. The analyzing crystal makes it possible to separate the diffraction and diffuse components with a high accuracy. In [4–6, 13], thin surface layers were investigated on a triple-crystal X-ray diffractometer. Since reflection curves for multilayer heterostructures have a

complex interference structure, the number of points measured at different angles $\Delta\theta$ should be several orders of magnitude larger than that necessary in analysis of surface layers. On the other hand, the measuring time for the diffraction reflection curve on the triple X-ray diffractometer is considerably longer than that on the double-crystal diffractometer. This circumstance renders triple-crystal diffractometry unsuitable for wide application.

In the double-crystal scheme, the diffuse background is suppressed using the system of slits S_1 and S_2 and also slit S_d ahead of the detector. Slits S_1 and S_2 and the crystal monochromator form the beam (incident on the studied crystal) with narrow distributions over the angles θ and wavelengths. Since X rays undergo diffraction from the crystal monochromator, the angular width $\delta\theta$ and the width $\delta\lambda$ of the distribution over wavelengths according to the Bragg–Wulf law are related by the expression

$$\delta\theta = \frac{\delta\lambda}{\lambda}\tan\theta_B. \quad (4)$$

With the aim of providing a high luminosity of the instrument, first and foremost, it is necessary to collect all X rays with wavelengths within the width of the characteristic line. On the other hand, in order to suppress background radiation, it is desirable to obtain a narrow angular distribution, which is achieved by the choice of slit widths and linear sizes of the setup. The simultaneous fulfillment of these conditions with due regard for expression (4) qualitatively changes the preliminary adjustment of the diffractometer. Unlike the standard scheme, additional slit S_d is placed ahead of the detector. This slit plays an important role and primarily prevents the incidence of the diffusion component (reflected from the studied crystal) on the detector. Note that, in addition to the rotation of the crystal sample through the angle θ, it is necessary to ensure the simultaneous rotation of the detector and slit S_d through the angle 2θ, so that diffractionally scattered X rays can arrive at the detector. The optimization of the experimental geometry makes it possible to increase considerably the coherent signal-to-diffuse background ratio and, hence, to extend the dynamic range of the measured diffraction reflection intensity by seven orders of magnitude.

The diffraction reflection curves were measured according to the double-crystal scheme (Fig. 4) with the use of a copper-anode sharp-focused X-ray tube as a source of the Cu$K_{\alpha1}$ characteristic X-ray radiation ($\delta\lambda/\lambda \sim 10^{-4}$). The projection of the size of a spot on the anode onto the direction of the X-ray beam was approximately equal to 0.2 mm. The tube power did not exceed 1.5 kW. The intensity of the X-ray beam after passing the collimating system of slits S_1 and S_2 (0.4×4 mm^2) and the monochromator was approximately equal to 75 000 pulses/s. A plane crystal with a single reflection and a slit monochromator with a triple reflection served as the crystal monochromator. The aperture angle for X rays incident on the sample was approximately equal to 1°. Owing to the additional slit S_d, X rays with an angular divergence of less than 0.1° arrived at the sample.

The sample was automatically scanned in the vicinity of the exact Bragg angle over a range of ~2° at twice the rotation rate of the detector (the so-called $\omega/2\theta$ scan mode). The measurements were carried out with a step of 10″ along the axis of rotation of the sample. Prior to the measurement of the diffraction reflection curve, angular calibration of the spectrometer was performed against Ge and Si reference single crystals. The scanning data in the range 5″–20″ were compared with the widths of natural reflection curves. The range 100″–600″ was controlled using the doublet splitting of the $K_{\alpha1}$ and $K_{\alpha2}$ lines at different reflection orders. Rotations angles of 1°–2° were checked from the separation of the K_α and K_β lines. The error in angular displacements was no more than 2% over the entire angle range. The reproducibility of measurements with respect to the scanning angle was no worse than 10″–15″ upon repeated scanning of any angle range in the course of the experiment. This error was associated with the inaccuracy in reproducing each angular displacement and the insufficient thermal stabilization of the spectrometer. The temperature in the room was maintained accurate to within ±1 K, which was insufficient for the angular stabilization of the X-ray beam reflected from the monochromator and led to an uncontrollable drift as large as 15″ over the course of a day.

Since the dynamic range of measured intensities and the angle range of scanning were wide, it was not possible to provide a constant statistic over the entire angle range. For this reason, the diffraction reflection curves were recorded in portions so that their ranges partially overlapped. The portions were matched reasoning from the best coincidence of interference maxima. The recording time was determined from the specified statistic. The measurements were carried out up to recording of 10 000 pulses or for no less than 2 s in the vicinity of the Bragg peak and up to recording of ~400 pulses or for no less than 20 s away from the peak. Note that, when measuring in the angle range ±200″, an absorber with $K = 4.5 \pm 0.5$ was placed ahead of the detector in order to avoid counting losses in the recording of signals.

4. MATHEMATICAL PRINCIPLES OF THE METHOD

Analysis of the diffraction reflection curve involves general standard stages, such as the choice of a model, the calculation of the spectra according to the chosen model, and the fitting of the experimental and theoretical spectra by using, for example, the χ^2 method [26–28]. At the same time, this analysis is characterized by a number of specific features. In particular, the

model can be refined without any limitations, the theoretical and experimental data can be ideally fitted at the parameter $\chi^2 \sim 1$, and a large amount of information on the structural parameters can be obtained from the experimental curves.

Let us assume that a multilayer system consists of a set of homogeneous layers. Each layer is characterized by the thickness l_j, the lattice parameter a_j, and the Debye–Waller static factor f_j determining the degree of amorphization of the layer, that is,

$$f_j = \exp(-w_j) = \exp(-\mathbf{K}_h^2\langle u_h^2\rangle_j). \quad (5)$$

Here, $\mathbf{K}_h$ is the reciprocal lattice vector and the parameter $\langle u_h^2\rangle_j$ describes root-mean-square random displacements of atoms from regular lattice sites. The parameters a_j and f_j are taken to be constant within each layer. At the first stage of analysis, the number of layers is chosen according to the technique of growing the multilayer system, it is assumed that each layer has abrupt interfaces, and the parameters of these layers are varied during the fitting. In the vast majority of cases, the initial model cannot adequately describe the diffraction reflection curves, because the interfaces between the layers cannot be ideally abrupt and are always diffuse to some extent. In order to describe the structure of interfaces, additional sublayers are introduced between the layers. Each sublayer is determined by the same set of the parameters *l*, *a*, and *f*. The number of these sublayers and, hence, the number of variable parameters gradually increase until a reasonable agreement between the experimental and theoretical data is achieved. The simplicity of the model and the possibility of refining it without limitations is one of the most important advantages of the method.

At rotation angles $|\Delta\theta| \gg \theta_0$, the reflection coefficient for the crystal is small and the amplitude of the diffraction reflection from the heterostructure can be written in the form

$$R(\Delta\theta) = \sum R_j(\Delta\theta) + R_0(\Delta\theta), \quad (6)$$

where $R_j(\Delta\theta)$ is the amplitude of scattering from the *j*th layer and $R_0(\Delta\theta)$ is the amplitude of scattering from the substrate. The scattering amplitude R_j can be calculated using the kinematic theory of X-ray scattering. According to this theory, the scattering amplitude R_j is defined by the relationship

$$R_j(\Delta\theta) = -\frac{i}{L_{ex}}\int_{L_j}^{L_{j+1}} \exp[-w(z)] \times \exp[iK_h z\gamma_0\Delta\theta - iK_h u(z) - \mu_0 z/\gamma_0]dz. \quad (7)$$

Here, L_{ex} is the so-called extinction length that determines the penetration depth of X rays into the crystal at the exact fulfillment of the Bragg condition; μ_0 is the linear absorption coefficient; L_j and L_{j+1} are the depths of the lower and upper interfaces of the *j*th layer, respectively; $\gamma_0 = \sin\theta_B$; and

$$u_j(z) = \int_{L_j}^{z}\Delta a(z')dz' + u(L_j) \quad (8)$$

is the total displacement of atomic planes in the layer at the depth *z* due to displacements of all lower lying layers of the structure $u(L_j)$ and also lower lying atomic layers in the *j*th layer.

The reflection coefficient $P_R(\Delta\theta)$ is determined from the scattering amplitude by the equation

$$P_R(\Delta\theta) = \frac{1}{\beta}|R(\Delta\theta)|^2. \quad (9)$$

In the case of the layer with constant parameters a_j and w_j, from formula (7), we easily find

$$R_j(\Delta\theta) = f_j\exp(-i\Phi_j(\alpha)) \times \frac{\exp[-ik(\alpha+\alpha_j)l_j - \mu_0 l_j/2\gamma_0] - 1}{L_{ex}(k(\alpha+\alpha_j) - i\mu_0/2\gamma_0)}. \quad (10)$$

Here, the complex phase can be represented in the form

$$\Phi_j(\alpha) = K_h u(L_j) + k\alpha L_j - i\mu_0 L_j/2\gamma_0; \quad (11)$$

$$k = 2\pi/\lambda, \quad \alpha = 2\sin(2\theta_B)\Delta\theta_B, \quad \alpha_j = 2\sin(2\theta_B)\Delta\theta_{B_j}, \quad (12)$$

and $\Delta\theta_{B_j}$ is the shift of the Bragg–Wulf angle as a result of a change in the interplanar distance in the layer, that is,

$$\Delta\theta_{B_j} = -\tan(\theta_B)\frac{\Delta a_j}{a}. \quad (13)$$

Under the assumption that the substrate thickness is considerably larger than the extinction length and at $|\Delta\theta| \gg \theta_0$, the amplitude $R_0(\Delta\theta)$ of the reflection from the substrate is given by the formula

$$R_n(\Delta\theta) = -f_n\frac{\exp(-i\Phi_n(\alpha))}{L_{ex}(k\alpha - i\mu_0/2\gamma_0)}, \quad (14)$$

where L_n is the depth of the lower layer of the substrate. Note that the parameters Δa_j are conveniently reckoned from the interplanar distance of the substrate. In this case, it is evident that $\Delta a_n = 0$ and $u(L_n) = 0$.

Formulas (6) and (9)–(13) can be directly applied to calculate the reflection curve almost over the entire range except for a narrow angle range $|\Delta\theta \sim \theta_0|$. In the central range, the calculation should be performed with equations of the dynamic theory of X-ray diffraction. In our case, these equations are conveniently used in the form of recurrent relationships [9, 20].

With allowance made for relationships (10) and (14), the reflection amplitude $R(\Delta\theta)$ can be represented

as the sum of the amplitudes for the interfaces between the layers, that is,

$$R(\Delta\theta) = \sum_{1}^{n} \tilde{R}_j(\Delta\theta), \quad (15)$$

where

$$\tilde{R}_j(\Delta\theta) = \exp[-i\Phi_j(\alpha)]\frac{1}{L_{ex}k}\left(\frac{f_j}{\alpha+\alpha_j} - \frac{f_{j+1}}{\alpha+\alpha_{j+1}}\right). \quad (16)$$

From formula (16), it follows that the interference pattern at sufficiently large angles $|\Delta\theta|$ is determined by the interface displacements $u(L_j)$ and the jumps of the parameters $f(L_j)$ and α_j at the interface. Moreover, formula (16) can easily be generalized to the case when the parameters $f(L_j)$ and α_j are not constant but slightly vary over the layer depth. Then, instead of formula (16), we have

$$\tilde{R}_j(\Delta\theta) = \exp[-i\Phi_j(\alpha)]\frac{1}{L_{ex}k}\left(\frac{f_j^{(+)}}{\alpha+\alpha_j^{(+)}} - \frac{f_{j+1}^{(-)}}{\alpha+\alpha_{j+1}^{(-)}}\right). \quad (17)$$

Here, $f_j^{(\mp)}$ are the Debye–Waller factors at the lower and upper interfaces of the jth layer, respectively. Similarly, the values of the parameter Δa_j are somewhat different at the lower ($\Delta a_j^{(-)}$) and upper ($\Delta a_j^{(+)}$) interfaces. The parameters $\Delta\alpha_j^{(\mp)}$ entering into relationship (17) are related to the parameters $\Delta a_j^{(\mp)}$ through formulas (12) and (13). Such a modification of the amplitude $\tilde{R}_j(\Delta\theta)$ is of importance, because all the parameters in relationship (17) are unrelated to the parameters of other layers. This circumstance substantially facilitates the fitting of the theoretical and experimental curves. However, it should be remembered that relationship (17) cannot be used to describe the entire reflection curve. The ranges with small quantities $\alpha + \alpha_j^{(+)}$ should be eliminated from consideration (see Section 5).

In calculations, it is necessary to take into account the diffuse scattering by thermal phonons and lattice imperfections in addition to the diffraction scattering. The exact calculation of the diffuse scattering is a sufficiently complex problem and requires the knowledge of many additional parameters, such as the type and density of different defects (dislocations, point defects, etc.). It is evident that, unlike the diffraction scattering, the diffuse scattering is incoherent and, hence, should not be oscillating in character. Therefore, the diffraction scattering can be approximated by a piecewise smooth function of the type

$$I_i^{(d)} = B_j + (B_{j+1} - B_j)\frac{\theta_i - \theta_j}{\theta_{j+1} - \theta_j} \quad (18)$$

at $\theta_i \in (\theta_j, \theta_{j+1})$, where the angle ranges (θ_j, θ_{j+1}) in which the function $I_i^{(D)}$ has a continuous derivative should be appreciably wider than the ranges corresponding to the periods of the oscillations observed in diffraction reflection curves. The coefficients B_j are variable parameters.

On the basis of the above formulas, the theoretical diffraction reflection curves are fitted to the experimental curves with the use of the χ^2 method. In terms of this method, the sought parameters can be obtained by minimizing the functional

$$\chi^2 = \frac{1}{N - N_p}\sum_{i=1}^{N}\frac{(I_i^{exp} - I_i^{th})^2}{\sigma_i^2}. \quad (19)$$

Here, N is the number of points in the diffraction reflection curve; N_p is the number of sought parameters; I_i^{exp} and I_i^{th} are the measured and calculated intensities of the reflected wave, respectively; and σ_i is the statistical error of measurements, which is determined by the total number of pulses recorded by the detector according to the Poisson law, that is,

$$\sigma_i = \sqrt{I_i^{exp}/t_i k_i}, \quad (20)$$

where t_i is the time of measurements and k_i is the attenuation coefficient due to the introduction of the additional absorber.

The parameter χ^2 is a random quantity with the distribution $\chi^2(r)$, which, at a large number of the degrees of freedom $q = N - N_p$, asymptotically tends to a normal distribution [13]. The normalizing coefficient $1/(N - N_p)$ in formula (19) is chosen so that, with due regard for the estimation technique, in the limit of large q, we have

$$\chi^2 = 1. \quad (21)$$

In this case, the root-mean-square difference of the parameter χ^2 from unity is written in the form

$$\Delta = \sqrt{2/(N - N_p)}. \quad (22)$$

The parameter χ^2 defined by formula (19) is used in statistical analysis not only as the minimized functional in the method for estimating the parameters of the model but also as the statistical criterion that makes it possible to evaluate the fitting quality or to choose the most optimum model when there are several ways of describing the spectra [26, 27]. The conclusion regarding the preference of a particular model can be drawn on the basis of the hypothesis theory. As follows from this theory (see, for example, [26]), for each model, there exists a characteristic r (referred to as the first-order error) that determines the probability of mistaken rejection of the model as erroneous.

Let us consider the model without sublayers and assume that this model is correct and a large value of

Table 1. Structural parameters specified by the growth technique and determined from the analysis of the diffraction reflection curves

Sample		Molecular-beam epitaxy			Diffraction reflection curve	
		t, °C	l_j, nm	x	l_j, nm	x
A	GaAs	610	100		107.60(2)	
	$In_xGa_{1-x}As$	580	13.5	0.08	12.13(2)	0.071(1)
	GaAs buffer	610	500		500	
B	GaAs	610	100		109.64(1)	
	$In_xGa_{1-x}As$	555	13.5	0.17	12.91(2)	0.155(1)
	GaAs buffer	610	500		500	

the parameter χ^2 results from a random fluctuation. For a true model, the χ^2 distribution at a large number of experimental points is described by the Gaussian function

$$P(\chi^2) = \frac{1}{\sqrt{2\pi}\Delta}\exp\left[-\frac{(\chi^2-1)^2}{2\Delta^2}\right], \quad (23)$$

where Δ is given by formula (22). The probability that, in a given experiment, a fluctuation results in a particular value of the parameter χ^2 is determined by the integral

$$r_1 = \frac{1}{\sqrt{2\pi}\Delta}\int_{\chi}^{\infty}\exp\left\{-\frac{(x-1)^2}{2\Delta^2}\right\}dx \quad (24)$$

and has the meaning of the first-order error. For the model with $|\chi^2 - 1| \sim \Delta$, it is easy to obtain a simpler estimate for the quantity r_1, that is,

$$r_1 = \frac{1}{\sqrt{2\pi}}\frac{\Delta}{\chi^2-1}\exp\left\{-\frac{(\chi^2-1)^2}{2\Delta^2}\right\}. \quad (25)$$

For example, in the case of a model giving $\chi^2 = 2$ for the number of experimental points $N \sim 800$ and $N_p \sim 10$, we obtain $r \sim 10^{-100}$. This means that the probability of making a mistake by rejecting this model as incorrect is extremely low. It should be noted that the smallness of the first-order error is primarily associated with the smallness of the quantity Δ, which is due to the large number N of experimental points. In experiments in which the number of experimental points is ten times smaller and the parameter χ^2 has the same value, the first-order error r is of the order of 10^{-10}.

5. INVESTIGATIONS OF MULTILAYER HETEROSTRUCTURES

The efficiency of double-crystal X-ray diffractometry for characterizing heterostructures will be demonstrated below using specific examples of investigation into the structure of low-dimensional systems GaAs/InAs/GaAs, $In_xGa_{1-x}As$/GaAs, and $Si_{1-x}Ge_x$/Si grown by molecular-beam epitaxy.

5.1. Structures with One Quantum Well

Two structures with an $In_xGa_{1-x}As$ quantum well in GaAs were grown using a Tsna-18 apparatus on GaAs(100) semi-insulating substrates with a misorientation angle of 3° along the [110] direction. The structures differ in the indium content in the well and the growth temperatures. The parameters of the samples and the growth temperatures are listed in Table 1 ("molecular-beam epitaxy" column).

The diffraction reflection curves for these samples are depicted in Fig. 5. The quantum wells have a relatively large thickness and strongly differ from GaAs in the lattice parameter. For this reason, additional peaks in the range of negative angles clearly manifest themselves in the diffraction reflection curves. The indium concentration and, hence, the difference in the lattice parameters for the quantum well in sample *B* are two times larger than those in sample *A*. The additional peak associated with the quantum well is pronounced in the diffraction reflection curve of sample *B*. This peak is less pronounced in the diffraction reflection curve of sample *A* (it overlaps the central peak and can be revealed from the strong asymmetry of the diffraction reflection curve as a whole). In both cases, a large number of oscillations are observed in the diffraction reflection curves, which indicates a relatively good quality of the quantum wells.

The parameters specified by the growth technique can be used as the starting approximation. In this case, the parameter χ^2 for sample *A* is equal to 88. A variation in the quantum well thickness, the indium concentration in the well, and the thickness of the upper layer lead to a decrease in χ^2 to 18.5. The positions of peaks and dips in the calculated and experimental curves (see Fig. 6a) are in good agreement, and the determined layer thicknesses and In concentrations in the layer differ from those specified by the growth technique by no more than 10% (see Table 1). However, according to the analysis performed in Section 4, the fitting with such a large parameter χ^2 cannot be considered satisfactory.

In order to achieve better agreement, there are additional possibilities. First, the parameters of the substrate and the upper layer can somewhat differ, because

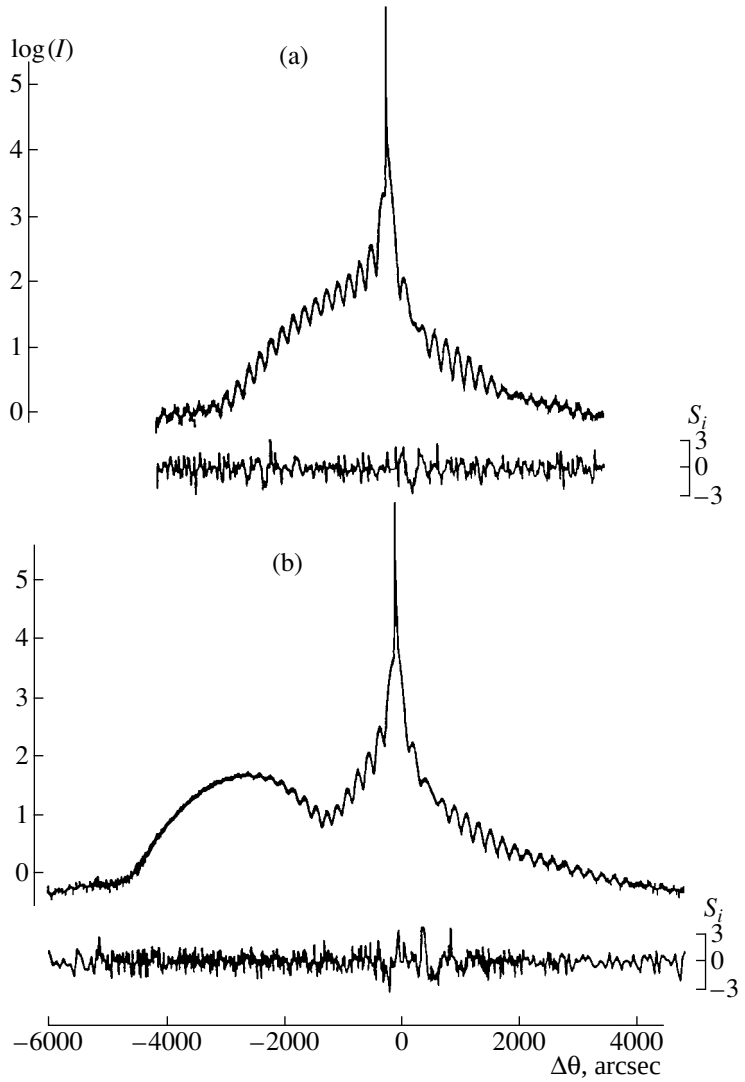

Fig. 5. Experimental (vertical dashes) and theoretical (solid lines) diffraction reflection curves for samples (a) *A* and (b) *B*. The theoretical curves are obtained for the final models at χ^2 = (a) 1.06 and (b) 1.07. The lower lines represent the differences S_i between the theoretical and experimental diffraction reflection curves in terms of standard deviations.

they were grown under different conditions. Furthermore, the quantum well can involve point defects or dislocations that deteriorate the perfection of the crystal lattice. In our approach, this is described by the Debye–Waller static factor f_j.

Defects of the crystal structure give rise to diffuse X-ray scattering. Moreover, there is diffuse scattering by crystal lattice vibrations. Finally, a change in the shape of the theoretical reflection curve can be caused by the smearing of the quantum well interfaces.

In the given case, the inclusion of the diffuse scattering according to the above scheme results in the most considerable decrease in the parameter χ^2 to 6.5. A variation in the parameters f_j and $\varepsilon_{\perp j} = \Delta a_j / a$ leads to a further decrease in χ^2 to ~2. The results of this fitting stage are presented in Table 2 and Fig. 6b.

Visually, the agreement between the experimental and calculated diffraction reflection curves in Fig. 6b can be treated as quite reasonable. As a rule, the fitting of a similar quality is regarded as final. However, as follows from the estimates made in the preceding section, there is a negligible risk by rejecting this model as incorrect.

The fitting quality can be improved owing to the inclusion of smearing of the quantum well interfaces by incorporating additional sublayers at the well interfaces. The addition of two sublayers on both sides of the quantum well leads to a decrease in the parameter χ^2 to 1.27. The fitting results are given in Table 3. However, according to formula (23), we have $r_1 \sim 10^{-5}$ for the last model. This is of course substantially less than the value of r_1 for the preceding model ($\chi^2 = 2$ and $r_1 \sim 10^{-100}$)

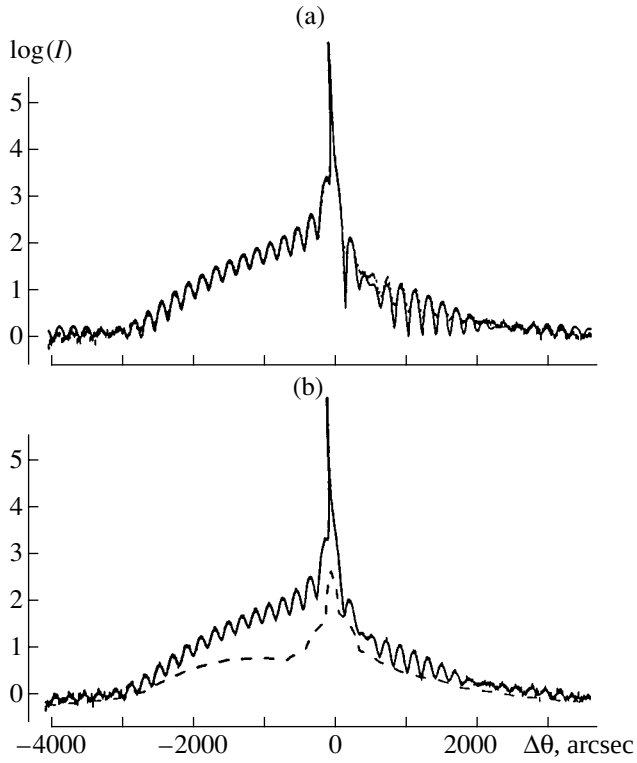

Fig. 6. (a) Experimental (vertical dashes) and theoretical (solid lines) diffraction reflection curves for sample *A*. The theoretical curve is obtained for the model with a variation in the parameters of the main layers ($\chi^2 = 18$). (b) The same curves calculated with due regard for the contribution of diffuse scattering (dashed line) for the model including sublayers ($\chi^2 = 1.27$).

but turns out to be rather small and calls for further refinement of the model.

The introduction of additional sublayers permits us to decrease the parameter χ^2 to 1.06 and, hence, to achieve an ideal fitting according to the criteria obtained in the preceding section. The parameters of the layers are listed in Table 3. The corresponding theoretical curve is depicted in Fig. 5a. The fitting quality is so high that the theoretical and experimental curves virtually coincide with each other on the figure scale.

A similar analysis was carried out for sample *B*. This sample is characterized by a higher indium concentration in the well ($x = 0.17$) and somewhat different growth conditions. The diffraction reflection curves for sample *B* were measured over a wider range of angles (Fig. 5b). The broad peak at –3000″ corresponds to the reflection from the quantum well. As in the case of sample *A*, a large number of oscillations are observed in the diffraction reflection curve, even though they are strongly attenuated in the range of the peak. This is associated with the fact that the structure of sample *B* is more defective than that of sample *A*. A variation in the layer thicknesses, the Debye–Waller static factors, and the interplanar distances; the incorporation of sublayers; and the inclusion of diffusion scattering make it possible to achieve excellent agreement between the calculated and experimental curves at $\chi^2 = 1.07$. The fitting results are presented in Fig. 5b and Table 3.

For an adequate theoretical description, the majority of points of the distribution

$$S_i = (I_i^{\exp} - I_i^T)/\sigma_i \qquad (26)$$

should fall in the range from –3 to +3 [13]. As can be seen from the curves $S_i(\Delta\theta)$ shown in Figs. 5a and 5b, the calculated errors are well within this range.

A detailed examination of technological aspects of the fitting results is beyond the scope of the present work. It should only be noted that we succeeded in revealing a thin transition layer 10 nm thick at the upper layer–vacuum interface in sample *B*. This is primarily explained by the fact that the diffraction reflection curve was measured over a wider range of angles. Moreover, this also allowed us to describe in more detail the interfaces between the layers in sample *B* as compared to sample *A*.

5.2. Parameters of $Si_{1-x}Ge_x$ *Quantum Wells in an* Si *Matrix*

Heterostructures $Si_{1-x}Ge_x$/Si with one (sample *A*1) and two (sample *A*2) quantum wells were grown on a RIBER SIVA 45 apparatus at the Institute of Semiconductor Physics (Linz, Austria). Prior to epitaxy, silicon substrates were cleaned by the method that was devel-

Table 2. Structural parameters of sample *A* according to the models with and without sublayers

Model without sublayers				Model with sublayers			
Layer	l_j, nm	$\Delta a_j/a$, %	f_j	Layer	l_j, nm	$\Delta a_j/a$, %	f_j
1	107.1(1)	–0.007(1)	0.854(4)	1	105.2(8)	–0.008(1)	0.83(1)
				2'	2.1(7)	0.12(8)	0.86(1)
2	12.8(1)*	0.952(5)*	0.91(1)*	2	10.7(2)*	0.962(8)*	0.86(1)*
				2"	3.2(1)	0.51(4)	0.82(1)
3	500	0	0.86(1)	3	500	0	0.88(1)

* Corresponds to the quantum well.

Table 3. Structural parameters of samples *A* and *B* according to the final models

Layer	Sample *A*			Layer	Sample *B*		
	l_j, nm	$\Delta a_j/a$, %	f_j		l_j, nm	$\Delta a_j/a$, %	f_j
				1	2.2(2)	–0.8(3)	0.29(4)
				2	2.8(1)	–0.19(6)	0.67(2)
1	106.5(2)*	–0.009(1)*	0.84(1)*	3	97.9(6)*	–0.001(1)*	0.81(1)*
2	1.6(2)	0.5(1)	0.95(2)	4	7.2(8)	–0.05(1)	0.74(1)
3	9.8(2)*	0.97(2)*	0.85(2)*	5	1.2(4)*	0.1(3)*	0.95(3)*
4	2.3(16)	0.6(2)	0.80(5)	6	10.1(3)*	2.23(2)*	0.90(3)*
5	2(1)	0.3(5)	0.90(6)	7	2.9(1)*	1.45(9)*	0.90(3)*
6	5(2)	0.01(2)	0.90(2)	8	3.9(3)	0.30(5)	0.86(2)
7	8(1)	–0.005(8)	0.86(2)	9	5.8(9)	0.04(2)	0.90(1)
				10	4.4(9)	–0.04(1)	0.88(1)
8	500	0	0.90(2)	11	500	0	0.93(1)

* Corresponds to the quantum well.

oped at the Radio Corp. of America and involved alkali ($NH_4OH : H_2O_2 : H_2O = 1 : 1 : 5$) and acid ($HCl : H_2O_2 : H_2O = 1 : 1 : 5$) treatments. In each etchant, the substrates were treated at the temperature $T \sim 80$°C for 15 min followed by washing in deionized water with a resistivity of no lower than MΩ cm. A thin oxide layer formed in the acid etchant was removed by heating for 5 min at $T = 1000$°C in the growth chamber. The Si buffer layer was grown at $T = 750$°C. Then, the temperature was decreased to 500°C and all subsequent layers were grown at this temperature. The structural parameters specified by the growth technique are listed in Table 4. The experimental diffraction reflection curves are depicted in Fig. 7. A large number of oscillations are observed in the diffraction reflection curves, which suggests a high quality of the grown layers with rather abrupt interfaces between the layers.

The structural parameters specified by the growth technique (Table 4) were used as the starting approximation in analysis of the diffraction reflection curves. A comparison of the calculated and experimental diffraction reflection curves indicates that the structural parameters of the grown structures only approximately correspond to those specified by the growth technique. This is quantitatively characterized by the large parameters $\chi^2 = 200$ and 138 for samples *A*1 and *A*2, respectively.

In order to describe the complete set of oscillations in the experimental diffraction reflection curve for sample *A*1, four additional sublayers were included in the sought model. Since the model for sample *A*2 initially involved very thin nanolayers, no additional sublayers were introduced. Moreover, for sample *A*2, the thicknesses of the quantum wells were varied and only the germanium concentration was varied in the course of the fitting. This is associated with the fact that the contribution of these nanolayers to the diffraction scattering is extremely small and the shape of the diffraction reflection curve is predominantly governed by the coherent displacement of atomic planes in the upper, rather thick Si layer with respect to the substrate, which is caused by the thin quantum wells.

The theoretical diffraction reflection curves for the final models are shown by the solid lines in Fig. 7. As can be seen from this figure, the calculated curves fit the experimental diffraction reflection curves over the entire range of Δθ angles rather well. This is also confirmed by the parameters $\chi^2 = 2.58$ and 1.96 for samples *A*1 and *A*2, respectively. The layer parameters obtained upon fitting are given in Table 5.

The crystal lattice parameters $\varepsilon_\perp = \Delta a_j(x)/a$, which, in the quantum wells, are due to the replacement of Si atoms by Ge atoms, are related to the calculated quantities $\Delta a_j^\perp/a$ through the known relationships [29]. The concentrations x determined according to the Vegard law were corrected with the use of the procedure proposed in [29].

The results of the investigation performed can be briefly summarized as follows. It was revealed that the quantum well in sample *A*1 have boundary layers whose thicknesses are equal to 3.3 nm for the upper (with respect to the quantum well) layer and 1.6 nm for the lower layer. A number of germanium atoms (approximately 6%) diffuse into these boundary layers; as a result, the germanium content in the quantum well decreases by about the same value. As was noted above, sample *A*2 contains a large number of thin layers. The thicknesses of the layers were not varied and only the crystal lattice parameters were varied in the course of

Table 4. Parameters of samples *A*1 and *A*2 according to the requirements of the growth technique

Layer	Sample *A*1	Layer	Sample *A*2
1	Si, l = 500 Å	1	Si, l = 500 Å
2	Si : $B^+(10^{19}cm^{-3})$, l = 16 Å	2	Si : $B^+(8 \times 10^{18}\ cm^{-3})$, l = 30 Å
3	Si, l = 100 Å	3	Si, l = 100 Å
4	$Si_{0.7}Ge_{0.3}$ quantum well, l = 150 Å	4	$Si_{0.8}Ge_{0.2}$ quantum well, l = 25 Å
5	Si buffer, l = 3000 Å	5	Si barrier, l = 35 Å
	Si(001) substrate	6	$Si_{0.8}Ge_{0.2}$ quantum well, l = 18 Å
		7	Si, l = 100 Å
		8	Si : $B^+(8 \times 10^{18}\ cm^{-3})$, l = 30 Å
		9	Si buffer, l = 1000 Å
			Si(001) substrate

Table 5. Layer parameters of samples *A*1 and *A*2 according to the final models

Sample *A*1				Sample *A*2			
Layer	l_j, Å	$\Delta a_j/a$, %	f_j	Layer	l_j, Å	$\Delta a_j/a$, %	f_j
1	41(3)	0	0.08(1)	1	544.3(2)	0.001(1)	0.95(1)
2	369(2)	0.009(1)	0.96(1)	2	30	–0.03(1)	0.95(1)
3	249(2)	–0.006(1)	1.00(1)	3	100	0.037(3)	0.95(2)
4	33(1)	0.32(2)	1.00(2)	4	25	0.94(2)	0.85(2)
5	150*	1.829(2)*	0.96(2)	5	35	0.12(1)*	0.75(3)*
6	16(1)	0.49(9)	0.98(2)	6	18	0.95(4)	0.70(3)
7	403(3)	–0.013(1)	0.97(1)	7	100	0.036(5)	0.71(2)
8	1047(7)	–0.001(1)	0.91(1)	8	30	–0.04(1)	0.71(2)
9	1329(8)	–0.002(1)	0.88(1)	9	1000	0.002(1)	0.71(2)
Substrate				Substrate			

* Corresponds to the quantum well.

the fitting. Analysis demonstrates that the germanium content in the quantum wells decreases by approximately 20%. This germanium diffuses into the layer separating the quantum wells and the boundary layers. As a whole, the total germanium content in the samples corresponds to the germanium amount introduced during their preparation.

Judging from Fig. 7, in which the theoretical and experimental curves almost coincide with each other, we can draw the inference regarding a very high quality of the fitting. However, according to the criteria described in Section 4, the fitting with the parameter $\chi^2 = 2.58$ or 1.96 cannot be treated as satisfactory and the model can be refined with the use of the available experimental data. However, no refinement was performed, because it is not directly associated with the quantum-well layers and is of little interest for the development of technology.

5.3. Heterostructure with Three Quantum Wells

The heterostructure depicted schematically in Fig. 8 was grown by molecular-beam epitaxy. A GaAs buffer layer 300 nm thick was grown on a GaAs substrate at a temperature of 600°C, after which the temperature was decreased to 520°C for 1.5 min. Then, an $In_xGa_{1-x}As$ layer 9 nm thick was grown and the process was suspended until the interface (for 1 min). Thereafter, a GaAs layer 60 nm thick was grown in such a way that the temperature of the substrate was gradually increased from 520 to 600°C over the course of the first minute of the growth. The same procedure was used for the growth of the two remaining $In_xGa_{1-x}As$ layers 6 and 3 nm in thickness. The experimental data are presented in Fig. 3.

Figure 3 shows the experimental diffraction reflection curve and the theoretical diffraction reflection curve calculated in the framework of a model that

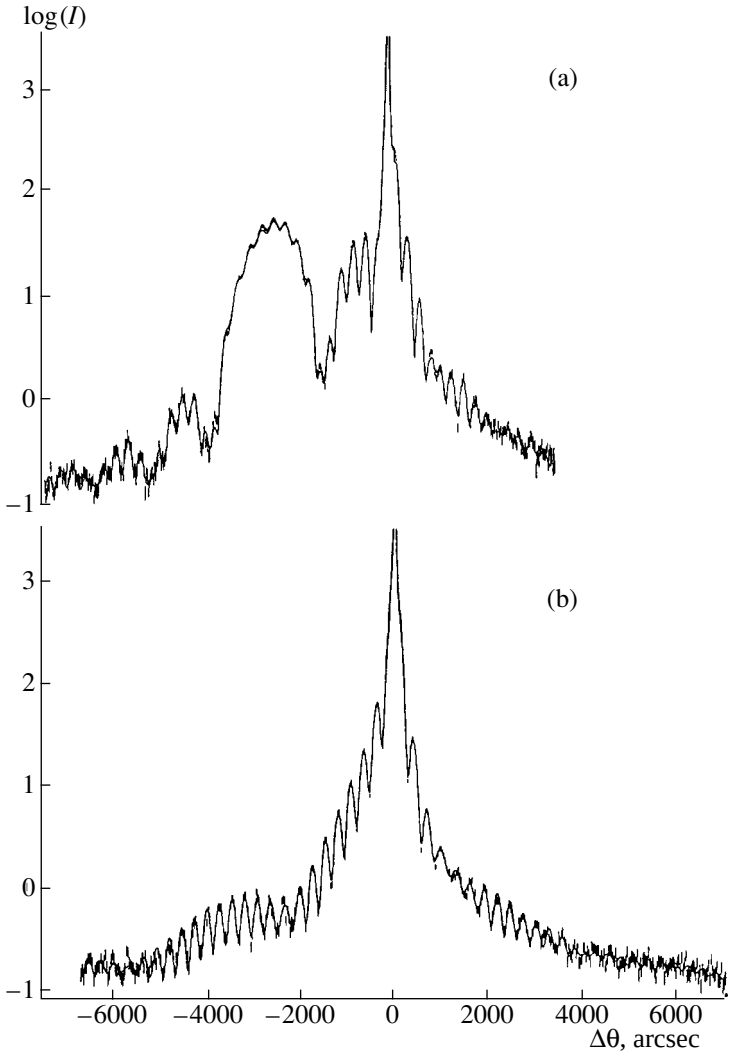

Fig. 7. Experimental (vertical dashes) and theoretical (solid lines) diffraction reflection curves for samples (a) *A*1 and (b) *A*2 of the $Si_{1-x}Ge_x$ structure. The theoretical curves are obtained for the final models at χ^2 = (a) 2.58 and (b) 1.96.

involves seven layers with the thicknesses corresponding to the structure depicted in Fig. 8. The factors f_j were taken equal to unity, and the relative changes $\varepsilon_\perp$ in the lattice parameter were assumed to be identical for all the $In_xGa_{1-x}As$ layers and equal to 0.028. This value corresponds to the indium concentration $x = 0.2$ under the assumption that the Vegard law [16] holds true for the given ternary compound.

It can be seen from Fig. 3 that, in this case, the experimental and theoretical curves disagree dramatically and the parameter χ^2 is very large in magnitude (3000). By varying the layer thicknesses and the indium concentration in the layers, it is possible to decrease the parameter χ^2 to 200. The inclusion of the diffuse scattering and a variation in the Debye–Waller static factors lead to a decrease in the parameter χ^2 to 6.2.

This disagreement between the theoretical and experimental data indicates that the model accounting for seven layers with abrupt interfaces does not correspond to the real structure. In this respect, additional layers were included at the next stage of analysis. The initial thicknesses of additional layers were taken equal to 1 nm, and the local In concentrations and the Debye–Waller static factors were assumed to be equal to the corresponding quantities for the adjacent main layers. As a result of the fitting, the parameter χ^2 decreases to 1.6. The theoretical curve obtained for this model is shown in Fig. 3 (curve *3*). It is visually difficult to distinguish between the theoretical and experimental curves.

The layer parameters determined are listed in Table 6. The analysis enabled us to describe the initial structure in greater detail. The $In_xGa_{1-x}As$ layers appear to be strongly diffuse, which can be explained by the segregation of indium during the heterostructure growth [10, 17, 18]. Moreover, it is important that the total indium contents (2.0, 3.7, and 5.6) in the

GaAs	60 nm
$In_xGa_{x-1}As$	3 nm
GaAs	60 nm
$In_xGa_{x-1}As$	6 nm
GaAs	60 nm
$In_xGa_{x-1}As$	9 nm
GaAs buffer	300 nm
Substrate	

Fig. 8. Schematic diagram of the profile of the $In_xGa_{1-x}As$–GaAs multilayer structure according to the requirements of the growth technique.

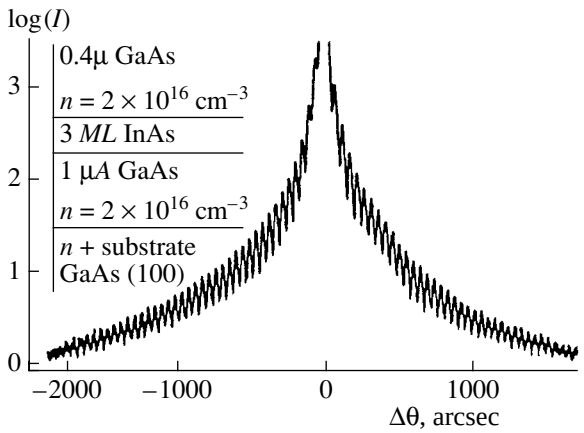

Fig. 9. Experimental (vertical dashes) and theoretical (solid line) diffraction reflection curves for the GaAs/InAs/GaAs structure shown in the inset. The theoretical curve is obtained for the model including additional layers.

$In_xGa_{1-x}As$ layers are close to the contents (2.0, 4.0, and 6.0) specified by the growth technique. Examination of the data presented in Table 6 demonstrates that the model of the structure composed of 14 layers is in some sense a limiting model. The model involves the upper layer ($j = 1$) with a thickness of 2.4 nm. Ignoring this layer leads to an increase in the parameter χ^2 by several tenths. The factor f_j for this layer turns out to be rather small. This is quite natural, because the crystal surface has a wavy relief, which can be clearly seen with an atomic-force microscope. In this case, the parameter f_j has the meaning of the filling factor [8]. The stress in the layer is determined with a very large error. It can be expected that the parameters of the additional sublayers are also evaluated with a low accuracy. This particular example clearly indicates an important feature of the method, namely, the possibility of determining the errors of the analyzed parameters restricts a more detailed description of the structure.

5.4. Determination of Small Total Displacements in a Heterostructure

As an example of the possible solution of this problem, we consider the curve of diffraction reflection (Fig. 9) from the (004) planes of a GaAs/InAs/GaAs heterostructure (depicted in the inset of Fig. 9). More than 80 oscillations are observed in this diffraction reflection curve, which primarily suggests a good quality of the grown structure. The thickness of the InAs layer is very small and does not exceed three monolayers. It is known that such layers are inhomogeneous and form island structures (the so-called quantum dots). However, as can be seen from the experimental diffraction reflection curve (the occurrence of a large number of oscillations), the stresses induced by the InAs layer are relieved rather rapidly. The role of the InAs layer is predominantly reduced to a displacement of atomic layers in the upper layer by a certain distance u of the order of an interatomic distance with respect to the lower layer. The contribution of the InAs layer to the diffraction scattering is rather small and, to a first approximation, can be disregarded. At the same time, the InAs layer shifts the main layers, which leads to the additional phase

$$\Phi = K_h u \tag{27}$$

in the scattering amplitude of the upper layer with respect to the lower layer.

Seemingly, the three-layer model (Fig. 10) with layers uniform in thickness and absolutely abrupt interfaces between them can serve as the starting model. However, it is easy to see that this model cannot be used to analyze the entire diffraction reflection curve. Actually, the grown layers are inhomogeneous and undergo small variations in the interplanar distance and the degree of their perfection. Therefore, this model is unsuitable for analyzing the central part of the curve in the immediate vicinity of the Bragg peak. At the same time, this model is also obviously inappropriate for examining the wings of the diffraction reflection curve, because the diffraction scattering in these angle ranges substantially depends on the structure of the interlayer interfaces. On the other hand, we can assume that, in a certain range of intermediate angles, the above model should adequately describe the diffraction reflection curve.

Table 6. Layer parameters according to different models

Model with $\chi^2 = 6.2$				Model with $\chi^2 = 1.6$			
j	l_j, nm	$\varepsilon_{\perp j}$, %	f_j	j	l_j, nm	$\varepsilon_{\perp j}$, %	f_j
				1	2.4(1)	–0.01(9)	0.34(2)
1	59.32(3)	0.007(2)	0.75(1)	2	54.9(4)	–0.001(1)	0.68(1)
				3	2.8(3)	0.3(2)	0.59(2)
2	4.61(3)	1.63(2)	0.75(1)	4	2.9(2)	1.99(8)	0.48(2)
				5	2.4(2)	0.56(4)	0.95(2)
3	57.73(3)	–0.005(1)	0.73(1)	6	56.2(1)	0.004(1)	0.80(1)
				7	2.8(1)	1.00(6)	1.00(2)
4	7.96(2)	1.920(4)	0.87(1)	8	1.5(5)	2.8(3)	0.97(5)
				9	4.2(4)	1.94(6)	0.82(2)
5	57.69(3)	–0.002(1)	0.69(1)	10	57.2(1)	0.003(2)	0.66(1)
				11	2.1(1)	1.21(5)	1.00(2)
6	12.03(4)	1.888(6)	0.45(1)	12	8.0(1)	2.07(1)	0.41(1)
				13	4.9(1)	0.67(2)	0.51(1)
Buffer			0.63(7)		Buffer		0.67(6)

For a three-layer system with abrupt interfaces, it is easy to derive a simple relationship for the diffraction reflection coefficient $R(\Delta\theta)$, which is valid over a wide angle range away from the Bragg peak [6]; that is,

$$R(\Delta\theta) = \left|\frac{1-\exp(i\Delta_q L)}{\Delta\theta} f_c + \frac{\exp(i\Delta_q L + i\Phi)}{\Delta\theta} f_s\right|^2 + R_b, \quad (28)$$

where $\Delta_q = -(2\pi/\lambda) \times 2\cos\theta_B \Delta\theta$ is the transferred momentum minus the reciprocal lattice vector; L is the thickness of the upper layer; f_c and f_s are the Debye–Waller static factors of the upper and buffer layers, respectively; and Φ is the phase defined by formula (27).

The reduced intensity can be written in the form

$$\tilde{I}(\Delta\theta) = P_R(\Delta\theta)\Delta\theta^2 = (B - A\sin(\Delta_q L + \varphi)), \quad (29)$$

where the quantities A and B are expressed though the parameters Φ, f_c, and f_s in the following way:

$$A = 2f_c\sqrt{(f_c - f_s)^2 + 4f_c f_s \sin^2(\Phi/2)}, \quad (30)$$

$$B = f_c^2 + (f_c - f_s)^2 + 4f_c f_s \sin^2(\Phi/2), \quad (31)$$

$$\tan\varphi = \frac{f_c - f_s\cos\Phi}{f_s\sin\Phi}. \quad (32)$$

The substrate and the buffer layer are usually grown with a sufficiently high degree of perfection and, hence, the factors f_c and f_s are close to unity. In this case, we obtain

$$A \approx 4\sin(\Phi/2), \quad B \approx 1 + i\sin^2(\Phi/2), \quad \varphi \approx \Phi/2. \quad (33)$$

Therefore, the amplitude, phase, and mean line of sinusoidal function (29) are directly determined by the sought phase Φ.

Now, we turn back to the experimental data presented in Fig. 9. For the left part of this curve, Fig. 11 shows the dependence of the reduced diffraction reflection intensity over a wide range of angles. In the angle range from –700″ to –100″, the character of oscillations resembles a typical sinusoid. The experimental

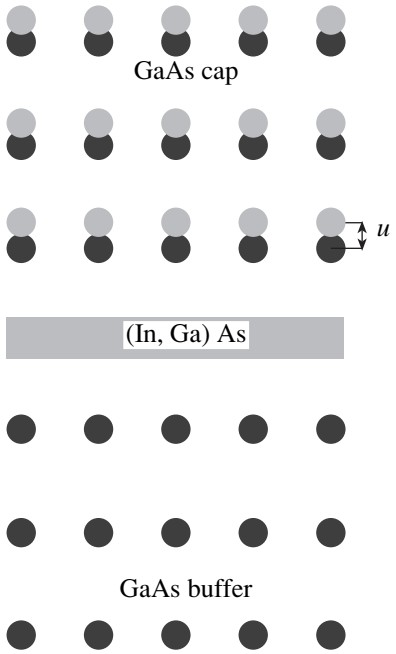

Fig. 10. A three-layer model of the GaAs/InAs/GaAs structure.

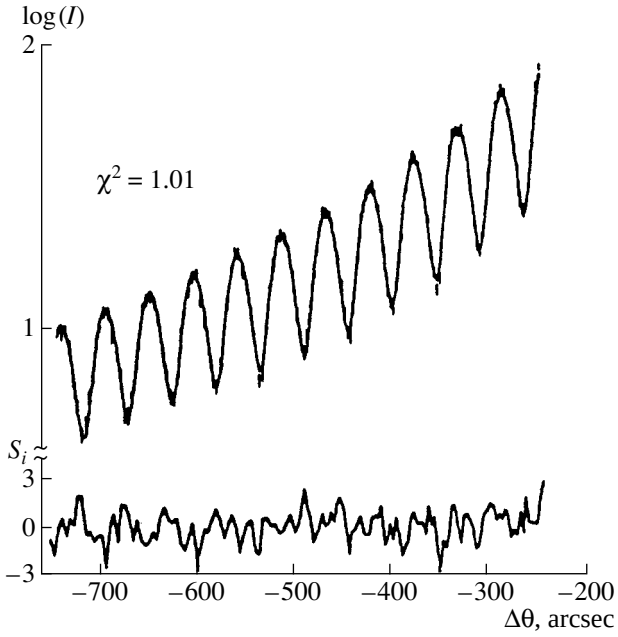

Fig. 11. Experimental reduced diffraction reflection intensity (vertical dashes), the theoretical curve (solid line) calculated from formula (29), and the difference curve S_i in the region of phase information.

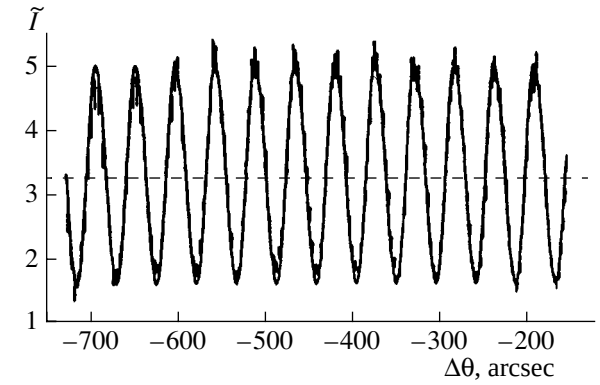

Fig. 12. Experimental (vertical dashes) and theoretical (solid line) diffraction reflection curves for the GaAs/InAs/GaAs sample. The theoretical curve is obtained for the three-layer model ($\chi^2 = 1.01$).

curve in this angle range and the curve calculated from formula (29) are depicted in Fig. 11. As can be seen, this simple formula describes the experimental data well. Thus, the portion of the diffraction reflection curve over a wide range (approximately 200 experimental points) provides a way of extracting phase information. The parameters of the sinusoid are readily determined to be $L = 412$ nm, $A = 1.7$, $B = 3.3$, and $\varphi = 1.4$. Using these data and relationships (29)–(32), it is easy to calculate the sought phase.

However, it should be taken into account that the convolution with the reflection curve for the crystal monochromator, rather than not the reflection curve for the sample, is measured in experiments. As a result, the reduced intensity cannot be described by simple analytical expressions similar to formulas (29)–(32). In this respect, we used the traditional fitting procedure. Figure 12 depicts the experimental diffraction reflection curve on the logarithmic scale in the aforementioned angle range. The theoretical curve for the three-layer model is also shown by the solid line in Fig. 12. The parameter χ^2 is equal to 1.01, which suggests the ideal quality of the fitting. This is confirmed by the curve indicating the differences S_i between the theoretical and experimental diffraction reflection curves (Fig. 12), according to which the values of S_i fall in the range from –3 to +3 [14].

As follows from the results obtained, the phase Φ is evaluated with a rather high accuracy (of the order of 10%). The corresponding displacement of the upper layer with respect to the buffer layer is determined to be $u = 0.1a$ (where $a = 5.65$ Å is the parameter of the GaAs crystal lattice), i.e., is equal to 0.56(5) Å. Therefore, double-crystal X-ray diffractometry without invoking additional phase-sensitive methods (for example, the X-ray standing-wave method [10, 31]) makes it possible to determine small displacements of individual layers in complex multicomponent systems.

6. CONCLUSIONS

Thus, the performed investigations clearly demonstrated that double-crystal X-ray diffractometry provides a way of obtaining detailed information on the parameters and the quality of grown thin layers with nanometer thicknesses. It is significant that the formation of the interference structure as a whole and, especially, on the wings of the diffraction reflection curve is primarily governed by the characteristics of interfaces. The proposed approach to analysis of diffraction reflection curves makes it possible (i) to obtain the mean parameters (and their errors) for individual layers; (ii) to determine the structure of interfaces with the highest accuracy; (iii) to elucidate the influence of the growth conditions on the quality of multilayer structures; (iv) to evaluate the indium and germanium distributions in $In_xGa_{1-x}As$ and Ge_xSi_{1-x} quantum wells and, thus, to determine the degree of imperfection and the thickness of interfaces on both sides of quantum wells; and (v) to reveal atomic-layer displacements (caused by foreign layers) comparable to or less than the interatomic distances.

An important factor is the choice of an adequate mathematical apparatus, because the finest details of the heterostructure are determined on the basis of quantitative criteria rather than from a visual similarity between the experimental and calculated diffraction reflection curves. The application of the χ^2 method for fitting of the theoretical diffraction reflection curves to the experimental data provided a high accuracy of

describing subtle effects in compound reflection curves even for the complex GaAs–$In_xGa_{1-x}As$/GaAs heterostructure, whose description requires a large number of parameters. The high reliability of the method is determined by the fact that the main differences between the structure specified by the grown technique and the grown structure can clearly be traced at all intermediate stages of analysis rather than being revealed only at the final stage.

ACKNOWLEDGMENTS

This work was supported by the Ministry of Industry, Science, and Technology of the Russian Federation (State Contract no. 37.029.11.0034) and the International Association of Assistance for the promotion of cooperation with scientists from the New Independent States of the former Soviet Union (project no. 01-0190).

REFERENCES

1. Jurgen H. Smet, T. P. E. Brockaert, and C. G. Fonstad, J. Appl. Phys. **71**, 2475 (1992).
2. F. Schaffler, Semicond. Sci. Technol., No. 12, 1515 (1997).
3. Zh. I. Alferov, Fiz. Tekh. Poluprovodn. (St. Petersburg) **32** (1), 3 (1998) [Semiconductors **32**, 1 (1998)].
4. A. M. Afanas'ev, P. A. Alexandrov, R. M. Imamov, *et al.*, Acta Crystallogr., Sect. A: Found. Crystallogr. **40**, 352 (1984).
5. S. S. Yakimov, V. A. Chaplanov, A. M. Afanas'ev, *et al.*, Pis'ma Zh. Éksp. Teor. Fiz. **39**, 3 (1984) [JETP Lett. **39**, 1 (1984)].
6. A. V. Afanas'ev, P. A. Alexandrov, R. M. Imamov, *et al.*, Acta Crystallogr., Sect. A: Found. Crystallogr. **41**, 227 (1985).
7. A. M. Afanas'ev, P. A. Alexandrov, S. S. Fanchenko, *et al.*, Acta Crystallogr., Sect. A: Found. Crystallogr. **42**, 116 (1986).
8. L. K. Robinson, Phys. Rev. B **33**, 3830 (1986).
9. L. Tapfer and K. Ploog, Phys. Rev. B **40** (14), 9802 (1989).
10. A. M. Afanas'ev, P. A. Aleksandrov, and R. M. Imamov, *X-ray Diffraction Diagnostics of Submicron Layers* (Nauka, Moscow, 1989).
11. B. K. Tanner, J. Cryst. Growth **99**, 1315 (1990).
12. L. Tapher, M. Ospelt, and H. von Kanel, J. Appl. Phys. **67**, 1298 (1990).
13. A. M. Afanas'ev, R. M. Imamov, A. A. Lomov, *et al.*, Surf. Sci. **275**, 131 (1992).
14. J. G. E. Klappe and P. F. Fewster, Acta Crystallogr., Sect. A: Found. Crystallogr. **67**, 1298 (1994).
15. C. Ferrari, M. R. Bruni, F. Martelli, and V. G. Simeone, J. Cryst. Growth **126**, 144 (1993).
16. M. Ilg and K. H. Ploog, Phys. Rev. B **48**, 11512 (1993).
17. J. M. Gerard, C. d'Anterroches, and J. Y. Marzin, J. Cryst. Growth **127**, 536 (1993).
18. C. Bocchi and C. Ferrari, J. Phys. D **28**, A164 (1995).
19. Z. G. Pinsker, *X-ray Crystal Optics* (Nauka, Moscow, 1982).
20. A. M. Afanas'ev, M. A. Chuev, R. M. Imamov, *et al.*, Kristallografiya **42** (3), 514 (1997) [Crystallogr. Rep. **42**, 467 (1997)].
21. A. M. Afanas'ev, M. A. Chuev, R. M. Imamov, *et al.*, Kristallografiya **43** (1), 139 (1998) [Crystallogr. Rep. **43**, 129 (1998)].
22. A. M. Afanas'ev, M. A. Chuev, R. M. Imamov, and A. A. Lomov, Kristallografiya **46** (5), 781 (2001) [Crystallogr. Rep. **46**, 707 (2001)].
23. A. M. Afanas'ev, A. P. Boltaev, R. M. Imamov, *et al.*, Mikroélektronika **37** (1), 3 (2002).
24. A. M. Afanas'ev, M. A. Chuev, R. M. Imamov, *et al.*, Kristallografiya **47** (6), 1130 (2002) [Crystallogr. Rep. **47**, 1058 (2002)].
25. A. M. Afanas'ev, M. A. Chuev, R. M. Imamov, *et al.*, Pis'ma Zh. Éksp. Teor. Fiz. **74** (10), 560 (2001) [JETP Lett. **74**, 498 (2001)].
26. H. Cramer, *Mathematical Methods of Statistics* (Princeton Univ. Press, Princeton, N.J., 1946; Mir, Moscow, 1975).
27. W. T. Eadie, D. Dryard, F. E. James, M. Roos, and B. Saboulet, *Statistical Methods in Experimental Physics* (North-Holland, Amsterdam, 1971; Atomizdat, Moscow, 1976).
28. A. M. Afanas'ev, R. M. Imamov, A. A. Lomov, *et al.*, Mikroélektronika **32** (2), 1 (2003).
29. J. P. Dismukes, L. Ekstrom, and R. J. Paff, J. Phys. Chem. **68**, 3021 (1964).
30. A. M. Afanas'ev, A. P. Boltaev, R. M. Imamov, *et al.*, Mikroélektronika **31** (1), 3 (2003).
31. A. M. Afanas'ev and V. G. Kon, Zh. Éksp. Teor. Fiz. **74**, 300 (1978) [Sov. Phys. JETP **47**, 154 (1978)].

Translated by O. Borovik-Romanova

Crystallography Reports, Vol. 48, No. 5, 2003, pp. 744–749. Translated from Kristallografiya, Vol. 48, No. 5, 2003, pp. 802–807.

STRUCTURE OF INORGANIC COMPOUNDS

Dedicated to the 60th Anniversary of the Shubnikov Institute of Crystallography of the Russian Academy of Sciences

Atomic Structure and Mechanism of Ionic Conductivity of $Li_{3.31}Ge_{0.31}P_{0.69}O_4$ Single Crystals

M. Kh. Rabadanov, A. Pietraszko**, V. V. Kireev*, A. K. Ivanov-Schitz*, and V. I. Simonov***

** Shubnikov Institute of Crystallography, Russian Academy of Sciences, Leninskiĭ pr. 59, Moscow, 119333 Russia*

e-mail: rab_mur@ns.crys.ras.ru

*** Institute for Low Temperature and Structure Research, Polish Academy of Sciences, PO Box 937, 50-950 Wroclaw, Poland*

Received October 28, 2002

Abstract—The atomic structure of $Li_{3.31}Ge_{0.31}P_{0.69}O_4$ single crystals was refined based on high-precision X-ray diffraction data at 293 K. The characteristic features of the crystal structure are considered, and their influence on high ionic conductivity (Li^+) of these crystals is discussed. *© 2003 MAIK "Nauka/Interperiodica".*

INTRODUCTION

Solid electrolytes with the γ-Li_3PO_4-type structure are model objects for studying the influence of various factors on ionic conductivity [1–4]. In solid solutions with a structure of this type, e.g., in the Li_4GeO_4–Li_3VO_4 or Li_4GeO_4–Li_3PO_4 systems, ionic conductivity ranges within 10^{-4}–10^{-5} Ω^{-1} cm^{-1} even at room temperature [1–3, 5]. These compounds hold promise for practical applications as electrolytes in solid-state lithium-based sources. The establishment of mechanisms of ion transport at the atomic level is an urgent problem, which can be solved using high-precision X-ray diffraction studies. This, in turn, opens up the way for the target control of conductivity by dosed isomorphous replacements. The present study was undertaken to obtain high-precision X-ray diffraction data for $Li_{3+x}P_{1-x}Ge_xO_4$ single crystals ($x = 0.31$) and establish the pathways of lithium-ion transport in these crystals.

The crystal structure of γ-Li_3PO_4 is described by the orthorhombic sp. gr. *Pnma*; the structure is a hexagonal close packing of oxygen atoms. One-eighth of the tetrahedral cavities in this packing are occupied by phosphorus cations, and three-eighths of the cavities are occupied by lithium. The structure contains two crystallographically different lithium atoms. The Li(1) atom occupies the 8*d* position (symmetry 1), and the Li(2) atom is located in the 4*c* position (symmetry *m*). The [PO_4] and [LiO_4] tetrahedra share oxygen vertices to form a loose three-dimensional framework (Fig. 1) favorable for ion transport.

GROWTH OF SINGLE CRYSTALS AND X-RAY DIFFRACTION STUDY

Single crystals in the Li_3PO_4–Li_4GeO_4 system were grown from flux. The solvent was the Li_2MoO_4–LiF mixture. Lithium orthophosphate and orthogermanate in equimolar amounts were used with the aim of preparing a solid solution with the composition $Li_{3.5}P_{0.5}Ge_{0.5}O_4$. The starting components and the solvent in the ~1 : 1 ratio were placed in a 60-ml platinum cup. The seed was a platinum rod. After complete dissolution of lithium orthophosphate and orthogermanate in the melt at 970°C, the reaction mixture was cooled to 911°C. Crystallization was performed by further cool-

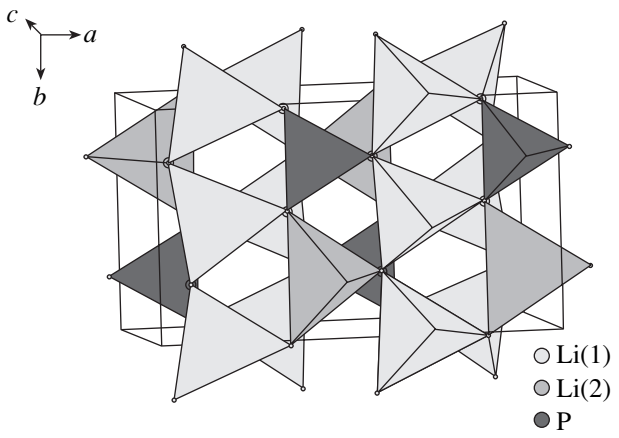

Fig. 1. Polyhedral representation of the unit cell of a γ-Li_3PO_4 single crystal.

1063-7745/03/4805-0744$24.00 © 2003 MAIK "Nauka/Interperiodica"

Table 1. Results of the atomic-model refinement: occupancies of positions, atomic coordinates, and anisotropic thermal parameters (for Li(3) and Li(4), isotropic thermal parameters)

Atoms		Occupancy	*x*/*a*	*y*/*b*	*z*/*c*	u_{11}	u_{22}	u_{33}	u_{12}	u_{13}	u_{23}
Li(1)	8*d*	0.850(7)	0.1643(2)	–0.0027(3)	0.3131(5)	0.022(1)	0.021(1)	0.028(1)	–0.0007(7)	0.005(1)	–0.004(1)
Li(2)	4*c*	0.830(5)	0.0742(3)	0.25	0.6885(7)	0.027(2)	0.021(1)	0.039(2)	0.0	0.012(2)	0.0
P/Ge	4*c*	0.69/0.31	0.41280(2)	0.25	0.32194(4)	0.0088(1)	0.00970(8)	0.0114(1)	0.0	–0.0011(1)	0.0
O(1)	8*d*	1.0	0.33968(6)	0.0363(1)	0.2141(1)	0.0339(3)	0.0374(3)	0.0344(4)	0.0027(3)	0.0003(3)	0.0016(3)
O(2)	4*c*	1.0	0.0556(2)	0.25	0.2834(3)	0.041(1)	0.025(1)	0.037(1)	0.0	–0.002(1)	0.0
O(3)	4*c*	1.0	0.0885(1)	0.75	0.1452(2)	0.0418(4)	0.0258(4)	0.0460(5)	0.0	0.0064(5)	0.0
Li(1*a*)	8*d*	0.102(5)	0.171(2)	0.037(3)	0.149(4)	as Li(1)					
Li(2*a*)	4*c*	0.082(4)	0.095(4)	0.25	0.844(8)	as Li(2)					
Li(3)	4*c*	0.063(6)	0.210(3)	0.25	1.009(8)	0.09(1)					
Li(4)	8*d*	0.088(6)	0.021(5)	–0.046(7)	0.428(9)	0.04(1)					

ing of the melt at a rate of 0.1 K/h to 858°C. The crystals synthesized were removed from the melt and cooled to room temperature at a rate of 30 K/h. Preliminary analysis of the single crystals grown showed that their composition is close to $Li_{3.31}Ge_{0.31}P_{0.69}O_4$.

Spherical samples suitable fox X-ray diffraction analysis were prepared from single crystals by abrasive grinding. X-ray diffraction study of a series of samples made it possible to select a single crystal 0.214(8) mm in diameter, which gave the best X-ray diffraction pattern. The high-precision X-ray diffraction experiment was performed on a Kuma-4 diffractometer equipped with a CCD coordinate detector using MoK_α radiation in the range $\sin\theta/\lambda < 1.20$ Å^{-1} at room temperature. The unit-cell parameters refined by the least-squares method based on 154 diffraction reflections are a = 10.690(1) Å, b = 6.1946(7) Å, and c = 5.0266(6) Å. All together, 8321 reflections were measured, of which 5076 reflections had $I > 2\sigma(I)$. The systematic absences indicated the sp. gr. *Pnma*. Averaging of integrated intensities of reflections equivalent within the sp. gr. *Pnma* gave 1343 independent reflections, with the reliability factor being R = 1.94%. The reflection intensities were corrected for the Lorentz and polarization factors. The absorption correction was applied with μr = 0.306. The best results were obtained by introducing the extinction correction according to the Becker–Coppens formalism (isotropic type I) under the assumption of the Lorentzian mosaic distribution.

STRUCTURE REFINEMENT

The structural parameters of $Li_{3.31}Ge_{0.31}P_{0.69}O_4$ single crystals were refined based on the X-ray diffraction data obtained by the least-squares method using the JANA software package [6]. At the first stage, the structure model was refined ignoring Li atoms and using high-angle reflections from the range of $0.60 < \sin\theta/\lambda < 1.20$ Å^{-1} (1033 independent experimental structure amplitudes and 30 structural parameters). Impurity Ge atoms isomorphously replace P atoms in tetrahedra. Assuming that the total occupancy of the [P,Ge] tetrahedra equals 100%, we refined the amount

Table 2. Interatomic distances (Å) in $Li_{3.31}Ge_{0.31}P_{0.69}O_4$ single crystals

Li(1)–O(1)	2.027(2)
Li(1)–O(1)	1.954(2)
Li(1)–O(2)	1.956(2)
Li(1)–O(3)	1.928(2)
Li(2)–O(1)	2.002(2) × 2
Li(2)–O(2)	2.045(4)
Li(2)–O(3)	1.930(3)
P/Ge–O(1)	1.6301(6) × 2
P/Ge–O(2)	1.616(2)
P/Ge–O(3)	1.6251(9)
Li(1*a*)–O(1)	1.83(2)
Li(1*a*)–O(1)	2.24(2)
Li(1*a*)–O(2)	1.93(2)
Li(1*a*)–O(3)	1.99(2)
Li(2*a*)–O(1)	2.02(2) × 2
Li(2*a*)–O(2)	2.25(4)
Li(2*a*)–O(3)	1.96(4)
Li(3)–O(1)	2.18(3) × 2
Li(3)–O(1)	2.37(3) × 2
Li(3)–O(2)	2.15(4)
Li(3)–O(3)	2.82(4)
Li(4)–O(1)	2.07(5)
Li(4)–O(1)	2.13(5)
Li(4)–O(2)	2.01(5)
Li(4)–O(2)	2.09(5)
Li(4)–O(3)	2.04(5)

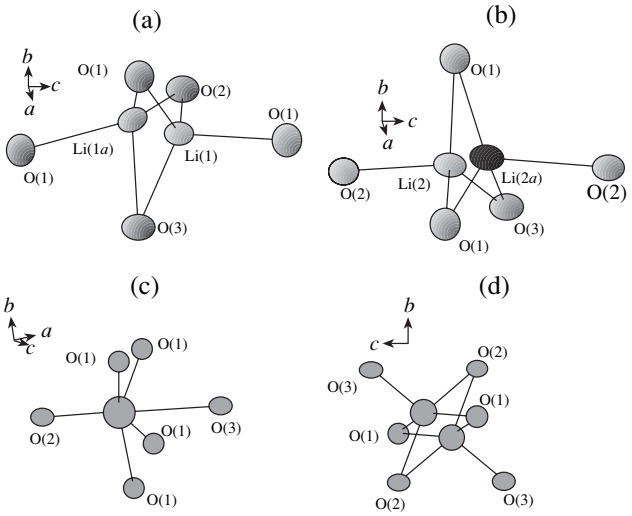

Fig. 2. Nearest environment of the (a) Li(1) and Li(1*a*), (b) Li(2) and Li(2*a*), (c) Li(3), and (d) Li(4) ions.

of phosphorus and germanium in this position by step-by-step scanning [7] of this position at a scan step of 0.5%. The minimum reliability factor corresponds to the occupancy of this position by Ge and P atoms in accordance with the formula $(Ge_{0.31}P_{0.69})$. This occupancy agrees well with the powder X-ray diffraction data according to Vegard's law. The high-angle refinement was independent of the lithium position in the structure, because the lithium contribution to these reflections is negligible. The atomic coordinates and thermal parameters of the atoms of a $[(P,Ge)O_4]$ tetrahedron determined at this stage were fixed and did not vary in the subsequent refinement.

Table 3. Interatomic distances and estimated energy barriers for hoppings of lithium ions

Hoppings	Energy barriers, eV	Interatomic distances, Å
Li(2) ⟶ Li(4)	0.29	1.72(5)
Li(4) ⟶ Li(2)	0.21	
Li(2*a*) ⟶ Li(2)	0.01	0.81(2)
Li(2) ⟶ Li(2*a*)	0.04	
Li(1*a*) ⟶ Li(2*a*)	0.24	2.19(4)
Li(2*a*) ⟶ Li(1*a*)	0.22	
Li(1) ⟶ Li(1*a*)	0.08	0.86(2)
Li(1*a*) ⟶ Li(1)	0.05	
Li(3) ⟶ Li(1)	0.25	2.24(3)
Li(1) ⟶ Li(3)	0.33	
Li(1) ⟶ Li(4)	0.29	1.66(5)
Li(4) ⟶ Li(1)	0.19	
Li(1) ⟶ Li(2)	0.70	2.634(3)
Li(2) ⟶ Li(1)	0.69	
Li(2*a*) ⟶ Li(3)	0.09	1.49(5)
Li(3) ⟶ Li(2*a*)	0.08	
Li(1*a*) ⟶ Li(3)	0.16	1.55(3)
Li(3) ⟶ Li(1*a*)	0.12	
Li(3) ⟶ Li(3)	0.60	4.08(3)
Li(3) ⟶ Li(4)	0.58	3.17(6)
Li(4) ⟶ Li(4)	0.40	2.53(6)
Li(4) ⟶ Li(4)	0.05	1.02(7)

The results of the high-angle refinement were used to construct difference electron-density syntheses based on the complete data set. For the centrosymmetric structure, the neglect of the lithium contribution does not change the signs of large structure amplitudes. The Li(1) and Li(2) positions were reliably localized from difference electron-density syntheses. The allowance for these lithium atoms reduced the R_w factor. However, the resulting difference electron-density syntheses still contained some weak additional peaks. To increase the sensitivity to the contributions of the lithium atoms, the next stage of the refinement was performed based on a limited data set with $\sin\theta/\lambda \le 0.9$ Å^{-1}, which contained these contributions. The refinement with due regard for the third- and fourth-order anharmonism of thermal vibrations of oxygen atoms made it possible to eliminate the residual peaks in the vicinity of the O(1), O(2), and O(3) atoms. However, the peaks in the neighborhood of the Li(1) and Li(2) positions persisted, which unambiguously indicated that the positions of these atoms are split. The refinement of the lithium positions with due regard for splitting of the positions into Li(1) and Li(1*a*) (100% total occupancy) and into Li(2) and Li(2*a*) (100% total occupancy) made it possible to eliminate the residual peaks in the vicinity of the lithium positions, with the standard and weighted *R* factors being decreased to 1.88 and 1.38%, respectively. Equal thermal parameters were attributed to lithium atoms in the split positions.

The difference syntheses calculated after this stage of the refinement of the structure model contained small peaks in the octahedral cavities of the structure. Using the analogy with study [8], we assumed that these positions are occupied by additional Li(3) and Li(4) atoms, which compensate the difference between the valences of Ge^{4+} and P^{5+} ions. The allowance for the Li(3) and Li(4) atoms in these positions and their refinement substantially improved the R_w factor (to 1.12%) and "cleaned" the zero electron-density maps.

Then, we lifted the assumption of 100% total occupancies of the Li(1)–Li(1*a*) and Li(2)–Li(2*a*) positions, which reduced the R_w factor to 1.08% and made the final total occupancies lower than 100%.

The final results of the refinement of the structure model are listed in Table 1.

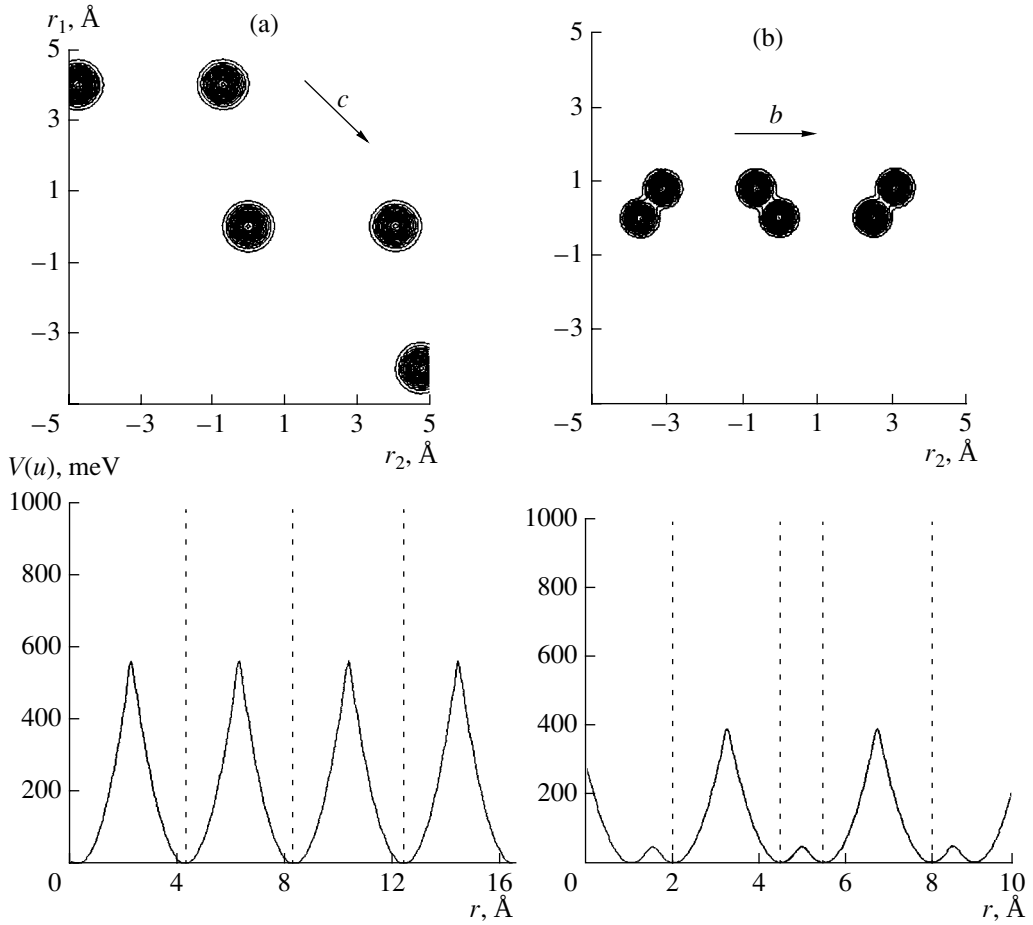

Fig. 3. Single-particle potentials along the (a) Li(3)–Li(3) and (b) Li(4)–Li(4) lines.

RESULTS AND DISCUSSION

First, it should be noted that all the thermal parameters of atoms in the $Li_{3.31}Ge_{0.31}P_{0.69}O_4$ structure are somewhat higher than those in pure γ-Li_3PO_4 [9]. This result is quite reasonable, because the partial replacement of P^{5+} cations by larger Ge^{4+} cations results in displacements of atoms in the structure and the necessary introduction of additional Li^+ ions compensating the difference between the charges of these cations. The additional lithium cations are located in the cavities of the structure. The average P–O and Ge–O distances (the coordination numbers are 4) are substantially different (1.54 and 1.76 Å, respectively) [10]. This leads to displacements of oxygen atoms, which was taken into account as the anharmonism of thermal vibrations of these atoms. The total occupancies of the main split Li(1) and Li(2) crystallographic positions are lower than 100%, which seems to indicate their involvement (together with the Li(3) and Li(4) ions) in the ion transport. According to the X-ray diffraction data, there are less than 3.31 lithium atoms per formula unit (see Table 1), i.e., a small portion of lithium ions are delocalized over the structure. These ions were difficult to localize because of their low scattering power.

The principal interatomic distances are given in Table 2. The nearest oxygen environment of all Li^+ ions is shown in Fig. 2.

In the $Li_{3.31}Ge_{0.31}P_{0.69}O_4$ solid solution, the main crystallographic positions of lithium ions are split. The Li(1*a*) and Li(2*a*) atoms are at distances of 0.86(2) and 0.81(4) Å from the Li(1) and Li(2) main positions, respectively. As can be seen from Figs. 2a and 2b, the Li(1*a*) and Li(2*a*) atoms occupy empty tetrahedra which share faces with the Li(1) and Li(2) tetrahedra, respectively. Such position splitting can be caused by both electrostatic perturbations associated with the different charges of the Ge and P cations and the incorporation of Li cations into empty octahedra (the octahedral cavities share faces with the Li tetrahedra). Therefore, all the lithium ions in the $Li_{3.31}Ge_{0.31}P_{0.69}O_4$ solid solution are disordered, which substantially enhances ionic conductivity.

It should be noted that the octahedral cavity is too large for the Li(4) ions and, hence, can simultaneously be occupied by two lithium ions. The coordination

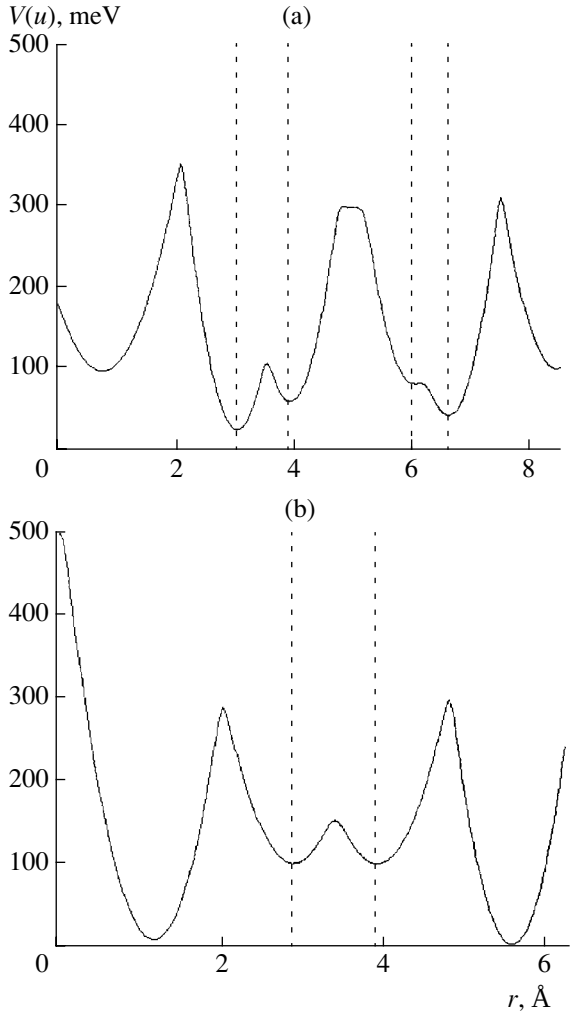

Fig. 4. Single-particle potentials along the (a) Li(3)–Li(1)–Li(1*a*)–Li(2*a*)–Li(2)–Li(4) and (b) Li(2)–Li(4)–Li(4)–Li(1) lines.

polyhedron of each ion in this cavity can be described as a tetragonal pyramid (Fig. 2d). The Li(4)–Li(4) distance is 1.02(7) Å. No splitting was observed for the Li(3) ions (Fig. 2c), but the isotropic thermal parameter of Li(3) is anomalously high.

In order to discuss the models of ion transport, we have to analyze the arrangement of lithium ions. The distances between different lithium ions and the corresponding potential barriers estimated from single-particle potentials are given in Table 3. This table allows one to analyze possible pathways of migration of lithium ions in the structure. Consider first the simplest mechanism of migration, which does not involve the Li(1), Li(2), Li(1*a*), or Li(2*a*) ions. In this case, only extra-stoichiometric Li(3) and Li(4) ions located in the octahedral cavities contribute to the conductivity. Consider the energy necessary for the charge transfer in this model. With this aim, we use the potential barriers between the Li(3) and Li(4) ions estimated from single-particle potentials of thermal vibrations of the atoms along the line connecting these atoms. As can be seen from Table 3, in order to jump from position 3 to position 4, a lithium ion must have an energy of 0.6 eV. The chains of the Li(3) and Li(4) ions and potentials along the lines connecting these ions are shown in Fig. 3. The barriers for hoppings along these chains are ~0.58 and ~0.4 eV for Li(3) and Li(4), respectively. The experimental activation energy of conductivity in the crystal under consideration is 0.54 eV [5]. Since the experimental activation energies are generally somewhat higher than their calculated values, it can be concluded that this model fails to adequately describe the experimental data. In order to adequately describe the experimental data on the activation energies, the mechanism of conductivity should include tetrahedrally coordinated lithium ions and lithium ions in the octahedral positions. Apparently, the ability of the former ions to migrate is explained by splitting of positions 1 and 2 (not observed in pure γ-Li_3PO_4) and disordering of positions (occupancies lower than 100%). In other words, high conductivity of germanium-substituted lithium orthophosphate is associated not only with the appearance of additional (compared to an undoped crystal) disordered lithium ions but also with disordering of the main lithium ions. One of the possible paths of migration of lithium ions in crystals with the γ-Li_3PO_4 structure was described earlier [8, 11] for $Li_{3.5}Ge_{0.5}V_{0.5}O_4$.[1] Using the migration path of lithium ions suggested in [8], we estimated the maximum potential barrier in the $Li_{3.31}Ge_{0.31}P_{0.69}O_4$ structure as ~0.35 eV, which agrees with the experimental data on the activation energy of conductivity [5]. The single-particle potentials of thermal vibrations of lithium ions along the lines connecting these ions are exemplified in Fig. 4. It should be noted that the maximum potential barrier for the direct Li(1)–Li(2) hopping is ~0.70 eV, whereas the by-pass Li(2)–Li(4)–Li(4)–Li(1) (Fig. 4b) has maximum potential barrier of ~0.35 eV.

In conclusion, it should be noted that our study shows that disorder of the lithium-ion sublattice is more pronounced than was indicated in [8], because we took into account additional splitting of the Li(1) and Li(4) positions, ignored in [8].

ACKNOWLEDGMENTS

This study was supported by the Russian Federation Government Program for Support of Leading Scientific Schools, project no. 00-15-96633.

[1] When considering the crystal structure and ion transport and comparing them with the results of earlier studies [5, 8, 11], one has to take into account that the crystallographic setting and notation of the positions of the Li(1) and Li(2) atoms used in these studies differ from those in the present study.

REFERENCES

1. A. K. Ivanov-Schitz and I. V. Murin, *Ionics of Solids* (S.-Peterb. Gos. Univ., St. Petersburg, 2000).
2. E. I. Burmakin, *Solid Electrolytes with Conductivity with Respect to Alkali Metal Cations* (Nauka, Moscow, 1992).
3. J. T. S. Irvine and A. R. West, in *High Conductivity Solid Ionic Conductors*, Ed. by T. Takahashi (World Sci., Singapore, 1989), p. 201.
4. A. K. Ivanov-Schitz, V. V. Kireev, O. K. Mel'nikov, and L. N. Dem'yanets, Kristallografiya **46** (5), 938 (2001) [Crystallogr. Rep. **46**, 864 (2001)].
5. A. K. Ivanov-Schitz and V. V. Kireev, Kristallografiya **48** (1), 117 (2003) [Crystallogr. Rep. **48**, 112 (2003)].
6. A. Petrichek and M. Duchek, *JANA98. Crystallographic Computing System* (Inst. of Physics, Acad. Sci. Czech Rep., Praha, 2000).
7. L. A. Muradyan, S. F. Radaev, and V. I. Simonov, *Methods of Structure Analysis* (Nauka, Moscow, 1989), p. 5.
8. I. Abrahams and P. G. Bruce, Acta Crystallogr., Sect. B: Struct. Sci. **47**, 696 (1991).
9. O. V. Yakubovich and V. S. Urusov, Kristallografiya **42** (2), 301 (1997) [Crystallogr. Rep. **42**, 261 (1997)].
10. *International Tables for Crystallography*, Ed. by A. J. C. Wilson (Kluwer Academic, Dordrecht, 1992).
11. P. G. Bruce and I. Abrahams, J. Solid State Chem. **95**, 74 (1991).

Translated by T. Safonova

Crystallography Reports, Vol. 48, No. 5, 2003, pp. 750–754. Translated from Kristallografiya, Vol. 48, No. 5, 2003, pp. 808–812.

STRUCTURE OF INORGANIC COMPOUNDS

New Data on Vlasovite: Refinement of the Crystal Structure and the Radiation Damage of the Crystal during the X-ray Diffraction Experiment

E. R. Gobechiya[1], I. V. Pekov[1], D. Yu. Pushcharovskiĭ[1,2], G. Ferraris[3], A. Gula[3], N. V. Zubkova[1], and N. V. Chukanov[4]

[1] *Faculty of Geology, Moscow State University, Vorob'evy gory, Moscow, 119899 Russia*
e-mail: elgob@mail.ru
[2] *Shubnikov Institute of Crystallography, Russian Academy of Sciences, Leninskiĭ pr. 59, Moscow, 119333 Russia*
[3] *Dipartimento di Scienze Mineralogishe e Petrologishe, Universita di Torino, Via Valpegra Caluso 35, 10125 Torino, Italy*
[4] *Institute of Problems of Chemical Physics, Russian Academy of Sciences, Chernogolovka, Moscow oblast, 142432 Russia*

Received April 1, 2003

Abstract—The crystal structure of vlasovite obtained from the Kipawa alkaline complex in Quebec is refined to $R_F = 0.053$ for 1515 unique reflections with $|F| > 4\sigma(F)$. The parameters of the monoclinic unit are as follows: $a = 11.063(8)$ Å, $b = 10.15(1)$ Å, $c = 8.60(1)$ Å, $\beta = 100.3(1)°$, space group $C2/c$, and $Z = 4$. The X-ray diffraction, electron microprobe, and IR spectroscopic data indicate that, under X-ray radiation, the specimen suffers radiation damage, which is accompanied by a partial removal of Na atoms, incorporation of H_2O molecules into the structure, and, possibly, a change in the configuration of the (Si,O) framework. © *2003 MAIK "Nauka/Interperiodica".*

INTRODUCTION

Vlasovite $Na_2ZrSi_4O_{11}$ is a typical zirconium concentrator in a number of alkaline complexes. In 1961, vlasovite was described as a new mineral from albitized eudialyte-microcline fenites and pegmatoid nepheline syenites of the exocontact zone of the Lovozero massif on the Kola Peninsula, where this compound occurs in the form of colorless transparent grains, replacing eudialyte and associated with microcline, albite, apatite, and fluorite [1].

The crystal structure of vlasovite (space group $C2/c$) was first determined by the photographic method in 1961 for a single crystal from the Lovozero massif [2] and later refined for the same specimen in the same space group [3]. It was found that vlasovite crystals from Ascensian Island in Atlantic are triclinic (space group $P\bar{1}$), but they become monoclinic after heating to 29°C [4]. However, the R factors reported in these studies are relatively large (0.149 and 0.116 for the $0kl$ and $hk0$ reflections, respectively [4]; and $R_{hkl} = 0.101$ for all reflections in [3]). For this reason, we refined the vlasovite structure for a specimen from the Kipawa alkaline complex in Quebec. In the course of our study, we observed the damage of the vlasovite crystal under X-ray irradiation. This phenomenon is of methodological interest and was studied specially. The results of both experimental studies are reported in this paper.

In the largest amounts, vlasovite occurs in the Kipawa alkaline complex in West Quebec (Canada) in the form of single-crystal insulations up to 15 cm long in pegmatites enriched with eudialyte and rinkite [5]. The specimen used in this study originates from Kipawa. In this specimen, transparent light-yellow isomorphic vlasovite grains up to 2 cm across, which are surrounded by a white gittensite border, grow into the assembly consisting of large grains of crimson eudialyte and black alkaline amphibole.

EXPERIMENTAL

The chemical composition of the mineral was determined using electron-microprobe analysis. When studying vlasovite on a Camebax SX 50 wave-dispersion electron microprobe analyzer, we came up against a serious problem of instability of the mineral under the effect of the electron beam: the sodium content measured varied widely with changing operating conditions. For example, at an accelerating voltage of 15 kV, current strength of 30 nA, and beam diameter of 2–3 μm, the Na_2O content was 4–6 wt % (instead of the calculated value of 14.6 wt %). Defocusing of the electron beam over areas 5×5 and 10×10 μm in size increased the Na_2O content to 7–8 and 9–10 wt %,

respectively. A similar dependence of the sodium content on the operating conditions was observed in the energy-dispersion studies of vlasovite on a JXA 50 microanalyzer equipped with an LINK spectrometer: a decrease in the beam current and an increase in the irradiated area resulted in an increase in the sodium content measured. For a current of 2 nA and a beam defocused over an area of 15×15 μm, the following content was obtained reproducibly (average of four determinations, wt %): Na_2O, 14.78; ZrO_2, 29.51; SiO_2, 56.27; total, 100.56. The contents of K, Ca, Sr, Ba, Mg, Mn, Fe, Zn, *REE*, Al, Ti, Hf, F, and Cl were beyond the determination limit. The empirical formula $Na_{2.02}Zr_{1.015}Si_{3.98}O_{11}$ is close to the ideal composition.

The X-ray diffraction intensities were measured from a fragment of the crystal that was subjected to the electron microprobe analysis. The crystal data, data-collection, and structure-refinement parameters are summarized in Table 1.

The unit cell parameters were obtained by the least-squares refinement of the angular parameters for 31 reflections in the range $6.89° \le 2\theta \le 47.83°$.

Absorption correction was introduced using the ψ-scan technique. The structure was solved by direct methods (independent of the earlier data) in space group *C*2/*c* with the SHELX97 program package [6] and refined with the JANA98 program [7]. At this stage, the partial occupancy of Na positions became obvious. Moreover, the difference Fourier synthesis contained peaks of the residual electron density around the Na(1), Na(2), and Zr positions. Correction for anharmonicity of thermal vibrations of these atoms improved R_F to 0.053 and lowered the heights of the residual maxima (Table 1). The final atomic coordinates and thermal displacement parameters are listed in Table 2. The valence-strength balance calculated according to [8] is presented in Table 3. The projection of the structure (drawn with the ATOMS program [9]) is shown in Fig. 1. The interatomic distances in the coordination polyhedra have normal values in the following ranges: Zr–O, 2.062(1)–2.116(1) Å; Na(1)–O, 2.386–2.870(1) Å; Na(2)–O, 2.368(1)–3.014(2) Å; Si(1)–O, 1.599(1)–1.624(1) Å; and Si(2)–O, 1.599–1.6282(7) Å.

The IR spectra of vlasovite (Fig. 2) were recorded with a Specord 75IR spectrophotometer (KBr pellets). The frequencies were measured to an accuracy of ±1 cm^{-1}. Polystyrene and ammonia were used as standards. To improve the accuracy in measurements of the intensities of the absorption bands, pure KBr was exposed to a reference ray.

Table 1. Crystal data and experimental parameters

Idealized formula	$Na_2Zr[Si_4O_{11}]$
Unit cell parameters, Å	a = 11.063(1), b = 10.15(1), c = 8.60(1), β = 100.3(1)°
Space group; Z	$C2/c$; 4
Cell volume V, $Å^3$	950.13(3)
Calculated density ρ, g/cm^3	2.975
Absorption coefficient μ, mm^{-1}	1.81
Molecular weight	425.56
F_{000}	824.0
Diffractometer	Ital Structures
Wavelength, Å	0.71073
Maximum 2θ angle, deg	67.98
Total number of reflections	4287
Number of unique reflections	1533
Number of unique reflections with $\|F\| > 4\sigma(F)$	1515
R_{av}, %	11.19
Number of parameters refined	131
R_F	0.053
$wR(\|F\|)$	0.054
$\Delta\rho_{max}$, $e/Å^3$	1.26
$\Delta\rho_{min}$, $e/Å^3$	–1.72

STRUCTURAL FEATURES AND THE RADIATION DAMAGE OF VLASOVITE

The structural elements of vlasovite are infinite chains of Si tetrahedra oriented along the [101] direction. The tetrahedra form four-membered centrosymmetric rings, which are linked through isolated Zr octahedra. Each Zr octahedron is connected with four chains. The Si tetrahedra share corners with one another and with Zr octahedral; that is, each oxygen atom is shared by two polyhedra. The cavities of the mixed zeolite-like framework accommodate the Na atoms in two inequivalent positions: the Na(1) and Na(2) atoms are located inside a seven-vertex polyhedron and a distorted octahedron, respectively.

In the specimen studied, the Na(1) and Na(2) positions are sodium-deficient. According to the refinement, the specimen contains only 1.72 Na atoms per formula unit instead of two atoms expected from the idealized vlasovite formula. The charge balance is attained by the formation of less (by half) vacancies, which are randomly distributed over the unit cell. These data are inconsistent with the results of the electron microprobe analysis, according to which the composition of the mineral agrees well with the ideal formula. The inconsistency of these data suggests that, in the course of the X-ray diffraction experiment, the mineral underwent some changes in composition and structure.

Table 2. Atomic coordinates, thermal displacement parameters, multiplicities (Q), and site occupancies (q)

Atom	x/a	y/b	z/c	Q	q	U^*_{eq}, Å$^2 \times 100$
Zr	0.25	0.25	0	0.5	0.5	1.61(2)
Na(1)	0	0.0746(1)	0.75	0.5	0.470(2)	3.21(3)
Na(2)	0	0.3996(2)	0.75	0.5	0.390(3)	5.31(6)
Si(1)	0.26433(3)	0.07226(4)	0.63854(5)	1	1	1.768(9)
Si(2)	0.04980(3)	0.21662(4)	0.42722(5)	1	1	1.846(9)
O(1)	0	0.1604(2)	0.25	0.5	0.5	2.44(4)
O(2)	0.1439(1)	0.1022(1)	0.5053(2)	1	1	3.33(3)
O(3)	0.1160(1)	0.3581(1)	0.4162(2)	1	1	3.22(3)
O(4)	0.0568(1)	0.2305(1)	0.9704(1)	1	1	2.40(3)
O(5)	0.2389(1)	0.1356(1)	0.7998(1)	1	1	2.93(3)
O(6)	0.2880(1)	0.0830(1)	0.1431(1)	1	1	2.18(2)

* The U_{eq} values are calculated from the parameters of anisotropic thermal displacements.

Table 3. Valence balance calculation*

Anion / Cation	O(1)	O(2)	O(3)	O(4)	O(5)	O(6)	Σ
Zr				$0.617^{[\times 2]}$	$0.713^{[\times 2]}$	$0.656^{[\times 2]}$	3.972
Na(1)	0.205	$0.055^{[\times 2]}$		$0.167^{[\times 2]}$	$0.094^{[\times 2]}$		0.837
Na(2)			$0.038^{[\times 2]}$	$0.132^{[\times 2]}$		$0.215^{[\times 2]}$	0.770
Si(1)		1.003	0.953		1.070	1.079	4.105
Si(2)	$0.989^{[\times 2]}$	1.005	1.003	1.070			4.067
Σ	2.183	2.063	1.994	1.986	1.877	1.950	

* The left and right superscripts indicate the valence strengths doubled in the calculations of valence balances at the anions and cations, respectively.

The weak fixation of Na atoms, especially Na(2), in the vlasovite structure was already noted in [3, 4] and is confirmed by our data on the partial occupancy of both Na positions (Table 2). The data of electron microprobe analysis clearly indicate that sodium can easily migrate in the bulk of the vlasovite crystal under high-energy radiation. These facts impelled us to perform an additional experiment in order to elucidate the effect of X rays on vlasovite. Rather large pieces (0.3–0.6 mm) of the mineral were cut from the single-crystalline specimen, whose fragments were used for the electron microprobe and X-ray diffraction studies, and exposed to X-ray radiation from a tube with an Mo anticathode operating at a voltage of 30 kV and a current of 5 mA for 19 h. The IR spectra of the mineral were recorded before and after the experiment under the same conditions.

Analysis of the IR spectra demonstrates that substantial changes take place in the vlasovite structure under irradiation. The changes observed in the spectrum of the specimen exposed to radiation, as compared to the spectrum of the starting mineral, are as follows: (1) intense absorption bands corresponding to molecular H_2O appeared at 3500 cm^{-1} (stretching vibrations) and 1645 cm^{-1} (bending vibrations); (2) the bands of stretching vibrations of the Si–O–Si bridge are shifted to lower frequencies (1126 $\longrightarrow$ 1117 and 1093 $\longrightarrow$ 1085 cm^{-1}), and the band of bending vibrations of the

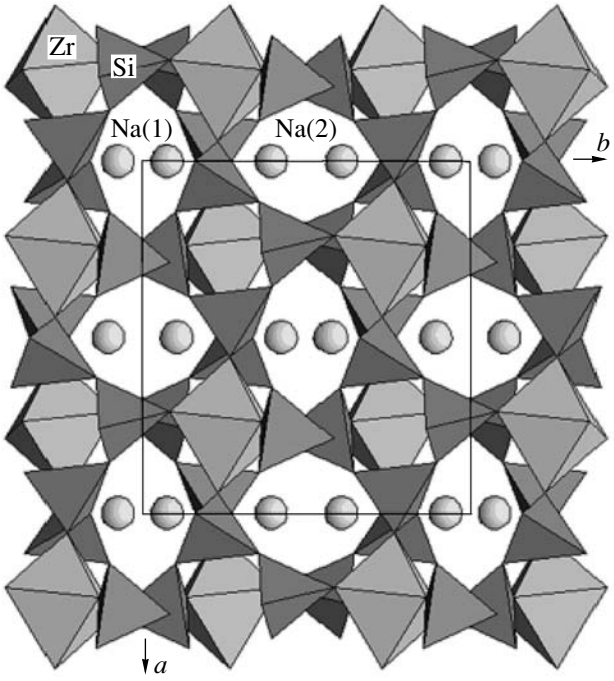

Fig. 1. Vlasovite structure in the projection onto the (001) plane.

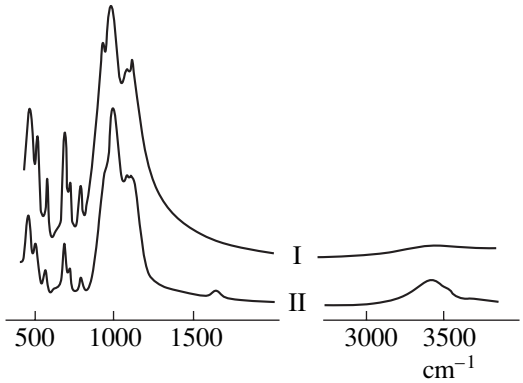

Fig. 2. IR spectra of the vlasovite samples: (I) the starting crystal and (II) the same crystal after 19-h exposure to X rays.

Si–O–Si bridge is shifted from 451 to 455 cm^{-1}; and (3) the band of Si–O stretching vibrations (involving the apical O atoms) at 942 cm^{-1}, which was clearly pronounced in the spectrum of the starting crystal, noticeably weakened and appeared as a shoulder at 945 cm^{-1}. All these changes in the IR spectra indicate the appearance of numerous defects in the framework and the hydration of structurally distorted vlasovite by absorption of atmospheric water. Note that the bands corresponding to the H_2O vibrations cannot be attributed to water molecules adsorbed by KBr. Since the structure analysis revealed a significant Na deficit, we assume that, in the irradiated specimen, water molecules are located in zeolite-like channels that accommodate Na. Most probably, water appeared in the distorted vlasovite structure after the radiation was switched off rather than in the course of irradiation. This provides an explanation of the absence of peaks corresponding to water oxygens in the difference synthesis. The position that could be occupied by a water molecule was calculated under the assumption that the shortest H_2O–O distance is 2.5 Å [10]. The coordinates of the resulting point (x = 0, y = 0.082, z = 0.75) are close to the Na(1) position (Table 2). The H_2O–O distances vary in the range 2.432(2)–3.097(3) Å. Thus, water molecules are presumably located in structural channels, provided these channels have Na vacancies. The Na deficit in the Na(1) and Na(2) positions can be explained within alternative models. First, Na atoms migrate inside the channels, which results in a decrease in the Na(1) and Na(2) site occupancies. In this case, the total Na content in the mineral and the charge balance in the $Na_2Zr[Si_4O_{11}]$ formula remain unchanged. Second, a portion of Na atoms leaves the crystal. The deficit of positive charge can be compensated either by a minor substitution of OH groups for O atoms of the bridging Si–O–Zr vertices or due to the appearance of anionic vacancies in the framework, which would make the framework defective. In the latter case, the general formula of the mineral is $Na_{2-n}Zr[Si_4O_{11-n/2}] \cdot nH_2O$, where $n < 1$. All the structural changes in vlasovite that were described above are irregular; otherwise, we should observe deviations from monoclinic symmetry similar to those described in [4]. We consider no more than possible displacements of Na atoms in the channels or even partial removal of sodium from the crystal, as is the case, for example, in the minerals of the lovozerite group, which undergo decationization and hydration in air [11].

In conclusion, we note that the radiation damage of the crystal in the course of the X-ray diffraction experiment observed in this study can be characteristic of other minerals. Taking this effect into account allows a more critical treatment of the results of structural determinations (particularly, site occupancies of weakly bound cations and water molecules) of unstable compounds, for example, high-alkaline zeolite-like silicates.

ACKNOWLEDGMENTS

We are grateful to L.A. Pautova and N.N. Kononkova for their aid in the determination of the chemical composition of the mineral and R.K. Rastsvetaeva for her critical remarks and useful discussion.

This study was supported by the Russian Foundation for Basic Research (project no. 03-05-64054) and by the Ministry of Education of the Russian Federation within the “Russian Universities” Program.

REFERENCES

1. R. P. Tikhonenkova and M. E. Kazakova, Dokl. Akad. Nauk SSSR **137** (4), 944 (1961).
2. Yu. A. Pyatenko and A. A. Voronkov, Dokl. Akad. Nauk SSSR **141** (4), 958 (1961).
3. A. A. Voronkov, T. A. Zhdanova, and Yu. A. Pyatenko, Kristallografiya **19** (2), 252 (1974) [Sov. Phys. Crystallogr. **19**, 152 (1974)].
4. S. G. Fleet and J. R. Cann, Miner. Mag. **36**, 233 (1967).
5. J. Gittins, E. L. Gasparrini, and S. G. Fleet, Can. Mineral. **12**, 211 (1973).
6. G. M. Sheldrick, *SHELX97, Program for the Solution and Refinement of Crystal Structures* (Siemens Energy and Automation, Madison, WI, 1997).
7. V. Petricek and M. Dusek, *JANA98: Crystallographic Computing System for Ordinary and Modulated Structures* (Inst. of Physics, Academy of Sciences of the Czech Republic, Prague, 1998).
8. N. E. Brese and M. O'Keeffe, Acta Crystallogr., Sect. B: Struct. Sci. **47**, 192 (1991).
9. E. Dowty, *Atoms 3.2: A Computer Program for Displaying Atomic Structures* (Kingsport, 1995), TN 37663.
10. G. Ferraris and G. Ivaldi, Acta Crystallogr., Sect. B: Struct. Sci. **44**, 341 (1988).
11. N. A. Yamnova, Yu. K. Egorov-Tismenko, and I. V. Pekov, Kristallografiya **46** (6), 1019 (2001) [Crystallogr. Rep. **46**, 937 (2001)].

Translated by I. Polyakova

Crystallography Reports, Vol. 48, No. 5, 2003, pp. 755–762. Translated from Kristallografiya, Vol. 48, No. 5, 2003, pp. 813–820.

STRUCTURE OF MACROMOLECULAR COMPOUNDS

Dedicated to the 60th Anniversary of the Shubnikov Institute of Crystallography of the Russian Academy of Sciences

Structure of Cellulose *Acetobacter xylinum*

V. V. Klechkovskaya*, Yu. G. Baklagina, N. D. Stepina*, A. K. Khripunov**, P. A. Buffat***, E. I. Suvorova*, I. S. Zanaveskina*, A. A. Tkachenko****, and S. V. Gladchenko****

** Shubnikov Institute of Crystallography, Russian Academy of Sciences, Leninskiĭ pr. 59, Moscow, 119333 Russia*

e-mail: klechvv@ns.crys.ras.ru

*** Institute of Macromolecular Compounds, Russian Academy of Sciences, Bol'shoĭ pr. 31, St. Petersburg, 199004 Russia*

**** Centre Interdisciplinaire de Microscopie Electronique, École Polytechnique Fédéralle de Lausanne, Lausanne, CH-1015 Switzerland*

***** St. Petersburg State University, Universitetskaya nab. 7–9, St. Petersburg, 199164 Russia*

Received April 2, 2003

Abstract—The data are presented on optimization of cellulose synthesis by *Acetobacter xylinum* (strain VKM V-880) and the structural characteristics of *A. xylinum* cellulose gel film synthesized during static cultivation. The structural changes caused by the removal of water from gel films are established and the structural organization of macromolecular chains in cellulose *A. xylinum* is studied. © *2003 MAIK "Nauka/Interperiodica".*

INTRODUCTION

The development of ecologically clean methods of cellulose synthesis is of great interest for the solution of the important problem of biosphere ecology, in general, and the problem of deforestation, in particular. It is also necessary to understand the evolution of the mechanism underlying biosynthesis of polysaccharides of various origins. In order to be able to use natural processes in practice, it is necessary to establish the structural hierarchy in biosynthesis—from monomer molecules up to the macrolevel.

The interest in fine details of biosynthesis and the structure of cellulose *A. xylinum* (CAX) is explained not only by the necessity of synthesizing chemically pure cellulose by ecological methods but also by a number of unique properties of this material and its possible application in various fields of medicine and technology [1–17].

The structural study of various celluloses (obtained from cotton, algae, animals, etc.) by various biochemical, genetic, physicochemical, and theoretical methods allowed one to establish the existence of two polymorphs of the native crystalline cellulose I—CI_α and CI_β [7–11]. It is established that the quantitative phase ratio in a two-phase structure depends on the sample nature, but the problem of precise ultrasonic localization of each phase is still unsolved.

Celluloses from various sources are characterized by various degrees of crystallinity. However, the I_α/I_β ratio of any cellulose sample is independent of the degree of its crystallinity. Thus, the *Valonia ventricosa* (V.V.) cellulose with the crystallinity index 100% is characterized by the ratio I_α/I_β = 60/40, whereas the cellulose of animal origin (from *Halocynthia*) with the same degree of crystallinity contains only 10% I_α, i.e., is characterized by the ratio I_α/I_β = 10/90 [14]. It is established that packing of cellulose chains in a metastable crystalline phase CI_α is described by a triclinic unit cell (sp. gr. *P*1) containing only one communicating chain. Under certain conditions, this phase is transformed into a thermodynamically stable monoclinic structure CI_β (sp. gr. $P2_1$) with two macrochains per unit cell [7, 11]. The method of calculating the profile functions suggested in [7] allowed one not only to separate the X-ray diffraction reflections from the CI_α and CI_β polymorphs in the ranges of interplanar spacings 0.59–0.62, 0.53–0.54, and 0.39–0.40 nm, but also to draw the conclusion that the composition ratios I_α/I_β for a number of celluloses of different origins depend on packing of molecular chains formed during biosynthesis. An attempt to interpret the fine details of the molecular mechanism of transformation of the I_α structure into I_β structure in solid state was made in [9] on an example of native cellulose samples possessing the same I_α/I_β ratios (60/40 for CAX and 58/42 for V.V. cel-

1063-7745/03/4805-0755$24.00 © 2003 MAIK "Nauka/Interperiodica"

lulose) but different crystallinity indices. It was established that 60-min-long thermal treatment of crystalline V.V. cellulose (crystallinity index 100%) in diglyme vapors at 270°C results in the transformation of 34% of the I_α phase into the I_β phase, whereas, in CAX samples (crystallinity index 100%), only 65% of the I_α phase undergoes a similar transformation.

At present, various research groups are attempting to understand why various samples are characterized by different I_α/I_β ratios. Most of the researchers studied phase ratios I_α/I_β and packings of macrochains in crystalline domains. It was established that the structural characteristics and the I_α/I_β ratio in the CAX depend on the strain and cultivation conditions used [13, 18–21] and, therefore, the *A. xylinum* cellulose can be considered as a model system for studying various factors that influence the structure formed.

The present article is dedicated to the structural organization of CAX macrochains during synthesis and the structural changes in the CAX synthesized in the form of a gel film during its drying. We also give some recommendations on the optimization of the CAX synthesis as a gel film by the strain VKM V-880. The structural studies of CAX samples were made by X-ray diffraction analysis, high-energy electron diffraction, and electron and atomic-force microscopy.

EXPERIMENTAL

Synthesis of A. xylinum Cellulose

The *A. xylinum* cellulose (CAX) was synthesized by VKM V-880 strain on a nutrient medium containing yeast extract, glucose, peptone, ethanol, and brewing wort at the concentrations determined in the course of optimization of the nutrient medium. The initial pH of the nutrient medium ranged from 5.9 to 6.0. The inaculated material was a 48-h culture of *A. xylinum* grown in a medium containing brewing water and brewing wort (6° B) at a 1 : 1 ratio with 2% of glucose and 1% of ethanol. In order to synthesize gel films, six-to-seven-day cultivation was performed at 29–30°C, then the CAX was separated and periodically washed with the 0.5–1.0% NaOH aqueous solution during boiling until the removal of *A. xylinum* cells. Then, the CAX was washed from the NaOH solution first with distilled water, then with the 0.5% acetic acid, and, finally, again with distilled water until the occurrence of the neutral reaction. The CAX thus obtained was stored in the form of a gel film at 5°C or, after sterilization in an autoclave, at room temperature, or, after drying at 40°C, in the dry form in vacuum.

Electron microscopy study was made using sterilized grids coated with 5 ml of the nutrient medium in a Petri dish and then with 1.5 ml of the inoculated material. The nutrient medium contained 3% of the yeast extract and 2% of glucose. The inoculated material contained 48-h *A. xylinum* culture grown on the medium of the same composition. In order to extract the cells from a CAX film, the content of the test tubes was thoroughly ground in a sterile homogenizer. For inoculation, the bacterial suspension free of fibers was used. Cultivation on nets was stopped after 3, 6, 9, and 18 h by drying the samples at 80°C.

Methods of Investigation

X-ray studies of the initial CAX gel films cleaned from the culture medium and also of the films upon the removal of a certain amount of water were studied on a DRON-2 diffractometer and in an RKV-86 X-ray diffraction chamber (Cu radiation, Ni filter).

Structure of thin films was studied by electron diffraction in an EMR-102 electron diffraction camera at the accelerating voltages 75 and 100 kV and in an EM430T electron microscope at the accelerating voltage 300 kV.

Dielectric losses ($\tan\delta$) of the 30- to 60-μm-thick films (preliminarily dried in vacuum at 60°C) were determined using a TR-9701 setup at frequencies from 1 to 100 kHz and temperatures from –140 to 120°C by a method described elsewhere [22].

The topographs of the surface of CAX films were obtained on an R4H atomic-force microscope (NT-MDT, Russia) in the tapping mode in air (Si cantilevers produced by Mikromasch, Estonia).

RESULTS AND DISCUSSION

It is well known that *A. xylinum* glucose-containing media and media containing other monosaccharides as sources of carbon and the yeast extract as a growth factor and source of nitrogen are favorable for development of *Acetobacter xylinum*. Earlier, it was shown that the CAX can also be synthesized on nutrient media with various inexpensive carbon sources: industrially hydrolyzed wood and peat and also molasses [23–25].

In order to determine the ability of the *A. xylinum* (VKM V-880) strain to synthesize cellulose, we optimized the initial nutrient medium containing glucose, yeast extract, and peptone. We also estimated the influence of organic additives (brewing wort and ethanol) on the cellulose biosynthesis. Optimization was made by the method of additive–network description of the experiment [26] according to which the cellulose yield was determined at five different medium components and five different levels of component concentrations. Using the combination of the components of the nutrient medium found, we managed to obtain up to 50 g of air-dry cellulose from one square meter of the reactor surface.

Using sedimentation and diffusion in cadoxen [23], we also managed to determine the molecular weight of the CAX (about 500 000 Da). According to the correlation laser spectroscopy data, the index of polydispersion in cadoxen is $M_Z/M_W \sim 1.1$. All these data are consistent with the known CAX characteristics [27].

At the first stage, we studied CAX gel films from their initial state up to the state of a dry polymer, which allowed us to establish the influence of the gradual removal of water from the film on its structural characteristics. The diffraction pattern from the initial gel film with the ratio dry polymer/water = 1 : 100 (Fig. 1, curve *1*) is characterized by a diffuse maximum in the range $2\theta = 20°–35°$. After removal of up to 50% of water from the initial gel film, four distinct reflections were seen against the halo background in the vicinity of the reflection angles $2\theta = 15°–16°$, 23°, 27°, 32°–34°, and 40°–42° (Fig. 1, curve *2*). All the reflections on the diffraction patterns are located in the regions characteristic of CI. After drying the sample without water in air at 20°C, the intensity of some the following reflections indexed within the CI_β modification increases, namely, of 110 ($2\theta = 16°50'$), 102 ($2\theta = 20°40'$), 200 ($2\theta = 23°$), 212 ($2\theta = 31°$), 004 ($2\theta = 34°30'$), and 204 ($2\theta = 41°30'$) (Fig. 1, curve *3*). Since the diffuse background was rather high (it disappeared only for the CAX films dried in vacuum at 40°C, Fig. 1, curve *4*), we believed that this sample would still preserve some amount of water.

This assumption was confirmed by the relaxation properties of the CAX measured by dielectric spectroscopy. Figure 2 shows the dependence of dielectric losses on temperature, $\tan\delta = F(t)$, for CAX samples. At negative temperatures, the maximum of dielectric losses $\tan\delta_m$ is observed in the vicinity of –60°C (at 1 kHz). According to the concepts of the relaxation properties of cellulose [22, 28, 29], this range of dielectric losses of the CAX films should be associated with relaxation of dipole polarization and mobility of primary hydroxyl groups of cellulose molecules. At temperatures above 0°C, dielectric losses become more pronounced, but, in the range from 40 to 80°C, they decrease, with the latter process being more intense the longer the storage time. This indicates the removal from the sample of those compounds which increase the electrical conductivity. In our case, the removal of water is most likely [29]. The repeated measurements show that drying of a CAX sample at 100°C results in an irreversible decrease of $\tan\delta_m$ (Fig. 2, curve *2*). Also, the maximum in the region of –60°C shifts toward higher temperatures, which indicates that no plastification associated with presence of water molecules forming hydrogen bonds with primary hydroxyls can take place. With destruction of the –OH–water complexes, no increase in the intensity of the $\tan\delta$ peak was observed, which can be explained by participation of the liberated OH–groups in the formation of a new system of intermolecular hydrogen bonds.

The further structural study of the CAX films was made by X-ray diffraction with the plane of the dried CAX film being parallel to the incident X-ray beam. The X-ray diffraction pattern obtained (Fig. 3, inset) shows the redistribution of the positions and intensities of some reflections. Close to the equator, we measured

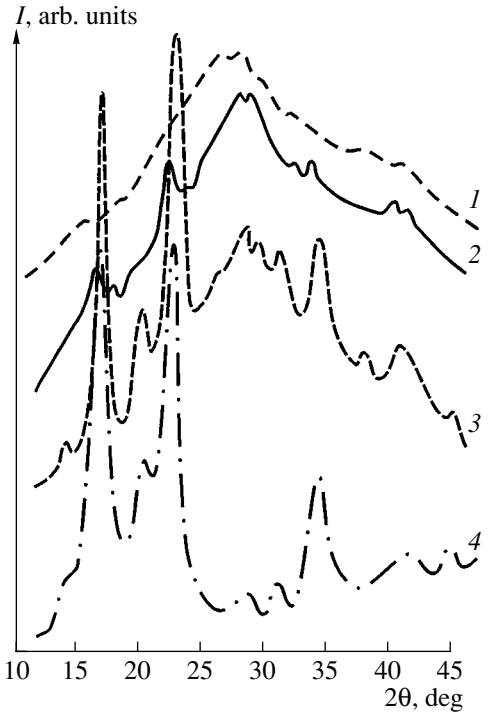

Fig. 1. Intensities of the diffraction pattern from CAX gel films with different water content: (*1*) 100%, (*2*) 50%, (*3*) 5–7%, and (*4*) dry film.

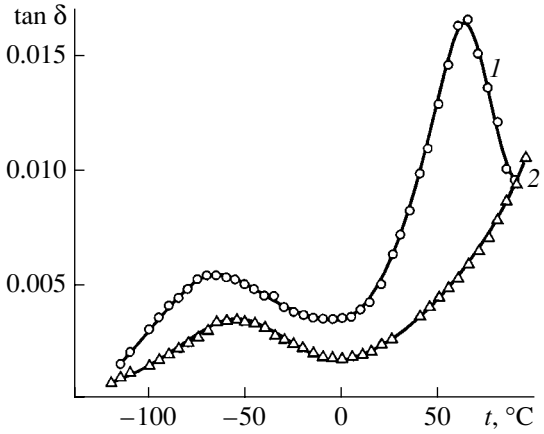

Fig. 2. Dielectric losses ($\tan\delta$) as a function of temperature, *t* from the (*1*) initial sample, (*2*) initial sample after heating up to 100°C.

the reflection with $d = 0.607$ nm ($2\theta = 15°$) corresponding to reflection from the $(1\bar{1}0)$ plane. We can also clearly see a reflection close to the meridian ($d = 0.523$ nm) against the background of the second ring ($2\theta = 17°$) identified as reflection from the (002) plane. No 110 reflection was observed on the equator; instead, we recorded only a weak ring from the (110) plane with $d = 0.532–0.535$ nm. Analyzing the intensity redistribu-

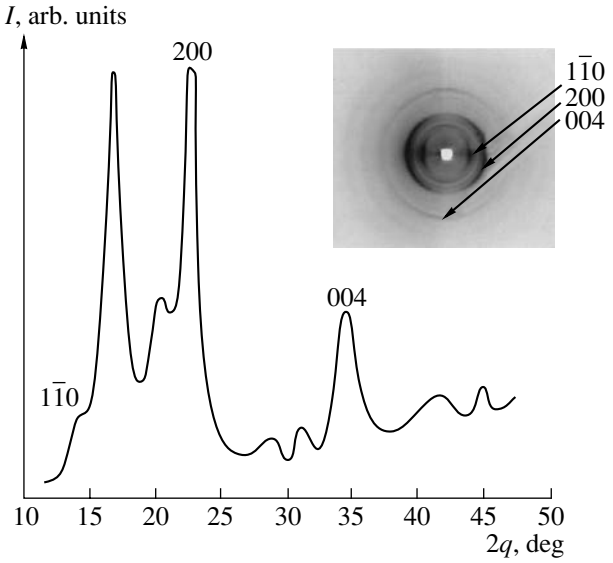

Fig. 3. Intensities of the diffraction pattern from a CAX dry film formed as a result of seven-day biosynthesis obtained at the normal incidence of an X-ray beam onto the film. In the inset: X-ray diffraction pattern obtained in the butt-end geometry with the sample plane being parallel to the X-ray beam.

tion for other reflections, we see that, e.g., a weak reflection close to $2\theta = 20°40'$ lies in the vicinity of the meridional region, which seems to be the superposition of reflections from the (102) and (012) planes of the monoclinic lattice ($d = 0.437$ and 0.432 nm). The most intense reflection in the vicinity of the equator is that with $d = 0.389$–0.392 nm, which corresponds to reflection from the (200) plane in which hydrogen-bonded molecules of cellulose chains form parallel layers. Finally, the reflection with $d = 0.259$–0.260 nm, which could have been the superposition of the reflections with noticeable intensities from the system of (004), (220), (031), and (023) planes on the X-ray diffraction pattern from the CAX films obtained in the "butt-end geometry" with the beam being parallel to the film surface (Fig. 3, inset), is clearly seen on the meridian. This reflection determines the parameter c of the polymer chain. The fact that the $1\bar{1}0$ reflection is observed on the equator of the diffraction pattern allows us to state that the $(1\bar{1}0)$ plane of the monoclinic unit cell in the crystalline domains forming the CAX ribbons is parallel to the plane of the macrosample, in other words, that the axial planar texture is formed. Thus, macrochains of the ordered CAX fragments (associates of microfibrils) are located in the plane of the dried film and form the axial texture.

Atomic force images of the surface and transverse section of the dry gel film are shown in Fig. 4. The image of the film surface (Fig. 4a) shows supramolecular CAX formations located in the planes practically parallel to the sample surface, which is also confirmed by the image shown in Fig. 4b. Thus, atomic force images are consistent with the X-ray diffraction data indicating the formation of a texture in the CAX films.

Considering diffraction patterns obtained from CAX samples (VKM V-880 and ATCC 53524 strains) [30], we see that reflection intensities are considerably different (Fig. 5, curves *1* and *3*). Most probably, this can be explained by different microstructures of the samples: in our case, the CAX films are textured, whereas the sample studied in [30] had the isotropic polycrystalline structure. Since these samples were prepared by different methods, we attempted to prepare samples by the method described and used in [30], i.e., by freezing gel films at –30°C with the subsequent lyophilization. As a result, the intensities were somewhat leveled but still remained noticeably different (Fig. 5, curve *2*). Most probably, this is associated with the considerable orientation of our samples associated with the specific features of their synthesis.

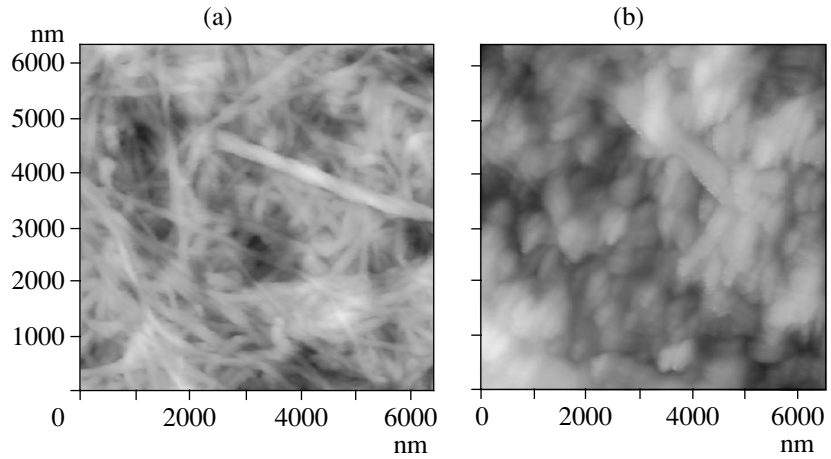

Fig. 4. Atomic force microscopy image of a CAX gel film: (a) image of the sample surface, (b) image of the transverse section.

The use of polycrystalline samples in [30] allowed Iwata *et al*. to analyze the intensity profiles and separate the reflections in the vicinity of the angles $2\theta = 15°$ and 17°. These reflections were attributed to the mixture of two crystalline modifications I_α and I_β. However, this method cannot be used for phase identification in textured CAX samples. However, the presence of the 002 reflection in the meridional region of the diffraction pattern obtained in the butt-end geometry (with the plane of the CAX film being parallel to the incident X-ray beam) indicates the formation of a considerable fraction of the monoclinic I_β phase in the gel CAX films.

More detailed information on the phase composition and structure of CAX films was obtained by electron diffraction. We used the possibilities offered by both electron microscope (selected area diffraction patterns) and electron diffraction camera (high-resolution diffraction patterns from rather large areas of the film).

Electron diffraction patterns obtained in an electron diffraction camera at the accelerating voltages 75 and 100 kV with the diameter of the electron beam 0.2 mm allowed us to study thin (up to 100 nm) gel CAX films, which were washed as was described above and dried at room temperature, and also samples dried directly on electron microscopy grids. Electron diffraction patterns obtained at normal incidence of an electron beam onto the sample showed a large number of ring reflections (Fig. 6a) characteristic of CI. The sample tilt with respect to the beam results in the transformation of these rings into arcs (Fig. 6b). This indicates the preferable orientation along the direction normal to the film plane (texture). Indexing of electron diffraction patterns obtained from the sample tilted at an angle of ~45° with respect to the electron beam shows that reflection occurs mainly from the (100) plane of the monoclinic lattice, the polymorph CI_β with the lattice parameters $a = 0.801$ nm, $b = 0.817$ nm, $c = 1.036$ nm (the axis of a macrochain) and $\gamma = 97°$ [10]. No reflections from the planes of the triclinic unit cell, the CI_α modification, were observed. However, the considerable angular width of the arc reflections on the oblique-texture electron diffraction patterns and the presence of a small number of additional reflections (e.g., $1\bar{1}0$ reflection along the [*h*00] direction) indicate the considerable deviation of the texture axis from its exact orientation.

The CAX structure at the microlevel was studied with an EM430T electron microscope. Electron microscopy images of the samples obtained at the initial stages of their syntheses show that bacteria synthesize cellulose microfibrils (ribbons) with the transverse dimension about 50 nm and move along the surface of the nutrient medium at random, although some rather long almost rectilinear portions with a length of 10 μm are also observed (Fig. 7a). The diffraction patterns from the unit ribbons chosen with the aid of a selective aperture always show the reflection with the spacing

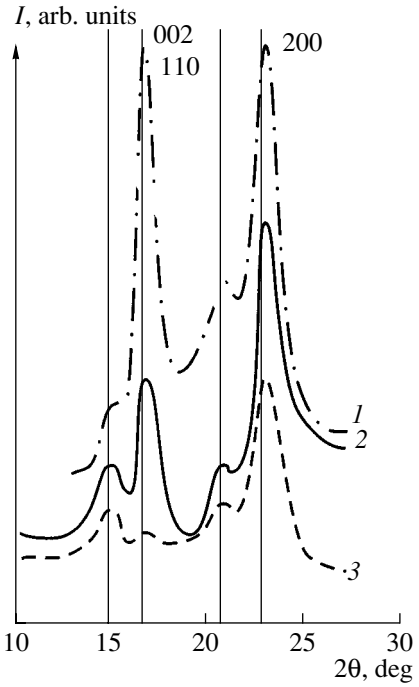

Fig. 5. Diffraction pattern from films synthesized by *A. xylinum*: *1* and *2* VKM V-880 strain; *3* ATCC 53524 strain. (*1*) CAX gel film dried at room temperature, (*2*) CAX gel film frozen at –30°C with the subsequent lyophilization, (*3*) CAX gel film frozen at –30°C with the subsequent lyophilization according to [31].

~0.260 nm oriented along the ribbon and the reflection with the spacing ~0.389 nm oriented in the perpendicular direction (Fig. 7b). These reflections can be identified as the 004 reflection within the polymorphous modification CI_β (cellulose chains parallel to microfibrils or ribbons) and the 200 reflection. Diffraction patterns from longer ribbons with the transverse dimension ~100 nm have a larger number of reflections, e.g., in addition to the 004 and 200 reflections, we also observed 102/012 reflections (d = 0.430–0.446 nm) complementing the (010) CI_β plane, the reflections with $d = 0.513$ and, sometimes, also with $d = 0.617$ nm, corresponding to 110 and 1-10 CCI_β. It should be noted that electron diffraction patterns from an isolated microfibril of the *Metandrocarpa uedai* tunic [31], an animal cellulose consisting mainly of CI_β, are characterized by the same set of reflections. Thus, under the conditions of synthesis of the *A. xylinum* cellulose, crystalline microfibrils with the structure CI_β are formed. No electron diffraction data indicating the coexistence of a CI_α polymorph was obtained.

Figure 8 shows the geometry of *A. xylinum* terminal complexes (TCs) and the CAX structure built by minisheets and minicrystals synthesized by one subunit of the terminal complex up to crystalline microfibril and associates (ribbons) of microfibrils. This geometry was suggested by Brown [3]. Twisted ribbons shown in

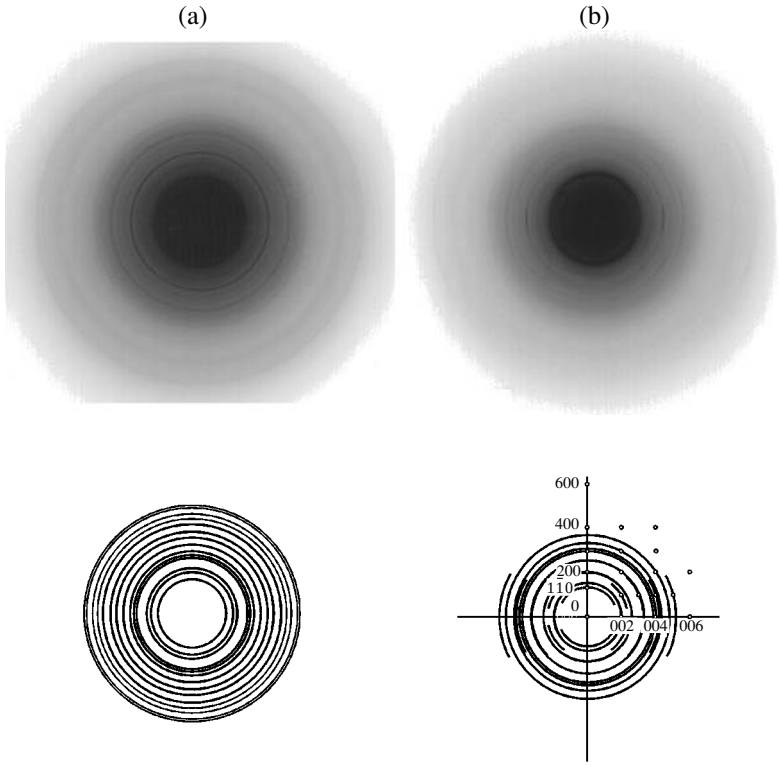

Fig. 6. Electron diffraction patterns and their schemes from a CAX gel film dried at room temperature obtained at (a) normal incidence of an electron beam onto the sample and (b) oblique incidence (45°) of an electron beam onto the sample.

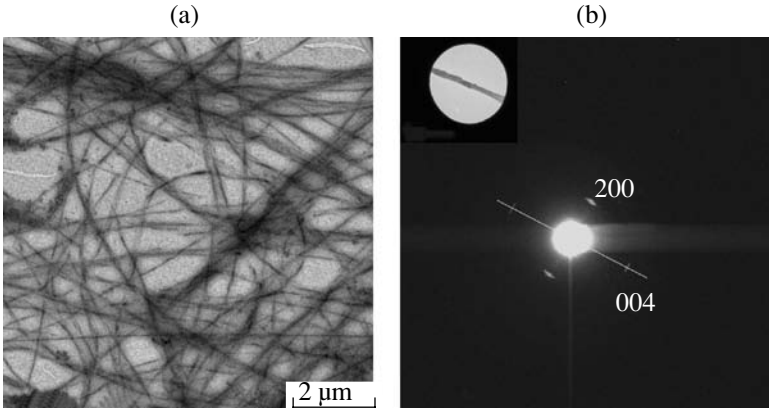

Fig. 7. Initial stages of a CAX gel film formation: (a) electron micrograph of an CAX microfibril formed within six hours of cultivation, (b) electron diffraction pattern from the portion of a microfibril with the transverse dimension ≤50 nm.

Fig. 8 can be explained by rotation of *A. xylinum* bacterium during its translational motion. The shear stresses arising in this planar CAX ribbon assemblies in the process of simultaneous crystallization and twisting are analyzed in [21, 30], where the authors also discuss the possible formation of various I_α/I_β ratios in CAX ribbon formations depending on the cultivation conditions. In particular, it is indicated that, during aggregation of microfibrils into broad ribbons, the stresses arising at their edges during twisting can give rise to the formation of a less symmetric crystal structure I_α, whereas, in the centers of these ribbons, the structure I_β is formed. The creation of the conditions for formation of less twisted ribbons or microfibrils with smaller transverse dimensions during synthesis would result in the formation of the regions of stable arrangement of CAX chains with the structure I_β. It seems that the chosen cultivation parameters provide free crystallization without twisting and formation of microfibrils mainly with the CI_β structure. However, detailed consideration

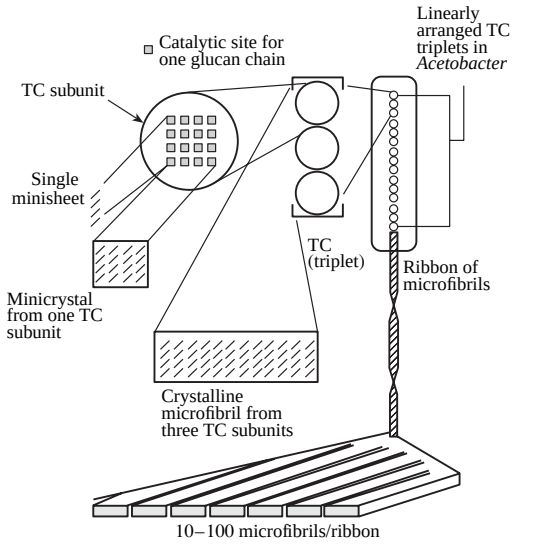

Fig. 8. Geometry of *A. xylinum* terminal complexes (TCs) and the hierarchy of microfibrils and ribbons suggested in [3].

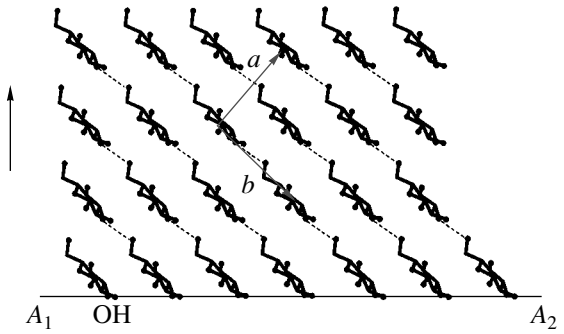

Fig. 9. Model packing of cellulose chains projected onto the *ab* plane for the monoclinic unit cell. A_1A_2 orientation of ribbon microfibrils in the macrofilm plane. Arrow indicates the directions of minisheets during biosynthesis.

of the atomic force microscopy images from the CAX films shows some twisted ribbons (Fig. 4a), but it is obvious that they are less characteristic—about one twisted ribbon per 10 images.

The results obtained allow us to suggest the following model of chain packing in CAX projected onto the *ab* plane of the monoclinic structure with two macrochains per unit cell (Fig. 9). We believe that minisheets suggested by Brown (indicated by arrows) are located normally to the surface of culture medium. Minisheets are bound by hydrogen bonds and, because of free crystallization (absence of shear stresses), the crystalline domains have the structure I_β and are oriented mainly by the (1–10) planes on the surface of the culture medium (A_1–A_2 line). In other words, they are oriented by their primary hydroxyl groups along the surface and create a network of hydrogen bonds with the aqueous medium, which is preserved during purification of the gel film and its storage.

It should be noted that CAX gel films can retain from 100 to 200 g of water per 1 g of dry polymer and preserve high intrinsic rupture strength (up to 2 kgf/mm^2). Analyzing the structural data, one can assume that the microfibril ribbons oriented in the film plane play not only the role of a reinforcing network but also of hydrophilic layers that can attach water molecules. According to the electron microscopy data, the diameter of such associates is ~50–100 nm, whereas their length exceeds the diameter by a factor of 1000 or even more. Thus, microfibril associates occupy only insignificant part of the gel-film volume.

CONCLUSIONS

(1) It is shown that in the static culture *A. xylinum* (VKM V-880 strain) may synthesize high-molecular cellulose (M_{SD} ~ 500 000 *D*) with a narrow molecular-weight distribution (M_Z/M_W ~ 1.1) and a considerable number of carbon sources. In order to obtain the maximum CAX yield, the composition of the nutrient medium is optimized.

(2) X-ray and electron diffraction and electron and atomic force microscopy studies indicate the formation of textured CAX gel films. In this case, the structures of microfibrils and ribbons correspond mainly to polymorphous CI_β modification.

(3) A model of packing of ribbon assemblies in the CAX film is suggested which shows that the minisheets forming these assemblies are located normally to the culture medium–air interface. The model allows one to describe the hierarchy of the structural organization during CAX biosynthesis—from a nanostructure to the formation of minicrystals and microfibrils to a textured macrosample.

ACKNOWLEDGMENTS

This study was supported by the Russian Foundation for Basic Research (project no. 01-03-33158), NWO (project no. 047.009.015), and Ministry of Industry and Science of the Russian Federation, program of the financial support of the development of the instrumental basis of scientific institutions.

REFERENCES

1. D. P. Delmer, Annu. Rev. Plant Physiol. Plant Mol. Biol. **50**, 245 (1999).
2. R. M. Brown, Jr. and J. M. Saxena, Plant Physiol. Biochem. **38** (1/2), 57 (2000).
3. R. M. Brown, Jr., J. Macromol. Sci., Pure Appl. Chem. A **33** (10), 1345 (1996).
4. B. Ranby, Cellul. Chem. Technol. **31**, 3 (1997).
5. A. C. O'Sullivan, Cellulose **4**, 173 (1997).
6. R. J. Vietor, K. Mazeau, M. Lakin, and S. Perez, Biopolymers **54**, 342 (2000).

7. M. Wada, T. Okano, and J. Sugiyama, Cellulose **4**, 221 (1997).
8. M. Wada, T. Okano, and J. Sugiyama, J. Wood Sci. **47**, 124 (2001).
9. E. M. Debzi, H. Chanzy, J. Sugiyama, *et al.*, Macromolecules **24** (25), 6816 (1991).
10. J. Sugiyama, R. Young, and H. Chanzy, Macromolecules **24** (14), 4168 (1991).
11. R. H. Atalla and D. L. VanderHart, Science **223**, 283 (1994).
12. S. K. Cousins and R. M. Brown, Jr., Polymer **38** (4), 897 (1997).
13. J.-F. Sassi, P. Tekely, and H. Chanzy, Cellulose **7**, 119 (2000).
14. H. Yamamoto and F. Horii, Macromolecules **26** (6), 1313 (1993).
15. A. Hirai and F. Horii, JCR Annu. Rep. **6**, 28 (1999).
16. US Patent No. 4,588,400; 4,655,758; 4,960,763; EP 186495; EP 323717.
17. US Patent No. 4,742,164; 5,009,797; 5,011,596; JP 3032726; 63295793.
18. S. Yamanaka, M. Ishihara, and J. Sugiyama, Cellulose **7**, 213 (2000).
19. H. Yamamoto and F. Horii, Macromolecules **26** (6), 1313 (1993).
20. H. Yamamoto, F. Horii, and A. Hirai, Cellulose **3**, 229 (1996).
21. A. Hirai, M. Tsuji, H. Yamamoto, and F. Horii, Cellulose **5**, 201 (1998).
22. Yu. G. Baklagina, A. K. Khripunov, A. N. Tkachenko, *et al.*, Zh. Prikl. Khim. (2003) (in press).
23. A. K. Khripunov, A. A. Tkachenko, Yu. B. Moskvicheva, *et al.*, *Biotechnology and Genetics* (N. Novgor. Gos. Univ., Nizhni Novgorod, 1991), p. 54.
24. S. Hestrin, in *Methods in Carbohydrate Chemistry*, Ed. by R. L. Whister (Academic, New York, 1963), Vol. 1, Chap. 8, p. 4.
25. A. K. Khripunov and A. A. Tkachenko, RF Patent No. 2,141,530 (20 November 1999); RF Patent No. 2,189,394 (20 October 2002).
26. V. V. Biryukov and V. M. Kantere, *Optimization of Periodical Processes of Microbiological Synthesis* (Nauka, Moscow, 1985), p. 32.
27. *Cellulose Chemistry and Its Applications*, Ed. by T. P. Nevell and S. H. Zeronian (Ellis Horwood, Chichester, 1985), Sect. 2.6.1.4.
28. T. I. Borisova, G. A. Petropavlovskiĭ, and N. E. Kotel'nikova, Vysokomol. Soedin. A **21** (9), 2031 (1979).
29. S. V. Gladchenko, T. I. Borisova, É. I. Larina, and G. A. Petropavlovskiĭ, Vysokomol. Soedin. B **34** (3), 21 (1992).
30. T. Iwata, L. Indrarti, and J.-I. Azuma, Cellulose **5**, 215 (1998).
31. S. Kimura and T. Itoh, Protoplasma **194**, 151 (1996).

Translated by L. Man

Crystallography Reports, Vol. 48, No. 5, 2003, pp. 763–767. Translated from Kristallografiya, Vol. 48, No. 5, 2003, pp. 821–825.

STRUCTURE OF MACROMOLECULAR COMPOUNDS

Dedicated to the 60th Anniversary of the Shubnikov Institute of Crystallography of the Russian Academy of Sciences

X-ray Diffraction Study of the Complex of the Enzyme SAICAR Synthase with Substrate Analogues

D. V. Urusova*, S. V. Antonyuk, A. I. Grebenko*, V. S. Lamzin***, and V. R. Melik-Adamyan***

** Shubnikov Institute of Crystallography, Russian Academy of Sciences, Leninskiĭ pr. 59, Moscow, 119333 Russia*
e-mail: dasha@ns.crys.ras.ru
e-mail: mawr@ns.cryst.ras
*** CCLRC Daresbury Laboratory, Daresbury, Warrington, Cheshire, WA4 4AD UK*
e-mail: S. Antonyuk@dl.ac.uk
**** European Molecular Biology Laboratory, EMBL Hamburg Outstation, c/o DESY, Notkestrasse 85, Hamburg, 22603 Germany*
e-mail: Victor@embl-hamburg.de
Received April 21, 2003

Abstract—The three-dimensional structure of the complex of the enzyme SAICAR synthase with analogues of natural substrates, namely, phosphoribosylaminoimidazolecarboxamide (AICAR) and succinic acid, was determined and refined by methods of protein crystallography. Two AICAR-binding sites were revealed in the protein molecule. One of these sites is located in the active center of the enzyme in the vicinity of the ATP-binding site, which has been found in the complex of SAICAR synthase with ATP that had been studied earlier. The second AICAR-binding site is located at the periphery of the protein molecule and coincides with the additional ATP-binding site present in the complexes studied earlier. The binding site of succinic acid was revealed in the active center of the enzyme in the vicinity of the AICAR molecule. The electron density distribution for the AICAR molecule in the active center is indicative of the possible lability of the atomic group of the adenine base. © *2003 MAIK "Nauka/Interperiodica".*

The enzyme SAICAR synthase (EC 6.3.2.6) catalyzes the seventh step of the biosynthesis of purine nucleotides in cells of different living organisms, such as bacteria, plants, and animals, thus providing the synthesis of 5'-phosphoribosyl-4-*N*-succinocarboxamide-5-aminoimidazole (SAICAR) from 5'-phosphoribosyl-5-aminoimidazole-4-carboxylate (CAIR) and aspartic acid in the presence of adenosinetriphosphate and Mg ions. The reaction is accompanied by hydrolysis of ATP to ADP and inorganic phosphate.

The present study is a continuation of our investigation of the structure of SAICAR synthase and mechanism of its enzymatic reaction. Earlier, we established the three-dimensional structures of the native enzyme (PDB, 1*a*48) [1, 2] and two its complexes with ATP (PDB, 1*obd*, 1*obg*) [3]. The active center of native SAICAR synthase has the cavity in the center of the molecule (presumably, the active center of the enzyme). Two sulfate ions were revealed in this cavity at a distance of about 17 Å from each other. The study of the three-dimensional structures of the complexes with ATP demonstrated that one of the phosphate groups of ATP occupies the site of one of the sulfate ions. This site was called the main ATP-binding site, because it is located in the active center of the protein molecule and binds the ATP molecule involved in the enzymatic reaction. An additional ATP-binding site was found in a small cavity at the periphery of the protein molecule (in its amino-terminal domain). Probably, this site fulfils the regulatory function in the action of the enzyme.

The aim of the present study was to determine the binding sites of CAIR and aspartic acid substrates in the enzyme. Instead of natural substrates, we used 5'-phosphoribosyl-5-amino-4-imidazolecarboxamide (AICAR), which is a more stable analogue of CAIR, and succinic acid, which is an analogue of aspartic acid, to prepare the enzyme–substrate complex. The only difference between AICAR and CAIR, which are nucleotides with an incomplete adenine base, is that AICAR contains the NH_2 group instead of the OH group of carboxylate present in CAIR. Succinic acid differs from aspartic acid by the absence of the amino group.

1063-7745/03/4805-0763$24.00 © 2003 MAIK "Nauka/Interperiodica"

Table 1. Statistical characteristics of the set of the X-ray diffraction data collected from the crystals of the SS + AIC + SUC complex

Wavelength, Å	0.8428
a, *b*, *c*, Å	61.03, 62.84, 78.60
Number of measured reflections	75822
R_{int}	0.033
Redundancy	6.0
Resolution range, Å	48.80–1.30
Resolution range for the last shell, Å	1.31–1.30
Completeness of the set, %	97.2
Completeness in the last resolution shell, %	86.8
$\langle I\rangle/\langle\sigma\rangle$	24.6
$\langle I\rangle/\langle\sigma\rangle$ in the last resolution shell	2.75

Table 2. Statistical characteristics of the refined model of the SS + AIC + SUC complex

R factor, %/number of reflections	18.1/69138
R_{free} factor, %/N_{free}	21.3/3693
Dispersion precision index (DPI), Å [9]	0.064
Number of protein atoms	2552
Number of solvent molecules	465
Number of atoms of AICAR in the major binding site	13
umber of atoms of AICAR in the additional binding site	22
Number of atoms of succinic acid in the major binding site	7
Number of sulfate ions	3
R.m.s. deviation from the ideal interatomic distances:	
1–2	0.015
1–3	0.035
1–4	0.032
$\langle B\rangle$ factor for main-chain atoms, Å^2	18.10
$\langle B\rangle$ factor for side-chain atoms, Å^2	24.46
$\langle B\rangle$ factor for solvent molecules, Å^2	31.87

The solution and refinement of the three-dimensional structure of this complex, which is hereinafter denoted as SS + AIC + SUC (SS is SAICAR synthase, AIC is AICAR, and SUC is succinic acid), revealed the binding sites of the substrate analogues.

MATERIALS AND METHODS

Crystallization of the Complex

Crystals of the SS + AIC + SUC complex were grown by cocrystallization of the protein with AICAR and succinic acid by the vapor-diffusion hanging-drop method at room temperature. The mother liquor consisted of the protein (24 mg/ml), 1 M ammonium sulfate, 0.1 M AICAR, 0.1 M succinic acid, and a 0.05 M Tris-HCl buffer (pH 7.5). The reservoir solution was composed of 2.25 M ammonium sulfate, 0.1 M succinic acid, and a 0.05 M Tris-HCl buffer (pH 7.5).

X-ray Data Collection

The X-ray-diffraction data were collected from crystals of the complex under study using synchrotron radiation in the European Molecular Biology Laboratory (Hamburg, Germany) on the DORIS storage ring (4.5 GeV) with the use of an Imaging Plate detector. The X-ray intensities were measured at 100 K. Before the low-temperature X-ray study, the crystals were soaked in a cryosolution containing a 30% saturated solution of glucose, 2.5 M ammonium sulfate, and a 0.05 M Tris-HCl buffer (pH 7.5).

The experimental X-ray data were processed using the DENZO/SCALEPACK program package [4]. The statistics of X-ray data collection are listed in Table 1.

Determination of the Structure of the Enzyme–Substrate Complex

The crystals of the SS + AIC + SUC complex were isomorphous with the crystals of the native enzyme. Hence, we used the atomic coordinates of native SAICAR synthase established at a resolution of 1.9 Å [1, 2] as the starting model for the refinement of the three-dimensional structure of the complex. The refinement was carried out using the REFMAC program [5] in combination with the ARP program [6], which allowed us to model the solvent structure. Manual improvement of the model was performed on a graphics station using the O program [7] by analyzing the difference electron-density syntheses, which were calculated with the coefficients $(2F_o - F_c, \varphi_c)$ and $(F_o - F_c, \varphi_c)$, where F_o and F_c are the observed and calculated magnitudes of structure amplitudes, respectively, and φ_c are the phases of structure factors calculated from the atomic model.

The atomic coordinates of the substrates (AICAR and succinic acid) were determined from the difference electron-density syntheses calculated with the coefficients $(F_o - F_c, \varphi_c)$ after several first cycles of the refinement and were partially included in the subsequent refinement of the model.

The results of the structure refinement for the complex of SAICAR synthase are listed in Table 2.

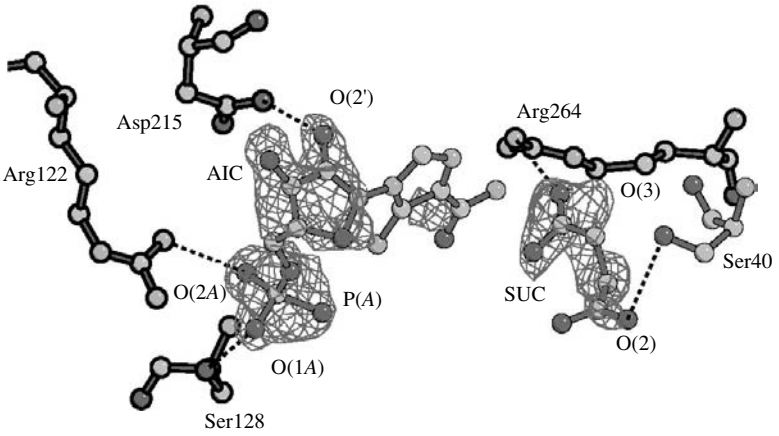

Fig. 1. Difference electron density and the model of the AICAR molecule in the active center of the enzyme. The contour lines correspond to the omitted synthesis ($F_o - F_c$, φ_c) at the 3σ level. The position of the incomplete adenine base, which was not supplied with a complete electron density, was determined from the arrangement of the ribose ring. Hydrogen bonds with amino acid residues of SAICAR synthase (Arg242 is omitted for clarity) are indicated by dashed lines.

RESULTS AND DISCUSSION

Analysis of the difference electron-density syntheses demonstrated that the SAICAR-synthase molecule has two AICAR-binding sites.

One of these sites is located in the active center of the enzyme, the positions of the phosphate group of AICAR coinciding with the binding site of one of the sulfate ions in the structure of the native enzyme [2]. Another AICAR-binding site is located at the periphery of the protein molecule and coincides with the additional ATP-binding site in the complexes studied previously [3].

The difference electron density corresponding to the AICAR molecule in the active center of the enzyme is rather complete only for the phosphate group and the ribose ring (Fig. 1). The atomic group of the incomplete adenine base is characterized by a poor electron density and relatively high temperature factors, which is indicative of the probable lability of this group. Because of this, the atomic coordinates of the adenine base were not used in the structure refinement, whereas the atoms of the phosphate group and the ribose ring were included in the last cycles of the refinement procedure together with the atoms of the protein. In the refined model, the oxygen atoms of the phosphate group of AICAR are fixed by hydrogen bonds with the amino-acid residues Arg122, Ser128, and Arg242 of the enzyme. The ribose ring forms the O(2')···O(D2) Asp125 hydrogen bond (Table 3).

As mentioned above, the second AICAR-binding site in the protein molecule coincides with the additional ATP-binding site in the ATP-containing complexes [3]. The adenine base is fixed by the N(1)···O Leu108, N(1)···O Val77, and O(6)···N Leu108 hydrogen bonds. The ribose ring forms the O(2')···O(E1) Glu62 hydrogen bond. The oxygen atoms of the phosphate group are bound to the protein only via the N(Z) Lys66···O(2A) interaction (Table 3). The temperature factors for the atoms of AICAR, like those for ATP, increase when one passes from the adenine base to the phosphate group, which is exposed to the surrounding

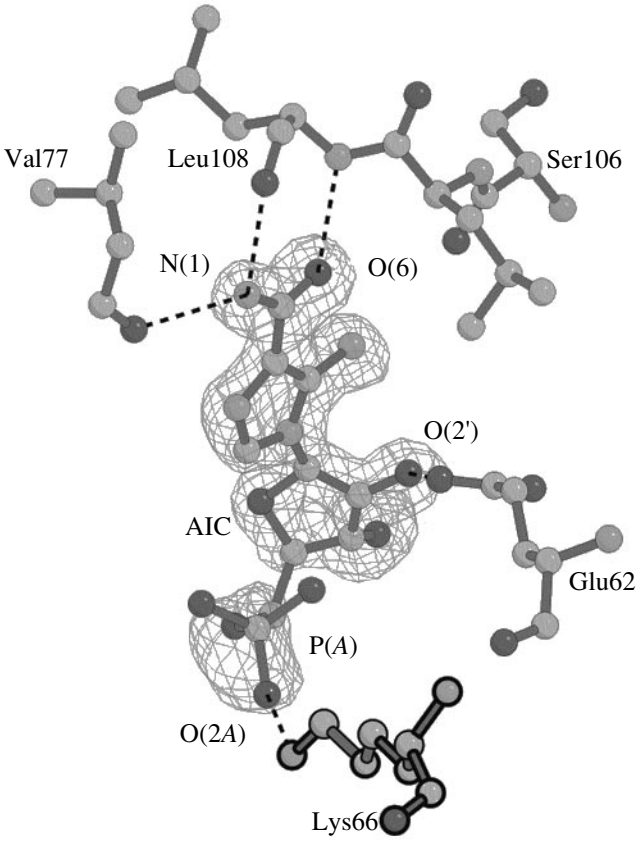

Fig. 2. Difference-electron density corresponding to the model of the AICAR molecule in the additional binding site. The omitted synthesis ($F_o - F_c$, φ_c) was calculated at the 3σ level. Hydrogen bonds with amino acid residues of SAICAR synthase are indicated by dashed lines.

Table 3. Hydrogen bonds between atoms of the protein and the substrates in the SS + AIC + SUC complex

Atoms	Bond length, Å
Major binding site of AICAR	
N(*H*1)Arg122···O(2*A*)	2.87
NSer128···O(2*A*)	2.95
O(*G*)Ser128···O(1*A*)	2.70
O(*D*2)Asp215···O(2')	2.83
N(*H*2)Arg242···O(2*A*)	3.00
Binding site of succinic acid	
O(*G*)Ser40···O(2)	3.18
N(*H*1)Arg264···O(3)	3.14
Additional binding site of AICAR	
O(*E*1)Glu62···O(2')	2.64
N(*Z*)Lys66···O(2*A*)	2.85
Oval77···N(1)	2.98
NLeu108···O(6)	2.79
OLeu108···N(1)	2.96

solution (Fig. 2). The role of this binding site in the complex under consideration, like that in the complex with ATP, remains unclear. Presumably, the similar mode of binding observed in these two complexes is related to the structural similarity of the ATP and AICAR molecules providing the formation of identical hydrogen bonds.

It should be noted that we initially prepared and studied the complex with AICAR and aspartic acid. However, we failed to reveal some atoms of the adenine base of AICAR as well as the atoms of aspartic acid. We hypothesized that the positive charges of the amino groups of AICAR, which is the synthetic substrate, and aspartic acid, which is the natural substrate, hinder the arrangement of these molecules in the sites of true substrates. Because of this, we chose succinic acid (which is devoid of the amino group) instead of aspartic acid. Certain advantages were gained, but, unfortunately, the desired results were not achieved. Nevertheless, analysis of the difference electron density suggested that the molecule of succinic acid in the SS + AIC + SUC complex faces the AICAR molecule in the vicinity of the loop that links the antiparallel sheets β*A*4 and β*A*5 [1] (Fig. 3). In spite of the absence of the electron density for the O(1) atom and relatively high temperature factors for all atoms of succinic acid, their coordinates were used to refine the structural model. The position of the molecule of succinic acid is fixed by hydrogen bonds with the amino-acid residues Ser40 and Arg264 (Fig. 1, Table 3).

Interestingly, difference Fourier maps of the SS + AIC + SUC complex showed an electron density in proximity to the residue Tyr42, which cannot be attrib-

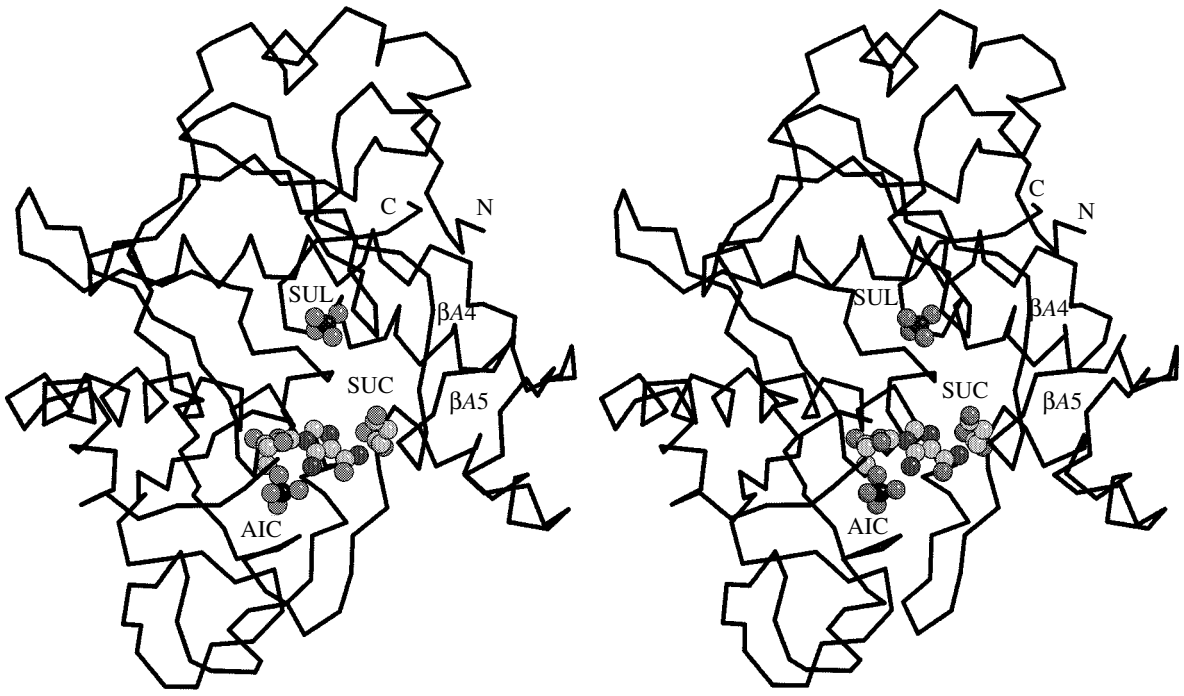

Fig. 3. Stereoview of the arrangement of substrate analogues in the molecule of SAICAR synthase; SUL is the sulfate ion corresponding to the position of one of the phosphate groups of ATP in the complexes with ATP [1, 2]. The N and C termini of the polypeptide chain and the β sheets (β*A*4 and β*A*5) are shown.

uted to the presence of bound water molecules. We fitted the second molecule of succinic acid to this electron density and included its coordinates in the refinement. Probably, the presence of this molecule is a consequence of the very high concentration of succinic acid used for preparation of the complex.

It is noteworthy that the main chain between the amino acid residues Leu231 and Val235 is statistically distributed over two positions. In complexes with ATP, this phenomenon was not observed. Apparently, the ATP binding in the active center of the enzyme stabilizes this region of the SAICAR-synthase molecule.

ACKNOWLEDGMENTS

This study was supported by the European Molecular Biology Organization (EMBO, grant no. PX310-1998) and the Russian Foundation for Basic Research (project nos. 99-04-48570 and 99-02-16191).

REFERENCES

1. V. M. Levdikov, A. I. Grebenko, V. V. Bapynin, *et al.*, Kristallografiya **41** (2), 293 (1996) [Crystallogr. Rep. **41**, 275 (1996)].
2. V. M. Levdikov, V. V. Barynin, A. I. Grebenko, *et al.*, Structure (London) **6**, 363 (1998).
3. S. V. Antonyuk, A. I. Grebenko, V. M. Levdikov, *et al.*, Kristallografiya **46** (4), 687 (2001) [Crystallogr. Rep. **46**, 620 (2001)].
4. Z. Otwinowski and V. Minor, Methods Enzymol. **276**, 307 (1997).
5. G. N. Murshudov, A. A. Vagin, and E. J. Dodson, Acta Crystallogr., Sect. D: Biol. Crystallogr. **53**, 240 (1997).
6. V. S. Lamzin and K. S. Wilson, Acta Crystallogr., Sect. D: Biol. Crystallogr. **49**, 129 (1993).
7. T. A. Jones, J. Y. Zou, S. W. Cowan, and M. Kjeldgaard, Acta Crystallogr., Sect. A: Found. Crystallogr. **47**, 110 (1991).
8. S. C. Hartman and J. M. Buchanan, J. Biol. Chem. **233**, 456 (1957).
9. W. J. Cruickshank, in *Proceedings of the CCP4 Study Weekend on Macromolecular Refinement* (1996), p. 11.
10. R. M. Esnouf, J. Mol. Graphics **15**, 132 (1997).

Translated by T. Safonova

Crystallography Reports, Vol. 48, No. 5, 2003, pp. 768–795. Translated from Kristallografiya, Vol. 48, No. 5, 2003, pp. 826–854.

REAL STRUCTURE OF CRYSTALS: REVIEWS

Dedicated to the 60th Anniversary of the Shubnikov Institute of Crystallography of the Russian Academy of Sciences

Magnetoplastic Effect: Basic Properties and Physical Mechanisms

V. I. Alshits, E. V. Darinskaya, M. V. Koldaeva, and E. A. Petrzhik

Shubnikov Institute of Crystallography, Russian Academy of Sciences, Leninskiĭ pr. 59, Moscow, 119333 Russia

e-mail: alshits@ns.crys.ras.ru

Received April 9, 2003

Abstract—This paper presents a review of the main results of investigations into the magnetoplastic effect, which manifests itself in motion of dislocations in crystals exposed to magnetic fields. The dependences of the mean free path of dislocations on the induction and direction of the magnetic field, the magnetic treatment time, the temperature, and the type and concentration of impurities are studied for NaCl, LiF, CsI, Zn, Al, and InSb crystals. The threshold magnetic field B_c below which the effect is absent, the saturation field B_0 above which the mean free paths of dislocations remain constant with an increase in the magnetic induction B, and the critical frequency ν_c of rotation of a sample in the magnetic field above which the effect disappears are examined. The quantities B_c, B_0, and ν_c are investigated as functions of the basic physical parameters. It is found that the magnetoplastic effect is highly sensitive to X-ray radiation at low doses and to simultaneous action of an electric field or mechanical loading. The hardening of NaCl(Pb) crystals in the magnetic field is revealed. The theoretical interpretation is proposed for all the findings and dependences observed. *© 2003 MAIK "Nauka/Interperiodica".*

CONTENTS

1. INTRODUCTION

The first experimental evidence for the possibility of modifying the properties of lattice defects in nonmagnetic crystals under the action of external magnetic fields has long since been obtained. In particular, Zagoruiko [1] studied the influence of external electric fields on the mobility of charged dislocations in NaCl crystals and incidentally revealed dislocation motion in pulsed magnetic fields. Taking into account that the majority of dislocations reversed their direction of motion with a change in the pulse polarity, this author made the assumption (most likely, fairly justified) that the driving force of the observed motion is the electrostatic effect of vortex electric fields on charged dislocations.

1063-7745/03/4805-0768$24.00

More recently, Sharp and Avery [2] argued that the treatment of NaCl and KCl crystals in external magnetic fields in their experiments led to weak, but measurable, magnetization of samples, which was explained by the magnetic ordering of spins in dislocation cores. That work had attracted the particular interest of experimenters and theorists, because the case in point was an observation of theoretically forbidden one-dimensional ferromagnetism. However, it should be noted that the justification of the interpretation proposed by those authors for the results obtained is open to question. In actual fact, the dislocation density was neither varied nor measured in [2]. Subsequent attempts to reproduce these data failed.

Distler *et al.* [3] found that the decoration pattern of the surface of NaCl crystals (containing $CdCl_2$ and $PbCl_2$ impurities) sharply changed within some time (from 10 to 25 days) after treatment in an ac magnetic field. The authors attributed this effect to magnetically stimulated decomposition of point-defect complexes in metals. These data raised lively debates among researchers, which, unfortunately, resulted neither in the understanding of the physical nature of the effect nor in the recognition of its existence. The problem was complicated by the indirect character of measurements and analysis of the observed changes on the basis of a qualitative comparison of the decoration patterns.

The history of investigations into the influence of the magnetic field on the macroplacticity of a number of nonmagnetic crystals appears to be even more dramatic [4–7]. Kravchenko theoretically predicted certain anomalies in the electron retardation of dislocations in metals in magnetic fields, which gave impetus to research in this direction. The relevant magnetic effects in low-temperature plasticity of copper and aluminum crystals were first found by Galigan and Pang [4]. Their results were subsequently reproduced by Bol'shutkin and Desnenko [7]. Then, they replaced stainless-steel dies (which were identical to those used in [4] and considered nonmagnetic) by textolite dies in a deformation-testing machine. As a result, the deformation kinetics became completely insensitive to the magnetic field. This is quite consistent with the results obtained by Grishin *et al.* [9], who showed that the anomalies predicted by Kravchenko should be observed only in the case when the magnetic field direction and dislocation lines are strictly parallel to each other. Certainly, this could not be expected for numerous bent dislocations under macroplastic deformation of metals. These findings cast aspersions not only on the data obtained in [4] but also on other investigations in this field. However, some of the above results have a direct relationship to the magnetoplastic effect discussed in the present work. The case at hand is a number of spin-dependent phenomena that determine the magnetosensitivity of interaction between lattice defects, primarily, between dislocations and paramagnetic impurity centers.

The magnetoplastic effect was originally discovered by our research group in 1985. This effect manifested itself as relaxation of the dislocation structure in NaCl crystals exposed to a constant magnetic field in the absence of mechanical loading. It was found that freshly introduced dislocations in samples subjected to magnetic treatment at $B = 0.2$–0.5 T for several minutes moved over distances of tens and hundreds of microns. The first response of the authors to this incidental observation was quite natural: "it is impossible." However, all attempts to "disprove" ourselves, to find a methodical error, and to elucidate the origin of the artefact led only to the accumulation of new well-reproducible regularities. As a result, within more than a year after the first observation, we prepared our first paper on this effect [10]. At that time, we did not have a clear idea of the physical mechanism of the phenomenon but were already strongly convinced that this is not artefact.

Within only a few years, we were led to the inference regarding the specific nature of the magnetoplastic effect [11, 12]. In this effect, the role played by the magnetic field is reduced not to an additional force action on dislocations that promotes their thermally activated depinning from local obstacles but to the breaking of local barriers due to specific spin processes in a dislocation–paramagnetic center system. In a large number of papers [11–37] published after our first work [10], we investigated different manifestations of magnetically stimulated mobility of individual dislocations in alkali halide crystals and nonmagnetic metals and semiconductors. All the obtained data count in favor of the initial hypothesis [12], according to which, in the magnetic field, the spin forbiddenness of a particular electronic transition in the dislocation–impurity system is removed with some time. This in turn leads to a considerable decrease in the energy of the dislocation–impurity interaction and the depinning of the dislocation from the point defect. A further motion of the dislocation to the next pinning center proceeds in the field of long-range stresses generated by other dislocations. Then, the process occurs over and over until the magnetic field is switched off or the dislocation appears to be in a region with low stresses. Therefore, the dislocation motion is associated with the self-organization of dislocations and results in their more equilibrium distribution.

Investigations performed by other researchers revealed that the magnetoplastic effect can manifest itself in macroplastic properties of crystals. In particular, according to [38–41], the active stressing of alkali halide crystals in a magnetic field at a constant strain rate ($\dot{\varepsilon}$ = const) leads to a substantial (severalfold) decrease in the yield stress. In this case, the lower the strain rate ε and the higher the magnetic induction B, the larger the decrease in the yield stress. Moreover, all stages of the plastic deformation are shortened; i.e.,

they occur in shorter strain ranges. The active stressing of PbS semiconductor crystals under the same conditions results in similar effects [42]. In [43], the influence of the magnetic field on the macroplasticity of NaCl crystals was studied under deformation at a constant rate of an increase in the stress ($\dot{\sigma}$ = const). In this case, the application of the magnetic field in the course of deformation leads to an increase in the slope of the curve $\varepsilon(\sigma)$, i.e., in the reciprocal of the hardening coefficient $d\varepsilon/d\sigma$. As follows from the data obtained in [44], the creep of crystals, i.e., the time dependence $\varepsilon(\sigma)$ at a constant load ($\dot{\sigma}$ = const), is also sensitive to the magnetic field. In [45, 46], it was demonstrated that the magnetic field appreciably affects the kinetics of amplitude-dependent internal friction in KCl, LiF, and Al crystals.

All the aforementioned macroplastic effects are observed only in an external magnetic field and disappear after switching off the field. Most likely, these are macroscopic manifestations of the magnetoplastic effect, which was studied in our works [10–36] for individual dislocations. However, Golovin and Morgunov [47–49] showed that there exists a magnetoplastic effect of another type when the preliminary magnetic treatment transforms the state of impurity complexes not in the course of their interaction with dislocations but prior to the introduction of fresh dislocations into a crystal; as a result, dislocations move more freely through the crystals with these complexes already after switching off the field. This effect first found in quenched alkali halide crystals [47–49] is also characterized by microplastic and macroplastic manifestations. Among these are an increase in the mobility of individual dislocations in NaCl [47–49] and Si [50] crystals and a decrease in the microhardness of alkali halide [51, 52], ferroelectric [53], and molecular [54, 55] crystals and even polymers [56, 57] subjected to magnetic treatment. It is quite possible the aforementioned phenomena observed by Distler *et al.* [3] (see also [58]) are also associated with the effect under consideration.

In the present work, we will restrict ourselves to detailed analysis of the magnetoplastic effect of the first type and its macroplastic manifestations studied in our works [10–37]. We will not dwell on methodical details and experimental techniques, which can be found in original papers. We also do not seek to describe in detail all the available experimental data. The emphasis will be given to the logic of research. Analysis of the experimental results, consideration of different hypotheses, and their experimental verification will gradually lead us to the understanding of the physical nature of the observed effect.

2. CHARACTERISTICS OF THE CRYSTALS STUDIED

We studied alkali halide crystals with different degrees of ionicity and cubic lattices of different types (LiF and NaCl with faced-centered lattices and CsI with a simple cubic lattice), Zn (faced-centered cubic lattice) and Al (hexagonal close-packed lattice) metal single crystals, and InSb semiconductor crystals of the sphalerite type. In the magnetic properties, NaCl, LiF, CsI, Zn, and InSb crystals are diamagnets and Al crystals are weak paramagnets.

The characteristics of the studied alkali halide crystals are listed in the table. The *metal single crystals* were grown from Zn (99.979) at the Institute for Low Temperature Physics and Engineering (Kharkov) and spectroscopically pure Al at the Institute of Metal Physics (Ural Division, Russian Academy of Sciences). The *semiconductor crystals* InSb had different types of conductivity and dopant contents: *n*-InSb (1×10^{14} and 1×10^{18} cm^{-3}) and *p*-InSb (5×10^{13}, 1.6×10^{14}, 1×10^{17}, and 1×10^{18} cm^{-3}).

The technique of preparing samples is described in detail in [10–16, 31]. The alkali halide crystals were preliminarily annealed, followed by chemical polishing and introduction of dislocations (by a weak shock). The density of introduced fresh dislocations $\rho_f \sim 10^4$ cm^{-2} was equal in order of magnitude to the density of initial aged dislocations. The Al crystals were not subjected to annealing. The dislocation density in these crystals was of the order of 10^4–10^5 cm^{-2}. The annealing of the Zn crystals resulted in an almost twofold decrease in the dislocation density to $(2–3) \times 10^{-5}$ cm^{-2}. Fresh dislocations were not introduced into these crystals. Therefore, the relative density of mobile dislocations in metal samples was always considerably lower than that in the alkali halide crystals.

3. EXPERIMENTAL TECHNIQUE AND RESULTS OF THE FIRST INVESTIGATIONS

After preliminary chemical etching of the surface with the aim of determining the initial positions of dislocations, samples $\sim 3 \times 3 \times 8$ mm^3 in size were exposed to a constant uniform field $B = 0.02$–2 T produced by an electromagnet for a time t from several seconds to 1 h (test experiments were also performed with a permanent magnet). In this case, the crystals were not subjected to mechanical loading or other external actions in addition to magnetic treatment. After switching off the magnetic field, the samples were etched once again. The etch patterns were examined and photographed with a Neophot-2 microscope. It was found that the treatment of crystals for several minutes in a relatively low constant magnetic field leads to noticeable displacements of dislocations by tens and hundreds of microns. Note that both edge and screw dislocations participate in the motion. However, a sufficient statistic for paths of screw dislocations could be achieved only for the LiF crystals. Therefore, all the data on screw dislocations were obtained for these crystals.

Characteristics of alkali halide crystals

Crystal	Impurity content			Yield stress τ_y, kPa	Manufacturer, growth method
	total, mol/mol	introduced impurity			
		designation	mol/mol		
NaCl-1	$<10^{-5}$			400	Nikol'sk, Kyropoulos method
NaCl-2	$\leq 10^{-5}$			500	Leningrad Optomechanical Plant, Kyropoulos method
NaCl-2(Ni)	$\leq 10^{-5}$		Ni: $<6\times10^{-8}$	500	
			Ni: $<6\times10^{-8}$	500	
NaCl-3(Ca)	$<5\times10^{-7}$	$C_{Ca}^{(1)}$	5×10^{-7}	150	Institute of Physics and Optics, Stockbarger method
		$C_{Ca}^{(2)}$	1×10^{-6}	200	
		$C_{Ca}^{(3)}$	1×10^{-5}	430	
		$C_{Ca}^{(4)}$	1×10^{-4}	790	
NaCl-3(Li)	Ca: 5×10^{-7}	C_{Li}	1×10^{-4}	230	
NaCl-3(Pb)	Ca: 5×10^{-7}	$C_{Pb}^{(1)}$	1×10^{-6}		
		$C_{Pb}^{(2)}$	1×10^{-5}		
CsI	$<1.2\times10^{-6}$			90	Leningrad Optomechanical Plant
LiF	Mg: 10^{-5}			300	Kharkov, Institute of Single Crystals

Figure 1 shows a typical etch pattern for the {100} face of the NaCl-1 crystal [10]. This etch pattern indicates that edge dislocations in the presence of magnetic field move in the {110} easy-slip plane along the ⟨110⟩ direction. Similar etch patterns were observed for all the crystals. Note that the basal slip of edge dislocations along the $[11\bar{2}0]$ direction was investigated in the Zn crystals. The directional distribution of dislocation motion over the sample as a whole is rather chaotic but is characterized by local correlations.

It turned out that, unlike the pulsed magnetic treatment [1], the change in the polarity of the constant magnetic field is not attended by a change in the direction of dislocation motion. However, the effect somewhat depends on the magnetic field orientation with respect to dislocations and the slip plane. In particular, no motion of rectilinear dislocations parallel to the magnetic field is observed in the alkali halide crystals.

The quantitative processing of the experimental data consisted in constructing the histograms of dislocations paths. Then, the mean free path l of dislocations under particular experimental conditions (the magnetic induction B, the time t of magnetic treatment of the sample, the temperature T, the impurity concentration C, the dislocation density ρ, etc.) was determined in a standard way. Typical histograms of dislocation paths in the NaCl crystals and the corresponding mean free paths of dislocations [18] are depicted in Fig. 2. It is important that the experimental data obtained in the magnetic fields produced by the electromagnet and the permanent magnet coincide with each other.

One more useful characteristic determined from the experimental data is the density ρ_m of mobile dislocations or, more precisely, the ratio of ρ_m to the density ρ_f of freshly introduced dislocations. The experimental data show that, with an increase in the induction B and the time t of magnetic treatment of the samples, the relative density ρ_m/ρ_f of dislocations moving in the magnetic field appreciably increases and can be as high as

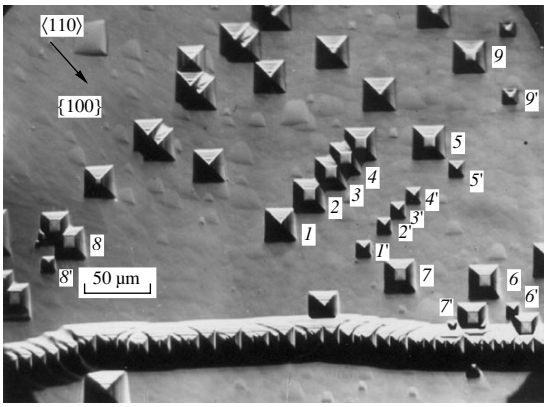

Fig. 1. Etch patterns illustrating the dislocation motion in NaCl crystals in a constant magnetic field: (*1*–*9*) initial dislocation positions and (*1*'–*9*') dislocations positions after applying a magnetic field of 0.5 T for 2 min.

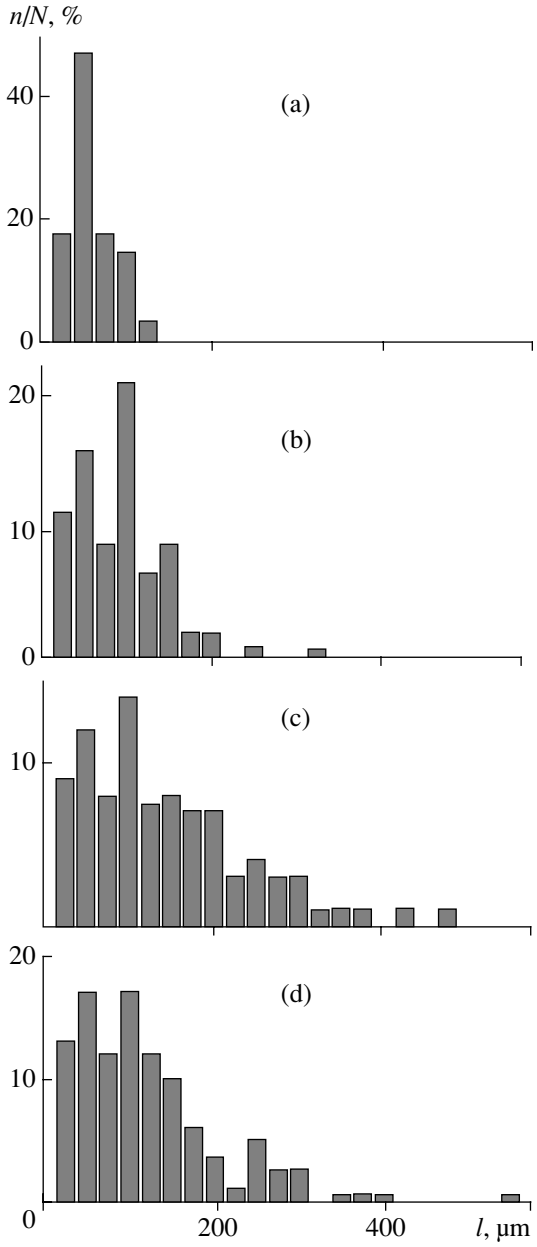

Fig. 2. Histograms of dislocation paths l in an NaCl crystal (at 293 K) for different times t of treatment in a magnetic field of 0.5 T. Treatment time t (min): (a) 1, (b) 3, (c) 5, and (d) 7. Mean free path of dislocations l (μm): (a) 48, (b) 75, (c) 128, and (d) 160.

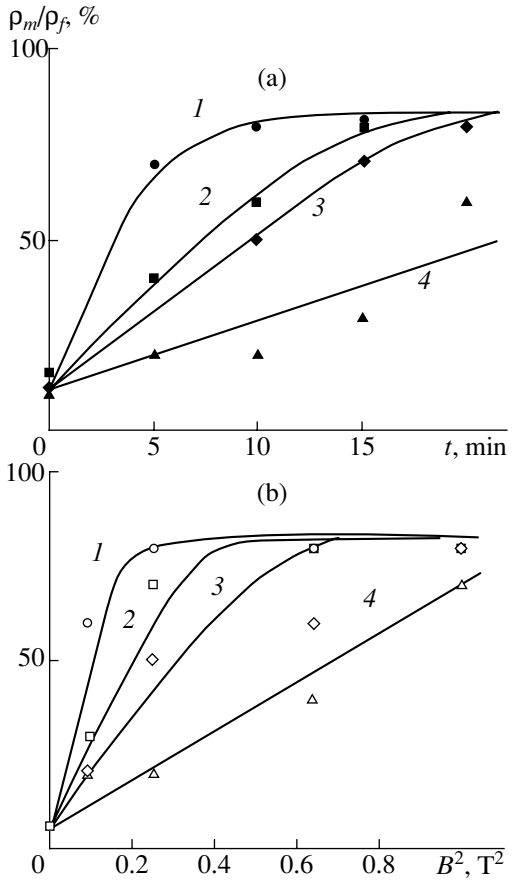

Fig. 3. Dependences of the relative density ρ_m/ρ_f of mobile dislocations in CsI crystals (at 293 K) on (a) the magnetic treatment time t at different magnetic inductions B and (b) the magnetic induction B at different magnetic treatment times t. Magnetic induction B (T): (a) (*1*) 1, (*2*) 0.8, (*3*) 0.5, and (*4*) 0.3. Treatment time t (min): (b) (*1*) 20, (*2*) 15, (*3*) 10, and (*4*) 5.

80–100% in the alkali halide crystals (see Fig. 3 for the CsI crystals [18, 20]).

As was noted above, fresh dislocations were not introduced into the metals. In this respect, the dislocation density ρ_m in these crystals was normalized to the total dislocation density ρ. The ratio ρ_m/ρ at saturation for the Al crystals was equal to 20%, which is sufficiently large. The dislocation density ρ in the Zn crystal was higher, and, correspondingly, the relative density ρ_m/ρ was lower. Note that the dislocation densities $\rho_m \sim 10^4$ cm^{-2} were high enough to be measured. It is clear that the higher the dislocation density ρ_m, the more representative the histogram and, hence, the smaller the number of samples that must be measured in order to obtain one point in the experimental curve.

4. DEPENDENCE OF THE MEAN FREE PATH OF DISLOCATIONS ON THE TIME, MAGNETIC FIELD ORIENTATION, AND DISLOCATION DENSITY

As follows from the experimental data, the mean free path l of dislocations linearly increases with an increase in the magnetic treatment time t for at least not too long times t and not too large values of the magnetic induction B and the dislocation density ρ. The linear dependences $l(t)$ measured for the NaCl-1 crystals at different orientations of the magnetic induction **B** (B = 0.5 T) with respect to the directions of lines **L** and Burgers vectors **b** of dislocations [11] are plotted in

Fig. 4. A regular increase in the mean free path l of dislocations with an increase in the magnetic treatment time and the sensitivity of this dependence to the field orientation **B** suggest that the observed dislocation motion in the magnetic field cannot be explained by the set of incident factors, such as the influence of the etchant, vortex fields, etc. However, these factors also manifest themselves as two spurious effects in the experimental dependences under consideration. The first effect, namely, the occurrence of nonzero background path $l(0)$ for linear dependences *1* and *3* in Fig. 4 is associated with the use of chemical etching for observing the dislocations. As was shown by Pariĭskiĭ *et al.* [59], the etching results in the depinning of a number of freshly introduced dislocations from surface obstacles and a weak related relaxation of the dislocation structure.

A parallel shift of linear dependence *2* with respect to linear dependence *3* is likely due to another spurious effect—the influence of vortex electric field (induced after switching on the electromagnet) on charged edge dislocations, which is similar to the aforementioned Zagoruiko effect [1]. Actually, in geometry *3*, this vortex field acts in the plane perpendicular to the slip plane of dislocations and does not affect their mean free path. By contrast, in geometry *2*, the vortex field is induced in the slip plane and can lead to the depinning of additional dislocations (occupying unstable positions) and to an increase in the mean free path. This assumption is supported by the observed increase in the background density $\rho_m(0)$ of mobile dislocations in geometry *2* and, primarily, by the disappearance of the spurious effect when the magnetic field increases gradually. The experimental verification demonstrated that, upon a sufficiently slow increase in the magnetic field, dependence *2* lowers and merges together with dependence *3*. On the other hand, additional switching-off and switching-on of the magnet results in an increase in the mean free path of dislocations in geometry *2* and does not affect this path in geometry *3* (Fig. 4).

The hypothesis of the electric origin of the switching-on effect is also confirmed by the fact that no similar changes were observed after switching on the magnet in experiments with the Zn [13] and Al [15] metal crystals, in which charged dislocations cannot exist. This effect is also not observed for screw and edge dislocations in the LiF crystals [16] but appears to be pronounced in the NaCl-3(Ca) [11] and CsI [16] crystals.

Returning to Fig. 4, we can make the inference that geometry *1*, in which the vector **B** is perpendicular to the dislocation line and makes an angle of 45° with the slip plane, is most preferable for observing the magnetoplastic effect in crystals of the NaCl type. As was noted above, the most unfavorable geometry is the parallel alignment of the field **B** and the dislocation line. In Fig. 4, this geometry corresponds to experimental point ◆ with the mean free path comparable to the background path associated with the etching. In the subsequent experiments, we, as a rule, used geometry *1*. Note that, for this geometry, the switching-on effect in the NaCl-1 crystals virtually does not lead to a change in the mean free paths of dislocations (Fig. 4) but changes the background density of mobile dislocations.

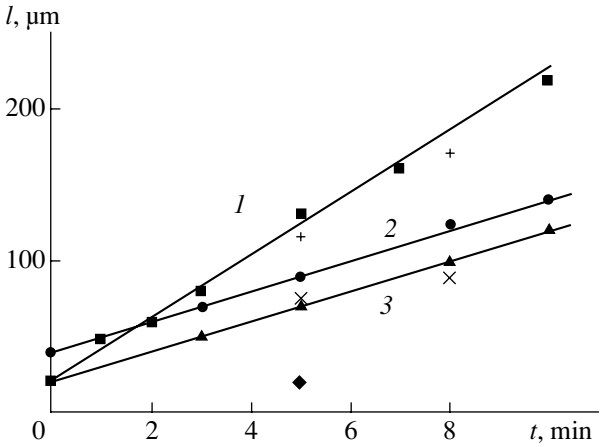

Fig. 4. Dependences of the mean free path l of dislocations in NaCl-1 crystals (at 293 K) on the magnetic treatment time t at different mutual orientations of the dislocation **L**, Burgers vector **b** of the dislocation, and the magnetic induction vector **B** (B = 0.5 T): (*1*) **B** ^ **b** = 45° and **B** ⊥ **L**, (*2*) **B** ⊥ **b** and **B** ⊥ **L**, (*3*) **B** ∥ **b** and **B** ⊥ **L**, (◆) **B** ⊥ **b** and **B** ∥ **L**, (+) the same as for orientation *2* with additional switching-off and switching-on of an electromagnet, and (×) the same as for orientation *3* with additional switching-off and switching-on of an electromagnet.

The dependences in Fig. 4 were obtained at the constant dislocation density $\rho \sim 10^4$ cm^{-2}. It was found that the mean free paths of dislocations in the samples with different dislocation densities differ from one another, all other factors being the same. Special investigations of the NaCl crystals at three dislocation densities $\rho \sim 10^4$, 10^5, and 2×10^5 cm^{-2} revealed that, at high dislocations densities ρ, the mean free path l of dislocations reaches a steady-state value. In this case, the higher the dislocation density ρ, the smaller the steady-state value (Fig. 5a). If the mean free path l of dislocations is normalized to the spacing of dislocations $1/\sqrt{\rho}$, this ratio $1/\sqrt{\rho}$ insignificantly depends on the dislocation density ρ (Fig. 5b) and reaches a steady-state value corresponding to the mean spacing of dislocations. A similar situation is characteristic of all the alkali halide and metal crystals (in particular, see Fig. 5c for Zn [13]). In essence, the parameter $1/\sqrt{\rho}$ determines the scale of measured relaxation paths of dislocations in the one-dimensional potential $U(x)$ formed by parallel dislocations in local crystal regions [35]. Hence, it follows that dislocations move in response to the long-range fields of internal stresses produced by surrounding dislocations and the magnetic field is responsible for the depinning of dislocations from local defects. In such a man-

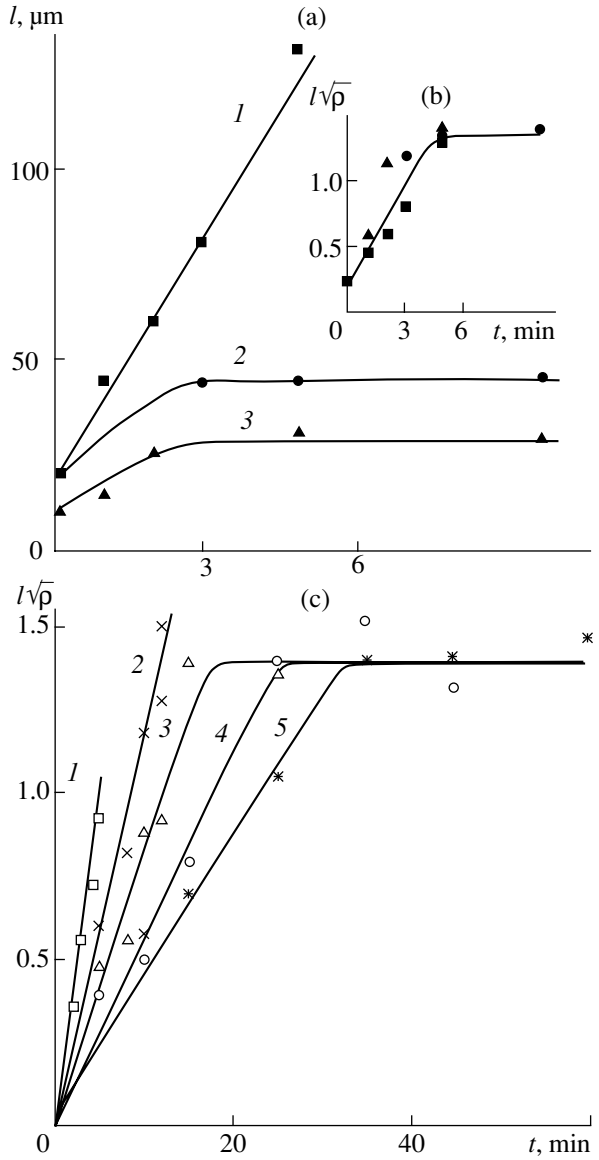

Fig. 5. Dependences of the mean free path l of dislocations in (a, b) NaCl-1 and (c) Zn crystals on the magnetic treatment time t at (a) different dislocation densities ρ (B = 0.5 T, T = 293 K) and (c) different magnetic inductions B (T = 293 K). (b) Dependences shown in panel (a) in the normalized coordinates. Dislocation density ρ (cm^{-2}): (a) (*1*) 1×10^4, (*2*) 1×10^5, and (*3*) 2×10^5. Magnetic induction B (T): (c) (*1*) 2, (*2*) 1.5, (*3*) 1.2, (*4*) 0.8, and (*5*) 0.5.

ner, the magnetically stimulated relaxation of the dislocation structure occurs in the crystal.

5. DEPENDENCE OF THE MEAN FREE PATH OF DISLOCATIONS ON THE MAGNETIC INDUCTION, PARAMAGNETIC IMPURITY CONCENTRATION, AND TEMPERATURE

As was noted above, the mean free path l and the density ρ_m of mobile dislocations increase with an increase in the magnetic induction B. The quantitative experimental investigation of the dependences $l(B)$ for the NaCl, CsI, LiF, Zn, and Al crystals demonstrated that these dependences are linear in B^2 in not very high fields at which the mean free path l is noticeably less than the steady-state value $1/\sqrt{\rho}$ [10–16]. This means that, under the given conditions, the mean free path l of dislocations can be written in the form

$$l = l_0 + aB^2, \tag{1}$$

where l_0 is the background mean free path associated with the aforementioned spurious effects. The corresponding dependences for the NaCl-3(Ca), NaCl-3(Pb), NaCl-2, and NaCl-2(Ni) crystals are plotted in Figs. 6a and 6b [11, 18].

The experimental study of the temperature dependence of the effect is extremely important for the subsequent interpretation of the phenomena. As can be seen from Fig. 6a, the mean free path of dislocations in the NaCl-3(Ca) crystals in the magnetic field does not depend on the temperature in the range 4.2–77 K and increases by only 15–20% with an increase in the temperature to 293 K. Similar temperature dependences of the mean free path of dislocations were observed for the Zn [13], Al [14], CsI, and LiF [16] crystals.

It turned out that the mean free path of dislocations in the magnetic field is sensitive to the type and concentration of impurities in the samples. For example, the presence of the Ni magnetically active impurity substantially increases the mean free path of dislocations in the NaCl-2(Ni) crystals as compared to that in the NaCl-2 crystals (Fig. 6b). It can be seen from Fig. 6b that no noticeable magnetoplasticity is observed for the NaCl-3(Pb) crystals. As will be shown below, these crystals are characterized not by the magnetoplasticity but by the magnetic hardening, which was revealed with the use of other experiments [30].

A number of the qualitative dependences $l_{B,C}(t)$ and $l_{t,C}(B)$ were measured for the NaCl-3(Ca) crystals at four different concentrations of Ca paramagnetic impurity [11]. The combined dependences $l_C(B^2t)$ (in the form of a fan of straight lines) are depicted in Fig. 7a. The section of these dependences $l_{B,t}(C)$ at fixed B = 0.5 T and t = 5 min (Fig. 7b) is of special interest. According to the data presented in Fig. 7b, we have

$$\Delta l = l - l_0 \propto 1/\sqrt{C}\,. \tag{2}$$

6. RELAY-RACE DISLOCATION MOTION

It can be seen from Fig. 3 that, after applying the magnetic field, the density ρ_m of mobile dislocations instantaneously increases to the background density ρ_0 due to the spurious effect. As the magnetic treatment time t or the magnetic induction B increases, the density ρ_m of mobile dislocations progressively increases and then reaches a steady-state value comparable to the density ρ_f of freshly introduced dislocations. The

dependences $\rho_m(B, t)$ for the other crystals studied exhibit a similar behavior [10, 12, 14]. Specifically, it was demonstrated in [14] for the Al crystals that both experimental dependences $\rho_m(t)$ and $\rho_m(B)$ can be represented as the universal dependence in the ρ_m–B^2t coordinates.

Such a progressive character of dislocation motion is impossible if all dislocations begin to move simultaneously. This leads us to the inference regarding a relay-race dislocation motion when dislocations initially begin to move in the most stressed crystal region and then their motion facilitates the depinning of neighboring dislocations. The direct experiment on the *in situ* observation of dislocation motion when the NaCl samples in the etchant were subjected to magnetic treatment [12] showed that dislocations do not simultaneously begin to move and stop and the mean time t_m of their motion is considerably shorter than the magnetic treatment time t and is proportional to it (at not very large B^2t).

The simplified phenomenological theory that made it possible to describe simply the found regularities was proposed in [12]. In particular, within this theory, the observed dependence $\rho_m(t)$ (Fig. 3a) is described by the simple formula

$$\rho_m(t) - \rho_0 = (\rho_m - \rho_0)_\infty[1 - \exp(-W_{st}t)], \qquad (3)$$

where $(\rho_m - \rho_0)_\infty$ is the maximum value of the difference $\rho_m(t) - \rho_0$ at $t \longrightarrow \infty$ in a given crystal and W_{st} is the probability of depinning dislocations at the beginning of motion. In [12, 14, 20], it was demonstrated that the processing of the experimental dependences $\rho_m(t)$ in the $\ln[1 - (\rho_m - \rho_0)/(\rho_m - \rho_0)_\infty]$–$t$ linearizing coordinates actually linearizes the dependences $\rho_m(t)$ for the NaCl-1, NaCl-3, CsI, and Al crystals. The results of this processing of the experimental data obtained in [12] for the NaCl-3 crystals at four different Ca concentrations are presented in Fig. 8a. The slopes of the straight lines determine the fitting parameters W_{st} for different concentrations C_{Ca}. According to [12], the parameter W_{st} has the meaning of the probability of beginning the dislocation motion per unit time. It can be seen from Fig. 8b that an increase in the Ca concentration from 5×10^{-7} to 1×10^{-4} mol/mol results in a decrease in the probability W_{st} by more than one order of magnitude; in this case, $W_{st} \propto 1/\sqrt{C}$. As follows from the data obtained in [12, 14], the probability W_{st} also depends on the magnetic induction B and the dislocation density ρ, that is,

$$W_{st} \approx \gamma B^2 \sqrt{\rho/C}. \qquad (4)$$

The probability W_{stop} of stopping the dislocation per unit time can be introduced in a similar way. According to [12, 14], this probability is characterized by the same dependence on B, ρ, and C with a constant that differs from γ by a multiplier of the order of unity. The phenomenological theory proposed in [12] permits us to derive the useful formula for the mean time t_m of dislocation motion, that is,

$$t_m \approx \begin{cases} \dfrac{1}{6}t, & t \ll (W_{st}^{-1} + W_{stop}^{-1}) \\ W_{stop}^{-1}, & t \gg (W_{st}^{-1} + W_{stop}^{-1}). \end{cases} \qquad (5)$$

Therefore, in the linear range of the dependence $l(t)$, the mean time t_m of dislocation motion should be six times shorter than the magnetic treatment time t. This

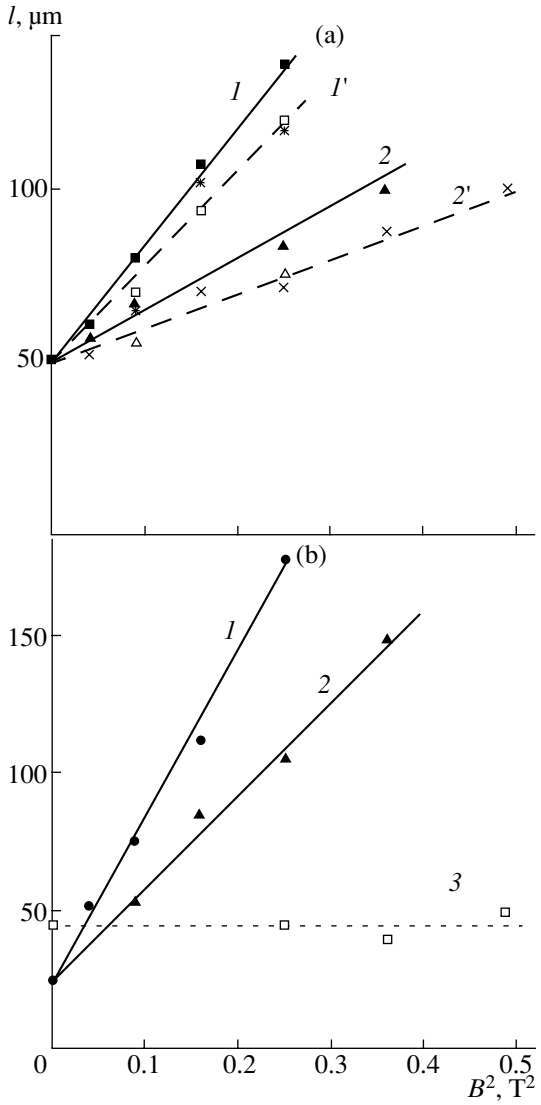

Fig. 6. Dependences of the mean free path l of dislocations on the magnetic induction B for (a) NaCl-3(Ca) crystals with different impurity concentrations at different temperatures T and (b) (*1*) NaCl-2(Ni), (*2*) NaCl-2, and (*3*) NaCl-3(Pb) crystals at T = 293 K. Impurity concentration (mol/mol): (a) (*1*, *1'*) $C_{Ca}^{(1)} = 5 \times 10^{-7}$ and (*2*, *2'*) $C_{Ca}^{(2)} = 1 \times 10^{-6}$. Temperature T (K): (a) (*1*, *2*) 293, (*1'*) (□) 77, (*2'*) (△) 77, (*1'*) (∗) 4.2, and (*2'*) (×) 4.2.

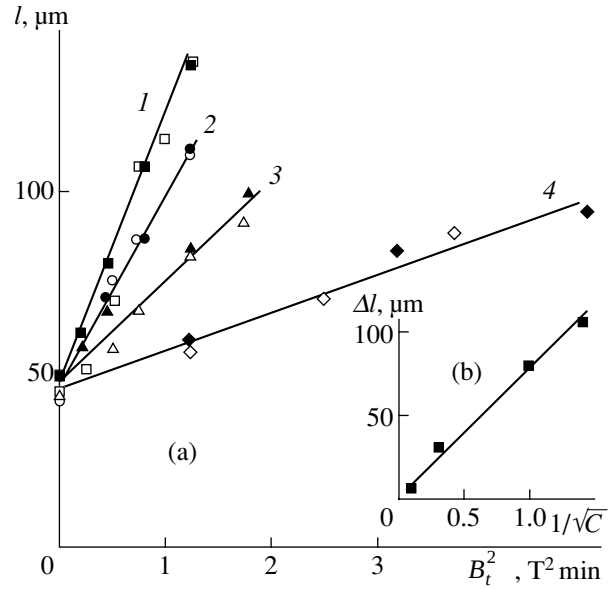

Fig. 7. (a) Dependences of the mean free path l of dislocations in NaCl-3(Ca) crystals on the product B^2t of the magnetic induction B squared by the magnetic treatment time t at different impurity concentrations C according to the experimental dependences $l(B)$ (■, ●, ▲, ◆) and $l(t)$ (□, ○, △, ◇) at T = 293 K. Impurity concentration C (mol/mol): (*1*) $C_{Ca}^{(1)} = 5 \times 10^{-7}$, (*2*) $C_{Ca}^{(2)} = 1 \times 10^{-6}$, (*3*) $C_{Ca}^{(3)} = 1 \times 10^{-5}$, and (*4*) $C_{Ca}^{(4)} = 1 \times 10^{-4}$. (b) Dependence of the mean free path Δl of dislocations on the Ca impurity concentration [section of dependences *1–4* in panel (a) at B = 0.5 T].

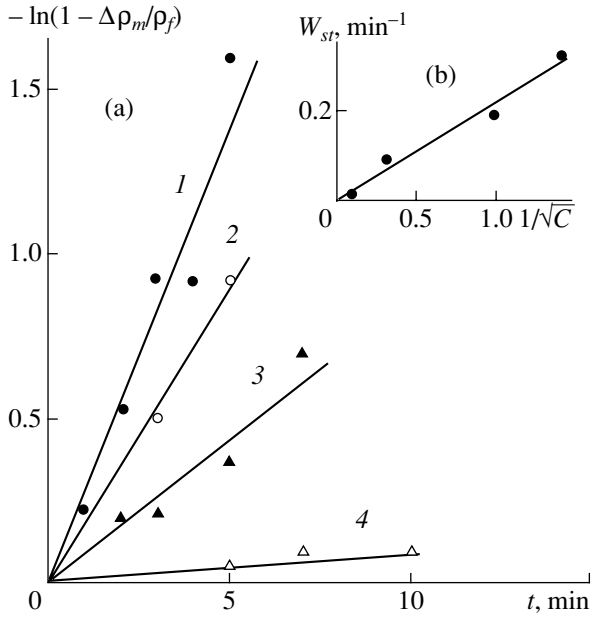

Fig. 8. (a) Dependences of the relative density ρ_m/ρ_f of mobile dislocations on the magnetic treatment time t at B = 0.5 T for NaCl-3(Ca) crystals with different Ca impurity concentrations C (mol/mol): (*1*) $C_{Ca}^{(1)} = 5 \times 10^{-7}$, (*2*) $C_{Ca}^{(2)} = 1 \times 10^{-6}$, (*3*) $C_{Ca}^{(3)} = 1 \times 10^{-5}$, and (*4*) $C_{Ca}^{(4)} = 1 \times 10^{-4}$. (b) Dependence of the probability W_{st} of beginning the dislocation motion on the Ca impurity concentration in NaCl-3(Ca) crystals.

theoretical result was experimentally corroborated for the NaCl, CsI, LiF, and Al crystals in [12, 14, 16].

7. KINEMATIC SCHEME OF THE EFFECT AND THE HYPOTHESIS OF ITS SPIN NATURE

The linear dependence of the mean free path of dislocations on the magnetic treatment time $\Delta l \propto t$ (Fig. 4) enables us to interpret the slope of this dependence as the effective mean velocity v_{ef} of dislocations. According to formula (5), this velocity and the true mean velocity v are related through the simple expression

$$v \approx 6v_{ef}. \quad (6)$$

As follows from expression (6) and the empirical formulas (1) and (2), the velocity v should obey the following relationship:

$$v \propto B^2/C^{0.5}. \quad (7)$$

On the other hand, the velocity v can be defined as the ratio of the mean distance Δx between local obstacles in the slip band to the time Δt of dislocation motion between adjacent rows of obstacles. The mean distance Δx can be estimated as

$$\Delta x \sim 1/\sqrt{C_0 D}, \quad (8)$$

where D is the diameter of an impurity complex and C_0 is the volume concentration of complexes. The concentrations C_0 and C are related by the expression

$$C = C_0 N, \quad (9)$$

where N is the mean number of impurity atoms in the complex. This mean number N is apparently proportional to the volume of the complex, i.e., can be estimated as follows:

$$N \approx (D/a_l)^3, \quad (10)$$

where a_l is of the order of the lattice parameter. It is evident that the quantity N should depend on the concentration C. This dependence will be considered below. Relationships (9) and (10) allow us to express Δx [see formula (8)] through the quantities C and N in the following way:

$$\Delta x = \frac{\sqrt[3]{N}}{\sqrt{a_l C}}. \quad (11)$$

The time Δt of dislocation motion to the next row of obstacles can be represented in the form of the product

$$\Delta t \approx n\tau_{dp}, \quad (12)$$

where τ_{dp} is the time of depinning the dislocation from one obstacle and n is the mean number of obstacles on the dislocation, which are sequentially overcome by the

dislocation in its motion from one row of impurity complexes to another. Consequently, the velocity $v = \Delta x/\Delta t$ can be estimated as

$$v \approx \sqrt[3]{N}/n\tau_{dp}\sqrt{Ca_l}. \quad (13)$$

By comparing this approximate formula with the empirical relationship (7), we obtain

$$\tau_{dp} \propto B^{-2}. \quad (14)$$

It should be noted that, according to the aforementioned experimental data, the time τ_{dp} of an elementary act of dislocation depinning from a local obstacle should be virtually independent of the temperature.

Therefore, the time τ_{dp} of depinning from the local barrier strongly depends on the magnetic field and is temperature independent, which is inconsistent with the conventional concept of the time of thermal activation. It is more reasonable to assume that any magnetically stimulated processes lead to the breaking or a considerable lowering of the barrier for the time τ_{dp}. Judging from the macroscopic deformation kinetics of alkali halide crystals in the magnetic field [41], we are dealing with a lowering of barriers.

The transformation of potential barriers in the magnetic field is a well-known phenomenon in chemical physics [60, 61]. The case in point is the spin evolution of radical pairs in a system of interacting chemical reagents in the magnetic field, which leads to the removal of the spin forbiddenness of a particular electronic transition in the system. This transition radically changes a configuration of the system and the energy of interaction between reagents (and, sometimes, even the interaction sign) virtually without changing the total energy. The last circumstance is quite natural, because the energy component $\mu_B B$ (where μ_B is the Bohr magneton) of the magnetic perturbation is very small even compared to the thermal energy kT (at $B = 1$ T and $T = 300$ K, $\mu_B B \sim 10^{-3}\, kT$). These spin-dependent electronic transitions in magnetic fields ($B = 0.02$–2 T), similar to those used in our experiments, substantially affect the rate of chemical reactions, photocurrent in semiconductors, viscosity of amorphous alloys, etc. [60–64].

The fact that the change in electronic states of pinning centers can strongly affect the interaction energy of centers with dislocations is well known and clearly manifests itself in the photoplastic effect in alkali halide crystals and semiconductors [65, 66]. The difference between the effects is that electronic transitions are caused by the photon capture in one case and the removal of the quantum forbiddenness due to the spin evolution in the magnetic field in another case.

The role of a radical pair in the dislocation–impurity system can be played, for example, by an unoccupied orbital with an unpaired spin in the dislocation core and a free spin of the paramagnetic center. At the same time, this can be a pair of spins in the impurity complex in the vicinity of the dislocation core. Unfortunately, the microscopic electronic structure of the dislocation–impurity complex system remains unknown to date. However, it is possible to solve a more general problem associated with the experimental verification of the hypothesis of the spin nature of the effect. For this purpose, we carried out a number of experiments on the study of the magnetoplastic effect in samples rotating in the magnetic field.

8. MAGNETOPLASTIC EFFECT IN ALTERNATING MAGNETIC FIELDS

The spin evolution in the system occurs in the course of spin precession about the direction of the magnetic field in which radical pairs relax to a new equilibrium distribution of spin states. As was shown above (Fig. 4), the kinetic of dislocation depinning depends on the mutual orientation of the magnetic field and dislocations. Therefore, the spin evolution depends not only on the field direction but also on the dislocation orientation, i.e., the crystal orientation (the possible reasons will be discussed below).

This leads to important features of the magnetoplastic effect observed in samples rotating in the magnetic field. Actually, the magnetoplastic effect in the rotating crystal can occur through the mechanism under consideration when a change $\Delta\varphi = 2\pi\nu\tau_{dp}$ in the magnetic field orientation with respect to the crystal for the spin evolution time $\tau \sim \tau_{dp}$ is small compared to the critical rotation angle $\Delta\varphi_c = 2\pi\alpha$, where α is a small parameter which will be estimated below from the experimental data. Consequently, there should exist the critical frequency

$$\nu_c = \alpha/\tau_{dp} \quad (15)$$

that separates two radically differing ranges of the dependence $l(\nu)$. At low rotation frequencies $\nu \ll \nu_c$, the mean free path l of dislocations should not substantially depend on the frequency ν. However, at sufficiently high frequencies $\nu \gg \nu_c$, the effect should disappear, because there is no direction to which spins can relax.

To put it differently, if our assumption regarding the spin nature of the magnetoplastic effect is correct, stepwise dependences $l(\nu)$ with a rather sharp decrease in the mean free path l of dislocations to the background path $l(0)$ in the frequency range $\nu \sim \nu_c$ should be expected in experiments. Moreover, the experimental dependence of the frequency ν_c should exhibit a specific behavior; namely, like the parameter τ_{dp}^{-1}, the frequency ν_c should not depend on the temperature but should be sensitive to the impurity type and the magnetic induction ($\nu_c \propto B^2$). Furthermore, it can be expected that edge and screw dislocations have different frequencies ν_c.

All these predictions were completely confirmed by the experimental data [12, 15]. As can be seen from Figs. 9–11, the dependences $l(\nu)$ have a stepwise shape.

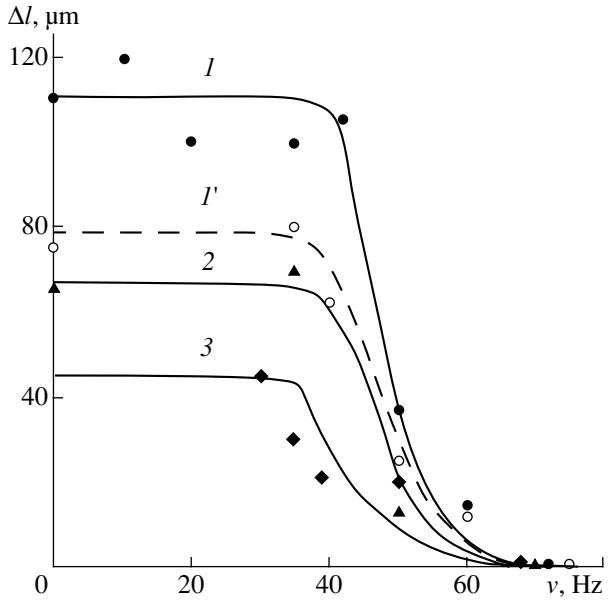

Fig. 9. Dependences of the mean free path l of dislocations on the rotation frequency ν of the sample in a magnetic field of 0.5 T for 5 min for (*1*, *1*') NaCl-2 and (*2*, *3*) NaCl-3(Ca) crystals with different Ca impurity concentrations C. Temperature T (K) = (*1*, *2*, *3*) 293 and (*1*') 77. Impurity concentration C (mol/mol): (*2*) $C_{Ca}^{(2)} = 1 \times 10^{-6}$ mol/mol and (*3*) $C_{Ca}^{(3)} = 1 \times 10^{-5}$.

Figure 9 shows the dependences $l(\nu)$ for the NaCl crystals (with different Ca concentrations) exposed to the magnetic field B = 0.5 T for 5 min at liquid-nitrogen and room temperatures [15]. It can be seen from Fig. 9 that, within the limits of experimental error, the critical frequency is independent of the temperature. With an increase in the Ca concentration by one order of magnitude, the critical frequency ν_c decreases only slightly, if at all. It was found that the value of ν_c does not depend on the magnetic treatment time. Similar dependences for the LiF and Al crystals subjected to magnetic treatment at two different magnetic inductions are depicted in Fig. 10 [15]. As can be seen from this figure, an increase in the magnetic induction from 0.5 to 0.7 T for the LiF crystals (Fig. 10a) and from 0.7 to 1.0 T for the Al crystals (Fig. 11b) leads to an increase in the critical frequency ν_c at which the effect is suppressed. However, in both cases, the critical frequency ν_c increases by a factor of no more than 1.5, which, even with due regard for our experimental errors, is less than a twofold increase predicted by the dependence $\nu_c \propto B^2$. It will be shown below that this disagreement is not accidental and reflects the fundamental features of spin conversion mechanism.

As could be expected, the critical frequencies ν_c differ for screw and edge dislocations. According to [15], for the LiF crystals, the critical frequency ν_c for screw dislocations is approximately three times higher than that for edge dislocations at the same magnetic inductions B. Small amounts of the magnetically active Ni impurity contained in the NaCl-2(Ni) crystals considerably affect the critical frequency ν_c [18, 20]. As can be seen from Fig. 11, the critical frequency ν_c in the NaCl-2(Ni) crystals is almost one order of magnitude higher than that in the initial NaCl-2 crystals. In this case, the value of ν_c does not depend on the Ni concentration in these crystals and is virtually proportional to the magnetic induction squared.

Thus, the results of the performed investigations into the magnetically stimulated dislocation mobility in the rotating crystals support the hypothesis of the spin nature of the microscopic mechanisms of the magnetoplastic effect.

9. THE INFLUENCE OF X-RAY IRRADIATION ON THE MAGNETOPLASTIC EFFECT IN NaCl AND LiF CRYSTALS

As was shown above, the impurity composition of crystals has a strong effect on the dependence $l(\nu)$ and the critical frequency ν_c. In this respect, it can be expected that, when the crystal contains several types of magnetosensitive obstacles to the dislocation motion, the dependence $l(\nu)$ should be represented by a multistep curve with a certain spectrum of the critical frequencies ν_{ci} (i = 1, 2, …).

These mixed states of the defect system in the studied crystals are conveniently produced by X-ray irradiation. It is well known that the exposure of alkali halide crystals to ionizing radiation of different nature and intensity brings about electronic excitations with energies and lifetimes varying in a wide range. High-energy electronic excitations decay to give the simplest structural defects of the electron–hole pair and exciton type, which, in turn, can form more complex lattice defects, including paramagnetic centers [67–69].

It turned out that the dependence $l(\nu)$ is highly sensitive to X-ray irradiation at low doses, which makes it possible to obtain a large amount of information characterizing the defect state of irradiated crystals.

The NaCl and LiF crystals served as objects of investigation [22, 25]. The preliminarily annealed samples were irradiated on an IRIS-M setup equipped with a Mo source at the wavelength λ = 0.7 Å (tube current I = 35 mA, tube voltage U = 45 kV). The irradiation time was t_{ir} = 5–30 s. The dose rate was approximately equal to 10 rad/s. The experimentally measured transmission factor for X rays was equal to 70–80% for the NaCl samples and 60–70% for the LiF samples. No coloration of the samples was observed upon irradiation.

After irradiation, fresh dislocations were introduced by shock into the sample followed by the exposure to the magnetic field in the dark in order to prevent the deexcitation of radiation-induced defects. The mean free path of dislocations was measured by the standard selective chemical etching. The test experiments

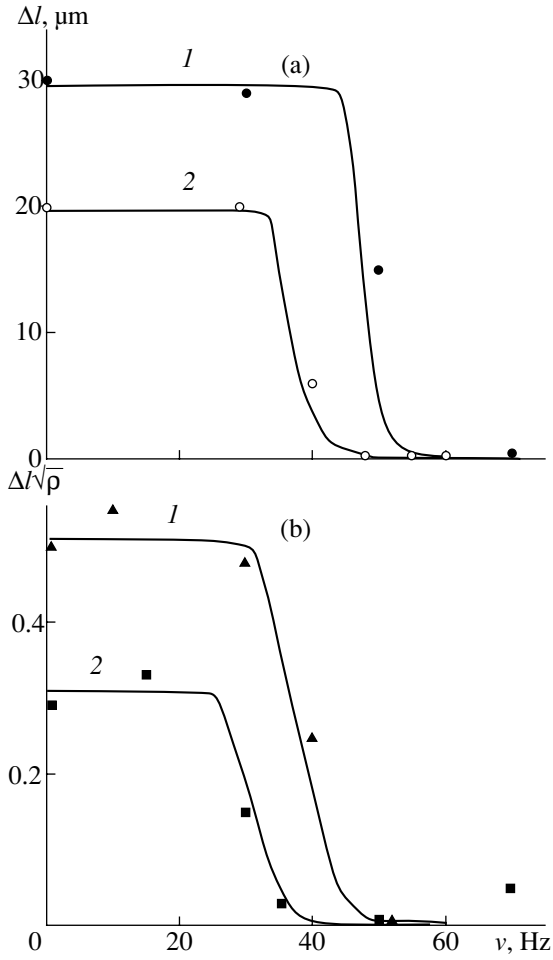

Fig. 10. Dependences of the mean free path l of dislocations in (a) LiF and (b) Al crystals on the rotation frequency ν of the sample in a magnetic field at inductions B = (a) (*1*) 0.7, (*2*) 0.5 (t = 5 min), (b) (*1*) 1, and (*2*) 0.7 (t = 15 min) T. T = 293 K.

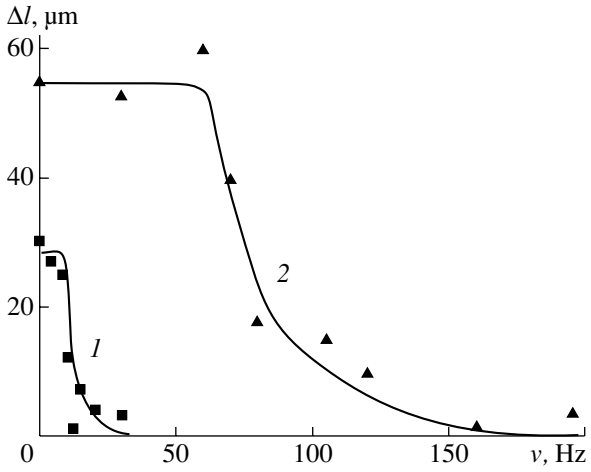

Fig. 11. Dependences of the mean free path l of dislocations in (*1*) NaCl-2 and (*2*) NaCl-2(Ni) crystals on the rotation frequency ν of the sample in a magnetic field of 0.3 T for 5 min.

showed that the mean free path of dislocations was approximately identical for all sample faces, including the face closest to the irradiation source.

Optical investigations of the samples in a wide range of wavelengths (from IR to UV) demonstrated that standard instruments cannot reveal changes induced by the irradiation at the doses used. The absorption bands corresponding to F^- centers and an increase in the transmission (by 5–20%) were observed only with an increase in the dose by two orders of magnitude (to 10^4 rad). At the same time, the magnetoplastic effect appeared to be sensitive to insignificant structural transformations caused by the irradiation at doses of the order of 10^2 rad.

The experiments showed that the X-ray irradiation of the samples even for a few seconds leads to a radical change in the dependence $l(\nu)$. This drastic change in the dependence $l(\nu)$ for the irradiated NaCl-3(Ca) crystals with the impurity concentration $C_{Ca}^{(1)} = 5 \times 10^{-7}$ mol/mol is illustrated in Fig. 12a. It can be seen from this figure that, as a result of irradiation, the effective dislocation velocity (i.e., the mean free path of dislocations) decreases and the one-step curve transforms into a two-step curve. The appearance of the second step indicates that irradiation generate magnetosensitive obstacles of a new type. It is of interest that an increase in the dose affects the first and second steps differently. An increase in the irradiation time t_{ir} from 5 to 30 s does not change the position of the second step at $\nu_{c2} \sim 150$ Hz for B = 0.5 T. On the other hand, as the irradiation dose increases, the first critical frequency ν_{c1} increases and becomes equal to ν_{c2} at t_{ir} = 30 s (Figs. 12a, 12b).

It should be noted that the Ca impurity concentration in the irradiated NaCl-3(Ca) crystals, like in the unirradiated crystals, very weakly affects the critical frequencies. A similar situation is observed for the NaCl-2 crystals.

The dependence of the effective velocity $\Delta l/t$ on ν for the irradiated NaCl-2(Ni) crystals also exhibits two steps. It was found that the positions of the first and second steps do not depend on the irradiated dose: $\nu_{c1} \sim$ 80 Hz and $\nu_{c2} \sim$ 145 Hz at B = 0.3 T (Fig. 13a). It is important that the frequency ν_{c1} for the NaCl-2(Ni) crystal virtually coincides with the frequency ν_{c2} for the NaCl-2 and NaCl-3(Ca) crystals (Fig. 13b). The second critical frequency ν_{c2} for the crystals containing Ni is nearly twice as high as the first critical frequency and has no analogs in the NaCl-2 and NaCl-3(Ca) crystals. Consequently, the spectrum of paramagnetic obstacles in the NaCl crystals is very sensitive to small additions of the Ni impurity.

The frequency dependences of the mean free path of edge and screw dislocations in the preliminarily irradiated LiF crystal differ radically. Like for the NaCl crys-

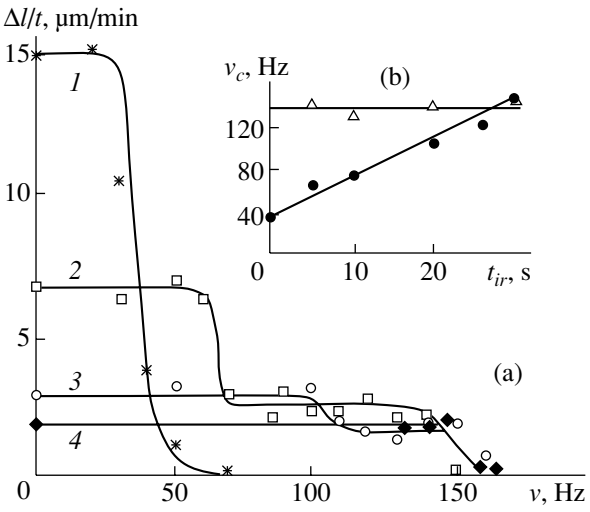

Fig. 12. (a) Dependences of the effective dislocation velocity $\Delta l/t$ on the rotation frequency ν of the sample in a magnetic field of 0.5 T for NaCl-3 crystals at the irradiation times t_{ir} = (*1*) 0, (*2*) 5, (*3*) 20, and (*4*) 30 s. (b) Dependence of the critical frequencies (●) ν_{c1} and (△) ν_{c2} on the irradiation times t_{ir}.

tals, for screw dislocations, the dependence $l(\nu)$ is characterized by two steps and the frequency ν_{c1} increases with an increase in the irradiation dose (Fig. 14a). At the same time, the one-step dependence $l(\nu)$ is retained for screw dislocations. In this case, the critical frequency ν_c^{ir} for the irradiated crystals is lower than the frequency ν_c and almost does not depend on the irradiation dose in the irradiation time range t_{ir} = 5–20 s (Fig. 14b). This implies that the crossover from the frequency ν_c to the frequency ν_c^{ir} occurs at doses corresponding to $t_{ir} < 5$ s.

The exposure of the irradiated samples to light of a tungsten lamp (prior to the introduction of fresh dislocations) leads to the natural de-excitation of radiation-induced defects and, at sufficiently long exposure times (1–5 h), restores the one-step dependence $l(\nu)$ and the initial frequency ν_c.

It is of interest to discuss why the two-step dependence $l(\nu)$ (for edge dislocations) rather than a strongly broadened one-step dependence is observed after irradiation of the crystals. Note that fresh dislocations (playing a key role in experiments) introduced into the unirradiated crystal are pinned at random positions but only where long-range internal stresses are too weak for their depinning from impurity centers. In the irradiated crystals after shock, fresh dislocations can be pinned at positions with larger stresses, because they can be held by impurities and new radiation-induced defects. In the magnetic field, only new obstacles are "switched off" at $\nu_{c1} < \nu < \nu_{c2}$. This leads to the depinning of a number of dislocations from the most stressed positions in the crystal. The dislocation motion is attended by a change in the distribution of internal stresses, which can initiate the motion of other dislocations. This results in the appearance of the second step in the dependence $l(\nu)$. All the effects of magnetically stimulated depinning are suppressed at $\nu > \nu_{c2}$.

It is unlikely that the origin of the new type of obstacles formed under irradiation can be uniquely elucidated on the basis of the obtained data. However, information accumulated to date on the formation of radiation-induced defects in alkali halide crystals under irradiation at small doses makes it possible to put forward a number of realistic hypotheses that provide the explanation for the results of our measurements. This was discussed in detail in our earlier work [25].

10. MAGNETOPLASTIC EFFECT AND SPIN–LATTICE RELAXATION

One of basic physical limitations on the possibility of realizing effects based on the spin evolution in the magnetic field is the requirement that a noticeable spin–lattice relaxation should not occur for the time of this evolution (in our case, for the time τ_{dp}) [61]. Otherwise, thermal fluctuations in the system mix spin states and virtually rule out the magnetically stimulated transitions and, hence, the depinning of dislocations. It was shown above [see relationship (14)] that the depinning time τ_{dp} of dislocations from paramagnetic centers rapidly increases with a decrease in the magnetic induction, that is,

$$\tau_{dp} = kB^{-2}. \tag{16}$$

Consequently, it can be expected that there is a threshold magnetic field B_c corresponding to the depinning time $\tau_{dp}(B_c)$ equal in order of magnitude to the spin–lattice relaxation time τ_{sl} in the dislocation–paramagnetic center system, because, at $B < B_c$, the above criterion for the existence of spin-dependent phenomena in the magnetic field is violated and the magnetoplastic effect should disappear.

Therefore, the observation of the threshold magnetic field is one more corroboration of the spin nature of the magnetoplastic effect. As was shown above, the mean free path l of dislocations in the case of the magnetoplastic effect linearly increases with an increase in the square of the magnetic induction B and the magnetic treatment time t (Figs. 4–7)

$$l = l_0 + \beta B^2 t. \tag{17}$$

Certainly, this linear dependence is observed at not very large values of B and t but also, as follows from the foregoing, at not very small values of B. In other words, when there is the threshold magnetic field of the magnetoplastic effect, the proportionality coefficient β =

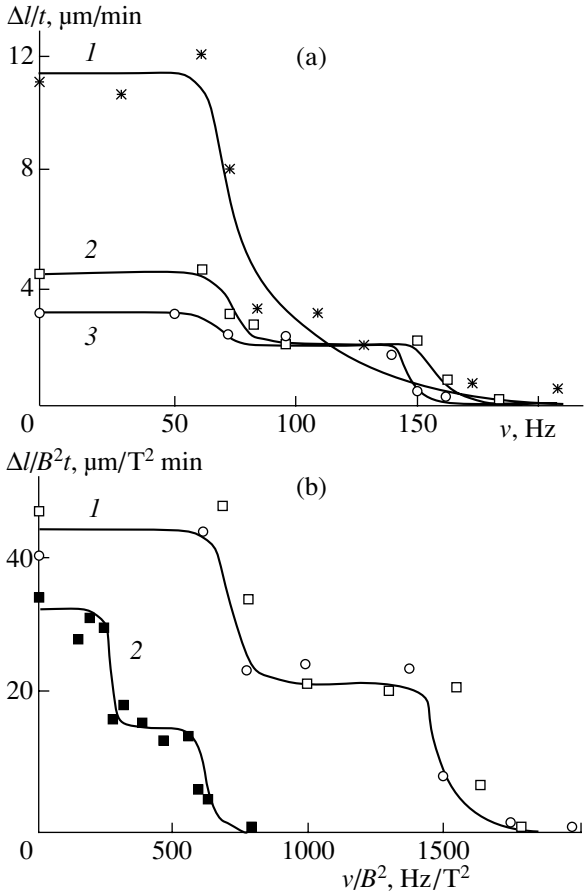

Fig. 13. (a) Dependences of the effective dislocation velocity $\Delta l/t$ on the rotation frequency ν of the sample in a magnetic field of 0.3 T for NaCl-2(Ni) crystals at irradiation times t_{ir} = (*1*) 0, (*2*) 5, and (*3*) 20 s. (b) Frequency dependences of the effective dislocation velocity normalized to the magnetic induction squared for (*1*) NaCl-2(Ni) and (*2*) NaCl-2 crystals (t_{ir} = 5 s) at magnetic inductions B = (*1*) (□) 0.2, (*1*) (○) 0.3, and (*2*) (■) 0.5 T.

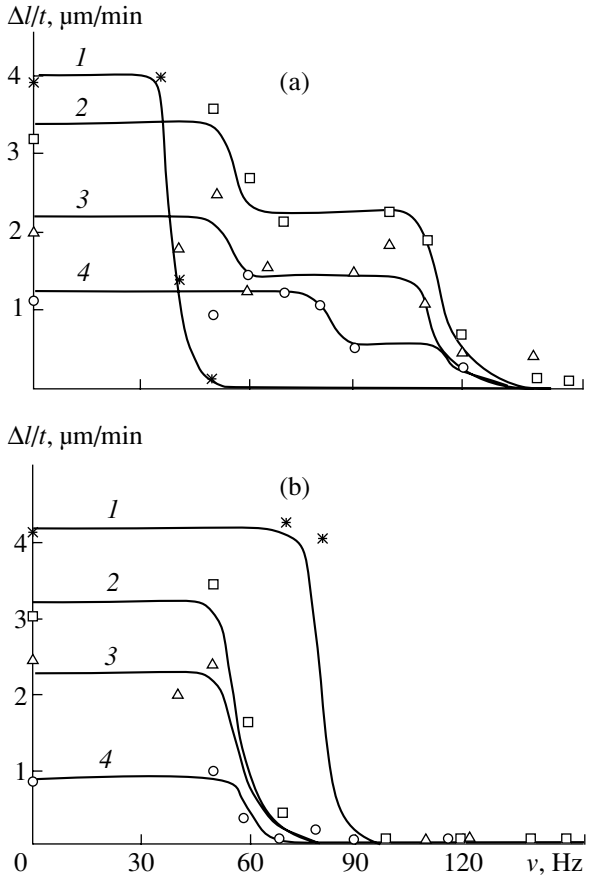

Fig. 14. Dependences of the effective velocity $\Delta l/t$ of (a) edge and (b) screw dislocations on the rotation frequency ν of the sample in a magnetic field of 0.5 T for LiF crystals at irradiation times t_{ir} = (*1*) 0, (*2*) 5, (*3*) 10, and (*4*) 20 s.

$(l - l_0)/B^2t$ should have the form of a step, that is,

$$\beta = \begin{cases} \text{const}, & B > B_c \\ 0, & B < B_c. \end{cases} \qquad (18)$$

In real experiments, we should expect a certain smearing of step (18) in the curves $\beta(B)$.

Figure 15 depicts the experimental dependences $\sqrt{\rho}\beta(B)$ for the NaCl-3(Ca) ($C_{\text{Ca}}^{(4)} = 1 \times 10^{-4}$ mol/mol) and Al crystals [23]. It can be seen from this figure that both dependences exhibit the predicted steps at close threshold fields $B_c \sim 0.2$ T. At $B > 0.2$ T, the coefficient β remains virtually constant, which provides the linear dependence of l on B^2t [see formula (17)]. At $B < 0.2$ T, the mean free path of dislocations drastically decreases to the background path and, hence, the magnetoplastic effect disappears.

Furthermore, it is necessary to verify whether the behavior of the threshold magnetic field B_c is consistent with the spin concept. The threshold field B_c determined from the balance condition

$$\tau_{dp}(B_c) = \tau_{sl}(T) \qquad (19)$$

according to formula (16) can be written in the form

$$B_c = \sqrt{\frac{k}{\tau_{sl}(T)}}. \qquad (20)$$

Consequently, taking into account that the spin–relaxation time τ_{sl} is a decreasing function of the temperature, the threshold field B_c should decrease with a decrease in the temperature. This inference was experimentally verified by measuring the dependence of the mean free path of dislocations in the LiF crystals on the magnetic induction B. When varying the magnetic induction B, the quantity B^2t was retained constant (B^2t = 5 T² min) by changing the magnetic treatment time. It can be seen from Fig. 16 that, with a decrease in the temperature from room temperature to 77 K, the

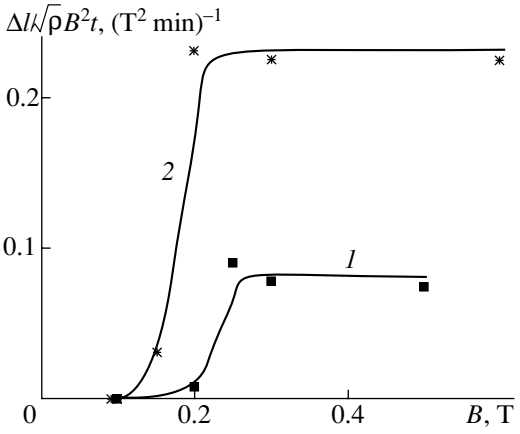

Fig. 15. Steps in the dependences of the normalized mean free path of dislocations $\Delta l\sqrt{\rho}/B^2t$ on the magnetic induction B for (*1*) NaCl-3(Ca) ($C_{Ca}^{(4)} = 1 \times 10^{-4}$ mol/mol) and (*2*) Al crystals.

step $\Delta l(B)$ is actually shifted toward the left and the corresponding decrease in the threshold field B_c is equivalent to an increase in the spin–lattice relaxation time τ_{sl} by a factor of approximately 2.5.

One more prediction that follows from our notions of the magnetoplasticity nature is associated with the behavior of the dependence $\beta(B) = (l - l_0)/B^2t$ for edge dislocations in the irradiated crystals. It was shown above that the exposure of the alkali halide crystals to X rays even at small doses leads to the formation of paramagnetic obstacles of a new type in addition to impurity complexes. This manifests itself in the appearance of the additional step in the dependence of the mean free path l of edge dislocations on the frequency ν of sample rotation in the magnetic field. In this case, the first critical frequency ν_{c1} increases with an increase in the irradiation dose and characterizes the radiation-activated impurity complex, whereas the frequency ν_{c2} of the second step does not depend on the dose and, likely, correspond to *Z* centers formed at individual impurity atoms [25]. It is reasonable to assume that spin systems of these defects on the dislocation have different spin–lattice relaxation times $\tau_{sl}^{(1)}$ and $\tau_{sl}^{(2)}$. Therefore, we can expect the appearance of the second step in the dependence $\beta(B) = (l - l_0)/B^2t$ for the irradiated crystal. Indeed, two steps are observed in the corresponding experimental dependence for edge dislocations in the LiF crystal irradiated using the same X-ray tube for 5 s (Fig. 17).

Experimental investigations of the NaCl-3 crystals with different Ca impurity concentrations showed that the threshold field B_c depends on the concentration C of this impurity (Fig. 18) [28]. As the concentration C increases, the threshold field B_c increases and tends to saturation at high concentrations. According to formula (20), this indicates a decrease in the spin–lattice relaxation time τ_{sl} with an increase in the concentration C. In [28], this behavior was interpreted in the following way. The well-annealed crystals were used in the experiments. Therefore, impurity atoms in the crystals have the tendency to coagulation with the formation of complexes. The higher the concentration C, the larger the size of the complex. Single impurity atoms and small-sized complexes should predominate in the pure crystals ($C_{Ca}^{(1)} = 5 \times 10^{-7}$ mol/mol and $C_{Ca}^{(2)} = 1 \times 10^{-6}$ mol/mol), whereas the mean size of complexes can be large in the crystals with a considerable impurity content ($C_{Ca}^{(3)} = 1 \times 10^{-5}$ mol/mol and $C_{Ca}^{(4)} = 1 \times 10^{-4}$ mol/mol). In the equilibrium structure of the NaCl crystal, for each Ca^{2+} ion replacing a univalent Na^+ ion, there are one cation vacancy and two Cl^- ions. With an increase in the number N of Ca atoms in the complex, the number $\bar{n}_v$ of vacancies among the nearest neighbors of each Ca atom increases and asymptotically approaches six. In a loose structure of large-sized complexes, Ca impurity atoms surrounded by vacancies should have a higher freedom for thermal motion and, correspondingly, larger amplitudes of thermal vibrations. In denser small-sized complexes, a similar increase in the amplitude of impurity atom motion is reached with an increase in the temperature, which results in a decrease in the time τ_{sl}. This is responsible for the increase in the threshold field B_c with an increase in the Ca concentration. In the framework of this model, the flattening of the dependence $B_c(C)$ corresponds to the change-over to sizes of complexes in the which the number of atoms in the bulk is substantially larger than the number of atoms on the surface.

11. EVALUATION OF THE TIME OF AN ELEMENTARY ACT OF DISLOCATION DEPINNING AND THE MODEL OF MAGNETICALLY STIMULATED UNZIPPING

Thus, all the experimental results obtained are quite consistent with the above hypothesis of the spin mechanism of the magnetoplastic effect. On the basis of a large amount of different available data, we will attempt to construct a model of the effect, which should be consistent with these data, on the one hand, and provide particular criteria for elucidating the spin mechanism, on the other hand. The role of these criteria can be played by the dependence of the time of elementary act on the magnetic field $\tau_{dp} \propto B^{-2}$ and the estimate of this time from the available experimental data. Let us first estimate the time of elementary act. Without any simplified model assumptions, we can only evaluate the lower and higher limits of the time τ_{dp}.

According to the experimentally verified relationship (15), we obtain

$$\tau_{dp} = \alpha/\nu_c. \quad (21)$$

The quantity α was introduced in relationship (15) as the small parameter determining the critical angle $\Delta\varphi_c = 2\pi\alpha$ that restricts the crystal rotation for the time τ_{dp} in order to provide the spin mechanism. Intuition suggests that this angle cannot be equal to tens of degrees and is less or of the order of several degrees. In this case, we have

$$\alpha \lesssim 10^{-2}. \quad (22)$$

As can be seen from Fig. 9, the critical frequency for the NaCl-2 and NaCl-3 crystals at $B = 0.5$ T is estimated at $\nu_c \sim 45$ Hz. With due regard for relationships (21) and (22), this gives the higher bounded estimate of the time τ_{dp}, that is,

$$\tau_{dp} \lesssim 10^{-4} \text{ s at } B = 0.5 \text{ T}. \quad (23)$$

However, in order to elucidate the spin mechanism, it is even more important to estimate from below the time τ_{dp}. By using the experimental values of the effective dislocation velocity v_{ef} and formulas (6) and (13), we find

$$\tau_{dp} \approx \sqrt[3]{N}/vn\sqrt{Ca_l}. \quad (24)$$

Since the dependence $N(C)$ is not reliably known, it is reasonable to make the estimate from the data for the NaCl-3(Ca) crystals with the lowest impurity concentration $C_{Ca}^{(1)} = 5 \times 10^{-7}$ mol/mol $= 1.18 \times 10^{16}$ cm^{-3}. At such a low impurity concentration, it is natural to assume that impurity atoms form not large-sized complexes but pinning centers with $N \sim 1$ (this also follows from Fig. 18). Then, the mean distance between impurity atoms in the slip plane can be estimated as

$$\Delta x \approx 1/\sqrt{Ca_l} \approx 0.3 \text{ μm}. \quad (25)$$

At the same time, according to our data for these crystals at $B = 0.5$ T, the dislocation velocity is estimated at $v = 6v_{ef} \approx 2$ μm/s. In this case, from relationship (24), we have

$$\tau_{dp} \sim \Delta x/vn \approx 10^{-1}/n \text{ s}. \quad (26)$$

From this estimate with allowance made for inequality (23), it follows that the number of sequentially overcome obstacles on the dislocation is rather large, that is,

$$n \gtrsim 10^3. \quad (27)$$

This is close to the maximum possible number n, which is equal to the total number of pinning points in the dislocation of length $L \sim 3$ mm:

$$n_{max} \sim L/\Delta x \approx 10^4. \quad (28)$$

From relationships (26) and (28), we find that, at $B = 0.5$ T,

$$\min\tau_{dp} \sim 10^{-5} \text{ s}. \quad (29)$$

As a result, taking into account inequality (23), we obtain

$$10^{-5} \lesssim \tau_{dp} \lesssim 10^{-4} \text{ s at } B = 0.5 \text{ T}. \quad (30)$$

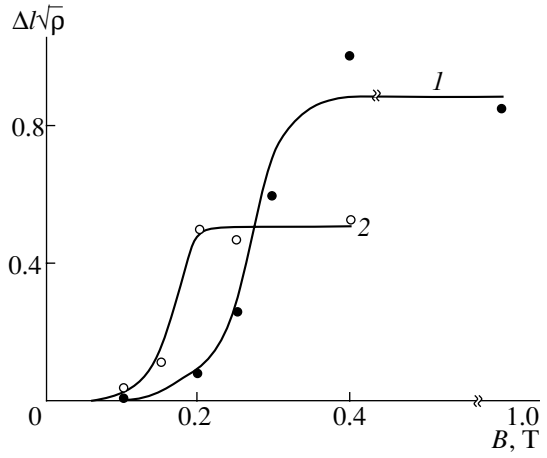

Fig. 16. Dependences of the normalized mean free path of dislocations in LiF crystals on the magnetic induction B at temperatures of (*1*) 293 and (*2*) 77 K. Crystals were exposed to a magnetic field for the time t chosen from the condition $B^2t = 5$ T^2 min.

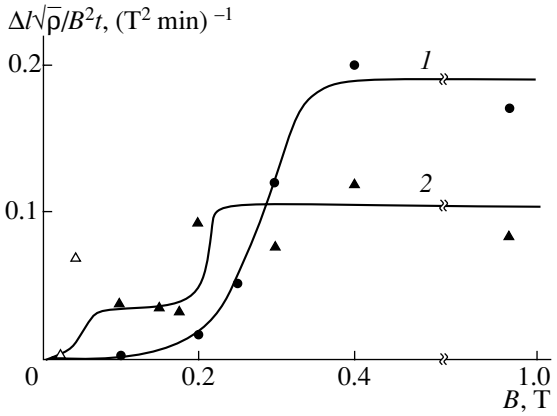

Fig. 17. Dependences of the normalized mean free path of dislocations in LiF crystals on the magnetic induction B for (*1*) unirradiated crystals and (*2*) crystals irradiated for 5 s in the absence of electric field (●, ▲) and in the magnetic and electric ($E = 10$ kV/m) fields (△).

Therefore, we have a sufficiently narrow range of times τ_{dp} permissible according to our experimental data and common sense. With due regard for relationships (21) and (22), the determined range (30) allows us to refine the estimate of the parameter α in expressions (15) and (21), that is,

$$\alpha \approx 10^{-3}\text{–}10^{-2}. \quad (31)$$

On the other hand, with the use of this estimate of the parameter α and relationships (19) and (21), the spin–lattice relaxation time τ_{sl} can be estimated in the order of magnitude as follows:

$$\tau_{sl} \approx \alpha/\nu_c(B_c). \quad (32)$$

For example, we experimentally determined that $B_c \sim 0.28$ T and ν_c (0.5 T) ~ 40 Hz for the LiF crystals. By

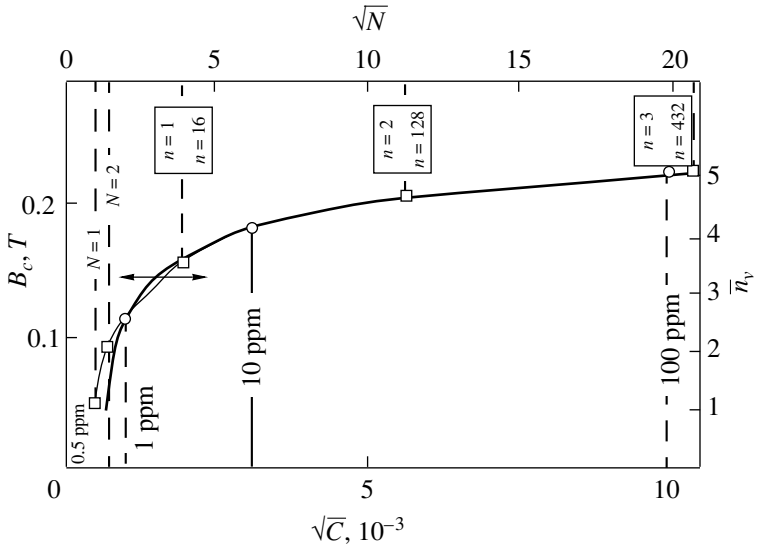

Fig. 18. Dependences of the threshold field B_c on the Ca impurity concentration C in NaCl-3(Ca) crystals (in the B_c–$\sqrt{C}$) and the mean number $\bar{n}_v$ of vacancies in the nearest environment of Ca impurity on the number N of Ca atoms in a complex (in the $\bar{n}_v$–$\sqrt{N}$ coordinates).

decreasing this frequency proportionally to the square of the induction ratio, we obtain $\nu_c(B_c) \sim 12$ Hz and, correspondingly, the sought estimate

$$\tau_{sl} \approx 10^{-4}\text{–}10^{-3} \text{ s}. \tag{33}$$

This estimate indicates that the spin–lattice relaxation time in the dislocation–paramagnetic center system is relatively long, which is likely the characteristic feature of defects in many crystals. For example, the spin–lattice relaxation time τ_{sl} for an *F*-center pair in KCl crystals at 50 K is approximately equal to 0.01 s [70] and the ^{23}Na nuclear spin–lattice relaxation time in NaCl single crystals at room temperature is of the order of 10 s [71].

In conclusion of this section, we discuss the possible physical reason for the sequential, magnetically stimulated depinning of dislocations from such a large number of obstacles over their length [see relationship (27)]. Apparently, this can be explained by the elastic repulsion between the dislocation and impurity center, which prevents their approach sufficient for the exchange interaction and formation of a radical spin pair. To put it differently, the spin conversion in a given impurity center can occur when the total force acting over the length Δl_{seg} of the nearest adjacent dislocation segments is larger than a critical force F_c; that is,

$$b\sigma_i \Delta l_{\text{seg}} > F_c, \tag{34}$$

where σ_i is the internal stress. Most likely, condition (34) is not satisfied for each obstacle and each dislocation. This leads to the relay-race dislocation motion and the sequential depinning of segments. Indeed, when condition (34) is fulfilled for a particular obstacle, after depinning the dislocation from this obstacle for the time τ_{dp} (if the obstacle is a single impurity atom), the critical conditions arise for the next obstacle, which is also overcome for the spin evolution time, etc. This results in the dislocation unzipping mechanism, which involves the sequential depinning from obstacles and is more known for the usual thermally activated motion of dislocations under the action of mechanical loads.

In principle, the mechanism of motion under consideration likely occurs irrespective of whether the impurity center is a single atom or a complex formed by a number of atoms. However, in the latter case, the overcoming of this center by the dislocation should involve a sequence of elementary acts of depinning from individual impurity atoms through the spin mechanism. It is reasonable to assume that the process of "cutting" the complex by the dislocation includes simultaneously all the atoms in direct contact with the dislocation and sequentially all the next rows of atoms appearing in the core of dislocation in its motion through the complex. Therefore, in terms of our model, the depinning time of the dislocation from the complex can be estimated as $\tau_{dp}\sqrt[3]{N}$. This enables us to rewrite relationship (13) in the simpler form

$$v \approx 1/n\tau_{dp}\sqrt{Ca_l}, \tag{34a}$$

where n is the specific number of complexes on the dislocation, which are sequentially overcome through the unzipping mechanism. As a result, the time $n\tau_{dp}$, as before, is the time Δt [see formula (12)] of dislocation motion to the next row of obstacles in the slip plane.

12. EXPERIMENTAL ELUCIDATION OF THE SPIN MECHANISM OF THE MAGNETOPLASTIC EFFECT

Estimate (30) obtained for the time τ_{dp} of the magnetically stimulated depinning of the dislocation from the impurity center is several orders of magnitude longer than times of spin processes usually considered in chemical physics. In any case, such a slow spin conversion is not encountered in chemical reactions in which the process should be completed for a very short time of approaching radicals (the so-called residence time in a cage). In chemical reactions, the recombination of chemical radicals in the magnetic field has been successfully described within the sufficiently fast Δg mechanism of spin evolution [60]. Unfortunately, this mechanism turns out to be too fast in our case. It should be noted that Molotskiĭ [72, 73] proposed a rather intricate model of the use of the Δg mechanism for describing the magnetoplastic effect. However, two variants of the developed theory resulted only in the renormalization of the mean dislocation velocity. In other words, when a dislocation moves past a point defect with a certain velocity v, the spin conversion in the magnetic field leads to an increase in this velocity to $v' = v(1 + kB^2)$. Consequently, under our experimental conditions, when dislocations pinned by impurity centers are at rest ($v = 0$) prior to the application of the magnetic field, they cannot be set in motion through the Molotskiĭ mechanism. This difficulty is absent in our model, and the sole problem is to find an appropriate (not very fast) mechanism of spin evolution.

At the same, the very slow mechanism alternative to the Δg mechanism is known in chemical physics. This mechanism, which is rejected in the theory of chemical reactions due to the slowness, is attractive for the magnetoplastic effect, because it predicts the spin conversion time inversely proportional to B^2. The case in point is the Brocklehurst mechanism of spin relaxation in the magnetic field [74] (see also [60]).

Physically, this mechanism of spin relaxation is associated with the anisotropy of the g factor (as a rule, estimated at $\Delta g \sim 10^{-2}$–10^{-3}), which leads to the magnetically stimulated transitions between the S and T states of radical pairs. In this case, it is necessary to distinguish the longitudinal and transverse spin relaxations that correspond to the $S \longleftrightarrow T_\pm$ and $S \longleftrightarrow T_0$ singlet–triplet transitions and are characterized by the times T_1 and T_2, respectively. The former time T_1 is determined by attainment of the equilibrium spin projection onto the field direction, and the latter time T_2 is governed by the decay of the spin magnetization components perpendicular to the field. These times decrease differently with an increase in the magnetic induction B; that is,

$$\begin{aligned} T_1^{-1} &= \tau^{-1} f(B^2/B_0^2), \\ T_2^{-1} &= \tau^{-1}[\alpha B^2/B_0^2 + \beta f(B^2/B_0^2)], \end{aligned} \tag{35}$$

where

$$\begin{aligned} \tau^{-1} &= \Delta g^2/5\tau_b, \quad B_0 = h/\mu_B\tau_b, \\ f(B^2/B_0^2) &= (B_0^2/B^2 + 1)^{-1}, \end{aligned} \tag{36}$$

α and β are coefficients of the order of unity, μ_B is the Bohr magneton, and τ_b is the correlation time of rotational motion of a radical. When describing the spin relaxation in the paramagnetic center–dislocation system, the correlation time τ_b is naturally replaced by the characteristic period τ_d of natural vibrations of dislocation segments pinned by paramagnetic impurities. The characteristic period τ_d can be estimated as

$$\tau_d \approx \Delta x/c_s \approx 10^{-10}\ \text{s}, \tag{37}$$

where Δx corresponds to estimate (25) and $c_s \sim 10^5$ cm/s is the velocity of sound.

As follows from relationships (35) and (36), at $B^2/B_0^2 \ll 1$, both functions $[T_1(B)]^{-1}$ and $[T_2(B)]^{-1}$ are proportional to B^2. However, in high fields ($B^2/B_0^2 \gg 1$), these dependences exhibit different behaviors, that is,

$$[T_1(B)]^{-1} \approx \text{const}, \quad [T_2(B)]^{-1} \sim aB^2 + b, \tag{38}$$

where a and b are constants. Therefore, in order to decide experimentally between the mechanisms of longitudinal and transverse spin relaxations, it is necessary to perform measurements in high fields.

The corresponding experiments were carried out using LiF crystals [32]. Figure 19 shows the dependences of the dimensionless mean free path of dislocations (reckoned from the background path) on the magnetic treatment time t in different magnetic fields at 293 and 77 K. It can be seen from Fig. 19 that, with an increase in the magnetic induction B, the slope of the linear dependence $l(t)$ first increases and then reaches a steady-state value in high fields. A decrease in the temperature to 77 K leads to a certain decrease in the slope dl/dt, but the mean free path of dislocations also reaches saturation in sufficiently high fields (Fig. 19, straight line *2*). This saturation is even more pronounced for the dependences $l(B)$ (Fig. 20). It is significant that a decrease in the treatment time t from 5 to 3 min and in the temperature (Fig. 20, curve *2'*) results in a decrease in the steady-state value. Consequently, this steady-state value is not associated with the geometric limit $\sim 1/\sqrt{\rho}$ typical of relaxation motion of dislocations (see Fig. 5).

Therefore, the behavior of the dependence $l(B)$ in the range of relatively high fields permits us to assume that the longitudinal spin relaxation in the magnetic field is responsible for the observed effect and to identify the depinning time τ_{dp} of the dislocation from the impurity with the time T_1 defined by formula (35). If

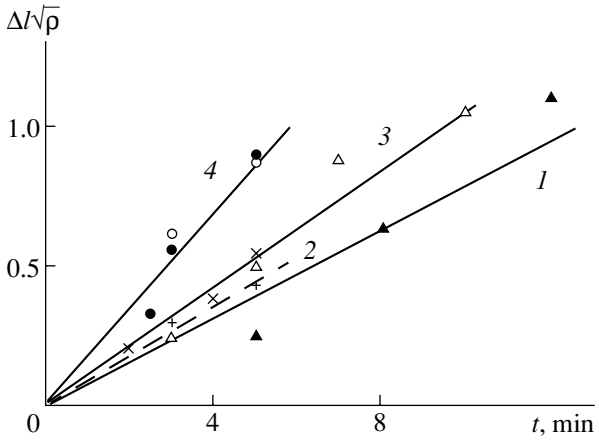

Fig. 19. Dependences of the normalized mean free path of dislocations $l\sqrt{\rho}$ on the magnetic treatment time t for LiF crystals at temperatures T = (*1*, *3*, *4*) 293 and (*2*) 77 K and magnetic inductions B = 0.6 (▲), 0.8 (△, +), 1 (○, ×), and 1.4 (●) T.

this assumption is correct, all the experimental curves in Fig. 20 should be described by the relationship

$$\Delta l\sqrt{\rho} = At[(B_0/B)^2 + 1]^{-1}. \quad (39)$$

Here, the parameter A is determined from the slope of the linear dependences $\Delta l\sqrt{\rho}(t)$ at $B \geq B_0$ (Fig. 19, straight lines *2*, *4*) and the field $B_0 = h/\mu_B\tau_d$ associated with the natural frequency of vibrations of dislocation segments can depend on the impurity concentration and should be independent of the temperature.

Actually, all the experimental data presented in Fig. 20 are described well in the $\Delta l\sqrt{\rho}/At$–$(B/B_0)^2$ coordinates by the expression

$$[(B_0/B)^2 + 1)]^{-1}, \quad (40)$$

which is typical of the mechanism of longitudinal spin relaxation (Fig. 21a). The solid line in Fig. 21a is calculated from expression (40) at B_0 = 0.8 T. Therefore, the experimental data for the LiF crystals allowed us to determine the fundamental parameter B_0 [see formulas (36)]:

$$B_0^{\mathrm{LiF}} \approx 0.8 \text{ T}. \quad (41)$$

As was shown above, the time $\tau_d = h/\mu_B B_0$ [see formulas (36)] depends on the mean length Δx of dislocation segments: $\tau_d = \Delta x/c_s$ [see relationship (37)]. It is reasonable to assume that an increase in the impurity concentration leads to a decrease in the mean length Δx and, hence, in the characteristic time τ_d. In [32], it was predicted that an increase in the concentration of point defects in crystals should result in an increase in the saturation field B_0 if the mechanism of longitudinal spin relaxation plays a decisive role in the depinning of dislocations from local obstacles in the magnetic field. In order to verify this prediction, comparative investigation of the magnetoplastic dynamics in the NaCl-3(Ca$^{(1)}$) and NaCl-3(Ca$^{(4)}$) crystals with the minimum and maximum Ca contents ($C_{\mathrm{Ca}}^{(1)} = 5 \times 10^{-7}$ mol/mol and $C_{\mathrm{Ca}}^{(4)} = 1 \times 10^{-4}$ mol/mol) was undertaken in [37]. Furthermore, for the same purpose, NaCl-3(Ca$^{(1)}$) crystals subjected to X-ray irradiation, which generate additional defects affecting the kinetics of the magnetoplastic effect, were studied in [22, 25].

The experimental technique in these investigations was identical to that used in [32] in the study of the LiF crystals. The results obtained for the above NaCl crystals are presented in Fig. 21b in the same coordinates as in Fig. 21a. As can be seen from Fig. 21b, an increase in the Ca concentration in the NaCl-3(Ca) from 5×10^{-7} to 10^{-4} mol/mol leads to an increase in the saturation field B_0 by a factor of 1.6: $B_0 \sim 0.5$ T for the NaCl-3(Ca$^{(1)}$) crystals and $B_0 \sim 0.8$ T for the NaCl-3(Ca$^{(4)}$) crystals. The X-ray irradiation of the NaCl-3(Ca$^{(1)}$) crystals for 5 and 10 s results in an increase in the saturation field B_0 from 0.5 to 0.7 T and to 0.8 T, respectively. The same tendency was observed in the study of the preliminarily irradiated LiF crystals. Therefore, the predicted increase in the saturation magnetic field with an increase in the concentration of paramagnetic centers [32] was confirmed completely. However, the question as to why an increase in the Ca concentration by a factor of 200 leads to an increase in the saturation field B_0 by a factor of only 1.6 remains open. This question will be considered below.

The saturation field B_0 measured for the NaCl-3(Ca$^{(1)}$) crystals corresponds to the time

$$\tau_d = h/\mu_B B_0 \approx 1.2 \times 10^{-10} \text{ s}, \quad (42)$$

which is in agreement with the above estimate (34) for the period of natural vibrations of dislocation segments for these crystals.

A good agreement between the theoretical dependence (40) and the experimental data and the coincidence of the estimated times τ_d (37) and (42) supports the hypothesis that the mechanism of longitudinal spin relaxation plays a governing role in the depinning of dislocations. The possibility of describing the dependences $l(B)$ for the LiF crystals at two strongly differing temperatures of 77 and 293 K (Fig. 21a) with the use of the same parameter B_0 = 0.8 T also favors this hypothesis.

Hence, there are strong grounds to identify the time τ_{dp} of the elementary act of dislocation depinning with the longitudinal spin relaxation time T_1 (35) and to write

$$\tau_{dp} = \frac{5\tau_d}{(\Delta g)^2}\left[\left(\frac{B_0}{B}\right)^2 + 1\right]. \quad (43)$$

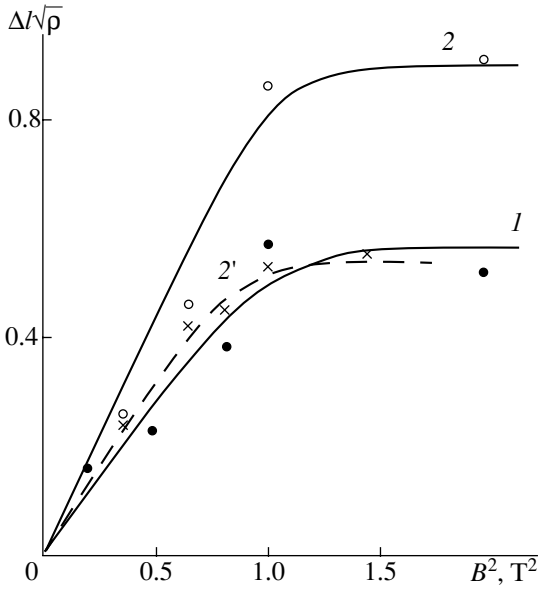

Fig. 20. Saturation of the normalized mean free path of dislocations in LiF crystals in high magnetic fields at temperatures T = (*1*, *2*) 293 and (*2*') 77 K and magnetic treatment times t = (*1*) 3 and (*2*, *2*') 5 min.

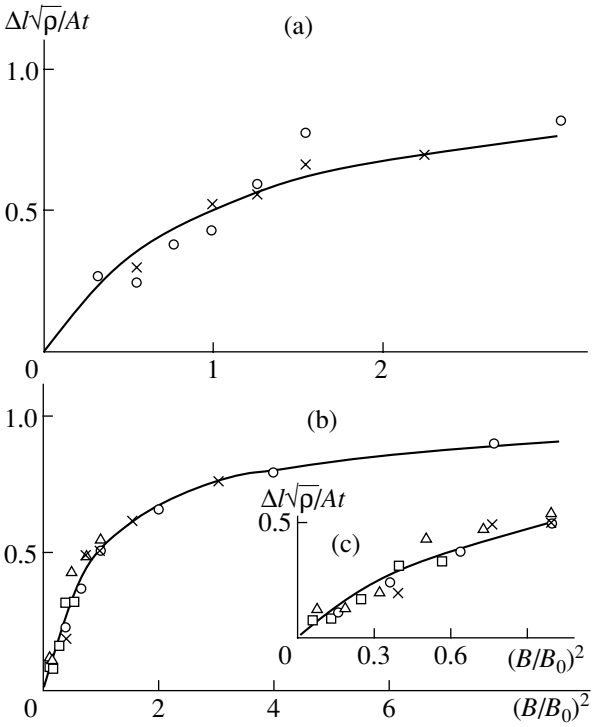

Fig. 21. Comparison of the experimental data (symbols) in the $\Delta l\sqrt{\rho}/At$–$(B/B_0)^2$ coordinates with the theoretical dependence $[(B_0/B)^2 + 1]^{-1}$ (solid lines) for (a) LiF crystals (according to the data presented in Fig. 20) at B_0 = 0.8 T and A = 0.23 (×) and 0.16 (○) min^{-1} and (b) NaCl-3 crystals at $C_{\mathrm{Ca}}^{(1)} = 5 \times 10^{-7}$ mol/mol, B_0 = 0.5 T, and A = 0.35 min^{-1} (○); $C_{\mathrm{Ca}}^{(4)} = 1 \times 10^{-4}$ mol/mol, B_0 = 0.8 T, and A = 0.16 min^{-1} (×); $C_{\mathrm{Ca}}^{(1)} = 5 \times 10^{-7}$ mol/mol, t_{ir} = 5 s, B_0 = 0.7 T, and A = 0.3 min^{-1} (△); $C_{\mathrm{Ca}}^{(1)} = 5 \times 10^{-7}$ mol/mol, t_{ir} = 10 s, B_0 = 0.8 T, and A = 0.28 min^{-1} (□).

It is of interest to compare this time with the aforementioned range (30) of permissible values for the NaCl-3(Ca$^{(1)}$) crystals at $B = B_0 = 0.5$ T. In this case, relationship (43) gives the formula

$$\tau_{dp}(B_0) = 10\tau_d/(\Delta g)^2. \quad (44)$$

By substituting estimate (37) or (42) for the time τ_d into formula (44), it is easy to check that the time $\tau_{dp}(B_0)$ falls in range (30) at quite reasonable anisotropies of the g factor $\Delta g \sim 3 \times 10^{-3}$–$10^{-2}$. This consistency of two different criteria is of prime importance, because it demonstrates that the Brocklehurst mechanism is slow enough for the magnetoplastic effect.

Note that this appears to be possible, because, in the system under investigation, there exists a relatively low frequency of natural vibrations of dislocation segments in the slip plane $\omega_d = 2\pi/\tau_d \sim 10^{11}$ s, which is several orders of magnitude lower than the Debye frequency. Most likely, this also leads to a lengthening of the spin–lattice relaxation time in the impurity–dislocation system. The specific feature of the situation is that the aforementioned low-frequency mode of dislocation vibrations exists only in one plane. Atomic vibrations in the dislocation core, along the dislocation line, and along the direction perpendicular to the slip plane have typical Debye frequencies. In other words, our spin system can be in equilibrium with a thermostat for particular spin components and undergoes a slow evolution for other spin components. Possibly, that is why the spin relaxation depend on the crystal orientation so that the crystal rotation at high frequencies $\nu > \nu_c$ suppresses the magnetoplastic effect.

13. THEORETICAL INTERPRETATION OF SOME PREVIOUSLY UNEXPLAINED DATA

Let us consider once again Fig. 10, which depicts two pairs of the experimental dependences $\Delta l(\nu)$ for the LiF and Al crystals at different magnetic inductions: 0.5 and 0.7 T for the LiF crystals and 0.7 and 1 T for the Al crystals. The magnetic inductions were chosen so that the ratio of the squares of the magnetic inductions in both cases was close to two. According to the predicted dependence $\nu_c \propto B^2$, we expected a twofold increase in the critical frequency for both crystals. However, an increase in the frequency was no more than one and a half. Now, it is clear that the dependences of the frequency $\nu_c = \alpha/\tau_{dp}$ and the mean free path $\Delta l(\nu = 0)$ on

the magnetic induction are somewhat more complex than those expected. According to expressions (39) and (43), these dependences are determined by the same function $f(B^2/B_0^2)$ defined by formula (36) and can be written as follows:

$$\nu_c(B) \propto (B_0^2/B^2 + 1)^{-1}, \quad \Delta l(B) \propto (B_0^2/B^2 + 1)^{-1}. \quad (45)$$

Only at $B \ll B_0$, the function $f(B^2/B_0^2)$ is reduced to B^2/B_0^2. However, earlier [see relationship (41)] we obtained $B_0 \sim 0.8$ T for the LiF crystals, which is not considerably larger than the used inductions (0.5 and, especially, 0.7 T). It can easily be shown that $f(0.7^2/0.8^2)/f(0.5^2/0.8^2) \sim 1.5$.

In principle, dependences (45) give an alternative method of determining the parameter B_0 from the experimental data by fitting it in such a way as to provide the best coincidence of the curves in Figs. 10a and 10b in the coordinates

$$\Delta l/f(B^2/B_0^2) - \nu/f(B^2/B_0^2). \quad (46)$$

The results of such a fitting for the LiF crystal are presented in Fig. 22a. The best agreement is observed at $B_0^{\mathrm{LiF}} \sim 0.75$ T. It can be seen from Fig. 22a that, at this parameter B_0^{LiF}, the experimental curves shown in Fig. 10a at different magnetic inductions B are reconstructed in coordinates (46) into the universal curve independent of the magnetic induction B. With allowance made for the errors of both methods, we can state that they give very close values of B_0. This means that the new method is valid and can be used for other crystals.

In particular, the saturation field B_0 was not previously measured for the Al crystals. As a result of a similar fitting for these crystals (Fig. 22b), the experimental points for two different magnetic inductions (Fig. 10b) satisfactorily fit the same curve, which enables us to determine the saturation field for the Al crystals, that is,

$$B_0^{\mathrm{Al}} \approx 0.9 \text{ T}. \quad (47)$$

Let us examine how the concentration of the Ca impurity in the NaCl-3 crystals affects the experimental dependences considered above. First, we analyze the experimental dependences $\Delta l(\nu)$ for the NaCl-3($Ca^{(2)}$) and NaCl-3($Ca^{(3)}$) crystals at $B = 0.5$ T (Fig. 9). As was noted above, an increase in the Ca concentration by one order of magnitude (from 10^{-6} to 10^{-5} mol/mol) results in a slight decrease in the critical frequency. Taking into account that $\nu_c \propto \tau_{dp}^{-1}$, we calculate the following ratio:

$$\frac{\tau_{dp}(C_{\mathrm{Ca}}^{(4)})}{\tau_{dp}(C_{\mathrm{Ca}}^{(1)})} = \frac{B_0^{(1)}}{B_0^{(4)}}\frac{(B_0^{(4)}/B)^2 + 1}{(B_0^{(1)}/B)^2 + 1} = \frac{1}{1.6}\frac{1.6^2 + 1}{2} = 1.11. \quad (48)$$

It can readily be checked that, for the approximated relationship $\tau_{dp} \propto C^{\gamma}$, ratio (48) corresponds to the exponent $\gamma = 0.02$, that is,

$$\tau_{dp} \propto C^{0.02} \text{ at } B = 0.5 \text{ T}. \quad (49)$$

Certainly, the time τ_{dp} depends not only on the concentration C but also on the magnetic induction B. Therefore, the fact that the time τ_{dp} is virtually independent of C is associated, to an extent, with the choice $B = 0.5$ T. The final estimate is as follows:

$$\frac{\nu_c^{(3)}}{\nu_c^{(2)}} \approx \left(\frac{C_{\mathrm{Ca}}^{(2)}}{C_{\mathrm{Ca}}^{(3)}}\right)^{0.02} = 10^{-0.02} \approx 0.95. \quad (50)$$

This result correctly represents the experimental data: with an increase in the impurity concentration, the critical frequency ν_c decreases only slightly, if at all.

Now, we return to the question arising in the preceding section: why an increase in the Ca concentration in the NaCl crystals by a factor of 200 leads to an increase in the saturation field B_0 by a factor of only 1.6. Let us reformulate the question in the following way: to which dependence $N(C)$ of the complex size on the impurity concentration this change in the saturation field B_0 corresponds. From the definition of the saturation field $B_0 = h/\mu_B\tau_d \sim hc_s/\mu_B\Delta x$ and formula (11), the ratio $B_0^{(4)}/B_0^{(1)}$ can be written in the form

$$\frac{B_0^{(4)}}{B_0^{(1)}} \approx \sqrt{\frac{C_{\mathrm{Ca}}^{(4)}}{C_{\mathrm{Ca}}^{(1)}}}\sqrt[3]{\frac{N^{(1)}}{N^{(4)}}} = \sqrt{200}\sqrt[3]{\frac{N^{(1)}}{N^{(4)}}} \approx 1.6. \quad (51)$$

By substituting $N \propto C^{\delta}$ into relationship (51), it can easily be found that $\delta \sim 1.23$, that is,

$$N(C) \propto C^{1.23}. \quad (52)$$

This approximate relationship is consistent with the data presented in Fig. 18 in which a linear dependence of N on C is traced. However, it should be remembered that relationship (52) is very rough. Indeed, the right-hand side of Eq. (51) is determined from the experimental data with a low accuracy. Moreover, the power dependence (52) is the approximation invalid for at least low concentrations C, because it is evident that $N \longrightarrow 1$ at $C \longrightarrow 0$. Nonetheless, relationship (52) can be used for semiqualitative estimates.

Let us use relationship (52) to justify theoretically the observed concentration dependence of the dislocation velocity. It can be seen from Figs. 7b and 8b that the mean free path Δl of dislocations (reckoned from the background path) and the probability W_{st} of beginning the dislocation motion per unit time decrease in the same manner with an increase in the impurity concentration C and are proportional to $C^{-0.5}$. This coincidence is not accidental, because both quantities are proportional to the mean dislocation velocity v [12, 14]. On the other hand, the fact that these dependences were obtained from different experimental data counts in favor of the empirical formula (7) according to which

$$v \propto C^{-0.5} \text{ at } B = 0.5 \text{ T}. \quad (53)$$

The left-hand side of relationship (53) can be calculated from the already checked expression (13) or, more precisely, its variant (34a) taking into account that the quantity n in the denominator should be proportional to $1/\Delta x$, i.e., to the ratio $\sqrt{C}/\sqrt[3]{N}$ [see formula (11)]. With the use of the approximate relationships (49) and (52), we obtain

$$v(C) \propto \frac{[N(C)]^{1/3}}{C\tau_{dp}(C)} \propto \frac{C^{0.41}}{C^{1.02}} \approx C^{-0.6}. \quad (54)$$

With allowance made for the low accuracy of our estimates, relationships (53) and (54) are in reasonable agreement, especially with due regard for the experimental errors in the determination of the exponent in relationship (53).

14. NEGATIVE MAGNETOPLASTIC EFFECT

The microscopic mechanism of the magnetoplastic effect under consideration is reduced to the removal of the spin forbiddenness of particular electronic transitions, which radically changes the configuration of the system and the energy of interaction of its components. However, this does not necessarily lead to a decrease in the interaction energy. In principle, the height of the local barrier associated with the impurity to the dislocation motion can decrease and increase in the magnetic field. In the preceding sections, we dealt with the plasticization only owing to the used method of examining the relaxation of the dislocation structure in the magnetic field in the absence of external actions. In this method, the magnetic hardening should manifest itself in our experiments as the absence of the magnetoplastic effect. A possible example can be seen from the data presented in Fig. 6b, according to which the mean free path of dislocations in the NaCl-3(Pb) crystal in the magnetic field remains equal to the background path and does not change with an increase in the magnetic induction. In order to reveal whether we deal with the absence (or a weak manifestation) of the magnetoplasticity or with the negative magnetoplastic effect, it is necessary to carry out experiments under the conditions of external loading.

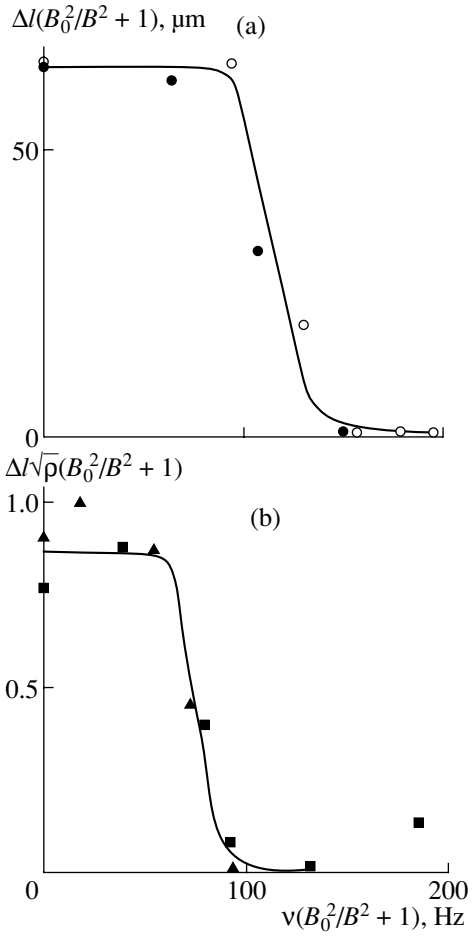

Fig. 22. Normalized dependences of the mean free path l of dislocations in (a) LiF and (b) Al crystals on the rotation frequency ν of the sample in a magnetic field (according to the data presented in Fig. 10) for magnetic inductions B = (a) 0.7 (●) and 0.5 (○) T at B_0 = 0.75 T and (b) 1 (▲) and 0.7 (■) T at B_0 = 0.9 T.

These investigations were performed in [30] with the use of a specially designed setup [75] for loading of crystals by compression pulses in the magnetic field. This setup made it possible to program and measure the amplitudes (0.05–100 N) and all time characteristics (from 0.3 ms to 1 h) of triangular and trapezoidal mechanical pulses.

Figure 23a depicts the dependences of the mean free path of dislocations on the amplitude of trapezoidal compression pulse for the NaCl-3 ($Pb^{(1)}$ and NaCl-3($Pb^{(2)}$) crystals ($C_{Pb}^{(1)} = 1 \times 10^{-6}$ mol/mol and $C_{Pb}^{(2)} = 1 \times 10^{-5}$ mol/mol). It can be seen from Fig. 23a that, in the absence of magnetic field, the mean free paths of dislocations in both crystals rapidly increase with an increase in the pulse amplitude and approximately correspond to the same experimental curve (curve *1*). Upon application of the magnetic field at B = 0.3 T, the situation changes drastically: at the same pulse amplitudes, the mean free path of dislocations considerably

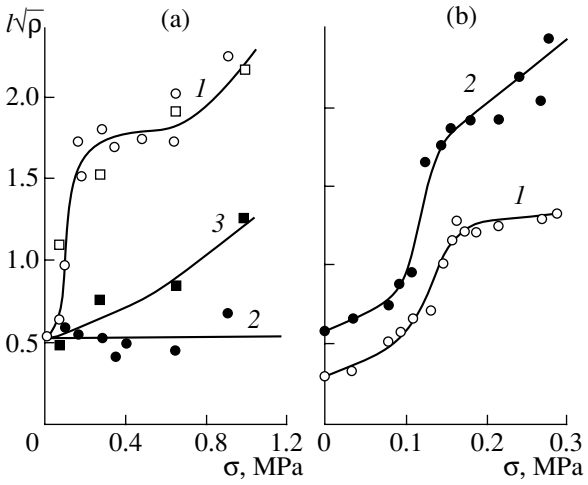

Fig. 23. Dependences of the normalized mean free path of dislocations $l\sqrt{\rho}$ on the amplitude of a trapezoidal mechanical compression pulse σ of length 5 min in a magnetic field at inductions B = (*1*) 0 and (*2*, *3*) 0.3 T for (a) NaCl-3(Pb) crystals at (*1*) (□) and (*2*) $C_{Pb}^{(2)} = 1 \times 10^{-5}$ mol/mol and (*1*) (□) and (*3*) $C_{Pb}^{(1)} = 1 \times 10^{-6}$ mol/mol and (b) NaCl-2 crystals.

decreases in the more pure NaCl-3(Pb$^{(1)}$) crystals (curve *3*) and remains equal to the background path in the NaCl-3(Pb$^{(2)}$) crystals. Consequently, the inference can be drawn that the lead impurity in the NaCl crystals results in the magnetic hardening effect.

For comparison, similar dependences for the NaCl-2 crystals containing the Ca impurity are plotted in Fig. 23b. As was shown above, the usual magnetic plasticization is observed in these crystals in the absence of addition mechanical loading. As could be expected, the magnetic field under pulsed deformation of these crystals also leads to an increase in the mean free path of dislocations.

Therefore, depending on the impurity type, the height of the barrier associated with the impurity to the dislocation motion can decrease and increase in the magnetic field. This opens up new possibilities of controlling the plastic properties of materials in the magnetic field with the use of doping.

15. MAGNETOPLASTIC EFFECT IN ALKALI HALIDE CRYSTALS UNDER SIMULTANEOUS ACTION OF AN ELECTRIC FIELD OR MECHANICAL LOADING

It is known that edge dislocations in alkali halide crystals bear an electric charge [76, 77]. This circumstance is responsible for the Stepanov effect [78], which manifests itself in the appearance of the electric polarization of samples under macrodeformation, and also for the inverse Stepanov effect, namely, the motion of dislocations in crystals in response to external electric fields. Different manifestations of the latter effect have been studied in many works (see the review [79]). Investigations were performed using rather high electric fields $E \sim 10^2$–10^3 kV/m. As a rule, lower electric fields do not affect the dislocation mobility. It was of interest to examine how the electric field affects the kinetic of the magnetoplastic effect.

For this purpose, the influence of weak electric fields (E = 0.25–9 kV/m) on the dislocation motion in the NaCl and LiF crystals in the magnetic field was investigated in [17, 24]. It is should be emphasized that, in the absence of the magnetic field, even the highest electric field used does not initiate the dislocation motion (except for background motions that do not depend on the field and are associated with the influence of etchants and the mechanical action on crystals upon application of contacts). However, even the minimum electric field E = 250 V/m applied to the NaCl-3(Ca$^{(1)}$) crystals results in a dramatic change in the dependence $l(B)$ obtained in [11] at E = 0 (see Fig. 24). It can be seen from Fig. 24 that the dependence $l(B)$ in the electric field reaches saturation corresponding to the mean spacing of forest dislocations $\sim 1/\sqrt{\rho}$ already at magnetic inductions higher than 0.15 T, at which an almost background path is observed at E = 0.

At E = 0, dislocations chaotically move over the crystal in the magnetic field, which reflects a chaotic distribution of internal stresses. The dislocation motion in the electric field is more ordered in character. The majority of edge dislocations reverse their direction of motion with a change in the polarity of the electric field. This agrees with a linear dependence of the mean free path of dislocations on the electric field strength. It was found that the dislocation mobility in the magnetic field strongly depends on the mutual orientation of the electric field, the dislocation line, and the Burgers vector of dislocation. The electric field aligned along the dislocation or perpendicular to the slip plane does not change the mean free path of dislocations in the magnetic field. The maximum dislocation mobility upon simultaneous application of fields is observed when the electric field vector lies perpendicular to the dislocation line in the slip plane.

All these facts suggest the force nature of the electric field effect on the dislocation mobility. Figure 25 presents the experimental data on the dislocation mobility in the LiF crystals rotating in the magnetic field upon application of the constant electric field. As can be seen from Fig. 25, the electric field increases the mean free path of edge dislocations and does not change the mean free path of screw (neutral) dislocations. The critical frequencies ν_c of rotation for edge and screw dislocations are different but remain unchanged upon application of the electric field. Consequently, the electric field has no effect on the time τ_{dp}

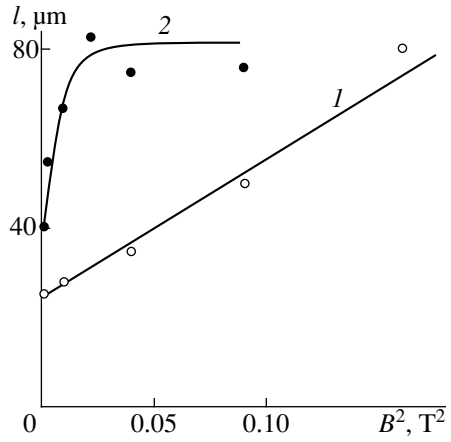

Fig. 24. Dependences of the mean free path of dislocations l in NaCl-3 crystals ($C_{Ca}^{(1)} = 5 \times 10^{-7}$ mol/mol) on the magnetic induction B under simultaneous exposure to an electric field E for 5 min. E = (*1*) 0 and (*2*) 0.25 kV/m.

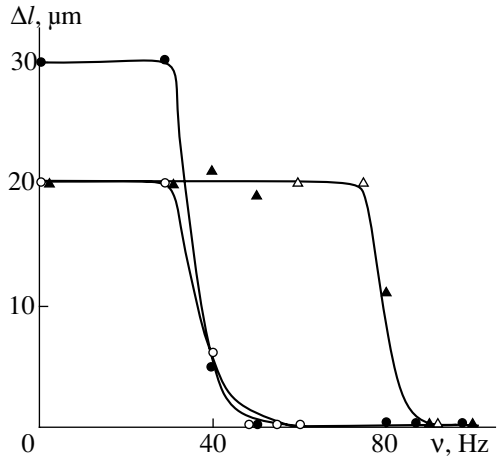

Fig. 25. Dependences of the mean free path of edge (●, ○) and screw (▲, △) dislocations l in LiF crystals on the rotation frequency ν of the sample in a magnetic field of 0.5 T for 5 min under simultaneous exposure to a dc electric field E. E = 2 (●, ▲) and 0 kV/m (○, △).

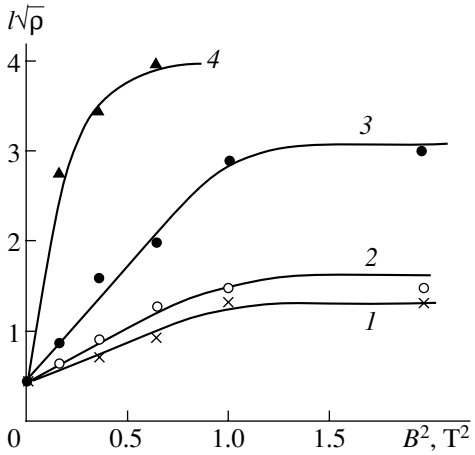

Fig. 26. Dependences of the normalized mean free path of edge dislocations $l\sqrt{\rho}$ in LiF crystals on the magnetic field induction B under simultaneous exposure to magnetic and electric fields (t = min). Electric field E (kV/m): (*1*) 0, (*2*) 3, (*3*) 6, and (*4*) 9.

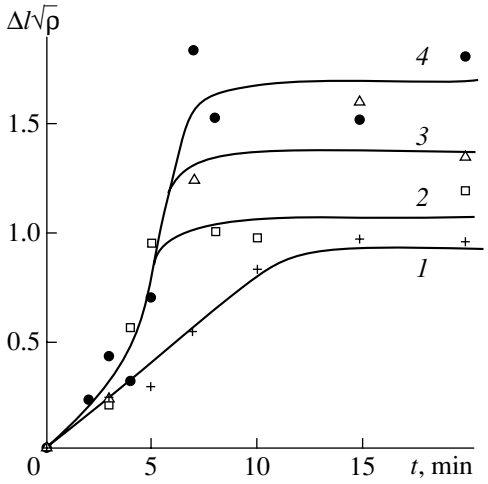

Fig. 27. Dependences of the normalized mean free path of dislocations $\Delta l\sqrt{\rho}$ in NaCl-2 crystals on the time t under simultaneous action of a magnetic field of 0.3 T and a trapezoidal mechanical pulse with the amplitudes σ = (*1*) 0, (*2*) 120, (*3*) 140, and (*4*) 220 kPa.

of elementary act of dislocation depinning from paramagnetic impurity centers.

Therefore, the force nature of the electric field effect on edge dislocations is beyond question. A sharp increase (by approximately two orders of magnitude) in the sensitivity of the dislocation mobility to the electric field under simultaneous exposure to the magnetic field is most likely explained by the fact that our crystals involve paramagnetic centers and also other obstacles insensitive to the magnetic field (forest dislocations and other impurity complexes). The numbers of the former and latter obstacles in the pure crystals differ substantially. In the magnetic field, paramagnetic centers do not pin dislocations and even internal stresses induce the forces sufficient for overcoming the other defects. Consequently, in the magnetic field, electric forces comparable to the driving force of internal stresses can lead to a noticeable increase in the dislocation mobility. In the absence of magnetic field, a similar effect can be caused by the electric forces that should be comparable to the forces associated with the stresses of the order of the yield stress, which, in our case, turns out to be two orders of magnitude larger than internal stresses.

It was demonstrated above that, when only the magnetic field is applied in the absence of other external actions, the dependence $l(B)$ at sufficiently large magnetic inductions B and magnetic treatment times t reaches a steady-state value corresponding to the mean

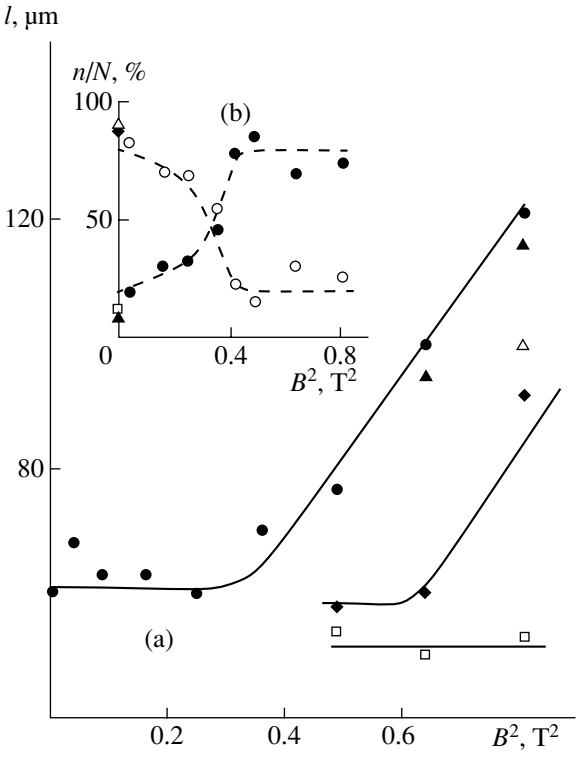

Fig. 28. Dependences of (a) the mean free path l and (b) the relative number n/N of diverging (●, ▲, △, □, ◆) and contracting (○) 60° dislocations on the magnetic field induction for different InSb single crystals subjected to preliminary mechanical loading at 15 (●, ○, ▲, △, □) and 10 (◆) MPa for t = 10 min at T = 273 K. InSb single crystals: n-InSb (1×10^{14} cm^{-3}) (●, ○, ◆), n-InSb(Te) (1×10^{18} cm^{-3}) (□), p-InSb(Ge) (1×10^{18} cm^{-3}) (▲), and p-InSb(Ge) (1×10^{17} cm^{-3}) (△).

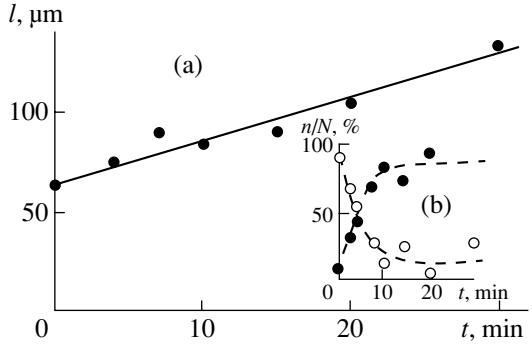

Fig. 29. Dependences of (a) the mean free path l and (b) the relative number n/N of diverging (●) and contracting (○) 60° dislocations in n-InSb (1×10^{14} cm^{-3}) single crystals on the magnetic treatment time t in a magnetic field of 0.7 T at a temperature of 473 K.

spacing of dislocations $1/\sqrt{\rho}$. The same situation is observed in the external electric field (Fig. 24) but at relatively low field strengths E. As can be seen from the experimental data presented in Fig. 26, the steady-state value in sufficiently high fields increases and is determined by the electric field strength E [33]. Most likely, this corresponds to the motion of such a large number of dislocations and such "deep" relaxation of the internal stress field when the local mean spacing of dislocations $1/\sqrt{\rho}$ increases noticeably. It is not accidental that a similar effect is observed for the same crystals in the magnetic field under the action of mechanical stresses rather than the electric field (Fig. 27).

16. MAGNETOPLASTIC EFFECT IN InSb CRYSTALS

The motion of individual dislocations in the InSb semiconductor crystal subjected to magnetic treatment in the absence of mechanical loading was first found in [31]. The first experiments were performed using pure n-InSb single crystals with a carrier concentration of 1×10^{14} cm^{-3}. In order to introduce fresh dislocations, a shallow scratch along the [110] direction on the (111) surface was cut by a corundum needle. Under subsequent deformation by the four-point probe technique at a temperature of 200°C and the load σ = 15 MPa for 5 min, dislocations were driven away from the scratch over a distance of 1000–2000 μm. The prepared samples were subjected to magnetic treatment at B = 0.2–0.9 T for the time t from several seconds to 50 min. The experiments were carried out at temperatures of 120, 150, 200, and 250°C with a preliminary slow heating for 50 min and a subsequent slow cooling. No external load was applied in the course of magnetic treatment. The check samples were prepared in the same way except for the exposure to the magnetic field, i.e., were annealed at B = 0. As usual, the chemical etching technique was used for observing fast 60° dislocations.

It was found that dislocations move both toward the scratch (contracting dislocation half-loops) and away of the scratch (diverging dislocation half-loops). In the check samples, the number of dislocations moving toward the scratch was as large as 90% of the total number of moving dislocations. In the samples subjected to magnetic treatment, with an increase in the magnetic induction B and the treatment time t, more and more dislocations move away from the scratch (see Figs. 28, 29). At sufficiently large B and t, the number of diverging mobile dislocations was as large as 90%. It is significant that, above a certain threshold field $B > B_c$, the mean free path of diverging dislocations becomes proportional to B^2 (Fig. 28a). Moreover, the dependence of the mean free path of diverging dislocations on the magnetic treatment time exhibits a linear behavior (Fig. 29). Note that the mean free path of contracting dislocations does not depend on the magnetic induction B.

The influence of the conductivity type and the degree of doping of the InSb single crystals on the mobility of 60° dislocations in the magnetic field was investigated in [36]. It was revealed that the doping of the pure InSb crystal with tellurium (n type) to a concentration of 10^{18} cm^{-3} (symbols □ in Fig. 28a) leads to

a decrease in the dislocation mobility to the background mobility. At the same time, the *p*-InSb crystals doped with germanium at the same carrier concentration (10^{18} cm^{-3}) are characterized by a pronounced magnetoplastic effect (symbols ▲ in Fig. 28a).

A decrease in the Ge dopant concentration ($C_{Ge} = 1 \times 10^{17}$ cm^{-3}) results in a decrease in the mean free path of diverging dislocations in the magnetic field (symbol △ in Fig. 28a). The magnetoplastic effect disappears with a further decrease in the Ge concentration to 1.6×10^{14} cm^{-3}. It should be noted that opposite tendencies were observed in mechanical testing of the same crystals in the absence of magnetic field [80]. The mean free path slightly increases with an increase in the Te concentration and appreciably decreases with an increase in the Ge concentration. It seems likely that the dislocation mobility in the magnetic field depends not only the conductivity type but also on the magnetic state of a dopant. It is not inconceivable that the magnetic treatment of the InSb crystal doped with tellurium leads to the hardening, as is the case for the aforementioned negative magnetoplastic effect in the NaCl-3(Pb) crystals [30].

17. CONCLUSIONS

Certainly, the above data on the magnetoplastic effect in InSb crystals are few in order to offer their complete interpretation. However, there are grounds to believe that, despite the specific features of the dislocation dynamics in these crystals, the basic idea underlying the explanation of the first findings remains the same, namely, the spin-dependent depinning of dislocations from impurity centers and the subsequent relaxation motion of dislocations in a very complex internal stress field superposed on the Peierls relief.

In this sense, much progress toward the understanding of similar processes in alkali halide and nonmagnetic crystals has been achieved. As a whole, it can be stated that the developed concept is self-consistent as applied to these crystals and makes it possible to explain (sometimes, even quantitatively) almost all specific features of our findings. Most likely, we succeeded in elucidating the particular microscopic mechanism responsible for the magnetoplastic effect. This is the longitudinal spin relaxation in the magnetic field, which was originally proposed by Brocklehurst [74]. As a result of the dislocation peculiarity, this mechanism is even slower than in the Brocklehurst theory developed for chemical reactions. However, owing to the slowness and the characteristic dependence on the magnetic field, the Brocklehurst mechanism adequately describes different qualitative and quantitative regularities of the magnetoplastic effect, which were found in our experiments.

Like any new phenomenon, the magnetoplastic effect opens up new possibilities in different directions. For example, the magnetoplastic effect allows one to measure the spin–lattice relaxation time of defects on dislocations. It is unlikely that there exists an alternative method that provides a way of separating defects on dislocations from defects in the bulk of a crystal in such measurements.

Owing to the unique sensitivity to small doses of radiation, the magnetoplastic effect can find application in dosimetry. Moreover, the idea of the development of new spectroscopy based on the magnetoplastic effect for analysis of radiation-induced defects in crystals after their irradiation at low doses seems to be quite realistic (see Figs. 12–14). However, this calls for further investigation with the use of a large set of different techniques.

The found enhancement of the inverse Stepanov effect in the magnetic field by two or three orders of magnitude offers strong possibilities of controlling the real structure of crystals through combined electromagnetic actions. We already use the magnetic treatment of crystals to stabilize the dislocation structure and to lower internal stresses. We experimentally proved that the magnetic treatment of crystals with the aim of lowering the internal stresses is quite competitive with the traditional mechanical vibrational loading [35].

The discovery of the negative magnetoplastic effect demonstrates that the controlled doping is promising for increasing the strength of materials intended for operation in high magnetic fields. At the same time, the potentialities associated with the optimization of processing of materials by controlling their plasticity with external magnetic fields hold the greatest promise. The data presented in the review on the influence of magnetic field on the mean free path of dislocations and the number of mobile dislocations unambiguously show that the magnetic field affects macroscopic characteristics of the plastic deformation, such as the yield stress, because the plastic shear is determined by the product of the mean free path of dislocations and the number of mobile dislocations. It was experimentally established [38–41] that a sufficiently slow deformation in a magnetic field of 0.5 T can lead to a severalfold decrease in the yield stress.

Undeniably, the above examples do not exhaust the possible fields of practical application of the magnetoplasticity and the magnetic hardening. However, turning back to the physical aspects of the magnetosensitive plasticity, we note an important lesson given by nature. Traditionally, microscopic processes on the dislocation level were predominantly described within mechanistic models in which impurity centers were identified with balls (dilatation centers) that mismatch occupied holes and, hence, dilate a lattice and generate internal stresses in a crystal. It was conventional to use these stresses to evaluate the energy of interaction of impurities with dislocations. Undoubtedly, these models cannot include such subtle spin effects with which we are faced. Therefore, when dealing with objects on the atomic level, it should be remembered that the case in

point is complex ensembles of particles, which are controlled not by classical mechanics but by quantum mechanics with the selection rules, Pauli principle, and other laws.

It should be noted that investigations into the influence of magnetic fields on the mechanical properties of crystals and their growth kinetics have attracted continuously increasing interest. At present, approximately ten scientific groups in Russia and other countries perform extensive research in this field. A new scientific direction is now in prospect. More than 15 years ago, when our scientific group was just formed, this was out of the question. Certainly, the results discussed above cover only a part of the data accumulated to date on the magnetoplasticity. It is hoped that our work will give impetus to new, more comprehensive publications, which will take into account our contribution to progress in this field.

ACKNOWLEDGMENTS

We are grateful to our coauthors and other colleagues for their participation at different stages of our investigation. Special thanks are due to V.A. Morozov and his coworkers. In our collaborative experiments performed in 1985, we first conceived the idea of the existence of the magnetoplasticity (see [34]).

This work was supported in part by the Russian Foundation for Basic Research (project no. 03-02-17021) and the Russian Academy of Sciences (the 6th Competition of Research Projects of Young Scientists of the Russian Academy of Sciences).

REFERENCES

1. N. V. Zagoruiko, Kristallografiya **10** (1), 81 (1965) [Sov. Phys. Crystallogr. **10**, 63 (1965)].
2. E. J. Sharp and D. A. Avery, Phys. Rev. B **158** (2), 511 (1967).
3. G. I. Distler, V. M. Kanevskiĭ, V. V. Moskvin, *et al.*, Dokl. Akad. Nauk SSSR **268** (3), 591 (1983) [Sov. Phys. Dokl. **28**, 43 (1983)].
4. J. M. Galigan and C. S. Pang, J. Appl. Phys. **50** (10), 6253 (1979).
5. V. P. Lebedev and V. S. Krylovskiĭ, Fiz. Tverd. Tela (Leningrad) **27** (5), 1285 (1985) [Sov. Phys. Solid State **27**, 777 (1985)].
6. V. A. Pavlov, I. A. Pereturina, and I. L. Pecherkina, Phys. Status Solidi **57**, 449 (1980).
7. D. N. Bol'shutkin and V. A. Desnenko, Fiz. Nizk. Temp. **7** (5), 652 (1981) [Sov. J. Low Temp. Phys. **7**, 321 (1981)].
8. V. Ya. Kravchenko, Pis'ma Zh. Éksp. Teor. Fiz. **12** (11), 551 (1970) [JETP Lett. **12**, 391 (1970)].
9. L. M. Grishin, É. A. Kaner, and E. R. Fel'dman, Zh. Éksp. Teor. Fiz. **70**, 1445 (1976) [Sov. Phys. JETP **43**, 753 (1976)].
10. V. I. Al'shits, E. V. Darinskaya, T. M. Perekalina, and A. A. Urusovskaya, Fiz. Tverd. Tela (Leningrad) **29** (2), 467 (1987) [Sov. Phys. Solid State **29**, 265 (1987)].
11. V. I. Al'shits, E. V. Darinskaya, and E. A. Petrzhik, Izv. Vyssh. Uchebn. Zaved., Chern. Metall., No. 10, 85 (1990).
12. V. I. Al'shits, E. V. Darinskaya, and E. A. Petrzhik, Fiz. Tverd. Tela (Leningrad) **33** (10), 3001 (1991) [Sov. Phys. Solid State **33**, 1694 (1991)].
13. V. I. Al'shits, E. V. Darinskaya, I. V. Gektina, and F. F. Lavrent'ev, Kristallografiya **35** (4), 1014 (1990) [Sov. Phys. Crystallogr. **35**, 597 (1990)].
14. V. I. Al'shits, E. V. Darinskaya, and E. A. Petrzhik, Fiz. Tverd. Tela (St. Petersburg) **34** (1), 155 (1992) [Sov. Phys. Solid State **34**, 81 (1992)].
15. V. I. Al'shits, R. Voska, E. V. Darinskaya, and E. A. Petrzhik, Fiz. Tverd. Tela (St. Petersburg) **35** (1), 70 (1993) [Phys. Solid State **35**, 37 (1993)].
16. V. I. Al'shits, E. V. Darinskaya, and E. A. Petrzhik, Fiz. Tverd. Tela (St. Petersburg) **35** (2), 320 (1993) [Phys. Solid State **35**, 162 (1993)].
17. V. I. Al'shits, E. V. Darinskaya, E. Yu. Mikhina, and E. A. Petrzhik, Fiz. Tverd. Tela (St. Petersburg) **35** (5), 1397 (1993) [Phys. Solid State **35**, 706 (1993)].
18. V. I. Al'shits, E. V. Darinskaya, O. L. Kazakova, *et al.*, Izv. Akad. Nauk, Ser. Fiz. **57** (11), 2 (1993).
19. V. I. Alshits, E. V. Darinskaya, and E. A. Petrzhik, Mater. Sci. Eng. A **164**, 322 (1993).
20. V. I. Alshits, E. V. Darinskaya, O. L. Kazakova, *et al.*, J. Alloys Compd. **211–212**, 548 (1994).
21. V. I. Alshits, E. V. Darinskaya, O. L. Kazakova, *et al.*, in *Applied Crystallography*, Ed. by H. Morawiec and D. Stoz (World Sci., London, 1994), p. 301.
22. V. I. Al'shits, E. V. Darinskaya, and O. L. Kazakova, Pis'ma Zh. Éksp. Teor. Fiz. **62** (4), 352 (1995) [JETP Lett. **62**, 375 (1995)].
23. V. I. Al'shits, E. V. Darinskaya, O. L. Kazakova, *et al.*, Pis'ma Zh. Éksp. Teor. Fiz. **63** (8), 628 (1996) [JETP Lett. **63**, 668 (1996)].
24. V. I. Al'shits, E. V. Darinskaya, E. Yu. Mikhina, and E. A. Petrzhik, Fiz. Tverd. Tela (St. Petersburg) **38** (8), 2426 (1996) [Phys. Solid State **38**, 1333 (1996)].
25. V. I. Al'shits, E. V. Darinskaya, and O. L. Kazakova, Zh. Éksp. Teor. Fiz. **111** (2), 615 (1997) [JETP **84**, 338 (1997)].
26. V. I. Alshits, E. V. Darinskaya, O. L. Kazakova, *et al.*, Mater. Sci. Eng. A **234–236**, 617 (1997).
27. V. I. Alshits, E. V. Darinskaya, O. L. Kazakova, *et al.*, Am. Soc. Test. Mater. **1304**, 153 (1997).
28. V. I. Al'shits, E. V. Darinskaya, and O. L. Kazakova, Fiz. Tverd. Tela (St. Petersburg) **40** (1), 81 (1998) [Phys. Solid State **40**, 70 (1998)].
29. V. I. Al'shits, E. V. Darinskaya, E. Yu. Mikhina, and E. A. Petrzhik, Pis'ma Zh. Éksp. Teor. Fiz. **67** (10), 788 (1998) [JETP Lett. **67**, 832 (1998)].
30. E. V. Darinskaya and M. V. Koldaeva, Pis'ma Zh. Éksp. Teor. Fiz. **70** (3), 226 (1999) [JETP Lett. **70**, 228 (1999)].
31. E. V. Darinskaya, E. A. Petrzhik, S. V. Erofeeva, and V. P. Kisel', Pis'ma Zh. Éksp. Teor. Fiz. **70** (4), 298 (1999) [JETP Lett. **70**, 309 (1999)].

32. V. I. Al'shits and E. V. Darinskaya, Pis'ma Zh. Éksp. Teor. Fiz. **70** (11), 749 (1999) [JETP Lett. **70**, 761 (1999)].
33. V. I. Alshits, E. V. Darinskaya, O. L. Kazakova, *et al.*, in *Trends in Continuum Physics (TRECOP'88)*, Ed. by B. T. Maruszewski, W. Muschik, and A. Radowicz (World Sci., Singapore, 1999), p. 14.
34. V. I. Al'shits, E. V. Darinskaya, M. A. Legen'kov, and V. A. Morozov, Fiz. Tverd. Tela (St. Petersburg) **41** (11), 2004 (1999) [Phys. Solid State **41**, 1839 (1999)].
35. V. I. Al'shits, E. V. Darinskaya, and M. V. Koldaeva, Fiz. Tverd. Tela (St. Petersburg) **43** (9), 1635 (2001) [Phys. Solid State **43**, 1703 (2001)].
36. E. A. Petrzhik, E. V. Darinskaya, S. A. Erofeeva, and M. R. Raukhman, Fiz. Tverd. Tela (St. Petersburg) **45** (2), 254 (2003) [Phys. Solid State **45**, 266 (2003)].
37. E. V. Darinskaya and E. Hartman, Fiz. Tverd. Tela (St. Petersburg) **45** (2003) (in press).
38. A. A. Urusovskaya, V. I. Al'shits, A. E. Smirnov, and N. N. Bekkauer, Pis'ma Zh. Éksp. Teor. Fiz. **65** (6), 470 (1997) [JETP Lett. **65**, 497 (1997)].
39. V. I. Al'shits, N. N. Bekkauér, A. E. Smirnov, and A. A. Urusovskaya, Zh. Éksp. Teor. Fiz. **115**, 951 (1999) [JETP **88**, 523 (1999)].
40. A. A. Urusovskaya, V. I. Al'shits, N. N. Bekkauer, and A. E. Smirnov, Fiz. Tverd. Tela (St. Petersburg) **42** (2), 267 (2000) [Phys. Solid State **42**, 274 (2000)].
41. V. I. Al'shits, A. A. Urusovskaya, A. E. Smirnov, and N. N. Bekkauer, Fiz. Tverd. Tela (St. Petersburg) **42** (2), 270 (2000) [Phys. Solid State **42**, 277 (2000)].
42. A. A. Urusovskaya, A. E. Smirnov, and N. N. Bekkauer, Vestn. Tambov Gos. Univ., Ser.: Estestv. Tekh. Nauki **5** (2–3), 389 (2000).
43. Yu. I. Golovin and R. B. Morgunov, Pis'ma Zh. Éksp. Teor. Fiz. **61** (7), 583 (1995) [JETP Lett. **61**, 596 (1995)].
44. B. I. Smirnov, N. N. Peschanskaya, and V. I. Nikolaev, Fiz. Tverd. Tela (St. Petersburg) **43** (12), 2154 (2001) [Phys. Solid State **43**, 2250 (2001)].
45. N. A. Tyapunina, V. L. Krasnikov, and É. P. Belozerova, Izv. Akad. Nauk, Ser. Fiz. **64** (9), 1776 (2000).
46. O. I. Datsko, Fiz. Tverd. Tela (St. Petersburg) **44** (2), 289 (2002) [Phys. Solid State **44**, 300 (2002)].
47. Yu. I. Golovin and R. B. Morgunov, Pis'ma Zh. Éksp. Teor. Fiz. **58** (3), 189 (1993) [JETP Lett. **58**, 191 (1993)].
48. Yu. I. Golovin and R. B. Morgunov, Zh. Éksp. Teor. Fiz. **115** (2), 605 (1999) [JETP **88**, 332 (1999)].
49. R. B. Morgunov and A. A. Baskakov, Fiz. Tverd. Tela (St. Petersburg) **43** (9), 1632 (2001) [Phys. Solid State **43**, 1700 (2001)].
50. A. A. Skvortsov, A. M. Orlov, and L. I. Gonchar, Zh. Éksp. Teor. Fiz. **120** (1), 134 (2001) [JETP **93**, 117 (2001)].
51. A. E. Smirnov and A. A. Urusovskaya, Fiz. Tverd. Tela (Leningrad) **29** (3), 852 (1987) [Sov. Phys. Solid State **29**, 485 (1987)].
52. Yu. I. Golovin, R. B. Morgunov, D. V. Lopatin, and A. A. Baskakov, Phys. Status Solidi A **160**, 3 (1997).
53. S. A. Gridnev, K. S. Drozhdin, and V. V. Shmykov, Fiz. Tverd. Tela (St. Petersburg) **42** (2), 318 (2000) [Phys. Solid State **42**, 326 (2000)].
54. Yu. A. Osip'yan, Yu. I. Golovin, R. B. Morgunov, *et al.*, Fiz. Tverd. Tela (St. Petersburg) **43** (7), 1333 (2001) [Phys. Solid State **43**, 1389 (2001)].
55. M. V. Koldaeva, in *Abstracts of 1st Russian Conference of Young Scientists on Physical Materials Science* (Manuskript, Kaluga, 2001), p. 39.
56. N. N. Peschanskaya and P. N. Yakushev, Fiz. Tverd. Tela (St. Petersburg) **39** (9), 1690 (1997) [Phys. Solid State **39**, 1509 (1997)].
57. Yu. I. Golovin, R. B. Morgunov, and S. Yu. Liksutin, Vysokomol. Soedin., Ser. B **40**, 373 (1999).
58. V. M. Kanevskiĭ, G. I. Distler, A. E. Smirnov, *et al.*, Izv. Akad. Nauk SSSR, Ser. Fiz. **48** (12), 2408 (1984).
59. V. B. Pariĭskiĭ, A. I. Landau, and V. I. Startsev, Fiz. Tverd. Tela (Leningrad) **5**, 1377 (1963) [Sov. Phys. Solid State **5**, 1002 (1963)].
60. A. L. Buchachenko, R. Z. Sagdeev, and K. M. Salikhov, *Magnetic and Spin Effects in Chemical Reactions* (Nauka, Novosibirsk, 1978).
61. Ya. B. Zel'dovich, A. L. Buchachenko, and E. L. Frankevich, Usp. Fiz. Nauk **155** (1), 3 (1988) [Sov. Phys. Usp. **31**, 385 (1988)].
62. V. V. Kveder, Yu. A. Osip'yan, and A. I. Shalynin, Zh. Éksp. Teor. Fiz. **83** (2), 699 (1982) [Sov. Phys. JETP **56**, 389 (1982)].
63. S. A. Dembovskiĭ, Pis'ma Zh. Éksp. Teor. Fiz. **41** (2), 74 (1985) [JETP Lett. **41**, 88 (1985)].
64. S. D. Savranskiĭ, Fiz. Khim. Stekla **13** (5), 659 (1987).
65. M. A. Golosovskiĭ, Yu. A. Osip'yan, and Ya. M. Soĭfer, Fiz. Tverd. Tela (Leningrad) **24** (2), 602 (1982) [Sov. Phys. Solid State **24**, 339 (1982)].
66. Yu. A. Osip'yan and I. V. Savchenko, Pis'ma Zh. Éksp. Teor. Fiz. **7** (4), 130 (1968) [JETP Lett. **7**, 100 (1968)].
67. N. Itoh, Adv. Phys. **31**, 491 (1982).
68. Ch. B. Lushchik and A. Ch. Lushchik, *Decay of Electronic Excitations with Defect Formation in Solids* (Nauka, Moscow, 1989), p. 263.
69. L. F. Mollenauer, S. Pan, and J. Winnacker, Phys. Rev. Lett. **26**, 1643 (1971).
70. P. A. Schnegg, C. Jaccard, and M. Aegerter, Phys. Status Solidi B **63**, 587 (1974).
71. I. O. Mavlonazarov and V. M. Mikushev, Fiz. Tverd. Tela (St. Petersburg) **34**, 2257 (1992) [Sov. Phys. Solid State **34**, 1206 (1992)].
72. M. I. Molotskiĭ, Fiz. Tverd. Tela (Leningrad) **33** (10), 3112 (1991) [Sov. Phys. Solid State **33**, 1760 (1991)].
73. M. I. Molotskiĭ, Fiz. Tverd. Tela (St. Petersburg) **35** (1), 11 (1993) [Phys. Solid State **35**, 5 (1993)].
74. B. Brocklehurst, Nature **221**, 921 (1969).
75. M. V. Koldaeva, E. V. Darinskaya, and V. N. Sytin, Prib. Tekh. Éksp., No. 3, 151 (1998).
76. A. A. Urusovskaya, Usp. Fiz. Nauk **96**, 39 (1968) [Sov. Phys. Usp. **11**, 631 (1968)].
77. R. W. Witworth, Adv. Phys. **24**, 203 (1975).
78. A. V. Stepanov, Z. Phys. B **81** (7–8), 560 (1933).
79. N. A. Tyapunina and É. P. Belozerova, Usp. Fiz. Nauk **156** (4), 683 (1988) [Sov. Phys. Usp. **31**, 1060 (1988)].
80. S. A. Erofeeva, Philos. Mag. A **70**, 943 (1994).

Translated by O. Borovik-Romanova

Crystallography Reports, Vol. 48, No. 5, 2003, pp. 796–812. Translated from Kristallografiya, Vol. 48, No. 5, 2003, pp. 855–872.

REAL STRUCTURE OF CRYSTALS: REVIEWS

Dedicated to the 60th Anniversary of the Shubnikov Institute of Crystallography of the Russian Academy of Sciences

The Influence of Magnetic Effects on the Mechanical Properties and Real Structure of Nonmagnetic Crystals

A. A. Urusovskaya*†, V. I. Alshits*, A. E. Smirnov*, and N. N. Bekkauer**

** Shubnikov Institute of Crystallography, Russian Academy of Sciences, Leninskiĭ pr. 59, Moscow, 119333 Russia*

e-mail: asmirnov@ns.crys.ras.ru, alshits@ns.crys.ras.ru

*** Peoples' Friendship University, ul. Miklukho-Maklaya 6, Moscow, 117198 Russia*

Received April 14, 2003

Abstract—This review for the first time systematizes the results of our investigations into the influence of magnetic effects on the mechanical properties and the real structure of nonmagnetic crystals. It is found that the preliminary magnetic treatment of alkali halide crystals leads to a decrease in their solubility and a change in the microhardness and yield stress. The magnetic field strongly affects the macroplasticity of LiF, NaCl, and PbS crystals under deformation in a magnetic field. This is accompanied by a change in the shape of stress–strain curves, a shortening of deformation stages, a change in the hardening coefficients, and a decrease in the yield stress. It is revealed that the magnetic effects exhibit threshold behavior. The yield stress is measured as a function of the magnetic induction and the strain rate. It is established that the magnetic and electric fields have a joint effect on the kinetics of plastic deformation. A kinematic model of the macroscopic magnetoplastic effect is proposed. © *2003 MAIK "Nauka/Interperiodica".*

CONTENTS

† Deceased.

1. INTRODUCTION

The problem of interaction of a field with a material is a fundamental problem in solid-state physics. The influence of electric and magnetic fields on different physical (including mechanical) properties of metals and experimental observations of the field effects on materials have long since been discussed thoroughly in the literature. However, the question of the possible effect of a magnetic field on the mechanical properties and real structure of nonmagnetic (e.g., alkali halide or semiconductor) crystals was not raised for a long time. This stems from seemingly obvious general considerations. A real crystal always contains dislocations and impurity centers. The energy acquired by one paramagnetic center (an impurity defect or an electron localized at a dislocation) in a field $B \sim 1$ T is estimated as $\Delta U \sim \mu_B B \sim 10^{-4}$ eV (where μ_B is the Bohr magneton), which is three orders of magnitude less than kT at $T = 300$ K. Hence, it seemingly follows that no effect of this field on the physical (especially, mechanical) properties of nonmagnetic crystals occurs. However, the results of the investigations performed in the last twenty years radically revised this inference.

In this review, we considered a number of physical effects observed in nonmagnetic crystals that are characterized by a strong response of an impurity subsystem to magnetic action. For the most part, we

1063-7745/03/4805-0796$24.00 © 2003 MAIK "Nauka/Interperiodica"

systematically analyzed the results obtained by our scientific group, which was among the first to be engaged in research in this new and nontrivial scientific direction. We discussed two types of effects associated with the magnetically stimulated evolution of electron states of the impurity subsystem. The first group involves the so-called magnetic memory effects, i.e., such an evolution that occurs with time after treatment in a magnetic field ("magnetization"), and can manifest themselves in a change in the mechanical and other properties of crystals. The effects of the second type are not associated with magnetic memory. In this case, the magnetic field *in situ* affects the dislocation–impurity system, changes local energy barriers to dislocation motion, and, as a rule, facilitates plastic deformation. Effects of this type disappear after switching off the magnetic field.

Note that the nature of the phenomena under consideration was not revealed immediately. It took a long time before we understood that the spin conversion in paramagnetic centers under exposure to external magnetic fields underlies the micromechansims of processes responsible for the observed macrochanges in the properties of crystals. In this case, the role of the magnetic field is reduced to the removal of the spin forbiddenness of a particular electronic transition in the system, which radically changes the configuration of the impurity center without changing the total energy of the center.

2. EFFECTS ASSOCIATED WITH THE MAGNETIC MEMORY PHENOMENON

2.1. Experimental Schemes

In this section, we will consider a number of magnetic memory effects which we found in NaCl, LiF, and NaCl : Ni crystals. The characteristic and nontrivial feature of these phenomena is that they manifest themselves not in the course of exposure to a field but within a time after magnetic treatment—the time it takes for certain transformations to occur in the real structure of a crystal. Historically, the phenomena of this group were first investigated in the framework of the given scientific direction, which, in our work, is referred to as the influence of magnetic effects on the mechanical properties and real structure of nonmagnetic crystals.

Further investigations demonstrated that the magnetic field affects electron states of the impurity subsystem. In order to reveal its evolution associated with the magnetic memory, we used two experimental schemes. According to the first scheme, the experiments were carried out in the following order: the preliminary magnetic treatment, storage, and measurements (see Sections 3.2, 3.3). The second scheme involved the following stages: the preliminary heat treatment, storage, magnetic treatment, and measurements (see Sections 3.4).

2.2. First Experiments on Preliminary Magnetic Treatment of Nonmagnetic Crystals

Distler *et al.* [1] investigated the influence of magnetic fields on NaCl crystals by the decoration technique and scanning electron microscopy. Analysis of the decoration patterns revealed that the preliminarily applied pulsed magnetic field considerably affects the state of impurities in the crystals. The effect of the magnetic field on the crystal was judged from the change in the morphology of the crystal surface due to magnetic treatment. According to [1], these observations suggest that the magnetic field can have a particular effect on impurity centers in the crystals, which, in turn, can lead to the disturbance of a quasi-stable (metastable) state of impurity complexes and the corresponding change in the defect–impurity structure of the crystals as a whole.

Concurrently and independently of Distler *et al.* [1], we found the mechanochemical effect in γ-irradiated NaCl crystals [2]. This effect lies in the fact that, when crystals are strained in a reactive medium, the yield stress and the strain hardening rate noticeably decrease as compared to those observed in the check experiment in air. It was then (in the very early 1980s) that we conceived the idea of performing two different types of experiments which would combine the magnetic treatment and decoration technique with solubility measurements and mechanical testing.

Experiments of the first type were carried out with the aim of quantitatively justifying the qualitative observations of changes in the morphology due to the magnetic treatment [1]. For this purpose, we studied how the preliminary exposure of NaCl crystals to a pulsed magnetic field affects their solubility [3]. A 70% aqueous solution of ethanol was used as the solvent. The dissolution was performed over the {100} faces of NaCl crystals. The parameters of the pulsed magnetic field were as follows: the peak strength of the magnetic field, 8×10^4 A/m; the pulse frequency, 12 Hz; the pulse duration, 3 ms; and the pulse rise time, 0.3 ms. The duration of magnetic field treatment was 10 min. The solubility of the crystals was measured by the gravimetric method (from the weight loss).

The experiments with the use of a number of samples demonstrated that the exposure of the crystals to the magnetic field leads to an approximately 30% decrease in the specific solubility as compared to the specific solubility of the unexposed (check) samples. Note that a maximum decrease in the specific solubility was observed within two days after treatment; i.e., there was a latent period (the magnetic memory effect).

According to the inference made in [1], we assumed in [3] that the magnetic field affects paramagnetic impurity centers, disturbs their metastable state, and brings about the redistribution of impurities and other point defects. It was found that, after magnetic treatment, the dissolution over a larger area of the crystal surface proceeds through the polishing mechanism, i.e., through a uniform layer-by-layer removal of the mate-

rial and only local regions 10–100 μm in size are characterized by a lower solubility. This implies that the magnetic treatment leads to a change in the state of impurities in certain local surface regions rather than over the entire surface.

Therefore, in our first work [3], the influence of the magnetic field on the physical properties of nonmagnetic materials was originally evaluated not only qualitatively but also quantitatively by using the solubility as an example. As was subsequently proved, the assumption drawn in this work that the magnetic field has a particular effect on the state of impurity centers appeared to be correct.

Experiments of the second type involved the preliminary magnetic treatment of γ-irradiated NaCl samples and their plastic compressive deformation. In this case, at all three experimental stages, we used the spectral characterization of the samples, namely, measured the spectra of the initial sample, the sample exposed to the magnetic field, and the strained sample. According to our unpublished data, the magnetic treatment led to the shift in the absorption band of colloidal Na toward the short-wavelength spectral range of the absorption spectrum from 665 to 655 nm. The active stressing of the "magnetized" sample resulted in an even more considerable shift in the absorption band from 655 to 624 nm. Mechanical testing revealed a variation in the yield stress that can be interpreted as the response to the magnetic treatment.

It should be noted that the mechanical properties of alkali halide crystals at standard temperatures are predominantly determined by the interaction of point defects primarily with moving dislocations. On this basis, we assumed that the mechanical treatment can lead to a change in the mechanical properties of nonmagnetic crystals, especially of crystals containing paramagnetic impurities. In this respect, in 1984, we undertook the first investigation into the influence of the preliminary magnetic treatment on the mechanical properties of nonmagnetic materials [4]. The microhardness of LiF crystals served as a measure of the effect of the magnetic treatment.

As in the case of investigation into the effect of the field on the solubility, the experiments involved the following stages: the preliminary magnetic treatment, storage, and measurements. The obtained results demonstrated that the magnetic treatment of LiF crystals containing 10^{-2} wt % Ni leads to a change in their microhardness and the sizes of dislocation rosettes. Note that the microhardness of the samples immediately after magnetic treatment virtually did not differ from the microhardness of the initial ("unmagnetized") crystal. The maximum effect was observed within two days after magnetic treatment. Subsequently, this effect weakened and disappeared gradually. Unfortunately, in this work, we made a methodical error, namely, did not measure the microhardness of check samples unexposed to the magnetic treatment. Therefore, an increase in the microhardness in time with a maximum within two days was taken for the magnetic hardening of the crystal. It is quite possible that, in actual fact, we only observed a usual aging of a fresh crystal cleavage in air. Indeed, without measurements of check samples, it is impossible to determine whether we dealt with magnetic hardening or with plasticization. However, we can state with assurance that the microhardness in our experiments was sensitive to the magnetic treatment: the higher the magnetic field strength and the longer the heat treatment, the stronger the effect. We assumed that the observed influence of the preliminary magnetic treatment on the microhardness is caused by the conversion of paramagnetic impurity centers.

This assumption made in our original woks [3, 4] was more recently confirmed by results of other authors, who performed experiments in which the magnetic and mechanical treatments were separated in time (according to the scheme: magnetic treatment–storage–measurements). For example, Golovin and Morgunov [5] observed an increase in the dislocation mobility and a decrease in the microhardness in NaCl crystals due to the preliminary magnetic treatment, which indicated a disordering effect. However, magnetic hardening was also observed in a number of works. In particular, Tyapunina *et al.* [6] studied the inelastic properties of KBr crystals subjected to preliminary magnetic treatment and found that, at certain ultrasound amplitudes, there arises the hardening which manifests itself in a decrease in the internal friction and an increase in the starting stresses of the onset of dislocation motion.

2.3. Effect of Preliminary Magnetic Treatment on the Yield Stress of NaCl : Ni Crystals

In [7], we investigated the influence of the preliminary magnetic treatment on the yield stress of NaCl crystals containing paramagnetic nickel impurities. Samples approximately $2 \times 3 \times 8$ mm^3 in size were cleaved along the cleavage planes. The preliminary magnetic treatment of the samples was performed in the field of a permanent magnet with an induction of 0.45 T. We carried out two series of experiments. In the first series, the duration of magnetic treatment varied from three hours to seven days and the samples were strained immediately after treatment. In the second series, the duration of the preliminary magnetic treatment was equal to one day for all the samples, which were strained within different times (from several hours to twenty five days) after magnetization. The deformation of the samples was examined using an original experimental setup specially designed by our group. This setup made it possible to compress crystals under simultaneous exposure to magnetic and (or) electric fields and also in the absence of fields. The experiments on the deformation in the presence and absence of magnetic field were performed on this compression-testing machine, whose parts operating in the magnetic field were produced from nonmagnetic materials (alumi-

num, bronze, and brass). Ruby cylinders were used as compressive dies. The strain rate varied from 10^{-5} to 10^{-3} s^{-1}. The experiments were performed at room temperature. Technically pure crystals NaCl, NaCl : Ni, LiF, and PbS served as objects of investigation. The magnetic field was created by a permanent magnet. The magnetic field induction could be varied from 0 to 0.5 T. The stress–strain curves were recorded with a KSP-4 automatic recorder. In both series of experiments, the crystals were strained in the absence of field and in the field with an induction of 0.45 T.

Figure 1 depicts the dependences of the yield stress σ_y of the NaCl : Ni crystals on the duration t_m of the preliminary magnetic treatment in the field $B = 0.45$ T (the crystals were strained immediately after cessation of the treatment). Under deformation without magnetic field (Fig. 1, curve *1*), the yield stress increases with an increase in the duration of the preliminary magnetic treatment to one day. A further increase in the magnetic treatment duration leads to a decrease in the yield stress. Note that the yield stress increases rather rapidly and decreases more slowly. A somewhat different situation is observed when crystals identically treated in the magnetic field are strained in the field $B = 0.45$ T (Fig. 1, curve *2*). Under these deformation conditions, the yield stress of the crystals exposed to the magnetic field for times shorter than one day decreases rather than increases with an increase in the magnetic treatment duration t_m. Only longer preliminary magnetic treatments lead to the hardening. The yield stress increases with an increase in t_m to three days and then decreases slowly. Therefore, a comparison of curves *1* and *2* in Fig. 1 indicates that the initial state of impurities (at $t_m = 0$) in our crystals is magnetosensitive in the sense that the yield stress of the crystals under deformation in the magnetic field decreases by $\Delta\sigma_y \sim 0.3$ MPa. The preliminary magnetic treatment of the crystals first leads to an increases in the magnetosensitivity of impurities. In this case, the quantity $\Delta\sigma_y(t_m)$ increases and reaches a maximum ($\Delta\sigma_y^{\max} \sim 1.15$ MPa) at $t_m = 1$ day. Then, as the magnetic treatment duration increases, the quantity $\Delta\sigma_y$ decreases and reaches a minimum ($\Delta\sigma_y^{\min} \sim 0.1$ MPa) at $t_m = 3$ days. With a further increase in the duration of the preliminary magnetic treatment, the "magnetic plasticization" $\Delta\sigma_y$ gradually increases and regains the initial value at $t_m = 6$ days. These nonmonotonic dependences of the yield stress of the crystals under two different conditions of their mechanical testing and, especially, the nonmonotonic behavior of the quantity $\Delta\sigma_y(t_m)$ suggests a complex combination of self-consistent aging processes and also magnetically and diffusion-stimulated transformations of the real impurity structure.

The fact that only diffusion processes rather than the preliminary magnetic treatment of the crystals predominantly contribute to the cupola-shaped dependence in

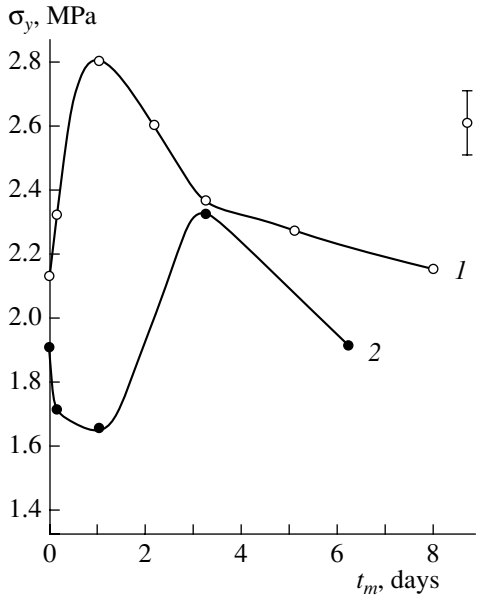

Fig. 1. Dependences of the yield stress σ_y of NaCl : Ni crystals strained (*1*) in the absence of magnetic field ($B = 0$) and (*2*) in the magnetic field $B = 0.45$ T at the strain rate $\dot{\varepsilon} = 2 \times 10^{-4}$ s^{-1} on the duration t_m of the preliminary magnetic treatment.

Fig. 1 (curve *1*) can be judged from the following series of experiments. In this series, the duration of the preliminary magnetic treatment was the same ($t_m = 1$ day) for all the samples and the time t_{am} between the cessation of the magnetic treatment and the beginning of the mechanical testing was varied in experiments. The obtained results are represented in Fig. 2. It can be seen from this figure that the dependences $\sigma_y(t_{am})$ under deformation at $B = 0$ and 0.45 T are similar to each other. After magnetic treatment for one day, storage for times shorter than one day leads to hardening. A further increase in t_{am} results in a monotonic decrease in the yield stress, which reaches an almost steady-state value within approximately a week. In this case, the quantity $\Delta\sigma_y$ only weakly depends on t_{am}. Most likely, this indicates that the preliminary magnetic treatment for a constant time somehow fixes the electronic impurity microstructure, which then, in contact with a dislocation in the course of deformation in the magnetic field, affects the spin kinetics. This microstructure is retained during storage of the crystals between the magnetic treatment and the deformation, even though impurity atoms diffuse, are joined into complexes, are located at dislocations, etc., which is responsible for the specific features in the behavior of the dependences $\sigma_y(t_{am})$ (Fig. 2).

Therefore, the magnetic treatment most likely does not contribute to the cupola-shaped time dependence of the yield stress. Consequently, this dependence is not characteristic of the magnetic treatment. On the other

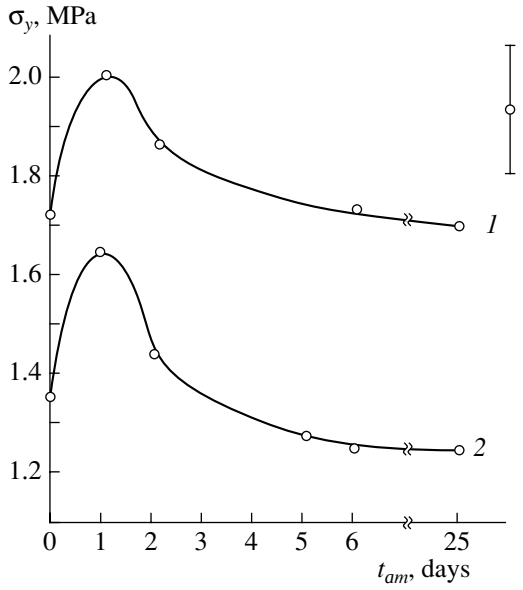

Fig. 2. Dependences of the yield stress σ_y under deformation (*1*) in the absence of magnetic field and (*2*) in the magnetic field $B = 0.45$ T at $\dot{\varepsilon} = 2 \times 10^{-4}$ s^{-1} on the time t_{am} elapsed after preliminary treatment in the magnetic field $B = 0.45$ T for 1 day.

hand, the quantity $\Delta\sigma_y$ is very sensitive to t_m, virtually does not depend on t_{am}, and can be treated as a characteristic of the magnetic treatment. It is this radical difference between the dependences $\Delta\sigma_y(t_m)$ and $\Delta\sigma_y(t_{am})$ that proves the effect of the preliminary magnetic treatment of the crystals on the state of their impurity subsystem.

It is evident that the experiments under consideration are conceptually similar to our earlier experiments on the solubility and microhardness of the crystals subjected to magnetic treatment [3, 4]. In all the cases, we are dealing with the magnetically stimulated evolution of the impurity subsystem with time. However, in the last series of experiments, new parameters associated with the deformation of the crystals in the magnetic field served as a measure of the effect of the magnetic treatment. This approach allowed us to demonstrate with confidence that the preliminary exposure to the magnetic field actually results in the transformation of the microstructure of impurity centers.

2.4. Effect of Preliminary Thermomagnetic Treatment on the Yield Stress of NaCl : Ni Crystals

Unlike the above experimental works concerned with the investigation into the effect of preliminary magnetic treatment on nonmagnetic crystals [7], in our recent work [8], we used a different experimental scheme involving the following stages: the preliminary heat treatment, storage, magnetic treatment, and measurements, which was previously proposed by Morgunov and Baskakov [9]. As was noted above, the magnetically stimulated evolution of the impurity subsystem is characterized by the magnetic memory effect, i.e., strongly depends on the storage time of the sample subjected to preliminary magnetic treatment. At first glance, the memory about the magnetically stimulated transformations of the real crystal structure should monotonically weaken with an increase in the time passed after magnetic treatment. As a consequence, the crystal after a time should "forget" these transformations due to usual thermal relaxation. However, as was shown in [9], the situation is not so simple.

According to [9], in order to provide the conditions required for the appearance of the sensitivity of crystals to the magnetic treatment, the initial impurity structure should be in a certain nonequilibrium state. This can be achieved, for example, through the preliminary heat treatment of crystals. Then, the evolution of the impurity subsystem can result in the formation of magnetosensitive states, namely, complexes of point defects that respond to the subsequent magnetic treatment. Consequently, the case in point is the formation of magnetosensitive electronic structures fixed in time.

Morgunov and Baskakov [9] showed that, after annealing (at 920 K for 2h) and quenching, the microhardness of NaCl : Eu crystals varies nonmonotonically with a change in the time between the quenching and the magnetic treatment (at 7 T for 10 ms) preceding the indentation. The maximum effect was observed at $t \sim 30$ h.

In contrast to the experiments performed in [9], in our experiments, a change not in the microhardness but in the yield stress under active stressing of crystals subjected to preliminary thermomagnetic treatment was used as a measure of the effect of the magnetic field. Moreover, we investigated NaCl : Ni crystals grown by the Kyropoulos method rather than NaCl : Eu crystals. The $NiCl_2$ impurity content in a batch was equal to 0.05 wt %. The total content of uncontrollable impurities did not exceed 10^{-3} wt %. Samples ($2 \times 3 \times 8$ mm^3 in size) cleaved along the cleavage planes were subjected to preliminary annealing at $T = 1000$ K for 3 h in the absence of magnetic field. Then, the samples were quenched in liquid nitrogen and held at room temperature for different times (from 0 to 240 h). Within required times after quenching, each group of samples was exposed to the constant magnetic field for 0.5 h immediately prior to the stressing. The crystals subjected to this thermomagnetic treatment were strained at a rate of 1.4×10^{-5} s^{-1} on the testing machine. The effect of the magnetic treatment was judged from the change in the measured yield stress. The experimental data obtained are presented in the table. Each experimental value of the yield stress was obtained by averaging the results of four measurements.

The investigation revealed that the dependence of the yield stress σ_y of the preliminarily quenched NaCl : Ni crystals on the storage time t before the short-term

magnetic treatment and deformation exhibits a nonmonotonic behavior. The storage of the samples for one day does not lead to a change in the yield stress. With a further increase in the storage time t, the yield stress first noticeably decreases (at t = 40 h) and then increases. Consequently, the maximum plasticization effect is observed at $t \sim 40$ h. This correlates with the data obtained in [9] and likely indicates that the preliminary thermomagnetic treatment provides a way of producing time-fixed magnetosensitive states of the impurity subsystem.

The experimental data on the influence of the preliminary quenching, storage time, and magnetic treatment of the samples on the yield stress give grounds to make the following inference. Before the preliminary heat treatment, the impurity structure is insensitive to the magnetic treatment of the crystal. Heat treatment (annealing) leads to the first transformation of the initial structure, which consists in decomposing the impurity complexes responsible for the retardation of dislocations. The next stage of the experimental procedure—the quenching—results in the "freezing" of decomposed impurity centers. During the subsequent long-term storage, the frozen impurity structure undergoes an evolution attended by an increase in the size of the formed small-sized paramagnetic centers (dislocation obstacles) owing to the diffusion. This implies that, as the paramagnetic centers increase in size, the impurity structure undergoes a series of transformations into different states. Among them, the states first and last in time, like the initial structural state, are insensitive to magnetic fields. Therefore, when the magnetic field is applied either too early or too late, no magnetosensitivity can be observed. Only at an optimum time between the quenching and the magnetic treatment (in our case, $t \sim 40$ h), the impurity structure, which arises by that time and is unstable with respect to spin-dependent electronic transitions, can respond to the magnetic excitation and experience a spin transition removing the forbiddenness of a particular electronic transition. This leads to a strong change in the configuration of complexes and their ability to retard dislocations in the course of the subsequent deformation in the absence of magnetic field. In other words, the preliminary magnetic treatment results in a lowering of energy barriers created by impurity centers to dislocation motion, which is equivalent of the plasticization of the structure. Experimentally, this is observed from a decrease in the yield stress.

In light of the foregoing, the results of the previous section can be interpreted in a somewhat different way. Possibly, the cleavage of the samples with the formation of fresh surfaces, which were not in equilibrium with the surrounding atmosphere, gave rise to the initial nonequilibrium state. The diffusion of impurities from the atmosphere initiated a certain evolution of the impurity structure of the crystals. At a certain stage (within one day), there arose a dominant structural motif sensitive to the magnetic field. Since the crystals were exposed to the magnetic field at this time, impurity complexes were formed in the crystals. Note that these complexes could not be formed in the absence of magnetic field. With a further increase in the time t_m of the preliminary magnetic treatment, the evolution of the structure gradually led to the disappearance of this motif and the complexes lost the capability of transforming in the magnetic field. In this equilibrium state, only the complexes located at dislocations could respond to the magnetic field, which actually manifested itself during the deformation in the magnetic field. Unfortunately, for the lack of reliable data, the proposed interpretation cannot be considered to be quite justified; however, it seems realistic and agrees reasonably with the results obtained for the quenched samples.

Dependence of the yield stress σ_y of NaCl : Ni crystals preliminarily quenched and subjected to magnetic treatment on the time t between the quenching and the magnetic treatment preceding the deformation

t, h	0	24	40	48	72	240
σ_y, MPa	2.30	2.35	1.60	2.30	3.15	3.10

Apparently, all the effects considered in this section of the review have one feature in common: the crystals in the described experiments are subjected to *preliminary* magnetic (or thermomagnetic) treatment. The preliminary treatment leads to the formation of an impurity structure that undergoes a time evolution, gradually transforms, and reverts to the original state. These structural transformations are revealed from the change in particular properties (for example, from a change in the surface morphology, a decrease in the solubility of crystals, and a variation in the microhardness or the yield stress). All these effects have the same origin associated with the magnetic memory of materials.

3. EFFECTS OBSERVED IN THE COURSE OF MAGNETIC TREATMENT

3.1. History of the Problem

Earlier experiments on the deformation of materials in magnetic fields were traditionally carried out for the most part with metals [10–13]. It was demonstrated that the magnetic field can lead to both hardening and plasticization.

In 1987, with the participation of the two authors of the present review, it was found that individual dislocations move in NaCl samples placed in a constant magnetic field without applying a mechanical load [14]. The specific feature of this effect is that the magnetic treatment and measurements are not separated in time. Dislocations *in situ* move beginning with the instant of time when the field is applied and do not move after the field is switched off. A further large series of investiga-

tions with the use of these and other nonmagnetic crystals made it possible to study the basic properties of the new phenomenon, which was termed the magnetoplastic effect.

First and foremost, it has been established that the role of the magnetic field resides in the depinning of dislocations from paramagnetic obstacles. It is believed that this is caused by the spin evolution in the magnetic field. The spin evolution removes the spin forbiddenness of a process that leads to a radical change in the configuration of the dislocation–impurity system and breaks (or substantially lowers) the barrier to dislocation motion. In the framework of this approach, the depinning time τ_{dp} of dislocations is limited by the spin evolution in the dislocation–paramagnetic center system. It is clear that such processes can proceed if the spin–lattice relaxation is insignificant for the depinning time τ_{dp} Otherwise, thermal disordering of spins should suppress the effect. Taking into account that the spin–lattice relaxation time τ_{sl} rather weakly depends on the magnetic field and $\tau_{dp} \propto B^{-2}$, it can be expected that there is the threshold field B_c (determined from the approximate relationship $\tau_{dp}(B_c) \simeq \tau_{sl}$) below which the magnetoplasticity should be absent. Indeed, this threshold field was experimentally found in [15].

The influence of the magnetic field on the mobility of individual dislocations in nonmagnetic crystals was investigated under conditions when the dislocation density ρ_d did not exceed 10^4–10^5 cm^{-2}. At these densities, dislocations relatively weakly pin each other. Actually, in this case, the mean spacing of forest dislocations crossing the slip plane is of the order of ~100 μm and the mean distance between impurity centers on the dislocation line typically does not exceed a fraction of a micron. Therefore, the "switching-off" of point obstacles on dislocations in the magnetic field decreases the dislocation motion drag by two or three orders of magnitude. This explains the dislocation motion experimentally observed in magnetic fields in response to extremely small internal stresses (of the order of 0.01 MPa) and also a high sensitivity of dislocation mobility to weak external actions [16].

At the same time, the problem associated with the possibility of using the magnetoplastic effect to control the macroplasticity of nonmagnetic materials is of prime practical interest. It should be noted that, under the conditions of macroplastic deformation, the dislocation density is usually several orders of magnitude higher than the initial density and the spacing of dislocation, which is equal to the reciprocal of the square root of the dislocation density, is correspondingly several orders of magnitude smaller than the initial spacing (for example, ~1 μm at $\rho_d \sim 10^8$ cm^{-2}). Therefore, under these conditions, the magnetic disordering of crystals can be not as pronounced as in experiments with individual dislocations. Note that Golovin and Morgunov [17] studied the deformation of a number of alkali halide crystals in the magnetic field under hydraulic pressure stressing ($\dot{\sigma}$ = const) and found a noticeable (almost twofold) increase in the strain rate with an increase in the magnetic field. Unfortunately, the experimental technique used in [17] did not permit the authors to reveal the influence of the magnetic field on the yield stress σ_y, which is a very fundamental characteristic. In our opinion, for this purpose, it is more appropriate to apply the active deformation method ($\dot{\varepsilon}$ = const). This method provides a way of measuring stress–strain curves $\sigma(\varepsilon)$ that correspond to many deformation stages and make it possible to determine the yield stress σ_y and the hardening magnitude at different deformation stages.

3.2. Effect of a Constant Magnetic Field on the Stress–Strain Curves for LiF, NaCl, and PbS Crystals

Samples of LiF crystals were prepared and the effect of a constant magnetic field on the stress–strain curves for these crystals was investigated using the technique described above [18–21]. The stress–strain curves corresponding to three deformation stages were measured under compression of the LiF crystals in the presence and absence of magnetic field. Figure 3 shows the stress–strain curves $\tau(\varepsilon)$ (where τ is the working shear stress) for two samples compressed at a constant rate of 5×10^{-5} s^{-1} in the absence of magnetic field (curves *1*, *2*) and three samples compressed in a magnetic field of 0.48 T (curves *3*, *4*, *5*). A comparison of the curves of these two series demonstrates that the initial straight-line segments corresponding to the elastic deformation of the crystals have the same slopes in the presence and absence of magnetic field. However, the yield stresses and the stresses of the onset of deformation stages II and III for the samples in the magnetic field appeared to be considerably smaller than those at $B = 0$. It is worth noting that, for the samples compressed in the magnetic field, the slopes of the curves $\tau(\varepsilon)$ at strain hardening stage II are smaller and the slopes $d\tau/d\varepsilon$ at deformation stage III are larger than the corresponding slopes of the curves measured at $B = 0$.

Figure 4 depicts the dependences of the shear yield stress τ_y (Fig. 4a), the strain hardening coefficient $\theta_{II} = (d\tau/d\varepsilon)_{II}$ (Fig. 4b), and the hardening coefficient at deformation stage III $\theta_{III} = (d\tau/d\varepsilon)_{III}$ (Fig. 4c) on the magnetic field induction B [18]. All the curves were measured at a strain rate of 5×10^{-5} s^{-1}. Similar dependences were also observed at a strain rate of 10^{-5} s^{-1}. However, at strain rates higher than 10^{-4} s^{-1}, the curves $\sigma(\varepsilon)$ became insensitive to the magnetic field.

Examination of the strained samples in transmitted polarized light revealed that, in the magnetic field with inductions B larger than the critical induction B_c (above which, as will be shown bellow, the effect manifests itself), only one pair of orthogonal slip planes partici-

pates in the deformation (Fig. 5a), whereas, in the absence of magnetic field, all four possible slip systems are always involved in this process (Fig. 5b). It is significant that, in the magnetic field, systems in which the edge dislocations are parallel to the field do not contribute to the deformation. This circumstance is in complete agreement with the previously established fact that the magnetoplastic effect is not observed for edge dislocations parallel to the field [22]. At the same time, a decrease in the number of slip systems naturally explains the observed decrease in the strain hardening coefficient in the magnetic field.

As is known, the changeover to deformation stage III occurs when dislocations generated by sources are compensated for by their annihilation, i.e., the cancellation of dislocations with opposite mechanical signs. This leads to a decrease in the hardening coefficient [the slope $\theta_{III} = (\partial\tau/\partial\varepsilon)_{III}$ at deformation stage III is smaller than the slope θ_{II} at stage II]. Most likely, the slip systems that are not involved in stage II of crystal deformation in the magnetic field provide an increase in the dislocation density, which can be responsible for the increase in the slope θ_{III} at $B > B_c$.

Similar dependences were obtained for NaCl crystals; in this case, the stress–strain curves for these crystals turned out to be magnetically sensitive over a wider range of strain rates [23–26]. This appreciably increased the amount of information on the influence of magnetic fields on the macroplasticity of nonmagnetic materials.

Figure 6 shows the stress–strain curves $\sigma(\varepsilon)$ (where σ is the uniaxial compressive stress) for annealed (Fig. 6a) and unannealed (Fig. 6b) samples in the absence of field (curves *1*, *1*') and in the magnetic field $B = 0.48$ T (curves *2*, *2*') at a strain rate of 5×10^{-4} s^{-1}. Curves *3* and *3*' in Fig. 6a were obtained for two different samples in the magnetic field $B = 0.2$ T. A comparison of these curves indicates a good reproducibility of the curves $\sigma(\varepsilon)$ for the annealed samples. At the same time, it can be seen from Fig. 6b that the reproducibility of the curves $\sigma(\varepsilon)$ is substantially worse for the unannealed samples. As could be expected, the annealed samples are softer compared to the unannealed samples: the initial yield stress (at $B = 0$) of the former samples is almost two times smaller than that of the latter samples. Correspondingly, the sensitivity of the annealed samples to the magnetic field is higher than that of the unannealed samples. As the induction B increases from 0 to 0.48 T, the yield stress decreases by a factor of approximately three for the annealed samples and by a factor of approximately one and a half for the unannealed samples at the same strain rate. Moreover, the strain and stress ranges of all the stages of the plastic flow of the annealed samples considerably decrease in the magnetic field. This means that the magnetic field promotes the changeover between the deformation stages in these crystals. On the other hand, it can be seen from the curves $\sigma(\varepsilon)$ in Fig. 6b that,

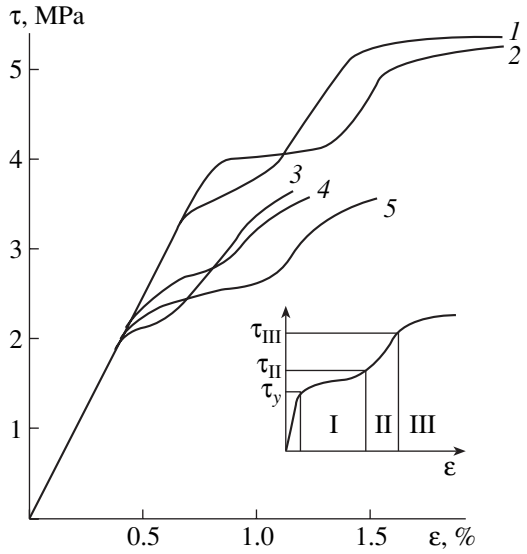

Fig. 3. Stress–strain curves for LiF crystals (*1*, *2*) in the absence of magnetic field and (*3*, *4*, *5*) in a magnetic field of 0.48 T at a strain rate of 5×10^{-5} s^{-1}. The inset shows the schematic stress–strain curve illustrating the deformation stages and characteristic parameters.

under deformation of the unannealed samples in the magnetic field, a decrease in the stress ranges of the stages is more pronounced than a decrease in the strain ranges.

Let us now consider our first experimental data on the plastic deformation of PbS crystals in the magnetic field [27]. These crystals are characterized by the ionic–covalent bonding and have the NaCl-type lattice. Figure 7 depicts the stress–strain curves for the PbS crystals in the absence of magnetic field (curve *1*) and in the magnetic field $B = 0.45$ T (curve *2*). As can be seen from this figure, the curves in both cases suggest the occurrence of three deformation stages. The application of the magnetic field leads to a decrease in the yield stress, a shortening of the easy-slip stage, and a reduction in the strain hardening rate at deformation stage II. These changes are similar to those observed for alkali halide crystals (see [18, 24]). However, unlike alkali halide crystals, in the PbS crystals, the application of the magnetic field does not result in the shortening of stage II but even leads to its lengthening. At the same time, the stress–strain curve measured in the magnetic field lies below the curve obtained in the absence of field. In our opinion, changes in the length and slopes of the segments corresponding to different deformation stages in the magnetic field is explained by the influence of the magnetic field on the participation of specific active slip systems in the deformation, in particular, by the magnetically stimulated faster changeover between the active and conjugate slip systems. In alkali halide crystals, the $\{110\}\langle 110\rangle$ system is the basic slip system. In the PbS crystals, there are several active systems, among which the $\{100\}\langle 110\rangle$ and $\{110\}\langle 110\rangle$

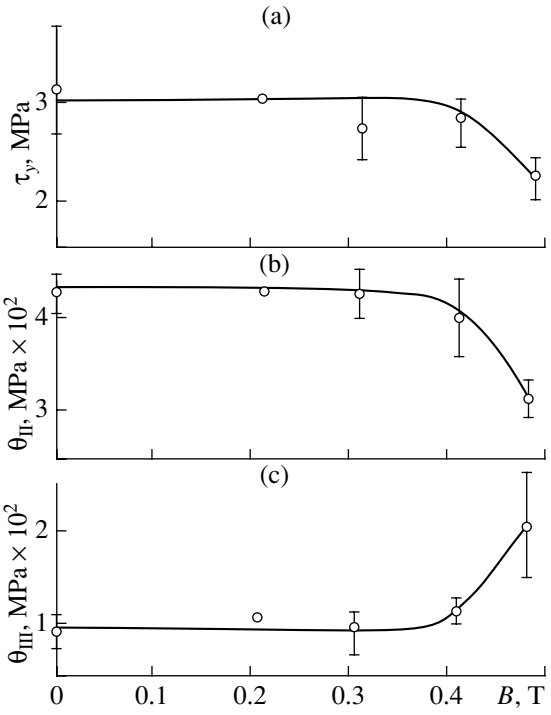

Fig. 4. Dependences of (a) the yield stress τ_y, (b) the strain hardening coefficient θ_{II}, and (c) the hardening coefficient θ_{III} at deformation stage III on the magnetic field induction *B*. The strain rate is equal to 5×10^{-5} s^{-1}.

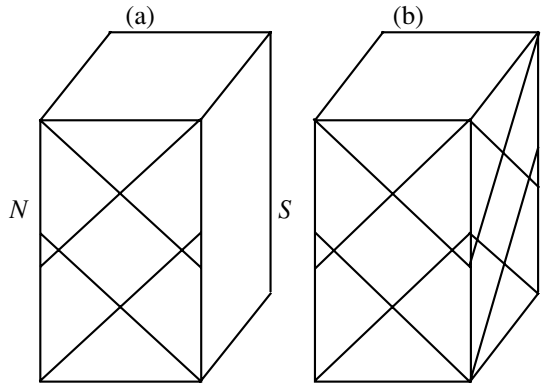

Fig. 5. A schematic representation of the active slip systems in LiF crystals under deformation in (a) the presence and (b) absence of the magnetic field.

systems are basic. The former system dominates under the action of a concentrated load, and the latter system dominates under compression along the ⟨100⟩ direction [29]. In the latter case, stress concentrators can also contribute to the deformation. Consequently, in the case of the PbS crystals, there are a larger number of degrees of freedom for the influence of the magnetic field on the plastic deformation.

Therefore, the effects of the constant magnetic field on the stress–strain curves for the LiF, NaCl, and PbS crystals bear obvious similarities and their own specific features. All the curves suggest the occurrence of three deformation stages. All the curves indicate that the magnetic field has a plasticizing effect. However, the slopes and lengths of the segments corresponding to particular deformation stages are different, which is associated with specific plastic characteristics of the crystals due to distinctive features of the real structure.

3.3. Effect of a Constant Magnetic Field on the Yield Stress of LiF, NaCl, and PbS Crystals

In addition to the influence of the magnetic field on the stress–strain curves, we studied how the magnetic field affects the yield stress of the crystals under consideration. With the aim of performing the necessary measurements for the LiF crystals, we modified our setup and extended the range of strain rates by more than one order of magnitude toward lower rates. This enabled us to change over from the semiqualitative results obtained in [18] to quantitative investigation into the dependences $\sigma_y(B)$ [20].

The dependences of the yield stress of the LiF crystals on the magnetic induction at different compression rates [20] are plotted in Fig. 8. It can be seen from this figure that the lower the strain rate, the larger the relative decrease in the yield stress $\sigma_y(0)/\sigma_y(B_{max})$, where $B_{max} = 0.48$ T. Specifically, the yield stress σ_y in the maximum field decreases by a factor of one and a half at the highest strain rate and by a factor of four at the lowest strain rate. Note that the independent results obtained by Tyapunina *et al.* [30] with the use of the acoustic method correlate with our experimental data on the ratio $\sigma_y(0)/\sigma_y(B_{max})$.

As can be seen from Fig. 8, a noticeable sensitivity of the yield stress of the LiF crystals to the magnetic field arises only beginning with a certain threshold field B_c above which the yield stress σ_y rather rapidly decreases with an increase in the induction *B* and asymptotically approaches a new, smaller yield stress $\sigma_y^{(I)}$. The observed effect of the magnetic field depends on the strain rate. In particular, the threshold magnetic field B_c remains constant ($B_c = B_c^{(0)}$) at low strain rates and considerably increases with an increase in the strain rate $\dot{\varepsilon}$ (although more slowly than $\dot{\varepsilon}$) at $\dot{\varepsilon} > \dot{\varepsilon}_c = 6 \times 10^{-6}$ s^{-1}. At the same time, this suggests that, at a constant induction $B > B_c^{(0)}$, a noticeable magnetosensitivity of the dependence $\sigma_y(\dot{\varepsilon})$ can be observed at strain rates $\dot{\varepsilon}$ in a range limited from above. It is this behavior that can be clearly seen from the experimental dependences $\sigma_y(\dot{\varepsilon})$ measured for a number of fixed inductions *B* (Fig. 9).

Each stress–strain curve measured for a particular sample reflects both general and individual properties of the studied material. In this respect, there is always a

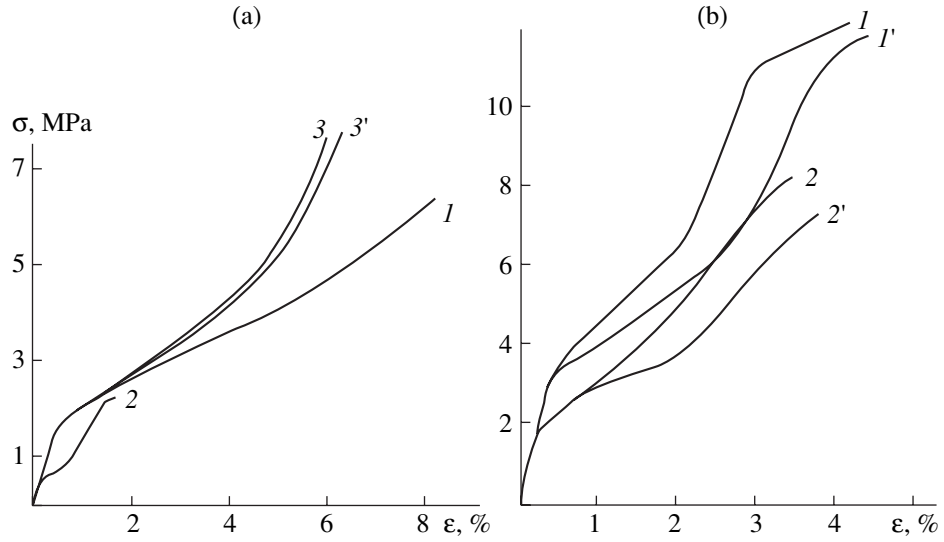

Fig. 6. Stress–strain curves for (a) annealed and (b) unannealed NaCl crystals under compression at $\dot{\varepsilon} = 5 \times 10^{-4}$ s^{-1} in magnetic fields B = (*1*, *1*') 0, (*2*, *2*') 0.48, and (*3*, *3*') 0.2 T.

spread of yield stresses determined for a series of samples under identical conditions. As a rule, this spread is substantially less for annealed samples, whose initial dislocation and impurity structure is more homogeneous and stabilized. Unfortunately, the number of annealed NaCl samples at our disposal was insufficient, and we could not carry out replicate measurements for all samples under identical conditions [24]. However, in the case of unannealed crystals (less "reliable" from the above viewpoint), replicate measurements of each stress–strain curve $\sigma_y(\dot{\varepsilon})$ at fixed parameters $\dot{\varepsilon}$ and B were performed for several samples. As will be shown below, the spread of the yield stresses $\sigma_y(\dot{\varepsilon})$ is appreciably smaller than the observed magnetic effects even for unannealed NaCl crystals.

Figure 10 depicts the dependences of the yield stress σ_y on the magnetic field induction B for the annealed (Fig. 10a) and unannealed (Fig. 10b) NaCl crystals. The dependence for the annealed samples clearly indicates the occurrence of three deformation stages. At the first stage of deformation (at inductions B less than the threshold field B_c), the yield stress σ_y remains constant and is insensitive to the magnetic field. At the second stage of deformation, the yield stress drastically decreases in a rather narrow range to the right of the threshold ($B \geq B_c$). Finally, at the third deformation stage (at $B > B_c'$), the yield stress σ_y is virtually unchanged to within the experimental error, even though it has a tendency toward slow decrease.

For unannealed crystals, the yield stress more smoothly decreases with an increase in the magnetic induction at $B > B_c$. Only at low compression rates, the dependence $\sigma_y(B)$ clearly demonstrates the occurrence of three deformation stages. Examination of these crystals at different strain rates in the range 1.4×10^{-5}–1.4×10^{-3} s^{-1} revealed that, as in the case of LiF crystals, the effect of the magnetic field on the yield stress appreciably increases with a decrease in the strain rate. It can be seen from Fig. 10b that this leads to a considerable decrease in the threshold magnetic field B_c (by a factor of approximately six) and the ratio $\sigma_y(B_{max})/\sigma_y(0)$.

A similar dependence of the yield stress on the magnetic induction is also observed for the PbS crystals (Fig. 11) [27]. It should be noted that, for these crystals, an increase in the magnetic induction B results in a smoother variation in the yield stress σ_y. In this case, the yield stress σ_y decreases slowly at $B < 0.3$ T and considerably faster at $B > 0.3$ T. However, within the limits of experimental error, we can likely state that the macro-

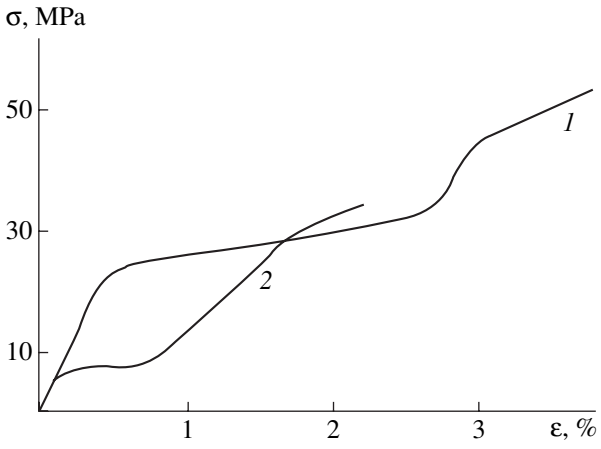

Fig. 7. Stress–strain curves for PbS crystals under active stressing (*1*) in the absence of magnetic field and (*2*) in the magnetic field B = 0.45 T.

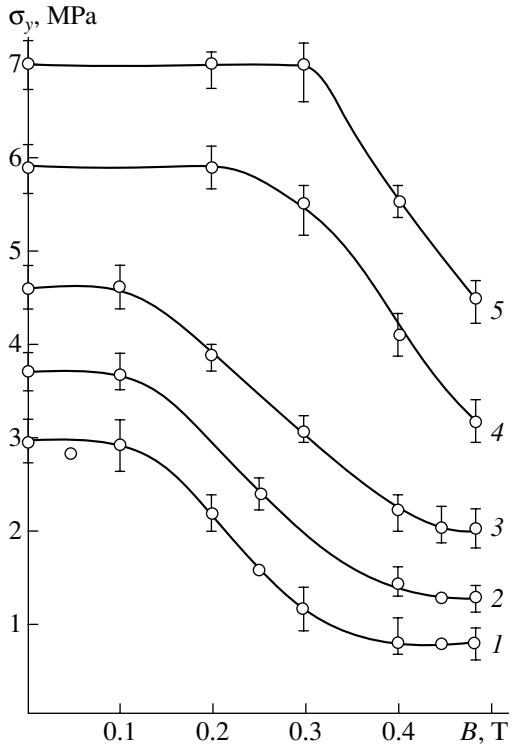

Fig. 8. Dependences of the yield stress σ_y of LiF crystals on the magnetic field induction B at strain rates $\dot{\varepsilon}$ = (*1*) 2×10^{-6}, (*2*) 3.5×10^{-6}, (*3*) 8×10^{-6}, (*4*) 2×10^{-5}, and (*5*) 5×10^{-5} s^{-1}.

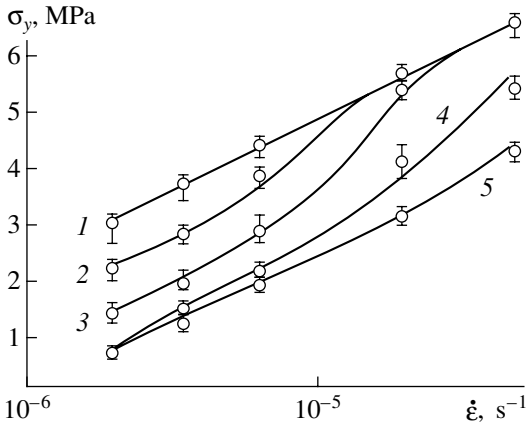

Fig. 9. Dependences of the yield stress σ_y of LiF crystals on the strain rate $\dot{\varepsilon}$ at magnetic field inductions B = (*1*) 0, (*2*) 0.2, (*3*) 0.3, (*4*) 0.4, and (*5*) 0.48 T.

scopic magnetoplastic effect in the PbS crystals has a threshold character. It is of interest that the sensitivity of this semiconductor material (which is substantially harder as compared to alkali halide crystals) to the magnetic field is no lower than the sensitivity of ductile alkali halide crystals.

Thus, the experimental investigations into the magnetosensitivity of the yield stress demonstrated that the magnetic-field dependences of the yield stress for all the studied LiF, NaCl, and PbS crystals suggest the occurrence of two or three deformation stages (the number of stages is determined by the degree of homogeneity and stabilization of the initial dislocation structure). Note that these dependences for alkali halide crystals exhibit a pronounced threshold behavior. At small magnetic inductions, the yield stress is magnetically insensitive. An increase in the magnetic induction first leads to a dramatic decrease in the yield stress. With a further increase in the magnetic induction, the yield stress (having different value) again becomes insensitive to the magnetic field. This suggests that there are two threshold magnetic fields: the lower threshold field B_c, below which the magnetoplastic effect does not manifest itself, and the higher threshold field B_c', above which the yield stress $\sigma_y^{(I)}$ decreased owing the magnetoplastic effect ceases to depend on the magnetic induction. It is significant that a decrease in the strain rate $\dot{\varepsilon}$ results in a decrease in both threshold magnetic fields.

3.4. Deformation of NaCl Crystals under Combined Exposure to Electric and Magnetic Fields

It is known [31–33] that, in alkali halide crystals, edge dislocations in their conservative motion can carry an uncompensated electric charge whose sign and magnitude are determined by the impurity composition of crystals and the supersaturation of anion and cation vacancies. This circumstance is responsible for the Stepanov effect [34], which manifests itself in the macropolarization of alkali halide crystals under deformation. The application of electric fields affects the behavior of crystals in the course of mechanical testing. It was found that this leads to a decrease in the yield stress [35, 36], acceleration of creep [37], and an increase in the internal friction [33].

In this respect, we experimentally investigated the strain hardening of NaCl crystals under the influence of electric field [38, 39]. The samples were compressed on a Regel–Dubov relaxometer at a rate of 10^{-3}–10^{-5} s^{-1} at room temperature. The electric field strength varied from 0.5 to 5 MV/m. The observed acceleration of the strain hardening in the stress–strain curves in the electric field is associated with the fact that the $\{111\}\langle 110\rangle$ secondary system is involved in the slip deformation, which retards the slip over the $\{110\}\langle 110\rangle$ primary system.

It should be noted that the observation of all the aforementioned effects requires the application of very high electric fields with a strength of the order of 10^3 kV/m. However, as was shown in [40, 41], the mean free paths of individual dislocations in their motion in alkali halide crystals under exposure to magnetic fields

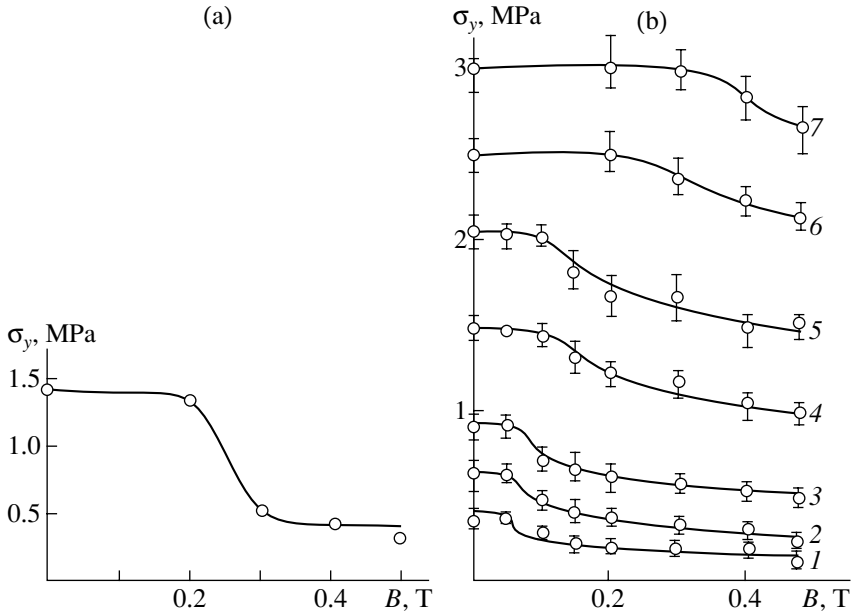

Fig. 10. Dependences of the yield stress on the magnetic field induction for (a) annealed and (b) unannealed NaCl crystals under compression at strain rates $\dot{\varepsilon}$ = (a) 5×10^{-4}, (b) (*1*) 1.4×10^{-5}, (*2*) 2×10^{-5}, (*3*) 3×10^{-5}, (*4*) 7.3×10^{-5}, (*5*) 1.75×10^{-4}, (*6*) 5×10^{-4}, and (*7*) 1.4×10^{-3} s^{-1}.

become highly sensitive to an external electric field. The application of even a low magnetic field (several tenths of a tesla) results in a decrease in the threshold electric field of the effect on individual dislocations by several orders of magnitude (from 10^2–10^3 to 0.1–1 kV/m). In this respect, it was of interest to study the macroplastic response of alkali halide crystals to the combined exposure to electric and magnetic fields.

For this purpose, we carried out experiments in which the constant magnetic field was applied perpendicular to the stressing axis of the compression-testing machine and the electric field was applied along this axis [42]. Brass electrodes were cemented to the jaws of corundum dies and were in contact with sample faces. The magnetic induction varied from 0 to 0.4 T, and the electric field strength ranged from 0 to 20 kV/m. The samples were strained at rates $\dot{\varepsilon}$ from 5×10^{-5} to 2×10^{-3} s^{-1} at room temperature.

Figure 12 shows the stress–strain curves measured under compression of NaCl crystals in the absence of both fields ($B = 0$, $E = 0$, curve *1*), only in the magnetic field B = 0.4 T (curve *2*), and in the magnetic (B = 0.4 T) and electric (E = 9 kV/m) fields (curve *3*). It can be seen from Fig. 12 that, upon application of the magnetic field, the corresponding stress–strain curve lies below curve *1*, the yield stress decreases, all the deformation stages become shorter, and the strain hardening coefficient θ_{II} is reduced. Compared to curve *2*, curve *3* is characterized by an additional decrease in the yield stress, a lengthening of the easy-slip stage, a reduction of the slope θ_I, and an increase in the hardening coefficient immediately after the yield stress and θ_{II} at the second hardening stage. It is significant that, in the absence of the magnetic field, the used electric fields did not affect the stress–strain curves of the NaCl crystals. The effect was observed only in electric fields with strengths of the order of 10^3 kV/cm [38].

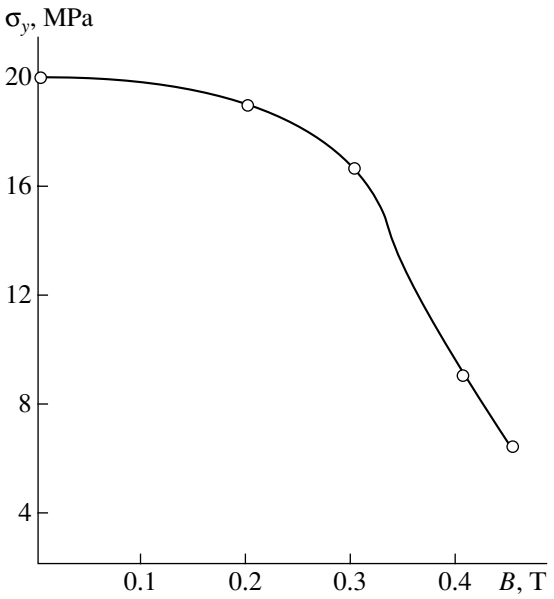

Fig. 11. Dependence of the yield stress of PbS crystals on the magnetic field induction at the strain rate $\dot{\varepsilon} = 4 \times 10^{-5}$ s^{-1}.

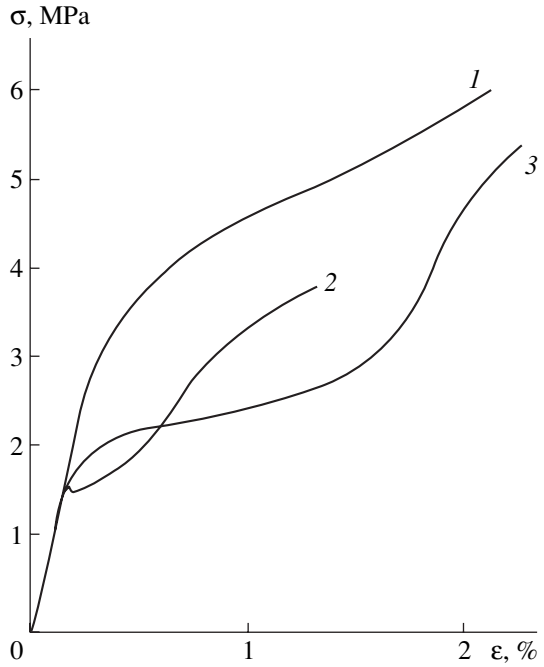

Fig. 12. Stress–strain curves for NaCl crystals under compression at $\dot{\varepsilon} = 8 \times 10^{-5}$ s^{-1} (*1*) in the absence of magnetic and electric fields, (*2*) in the magnetic field $B = 0.4$ T, and (*3*) in the magnetic (0.4 T) and electric ($E = 9$ kV/m) fields.

As was noted above, the shortening of deformation stages and a decrease in the slope θ_{II} in the magnetic field is explained by the fact that the magnetic field stimulates a faster changeover between the active slip systems [18, 24]. By contrast, the electric field, as can be judged from the lengthening of the first deformation stage and the decrease in the slope θ_I, provides the conditions for a longer participation of the primary slip system in the initial deformation stages. An increase in the strain hardening coefficients θ_{II} under the combined action of the magnetic and electric fields can likely be interpreted by the electrically stimulated increase in the dislocation density according to the known relationship [43]

$$\theta_{II} \sim Gb\sqrt{\rho},$$

where G is the shear modulus, b is the magnitude of the Burgers vector, and ρ is the dislocation density.

The dependences of the yield stress σ_y on the electric field strength E at different magnetic inductions B are plotted in Fig. 13a. It can be clearly seen from this figure that the experimental dependences involve two segments corresponding to the initial decrease in the yield stress and its subsequent saturation at $E > 1$–1.5 kV/m. The larger the magnetic induction, the larger and steeper the decrease in the yield stress σ_y.

Similar dependences were obtained at the fixed magnetic induction B and different strain rates $\dot{\varepsilon}$ (Fig. 13b). The electric field strengths of the saturation are the same as for the dependences depicted in Fig. 13a. The lower the strain rate $\dot{\varepsilon}$, the steeper and larger the decrease in the yield stress. Furthermore, it was shown that, at $\dot{\varepsilon} = 8 \times 10^{-5}$ s^{-1}, the yield stress corresponding to the saturation in the dependences is retained up to $E \geq 20$ kV/m.

Therefore, the sensitivity of the parameters of the macroplasticity to the electric field increases by several orders of magnitude. Actually, the effects found under the combined action of weak magnetic and electric fields $B \leq 0.4$ T and $E \sim 1$ kV/m (a decrease in the yield stress and an increase in the strain hardening rate and the dislocation density) can be observed in the absence of magnetic field only in considerably higher electric fields $E \geq 10^3$ kV/m.

The reason for this behavior seems to be quite evident. Indeed, in both cases, the threshold of sensitivity to the electric field is determined from the condition that the electric force acting on a dislocation should be comparable to the dislocation motion drag. Consequently, a drastic increase in this threshold upon application of the magnetic field is likely associated with the corresponding decrease in the dislocation motion drag when the interaction of the dislocation with main impurity centers is suppressed owing to particular spin-dependent transitions in the dislocation–impurity system in the external magnetic field.

The saturation of the observed decrease in the yield stress σ_y with an increase in the electric field strength most likely reflects the "residual" role of screw components of dislocation loops in the macroplasticity. Recall that screw dislocations in basic slip systems in alkali halide crystals are neutral. The dislocation motion with a velocity controlled by a given strain rate requires the application of a certain mechanical stress that possibly corresponds to the yield stress σ_y at $E \longrightarrow \infty$.

Note that an increase in the strain rate $\dot{\varepsilon}$ leads to a decrease in the maximum reduction of the yield stress σ_y under the action of the electric field (Fig. 13b). This correlates with the previously observed decrease in the dynamic charge on edge dislocations with an increase in the strain rate [44].

3.5. The Kinematic Model of the Macroscopic Magnetoplastic Effect

The established experimental regularities were interpreted within a simple kinematic model of the macroscopic magnetoplastic effect [20, 24].

As was noted above, according to the independent data obtained by different authors in the study of the microplasticity of nonmagnetic crystals, the role of the magnetic field in the plasticization of crystals is reduced to the depinning of dislocations from point defects [22, 45]. Let us consider the active deformation of a crystal at a strain rate $\dot{\varepsilon} = \text{const}$ in the magnetic field B in the framework of a simplified model under the

assumption that the yield stress σ_y at $B = 0$ is limited by identical magnetosensitive impurity centers coexisting with obstacles insensitive to the magnetic field. At a given magnetic field B, the depinning time τ_B of dislocations from obstacles of the first type due to spin-dependent transitions is proportional to B^{-2} [46], that is,

$$\tau_B = \alpha B^{-2}. \quad (1)$$

According to [46], these transitions and, hence, the corresponding depinning can occur only in magnetic fields higher than a certain threshold field $B_c^{(0)}$. On the other hand, even at $B > B_c^{(0)}$, the magnetically stimulated depinning of dislocations does not affect the macroplasticity if the depinning time τ_B defined by formula (1) is considerably longer than the time of thermally activated depinning of dislocations

$$\tau_{th} = \tau_0 \exp[(U_0 - \gamma\sigma)/kT] \quad (2)$$

from the same obstacle under the stress $\sigma = \sigma_y$ given by the strain rate

$$\dot{\varepsilon} = \dot{\varepsilon}_0 \exp[-(U_0 - \gamma\sigma)/kT]. \quad (3)$$

In formulas (2) and (3), U_0 is the activation energy for overcoming of the potential barrier associated with the impurity center and γ is the activation volume. Therefore, the deformation kinetics determines its own threshold of the magnetosensitive macroplasticity, because the inequality $\tau_B < \tau_{th}$ with due regard for relationships (1)–(3) is equivalent to the following inequality:

$$B^2 > \alpha\dot{\varepsilon}/\tau_0\dot{\varepsilon}_0. \quad (4)$$

To put it differently, a pronounced effect of the magnetic field on the stress–strain curves $\sigma(\varepsilon)$ in terms of the model under consideration should be observed only at $B > B_c$, where the threshold field B_c is represented by the expression

$$B_c = \max\{B_c^{(0)}, k\sqrt{\dot{\varepsilon}}\}, \quad k = \sqrt{\alpha/\tau_0\dot{\varepsilon}_0}. \quad (5)$$

The dependence of the threshold field B_c on the strain rate can be written in the following, more convenient form [equivalent to expression (5)]:

$$B_c = \begin{cases} B_c^{(0)}, & \dot{\varepsilon} < \dot{\varepsilon}_m \\ k\sqrt{\dot{\varepsilon}}, & \dot{\varepsilon} > \dot{\varepsilon}_m, \end{cases} \quad (6)$$

where

$$\dot{\varepsilon}_m = (B_c^{(0)}/k)^2. \quad (7)$$

The dependences $B_c(\dot{\varepsilon})$ calculated within the proposed model and the experimental data obtained by processing the dependences $\sigma_y(B)$ measured for the LiF (Fig. 8) and NaCl (Fig. 10b) crystals at different strain rates are compared in Fig. 14 (curves *1*, *2*). It can be seen from this figure that the predicted dependences [calculated from formulas (5) and (6)] and the experimental data are in good agreement, which counts in favor of the aforementioned physical model.

In principle, this model also explains a further behavior of the dependence $\sigma_y(B)$. Indeed, according to formula (1), the depinning time of dislocations from obstacles of the main type in magnetic fields higher than the threshold field B_c should rapidly decrease with an increase in the induction B. In sufficiently high fields, the depinning time τ_B becomes substantially shorter than both the time τ_{th} [relationship (2)] and the time of thermally activated overcoming of the remaining weaker magnetically insensitive obstacles, which

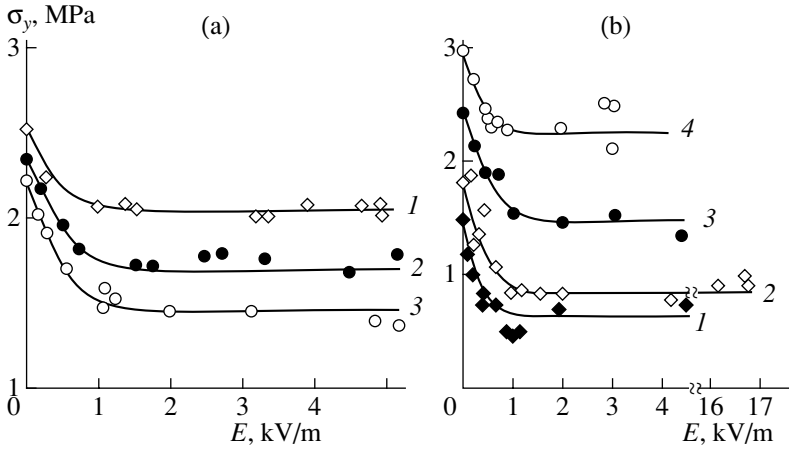

Fig. 13. Dependences of the yield stress on the electric field strength at (a) different magnetic field inductions B ($\dot{\varepsilon} = 5 \times 10^{-4}$ s^{-1}) and (b) different strain rates $\dot{\varepsilon}$ (B = 0.4 T). Magnetic field induction B (T): (a) (*1*) 0.2, (*2*) 0.3, and (*3*) 0.4. Strain rates $\dot{\varepsilon}$ (s^{-1}): (b) (*1*) 5×10^{-5}, (*2*) 8×10^{-5}, (*3*) 2×10^{-4}, and (*4*) 2×10^{-3}.

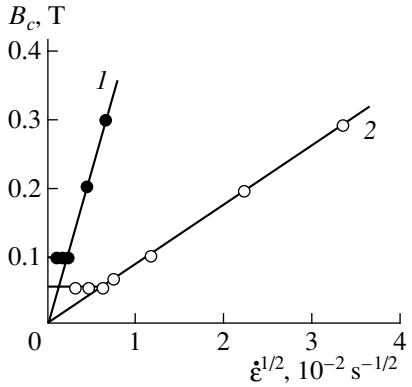

Fig. 14. Dependences of the threshold magnetic field induction B_c on the strain rate $\dot{\varepsilon}$ for (*1*) LiF and (*2*) NaCl crystals. Solid lines are the theoretical dependences calculated from formulas (5) and (6). Experimental points are obtained by processing the dependences depicted in Figs. 8 and 10b.

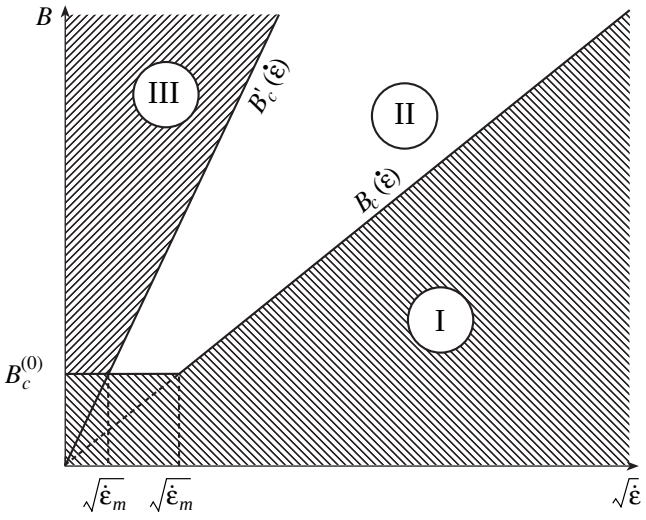

Fig. 15. Dependences $B_c(\dot{\varepsilon})$ and $B_c'(\dot{\varepsilon})$ and regions I, II, and III of the physical parameters $\{B, \dot{\varepsilon}\}$ corresponding to three ranges of a variation in the yield stress with an increase in the magnetic induction B.

can be written in the form

$$\tau_{th}' = \tau_0' \exp[(U_0' - \gamma'\sigma)/kT], \quad (8)$$

where U_0' is the activation energy for overcoming of the potential barriers associated with these obstacles and γ' is the activation volume. Consequently, with an increase in the magnetic induction, the yield stress σ_y should change from the initial value $\sigma_y(B = 0) \equiv \sigma_y^{(0)}$ determined from relationship (3) at $\sigma = \sigma_y^{(0)}$,

$$\sigma_y^{(0)} = (U_0/\gamma) + [(kT/\gamma)\ln(\dot{\varepsilon}/\dot{\varepsilon}_0)], \quad (9)$$

to the yield stress $\sigma_y^{(1)}$ corresponding to the activation parameters U_0' and γ', that is,

$$\sigma_y^{(1)} = (U_0'/\gamma') + [(kT/\gamma')\ln(\dot{\varepsilon}/\dot{\varepsilon}_0')]. \quad (10)$$

Therefore, in our model, the fact that the dependence $\sigma_y(B)$ involves three characteristic segments is determined by the occurrence of three characteristic ranges of variations in the time of the magnetically stimulated depinning of dislocations from impurities: $\tau_B > \tau_{th}$, $\tau_{th}' < \tau_B < \tau_{th}$, and $\tau_B < \tau_{th}'$. These time ranges correspond to the following magnetic induction ranges:

$$B < B_c, \quad B_c < B < B_c', \quad B > B_c', \quad (11)$$

where the second threshold field B_c' is given by expressions similar to formulas (5) and (6) after substitution

$$k \longrightarrow k' = \sqrt{\alpha/\tau_0'\dot{\varepsilon}_0'}, \quad \dot{\varepsilon}_m \longrightarrow \dot{\varepsilon}_m' = (B_c^{(0)}/k')^2. \quad (12)$$

Figure 15 shows the dependences $B_c(\dot{\varepsilon})$ and $B_c'(\dot{\varepsilon})$ and also the regions of the physical parameters $\{B, \dot{\varepsilon}\}$ corresponding to three ranges (11) of variations in the yield stress with an increase in the magnetic induction B. The thermally activated processes of depinning from defects of all types are dominant at parameters corresponding to region I ($B < B_c$). The yield stress in region III ($B > B_c'$) is limited by the thermally activated depinning from obstacles insensitive to the magnetic field. In the framework of this model, the yield strength should substantially depend on the magnetic field only in intermediate region II. As can be seen from Fig. 15, the width of this region on the magnetic induction scale should remain minimum and independent of the strain rate at $\dot{\varepsilon} < \dot{\varepsilon}_m' = (B_c/k')^2$. At strain rates lying in the range $\dot{\varepsilon}_m' < \dot{\varepsilon} < \dot{\varepsilon}_m = (B_c/k')^2$, the width of region II increases with an increase in the strain rate $\dot{\varepsilon}$. In this case, the left boundary of the region remains unchanged and the right boundary is shifted proportionally to $\sqrt{\dot{\varepsilon}}$. Finally, at high strain rates $\dot{\varepsilon} > \dot{\varepsilon}_m$, both boundaries of the intermediate region are shifted proportionally to $\sqrt{\dot{\varepsilon}}$ and the region width can be estimated as $\Delta B \sim (k' - k)\sqrt{\dot{\varepsilon}}$. It can be seen from Figs. 8 and 10b that an increase in the strain rate $\dot{\varepsilon}$ leads to an increase in the range ΔB of a main decrease in the yield stress σ_y, which correlates qualitatively with the proposed model. Certainly, the width of the step in the dependence $\sigma_y(B)$ can also be governed by other factors that are disregarded within the simplified approach used.

One of these factors can be associated with the occurrence of several types of magnetosensitive barriers. However, as can be seen from Fig. 9, curve *1* describing the deformation of the LiF crystals at $B = 0$ indicates that the dependence of the yield stress on

$\log\dot{\varepsilon}$ exhibits a linear behavior in complete agreement with the our model formula (9), which likely disproves the above assumption. Moreover, the dependences shown in Fig. 9 carry information that is possibly even more important for the understanding of the processes under investigation. Curve *5* measured at the largest induction ($B \sim 0.5$ T) almost completely lies in region III, and the slope of its straight-line segment described by relationship (10) in our model virtually coincides with the slope of curve *1*. This implies that the activation volumes of the initial and final potential barriers are equal to each other ($\gamma = \gamma'$). Hence, it follows that the initial magnetosensitive centers responsible for the deformation macrokinetics in region I and defects controlling the yield stress in region III occupy the same positions. In other words, the final barriers result from the initial barriers after spin-dependent electronic transitions in the impurity–dislocation system. Therefore, in at least the LiF crystals, the magnetic field leads only to a strong lowering of the barriers rather than to their complete breaking (suppression), as was commonly believed earlier. This fundamentally important conclusion was first drawn in our work [20].

4. CONCLUSIONS

Thus, in the series of works under consideration, we revealed and investigated the influence of magnetic effects on the real structure of nonmagnetic crystals and their deformation kinetic. We studied two groups of phenomena: the magnetic memory effects caused by the preliminary heat treatment and the *in situ* magnetic effects that are not governed by the magnetic memory. The effects of the former group result in such transformations of the impurity structure that are accompanied by a gradual formation of the magnetosensitive state, which disappears with time. The effects of the latter group are directly associated with magnetoplasticity, which manifests itself only during the application of the magnetic field.

The effect of the magnetic treatment on the real structure was judged from the change in the physical properties of the samples. It was established for the first time that the preliminary magnetic treatment of alkali halide crystals results in a decrease in the solubility and a change in the microhardness. The effect of the preliminary thermomagnetic treatment of the crystals on the time evolution of the their impurity structure was revealed from the measured changes in the yield stress.

Moreover, it was found that the yield stress of the NaCl : Ni crystals nonmonotonically varies (gradually decreases and then regains the initial value) with a variation in the time between the quenching and the preliminary magnetic treatment of the samples. It was demonstrated that a long-term preliminary exposure of the freshly cleaved NaCl : Ni samples to the magnetic field affects the electronic structure of their impurity centers. This manifests itself in the nonmonotonic dependence of the magnetoplastic response (the difference between the yield stresses measured in the presence and absence of magnetic field) on the magnetic treatment duration.

The macroscopic manifestations of the magnetoplastic effect were investigated under active deformation of crystals in the magnetic field. It was shown that the application of the magnetic field leads to a change in the stress–strain curves and a decrease in the yield stress of the LiF, NaCl, and PbS crystals. The existence region of the magnetoplastic effect was studied as a function of the strain rate and the magnetic induction. It was revealed that there is a lower threshold of the effect, namely, the threshold magnetic field B_c dependent on the strain rate $\dot{\varepsilon}$. At $B > B_c$, the yield stress strongly decreases and then reaches the steady-state value, which is determined by the barrier height lowered owing to the magnetically stimulated evolution of the electronic structure of the dislocation–impurity system.

It was established that the simultaneous exposure of alkali halide crystals to the magnetic and electric fields sharply reduces the threshold of the sensitivity of these crystals to the electric field. The degree of plasticization of materials in the electric field $E \sim 1$ kV/m and the magnetic field is identical to that in the electric field $E \sim 10^3$ kV/m in the absence of magnetic field.

The physical interpretation was proposed for all the observed properties and the specific features of the deformation kinetics in the magnetic field. The kinematic model of the macroscopic magnetoplastic effect was constructed. The model is based on the competition between the processes of thermally activated and magnetically stimulated depinning of dislocations from paramagnetic impurity centers (dislocation obstacles). This model allowed us to analytically describe many experimental dependences and characteristics. In particular, the theory was developed for the dependence of the yield stress on the strain rate and the magnetic field induction that corresponds to three deformation stages. This theory is in good agreement with the experimental dependences $\sigma_y(B, \dot{\varepsilon})$ and $B_c(\dot{\varepsilon})$.

ACKNOWLEDGMENTS

The series of investigations was supported by the Russian Foundation for Basic Research, project nos. 97-02-16327 and 00-02-16233. This work was also supported in part by the Russian Foundation for Basic Research, project no. 03-02-16423.

REFERENCES

1. G. I. Distler, V. M. Kanevskiĭ, V. V. Moskvin, *et al.*, Dokl. Akad. Nauk SSSR **268** (3), 591 (1983) [Sov. Phys. Dokl. **28**, 43 (1983)].
2. A. E. Smirnov, A. A. Urusovskaya, and V. R. Regel', Dokl. Akad. Nauk SSSR **280** (5), 1122 (1985) [Sov. Phys. Dokl. **30**, 155 (1985)].

3. V. M. Kanevskiĭ, G. I. Distler, A. E. Smirnov, *et al.*, Izv. Akad. Nauk SSSR, Ser. Fiz. **48** (12), 2408 (1984).
4. A. E. Smirnov and A. A. Urusovskaya, Fiz. Tverd. Tela (Leningrad) **29** (3), 852 (1987) [Sov. Phys. Solid State **29**, 485 (1987)].
5. Yu. I. Golovin and R. B. Morgunov, Pis'ma Zh. Éksp. Teor. Fiz. **58** (3), 189 (1993) [JETP Lett. **58**, 191 (1993)].
6. N. A. Tyapunina, V. L. Krasnikov, and É. P. Belozerova, Kristallografiya **45** (1), 156 (2000) [Crystallogr. Rep. **45**, 150 (2000)].
7. A. A. Urusovskaya, A. E. Smirnov, and N. N. Bekkauer, in *Proceedings of XXXVI International Seminar "Topical Problems of Strength," Vitebsk, Russia, 2000*, Part 1, p. 294.
8. A. E. Smirnov, N. N. Bekkauer, and V. V. Sadchikov, Kristallografiya **48** (2003) (in press).
9. R. B. Morgunov and A. A. Baskakov, Fiz. Tverd. Tela (St. Petersburg) **43** (9), 1632 (2001) [Phys. Solid State **43**, 1700 (2001)].
10. J. M. Galligan and C. S. Pang, J. Appl. Phys. **50** (10), 6253 (1979).
11. V. S. Krylovskiĭ, V. P. Lebedev, and V. I. Khotkevich, Fiz. Nizk. Temp. **7** (12), 1550 (1981) [Sov. J. Low Temp. Phys. **7**, 750 (1981)].
12. V. A. Pavlov, I. A. Pereturina, and I. L. Pecherkina, Fiz. Met. Metalloved. **47** (11), 171 (1979).
13. D. N. Bol'shutkin and V. A. Desnenko, Fiz. Nizk. Temp. **7**, 652 (1981) [Sov. J. Low Temp. Phys. **7**, 321 (1981)].
14. V. I. Al'shits, E. V. Darinskaya, T. M. Perekalina, and A. A. Urusovskaya, Fiz. Tverd. Tela (Leningrad) **29** (2), 467 (1987) [Sov. Phys. Solid State **29**, 265 (1987)].
15. V. I. Al'shits, E. V. Darinskaya, O. L. Kazakova, *et al.*, Pis'ma Zh. Éksp. Teor. Fiz. **63** (8), 628 (1996) [JETP Lett. **63**, 668 (1996)].
16. V. I. Al'shits, E. V. Darinskaya, E. Yu. Mikhina, and E. A. Petrzhik, Fiz. Tverd. Tela (St. Petersburg) **38**, 2426 (1996) [Phys. Solid State **38**, 1333 (1996)].
17. Yu. I. Golovin and R. B. Morgunov, Pis'ma Zh. Éksp. Teor. Fiz. **61** (7), 583 (1995) [JETP Lett. **61**, 596 (1995)].
18. A. A. Urusovskaya, V. I. Al'shits, A. E. Smirnov, and N. N. Bekkauer, Pis'ma Zh. Éksp. Teor. Fiz. **65** (6), 470 (1997) [JETP Lett. **65**, 497 (1997)].
19. A. A. Urusovskaya, A. E. Smirnov, and N. N. Bekkauer, Izv. Akad. Nauk, Ser. Fiz. **61** (5), 937 (1997).
20. V. I. Al'shits, A. A. Urusovskaya, A. E. Smirnov, and N. N. Bekkauer, Fiz. Tverd. Tela (St. Petersburg) **42** (2), 270 (2000) [Phys. Solid State **42**, 277 (2000)].
21. A. A. Urusovskaya, V. I. Alshits, A. E. Smirnov, and N. N. Bekkauer, in *20th Europian Crystallographic Meeting, Book of Abstracts and Programme, Krakow, Poland, 2001* (Errata, Krakow, 2001), p. 6.
22. V. I. Al'shits, E. V. Darinskaya, O. Ya. Kazakova, *et al.*, Izv. Akad. Nauk, Ser. Fiz. **57** (11), 2 (1993).
23. A. A. Urusovskaya, V. I. Al'shits, A. E. Smirnov, and N. N. Bekkauer, Vestn. Tambov. Univ. **3** (3), 213 (1998).
24. V. I. Al'shits, N. N. Bekkauér, A. E. Smirnov, and A. A. Urusovskaya, Zh. Éksp. Teor. Fiz. **115**, 951 (1999) [JETP **88**, 523 (1999)].
25. V. I. Al'shits, A. A. Urusovskaya, A. E. Smirnov, *et al.*, in *Proceedings of All-Russian Conference "Structural Defects and Strength of Crystals," Chernogolovka, Russia, 2002*, p. 160.
26. V. I. Al'shits, N. N. Bekkauer, A. E. Smirnov, and A. A. Urusovskaya, Izv. Akad. Nauk, Ser. Fiz. **67** (6), 775 (2003).
27. A. A. Urusovskaya, A. E. Smirnov, and N. N. Bekkauer, Vestn. Tambov. Univ., Ser. Estestv. Tekh. Nauki **5** (2–3), 389 (2000).
28. A. A. Urusovskaya, N. L. Sizova, K. Sangwal, and S. P. Smirnov, Fiz. Tverd. Tela (Leningrad) **20** (5), 1451 (1978) [Sov. Phys. Solid State **20**, 835 (1978)].
29. A. A. Urusovskaya and G. G. Knab, Phys. Status Solidi A **61** (1), 203 (1980).
30. N. A. Tyapunina, V. L. Krasnikov, and É. P. Belozerova, Fiz. Tverd. Tela (St. Petersburg) **41** (6), 1035 (1999) [Phys. Solid State **41**, 942 (1999)].
31. A. A. Urusovskaya, Usp. Fiz. Nauk **96** (1), 39 (1968) [Sov. Phys. Usp. **11**, 631 (1968)].
32. R. W. Whitworth, Adv. Phys. **24** (2), 203 (1975).
33. N. A. Tyapunina and E. P. Belozerova, Usp. Fiz. Nauk **156** (4), 683 (1988) [Sov. Phys. Usp. **31**, 1060 (1988)].
34. A. W. Stepanov, Z. Phys. **81** (7/8), 560 (1933).
35. A. N. Kulichenko and B. I. Smirnov, Fiz. Tverd. Tela (Leningrad) **23** (4), 1029 (1981) [Sov. Phys. Solid State **23**, 595 (1981)].
36. A. N. Kulichenko and B. I. Smirnov, Fiz. Tverd. Tela (Leningrad) **25** (5), 1523 (1983) [Sov. Phys. Solid State **25**, 876 (1983)].
37. N. V. Zagoruĭko and E. D. Shchukin, Kristallografiya **13** (5), 908 (1968) [Sov. Phys. Crystallogr. **13**, 789 (1968)].
38. A. A. Urusovskaya, N. N. Bekkauer, and A. E. Smirnov, Fiz. Tverd. Tela (Leningrad) **33** (11), 3169 (1991) [Sov. Phys. Solid State **33**, 1790 (1991)].
39. A. A. Urusovskaya, A. E. Smirnov, and N. N. Bekkauer, Izv. Vyssh. Uchebn. Zaved., Chern. Metall., No. 8, 55 (1993).
40. V. I. Al'shits, E. V. Darinskaya, E. Yu. Mikhina, and E. A. Petrzhik, Fiz. Tverd. Tela (St. Petersburg) **35** (5), 1397 (1993) [Phys. Solid State **35**, 706 (1993)].
41. V. I. Al'shits, E. V. Darinskaya, E. Yu. Mikhina, and E. A. Petrzhik, Fiz. Tverd. Tela (St. Petersburg) **38** (8), 2426 (1996) [Phys. Solid State **38**, 1333 (1996)].
42. A. A. Urusovskaya, V. I. Al'shits, N. N. Bekkauer, and A. E. Smirnov, Fiz. Tverd. Tela (St. Petersburg) **42** (2), 267 (2000) [Phys. Solid State **42**, 274 (2000)].
43. N. F. Mott, Philos. Mag. **43** (7), 1151 (1952).
44. V. I. Al'shits, M. V. Galustashvili, and I. M. Paperno, Kristallografiya **20** (6), 1113 (1975) [Sov. Phys. Crystallogr. **20**, 679 (1975)].
45. Yu. I. Golovin and R. B. Morgunov, Zh. Éksp. Teor. Fiz. **115** (2), 605 (1999) [JETP **88**, 332 (1999)].
46. V. I. Al'shits, E. V. Darinskaya, O. Ya. Kazakova, *et al.*, Pis'ma Zh. Éksp. Teor. Fiz. **63**, 628 (1996) [JETP Lett. **63**, 668 (1996)].

Translated by O. Borovik-Romanova

Crystallography Reports, Vol. 48, No. 5, 2003, pp. 813–818. Translated from Kristallografiya, Vol. 48, No. 5, 2003, pp. 873–878.

REAL CRYSTAL STRUCTURE

Dedicated to the 60th Anniversary of the Shubnikov Institute of Crystallography of the Russian Academy of Sciences

Hardening of Crystals Caused by the Dynamic Aging of Dislocations

B. V. Petukhov

Shubnikov Institute of Crystallography, Russian Academy of Sciences, Leninskiĭ pr. 59, Moscow, 119333 Russia

e-mail: petukhov@ns.crys.ras.ru

Received February 27, 2003

Abstract—A model relating the pronounced effect of mobile impurities on the processes of plastic deformation in crystals to the dynamic aging of dislocations is proposed. The model is based on the concept of internal stresses depending individually on the age of dislocations due to the difference in the impurity environment. The concentration dependence of the impurity contribution to the hardening of materials is calculated. The theory is illustrated by the experimental data for a GeSi solid solution. © *2003 MAIK "Nauka/Interperiodica".*

INTRODUCTION

Many crystalline materials are characterized by a very strong variation in the yield point caused by doping. Such a behavior is rather promising for controlling the mechanical characteristics of crystals, and, in particular, for the enhancement of their strength. As a rule, the magnitude of so-called solid-solution hardening far exceeds the values expected from the mean-field estimates. The latter are obtained by interpolation between the values of the yield point for the materials formed by each sort of atoms of which the initial compound is composed (see, for example, [1–3]). One of the goals of the theory is the search for mechanisms underlying the enhanced effect of impurities on the plasticity of crystalline materials. In this paper, we discuss one such mechanism related to the so-called dynamic aging of dislocations, which is an alternative to the mechanisms of static hardening [4].

Experimental data demonstrate that dislocations can be considered as sinks for mobile impurities. In addition, the dislocation moving through the crystal can trap in its core and entrain into motion even low-mobile impurities. As a result, the dynamic properties of the dislocations themselves change drastically until the dislocations become completely immobile. The pinning by impurities impedes the motion and multiplication of dislocations. These phenomena have important consequences for the production and operation of semiconductor devices in microelectronics [5, 6] and for the characteristics of structural materials [1–4].

The evolution of dislocation ensembles in many pure crystalline materials with a pronounced temperature dependence of the yield point (semiconductors, alkali halide crystals, etc.) is described satisfactorily by the well-known Johnston–Gilman [7] and Alexander–Haasen [8, 9] theories. The corresponding theory for materials with impurities and solid solutions is far from well elaborated. We should mention [10], where the Alexander–Haasen model is supplemented by a numerical solution of the equation describing the diffusion of oxygen atoms in silicon toward moving dislocations. In this study, we analyze another case, when an extended cloud of impurities is not formed around rapidly moving dislocations and the direct contact interaction of impurities with the dislocation cores plays a dominant role. This process is accompanied by the entrainment of impurities, which results in their excess concentration in the dislocation core. The corresponding changes in the dislocation mobility are usually referred to as the dynamic aging of dislocations. The aged dislocations, which have trapped a lot of impurities, loose their mobility and drop out of the plastic flow of the material. The newly formed dislocations take their place. The motion of dislocations with the excess impurity content requires a stronger driving force. This is the direct reason for the increase in the magnitude of the deforming stress. The aim of this study is to quantitatively analyze this hardening mechanism. First, we briefly recall the model of plastic deformation in pure materials; then, we generalize this model taking into account the effect of dynamic aging of dislocations.

1063-7745/03/4805-0813$24.00

DEFORMATION OF PURE CRYSTALS

We shall consider deformation beyond the yield point (when it is mainly plastic). The plastic-deformation rate $\dot{\varepsilon}$ is given by the Orowan relation $\dot{\varepsilon} = NbV(\tau)$, where b is the length of the Burgers' vector of dislocations; N is the density of dislocations; and $V(\tau)$ is the velocity of dislocations, which depends on the applied stress τ and temperature T. In particular, the velocity of dislocations in pure crystalline semiconductors, such as germanium, silicon, and the like, obeys the empirical equation

$$V = B\tau^m, \quad (1)$$

where the exponent m is of the order of unity and nearly independent of temperature. In this case, the temperature dependence is mainly due to the coefficient B [11–13] (it is usually characterized by an Arrhenius-type temperature dependence with a certain activation energy E). For other materials, such as alkali halide crystals and some metals, Eq. (1) is also valid, but the exponent m may be quite large and temperature dependent. For many materials, the activation energy E itself depends on the applied stress.

The kinetic equation describing the evolution of the dislocation ensemble has the form

$$\frac{dN}{dt} = wN\tau^n V(\tau). \quad (2)$$

Here, w is the self-multiplication factor for dislocations. The exponent n is different for different models. For example, $n = 0$ in the Johnston–Gilman model and $n = 1$ in the Alexander–Haasen model. We discuss here the general case with an arbitrary value of n.

In order to take into account the strain hardening, the applied stress τ is usually substituted by the effective stress $\tau_e = \tau - \tau_i$ in (1) and (2). Here, τ_i is the so-called internal stress, related, for example, to the long-range elastic fields of dislocations. To describe pure crystals, we assume the internal stresses to be the same for all dislocations. In crystals with impurities, the driving force for dislocations may depend on the crystal age owing to the aging effect. This circumstance calls for the modification of the usual approach.

CRYSTALS WITH IMPURITIES: THE EFFECT OF DYNAMIC AGING OF DISLOCATIONS

We shall discuss below the case of lightly doped crystals or diluted solid solutions (when it is possible to neglect the changes in the elastic moduli and other characteristics of the starting materials). In this case, the effect of clusters is rather small and may be neglected. For brevity, the minority atoms in the solid solution will also be referred to as impurities. As shown in [14, 15], it is necessary to distinguish between the cases of mobile and low-mobile impurities. The trapping radius for mobile impurities trapped by edge dislocations is determined by the expression $r = 2(2AD/kTV)^{1/2}$. Here, the factor $A = \frac{1}{3\pi}\frac{1+\nu}{1-\nu}Gb\Delta v$ characterizes the long-range elastic interaction of a dislocation with an impurity atom generating dilatation Δv, G is the shear modulus, ν is the Poisson's ratio, and D is the impurity diffusivity. In the case of low-mobile impurities with low diffusivity, the trapping radius for impurities may decrease to its minimum value r_0 with the same order of magnitude as the dislocation-core size ~b. In our calculations, the condition $r \le b$ will be the criterion for low mobility of impurities. Note that this criterion depends not only on the type of impurities, but also on the characteristics of their interaction with dislocations and, in particular, on the type of dislocations. In contrast to edge dislocations, which are characterized by long-range elastic interaction with impurities and for which the trapping radius r may far exceed the lattice constant, screw dislocations may have an environment of only a small radius. When the size of the impurity environment $r_0 \sim b$, for both dislocation types, we should talk of a nonlinear drift (or simply a forced entrainment of impurities) rather than the diffusion of impurities trapped by moving dislocations.

The amount of impurities trapped per unit time is given by their amount within a layer of area rV. Disregarding the processes in which trapped impurities detach from the dislocations, we can describe the entrainment of impurities by the equation

$$\frac{dc}{dt} = \frac{rc_0}{a^2}V. \quad (3)$$

Here, c_0 is the impurity concentration in the crystal bulk per lattice site and c is the concentration of impurities trapped by dislocations.

When a dislocation is displaced by a distance of several lattice constants, the impurity concentration within its core becomes considerably higher than the bulk concentration c_0. In the theories of aging of dislocations, it is assumed that the excess of impurity atoms in their cores results in the braking stress of the dry-friction type. It can be written as βc [16], where the factors β are determined by the short-range contact interaction of an impurity with a dislocation. This contribution also reduces the value of effective stress τ_e, which drives the dislocation. As a result, we have $\tau_e = \tau - \tau_i - \beta c$.

The number of impurities trapped by a dislocation is determined by its mean free path, which depends on the moment of creation of this dislocation. Consequently, as was mentioned in [17], the effective stress affecting dislocations created at different moments of time should also be different. Below, we illustrate this idea by calculations for the case of constant applied stress. That is why the generation rate of new dislocations will be different for dislocations with a different history. In order to take into account this phenomenon in our calculations, we should explicitly take into consideration the age of dislocations. With this purpose, we introduce

the quantity $\rho(t)$ defined as the number of dislocations created in the unit volume per unit time. Then the increase in the dislocation density dN during time dt will be given by the relation $dN = \rho(t)dt$. The total density is the sum of contributions from all dislocations created at different moments of time. As a result, we come to the formula

$$\rho(t) = w\int_0^t dt_1\rho(t_1)V(\tau-\tau_i-\beta c(t,t_1)) \times[\tau(t)-\tau_i-\beta c(t,t_1)]^n, \quad (4)$$

which should replace Eq. (2).

Due to the difference in the impurity content, the dislocations created at different moments of time t_1 move with different velocities $V(t, t_1)$ at a given moment t and, hence, make different contributions to the rate $\dot{\varepsilon}$ of the plastic flow of the sample. Summing all these contributions, we obtain the generalized Orowan relation

$$\dot{\varepsilon} = \int_0^t dt_1\rho(t_1)bV(t,t_1). \quad (5)$$

The steady-state deforming stress that is established beyond the yield point (at the easy glide stage) changes relatively slowly with time. Therefore, we shall use the quasi-static approximation to find the contribution of the impurity hardening to the deforming stress. In other words, we neglect the time dependence of τ. In this case, the variables in Eq. (3) are separated for arbitrary stress dependence of the dislocation velocity:

$$\frac{dc}{rV(\tau-\tau_i-\beta c)} = \frac{c_0}{a^2}dt. \quad (6)$$

The integration of this expression allows us to calculate the impurity concentration in the dislocation core and find the variation in time of the effective stress τ_e, which drives the dislocation. In the case of the power-law dependence of the dislocation velocity on stress (1), for sufficiently mobile impurities (that is, for $r \sim 1/V^{1/2}$), we obtain

$$\tau_e = \left[(\tau-\tau_i)^{1-m/2} + \left(\frac{m}{2}-1\right)\frac{\beta c_0}{a^2}\sqrt{\frac{8ADB}{kT}}(t-t_1)\right]^{\frac{1}{1-m/2}}. \quad (7)$$

Figure 1 shows the kinetics of the effective stress (time is normalized to $\frac{a^2(\tau-\tau_i)^{1-m/2}}{\beta c_0}\sqrt{\frac{kT}{8ADB}}$). At $m < 2$, the effective stress vanishes and the dislocation stops after a finite time. At $m \geq 2$, the motion of the dislocation slows down smoothly, but the velocity does not become zero during the whole time interval under study. In the case of low-mobile impurities, when $r = r_0 = \text{const}$, the right-hand side of the above inequalities should contain 1 instead of 2.

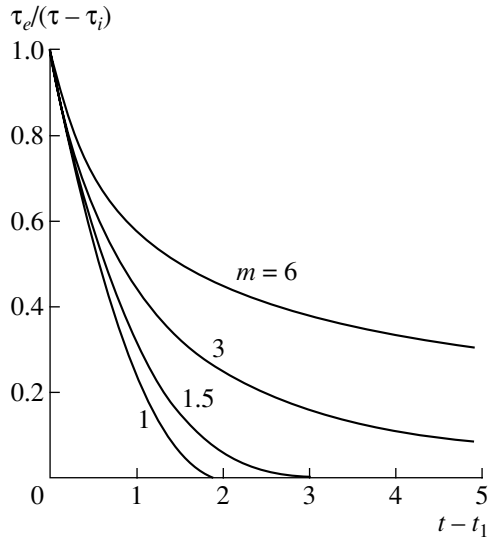

Fig. 1. Kinetics of the effective stress depending on the age of dislocations at different values of exponent m in the relation between the dislocation velocity and the stress.

Thus, permanent immobilization of aged dislocations occurs. To support the process of the plastic flow, these dislocations should be replaced by the newly created ones. Such a situation requires a higher level of applied stress as compared to the case of a pure crystal. The higher the concentration of impurities, the larger the stress required. Let us find the necessary level of applied stress. The impurity environment $c(t, t_1)$ trapped by a dislocation with a constant applied stress depends on the difference $t - t_1$ only. This circumstance makes it possible to replace the variable t in integral (4) by τ_e. Let us substitute expression (6) into Eq. (4). We assume $\rho(t)$ to be constant (ρ_∞) at $t \longrightarrow \infty$. This constant value turns out to be a common multiplier for the left- and right-hand sides of Eq. (4) and can be canceled. As a result, we obtain the following equation for determining the deforming stress as a function of the impurity concentration and other parameters:

$$\frac{wa^2}{\beta c_0}\int_0^{\tau-\tau_i} d\tau_e\frac{\tau_e^n}{r} = 1. \quad (8)$$

The steady-state generation rate ρ_∞ of dislocations is found from the generalized Orowan relation (5)

$$\rho_\infty = \frac{\beta c_0\dot{\varepsilon}}{ba^2}\Big/\int_0^{\tau-\tau_i}\frac{d\tau_e}{r}. \quad (9)$$

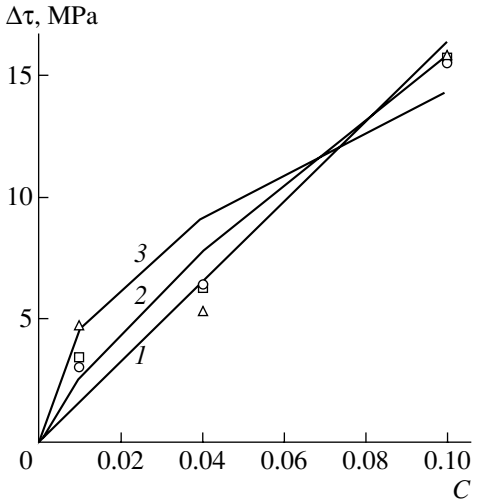

Fig. 2. Concentration dependence of the solid-solution hardening of $Ge_{1-c}Si_c$ at different temperatures according to the data from [18]: T = (triangles) 900, (squares) 800, and (circles) 700°C. Curves *1*, *2*, and *3* correspond to $\Delta\tau \sim c^{0.8}$, $\Delta\tau \sim c$, and $\Delta\tau \sim c^{1/2}$, respectively.

Equation (8) describes the additive contribution of impurity atoms entrained by the dislocation ensemble, which enhances the internal stresses, i.e., leads to the hardening of the crystal. The concentration and temperature dependences of this contribution may be rather different under various conditions. For sufficiently mobile impurities, when $r \sim 1/V^{1/2}$, we can expect a pronounced temperature dependence on the impurity contribution. For example, in the case of the power-law dependence (1) of the dislocation velocity on stress, we find the following expression by calculating the integral in (8):

$$\tau = \left[\frac{(n + m/2 + 1)\beta c_0}{wa^2}\sqrt{\frac{8AD}{kTB}}\right]^{1/(n+m/2+1)} + \tau_i. \quad (10)$$

The first term in (10) describes the impurity contribution to the deforming stress and includes the parameters D and B with the exponential temperature dependence. The temperature dependence of m is also possible. Eventually, all these factors lead to a complicated temperature dependence of τ, and, at certain values of the parameters, this dependence can be anomalous; i.e., the deforming stress may increase with temperature.

In the case of low-mobile impurities, when $r = r_0 =$ const, the situation is different. Calculating the integral in (8), which is independent of the dislocation mobility in this case, we find for any form of $V(\tau)$

$$\tau = \left[\frac{(n + 1)\beta c_0 r_0}{wa^2}\right]^{1/(n+1)} + \tau_i. \quad (11)$$

It is interesting to note that the concentration dependence of the impurity hardening is governed in this case by the dynamics of the multiplication of dislocations rather than by their mobility. For the Johnston–Gilman model at $n = 0$, expression (11) describes the impurity contribution to the deforming stress, which is linear with respect to the concentration c_0:

$$\tau = \frac{\beta r_0}{wa^2}c_0 + \tau_i. \quad (12)$$

In the Alexander–Haasen model, $n = 1$ and the impurity contribution has a square-root dependence on c_0:

$$\tau = \sqrt{\frac{2\beta r_0 c_0}{wa^2}} + \tau_i. \quad (13)$$

These two types of behavior are observed most frequently in experiments (see, for example, [1–4] and the references therein). However, in both the cases of (12) and (13), the impurity hardening is not characterized by a pronounced temperature dependence of the thermal-activation term, which enters the dislocation mobility (1) but is canceled in the final expression. Therefore, the impurity contribution should make the plasticity less sensitive to temperature, whereas, in pure semiconductors and some other materials, the deforming stress steeply decreases with increasing temperature. The above is also valid for the sensitivity to the plastic-flow rate (the dependence of the deforming stress on $\dot{\varepsilon}$ also becomes weaker in comparison with pure materials).

Such an effect of doping was observed, for example, for the $Ge_{1-c}Si_c$ solid solution by Yonenaga [18], who suggested that this phenomenon may be to a certain extent related to the formation of a dynamic environment of the solution atoms around dislocations. Therefore, let us try to apply the model discussed in this study to the interpretation of specific features of the experimental data. The mobility of dislocations in pure and low-doped germanium is characterized by parameter $m \sim 1.7$ and activation energy $E \sim 1.62$–1.7 eV. In pure germanium, such values result in a pronounced temperature dependence of the deforming stress. However, the situation for a solid solution is different.

Figure 2 shows the increments of deforming stress with respect to the deforming stress in pure germanium caused by dissolved silicon atoms calculated on the basis of the experimental data from [18] for three temperatures: $T_1 = 900$°C, $T_2 = 800$°C, and $T_3 = 700$°C. We can see that, for all the concentrations of the solution, these increments are nearly the same for all three temperature values, which, apparently, corresponds to the case of low-mobile impurities. The fitting of the concentration dependence yields the dependence $\sim c^{0.8}$ (Fig. 2, curve *1*); i.e., the exponent is closer to 1 (the Johnston–Gilman model) than to 1/2 (the Alexander–Haasen model). Assuming linear behavior, we find from the experimental data the coefficient $\beta r_0/(wa^2)$ to

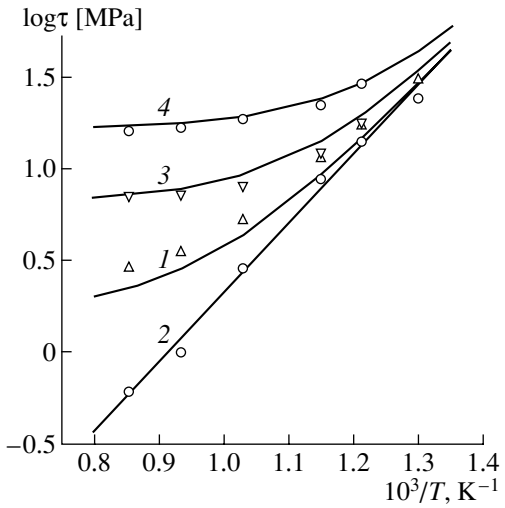

Fig. 3. Temperature dependence of the deforming stress τ for the $Ge_{1-c}Si_c$ solid solution at different concentrations of silicon atoms: c = (*1*) 0, (*2*) 0.01, (*3*) 0.04, and (*4*) 0.1. The data are from [18]. Solid lines show the results of calculations.

be about 164 MPa (Fig. 2, curve *2*). Using the derived concentration dependence of the impurity contribution and the known temperature dependence of the deforming stress in pure germanium, we can plot the temperature dependences for the $Ge_{1-c}Si_c$ solid solution with different contents of silicon. The results of the calculations are shown in Fig. 3 for three values of Si content: c = 0.01, 0.04, and 0.1. One can see that the calculations agree well with the experimental data [18].

Similar behavior is also observed for other materials, such as solid solutions based on the bcc metals [3]. One should bear in mind that, along with the effect of impurities and dissolved atoms, the deceleration of dislocations may be due to intrinsic point defects [19]. The coexistence of dislocations moving at different velocities (in agreement with the predictions of our model), which was observed in *in situ* experiments with γ-TiAl, was also reported in [19]. At the same time, the experiment indicates the limitations of the applicability of the model suggested, which are related to the possibility that impurities may become detached from dislocations at the later stages of the accumulation of impurities. In particular, collective detachment of impurities may lead to instabilities of the plastic flow such as the Portevin–Le Chatelier instabilities [16]. However, the discussion of such instabilities is beyond the scope of the present paper.

In conclusion, note that in the model considered the hardening effect turns out to be so strong (in comparison with the estimates based on the mean-field theory) due to the collective influence of impurities trapped along the mean free path of dislocations (which is fairly long). For example, in the case of the impurity contribution described by Eq. (12), the quantity $1/w$ plays the role of such a path. This quantity is the mean distance, far exceeding the lattice constant, at which multiplication of dislocations occurs. As a result, the calculations we performed explicitly demonstrate that the effect of the dynamic aging of dislocations can drastically change the characteristics of the plastic flow typical of a pure crystal. The identification of the specific mechanisms underlying the dislocation dynamics calls for a more detailed comparison of experimental data with the theoretical predictions.

CONCLUSIONS

Let us formulate the main results obtained here.

We presented the concept of effective internal stresses depending individually on the age of dislocations owing to the difference in their impurity environment. The impurity contribution to the macroscopic deforming stress that is established beyond the yield point at the easy glide stage was calculated by averaging over the ensemble of dislocations of different age.

According to our calculations, the effect of sufficiently mobile impurities is controlled by their diffusion mobility, which may give rise to an anomalous temperature dependence of the deforming stress. The effect of low-mobile impurities is less sensitive to the temperature and deformation rate and reduces the corresponding dependence of the deforming stress in comparison with that for pure crystals.

The magnitude of the impurity hardening is related to the cooperative effect of impurities trapped by the dislocations that have a rather long mean free path and far exceeds that expected from the mean-field estimates.

REFERENCES

1. J. Friedel, *Dislocations* (Pergamon, Oxford, 1964; Mir, Moscow, 1967).
2. T. Suzuki, H. Yosinaga, and S. Takeuchi, *Dislocation Dynamics and Plasticity* (Syokabo, Tokyo, 1986; Mir, Moscow, 1989; Springer, Berlin, 1991).
3. N. I. Noskova, *Defects and Deformation of Single Crystals* (Ural. Otd. Ross. Akad. Nauk, Ekaterinburg, 1995).
4. H. Neuhauser, *Multiscale Phenomena in Plasticity*, Ed. by J. Lepinoux *et al.* (Kluwer, Dordrecht, 2000), p. 99.
5. K. Sumino, *Defects and Properties of Semiconductors: Defect Engineering*, Ed. by J. Chikawa *et al.* (KTK Scientific, Tokyo, 1987), p. 227.
6. M. G. Mil'vidskiĭ and V. B. Osvenskiĭ, *Structural Defects in Single Crystals of Semiconductors* (Metallurgiya, Moscow, 1984).
7. W. G. Johnston and J. J. Gilman, J. Appl. Phys. **30**, 129 (1959).
8. H. Alexander and P. Haasen, Solid State Phys. **22**, 27 (1968).
9. H. Alexander, *Dislocations in Solids*, Ed. by F. R. N. Nabarro (North-Holland, Amsterdam, 1986), Vol. 7, p. 113.

10. D. Maroudas and R. A. Brown, J. Mater. Res. **6**, 2337 (1991).
11. V. I. Nikitenko, *Dynamics of Dislocations* (Naukova Dumka, Kiev, 1975), p. 7.
12. K. Sumino and M. Imai, Philos. Mag. A **47**, 753 (1983).
13. A. George and J. Rabier, Rev. Phys. Appl. **22**, 941 (1987).
14. H. Yoshinaga and S. Morozumi, Philos. Mag. **23**, 1351 (1971).
15. B. V. Petukhov, Fiz. Tverd. Tela (Leningrad) **26**, 3160 (1984) [Sov. Phys. Solid State **26**, 1903 (1984)].
16. Y. Estrin and L. P. Kubin, *Continuum Models for Materials with Micro-Structure*, Ed. by H.-B. Mulhaus (Wiley, New York, 1995), p. 395.
17. B. V. Petukhov, Fiz. Tekh. Poluprovodn. (St. Petersburg) **36**, 129 (2002) [Semiconductors **36**, 121 (2002)].
18. I. Yonenaga, Physica B (Amsterdam) **273–274**, 612 (1999).
19. D. Haussler, M. Bartsch, M. Aindow, *et al.*, Philos. Mag. A **79**, 1045 (1999).

Translated by K. Kugel

Crystallography Reports, Vol. 48, No. 5, 2003, pp. 819–822. Translated from Kristallografiya, Vol. 48, No. 5, 2003, pp. 879–883.

LATTICE DYNAMICS AND PHASE TRANSITIONS

Dedicated to the 60th Anniversary of the Shubnikov Institute of Crystallography of the Russian Academy of Sciences

The Domain Structure of $Cs_3H(SeO_4)_2$ Crystals

L. F. Kirpichnikova*, M. Polomska, L. Szczesniak**, and B. Hilczer****

** Shubnikov Institute of Crystallography, Russian Academy of Sciences, Leninskiĭ pr. 59, Moscow, 119333 Russia*

e-mail: luba@ns.crys.ras.ru

*** Institute of Molecular Physics, Polish Academy of Sciences, Smoluchowskiego 17, 60-17 Poznan, Poland*

e-mail: polomska@ifmpan.poznan.pl

Received April 21, 2003

Abstract—The characteristics of the changes in the domain structure of $Cs_3H(SeO_4)_2$ crystals have been studied in a wide temperature range. An anomalous change in the domain structure in the temperature range near the superprotonic phase transition was found. The anomalies in this temperature range were also found by differential scanning calorimetry. The characteristics of the changes in the domain structure in different phases are compared. *© 2003 MAIK "Nauka/Interperiodica".*

$Cs_3H(SeO_4)_2$ crystals are known to undergo several phase transitions. At $T_S = 456$ K, an improper first-order phase transition from the superprotonic phase I ($R\bar{3}m$) to the ferroelastic phase II ($A2/a$) occurs. Then, at 369 K, the transition to the ferroelastic phase III ($C2/m$) is observed, and, at 50 K, phase IV appears [1–3]. The structures of phases II and III are similar to the slightly distorted structure of phase I; thus, the I–II–III transitions are caused by small deformations with slight displacements of nonhydrogen atoms [4–7]. The most essential changes at the phase transitions occur in proton subsystems: at the II–I transition, an ordered system becomes dynamically disordered [6]. According to [7], at room temperature, the SeO_4 tetrahedra in phase III are linked by hydrogen bonds into isolated pairs (dimers). Only one bond is retained at the II–III phase transition; the other bond breaks and a new bond directed at an angle of 120° to the previous one is formed. According to another model [3], at the III–II transition, all the hydrogen bonds are disrupted, and new reoriented bonds are formed between the adjacent SeO_4^{2-} groups. The domain structure of $Cs_3H(SeO_4)_2$ crystals was studied by Komukae *et al.* [3], who proposed the crystalline models of twins and showed that the components of the spontaneous-strain tensor are about 10^{-3}, which is typical of crystals of the $Me_3H(XO_4)_2$ family.

This aim of this study was to investigate the domain structure of $Cs_3H(SeO_4)_2$ crystals in the temperature range from room temperature to the temperature of the transition to the superprotonic phase. This problem is of interest because the relatively high spontaneous strain disappears in the vicinity of the superprotonic transition and the conductivity begins to increase significantly. In addition, in contrast to crystals of the $Me_3H(XO_4)_2$ family, $Cs_3H(SeO_4)_2$ crystals undergo an additional phase transition from one ferroelastic phase to another above room temperature. The characteristics of the changes in the domain structure in this temperature range deserve to be studied in more detail.

The domain structure of $Cs_3H(SeO_4)_2$ crystals was studied by the polarization-optical method using a VTO 232 M1 video system (LINKAM, England) in a wide temperature range. The samples were placed into a special THMS600 unit. The precision control, programmable variations, and temperature stabilization were performed using a TMS91 unit. Changes in the domain structure observed were recorded on a videocassette, checked on a TV screen, and photographed. The temperature change was checked accurate to 0.01 K. The differential scanning calorimetry studies were performed using an NETSCH DSC-200 instrument; the samples were heated at a rate of 0.2 K/min.

$Cs_3H(SeO_4)_2$ crystals usually have a pseudohexagonal habit with well-pronounced (001) faces. In the phase above the superprotonic transition, the crystals become transparent and optically uniaxial, the optical axis being directed normally to the (0001) face. With the symmetry reduction from the trigonal paraelastic superprotonic $\bar{3}m$ phase (Fig. 1a) to the monoclinic

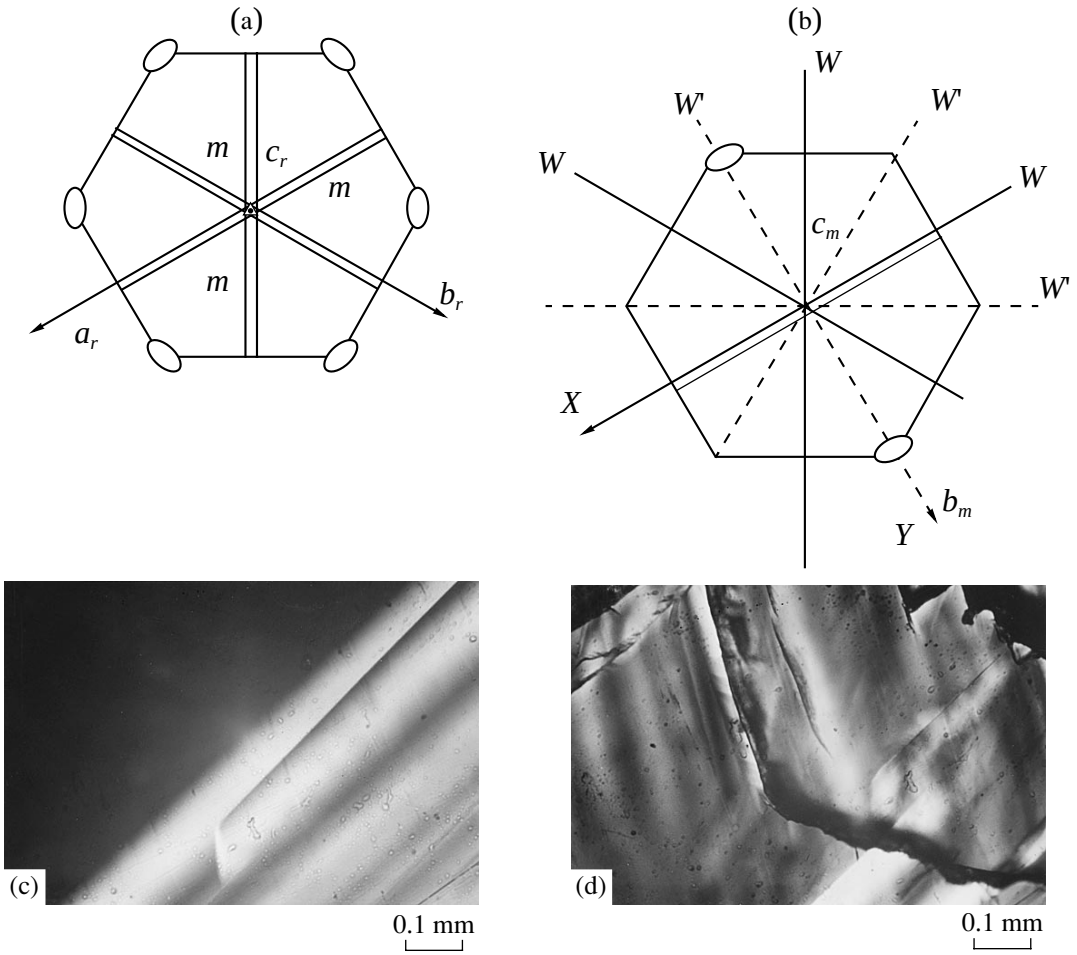

Fig. 1. (a) Schematic of the point groups and symmetry elements $\bar{3}m$ and 2/*m* and (b) the orientation of the domain walls *W* and *W*'. Photographs of the ferroelastic domain structure of the (001) cut of $Cs_3H(SeO_4)_2$ crystals at (c) 300 and (d) 370 K.

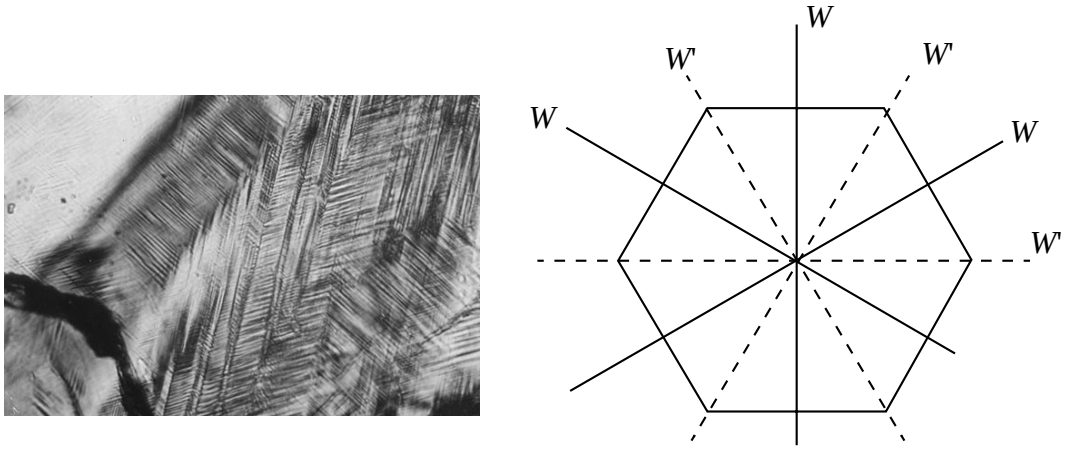

Fig. 2. Small-domain structure occurring on the (001) cut of $Cs_3H(SeO_4)_2$ crystals at T_S = 1.3 K.

ferroelastic 2/*m* phase (Fig. 1b), three orientation states, S_1, S_2, and S_3 (or three domains), and six types of domain walls arise according to [8]. Two types of domain walls, *W* and *W*', exist. The domain wall *W* corresponds to the plane of reflection symmetry lost during the transition; it is always perpendicular to the (001) plane and does not vary with temperature. The domain wall *W*' corresponds to the symmetry axis lost during

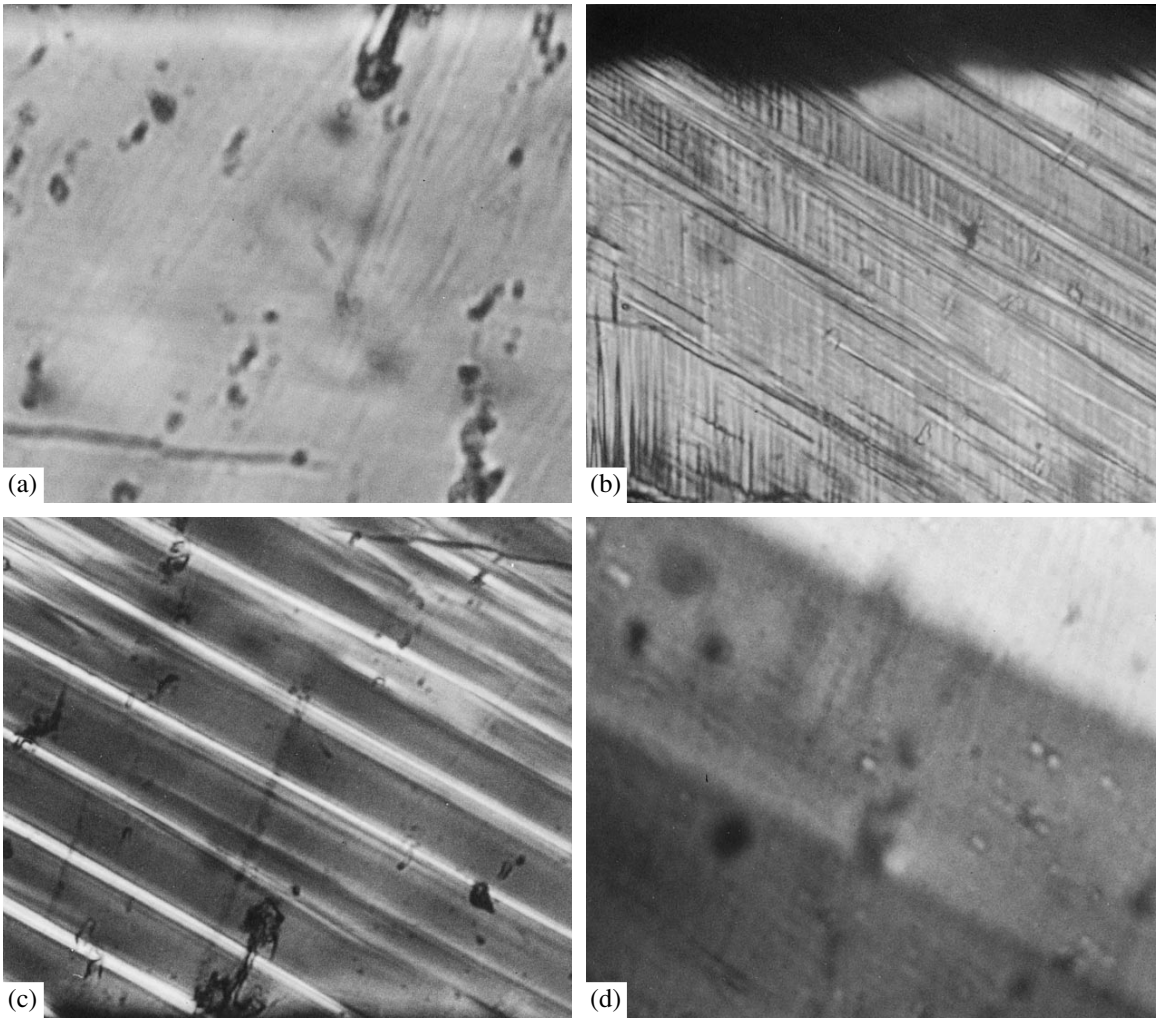

Fig. 3. Transformation of the (001) cut of a $Cs_3H(SeO_4)_2$ crystal due to the transition from the superprotonic phase (a) with decreasing temperature, (b) at T_S = 1 K, (c) in the *A*2/*a* phase, and (d) in the *C*2/*m* phase.

the transition; it is tilted with respect to the face of the hexagonal prism and may rotate with temperature. The photograph of the (001) cut of a $Cs_3H(SeO_4)_2$ crystal with the domain structure of *W*' type at room temperature is shown in Fig. 1c. With an increase in the temperature, the shape of the domain bands practically does not change up to the III–II phase transition. At 369 K, a motion of the phase front characteristic of the first-order phase transition is observed, cracks appear, and a partial crystal fracture occurs. A significant number of new domains appear (Fig. 2d); however, the domains in phase II are oriented similarly to those in phase III (with regard to the distortions caused by cracks in the crystal). With a further increase in temperature, the domain structure of phase II practically does not change, and a significant domain restructuring is observed only as the superprotonic phase transition is approached. At a temperature 1.3 K below that corresponding to the appearance of the superprotonic phase, new small domains arise (Fig. 2), which disappear at the phase transition to the superprotonic phase. If the temperature of the transition from the superprotonic to the ferroelastic phase decreases, small domains appear, which are replaced by larger domains with further decreasing temperature (Fig. 3). Small domains exist in a narrow temperature region ~1.3 K below the temperature of the superprotonic transition. Such an abnormal change in the domain structure in the vicinity of the superprotonic transition was not observed in the previous studies and, therefore, is of certain interest. The variety of domains, their small size, and the presence of numerous lens-shaped domains do not allow us to assign the domains observed either to the monoclinic or to the triclinic phase with complete certainty. The differential scanning calorimetry showed an abnormal increase in the signal below the main peak due to the transition to the superprotonic phase (Fig. 4). At temperatures below that corresponding to the sharp peak

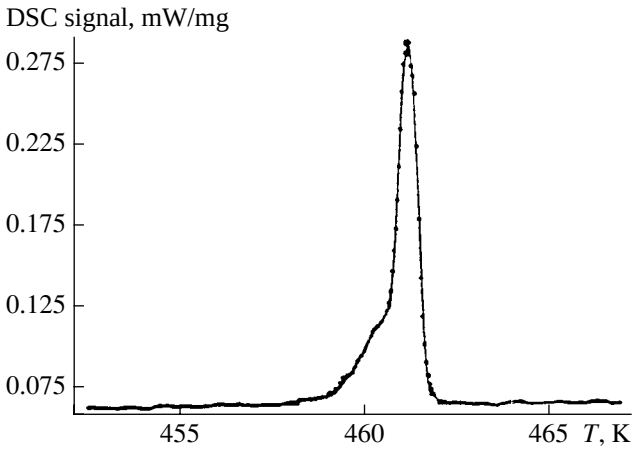

Fig. 4. Differential-scanning calorimetry (DSC) curve for the $Cs_3H(SeO_4)_2$ crystals.

with $\Delta S_1 = 7.25$ J mol^{-1} K^{-1} due to the transition to the superprotonic phase, a step with $\Delta S_2 = 2.07$ J mol^{-1} K^{-1} is observed. Thus, the total change in the entropy is 9.32 J mol^{-1} K^{-1}.

The appearance of a new domain structure near the transition from the superprotonic to the ferroelastic phase accompanied by an anomaly on the differential-scanning-calorimetry curve shows that the transition to the high-conductivity phase is of more complex nature than described previously. The appearance of small domains, which has not been described in the literature, occurs at the same temperature as that at which the conductivity begins to rise. This anomalous phenomenon requires more detailed consideration since the reason for the unusual behavior of the domains is not yet clear. One may suggest that the appearance of the domains is caused by the occurrence of internal stresses in the region of active restructuring of the proton subsystem. If there are significant internal stresses in the material, there is a chance that the ferroelastic transition will split under the action of these stresses.

It is also possible that the appearance of the new domains is caused by the transition to an intermediate phase (triclinic or monoclinic) occurring in a narrow temperature range below the temperatures corresponding to the superprotonic phase. However, it is rather difficult to confirm or disprove this suggestion because the temperature range in which such a phase may exist is narrow and also because the appearance of many small domains in this temperature range leads to structural distortion. One may also suggest that the internal stresses are caused by the presence of antiphase domains appearing as a result of the improper character of the transition from the superprotonic to the ferroelastic phase. Of course, these stresses cannot lead to a splitting of the transition, but they can cause restructuring of the ferroelastic domains due to the fairly low coercive stress near the transition.

ACKNOWLEDGMENTS

We are grateful to A. Pavlovskiĭ for supplying the crystals for analysis.

This study was supported by the Russian Foundation for Basic Research, project no. 03-02-16190.

REFERENCES

1. M. Komukae, T. Osaka, T. Kaneko, and Y. Makita, J. Phys. Soc. Jpn. **54**, 3407 (1985).
2. A. I. Baranov, A. V. Tregubchenko, L. A. Shuvalov, and N. M. Shchagina, Fiz. Tverd. Tela (Leningrad) **29** (8), 2513 (1987) [Sov. Phys. Solid State **29**, 1448 (1987)].
3. M. Komukae, K. Sakata, T. Osaka, and Y. Makita, J. Phys. Soc. Jpn. **63**, 1009 (1994).
4. B. V. Merinov, A. I. Baranov, A. V. Tregubchenko, and L. A. Shuvalov, Dokl. Akad. Nauk SSSR **302**, 406 (1988).
5. B. V. Merinov, N. B. Bolotina, A. I. Baranov, and L. A. Shuvalov, Kristallografiya **33** (6), 1131 (1988) [Sov. Phys. Crystallogr. **33**, 824 (1988)].
6. B. V. Merinov, A. I. Baranov, and L. A. Shuvalov, Kristallografiya **35** (2), 355 (1990) [Sov. Phys. Crystallogr. **35**, 200 (1990)].
7. B. V. Merinov, N. B. Bolotina, A. I. Baranov, and L. A. Shuvalov, Kristallografiya **36** (5), 1131 (1991) [Sov. Phys. Crystallogr. **36**, 639 (1991)].
8. J. Sapriel, Phys. Rev. B **12** (11), 5128 (1975).

Translated by T. Dmitrieva

Crystallography Reports, Vol. 48, No. 5, 2003, pp. 823–831. Translated from Kristallografiya, Vol. 48, No. 5, 2003, pp. 884–892.

PHYSICAL PROPERTIES OF CRYSTALS

Dedicated to the 60th Anniversary of the Shubnikov Institute of Crystallography of the Russian Academy of Sciences

The Influence of Optical Activity on the Intensity and Polarization Parameters of Transmitted Light in Crystals

A. F. Konstantinova*, K. A. Rudoy, B. V. Nabatov*, E. A. Evdishchenko*, V. I. Stroganov**, and O. Yu. Pikul'****

** Shubnikov Institute of Crystallography, Russian Academy of Sciences, Leninskiĭ pr. 59, Moscow, 119333 Russia*

e-mail: AFKonst@ns.crys.ras.ru

*** Far Eastern State Transport University, ul. Serysheva 47, Khabarovsk, 680000 Russia*

Received June 4, 2003

Abstract—The ellipticity and azimuth of light transmitted through an optically active plate and the intensity of this light transmitted through an analyzer are theoretically investigated as functions of the rotation angle of the plate. Relationships describing these parameters are considered. It is demonstrated that, depending on the angle of inclination of the plate, the optical activity can affect the characteristics of the transmitted light differently. A technique for determining the optical activity parameters is proposed from analyzing the relationships for the light intensity. The conoscopic figures of uniaxial and biaxial optically active crystals are described. © *2003 MAIK "Nauka/Interperiodica".*

INTRODUCTION

Although optically active crystals have long been studied, a number of problems concerning their properties remain unclear and call for detailed investigation. As a rule, the effect of optical activity on the characteristics of transmitted light can be determined using different polarizing devices and varying the wavelength of the incident light [1, 2]. The characteristics of transmitted light upon rotation of samples were experimentally studied in [3–6] by measuring the change in the intensity of the light transmitted through an optically active plate located between an arbitrarily oriented polarizer and analyzer. The change in the intensity of the transmitted light was caused by the rotation of the plate. Earlier, Buzylov *et al.* [7] analyzed the dependence of the transmittance of a polarizing system on the angle of inclination to the optic axis and developed a device for modulation of a monochromatic parallel optical beam with the use of uniaxial gyrotropic crystals.

However, as far as we know, a comprehensive analysis of the characteristics of transmitted light as functions of the angle of rotation of the plate prepared from uniaxial or biaxial optically active absorbing crystals has never been performed before. The aim of the present work was to investigate this problem theoretically.

INTENSITY, ELLIPTICITY, AND AZIMUTH OF THE LIGHT TRANSMITTED THROUGH AN OPTICALLY ACTIVE ABSORBING PLATE

Let us consider the general case where an anisotropic optically active absorbing plate with an optic axis arbitrarily oriented at an angle θ to the normal is located between an arbitrarily oriented polarizer and analyzer. The plate can be rotated about the axis parallel to the plate surface through an angle ϕ_i (i.e., it can be inclined).

With due regard for the optical activity and absorptivity, the complex refractive indices of eigenwaves propagating in the crystal can be represented by the relationship $N_{1,2} = n_{1,2} + i\kappa_{1,2}$, where n_1 and n_2 are the refractive indices and κ_1 and κ_2 are the absorption indices. The average refractive index n_s and the average absorption index κ_s are determined as $n_s = (n_1 + n_2)/2$ and $\kappa_s = (\kappa_1 + \kappa_2)/2$. The angle ϕ_s is defined as the average value of the angles formed by waves refracted by the crystal and can be obtained from the Snell's law: $\sin\phi_s = \sin\phi_i/n_s$, where ϕ_i is the angle of incidence.

When analyzing the relationships for the polarization parameters of the transmitted light, we assume that the light is incident along the normal but, in this case, the orientation of the optic axis changes and becomes equal to $|\theta - \phi_s|$. The angle ϕ_s is determined under the assumption that, upon an oblique incidence of the light, both eigenwaves have an identical angle of refraction

1063-7745/03/4805-0823$24.00 © 2003 MAIK "Nauka/Interperiodica"

and the refractive index is taken as the average of the corresponding refractive indices. This approximation is fairly justified, because, upon an oblique incidence of the light, the angles of refraction of the eigenwaves differ insignificantly. Moreover, it should be taken into account that the calculated thickness of the plate d_s depends on the angle ϕ_s and can be determined from the expression $d_s = d/\cos\phi_s$, where d is the plate thickness measured along the normal to the plate surface.

It should be noted that, in many cases, multiple reflections are ignored in analyzing the results of measurements of the intensity of the light transmitted through a crystal plate. This is associated with the fact that, as a rule, the relative change in the light intensity as a function of a particular parameter is considered instead of the change in its absolute value. However, if more detailed information is required, multiple reflections must be taken into account, especially when the measurements are performed with very thin samples. In this case, the inclusion of multiple reflections in the expressions for parameters of the transmitted light can be accomplished only with computer calculations. In order to estimate the transmittance of the plate, i.e., when there is no need to account for multiple reflections and it will suffice to consider only the reflections from the first and second faces, we use the following approximation. If we disregard the small difference between the transmission coefficients of the eigenwaves, which is determined by the birefringence, the multiple reflections in the majority of cases can be described, to sufficient accuracy, in terms of the coefficient T, which characterizes the transmission of an isotropic plate [8].

In the general case, the coefficient T can be expressed through the average refractive index n_s and the average absorption index κ_s; that is,

$$T = [(1-R)^2(1+\kappa_s^2/n_s^2)]/[(e^{\eta} - Re^{-\eta})^2 + 4R\sin^2(\varphi+\varphi_0)], \quad (1)$$

where λ is the wavelength of the incident light; $\varphi = (2\pi/\lambda)n_s d$ is the change in the phase due to multiple reflections; $\eta = (2\pi/\lambda)\kappa_s d = Kd/2$; R is the reflection coefficient, which is defined by the relationship

$$R = [(n_s-1)^2 + \kappa_s^2]/[(n_s+1)^2 + \kappa_s^2];$$

$$\tan\varphi_0 = 2\kappa_s/(n_s^2 + \kappa_s^2 - 1).$$

For sufficiently thick plates, the transmittance is determined by the averaged value of the coefficient T defined by expression (1), which is obtained upon integrating with respect to φ; that is,

$$\langle T\rangle = [(1-R)^2(1+\kappa_s^2/n_s^2)]e^{-Kd}/(1-R^2e^{-2Kd}). \quad (2)$$

In the case of samples with a small transmittance, i.e., when the average absorption index κ_s (and, hence, Kd) can be considered to be small, relationship (2) takes the form

$$\langle T\rangle = (1-R)/(1+R) = 2n_s/(1+n_s^2). \quad (3)$$

As a rule, even transparent samples are characterized by a transition layer on their surface and scattering centers in the bulk. These samples can be treated as weakly absorbing materials. It should be emphasized that, in this case, the average absorption index κ_s is of the order of 10^{-3}–10^{-6} and its variations lead to a change in the amplitude but do not affect the phase.

On this basis, the intensity J of the light transmitted through a plate located between an arbitrarily oriented polarizer and analyzer can be written in the form

$$J = T[1 - \cos 2\upsilon\cos 2(\chi-\beta)]/2, \quad (4)$$

where α and β are the azimuths of the directions of the maximum transmission of the polarizer and the analyzer, respectively, and χ and υ are the azimuth and the ellipticity angle of the light that is transmitted through the polarizer and the plate prepared from the studied crystal and is then incident on the analyzer, respectively.

The ellipticity $\tau = \tan\upsilon$ and the azimuth χ can be determined from the following expressions (provided the azimuth of the instantaneous axis of the plate is equal to zero, i.e., the plate is oriented along its own principal axes) [2]:

$$\sin 2\upsilon = \pm[\sinh\delta_{el}\sin 2\gamma + \cos 2\gamma((\cosh\delta_{el} - \cos\Delta_{el})\sin 2\gamma\cos 2\alpha + \sin 2\alpha\sin\Delta_{el})]/[\cosh\delta_{el} + \sinh\delta_{el}\cos 2\gamma\cos 2\alpha], \quad (5)$$

$$\tan 2\chi = [\sin 2\alpha\cos\Delta_{el} \pm \sin 2\gamma\cos 2\alpha\sin\Delta_{el}]/[\sinh\delta_{el}\cos 2\gamma + \cosh\delta_{el}\cos^2 2\gamma\cos 2\alpha + \sin^2 2\gamma\cos\Delta_{el} \pm \sin 2\gamma\sin 2\alpha\sin\Delta_{el}], \quad (6)$$

where

$$\Delta_{el} = 2\pi d(n_2 - n_1)/(\lambda\cos\phi_s),$$
$$\delta_{el} = 2\pi d(\kappa_2 - \kappa_1)/(\lambda\cos\phi_s), \quad (7)$$

$\sin 2\gamma = 2k/(1+k^2)$, and $k = \tan\gamma$ is the ellipticity of the eigenwaves. For the majority of optically active crystals, it is assumed that the ellipticities k_1 and k_2 of the eigenwaves are equal in magnitude but opposite in sign. As a result, the ellipticity of the eigenwaves k can be calculated from the relationship given in [9]:

$$k = [(n_{02}^2 - n_{01}^2) - \sqrt{(n_{02}^2 - n_{01}^2)^2 + 4G^2}]/(2G), \quad (8)$$

where n_{01} and n_{02} are the refractive indices of the eigenwaves propagating in the crystal along the specified direction of the wave normal without regard for the optical activity and G is the scalar parameter of gyra-

tion. The parameter G depends on the crystal symmetry and the direction of the wave normal [2]. In the general form, we can write

$$G = g_{11}\theta_1^2 + g_{22}\theta_2^2 + g_{33}\theta_3^2 + (g_{12} + g_{21})\theta_1\theta_2 + (g_{13} + g_{31})\theta_1\theta_3 + (g_{23} + g_{32})\theta_2\theta_3, \quad (9)$$

where θ_1, θ_2, and θ_3 are the direction cosines and g_{ij} stands for the components of the gyration pseudotensor. As was shown in our previous work [10], the components g_{ij} and α_{ij} of the gyration pseudotensors in the approximate (g_{ij}) and exact (α_{ij}) theories are related by the following expressions:

$$g_{11} \approx (\alpha_{22} + \alpha_{33})n_s, \quad g_{22} \approx (\alpha_{11} + \alpha_{33})n_s, \quad g_{33} \approx (\alpha_{22} + \alpha_{11})n_s, \quad g_{ij} \approx \alpha_{ij}n_s. \quad (10)$$

The situations where these relationships must be taken into account in terms of the exact theory were described in [10].

Strictly speaking, the polarization parameters of the transmitted light upon inclination of the plate can depend on the antisymmetric component g_{12} of the gyration pseudotensor (in symmetry classes *3*, *4*, *6*, *3m*, *4mm*, and *6mm*) [2]. However, in symmetry classes *3*, *4*, and *6*, the optical activity is determined primarily by the symmetric part of the gyration pseudotensor and the antisymmetric component is of little significance. In the symmetry classes *3m*, *4mm*, and *6mm*, the ellipticity of eigenwaves associated with this component is approximately equal to 10^{-6} [2]; hence, these symmetry classes were excluded from our consideration.

The quantity Δn_{el} can be calculated using the principle of birefringence superposition [9]:

$$\Delta n_{el}^2 = \Delta n_l^2 + \Delta n_c^2, \quad (11)$$

where $\Delta n_l = (n_{02} - n_{01})$ is the linear birefringence and $\Delta n_c = G/\sqrt{n_{01}n_{02}}$ is the circular birefringence.

From relationship (6), the quantity 2χ can be exactly determined if it is remembered that the sign of $\sin 2\chi$ is the sign of the numerator and the sign of $\cos 2\chi$ is the sign of the denominator. This correspondence can be explained by the fact that expressions (5) and (6) are derived within the formalism of Müller matrices [11].

After substituting expressions (5) and (6) into relationship (4), we obtain

$$J = T\{2\cosh\delta_{el}\cos^2(\alpha - \beta) - (\cosh\delta_{el} - \cos\Delta_{el})\sin 2\alpha\sin 2\beta - (\cosh\delta_{el} - \cos\Delta_{el})\cos 2\alpha\cos 2\beta\sin^2 2\gamma \pm \sin 2(\alpha - \beta)\sin 2\gamma\sin\Delta_{el}\}/2). \quad (12)$$

In relationships (5), (6), and (12), the plus and minus signs refer to the right- and left-handed crystals, respectively. Expression (12) is written without regard for the circular dichroism, because the imaginary part of the gyration tensor, which characterizes the circular dichroism, is a small quantity (~10^{-6}–10^{-8}). It is obvious that, if the crystal is nonabsorbing ($\kappa_{1,2} = 0$), we have $\delta_{el} = 0$ and expression (12) can be simplified significantly.

All the above relationships are applicable to uniaxial optically active absorbing and transparent crystals, as well as to biaxial transparent and biaxial absorbing crystals for directions in which the ellipticity of eigenwaves is associated only with the optical activity.

ANALYSIS OF THE CHARACTERISTICS OF TRANSMITTED LIGHT

Now, we consider the case where the polarizer and the analyzer are crossed ($\beta = \alpha = 90°$) and the studied plate is located between them. If the principal plane of the plate is aligned with the direction of transmission of the polarizer ($\alpha = 0°, 90°$), the expression for the intensity of the light transmitted through the polarizer–plate–analyzer system and the expressions for the ellipticity $\tau = \tan\upsilon$ and azimuth χ of the light that is transmitted through the polarizer and the plate and is then incident on the analyzer can be represented in the form

$$J = T\sin^2 2\gamma\sin^2(\Delta_{el}/2), \quad (13)$$

$$\sin 2\upsilon = \pm\sin 4\gamma\sin^2(\Delta_{el}/2), \quad (14)$$

$$\tan 2\chi = [\pm\sin 2\gamma\sin\Delta_{el}]/[1 - 2\sin^2 2\gamma\sin^2(\Delta_{el}/2)]. \quad (15)$$

It should be emphasized that all the above quantities are proportional to the ellipticity of the eigenwaves due to the optical activity. For inactive crystals, the right-hand sides of expressions (13)–(15) vanish; i.e., the crystal is in the extinction position. It is evident that the quantities defined by expressions (13)–(15) for optically active crystals oscillate with changes in the phase difference Δ_{el}. As a rule, these changes are caused by variations in the wavelength of incident light [2]. In some cases, these changes are induced under external actions, for example, under variations in the temperature or upon exposure to electric or magnetic fields.

Let us now analyze how the rotation of the plate through an angle ϕ_i affects the parameters under investigation. Upon rotation of the plate, the change in the birefringence leads to a change in the phase difference Δ_{el} and the quantities $\sin^2(\Delta_{el}/2)$ and $\sin\Delta_{el}$ oscillate, whereas the quantities $\sin^2 2\gamma$, $\sin 4\gamma$, and $\sin 2\gamma$ related to the optical activity vary in a gradual way. Therefore, the curves $\sin^2 2\gamma(\phi_i)$ and $\sin 4\gamma(\phi_i)$ represent envelopes of the dependences $J(\phi_i)$ and $\sin 2\upsilon(\phi_i)$, respectively [see expressions (13) and (14)]. For $\Delta_{el}/2 = j\pi/2$ (where j = 1, 3, 5, …), the functions $J(\phi_i)$ and $\sin 2\upsilon(\phi_i)$ have maximum values. In the case when $\sin^2 2\gamma$ is a small quantity, the curve $\sin 2\gamma(\phi_i)$ is an envelope of the depen-

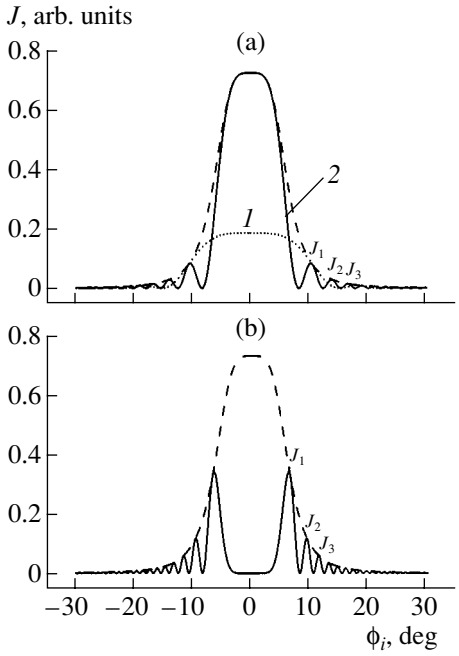

Fig. 1. Dependences of the intensity J of the transmitted light on the angle of rotation ϕ_i of plates cut out normally to the optic axis of a paratellurite crystal for d = (a) (*1*) 0.35, (*2*) 1.034, and (b) 2.069 mm. Dashed lines indicate the dependence $\sin^2 2\gamma(\phi_i)$.

dence $\tan 2\chi(\phi_i)$ [expression (15)] and maximum values of $\tan 2\chi(\phi_i)$ are attained at $\Delta_{el} = j\pi/2$, where j = 1, 3, 5, …. If the light propagates along the optic axis, we obtain $\sin 2\gamma = \mp 1$ (the upper and lower signs correspond to right-handed and left-handed crystals, respectively) and the phases difference $\Delta_{el} = \Delta_c = 2\rho d$, where $\rho = g_{33}\pi/\lambda n_o$ is the specific rotation of the polarization plane. For $\alpha \neq 0°$ and crossed polarizers, expression (12) takes the form

$$J = T\sin^2(\Delta_{el}/2)(\sin^2 2\alpha + \sin^2 2\gamma\cos^2 2\alpha). \quad (16)$$

As follows from formula (16), the intensity J of light propagating along the optic axis does not depend on the angle α. When the light propagates along directions differing from the optic axis, the quantity $\sin^2 2\gamma$ becomes small and the intensity $J(\phi_i)$ at α = const is determined by the quantity $T\sin^2(\Delta_{el}/2)$.

UNIAXIAL OPTICALLY ACTIVE CRYSTALS

We consider uniaxial crystals of the symmetry classes *3*, *4*, *6*, *3* : *2*, *4* : *2*, and *6* : *2*, for which the refractive indices and the scalar parameter of gyration can be calculated from the relationships

$$n_{02}^2 = n_o^2 n_e^2/[n_o^2 + (n_e^2 - n_o^2)(\mathbf{n}_s\mathbf{c})^2], \quad (17)$$

$$G = g_{33}\cos^2\phi_s + g_{11}\sin^2\phi_s, \quad (18)$$

where n_o and n_e are the principal refractive indices of the ordinary and extraordinary waves, respectively; $\mathbf{n}_s$ is the unit vector oriented along the average direction of the wave normals of the refracted waves; $\mathbf{c}$ is the unit vector directed along the optic axis; $(\mathbf{n}_s\mathbf{c}) = \cos\theta$; and θ is the angle formed by the optic axis and the wave normal $\mathbf{n}_s$.

The Case of a Plate Cut out Normally to the Optic Axis of the Crystal

Upon normal incidence on a plate cut out perpendicularly to the optic axis of the crystal, the light propagates along the optic axis. Figure 1 shows the dependences of the intensity of the transmitted light on the rotation angle ϕ_i for plates of different thicknesses. The calculation was performed for a paratellurite crystal at the wavelength λ = 0.6328 μm, refractive indices n_o = 2.2597 and n_e = 2.4119, specific rotation ρ = 87 deg/mm, and gyration tensor component $g_{33} = -6.9114 \times 10^{-4}$ [12].

It can be seen from Fig. 1 that, upon propagation of the light along the optic axis of the crystal, the polarizing system, depending on the phase difference $\Delta_c/2$, can transmit light with an intensity ranging from the maximum value, when $\Delta_c/2 = \pi/2$ (Fig. 1a, curve *2*), to the minimum value (zero), when $\Delta_c/2 = \pi$ (Fig. 1b). The maximum intensities J_m are obtained at $\Delta_{el}/2 = j\pi/2$ (j is an odd integer). The j value for the first maximum is determined by the phase difference $\Delta_c/2$. In Fig. 1b, the first maximum J_1 corresponds to the phase difference $\Delta_{el}/2 = 3\pi/2$, the second maximum J_2, to the phase difference $\Delta_{el}/2 = 5\pi/2$, etc. For any value of $\Delta_{el}/2$, the curve $T\sin^2 2\gamma(\phi_i)$ is an envelope of the dependence $J_m(\phi_i)$, which is clearly seen in Fig. 1.

The above analysis makes it possible to determine the parameters of the optical activity upon rotation of the plate through an angle ϕ_i. The ellipticity of the eigenwaves can be calculated from the dependence $J(\phi_i)$ measured for the crossed analyzer and polarizer and the azimuth of the incident light α = 0°, 90° (Fig. 1). In this case, the intensity J can be determined from expression (13). Taking into account that $\sin^2(\Delta_{el}/2) = 1$, we can write the following expression for the mth maximum:

$$J_m = T\sin^2 2\gamma_m. \quad (19)$$

By using the expression $\sin 2\gamma_m = 2k_m/(1 + k_m^2)$, the ellipticity of the eigenwaves can be calculated from the relationship

$$k_m = (1 - (1 - J_m/T)^{1/2})/(J_m/T)^{1/2}. \quad (20)$$

Since the phase difference Δ_{el} specifies the positions of the maxima and minima, its value can be obtained by measuring the light intensity J at any azimuth α of incident light [expression (16)]. From the measured depen-

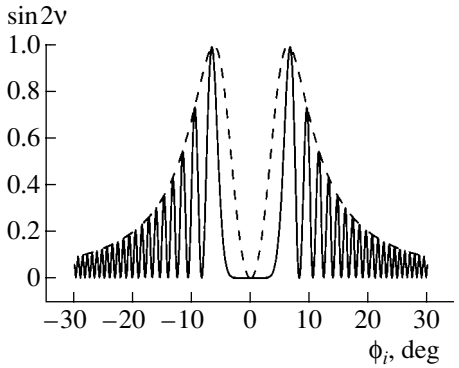

Fig. 2. Dependence of sin2υ on the angle of rotation ϕ_i of a 2.069-mm-thick plate cut out normally to the optic axis of a paratellurite crystal. The dashed line indicates the dependence sin4γ(ϕ_i).

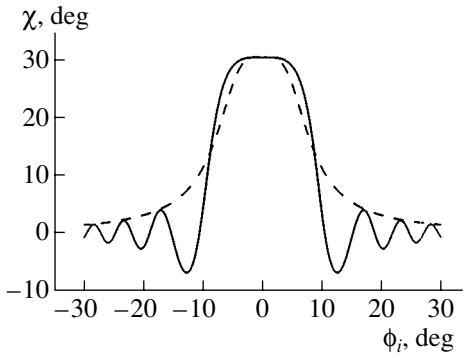

Fig. 3. Dependence of the azimuth χ on the angle of rotation ϕ_i of a 0.35-mm-thick plate cut out normally to the optic axis of a paratellurite crystal. The dashed line indicates the dependence sin2γ(ϕ_i).

dence $J(\phi_i)$ with due regard for Δ_c, it is possible to determine the order of maxima $(\Delta_{el}/2)_{max} = j\pi/2$ or minima $(\Delta_{el}/2)_{min} = l\pi$ (where $l = 1, 2$) of the intensity. The elliptic birefringence Δn_{el} can be calculated from formula (7).

Unlike the dependence $J(\phi_i)$, the dependence sin2υ(ϕ_i) that characterizes the ellipticity of the light transmitted though the plate is bounded by the envelope sin4γ (Fig. 2). For the light propagating along the optic axis, we have sin4γ = 0 and, hence, the light is always linearly polarized. It can be seen from Fig. 2 that, at the plate thickness d = 2.069 mm, the light is also almost linearly polarized for directions close to the optic axis ($\phi_i \sim 0°$–3.5°).

The dependence of the azimuth χ on the angle of rotation ϕ_i of the plate 0.35 mm thick is plotted in Fig. 3. This dependence characterizes the rotation of the polarization plane for the light propagating along the optic axis and a change in the rotation of the major axis of the polarization ellipse when the light propagates along directions differing from the optic axis. A change in the sample thickness does not lead to a radical change in the dependence χ(ϕ_i): as the angle of rotation ϕ_i of the plate increases, the angle of rotation of the major axis of the polarization ellipse decreases, becomes equal to zero (χ = 0) at a certain angle $\phi_i = \phi_0$ (in our case, ϕ_0 = 10.55°), and then oscillates about zero. An increase in the samples thickness leads to a decrease in the angle ϕ_0. If the light propagates along directions strongly deviating from the optic axis, the ellipticity k of eigenwaves becomes small and the quantity k^2 can be ignored. In this case, sin2γ ~ 2k, relationship (15) is simplified, and we obtain $\tan 2\chi = \pm 2k \sin\Delta_{el}$. Under these conditions, the curve $k(\phi_i)$ is the envelope of the dependence χ(ϕ_i).

The Case of a Plate Cut out at an Angle to the Optic Axis of the Crystal

If the plate is cut out at an angle to the optic axis and the angle θ is relatively small, it is clear that the plate can be rotated in such a way as to provide the light propagation along the optic axis. The dependence of the intensity of the transmitted light on the angle of rotation ϕ_i of the plate is shown in Fig. 4a. The plate is cut from a quartz crystal at the angle θ = 10° to the optic axis. From Fig. 4a, according to the Snell's law, we obtain ϕ_i = 15.58° and then $\phi_s = \theta$ = 10°.

In our earlier work [13], we described and calculated the conoscopic figure for a plate cut out normally to the optic axis of an optically active crystal. Relationship (12) allows us to calculate the conoscopic figure for any cross section of the crystal with the use of the Mathematica-4.1 package [14]. The conoscopic figure of the same plate is depicted in Fig. 4b. It can be seen from Fig. 4b that the isogyre cross is shifted and the dependence in Fig. 4a is the cross section of the conoscopic figure in Fig. 4b along the *OX* axis.

The Case of a Plate Cut out Parallel to the Optic Axis of the Crystal

This case is of special interest because the parameters J, sin2υ, and $\tan 2\chi$ obtained for this orientation of the plate make it possible to determine the components of the gyration pseudotensor, which cannot be derived when the plate is cut out normally to the optic axis. Similar investigations were performed for plates cut out parallel to the optic axis by varying the wavelength of incident light [1, 2]. The dependences of the intensity, ellipticity, and azimuth of the transmitted light on the angle of rotation of the plate 0.35 mm thick are plotted in Fig. 5. The plate is rotated so that the angle between the wave normal and the optic axis changes. Note that

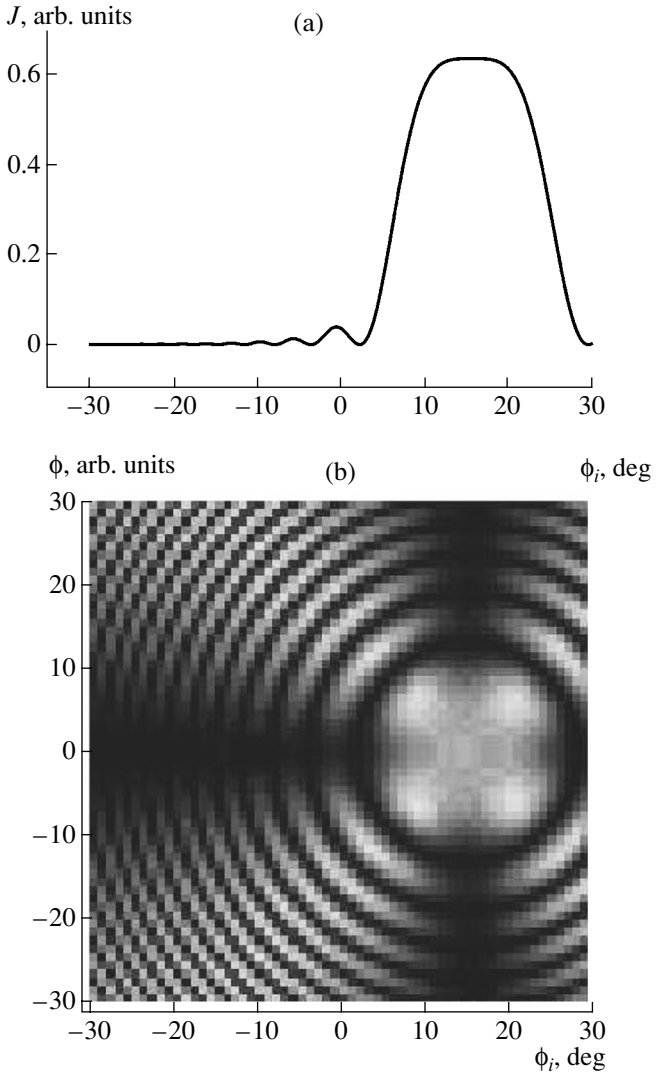

Fig. 4. (a) Dependence of the intensity J of the transmitted light on the angle of rotation ϕ_i of a 3-mm-thick plate cut from a quartz crystal at an angle ($\theta = 10°$) to the optic axis and (b) the conoscopic figure of this plate. Optical parameters: $\lambda = 0.6328$ μm, $n_o = 1.54263$, $n_e = 1.55169$, $g_{11} = 5.39 \times 10^{-5}$, and $g_{33} = -10.528 \times 10^{-5}$.

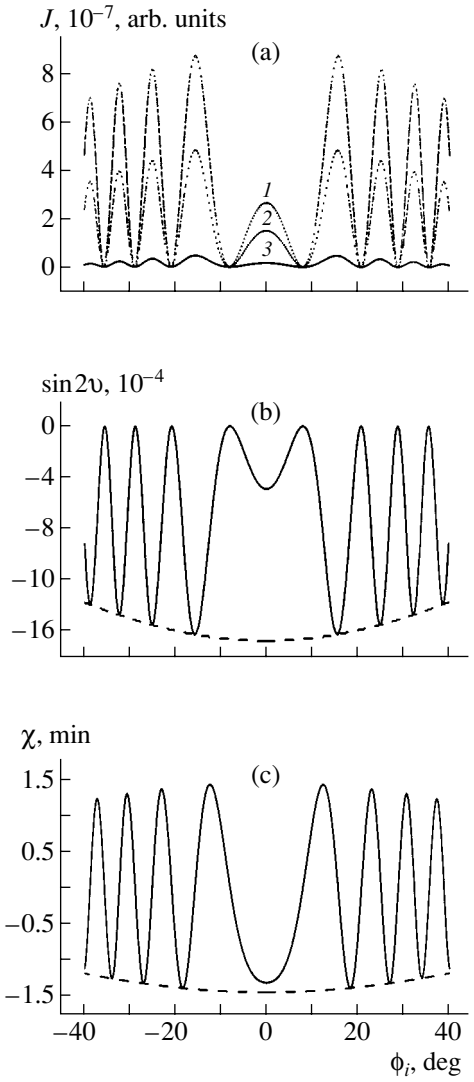

Fig. 5. Dependences of (a) the intensity J, (b) sin2υ, and (c) the azimuth χ of the transmitted light on the angle of rotation ϕ_i of a 0.35-mm-thick plate cut out parallel to the optic axis of a paratellurite crystal. (a) $g_{11} = (1)\ 4 \times 10^{-4}$, $(2)\ 3 \times 10^{-4}$, and $(3)\ 10^{-4}$. Dashed lines indicate the dependences (b) $\sin 4\gamma(\phi_i)$ and (c) $\sin 2\gamma(\phi_i)$.

the plate cut out parallel to the optic axis can be rotated with respect to the optic axis. In this case, the light beam is perpendicular to the optic axis at any rotations of the plate.

If the plate is cut out normally to the optic axis, the component g_{33} of the gyration pseudotensor predominantly affects the intensity and the polarization parameters of the transmitted light. By contrast, if the plate is cut out parallel to the optic axis, the component g_{11} of the gyration pseudotensor has a dominant effect. Figure 5a shows the dependences of the intensity of the transmitted light that are calculated at different components g_{11}.

For a plate orientation parallel to the optic axis, all the parameters $J(\phi_i)$, $\sin 2\upsilon(\phi_i)$, and $\tan 2\chi(\phi_i)$, as a rule, are small, because they are proportional to the ellipticity of eigenwaves. In this situation, we have $k = g_{11}/(2n_s\Delta n_{el})$. However, if there exists the so-called isotropic birefringence point when the refractive indices coincide at a particular light wavelength, the ellipticity of eigenwaves becomes equal to unity and the crystal exhibits an isotropic behavior.

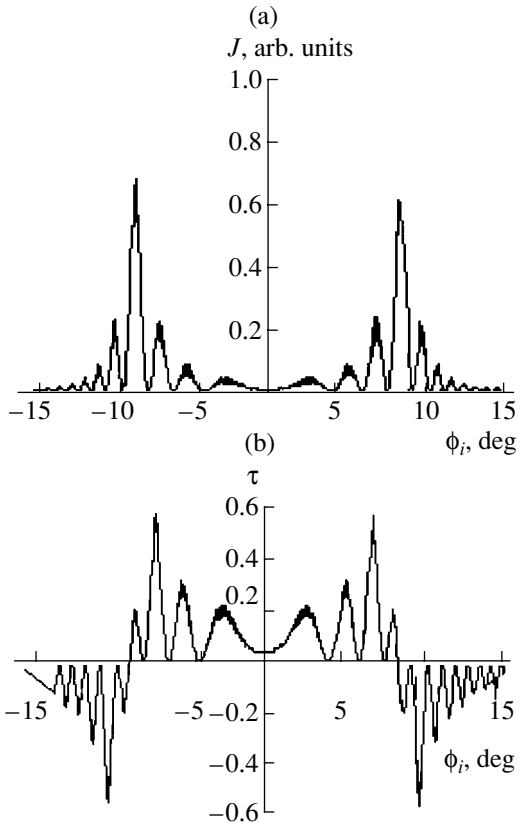

Fig. 6. Dependences of (a) the intensity J and (b) the ellipticity τ of the transmitted light on the angle of rotation ϕ_i of a plate cut out normally to the acute bisectrix of the angle between the optic axes of an biaxial optically active crystal. Optical parameters: $n_{01} = 1.6$, $n_{02} = 1.6004$, $n_{03} = 1.65$, $g_{11} = 4.706 \times 10^{-5}$, $g_{22} = 5.818 \times 10^{-5}$, $g_{33} = -11.705 \times 10^{-5}$, $V = 5.25°$, and $d = 6$ mm.

BIAXIAL OPTICALLY ACTIVE CRYSTALS

As was noted above, relationships (4)–(6) also hold for biaxial crystals. In this respect, we examine crystals belonging to the orthorhombic crystal system when the plate that is cut normally to the acute bisectrix of the angle formed by the optic axes is located between the crossed polarizer and analyzer.

If the principal plane of the plate coincides with the direction of transmission of the polarizer ($\alpha = 0°, 90°$), the regularity characteristic of uniaxial crystals for directions close to the optic axis should be valid for each optic axis of the biaxial crystal. The dependences of the intensity and the ellipticity of the transmitted light on the angle of rotation of the biaxial-crystal plate are depicted in Fig. 6. It is obvious that the birefringence and the scalar parameter of gyration should be correctly included in the calculation. In crystals of this crystal system, the rotation of the polarization plane along the optic axes is identical and, hence, the intensities of the transmitted light along the optic axes are equal to each other. For calculations, the optical parameters of the crystal are chosen so that the angle $2V$ between the optic axes is small and the main regularities manifest themselves. For directions considerably deviating from the optic axis, the main regularities of the characteristics of the transmitted light should be similar to those for the uniaxial crystal with allowance made for the refractive indices and the scalar parameter of gyration for these directions. It should be emphasized once again that the intensity, ellipticity, and azimuth of the transmitted light are proportional to the ellipticity of eigenwaves for optically active crystals and equal to zero for inactive crystals.

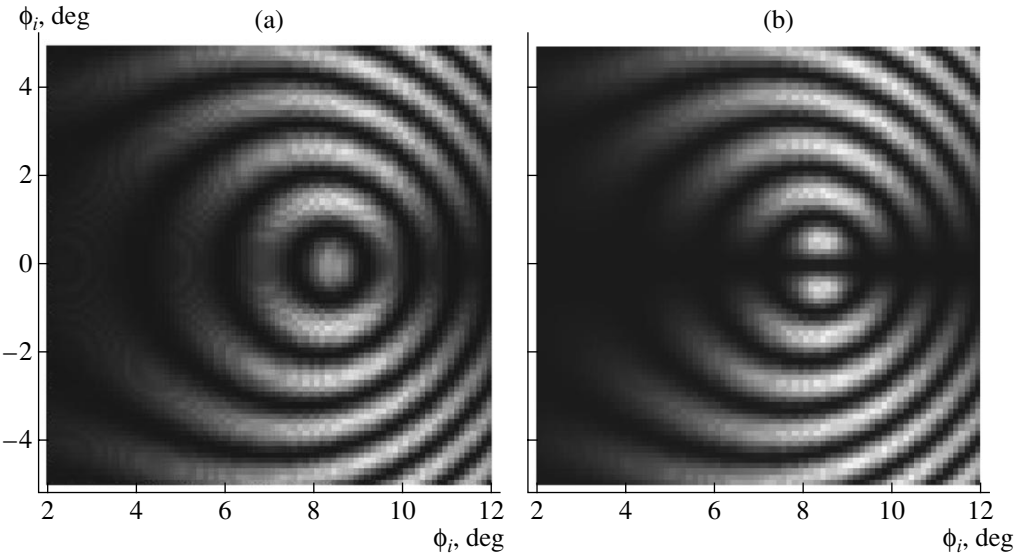

Fig. 7. Enlarged fragments of the conoscopic figures in the region of one of the optic axes of biaxial optically (a) active and (b) inactive crystals. The optical parameters are the same as in Fig. 6 ($g_{jj} = 0$ for an inactive crystal).

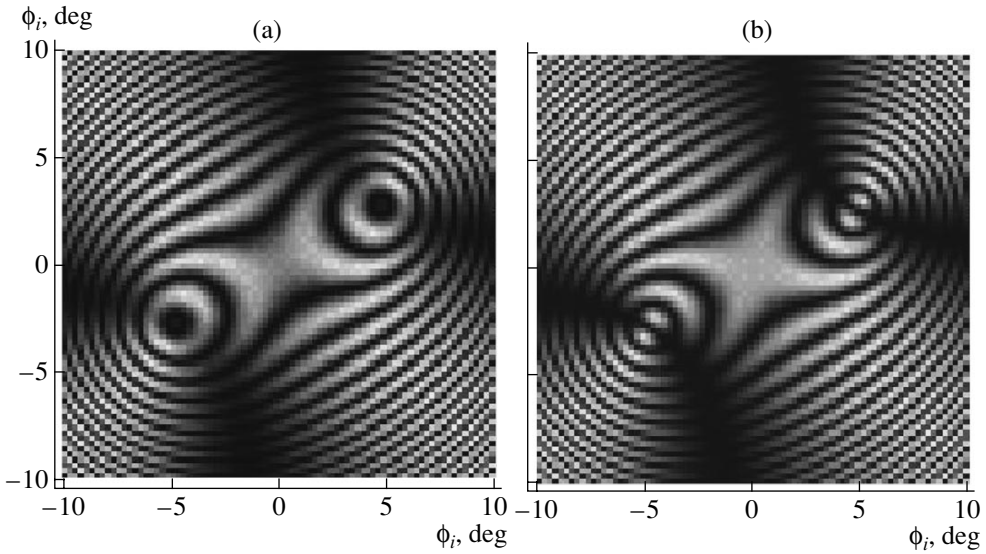

Fig. 8. Conoscopic figures of biaxial optically (a) active and (b) inactive crystals. The plate is rotated through an angle of 30° about the normal to the crossed polarizer and analyzer. Optical parameters of crystals: $n_{01} = 1.5$, $n_{02} = 1.5002$, $n_{03} = 1.55$, $g_{11} = 4.706 \times 10^{-5}$, $g_{22} = 5.818 \times 10^{-5}$, $g_{33} = -11.705 \times 10^{-5}$, $V = 3.71°$, and $d = 8$ mm ($g_{jj} = 0$ for an inactive crystal).

As in the case of uniaxial crystals, the conoscopic figures for biaxial crystals can be described by relationship (12). It can be seen from Figs. 7a and 7b that the difference between the active and inactive crystals is especially pronounced along the optic axis. For an optically active crystal, the light intensity at the center of the conoscopic figure differs from zero, because the crystal rotates the polarization plane in this direction. Similar differences are clearly seen in the case when the plate is rotated through a certain angle between the crossed polarizer and analyzer (Fig. 8).

In the crystals belonging to monoclinic or triclinic systems, the rotation of the polarization plane along the optic axes occurs variously and can even be opposite in sign, for example, in the case of sugar ($\rho_1 = 22°$ and $\rho_2 = -6.4°$). Consequently, the dependences of the intensity, ellipticity, and azimuth for a plate cut out normally to the acute bisectrix of the angle between the optic axes of this crystal, unlike an orthorhombic crystal, appear to be asymmetric in shape and there exist a number of variants depending on the optical parameters of the crystal.

CONCLUSIONS

Thus, we analyzed the relationships for the ellipticity and azimuth of the light transmitted through a polarizer and an optically active absorbing plate upon its inclination.

The expressions determining the intensity of the light transmitted through the polarizer–plate–analyzer system as a function of the angle of inclination of the plate were considered. It was demonstrated that, in the case when the plate is oriented along its own principal axes, the intensity of the transmitted light for the crossed polarizer and analyzer is related to the optical activity and is proportional to the ellipticity of the eigenwaves. A technique was proposed for determining the parameters of the optical activity from experimental data on the intensity of the transmitted light upon inclination of the plate. The conoscopic figures of uniaxial and biaxial optically active crystals were described, and the difference between the optically active and inactive crystals was established with the use of the formulas for the intensity of the transmitted light.

ACKNOWLEDGMENTS

This work was supported by the Russian Foundation for Basic Research, project no. 03-02-16871.

REFERENCES

1. J. R. L. Moxon and A. R. Renshaw, J. Phys.: Condens. Matter **2**, 6807 (1990).
2. A. F. Konstantinova, B. N. Grechushnikov, B. V. Bokut', and E. G. Valyashko, *Optical Properties of Crystals* (Nauka i Tekhnika, Minsk, 1995).
3. I. Bodnar, in *Proceedings of Bianisotropics'98, Braunschweig, Germany* (1998), p. 61.
4. I. Bodnar and M. P. Anatska, in *Proceedings of Bianisotropics 2000, Lisbon, Portugal* (2000), p. 84.
5. K. A. Rudoy and V. I. Stroganov, *Nonlinear Properties of Optical Media*, Ed. by V. I. Stroganov (DVGUPS, Khabarovsk, 2001), p. 49.
6. K. A. Rudoy, O. Yu. Pikul', and V. I. Stroganov, *Optical Properties of Condensed Matter*, Ed. by V. I. Stroganov (DVGUPS, Khabarovsk, 2002), p. 48.

7. V. P. Buzylov, O. G. Vlokh, V. K. Zaĭtsev, *et al.*, USSR Inventor's Certificate No. 366,809 (October 28, 1972).

8. M. Born and E. Wolf, *Principles of Optics: Electromagnetic Theory of Propagation, Interference, and Diffraction of Light*, 2nd ed. (Pergamon Press, Oxford, 1964; Nauka, Moscow, 1970).

9. J. F. Nye, *Physical Properties of Crystals: Their Representation by Tensors and Matrices* (Clarendon Press, Oxford, 1957; Inostrannaya Literatura, Moscow, 1960).

10. A. F. Konstantinova, B. V. Nabatov, E. A. Evdishchenko, and K. K. Konstantinov, Kristallografiya **47** (5), 879 (2002) [Crystallogr. Rep. **47**, 815 (2002)].

11. W. A. Shurcliff, *Polarized Light: Production and Use* (Harvard Univ. Press, Cambridge, Mass., 1962; Mir, Moscow, 1965).

12. A. W. Warner, D. L. White, and W. A. Bonner, J. Appl. Phys. **43** (11), 4489 (1972).

13. K. A. Rudoĭ, B. V. Nabatov, V. I. Stroganov, *et al.*, Kristallografiya **48** (2), 359 (2003) [Crystallogr. Rep. **48**, 300 (2003)].

14. A. F. Konstantinova, K. K. Konstantinov, B. V. Nabatov, and E. A. Evdishchenko, Kristallografiya **47** (4), 702 (2002) [Crystallogr. Rep. **47**, 645 (2002)].

Translated by O. Borovik-Romanova

Crystallography Reports, Vol. 48, No. 5, 2003, pp. 832–835. Translated from Kristallografiya, Vol. 48, No. 5, 2003, pp. 893–896.

PHYSICAL PROPERTIES OF CRYSTALS

Dedicated to the 60th Anniversary of the Shubnikov Institute of Crystallography of the Russian Academy of Sciences

Composite Phase Plates with Elements of Different Thickness

V. S. Chudakov

Shubnikov Institute of Crystallography, Russian Academy of Sciences, Leninskiĭ pr. 59, Moscow, 119333 Russia

Received May 3, 2003

Abstract—A calculation method is proposed for composite phase plates consisting of two elements of different thickness. These crystal-optics elements make it possible to vary the type of polarization of radiation. For the known values of the phase shifts produced by the elements, the required type of polarization is attained by specific orientation of the fast axes of both elements with respect to the direction of maximum transmission of the polarizer. The azimuthal angles of the fast axes of these elements are set according to the formulas listed below.

Polarized radiation, especially in the infrared range, is effectively used in the defectoscopy of insulating and semiconductor crystals belonging to the cubic system. Polarization optical methods make it possible to study a number of widespread phenomena related to defects: the optical anisotropy induced by internal stresses, local deviations from stoichiometry, weak optical absorption, induced optical polarizability, and so on. Phase plates of different kinds must be used in these methods to change the type of polarization of radiation used.

Composite phase plates (CPPs), especially those made of mica, are most popular and efficient in practice. The advantages of a CPP consisting of two identical inactive birefringent plates were discussed in detail in [1]. Such a CPP can be used both as a half-wave and a quarter-wave phase plate, as well as a compensator.

However, experience in operating such devices has shown that CPPs with elements that produce significantly different phase shifts are much more efficient in some cases. For example, the phase difference introduced by the input (with respect to the incident light) plate may exceed many times that introduced by the output plate. The latter provides a precise tuning of a CPP with respect to the required parameter.

In order to implement a CPP as a specific phase plate, it is necessary to know the phase shifts for the elements at the chosen wavelength and the orientation of the fast axes of both elements with respect to the direction of maximum transmission of the polarizer. The phase shift can be determined by different methods using a polariscope or, as in the case of mica, by calculations based on the reference data on the birefringence [2] and the measured thickness of the plate. The potentialities of polariscopic techniques depend in many respects on the required spectral range. In the visible range, it is possible to apply the method described in [1]. The same method can also be used in the near-infrared range if a polariscope is equipped with an electron-optical or some other image converter. A photoelectric polariscope with a rotating analyzer [3] allows one, with the use of a phase detector, to determine more easily the desired value of the phase shift δ_1 for the plate studied directly in the chosen spectral range. There are two possible ways of doing this:

$$\delta_1 = \arccos U_{\min}/U_{\max} + \pi n, \tag{1}$$

$$\delta_1 = \delta_c[(\arccos U_{\Sigma+} + \arccos U_{\Sigma-})/(\arccos U_{\Sigma+} - \arccos U_{\Sigma-})] + 2\pi n, \tag{2}$$

where $U_{\min}$ and $U_{\max}$ are the magnitudes of signals (with regard to their sign) for the diagonal (at an angle of 45°) and parallel orientations of the fast axis of the plate with respect to the direction of maximum transmission of the polarizer. In variant (2), a calibrated plate with a small phase shift δ_c is used in addition. First of all, the plate with unknown δ_1 is set diagonally with respect to the direction of maximum transmission of the polarizer. Then, for two orientations of the calibrated plate (with its fast axis either parallel or perpendicular to the fast axis of the plate under study), we measure the signals $U_{\Sigma+}$ and $U_{\Sigma-}$. Hereinafter, we use only the absolute value of δ_1. Therefore, it is sufficient to determine the values of the maximum and minimum signals during the rotation of the calibrated plate. If $\delta_1 > \pi$, the order of interference n should be refined.

1063-7745/03/4805-0832$24.00 © 2003 MAIK "Nauka/Interperiodica"

When it is possible to measure the phase shifts of the plates at two wavelengths (λ_1 and λ_2) that differ from each other by no more than 30%, the value of n can be determined from the relations

$$n = |\arccos(U_{1\min}/U_{1\max}) - m\arccos(U_{2\min}/U_{2\max})/\pi(m-1), \quad (3)$$

$$n = |\arccos(U_{1\min}/U_{1\max}) - m\arccos(U_{2\min}/U_{2\max})/\pi(m-1), \quad (4)$$

where $m = \lambda_2/\lambda_1 > 1$. If the result is correct, n is an integer or only slightly differs from it. This difference may be caused by the measurement error for $U_{\min}$ and $U_{\max}$, as well as by the dispersion of the birefringence within the spectral range λ_2–λ_1.

If the phase shifts produced by both elements of the CPP for the radiation chosen are known, in order to obtain a desired transformation of polarized light, one should also know the azimuthal angles for the fast axes of these elements with respect to the direction of maximum transmission of the polarizer. As an example, Fig. 1 shows a graphical solution to the problem concerning the transformation of the linear polarization of radiation into the circular polarization. The different projections of the Poincaré sphere and the methods of analytical geometry are used to find this solution.

The input (with respect to the linearly polarized radiation) plate characterized by the phase shift δ_1 is set in such a way that its fast axis fa_1 is set at the angle α_1 with respect to the direction of maximum transmission of the polarizer. At the sphere, such angles are mapped to doubled angles $2\alpha_1$. Due to the effect of the input plate, the linear polarization of the radiation is changed into elliptical polarization. The parameters of the latter can be determined by the coordinates of the point *B*. The transformation of the linear polarization into elliptical polarization is shown by the arc L_1 and its projection onto the equatorial plane of the sphere in the form of the segment *AB*. The fast axis fa_1 is perpendicular to this segment.

The output plate, which is characterized by the parameters δ_2 and α_2, changes the elliptical polarization of radiation into circular polarization. The fast axis fa_2 of the output plate is perpendicular to the segment *BZ*, which is the projection of the arc L_2. The point *Z* is the pole of the sphere. The polar axis itself is perpendicular to the plane of the figure. The plots presented allow us to determine numerically the azimuths α_1 and α_2. For simplicity, we assume the sphere radius to be equal to unity. For the length of segment *AB*, we have $AB = (1 - \cos\delta_1)\cos 2\beta$. This relation is the equation of a circle in the polar coordinates. The center of the circle lies at the polar axis, and its radius ρ_1 and the coordinate x_1 (the distance from the point *Z*) are determined from the equations

$$\rho_1 = (1 - \cos\delta_1)/2, \quad x_1 = (1 + \cos\delta_1)/2. \quad (5)$$

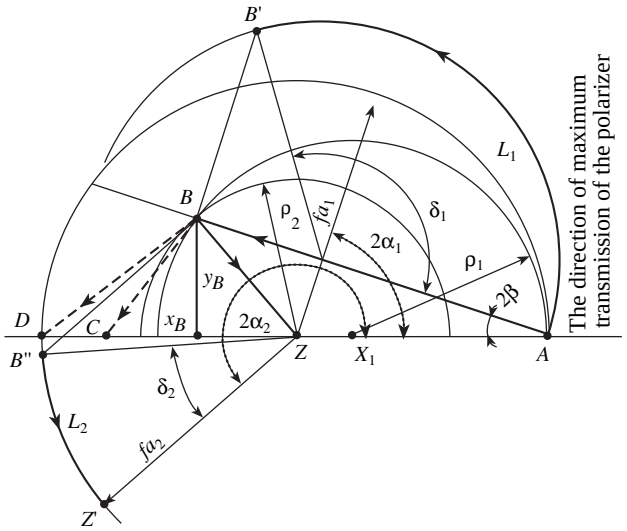

Fig. 1. Graphical solution to the problem of finding the parameters of composite phase plates consisting of elements with different thicknesses obtained with the use of the Poincaré sphere and the methods of analytical geometry. L_1 and L_2 are the arcs corresponding to the transformation of linear polarization of radiation into elliptical polarization and that of elliptical polarization into circular polarization in the 90° CPP for the input and output plates, respectively. δ_1 and δ_2 are the phase shifts, *AB* and *BZ* are the projections of L_1 and L_2 on the equatorial plane of the sphere, α_1 and α_2 are the azimuthal angles for the fast axes fa_1 and fa_2 of the plates, *BD* and *BC* are the projections of the arcs corresponding to the transformation of elliptical polarization into 90°-linear polarization and that of elliptical polarization into 90°-elliptical polarization, and ρ_1 and ρ_2 are the radii of auxiliary circles used for determining the Cartesian coordinates of the point *B*.

The parameters of the second circle, which describe the changes in the length of segment *BZ* with varying azimuthal angle of the fast axis fa_2 are determined by the fact that the center of the second circle x_a coincides with the point *Z*. Thus, we have

$$\rho_2 = \sin\delta_2, \quad x_2 = 0. \quad (6)$$

The point *B* coincides with the point of intersection of the circles. Its Cartesian coordinates in the equatorial plane of the sphere can be determined by solving the system of equations

$$(x_B - x_1)^2 + y_B^2 = \rho_1^2, \quad (x_B - x_2)^2 + y_B^2 = \rho_2^2. \quad (7)$$

The coordinates x_B and y_B allow us to find the values of the sought azimuthal angles of the fast axes fa_1 and fa_2:

$$\alpha_1 = 45° - 0.5\arctan[y_B/(1 - x_B)], \quad \alpha_2 = 45° + 0.5\arctan(y_B/x_B). \quad (8)$$

The last condition to be met for the correct choice of a CPP with plates of different thickness, which should

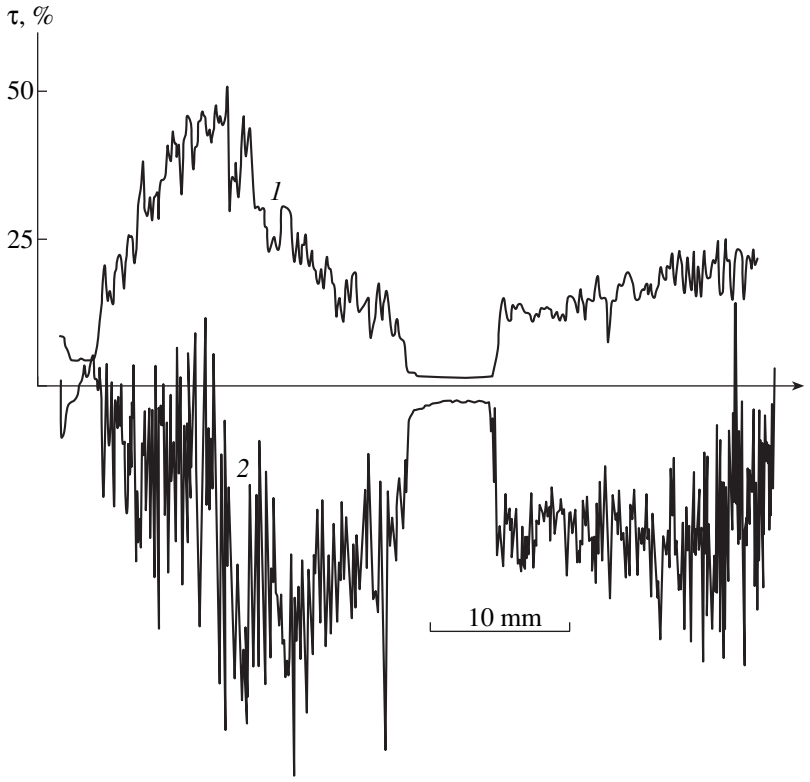

Fig. 2. Optical inhomogeneity of single-crystal cadmium telluride. Curve *1* illustrates the local distribution of integrated optical transmission within the 0.85–1.25 μm wavelength range. Curve *2* demonstrates the optical inhomogeneity revealed by the spectral modulator using a CPP with a large phase shift produced by the input plate.

serve as a quarter-wave phase plate, is as follows:

$$[1 - \cos(\delta_1 + \delta_2)] \geq 1 \geq [1 - \cos(\delta_1 - \delta_2)]. \quad (9)$$

Half-wave phase plates are used to rotate the plane of polarization. Their phase shift is equal to 180°. Similar to CPPs with a 90° phase shift, the angle between the fast axes of the input and output plates in a 180° CPP is set depending on the chosen values of the phase shifts δ_1 and δ_2. We shall demonstrate how to find this angle corresponding to the rotation of the plane of polarization by 90° using the 180° CPP as an example. For simplicity, we show in Fig. 1 the same input plate as that used for 90° CPPs. The output plate (the projection *BD*) differs from those used in 90° CPPs both in value of the phase shift and in the azimuthal angle of the fast axis fa_2. When the angle α_2 is varied, the length of the segment *BD* varies similarly to that of the projection *AB*. Therefore, the parameters of the second circle, which is not shown in Fig. 1, have the form

$$\begin{aligned} \rho_2 &= (1 - \cos\delta_2)/2, \\ x_2 &= -(1 + \cos\delta_2)/2. \end{aligned} \quad (10)$$

Similar to the calculations of the 90° CPP, we determine α_1 and α_2 using the values of ρ_1, x_1, ρ_2, and x_2. The sought angle between the fast axes fa_1 and fa_2 is equal to $(\alpha_1 - \alpha_2)$. Note one substantial drawback of the 180° CPP. In contrast to the single-element 180° plates, 180° CPPs are unsuitable for the modulation of polarized light by continuous rotation of the single-element 180° plate when the analyzer is at rest. It is possible to construct a half-wave CPP if the following conditions are met:

$$(\delta_1 + \delta_2) \geq 180° \geq (\delta_1 - \delta_2). \quad (11)$$

A CPP with elements of different thickness can also be used to convert linear polarization of radiation to elliptical polarization with the specified parameters. A solution to this, more complicated, problem is of special interest because such a solution is universal and allows us also to determine the parameters of elements both for 90° and 180° CPPs. To simplify Fig. 1, let us consider the variant where a known input plate is supplemented by an output plate with the projection mapped by the segment *BC*.

Let us specify the ellipticity of the output light by the value of the phase shift Δ by which this CPP differs from 180° CPPs. The effective fast axis of the CPP is directed at an angle of 45° with respect to the direction of maximum transmission of the polarizer. The parameters ρ_1 and x_1 for the CPP converting linear polarization of light to elliptical are determined in the same way as for 90° and 180° CPPs. At the same time, the param-

eters ρ_2 and x_2 are calculated in a more complicated manner:

$$\rho_2 = \sin\Delta\sin\delta_2 + \cos\Delta[1 - \cos(\Delta + \delta_2)]/2,$$
$$x_2 = -\cos\Delta[1 + \cos(\Delta + \delta_2)]/2. \quad (12)$$

The azimutal angle for the fast axis of the output plate is also calculated in a different way:

$$\alpha_2 = 45° + 0.5\arctan[y_B/(x_B + \cos\Delta)]. \quad (13)$$

Thus, the parameters ρ_2, x_2, and α_2 for 90° and 180° CPPs are determined using (12) and (13) provided that $\Delta = 90°$ and $\Delta = 0°$, respectively.

As mentioned above, in order to enhance the sensitivity and accuracy of some methods for the study of structural defects in crystals, the optical path difference created by the input plate should far exceed that created by the output plate. For example, it was ascertained that such CPPs significantly increase the efficiency of the method in which a spectrum modulator is used to visualize the local spectral inhomogeneity of the objects under study [4].

In this method, a scanning photoelectric device is equipped by a polarizing unit that includes a polarizer, a CPP, and a rotating analyzer. This unit is installed either before or after the object under study. The recorded modulated signal from the photodetector is proportional to the integral characteristic:

$$U \approx \int_{\nu_1}^{\nu_2} \tau(\nu) I(\nu) \cos\delta(\nu) d\nu, \quad (14)$$

where ν_1 and ν_2 are the frequencies corresponding to the edges of the operating spectral range; $\tau(\nu)$ is the distribution of the transmission within the spectral range; $I(\nu)$ is the spectral sensitivity of the instrument with regard to the contributions of all its elements, including the polarization unit; and $\delta(\nu)$ is the variation in the phase shift as a function of ν. As an example of efficient application of a CPP with a very large phase shift produced by the input plate, Fig. 2 shows the results of studying single-crystal cadmium telluride. Curve *2* demonstrates the local deviations from stoichiometry in the crystal under investigation. The crystal was studied using an FPD-1 photoelectric polariscope for defectoscopy. Curve *2* was recorded in a wide spectral range: 0.85–1.25 μm. The composite phase plate consisted of two mica plates, 265 and 17 μm thick. It served as a quarter-wave plate tuned to a wavelength of 1.05 μm. At this wavelength, the phase shifts produced by the input and output plates were equal to 454° and 29°, respectively. The calculations show that the sensitivity will be reduced by more than a factor of 4 if we use a single-element 90° plate instead of the CPP. To compare the results of the study of the spectral inhomogeneity of the crystal with the distribution of the integrated optical transmission $\tau = \int_{\nu_1}^{\nu_2} \tau(\nu) d\nu$, we present curve *1*. It is clear that curve *1* is not a direct mapping of curve *2*.

In conclusion, we should note that the method developed for designing composite phase plates makes it possible to calculate in a simplified form with high accuracy the parameters of such plates independent of the relation between the phase shifts produced by their elements.

REFERENCES

1. B. N. Grechushnikov, A. I. Vislobokov, E. A. Evdishchenko, *et al.*, Kristallografiya **38** (2), 55 (1993) [Crystallogr. Rep. **38**, 164 (1993)].
2. E. M. Voronkova, B. N. Grechushnikov, G. I. Distler, and I. P. Petrov, *Optical Materials for Infrared Technology* (Nauka, Moscow, 1965).
3. V. S. Chudakov, Prib. Tekh. Éksp., No. 5, 210 (1977).
4. V. S. Chudakov and B. N. Grechushnikov, Opt. Mekh. Prom., No. 7, 49 (1977).

Translated by K. Kugel

Crystallography Reports, Vol. 48, No. 5, 2003, pp. 836–850. Translated from Kristallografiya, Vol. 48, No. 5, 2003, pp. 897–911.

SURFACE, THIN FILMS: REVIEWS

Dedicated to the 60th Anniversary of the Shubnikov Institute of Crystallography of the Russian Academy of Sciences

X-ray Investigations of Surface Roughnesses

V. E. Asadchikov, I. V. Kozhevnikov, and Yu. S. Krivonosov

Shubnikov Institute of Crystallography, Russian Academy of Sciences, Leninskiĭ pr. 59, Moscow, 119333 Russia

e-mail: asad@ns.crys.ras.ru

Received February 18, 2003

Abstract—The unique potentialities and prospects for practical use of the X-ray scattering method as applied to the study and testing of surface roughnesses are considered. The high sensitivity, informative capability, and reliability of this method are demonstrated by using numerous examples. The results obtained by the X-ray scattering method at different wavelengths are compared with the available data of atomic-force microscopy.

CONTENTS

1. INTRODUCTION

Surfaces and thin-film coatings of superhigh quality (with a roughness height of less than 1 nm) are required in many fields of modern science, engineering, and technology. First and foremost, these are laser engineering, optics, X-ray optics, high-precision machine engineering, and microelectronics. At present, surface treatment and coating deposition techniques that, in principle, make it possible to produce perfect surfaces have been devised and introduced extensively. However, the problem regarding reliable quantitative characterization of these surfaces is still far from resolved, particularly in the case of thin-film and multilayer coatings and surfaces of complex shape.

Methods of testing individual surfaces have been well developed to date and can be subdivided into the following four groups: mechanical, optical, tunneling and atomic-force, and X-ray methods. These methods are based on different physical principles and complement each other. Certainly, each of them has its own advantages and disadvantages.

For example, the disadvantage of mechanical profilometers is that a measuring probe (diamond needle) is in contact with the surface and, hence, damages it to some extent. Moreover, the measurement procedure takes a good deal of time, especially in the case when it is necessary to examine the surface over the entire area.

The most widely used optical methods involve a large number of quite different approaches. Among these are different modifications of interference techniques, optical profilometry, and methods based on the measurement of radiation scattering in the visible region. Many of these methods are not quantitative, because they require the use of reference samples. The principal disadvantage of all optical methods is that the minimum longitudinal (along the surface) size of detectable roughnesses is limited in order of magnitude by the wavelength of probe radiation; i.e., it cannot be less than 0.5 μm.

Tunneling and atomic-force microscopies have the highest sensitivity and accuracy and provide a means for observing the atomic structure of the surface. However, the field of vision (the studied sample area) in this case is no more than several units or tens of microns, which is unsuitable for solving many applied problems. Moreover, samples should be small in size and weight.

The limited capabilities of all the profilometric and optical methods most clearly manifest themselves in the study of hidden interfaces, such as the boundary between a substrate and a nontransparent (e.g., metal) film deposited on this substrate.

1063-7745/03/4805-0836$24.00

In our opinion, the application of methods based on analysis of the X-ray scattering indicatrix opens up new possibilities of testing surface and interface roughnesses. The small radiation wavelength and the possibility of changing the depth of radiation penetration into a material from several nanometers (under the conditions of total external reflection) to several tens of micrometers render X-ray radiation indispensable in investigating surface and volume nanoinhomogeneities, including roughnesses of hidden interfaces.

The purpose of this work was to demonstrate the unique potentialities of the X-ray methods for studying the roughness, their high informative capability and reliability, and prospects for use as a metrological basis for further development of modern technologies of processing supersmooth surfaces. This is an important problem of modern optics, X-ray optics, and microelectronics.

This paper presents a review of our investigations. For the most part, the experiments were performed on an X-ray diffractometer designed at the Shubnikov Institute of Crystallography, Russian Academy of Sciences. A number of experimental data were obtained at the European Synchrotron Radiation Facility (ESRF, Grenoble, France) in collaboration with C. Morawe, E. Ziegler, and T. Metzger. Moreover, we carried out a comparative analysis of the data obtained on the surface roughness with the use atomic-force microscopy and soft X-ray, hard X-ray, and UV scattering. These experiments were performed in collaboration with V.I. Ostashev and A. Duparré.

2. MODEL OF THE SURFACE AND THEORETICAL PRINCIPLES OF THE METHOD

It should be emphasized that, unlike profilometric techniques, the X-ray scattering method is indirect and strongly depends on the used theory of interaction of short-wavelength electromagnetic radiation with a rough surface and the particular model of a material–vacuum interface. Therefore, the problem associated with the choice of an adequate theoretical approximation and a realistic model of the surface is of special importance in developing practical methods for examining the roughness with the use of the X-ray scattering. In this case, the theory should describe all the experimentally observed features of X-ray scattering, on the one hand, and be simple enough to determine uniquely the roughness parameters, on the other.

Within the simplest model of the rough surface, it is assumed that the vacuum–material interface is described by the two-dimensional function $z = \zeta(\boldsymbol{\rho})$ and the permittivity at the interface jumpwise changes from unity to its value ε_+ in the bulk of the material, that is,

$$\varepsilon_0(\mathbf{r}) = 1 + (\varepsilon_+ - 1)\theta[z - \zeta(\boldsymbol{\rho})]. \quad (1)$$

Here, $\theta(z)$ is the Heaviside step function $\theta(z > 0) = 1$ and $\theta(z < 0) = 0$ and the vector $\boldsymbol{\rho} \equiv (x, y)$ lies in the plane of the ideally smooth interface.

In this work, the rough surface will be analyzed in terms of model (1), which, despite its simplicity, allows us to describe almost all the experimentally observed features of X-ray scattering. A more complex model of the surface with due regard for volume inhomogeneities of the electron density in a surface layer of the material will be considered in the separate paper [1], which is a continuation of the present work.

For the most part, the modern approaches to investigation of the surface roughness are based on the probability theory. In this case, the rough surface profile $\zeta(\boldsymbol{\rho})$ is treated as the realization of a random process that can be described using particular statistical characteristics. As a rule, the description of properties of the rough surface is restricted to consideration of the correlation function $C(\boldsymbol{\rho})$ or, what is the same, the two-dimensional power spectral density $\mathrm{PSD}_{2D}(\mathbf{q})$ of the surface roughness, that is,

$$\begin{aligned} C(\boldsymbol{\rho}) &= \langle \zeta(\boldsymbol{\rho} + \boldsymbol{\rho}')\zeta(\boldsymbol{\rho}')\rangle; \\ \mathrm{PSD}_{2D}(\boldsymbol{\nu}) &= \int C(\boldsymbol{\rho}) e^{2\pi i \boldsymbol{\nu}\boldsymbol{\rho}} d^2\boldsymbol{\rho}, \end{aligned} \quad (2)$$

where the angle brackets indicate averaging over realizations. In particular, $\sigma \equiv \sqrt{C(0)} \equiv \sqrt{\langle \zeta^2(0)\rangle}$ is the root-mean-square roughness height.

The surface relief can be represented in the form of the Fourier integral with random amplitudes of spatial harmonics

$$\zeta(\boldsymbol{\nu}) = \int \zeta(\boldsymbol{\rho}) e^{2\pi i \boldsymbol{\nu}\boldsymbol{\rho}} d^2\boldsymbol{\rho}. \quad (3)$$

As a result, from formulas (2), we found that the PSD function and the roughness spectrum of the homogeneous surface are related by the expression

$$\langle \zeta(\boldsymbol{\nu})\zeta^*(\boldsymbol{\nu}')\rangle = \mathrm{PSD}_{2D}(\boldsymbol{\nu})\delta(\boldsymbol{\nu} - \boldsymbol{\nu}'). \quad (4)$$

Expression (4) clearly demonstrates the physical meaning of the PSD function. Actually, since expansion (3) represents the rough surface relief in the form of a set of two-dimensional diffraction gratings with the periods $d_x = 1/\nu_x$ and $d_y = 1/\nu_y$ (along the x and y axes, respectively), the PSD function characterizes the root-mean-square amplitude of these gratings. The characteristic range of a variation in the function $C(\boldsymbol{\rho})$ is referred to as the correlation length of roughness heights.

Our experimental techniques are theoretically based on the approach according to which the amplitude of wave scattering by the rough surface is expanded in terms of the roughness height $\zeta(\boldsymbol{\rho})$. In actual fact, the principles of such an approach were developed by Andronov and Leontovich [2]. At present, this approach is widely used in analysis of the visible radiation scattering [3]. The applicability of the perturbation theory to analysis of X-ray scattering with allow-

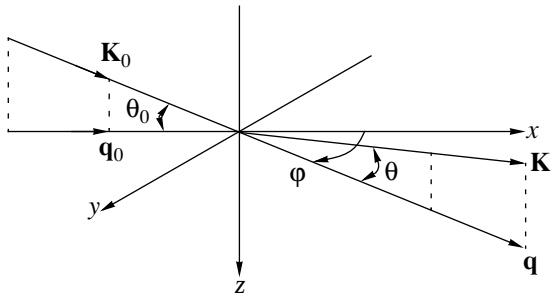

Fig. 1. Schematic representation of the interaction of an X-ray wave with a rough interface. $\mathbf{K}_0$ and $\mathbf{K}$ are the wave vectors of incident and scattered radiation, respectively; $\mathbf{q}_0$ and $\mathbf{q}$ are the projections of these vectors onto the *XY* plane; θ_0 is the grazing angle of the probe beam; and θ and φ are the scattering angles.

ance made for the specific features of this wavelength range was justified in [4–7].

For the rough surface with the stepwise change in the permittivity [formula (1)], the relationship for the scattering indicatrix in the first nonvanishing order of the perturbation theory has the very simple form

$$\begin{aligned}\Phi(\theta, \varphi) &= \frac{1}{Q_0}\frac{dQ}{d\Omega} \\ &= \frac{k^4|1-\varepsilon_+|^2}{16\pi^2\sin\theta_0}|t(\theta_0)t(\theta)|^2\mathrm{PSD}_{2D}(\boldsymbol{\nu}),\end{aligned} \tag{5}$$

$$2\pi\boldsymbol{\nu} = \mathbf{q} - \mathbf{q}_0 = k\{\cos\theta\cos\varphi - \cos\theta_0;\ \cos\theta\sin\varphi\}, \tag{6}$$
$$k = 2\pi/\lambda.$$

Here (see Fig. 1), θ_0 is the grazing angle of a probe beam, θ and φ are the scattering angles, $\mathbf{q}_0$ and $\mathbf{q}$ are the projections of the wave vectors of the incident and scattered radiations onto the *XY* plane, Q_0 is the power of incident radiation, dQ is the power of the radiation scattered into the solid angle $d\Omega$, and $t(\theta)$ is the field amplitude of the unperturbed wave on the ideally smooth surface (amplitude transmission coefficient)

$$t(\theta) = \frac{2\sin\theta}{\sin\theta + \sqrt{\varepsilon_+ - \cos^2\theta}}.$$

Equation (6) represents the usual condition for the diffraction of the X-ray wave by a two-dimensional diffraction grating and implies that, within the first order of the perturbation theory, the sole harmonic with the frequency $\boldsymbol{\nu}$ in the roughness spectrum (4) scatters the radiation along the direction $\mathbf{q}$ when the beam is incident along the direction $\mathbf{q}_0$ on the surface.

Note that, in the X-ray region, it is reasonable to analyze small grazing angles $\theta_0 \le \theta_c \ll 1$ at which the reflectivity is large in magnitude. In this situation, the indicatrix width $\Delta\theta$ in the scattering plane and the indicatrix width $\Delta\varphi$ in the perpendicular (azimuthal) plane are related by the expression

$$\Delta\varphi \approx \theta_0\Delta\theta \ll \Delta\theta.$$

Since the grazing angle θ_0 of the probe beam usually varies from 0.2° to 0.5° at the wavelength $\lambda = 0.154$ nm, the indicatrix width for the scattering angle φ appears to be 300–750 times smaller than that for the scattering angle θ. Therefore, the experimental determination of the scattering indicatrix $\Pi(\theta)$ integrated over the angle φ (i.e., over the direction perpendicular to the incidence plane) turns out to be simple in the X-ray region. The relationship derived in [6, 7] for the scattering indicatrix $\Pi(\theta)$ in the case of isotropic surfaces, which will be considered below, takes the form

$$\begin{aligned}\Pi(\theta) &= \frac{1}{Q_0}\frac{dQ}{d\theta} = \int\Phi(\theta, \varphi)d\varphi \\ &= \frac{k^3|1-\varepsilon_+|^2|t(\theta_0)t(\theta)|^2}{16\pi\sin\theta_0\sqrt{\cos\theta_0\cos\theta}}\mathrm{PSD}_{1D}(p),\end{aligned} \tag{7}$$

$$\mathrm{PSD}_{1D}(p) = 4\int_0^\infty C(\rho)\cos(2\pi p\rho)d\rho;$$

$$2\pi p = |q_0 - q| = k|\cos\theta - \cos\theta_0|,$$

where dQ is the power of the radiation scattered in the angle range $d\theta$.

It should be noted that the changeover from the differential indicatrix $\Phi(\theta, \varphi)$ to the indicatrix $\Pi(\theta)$ integrated over the angle φ is always valid in the X-ray region but can be incorrect for the visible radiation, because formula (7) was obtained within the approximation $ka \gg 1$, $ka\cos\theta \gg 1$, and $ka\cos\theta_0 \gg 1$ (where a is the correlation length of roughness heights). These inequalities hold for the X-ray region at small grazing angles but are not satisfied for the visible radiation, especially upon normal incidence.

Consequently, from the scattering indicatrix $\Phi(\theta, \varphi)$ or $\Pi(\theta)$ measured in the X-ray region, it is easy to calculate the spectral function $\mathrm{PSD}_{2D}(\nu)$ or $\mathrm{PSD}_{1D}(p)$, which is governed only by the statistical properties of the surface. The difference lies only in the fact that the scattering indicatrix $\Phi(\theta, \varphi)$ involves the two-dimensional PSD function determined by the two-dimensional Fourier transform of the correlation function, whereas the scattering indicatrix $\Pi(\theta)$ includes the one-dimensional PSD function, which is the cosine of the Fourier transform of the function $C(\rho)$. For the isotropic surfaces under consideration, these functions are

related by the following expressions:

$$\mathrm{PSD}_{2D}(\nu) = -\frac{1}{2\pi}\int_{\nu}^{\infty}\frac{d}{dp}(\mathrm{PSD}_{1D}(p))\frac{dp}{\sqrt{p^2-\nu^2}},$$
$$\mathrm{PSD}_{1D}(p) = 4\int_{p}^{\infty}\mathrm{PSD}_{2D}(\nu)\frac{\nu d\nu}{\sqrt{\nu^2-p^2}}. \quad (8)$$

Relationships (5) and (7) were derived in the scalar approximation. This is justified, because the grazing angle of the probe beam in practice is small and, as a rule, does not exceed the critical angle of the total external reflection. In this case, the effects associated with the polarization of the incident radiation are negligible. With an increase in the grazing angle, both the reflectivity and the intensity of scattered radiation rapidly become negligible in magnitude.

The conditions for the applicability of the perturbation theory were analyzed in detail by Kozhevnikov and Pyatakhin [8]. Let us make two assumptions (which, as will be shown below, represent the facts), namely, the PSD function can be described within the fractal model of the surface, i.e., decreases according to the inverse power law with an increase in the spatial frequency, and the probe beam is incident on the surface at the grazing angle θ_0 of the order of the critical angle θ_c of the total external reflection. Then, the condition for the applicability of the perturbation theory can be written in the form

$$k\sigma\theta_c \ll 1. \quad (9)$$

This means that the perturbation theory can be used to examine experimental data only for supersmooth surfaces when the roughness height σ does not exceed 1.0–1.5 nm. It is these surfaces that are of prime interest for optics, X-ray optics, and microelectronics.

The fundamental significance of the perturbation theory is primarily associated with the fact that it becomes absolutely exact (in the framework of the used model of the surface) with a decrease in the roughness height $\sigma \longrightarrow 0$. Therefore, any theory that lays claim to a greater generality should transform into the perturbation theory at $\sigma \longrightarrow 0$.

Furthermore, relationships (5) and (7) were obtained without any additional assumptions about either the scattered-wave field or the properties of the surface roughness. In particular, there is no need for the assumption regarding a normal distribution of their heights.

Finally, the formulas of the perturbation theory permit one to determine the PSD function of roughness directly from the measured scattering indicatrix without any *a priori* assumptions about the form of the correlation function. This cannot be done in terms of more general theories. Moreover these theories do not enable one to uniquely determine the roughness parameters even with the use of a model correlation function. These problems were considered in greater detail in [8].

Note that, in practice, the PSD function can be determined only in the finite spatial frequency range $\nu \in [\nu_{\min}, \nu_{\max}]$. Indeed, with a variation in the angles θ_0, θ, and φ but at a fixed wavelength of the incident radiation, the frequency ν cannot exceed $\nu_{\max} = 2/\lambda$. This leads to the obvious inference: the smaller the wavelength of the probe radiation, the higher the accuracy in the determination of the surface microgeometry. The minimum longitudinal sizes of detectable surface inhomogeneities are of the order of $a_{\min} = 1/\nu_{\max} = \lambda/2$. In real experiments, the achievable frequency $\nu_{\max}$ is limited by the radiation source power and the sensitivity of a measuring setup, because high spatial frequencies correspond to indicatrix wings, where the scattered radiation has an extremely low intensity. In our experiments described below, the typical values of $\nu_{\max}$ with the use of X-ray tubes and synchrotron sources are equal to 4–5 and 100–150 μm^{-1}, respectively.

The frequency ν is limited from below by a finite width s of the incident beam, because scattered X-ray photons are indistinguishable from specularly reflected X-ray photons in at least the observation angle range from $\theta_0 - \delta\theta/2$ to $\theta_0 + \delta\theta/2$ (where $\delta\theta = s/L$ and L is the distance between a sample and a detector). From this condition, we find that $\nu_{\min} \sim 2\delta\theta\sin\theta_0/\lambda$ and $a_{\max} = 1/\nu_{\min} \sim \lambda/(\delta\theta\sin\theta_0)$. In our experiments, the specularly reflected and diffusely scattered radiations can reliably be separated beginning with the spatial frequency $\nu_{\min} \sim 0.02$–0.05 μm^{-1}.

Figure 2 shows the characteristic ranges of spatial frequencies measured in different methods of investigating the surface roughness. Optical (and mechanical) profilometers make it possible to determine the PSD function in the range of low spatial frequencies. By contrast, the scattering methods and atomic-force microscopy provide a way of determining the PSD function in the range of high spatial frequencies. Compared to the UV scattering method, the X-ray scattering method even with the use of tubes as radiation sources is characterized by a noticeably wider range of measured spatial frequencies. Moreover, the upper frequency ν is limited by the fundamental factor (the radiation wavelength) in the UV scattering method and by technical factors (the source power and the sensitivity of instruments) in the X-ray scattering method. When synchrotrons are used as radiation sources, the measured frequency range covers at least five orders of magnitude even for supersmooth surfaces. The possibility of performing experiments in the range of very high frequencies is explained by the high power of the synchrotron radiation beam. The extension of the measurement range toward the low-frequency range is associated with the considerably larger distance between a sample and a detector (1–2 m) in special channels of the synchrotron radiation

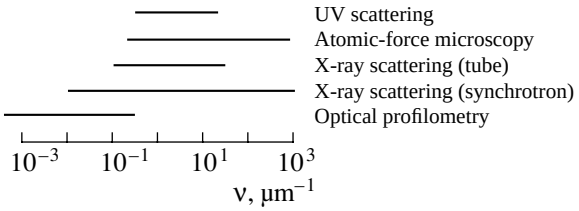

Fig. 2. Characteristic ranges of spatial frequencies measured in different methods of investigating the surface roughness: UV and X-ray scatterings with the use of tubes and synchrotrons as radiation sources, atomic-force microscopy, and optical profilometry.

as compared to that (20–30 cm) in conventional X-ray diffractometers. However, the range of measured frequencies is limited from above and below for any method of examining the roughness.

In conclusion of this section, we note that, although the PSD function enables one to describe most completely and precisely the surface roughness, for clearness, it is often expedient to introduce crude (integrated or approximate) roughness parameters. In particular, it is sometimes convenient to characterize the quality of the surface by the sole parameter. For this purpose, the effective roughness height σ_{eff} is introduced using one of the following relationships:

$$\sigma_{eff}^2 = 2\pi \int_{\nu_{min}}^{\nu_{max}} PSD_{2D}(\nu)\nu d\nu;$$
$$\sigma_{eff}^2 = \int_{p_{min}}^{p_{max}} PSD_{1D}(p)dp. \quad (10)$$

It is evident that the effective roughness height (10) has meaning when the spatial frequency range of integration is determined. Specifically, at p_{min}, $\nu_{min} \longrightarrow 0$ and p_{max}, $\nu_{max} \longrightarrow \infty$, the parameter σ_{eff} is reduced to the mathematically exact root-mean-square roughness height σ.

In order to represent more pictorially the surface microgeometry and to describe the surface properties with only a few parameters, the measured PSD functions are often approximated in terms of a particular model. In our case, we will use the so-called *ABC* model of the PSD function [9]:

$$PSD_{2D}(\nu) = \frac{4\pi\sigma^2 a^2 h}{[1 + (2\pi\nu a)^2]^{1+h}},$$
$$PSD_{1D}(p) = \frac{4\sqrt{\pi}\Gamma(h + 1/2)}{\Gamma(h)} \frac{\sigma^2 a}{[1 + (2\pi p a)^2]^{h+1/2}}. \quad (11)$$

Here, the fitting parameters have a clear physical meaning, namely, σ is the root-mean-square roughness height, a is the correlation length, and h is the fractal parameter that characterizes the behavior of the intensity of scattered radiation in the range of high spatial frequencies. The PSD functions defined by formulas (11) satisfy conditions (8).

3. EXPERIMENTAL SETUP AND MEASUREMENT PROCEDURE

Our approach to investigation of the surface roughness consists in determining the one- or two-dimensional PSD function directly from the measured X-ray scattering indicatrix with the use of formulas (5) or (7). The properties of the rough surface are completely characterized by the PSD function, which allows one to predict the scattering intensity and its angular distribution at different wavelengths on the basis of experimental data obtained for one wavelength.

In order to extract the maximum amount of information on the statistical parameters of surface roughnesses from X-ray scattering data, measurements should be performed in the widest possible range of spatial frequencies. This means that small angular displacements in the immediate vicinity of the specularly reflected beam should be recorded with a high accuracy. At the same time, it is necessary to measure reliably extremely low signals in the scattering indicatrix wings, where the intensity of scattering radiation is five or six orders of magnitude lower than that of the incident beam.

Therefore, when designing an experimental setup intended for investigating the microroughness of supersmooth surfaces, it was essential to provide a high accuracy in the determination of all angular displacements, a high counting rate of a detector, and its low noise. Furthermore, the X-ray scattering from collimator slits should be minimized and the width of an entrance slit of a detector could be automatically varied in the course of measurements. These requirements were taken into account in the design of the experimental setups described in [10, 11].

The basic results presented in our work were obtained using the experimental setup schematically depicted in Fig. 3. The setup was designed on the basis of a goniometer of a triple-crystal X-ray spectrometer and a standard radiation source—an X-ray tube. In order to ensure the required spatial characteristics of an X-ray beam, we used the three-slit collimation scheme. The width of the first (nearest to the source) slit is constant and equal to 100 μm. On the other hand, the widths of the second and third slits can be continuously varied in the range from 0 to 2 mm with an accuracy of 2 μm. Note that blinds of the third slit moved independently of one another. Moreover, the second and third slits could be rotated about the horizontal axis perpendicular to the slit plane, which made it possible to arrange them parallel to the X-ray beam and each other.

An X-ray monochromator, which was a polished germanium single crystal [the (220) reflection, CuK_α1, λ = 0.154 nm], was located between the first and second slits.

The radiation was recorded by a conventional scintillation detector. The entrance slit of the detector is similar in design to the second slit of the collimator. In the course of measurements, as the intensity of the scattered radiation decreased, the width of the former slit increased from 30 μm to 1 mm. Owing to the use of a highly stabilized power supply of the detector and a two-level discriminator, the intrinsic noise of the counting channel did not exceed 0.07 pulse/s.

The sample and the detector were automatically rotated with two step motors. The third step motor controlled the entrance slit of the detector. Instrumentation equipment conformed to the CAMAC standard. The experiment was controlled with a personal computer.

The typical X-ray scattering indicatrix is represented by curve *1* in Fig. 4. The scattering intensity was measured as follows. The sample was rotated through the angle θ_0, and its position was fixed. Then, the intensity of the scattered intensity was recorded upon rotation of the detector. During measurements, the width of the entrance slit of the detector was changed several times with the aim of improving the statistical parameters of the experiment. Note that the radiation intensity in the indicatrix wings is approximately 10^6 times lower than the radiation intensity in the direction of the specular reflection. No less than 10^3 X-ray photons were recorded at each point, so that the statistical error of measurements did not exceed 3%.

It should be noted that, when studying supersmooth surfaces with a roughness height of 0.2 nm or less, there arises the problem of separation of the desired signal from the parasitic scattering, which, in our opinion, is due to the scattering of the X-ray beam by air and edges of the collimator slits. The intensity of this parasitic scattering can be comparable to the desired signal in the indicatrix wings.

In order to decrease the intensity of parasitic scattering, a special cell of a certain volume evacuated to vacuum was placed between the sample and the entrance slit of the detector. The use of this element in the setup led to a decrease in the intensity of parasitic scattering by a factor of six or seven. This permitted us to improve the reliability of measurements, especially in the case of supersmooth surfaces. The direct-beam profiles measured with and without an evacuated cell are shown in Fig. 4. A comparison of the direct-beam profiles with the measured scattering indicatrix for a very smooth sample clearly demonstrates the necessity of decreasing the intensity of parasitic scattering.

The experimental scattering indicatrix shown in Fig. 4 permits us to determine the one-dimensional PSD function of roughness from relationship (7) when the optical constants (i.e., the real and imaginary parts of the permittivity ε_+) are available for the studied sample. If the chemical composition or the density of the sample is unknown, the optical constants should be found experimentally.

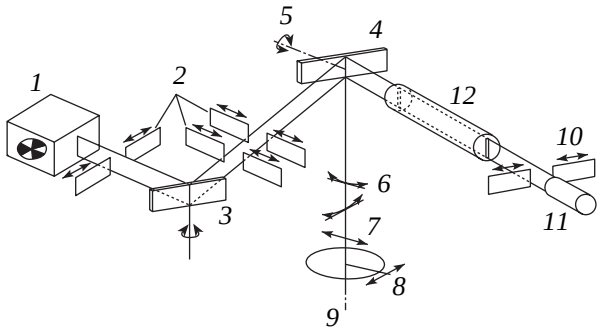

Fig. 3. Schematic drawing of the experimental setup. Designations: (*1*) X-ray tube, (*2*) three-slit collimator, (*3*) crystal monochromator, (*4*) studied sample, (*5*)–(*7*) adjusting gears, (*8*) rotation gear of the sample and detector, (*9*) principal axis of the goniometer, (*10*) entrance slit, (*11*) detector, and (*12*) cell evacuated to vacuum.

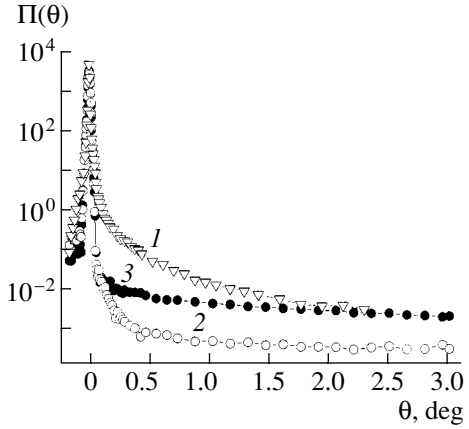

Fig. 4. (*1*) Scattering indicatrix for a polished quartz substrate with the roughness height σ_{eff} = 0.2 nm (the specular component is not subtracted) and direct-beam profiles measured (*2*) with and (*3*) without an evacuated cell.

For this purpose, the total X-ray reflectivity is measured as a function of the grazing angle: $R_\Sigma(\theta_0) = R_{spec}(\theta_0) + \mathrm{TIS}(\theta_0)$, where R_{spec} is the specular reflectivity and $\mathrm{TIS} = \int \Pi(\theta) d\theta$ is the integrated intensity of scattering into vacuum. Then, by treating the real and imaginary parts of the permittivity ε_+ as unknown parameters, the theoretical reflectivity curve is fitted to the experimental data according to the least-squares technique. Examples of fittings are presented in Fig. 5, in which the theoretical curves are calculated under the assumption of ideally smooth surfaces. This simplified approach is supported by the following circumstances. First, we are interested in supersmooth surfaces when the roughness only slightly affects the reflectivity for at

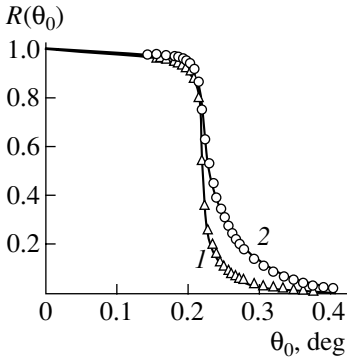

Fig. 5. Dependences of the experimental reflectivity on the grazing angle of incident radiation (λ = 0.154 nm) for (*1*) polished quartz substrate and (*2*) 5.7-nm-thick Al_2O_3 film deposited onto this substrate. Solid lines represent the results of theoretical fitting.

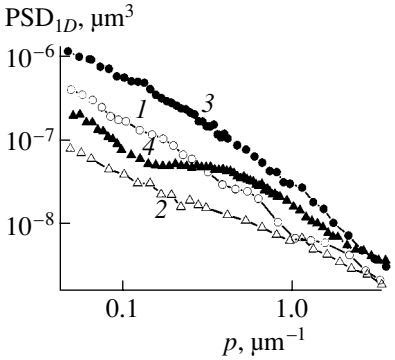

Fig. 6. Experimental spectral functions of the roughness for (*1, 2*) polished quartz substrates, (*3*) glass prepared by the float method, and (*4*) tungsten film on a polished glass substrate.

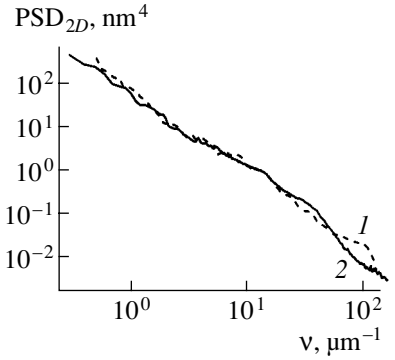

Fig. 7. Two-dimensional PSD functions determined from (*1*) X-ray scattering (wavelength, 0.15 nm) and (*2*) atomic-force microscopic data for a superpolished silicon wafer.

least small grazing angles. Second, as was shown in [7], roughnesses with a large correlation length $a \gg \lambda/(\pi\theta_c^2)$ (where θ_c is the critical angle of the total external reflection) do not result in an additional absorption of radiation in a material and only redistribute its intensity between the components specularly reflected and scattered into vacuum. Therefore, the inclusion of the total intensity of radiation backscattered from the surface into vacuum (rather than only the specular reflectivity) enables us to reduce, to a maximum degree, the effect of the surface roughness on the reflectivity curve.

The dependence of the reflectivity on the grazing angle is experimentally determined using a traditional θ–2θ geometry. The entrance slit of the detector should be wide enough to prevent the influence of a further increase in the slit width on the measured total reflectivities.

Figure 6 depicts the one-dimensional PSD functions of the surface roughness, which were directly obtained from the X-ray scattering indicatrices measured at the wavelength λ = 0.154 nm. The measurements were carried out with the use of the X-ray tube as the radiation source. The low intensity of the source and the small distance between the sample and the detector (of the order of 20 cm) make measurements of the more informative two-dimensional PSD function impossible. Table 1 presents a brief description of the samples and the effective roughness heights σ_{eff} calculated from formula (10), in which the integration is performed over the measured range of spatial frequencies p from p_{min} = 0.05 μm^{-1} to p_{max} = 4 μm^{-1}. It can be seen from Table 1 that the effective roughness heights for the studied samples vary from 0.15 to 0.4 nm. This clearly demonstrates the high sensitivity of the X-ray scattering method even in the case when the X-ray tube serves as the radiation source.

In Fig. 6, curves *1* and *2* represent the PSD functions of the surface of silica glass substrates subjected to fine grinding and polishing. Curve *3* corresponds to the glass substrate prepared using the so-called fire polishing or the float method. This method consists in solidifying a glass melt on the surface of molten tin and has the advantage that the resulting surface of such a glass is rather smooth in itself without any additional mechanical polishing. Curve *4* describes the surface roughness of a tungsten film (approximately 0.2 μm thick) deposited onto a polished glass substrate.

The two-dimensional PSD function for the surface of a superpolished silicon wafer is presented in Fig. 7. The experimental data were obtained on the synchrotron (ESRF, ID01 beamline [12]) at the wavelength λ = 0.15 nm. The effective roughness height was determined to be only $\sigma_{eff} \simeq 0.068$ nm (in the measured range of spatial frequencies); i.e., in essence, the sample was atomically smooth. However, the use of the synchrotron as the radiation source, which is characterized by a high beam power and the possibility of measuring the scattering at large distances from the sample (approximately 1 m in our experiments), made it possible to determine the two-dimensional PSD function up to very high spatial frequencies $\nu \sim 120$ μm^{-1}. These

Table 1. Effective roughness heights σ_{eff} for the samples whose PSD functions are shown in Figs. 6–10

Figure no.	Curve no.	Sample	σ_{eff}, nm
6	*1*	Polished quartz substrate	0.15
	2	Polished quartz substrate	0.26
	3	Glass substrate prepared by the float method	0.41
	4	W film (0.2 μm) on polished substrate	0.23
7	*1*	Polished silicon wafer	0.068
8	*1*, *2*	Initial quartz substrates on chuck plate	0.56
	3	One of the substrates after additional polishing	0.43
9	*1*	Substrate polished with iron oxide	0.41
	2	Substrate polished with cerium oxide	0.54
	3	Substrate *2* repolished with iron oxide	0.42
10	*1*	Initial substrate	0.32
	2	Initial substrate	0.67
	3	Both substrates treated with Ar^+ ions	1.05
	4	Carbon film surface	0.56

frequencies correspond to the upper limit of measurements with atomic-force microscopy.

Note that the PSD functions of polished substrates are well approximated by relationships (11) in the framework of the *ABC* model. On the other hand, the PSD functions of film coatings (for example, curve *4* for the tungsten film in Fig. 6), as a rule, exhibit a more complex behavior, in particular, a maximum in the range of high spatial frequencies, and, hence, cannot be described by relationships (11) with the sole correlation length. This implies that the surface structure of film samples involves two (or more) statistically independent systems of roughnesses with different correlation lengths. In general, their physical origin is clear. It is well known from the literature and, recently, has been clearly demonstrated by atomic-force microscopy [13, 14] that the deposition of film coatings very often leads to a rapid growth of small-scale roughnesses associated with the columnar structure of many dielectric films and the polycrystalline structure of metal films. Therefore, it is reasonable to assume that the low-frequency portion of the roughness spectrum of the studied tungsten film is due to the roughness of the initial substrate and the high-frequency portion is governed by the roughnesses formed during the deposition of the film coating.

4. X-RAY SCATTERING METHOD AS APPLIED TO MODERN TECHNOLOGIES OF SURFACE TREATMENT

Owing to the high sensitivity and informative capability, the X-ray scattering method can serve as a metrological basis for further development of technologies of processing supersmooth surfaces in optics and microelectronics and also for the deposition of film coatings. Let us dwell on certain examples of such applications of the X-ray scattering method.

The characteristic feature of mechanical grinding and polishing of optical elements is that several elements are fastened on a technological chuck plate, which carriers them to the completion of the polishing process. Moreover, the development of the superpolishing technology requires the control over the smoothness of treated surfaces after each stage of the technological process (for example, in order to optimize the time of grinding and polishing by powders with a particular particle size). Apparently, it is this X-ray scattering method that is best suited for this purpose, because the size and weight of studied samples are strongly limited, for example, in the case of the existing atomic-force microscopes. We constructed a special adjusting gear integrated with a sample holder. This gear provides the necessary adjustment accuracy and makes it possible to investigate samples of diameter as large as

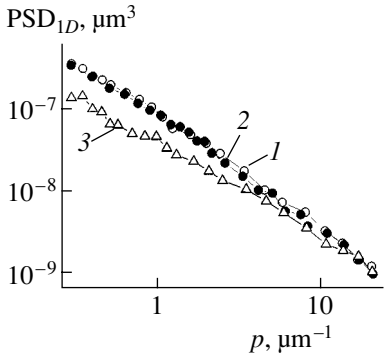

Fig. 8. PSD functions of the roughness for (*1, 2*) quartz substrates fastened at the center and periphery of the technological chuck plate and (*3*) one of these substrates after additional polishing.

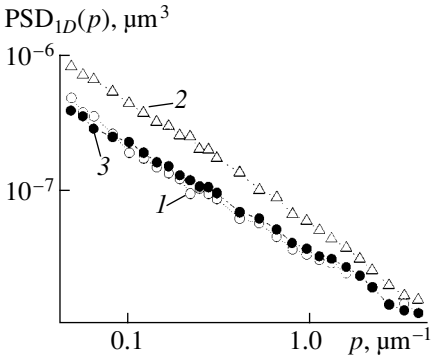

Fig. 9. PSD functions of the roughness for quartz substrates polished with (*1*) iron oxide and (*2*) cerium oxide and (*3*) substrate *2* repolished with iron oxide.

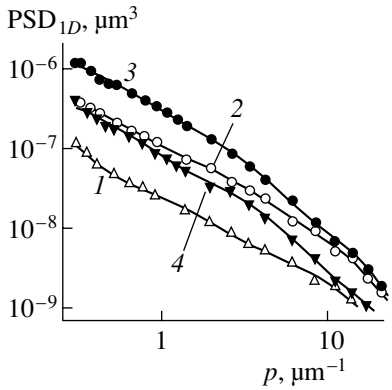

Fig. 10. Experimental spectral functions of the roughness for (*1, 2*) the initial surfaces of two quartz substrates with different surface finish, (*3*) the same surfaces after treatment with a directed Ar^+ ion beam, and (*4*) the surface after deposition of a diamond-like carbon film.

200 mm. Furthermore, any one of the samples fastened on the chuck plate and even any surface region 10 × 10 mm^2 in size in each sample can be examined with the use of our setup [15].

Figure 8 shows the measured PSD functions for two quartz substrates fastened at the center and periphery of the chuck plate (curves *1*, *2*). As can be seen from Fig. 8, the quality of the substrate surface virtually does not depend on the location of the substrate on the chuck plate. After X-ray testing, which revealed an insufficiently high quality of the substrates, the chuck plate was removed from the measuring setup, and the substrates were subjected to additional polishing. The PSD function of one of the substrates after additional polishing is shown by curve *3* in Fig. 8. It can be seen from Fig. 8 and Table 1 that the additional polishing of the samples results in a considerable smoothing of their surfaces. Note that this effect is most pronounced in the low-frequency range of the roughness spectrum.

Our investigations of the polishing process [16] clearly demonstrated that the surface finish is predominantly determined by the polishing agent used at the last polishing stage. As an illustration, Fig. 9 shows the PSD functions of quartz substrates polished with the use of iron oxide (curve *1*) and cerium oxide (curve *2*) characterized by a larger size of powder particles. It can be seen from this figure (see also Table 1) that, in the former case, the substrate surface has a substantially higher quality. However, if substrate *2* is repolished with iron oxide, the quality of the substrate surface becomes identical to that of substrate *1*.

The investigations performed made it possible to improve the technological process of fabricating supersmooth quartz substrates and to prepare samples with an effective roughness height of 0.26 nm (Fig. 6, curve *2*), whereas effective roughness heights of 0.4–0.45 nm were typical of substrates produced according to the old technology.

One more example of the possibilities of applying the X-ray scattering method is provided by investigation of a change in the surface microrelief upon deposition of diamond-like carbon films (Fig. 10). The deposition process involved two stages: the cleaning of the substrate surface with a directed Ar^+ ion beam and the film deposition through the cyclohexane destruction. Curves *1* and *2* in Fig. 10 indicate the measured PSD functions for two polished quartz substrates substantially differing in the surface finish (see Table 1). It was found that the ion bombardment leads to an increase in the roughness of both substrates. Moreover, the roughness spectra of both surfaces become identical to each other (Fig. 10, curve *3*). In other words, the ion beam etches away initial roughnesses but results in the formation of new roughnesses determined by parameters of the ion beam.

In this respect, we note that, under different conditions, the ion etching can lead to a considerable smoothing of surface roughnesses [17, 18]. In particular, this effect was observed in our earlier work [19].

After ion-beam treatment, the diamond-like carbon film approximately 0.1 μm thick was deposited onto the substrate surface. The roughness spectrum after film

deposition is depicted by curve *4*, which lies appreciably lower than curve *3*. This means that the deposition of the carbon film results in the surface smoothing.

Consequently, the surface resulting from all the technological operations appears to be smoother than the surface of substrate *2* but rougher than the surface of substrate *1*. In this case, the quality of the film surface does not depend on the quality of the initial substrate. These investigations showed that the deposition of the carbon film leads to the smoothing of roughnesses, but the preliminary ion-beam treatment results in the their noticeable growth. Therefore, in the above technological process, the surface cleaning is the limiting stage and should be modified in such a way as to prevent the surface roughness growth.

The use of the X-ray scattering data in the technology of depositing thin-film coatings is illustrated in Fig. 11, which shows the change in the root-mean-square roughness height during growth of a B_4C film deposited onto a superpolished silicon wafer by magnetron sputtering. The X-ray measurements were carried out on the ID01 beamline (ESRF) at the wavelength λ = 0.15 nm. Note that the polarizabilities of Si and B_4C virtually coincide at this wavelength. Therefore, the scattering from the inner interface was disregarded when determining the PSD function of the external surface of B_4C films. In addition to the X-ray measurements, the film roughness was examined with atomic-force microscopy. The effective roughness heights σ_{eff} determined by both methods are in good agreement with each other.

As can clearly be seen from Fig. 11, the effective roughness height exhibits a nonmonotonic behavior with the film growth, which can easily be explained. An increase in the effective roughness height at small film thicknesses is associated with the formation of islands at the initial stage of the film growth. With a further film growth, the film becomes continuous and its roughness is smoothed owing to surface relaxation occurring through particular mechanisms. It can be seen from Fig. 11 that, most likely, the studied film becomes continuous at a thickness of an order of 0.6–0.8 nm (two or three monolayers of B_4C molecules).

The aforementioned examples and other investigations performed in our earlier works [15, 16, 20–22] demonstrate the high potentialities of the X-ray scattering method for the study of the microroughness of supersmooth surfaces. Further development of the method holds promise from the viewpoint of both basic research and its use as the metrological basis for a number of modern technologies in optics, laser engineering, microelectronics, and high-precision machine engineering. This raises the very important question as to the reliability of the results obtained by the X-ray scattering method, which is the subject matter of the next section.

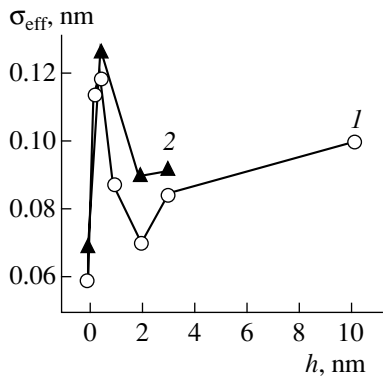

Fig. 11. Change in the effective height of roughnesses (in the spatial-frequency range 0.3–100 μm^{-1}) in a growing B_4C film according to (*1*) atomic-force microscopic and (*2*) X-ray scattering data.

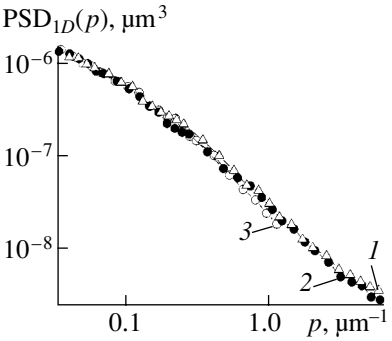

Fig. 12. PSD functions determined for a polished quartz substrate from X-ray scattering indicatrices measured at different grazing angles of the probe beam θ_0 = (*1*) 350″, (*2*) 450″, and (*3*) 600″.

5. COMPARATIVE INVESTIGATIONS OF THE SURFACE ROUGHNESS BY DIFFERENT METHODS

A large number of experiments were carried out with the aim of confirming the correctness of the used experimental technique.

First and foremost, we measured and analyzed the indicatrices of X-ray scattering from the same samples at different grazing angles of incident beam. A change in the grazing angle leads to a change in the intensity of scattered radiation and in the width and even shape of its angular distribution. At the same time, the PSD function that is extracted from the experimental data and describes the surface properties should not depend on the grazing angles of the incident beam. The performed investigations showed that the PSD functions found from the experimental data obtained at different grazing angles of the incident beam coincide with each other (Fig. 12). The independence of the experimental

Table 2. Effective roughness heights σ_{eff} (at spatial frequencies in the range from 0.06 to 3 μm^{-1}) according to atomic-force microscopy and hard X-ray (λ = 0.154 nm), soft X-ray (λ = 4.47 nm), and UV (λ = 325 nm) scattering data

Sample designation	Sample	σ_{eff}, nm			
		atomic-force microscopy	hard X-ray scattering	soft X-ray scattering	UV scattering
VK-7	Polished VK-7 glass substrate	0.25	0.27	0.34	
*SQ*1	Polished quartz substrate	0.64	0.64	0.53	
Al_2O_3	Al_2O_3 film (d = 0.1 μm) on *SQ*1	0.50	0.48	0.60	
MgF_2	MgF_2 film (d = 0.18 μm) on *SQ*1	0.95	0.76	1.03	
Ag	Ag film coated with a protective layer of thickness d = 0.3 μm	0.55*	0.47*		
			0.73**		0.80**

* Surface of the protective layer.
** Surface of the silver film.

PSD function from the grazing angle θ_0 of the probe beam supports the validity of our approach, i.e., the possibility of applying the perturbation theory to process the X-ray experimental data.

Undeniably, the most conclusive proof can be provided by a comparison of the X-ray scattering data with independent results obtained by other methods, primarily, one of direct profilometric methods. Such a comparison was performed on the basis of the data obtained by the X-ray (at wavelengths of 0.154 and 4.47 nm) and UV (at a wavelength of 325 nm) scattering methods and atomic-force microscopy. Note that, in recent years, the last method has been widely used to study the surface roughness [13, 14, 23, 24].

It should be emphasized that atomic-force microscopy and the X-ray scattering method allow one to investigate surface roughnesses with longitudinal sizes that are many times smaller than wavelengths of visible radiation. These methods are based on quite different physical phenomena: attractive and repulsive molecular interactions and the diffraction of electromagnetic radiation by an inhomogeneous interface. Furthermore, these methods provide quite different experimental information, namely, a two-dimensional surface relief in atomic-force microscopy and an angular distribution of the intensity of scattered radiation in the X-ray scattering method. Finally, the technique of extracting the data on the sample microgeometry from the scattering indicatrices strongly depends on the used model of the surface and the theory of interaction between radiation and a rough scatterer. Therefore, a comparison of the X-ray scattering and atomic-force microscopic data for the same samples is not only of practical importance but also of considerable scientific interest.

In our experiments, we examined polished glass and quartz substrates of different quality and Al_2O_3, MgF_2, and Ag films. Table 2 presents a brief description of the studied samples.

The surfaces of the substrates and film coatings were investigated on a DIMENSION 300 atomic-force microscope. The techniques of measurements and processing of experimental data are described in [13]. The measurements were carried out in the range of spatial frequencies from approximately 0.05–0.07 to 120 μm^{-1}.

The UV scattering was studied upon normal incidence of the radiation with the wavelength λ = 325 nm (a He–Cd laser). The scattering intensity was measured in the range of angles (reckoned from the normal to the surface) from 0.3° to 85°. This enabled us to determine the two-dimensional PSD function of surface roughness in the range of spatial frequencies ν from 0.06 to 3 μm^{-1}.

The VK-7, *SQ*1, Al_2O_3, and MgF_2 samples (Table 2) were examined by the hard (λ = 0.154 nm) and soft (λ = 4.47 nm) X-ray scattering and atomic-force microscopy. The one-dimensional PSD functions determined from the X-ray scattering data obtained at two different wavelengths are depicted in Fig. 13a. It can be seen from this figure that the experimental data agree well with each other.

In order to compare the X-ray scattering and atomic-force microscopic data, it is necessary to derive the two-dimensional PSD functions from the one-dimensional functions found from the X-ray scattering data. For this purpose, we used the *ABC* model [see relationships (11)] (or the sum of two *ABC* model functions). The parameters σ, a, and h of this model were determined by fitting the calculated $PSD_{1D}(p)$ curves to the experimental data. On the basis of the obtained parameters, we calculated the two-dimensional PSD functions. These functions are compared with the corre-

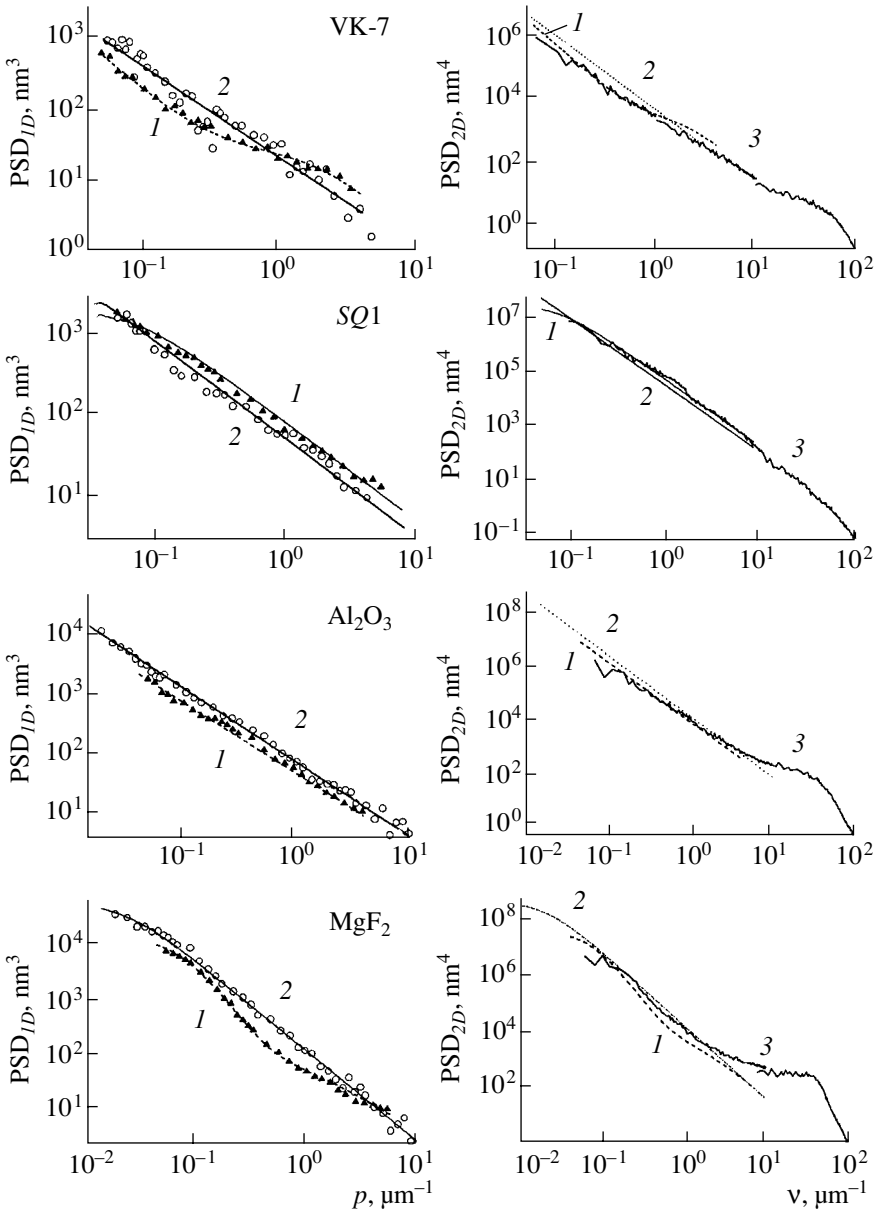

Fig. 13. (a) One-dimensional PSD functions of the surface roughness for the VK-7, *SQ*1, Al_2O_3, and MgF_2 samples according to (*1*) hard ($\lambda = 0.154$ nm) and (*2*) soft ($\lambda = 4.47$ nm) X-ray scattering data. Circles and triangles are the experimental results. Curves passing through circles and triangles correspond to the results of fitting of the experimental functions with the use of the *ABC* model. (b) Two-dimensional PSD functions (*3*) measured using atomic-force microscopy and (*1*, *2*) calculated from the X-ray scattering data.

sponding two-dimensional PSD functions determined from the atomic-force microscopic data in Fig. 13b.

Moreover, the effective roughness heights σ_{eff} obtained for the range of spatial frequencies from 0.06 to 3 μm^{-1} are listed in Table 2. This range is common to all the used methods of investigating the surface roughness and is determined by the capabilities of the UV scattering technique. As can be seen from Table 2, the effective roughness heights σ_{eff} calculated from the atomic-force microscopic and X-ray scattering data are sufficiently close to each other.

The two-dimensional PSD functions determined by the two methods for the VK-7, *SQ*1, Al_2O_3 samples are in surprisingly good agreement over the entire overlapping range of spatial frequencies. For the MgF_2 sample, the discrepancy between the PSD functions is somewhat larger in the range of high spatial frequencies $\nu > 5$ μm^{-1}.

The two-dimensional PSD functions determined for the superpolished silicon wafer from the X-ray scattering and atomic-force microscopic data are compared in Fig. 7. Like for the aforementioned samples, the functions are in good agreement, except for the range of

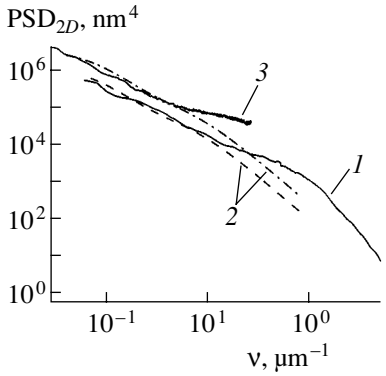

Fig. 14. Two-dimensional PSD functions of the surface roughness for a silver mirror with a protective coating according to (*1*) atomic-force microscopy and (*2*) X-ray (λ = 0.154 nm) and (*3*) UV (λ = 325 nm) scattering data. Upper and lower curves *2* corresponding to the X-ray scattering data are obtained at two grazing angles of the probe beam θ_0 = 0.35° and 0.17°, respectively.

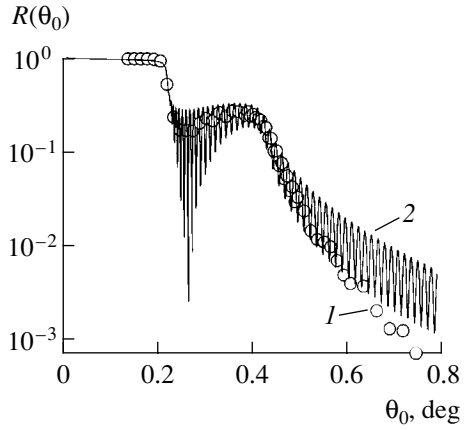

Fig. 15. (*1*) Experimental dependence of the X-ray reflectivity (λ = 0.154 nm) on the grazing angle for a silver mirror. Curve *2* indicates the results of the theoretical fitting performed with the aim of determining the optical constants of protective and silver films.

high spatial frequencies. The root-mean-square roughness heights (in the overlapping range of spatial frequencies from 0.3 to 120 μm^{-1}) calculated from the X-ray scattering and atomic-force microscopic data are equal to approximately 0.068 and 0.060 nm, respectively.

The observed discrepancy between the PSD functions found by both methods in the range of high spatial frequencies can be associated with the following factors. First, this is the limited validity range of the perturbation theory used for processing the X-ray scattering data. Second, this is the simplified model of the surface according to which the properties of a material jumpwise change at the interface. In actual fact, an adhesion layer with a typical thickness of an order of 1 nm occurs on any surface. It seems likely that the surface of just the adhesion layer rather than the true surface of the sample is examined by atomic-force microscopy. In turn, the deposition of any film leads to a change in the surface roughness spectrum in the range of high spatial frequencies. Furthermore, the surface layer has an effect on the angular distribution of the X-ray scattering intensity. Note that this effect is stronger in the scattering indicatrix wings. Third, the two-dimensional PSD function is determined using a particular extrapolation of the experimental one-dimensional PSD function to the range of high spatial frequencies. For this purpose, we used the *ABC* model [relationships (11)], which, in general, can be insufficiently adequate to the reality.

Let us now consider the two-dimensional PSD functions of roughness for a silver mirror (Fig. 14), which were determined from the atomic-force microscopic and UV scattering data. It can be seen from Fig. 14 that these functions differ substantially. However, the origin of this difference is quite clear and can easily be explained. The point is that an additional (transparent for the UV radiation) protective polymer coating approximately 0.3 μm thick was deposited onto the silver film in order to protect it against degradation in an air medium. It is obvious that only the PSD function of the outer surface of the protective coating can be determined from atomic-force microscopic measurements. On the other hand, the UV radiation is predominantly scattered from a well-reflecting silver layer. This accounts for the difference between the PSD functions (Fig. 14) derived from the atomic-force microscopic and UV scattering data.

In turn, the penetration depth of X-ray radiation into a material can vary over a wide range (from several nanometers to several micrometers) with an increase in the grazing angle of incident beam. The angular dependence of the hard X-ray reflectivity for the silver sample is plotted by points in Fig. 15. At small grazing angles $\theta_0 < 0.2°$, the radiation is totally reflected from the surface of the protective film. In this case, the penetration depth of the wave field into the material is equal to several nanometers and, hence, the scattering is associated with the roughness only of the outer surface of the protective coating.

As the grazing angle θ_0 increases, the X-ray wave penetrates into the protective film but totally reflects from the heavier silver layer at $0.2° < \theta_0 < 0.4°$. In this range of grazing angles θ_0, the difference of the reflectivity from unity is caused by the partial absorption of the radiation in the protective film. Note that, at $\theta_0 \sim 0.4°$, the reflectivity from the outer surface of the protective coating does not exceed 0.5% and, hence, the radiation scattering is almost completely governed by the roughness of the silver layer.

The solid line in Fig. 15 indicates the results of the theoretical fitting carried out with the aim of determining the optical constants of the protective and silver

films. Oscillations in the calculated curve arise from interference effects. Owing to the finite angular width of the incident beam, these oscillations cannot be seen in the experimental curve.

Therefore, the X-ray scattering indicatrices measured at two different grazing angles $\theta_0 \simeq 0.17°$ and 0.37° permit us to obtain information on the roughness of either of the two interfaces. The two-dimensional PSD functions determined by the X-ray scattering method for both surfaces are represented in Fig. 14. The indicatrix of scattering from the silver film was analyzed with due regard for the absorption of radiation in the protective film. It can be seen that the PSD functions derived from the X-ray scattering data are in good agreement with those obtained from the UV scattering and atomic-force microscopic data in the range of not very high spatial frequencies. The difference between the functions at high frequencies can be explained by the factors considered above and the errors in the determination of the optical constants for the protective and silver films.

Figure 14 clearly demonstrates the potentialities of the X-ray scattering method in the study of hidden interfaces. The results obtained in the investigation of surface layers of solids and the roughness of thin-film coatings will be analyzed in more detail in the separate paper [1], which is a continuation of the present work.

6. CONCLUSIONS

Thus, the analysis performed clearly demonstrated that X-ray scattering methods possess a number of unique potentialities and advantages over all other methods. Their main capabilities are as follows:

(1) These are nondestructive testing methods.

(2) X-ray methods allow one to obtain quantitative information on the structure of the material and surface.

(3) Their informative capabilities are higher than those of optical methods, because the minimum longitudinal size of detectable inhomogeneities corresponds in order of magnitude to the wavelength of probe radiation.

(4) The methods under consideration have a very high sensitivity and provide a means of investigating surface layers and thin films with thicknesses as small as a monoatomic layer and roughnesses with a root-mean-square height of 0.1–0.2 nm or less [16, 20].

(5) X-ray methods make it possible to examine hidden interfaces (for example, film–substrate interfaces) [20, 21, 25] and surface layers of solids and liquids [26–29].

(6) The methods can be used to control the roughness of concave surfaces with arbitrary shapes and sizes. This approach is based on the whispering gallery effect in the X-ray region [30, 31].

(7) These methods permit one to analyze large-area samples, including semiconductor wafers, optical elements, magnetic and optical memory disks, and products of machine building [15, 16, 22].

(8) The X-ray methods can easily be adapted to *in situ* measurements.

A wealth of experience in the use of X-ray methods in industrial defectoscopy, materials science, and medicine has been accumulated to date. This has given impetus a rapid practical implementation of recent advances in X-ray physics. The case in point is the design of new devices for testing products processed with a subnanometer accuracy [10, 32, 33]. These devices can be used directly in production without changing or interrupting a technological cycle.

ACKNOWLEDGMENTS

We would like to thank B.V. Mchedlishvili for his interest in this work.

REFERENCES

1. V. E. Asadchikov, I. V. Kozhevnikov, and Yu. S. Krivonosov, Kristallografiya (in press).
2. A. A. Andronov and M. A. Leontovich, in *Collected Works of A. A. Andronov* (Akad. Nauk SSSR, Moscow, 1956), p. 5; Z. Phys. B **38**, 485 (1926).
3. J. M. Bennett and L. Mattsson, *Introduction to Surface Roughness and Scattering* (Opt. Soc. Am., Washington, 1989).
4. A. V. Andreev, Usp. Fiz. Nauk **145** (1), 113 (1985) [Sov. Phys. Usp. **28**, 70 (1985)].
5. A. V. Vinogradov, N. N. Zorev, I. V. Kozhevnikov, and I. G. Yakushkin, Zh. Éksp. Teor. Fiz. **89** (6), 2124 (1985) [Sov. Phys. JETP **62**, 1225 (1985)].
6. A. V. Vinogradov, N. N. Zorev, I. V. Kozhevnikov, *et al.*, Zh. Éksp. Teor. Fiz. **94** (8), 203 (1988) [Sov. Phys. JETP **67**, 1631 (1988)].
7. A. V. Vinogradov and I. V. Kozhevnikov, Tr. Fiz. Inst. im. P.N. Lebedeva, Akad. Nauk SSSR **196**, 18 (1989).
8. I. V. Kozhevnikov and M. V. Pyatakhin, J. X-Ray Sci. Technol. **8**, 253 (2000).
9. E. L. Church and P. Z. Takacs, Proc. SPIE **1530**, 71 (1991).
10. B. M. Alaudinov, V. E. Asadchikov, I. V. Kozhevnikov, *et al.*, Nauchn. Priborostr. **5** (1–2), 95 (1995).
11. I. V. Kozhevnikov, V. E. Asadchikov, A. Duparré, *et al.*, Proc. SPIE **3739**, 348 (1999).
12. M. J. Capitan, D. Thiaudiere, L. Goirand, *et al.*, Physica B (Amsterdam) **283**, 256 (2000).
13. V. E. Asadchikov, A. Duparre, S. Jakobs, *et al.*, Appl. Opt. **38**, 684 (1999).
14. C. Ruppre and A. Duparré, Thin Solid Films **288**, 8 (1996).
15. V. E. Asadchikov, E. E. Andreev, A. V. Vinogradov, *et al.*, Poverkhnost, No. 7, 17 (1998).
16. V. E. Asadchikov, A. V. Vinogradov, V. N. Zryuev, *et al.*, Zavod. Lab. **67** (67), 19 (2001).
17. K. Oyoshi, T. Tagami, and S. Tanaka, Jpn. J. Appl. Phys. **30**, 1854 (1991).

18. E. Spiller, Appl. Phys. Lett. **54**, 2293 (1989).
19. I. V. Kozhevnikov, V. E. Asadchikov, and B. M. Alaudinov, Proc. SPIE **2453**, 141 (1995).
20. V. E. Asadchikov, I. N. Bukreeva, A. Duparre, *et al.*, Proc. SPIE **4449**, 253 (2001).
21. I. V. Kozhevnikov, V. E. Asadchikov, I. N. Bukreeva, *et al.*, Proc. SPIE **4099**, 267 (2000).
22. V. E. Asadchikov, A. Yu. Karabekov, I. V. Kozhevnikov, *et al.*, Izv. Vyssh. Uchebn. Zaved., Mater. Élektron. Tekh., No. 1, 65 (1999).
23. V. V. Protopopov, K. A. Valiev, and R. M. Imamov, Kristallografiya **42** (4), 747 (1997) [Crystallogr. Rep. **42**, 686 (1997)].
24. P. A. Arutyunov and A. L. Tolstikhina, Mikroélektronika **26** (6), 426 (1997).
25. V. E. Asadchikov, A. Duparre, I. V. Kozhevnikov, *et al.*, Proc. SPIE **3738**, 387 (1999).
26. B. M. Alaudinov, I. A. Artyukov, V. E. Asadchikov, *et al.*, Kristallografiya **39** (4), 605 (1994) [Crystallogr. Rep. **39**, 540 (1994)].
27. I. A. Artyukov, V. E. Asadchikov, and I. V. Kozhevnikov, J. X-Ray Sci. Technol. **6**, 223 (1996).
28. O. N. Gilev, V. E. Asadchikov, A. Duparre, *et al.*, Proc. SPIE **4099**, 279 (2000).
29. A. M. Afanas'ev, P. A. Aleksandrov, and R. M. Imamov, *X-ray Diffraction Diagnostics of Submicron Layers* (Nauka, Moscow, 1989).
30. V. E. Asadchikov, I. I. Bukreeva, A. V. Vinogradov, *et al.*, Kvantovaya Élektron. (Moscow) **24** (8), 845 (1997).
31. I. N. Bukreeva, V. E. Asadchikov, O. N. Gilev, *et al.*, Proc. SPIE **3739**, 395 (1999).
32. K. A. Valiev, V. V. Protopopov, V. V. Danilov, *et al.*, Preprint No. 21, FTI RAN (Physicotechnical Inst., Russian Academy of Sciences, St. Petersburg, 1997).
33. A. G. Tur'yanskiĭ, A. V. Vinogradov, and I. V. Pirshin, Prib. Tekh. Éksp., No. 1, 105 (1999).

Translated by O. Borovik-Romanova

Crystallography Reports, Vol. 48, No. 5, 2003, pp. 851–859. Translated from Kristallografiya, Vol. 48, No. 5, 2003, pp. 912–920.

SURFACE, THIN FILMS

Dedicated to the 60th Anniversary of the Shubnikov Institute of Crystallography of the Russian Academy of Sciences

Influence of Defects on the Formation of Thin Porous GaP(001) Films

V. A. Karavanskiĭ*, A. A. Lomov, A. G. Sutyrin**, R. M. Imamov**, V. I. Dravin***, N. N. Mel'nik***, and T. N. Zavaritskaya*****

** Natural Science Center, Institute of General Physics, Russian Academy of Sciences, ul. Vavilova 38, Moscow, 119991 Russia*

e-mail: karavan@kapella.gri.ru

*** Shubnikov Institute of Crystallography, Russian Academy of Sciences, Leninskiĭ pr. 59, Moscow, 119333 Russia*

e-mail: a.lomov@ns.crys.ras.ru

**** Lebedev Institute of Physics, Russian Academy of Sciences, Leninskiĭ pr. 53, Moscow, 119991 Russia*

Received January 27, 2003

Abstract—The results are presented of the optical and X-ray studies of the structure of *n*-type subsurface GaP(001) layers implanted with 300 keV-He^+- ($D = 10^{16}$ at./cm^2) and 600 keV-Xe^{2+}-ions ($D = 10^{12}$ at./cm^2) and then subjected to electrochemical anodizing in aqueous 0.25 M H^+ solution. It is shown that defects formed in the crystal lattice as a result of this treatment considerably influence the character of electrochemical etching and the structural parameters of the formed layers. It is shown that anodic etching proceeds over the defects, which allows one to obtain oriented systems of pores by choosing the appropriate conditions of preliminary implantation. © *2003 MAIK "Nauka/Interperiodica".*

INTRODUCTION

Defects present in a crystal lattice determine, to a high extent, the physical properties of solids. The size and type of defects influence nucleation of pores during etching of the substrate material. In particular, pores change the potential distribution in the crystal bulk and affect the electrochemical processes at the solid–electrolyte interface [1]. It is well known that the structure of layers in semiconductors with nanopores obtained by anodic etching considerably depends on orientation, conductivity type, and defects in the initial substrate [2–4]. Thus, controlling the defect distribution in the subsurface region of the sample, one can obtain porous layers possessing various properties.

One of the promising methods of producing numerous defects of various types in crystals is their implantation with high-energy ions. The type of defects and their distribution in the subsurface layers are determined not only by the kind and energy of implanted ions but also by the kinetics of defect formation, interaction, accumulation, and migration.

Traditionally, ion implantation has been widely used in technology of micro- and optoelectronics for obtaining semiconductor layers of the given thickness and conductivity type and magnitude [5]. In recent years, ion implantation has also been widely used in nanotechnology, in particular, in synthesis of semiconductor structures with nanometer dimensions and set compositions [6–9]. It is shown [10] that preliminary ion implantation allows one to obtain layers with the ordered pore orientation and control the degree of material porosity. However, up to now, no detailed studies of the influence of the kind of implanted ions, their energy, and dose on the formation of porous layers and their structural parameters have been made.

Below, we describe our experiments on the influence of defects formed after preliminary implantation of gallium phosphide samples with Xe^{2+} and He^+ ions on the morphology and parameters of porous layers obtained after electrochemical anodizing in a 0.25-M H_2SO_4 aqueous solution performed by the methods of Raman scattering and X-ray diffractometry and reflectometry.

SAMPLES AND METHODS OF MEASUREMENTS

The substrates were standard *n*-type crystalline GaP(001) wafers doped with sulfur up to the concentra-

1063-7745/03/4805-0851$24.00 © 2003 MAIK "Nauka/Interperiodica"

tion $N \sim 3 \times 10^{17}$ cm^{-3}. Defects in the subsurface layer were obtained after ion implantation of samples on an accelerator produced by the High-Voltage Engineering B.V. company (Holland). The ions for implantation were selected proceeding from the following. On the one hand, these ions should not directly affect the process of subsequent anodic etching (e.g., owing to the formation of new compounds or electrically active states). On the other hand, in order to obtain qualitatively different effects on the subsurface layers, the selected ions should have considerably different masses. It is well known that implantation with heavy ions change the defect density along the particle track and that the clusters of radiation-induced defects thus formed are oriented along the tracks. In this case, the low ion density after anodic etching can result in the formation of a layer with columnar pores oriented along ion tracks. On the contrary, implantation with light ions gives rise to a more uniform distribution of defects. It is natural to expect that the subsequent anodic etching would result in the formation of porous layers with different structures.

Proceeding from the above criteria, we implanted our samples with helium and xenon ions. The energy E, dose D, and ionic current J were equal to 600 keV, 10^{12} ion/cm^2, and 0.005 μm A/cm^2 for Xe^{++} ions and 300 keV, 10^{16} ion/cm^2, and 0.7 μmA/cm^2 for He^+ ions. The penetration depth of ions, R_p, estimated using the SRIM 2000 program [11] was 0.165 and 1.31 μm for Xe^{2+} and He^+, respectively.

Anodic etching was performed for 20 s in a two-chamber cell with platinum electrodes at the current density $j = 40$ mA/cm^2 in darkness. The electrolyte was a 0.25-M H_2SO_4 aqueous solution. During anodizing, the following processes can occur: complete etching of the material (electropolishing mode), formation of a porous layer with the preservation of the initial external interface, and formation of a porous layer with the displacement of the external interface toward the substrate. Taking into account the fact that, during anodic etching of crystalline GaP, the removal of a pair of Ga and P atoms requires the participation in the process of six to eight charge carriers [12–14], the current flowing in the circuit in the first case provides the removal of a layer of the thickness $t_a \sim 10.15$ μm. If anodizing proceeds by etching away from pores (the second case), then the thickness of the layer thus formed is

$$t_a \approx 0.15/(1 - \nu), \quad (1)$$

where $\nu = \rho/\rho_0$ and ρ and ρ_0 are the densities of the layer formed and the initial substrate, respectively. The third process can proceed if a porous layer contains nanocrystals weakly bound to one another. This results in the detachment of the upper part of the anodized layer and its "inclusion" into the electrolyte. In this case Eq. (1) relating the charge, density, and thickness of the anodized layer becomes invalid. The real porous layer can be noticeably thinner.

Photoluminescence and Raman spectra were recorded on a U-1000 Jobin-Yvon spectrometer with an attached microscope in the mode of studying microsamples in the back reflection geometry at the normal incidence of the radiation onto the sample. The Raman spectra were recorded in the region of the longitudinal (LO) and transverse (TO) optical phonons of a crystalline GaP sample (360 to 420 cm^{-1}). Excitation was attained using the radiation of the 488 nm line of an argon laser focused to a spot with the diameter $d \sim 40$ μm. The intensity was selected empirically below the level at which the laser beam can give rise to radiation damages in the sample. Studying microsamples, we collected the scattered radiation from the region determined by the size of the focal spot and the penetration depth of light in the material or by the depth of focus of a micro-objective (~3–4 μm). For the initial GaP crystal, the penetration depth is ~10 μm (the absorption coefficient equals ~900 cm^{-1}) [14]. Therefore, the thickness of the layer probed is determined by the depth of focus of the micro-objective used. For highly absorptive materials, the region probed is determined only by the depth of the radiation penetration into the sample.

The surface morphology and distortions of the subsurface layers were studied using rocking curves and X-ray reflectometry. The experimental curves were recorded on a TRC-1 triple-crystal X-ray diffractometer. The radiation source was a 1.1-kW X-ray tube with a copper anode ($\lambda = 0.154$ nm). The crystal–monochromator was a grooved Ge single crystal with the triple 004 reflection. The rocking curves (004 reflection) from GaP samples were recorded using the parallel quasidispersion-free geometry of crystals (n, $-m$). The dispersion of the chosen scheme did not exceed a few angular seconds. In order to record the intensity of a specular-reflection signal in X-ray reflectometry, we used a horizontal slit (3 arcmin) before the detector. The curves were recorded in the $\theta/2\theta$ scanning mode. The diffuse-scattering intensity was recorded in the mode of detector scanning at the fixed position of the sample (θ scanning).

DISCUSSION OF RESULTS

It should be noted that the samples prepared from a standard GaP wafer had a mirror-smooth surface. Ion implantation at the selected modes resulted in visible changes of the GaP-substrate surface. Irrespectively of the type of ion implantation, this manifested itself in the formation of a layer with an elevated optical density poorly seen after implantation with Xe^{2+} ions and almost nontransparent with metal luster after implantation with He^+ ions. Upon anodizing, the mirror-smooth portions remained smooth but could be easily observed in the reflected light. The transmission study showed that preliminarily Xe^{2+}-implanted samples looked

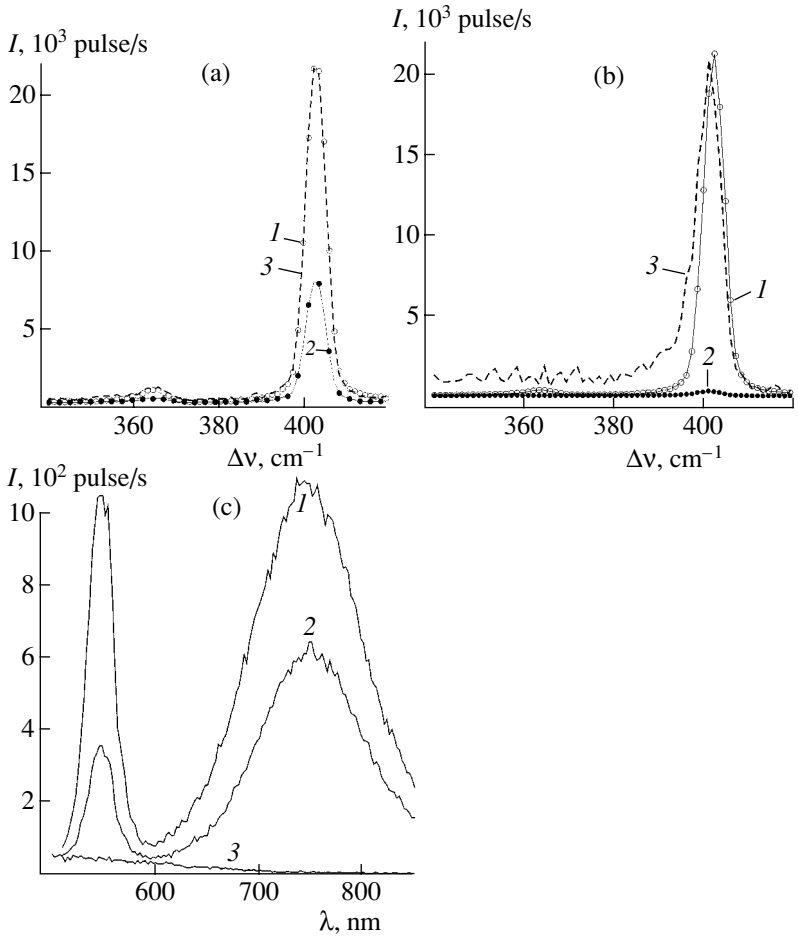

Fig. 1. (a) Raman spectra from the (*1*) initial and (*2*) Xe^{++}-implanted GaP crystals and (*3*) Raman spectrum normalized to the maximum Raman amplitude of the initial GaP sample shown by curve *2*. (b) (*1*) Raman spectra from the initial and (*2*) He^{+}-implanted GaP crystals and (*3*) spectrum from implanted GaP normalized to the Raman amplitude of the initial GaP spectrum. (c) Photoluminescence spectra of the (*1*) initial and (*2*) Xe^{++}- and (*3*) He^{+}-implanted GaP crystals.

lighter, whereas the sample implanted with He^{+} ions remained unchanged.

Raman Scattering

The Raman scattering data for the initial and implanted samples are shown in Fig. 1. Analysis of the spectra shows that they are highly sensitivity to lattice distortions in the subsurface layers. It is seen that, for Xe^{2+}-implanted samples, the intensity of Raman spectra (Fig. 1a) decreases by a factor of about 2.75, whereas the shape of the line of LO vibrations remains practically the same. In this case, we deal with low deformations and small thickness of the disturbed layer, L_{Xe} lower than the depth of focus of the micro-objective and penetration depth of radiation. It is natural to assume that the main contribution to the recorded signal comes from the Raman scattering from the substrate and undisturbed regions of the layer. A decrease in the scattering intensity observed is explained by low *efficiency of Raman scattering* from the implanted layer and higher absorption of both exciting radiation and recorded signal because of the formation of additional levels in the band gap [15].

On the contrary, the Raman spectra from the He^{+}-implanted sample (Fig. 1b) show both qualitative and quantitative changes. The intensity of the LO line decreases by about 70 times; its position is shifted by 1.2 cm^{-1} to the low-frequency range. Moreover, the LO line is broadened and asymmetric. In this case, the Raman spectrum is recorded from a considerably deformed layer with a considerably larger number of defects, which reduce the efficiency of the Raman scattering and give rise to additional absorption. Therefore, no Raman signal is observed from the substrate. This signifies that the penetration depth of the radiation in the defect layer is considerably less than the layer thickness L_{He}. The conclusions made are confirmed by the photoluminescence spectra shown in Fig. 1c. Curve *1* corresponds to photoluminescence from the initial crystal (the band 2.2–2.3 eV corresponds to the transition between the levels formed by impurity *S* acceptors

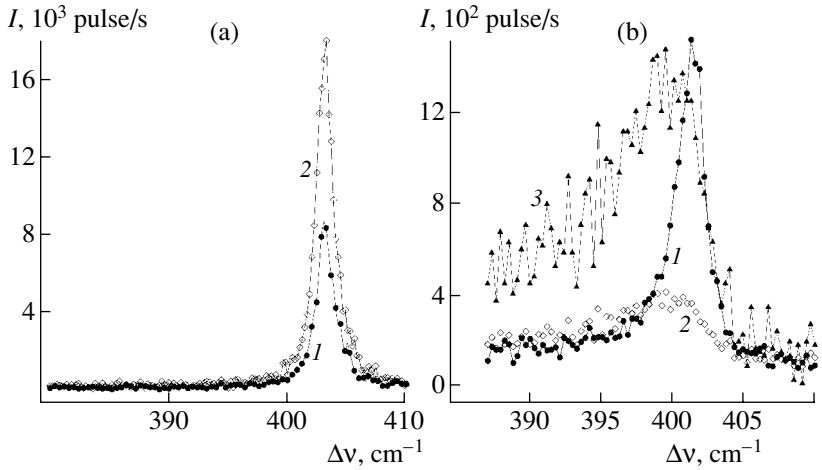

Fig. 2. (a) Raman spectra from a Xe^{++}-implanted GaP sample (*1*) before and (*2*) after anodizing. (b) Raman spectra from a He^{+}-implanted GaP sample (*1*) before and (*2*) after anodizing and (*3*) spectrum shown by curve *2* normalized to the maximum Raman amplitude from the implanted sample.

and Cd donors, whereas the band 1.6–1.8 eV corresponds to the recombination of an exciton of the Cd–O complex to the level of the Cd acceptor [16]. For a Xe^{2+}-implanted sample, the photoluminescence intensity decreases (curve *2*), whereas, for a He^{+}-implanted sample, the photoluminescence signal practically disappears (curve *3*). This indicates that, in the latter case, the exciting radiation cannot penetrate the substrate through the absorbing defect layer L_{He}.

The Raman spectra from anodized samples are shown in Fig. 2. It is seen that, for a Xe^{2+}-implanted sample, the form of the spectrum remains the same (Fig. 2a). Despite a twofold increase in the intensity of the line of LO vibrations, its value is lower than the Raman amplitude from the initial substrate. Therefore, the quenching centers of Raman scattering were not completely removed, and the thickness t_a of the anodized layer seems not to exceed the total thickness L_{Xe} of the disturbed layer. Analysis of the Raman spectra (Fig. 2b) from He^{+}-implanted GaP sample before and after anodizing shows that, in this case, the Raman spectra are qualitatively different. The intensity of the LO line decreases almost by a factor of five and the shape of the spectrum is considerably changed. A broad "band" is observed in the frequency range between the TO and LO vibrations, the so-called Fröhlich mode. Similar bands were also observed in nanocrystalline GaP films obtained by vacuum deposition [17]. The appearance of these modes is associated with vibrational eigenmode of nanocrystals in the frequency range between the TO and LO modes, where the real part of permittivity is negative and the exact resonance position depends on the nanocrystal shape [18]. In this case, a decrease in the intensity of the LO vibrations and the broad line of the Fröhlich mode can be explained by the formation after etching of a layer of rather small GaP nanocrystals of different shapes. It should also be noted that no Raman signal from the substrate is observed and, therefore, the thickness of the anodized layer, t_a, is much less than L_{He}.

X-ray Studies

To confirm the results of optical measurements and obtain the information on the surface state and the structural parameters of the subsurface layers, we performed X-ray studies. The allowance for the background component and appropriate selection of the experimental geometry allowed us to measure the intensity of the specular component of scattering. Figure 3a shows the experimental reflectometry curves obtained from the initial samples in the $\theta/2\theta$ scanning mode (curve *1*) and after ion implantation (curves *3*, *5*) and subsequent anodizing of the samples (curves *7*, *8*). The solid lines show the corresponding theoretical specular-reflection curves (curves *2*, *4*, *6*) calculated within the theory of recurrence relationships [19]. As is seen from Fig. 3a, in the vicinity of $\theta = 0$, the reflectometry curves show a clearly pronounced maximum, a part of the direct beam. The intensity of this beam $I = 0.5I_0$ (where I_0 is the intensity of the X-ray beam in the detector without a crystal–sample) was used to normalize the data when fitting the theoretical and experimental reflectometry curves. This fitting was performed by the least-squares method using the nonlinear algorithm for minimizing the functional χ^2 [20] and a specially developed procedure [21] for processing X-ray diffraction data. Constructing the model of a subsurface layer, we assumed that the sample surface is coated with a film with the thickness t and the roughness σ_i ($i = 0, 1$) at the vacuum–film and film–substrate interfaces, respectively. The roughness was taken into account using the approximation described in [22]. The fitting parameters were thickness t, relative film density ν, and

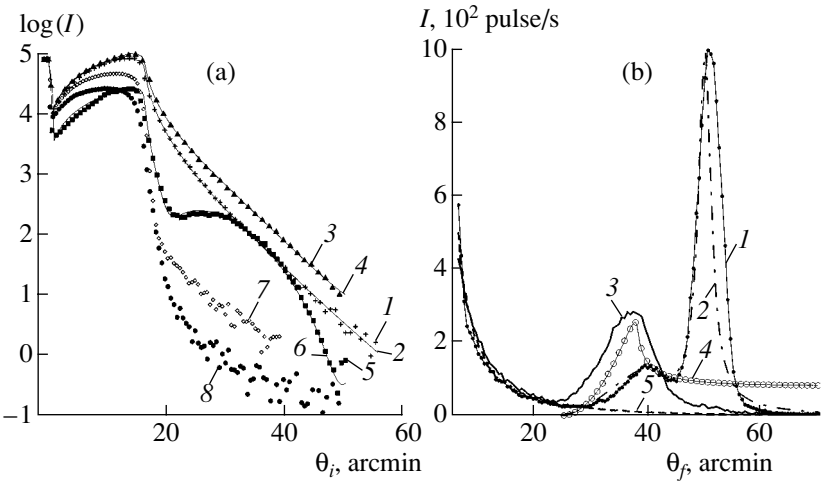

Fig. 3. (a) Fitting of experimental (symbols) and calculated (lines) specular reflection curves from the samples subjected to (*1*, *2*) chemical–mechanical polishing, (*3*, *4*) Xe^{++}-implantation plus (*7*) anodizing, (*5*, *6*) He^{+}-implantation plus (*8*) anodizing. (b) Scattering diagrams obtained at the grazing angle θ_i = 25 arcmin for samples subjected to (*1*, *2*) chemical–mechanical polishing (*1* is the experimental curve and *2* is the calculated curve), and (*3*) Xe^{++}-implantation plus anodizing. (*4*) Transmission coefficient (calculated for a layer with $\nu = 0.63$) and (*5*) the background component Cu$K_{\alpha 1}$ radiation.

roughness at the interfaces σ_i. The theoretical θ_{c0} values and the densities ρ_0 for bulk GaP crystals are 16.6 arcmin and 4.14 g/cm^3, respectively.

The good agreement of the experimental and model curves (Fig. 3a) indicates that total scattering from both initial and implanted samples consists mainly of the specular component. The surface of the initial sample has the roughness $\sigma_0 \sim 1.6$ nm. Proceeding to the analysis of the reflectometry curves from implanted sample (curves *3* and *5* in Fig. 3a), we should like to note that the dependence of the scattering intensity *I* on the grazing angle θ_i at angles exceeding θ_c considerably differs from the corresponding dependence for the initial sample. The rocking curve from the He^{+}-implanted sample (curve *5*) has a broad hump because of thickness oscillations—a result of the interference of the waves scattered from the internal and external interfaces of the thin film on the sample surface. At an angle ~50 arcmin, the curve dramatically rises, which is associated with the beginning of the next oscillation. The fixed film has the following parameters: thickness $t \approx 8$ nm, density equal to 46% of the substrate density, roughness 1.3 nm on the surface and 1.1 nm at the lower film–substrate interface. The characteristics of the reflectometry curve from the Xe^{++}-implanted sample (curve *3*) are less impressive: thickness oscillations of the intensity at angles $\theta_i > \theta_c$ are practically absent. However, processing the results obtained, we see that the surface is also coated with a 23-nm-thick film with the density higher by 3–5% than the density of the bulk sample. The data on fitting of the film parameters and the interface roughness are listed in the table. Existence of films with relatively sharp boundaries on the surface of the implanted samples was established earlier [23]. We believe that the formation of these films as a result of interactions of ions with the substrate matrix (due to amorphization of subsurface layers, atomization of the material, formation of the radiation-induced vacancies during He^{+} implantation or interstitials during X^{++} implantation) is hardly probable. Most probably, their appearance is associated with the deposition of the residual impurity atoms in the chamber during ion implantation. We should like to indicate that the thicknesses fixed at the GaP surface by reflectometry are much less than the depth of light penetration into the substrate. Therefore, the transformation of the optical spectra observed (Fig. 1) is associated with the distortion of the crystal lattice of deeper layers of the sample.

After anodizing, the reflectometry curves become different. At grazing angles exceeding the critical angle, the specular-reflection intensity becomes practically zero (Fig. 3a, curves *7* and *8*). The additional experiments in the θ-scan mode show (Fig. 3b, curve *3*) that, at grazing angles exceeding θ_c, scattering is determined mainly by the diffuse component, which results in the appearance of an intense Yoneda peak at the reflection angles $\theta_f = \theta_i + 0.9\theta_c$ [24] and the low-intensity specular-reflection component at $\theta_f = 2\theta_i$ on the scattering diagram. For comparison, the same figure also shows the experimental and theoretical scattering diagrams (curves *1* and *2*, respectively) for the initial GaP substrate. In simulation, we assumed that the substrate surface has the roughness $\sigma_0 = 1.6$ nm. The diffuse-scattering intensity from the Xe^{++}-implanted and then anodized sample (Fig. 3b, curve *3*) exceeds the intensity of scattering from the initial substrate, whereas the diffuse-scattering maximum is displaced toward smaller angles. Comparing the angular positions of the maxima of transmission coefficients (curve *4*) and diffuse scattering (curve *3*), we managed

Parameters of subsurface layers of GaP samples according to X-ray reflectometry data

Mode of processing of GaP(001) substrates	Layer parameters			
	t, nm	σ_0, nm	σ_1, nm	$\nu = \rho/\rho_0$
Chemical–mechanical polishing	>500	1.6(2)		1.00(1)
Implantation: He^+, E = 300 keV, $D = 10^{16}$ atoms/cm^2	8.3(2)	1.3(2)	1.1(2)	0.50(2)
Implantation: He^+, E = 300 keV, $D = 10^{16}$ atoms/cm^2 and anodizing: current I = 2 mA/cm^2, etching time 5 min	>100			0.55(3)
Implantation: Xe^{++}, E = 600 keV, $D = 10^{13}$ atoms/cm^2	6.0(8)	1.2(1)		1.06(3)
Implantation: Xe^{++}, E = 600 keV, $D = 10^{13}$ atoms/cm^2 and anodizing: current I = 2 mA/cm^2, etching time 5 min	>100			0.63(3)

to estimate the density of the anodized layer as ~63 and ~55% for samples preliminarily implanted with Xe^{++} and He^+ ions, respectively. However, the experimental data obtained yielded only the average layer density. The known theories of X-ray specular reflection and diffuse scattering at small grazing angles are valid only in the first approximation of the perturbation theory, i.e., at roughness $\sigma \sim 10\lambda$ [22], and, therefore, no attempts were made to fit curves *7* and *8* in Fig. 3a.

The data obtained allow us to state that anodizing results in the formation of porous layers of various densities in the subsurface layer, which, depending on the structure and morphology of these layers, differently suppress the specular component of scattering and give rise to intense diffuse scattering. In this case, the pore structure depends on the parameters of preliminary implantation.

To answer the question of whether the disturbed or nondisturbed layers can be etched away at the initial stage of anodizing, we have to analyze the results of X-ray diffraction measurements.

Figure 4 shows the rocking curves obtained before (*1*) and after (*2*) anodizing of Xe^{++}- (Fig. 4a) and He^+-implanted (Fig. 4c) GaP samples and the rocking curves from the initial substrate (*3*). It is seen that, in addition to the basic Bragg maximum from the substrate at the angle $\Delta\theta = \theta - \theta_B = 0$, the rocking curves have additional diffraction regions on the side of angles smaller than the Bragg angle θ_B. This signifies that implantation results in the formation of a subsurface layer with an elevated lattice parameter $\Delta d/d = -\cot\theta_B\Delta\theta$ along the surface normal. The intensity of additional scattering and the shapes of the curves in Figs. 4a and 4c depend on the thickness L of the disturbed layers, the deformation $\Delta d(z)/d$, and the static Debye–Waller factor $\exp(-w(z))$. Within the framework of the discrete model [21], we fitted ($\chi^2 \approx 7$) the theoretical and experimental curves. Curve *4* in Fig. 4a corresponds to the calculated rocking curve for the Xe^{++}-implanted sample. The profiles of the distributions of deformations $\Delta d(z)/d$ and concentrations $C(z)$ of incorporated atoms over the depths of the same sample are shown in Fig. 4b. It is seen that the deformation maximum is observed at a depth of ~0.16 μm, which corresponds to the average penetration depth R of xenon ions obtained by simulation using the program from [11]. According to the X-ray diffraction data, the thickness L_{Xe} of a disturbed layer is ~0.25 μm. After anodizing, the rocking curve (Fig. 4a, curve *2*) changed considerably: it became practically symmetric and lost its characteristic features at the tails. Therefore, the selected anodizing mode practically etches away lattice defects from the implanted layer of the thickness L_{Xe}, which, in this case, should be comparable with the assumed anodizing depth t_a. At the average density of a formed layer ν (see table), Eq. (1) yields that the thickness of the anodized layer $t_a \sim 0.4$ μm. This agrees well with the data on Raman scattering (the intensity of the mode of LO vibrations is reconstructed only partly) and X-ray reflectometry (anodizing results in the formation of a large number of etched pores in a layer with the thickness exceeding 0.1 μm). Moreover, the layer-by-layer etching of the sample for a depth of $t_a \sim 0.15$ μm (effect of electropolishing) results in the removal of only a part of the disturbed layer (Fig. 4b). Obviously, in a sample preliminarily implanted with Xe^{++} ions, anodizing proceeds with the formation of pores, whereas the upper boundary of the sample remains practically unchanged.

The anodizing mode used in the case of a preliminarily He^+-implanted sample cannot remove the disturbed layer. It is seen from Fig. 4c that the rocking curves (curves *1*, *2*) are not considerably changed—neither the angular positions ($\Delta\theta = -510$ arc s) nor the intensity of the main diffraction peak from the layer are changed. However, the anodizing process took place, which is confirmed by the absence of a broad hump (*M*) on curve *2* (Fig. 4c) and the rocking-curve tail corresponding to the layer regions characterized by low deformations. Moreover, a slight increase in the oscillation period indicates the change in the disturbed-layer thickness L_{He} by δL_{He}, which, in the kinematical approximation, can be obtained from the relationship [25]

$$L = \lambda\gamma_0/\Delta\theta\sin 2\theta_B, \qquad (2)$$

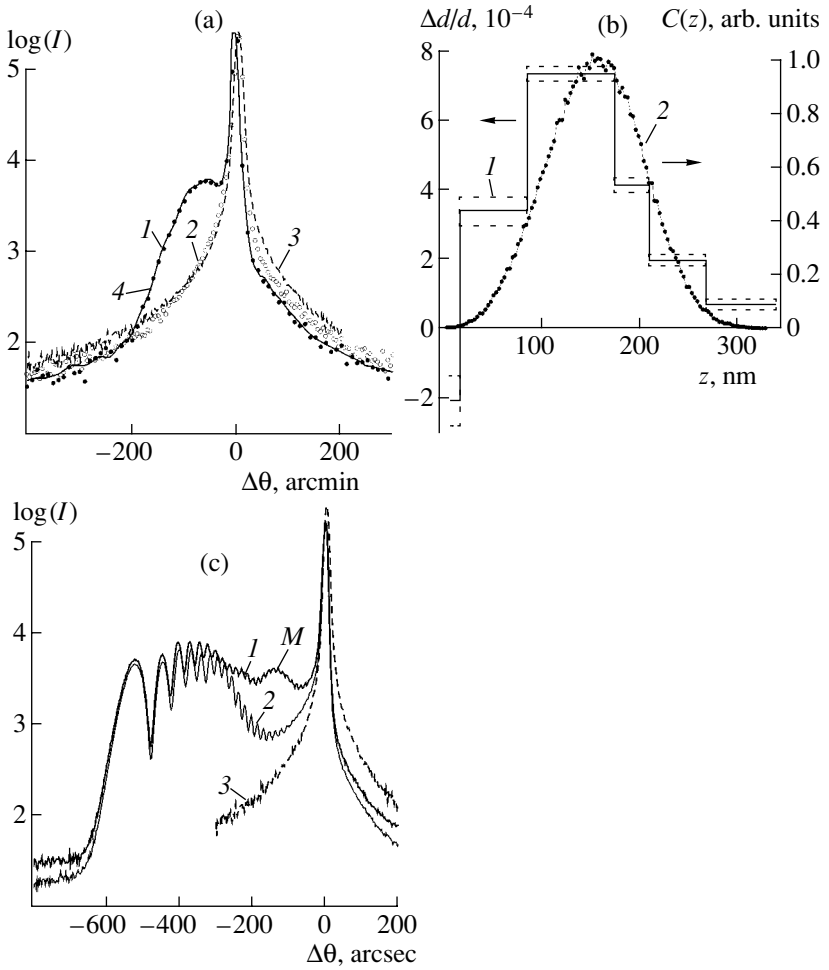

Fig. 4. (a) Rocking curves from Xe^{++}-implanted samples (*1*) before and (*2*) after anodizing and from (*3*) the initial sample. (*4*) Fitting of the calculated ($\chi^2 = 7.5$) and experimental curves. (b) (*1*) Reconstructed distribution of deformation $\Delta d/d$ in the subsurface layer of the Xe^{++}-implanted sample and (*2*) ion distribution $C(z)$ over the depth of the subsurface layer obtained by the Monte Carlo method. (c) Rocking curves from He^{+}-implanted samples (*1*) before and (*2*) after anodizing and from (*3*) the initial sample. For *M* see the text.

where γ_0 is the directional cosine and $\Delta\theta$ is the period of oscillations. Differentiating this equation with respect to $\Delta\theta$, we obtain

$$\delta L \approx -\lambda\gamma_0\delta(\Delta\theta)/((\Delta\theta_{av})^2 \sin 2\theta_B). \quad (3)$$

It follows from the rocking curves in Fig. 4c that $\delta(\Delta\theta) = \Delta\theta_{av}/16$, where $\Delta\theta_{av}$ is the average period of oscillations. Then, the corresponding average change in the thickness is $\delta L_{He} = 0.06$ μm, and the layer thickness is $L_{He} \sim 1.2$ μm. A decrease by δL_{He} in the thickness of an implanted layer after anodizing is much less (even in the case of electropolishing) than the assumed value t_a. Thus, for He^{+}-implanted samples, anodic etching removes the regions subjected to considerable amorphization, which give no noticeable contribution to diffraction scattering. Then, anodizing proceeds in the near-boundary regions of slightly distorted layers and propagates into the sample bulk. The analogous etching mechanism was observed in GaAs(001) samples [23]. Comparing the results obtained with the optical data, we see that nanocrystals that contribute to the Fröhlich mode of Raman scattering are formed in the subsurface layer with the density $\nu \sim 0.5$ (see table) and thickness $t_a \sim 0.3$ μm. During anodizing, some etched nanocrystals become free and precipitate in electrolyte, whereas the remaining ones, still bound to the substrate, are misoriented under the action of surface tension. As a result, the upper subsurface layer of the sample stops scattering X-ray radiation coherently, which results in the disappearance of the hump *M* on curve *2* (Fig. 4c). The thickness of a layer scattering kinematically, which is determined from the half-width of the hump *M*, ranges, in accordance with Eq. (2), from 0.36 to 0.40 μm, which confirms the assumption about the propagation of the anodizing process to strongly amorphized regions.

Scanning electron microscopy. The optical and X-ray diffraction data obtained unambiguously indicate the formation of micropores in the subsurface GaP

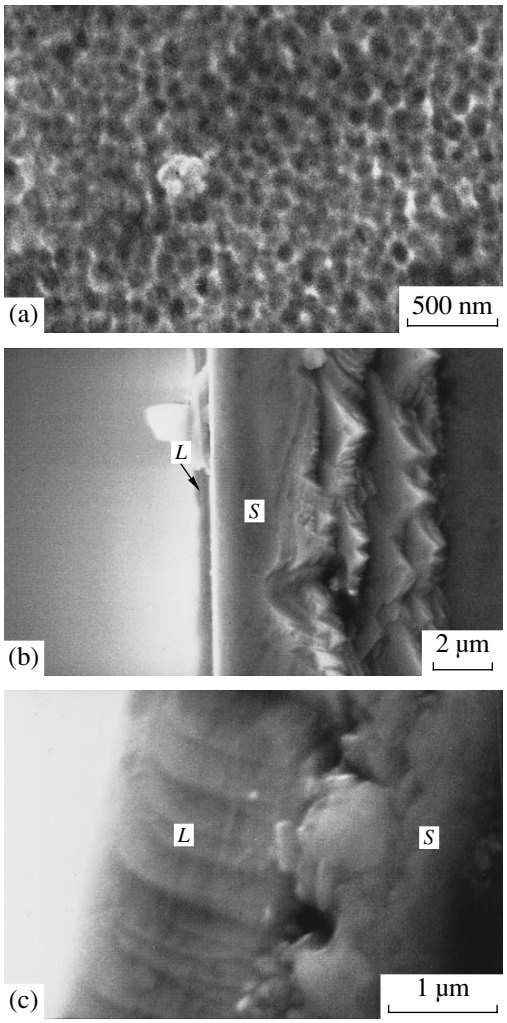

Fig. 5. Micrographs of (a) the surface of Xe^{++}-implanted anodized sample; (b) Xe^{++}-implanted and (c) He^{+}-implanted cleavages obtained on an FEI XL30 scanning electron microscope at the accelerating voltage 15 keV. *L* and *S* denote the layer and the substrate, respectively.

(001) layer. This result agrees well with the micrographs of the sample surfaces obtained in secondary electrons with a Philips XL30 TMP scanning electron microscope. It is seen from Fig. 5a that, during anodizing of a Xe^{++}-implanted sample, a porous layer is formed with the pore size ranging from 30 to 90 nm. A similar surface state is also observed for a He^{+}-implanted sample, but in this case, the sample surface shows the presence of inhomogeneities on two different scales. Along with rather few pores with the size ranging from ~100 to 120 nm, there are some regions with pores about 30 nm in size and even less. Figures 5b and 5c show the micrographs of the cleavages of the Xe^{++}- and He^{+}-implanted samples, respectively. It is seen that the subsurface layers of these samples have the thicknesses ~0.4 and 1.6 μm, respectively.

CONCLUSIONS

Thus, the use of the methods of X-ray diffractometry and reflectometry and Raman scattering and photoluminescence allowed us to characterize in detail porous layers formed in the subsurface region of single-crystal gallium phosphide wafers first implanted with Xe^{++} and He^{+} lions and then etched electrochemically in the anodizing mode. The characteristics of anodizing are studied depending on the dose and mass of implanted ions. It is shown that the formation of porous structure takes place mainly because of etching away defects, which allows one to use the preliminary ion implantation for more efficient control of the parameters of porous layers. It is established that anodizing of GaP(001) substrates preliminarily implanted with He^{+} ions at a dose of 10^{16} at./cm^2 results in the formation of porous layers containing nanocrystals.

ACKNOWLEDGMENTS

The authors are grateful to A.L. Vasil'ev for obtaining electron micrographs of the samples and G.V. Ganin for his help in preparing illustrations.

This study was supported by the Russian Foundation for Basic Research, project nos. 00-02-17716, 00-02-17864, and 00-02-17521, the programs Integration of Higher School and Fundamental Sciences, project no. B-0094, the program *Low-Dimensional Quantum Nanostructures*, of the Presidium of the Russian Academy of Sciences, projects 2.3 and 6.8, and Federal Scientific–Technological Program, project Nonequilibrium Phenomena and Fast Processes in Nanostructures.

REFERENCES

1. P. Schmuki and L. E. Erickson, Appl. Phys. Lett. **73** (18), 2600 (1998).
2. P. Schmuki, L. E. Erickson, and D. J. Lockwood, J. Porous Mater. **7** (1/3), 233 (2000).
3. P. Schmuki, L. E. Erickson, and D. J. Lockwood, Phys. Rev. Lett. **80**, 4060 (1998).
4. B. Surma, A. Wnuk, A. Misiuk, *et al.*, Cryst. Res. Technol. **34**, 689 (1999).
5. L. Hanley and S. B. Sinnott, Surf. Sci. **500**, 500 (2002).
6. Y. Kanemitsu, H. Tanaka, T. Kushida, *et al.*, Physica E (Amsterdam) **7** (3–4), 322 (2000).
7. O. González-Varona, A. Pérez-Rodriguez, O. Garrido, *et al.*, Nucl. Instrum. Methods Phys. Res. B **161–163**, 904 (2000).
8. J. K. N. Lindner and B. Stritzker, Nucl. Instrum. Methods Phys. Res. B **148** (1–4), 528 (1999).
9. A. Tchebotareva, J. L. Brebner, S. Roorda, *et al.*, J. Appl. Phys. **92** (8), 4664 (2002).
10. I. M. Tiginyanu, C. Schwab, J.-J. Grob, *et al.*, Appl. Phys. Lett. **71** (26), 3829 (1997).
11. J. F. Ziegler and J. P. Biersack, SRIM-2000.39, Version available at http://www.research.ibm.com/ionbeams.

12. H. H. Goossens and W. P. Gomes, Electrochim. Acta **37** (5), 811 (1992).
13. P. Shmuki, J. Fraser, C. M. Vitus, *et al.*, J. Electrochem. Soc. **143** (10), 3316 (1996).
14. *Semiconductors and Semimetals*, Vol. 3: *Optical Properties of III–V Compounds*, Ed. by R. K. Willardson and A. C. Beer (Academic, New York, 1967; Mir, Moscow, 1970).
15. H. Takamatsu, S. Sumie, T. Morimoto, *et al.*, J. Appl. Phys. **78** (3), 1504 (1995).
16. K. Seeger, *Semiconductor Physics* (Springer, Vienna, 1973; Mir, Moscow, 1977).
17. S. Hayashi and R. Ruppin, J. Phys. C **18**, 2583 (1985).
18. E. F. Venger, A. V. Goncharenko, and M. L. Dmitruk, *Optics of Small Particles and Disperse Media* (Naukova Dumka, Kiev, 1999).
19. V. A. Bushuev, A. A. Lomov, and A. G. Sutyrin, Kristallografiya **47** (4), 741 (2002) [Crystallogr. Rep. **47**, 683 (2002)].
20. W. T. Eadie, D. Dryard, F. E. James, M. Roos, and B. Saboulet, *Statistical Methods and Experimental Physics* (North-Holland, Amsterdam, 1971; Atomizdat, Moscow, 1976).
21. A. M. Afanas'ev, M. A. Chuev, R. M. Imamov, *et al.*, Kristallografiya **42** (3), 514 (1997) [Crystallogr. Rep. **42**, 467 (1997)].
22. L. Nevot and P. Croce, Rev. Phys. Appl. **15** (4), 761 (1980).
23. A. A. Lomov, V. A. Karavanskiĭ, R. M. Imamov, *et al.*, Kristallografiya **47** (6), 1122 (2002) [Crystallogr. Rep. **47**, 1051 (2002)].
24. V. A. Bushuev and A. P. Petrakov, in *Proceedings of National Conference on Use of X-Ray and Synchrotron Radiations, Neutrons, and Electrons in Studies of Materials* (Dubna, 1998), Vol. 2, p. 188.
25. D. K. Bowen and B. K. Tanner, *High Resolution X-Ray Diffractometry and Topography* (Taylor and Francis, London, 1998; Nauka, St. Petersburg, 2002).

Translated by L. Man

Crystallography Reports, Vol. 48, No. 5, 2003, pp. 860–867. Translated from Kristallografiya, Vol. 48, No. 5, 2003, pp. 921–929.

SURFACE, THIN FILMS

Dedicated to the 60th Anniversary of the Shubnikov Institute of Crystallography of the Russian Academy of Sciences

Restoration of Structure of Thin Multilayer Films from Reflectivity Data by Stepwise Model Refinement

L. G. Yanusova[1], S. F. Borisova[1], V. V. Volkov[1], S. B. Astaf'ev[1], and B. M. Shchedrin[1, 2]

[1] *Shubnikov Institute of Crystallography, Russian Academy of Sciences, Leninskiĭ pr. 59, Moscow, 119333 Russia*

e-mail: yanusova@ns.crys.ras.ru

[2] *Moscow State University, Vorob'evy gory, Moscow, 119992*

Received October 9, 2002

Abstract—The computational experiment on the restoration of the model parameters of the cross-section profile of the scattering density of thin multilayer films is described. It is shown that the use of the stepwise model of the structure, which is described by the thickness, density, absorption, and roughness parameters makes the problem of profile restoration multimodal and ill-conditioned. The analysis of the numerical experiments performed allowed us to propose a procedure of consecutive refinement of the initial-model parameters using the results of the local minimization of the discrepancy functional applied for the characteristic segments of the reflectivity curve. The methods proposed were used to restore the structure of a multilayer film deposited on a silicon substrate by the Langmuir–Blodgett method. © *2003 MAIK "Nauka/Interperiodica".*

INTRODUCTION

The development of the nanotechnologies that require the use of multilayer film structures gave rise to creation of methods of reliable control of the thickness and electron density of layers and other film parameters, because even slight deviations from the necessary parameters during film deposition can considerably change the characteristics of the elements made on the basis of these films. The method of X-ray reflectometry enables one to restore the transverse electron-density profile by analyzing specular-reflection intensity curves. To date, there is no reliable method of solving this problem for an arbitrary sample, and, therefore, the successive solution of the problem is determined by researchers' experience and favorable circumstances. Numerous attempts has been made to develop general methodological recommendations to facilitate the solution of this problem.

The interpretation of experimental reflectometry data is associated with best possible fitting of the experimentally measured intensities of reflections and the values computed based on the mathematical model of the film structure. For the successful solution of this problem, it is necessary not only to have reliable scattered intensities from the sample but also a sufficiently adequate mathematical model of its structure.

The initial parameters of the model are usually selected proceeding from the available information on the object studied. Hereafter, this set of values is referred to as the "initial model." The objective function that describes the agreement between the experimental, I_{exp}, and theoretical, I_{mod}, curves is selected in accordance with the Fisher maximum likelihood principle [1]. However, it is frequently forgotten that the conclusion made from the mathematical statistics that the following squared objective function is preferable

$$\Phi = \chi^2 = \frac{1}{M-N}\sum_{i=1}^{M} w_i(I_{exp} - I_{mod})^2, \qquad (1)$$

where M is the number of points on the curve (the number of angular counts) and N is the number of the model parameters, is valid only if the estimated weight functions w_i (the reciprocal values of the dispersion of deviations) are known. It is shown in [2, 3] that in practice some other objective functions correspond to the maximum likelihood principle. Thus, the selection of the weight function is very important for minimization of the functional Φ. Below, we sought the optimum model parameters using the squared functional described by Eq. (1).

One has to develop not only the methods of the search for the minimum value but also the tactics of their application to real objects, because, searching for the local minima, one has to be able to be sure that the minimum value obtained in the process of descent is the estimate of an isolated point of the minimum and not

1063-7745/03/4805-0860$24.00 © 2003 MAIK "Nauka/Interperiodica"

the "bottom of a ravine" [4]. When searching for the global minimum, one can be "lost" among the valley hills of if there are no appropriate physical criteria for diagnostics of the global minimum.

The practice of density-profile restoration from the reflectivity curve using the REFLAN and FITRXN software packages [5, 6] for determining model parameters of the film structure and the algorithms of the search for the global minimum [7] showed that, in some instances, no solution can be obtained.

To solve the above problems, we performed the computation experiment in order to restore the structures of some multilayer films with various layer compositions. The basic experiment covered the film models consisting of one to five layers of various densities and thicknesses (we also considered the variants with the periodic repetition of the chosen set of layers, hereafter referred to as "the unit cell"). One should note that the periodic repetition of the layers does not change the number the model parameters, because the number of these periodic repetitions is specified, with the period being determined by the total thickness of the unit-cell layers.

The REFLAN and FITRXN software packages used in our study are based on the different algorithms of local minimization, NL2SOL [8] and AMOEBA [9], respectively. Some comparative characteristics of the packages will be considered in the description of the computational experiment, but here, we should like to note that the comparison of advantages and disadvantages of these programs was out of the scope of this paper.

EXPERIMENTAL

Mathematical Model of Film and Corresponding X-ray Scattering Intensity Curve

The profile of the scattering density $\mathrm{Re}\rho(z)$ is represented as a set of homogeneous layers of finite thicknesses deposited onto a semi-infinite substrate. Each *i*th layer is characterized by the following four parameters: d_i is the width, $\mathrm{Re}\rho_i$ is the scattering density, $\beta_i = \mathrm{Im}\rho_i$ is the radiation absorption, and σ_i is the roughness, which simulates statistical disturbance of the film layers at their interfaces (width of the disturbed layer). In the analytical form, the scattering density for the given set of *n* layers can be written as

$$\rho(z) = \sum_{i=1}^{n} \rho_i [f(-(z - z_i)/\sigma_i) - f(-(z - z_{i-1})/\sigma_{i-1})] + \rho_{n+1}, \quad (2)$$

where ρ_{n+1} is the substrate density, $z_0 = 0$, *n* is the number of layers, z_i is coordinate of the interface between the $(i + 1)$th and *i*th layers, and $d_i = z_{i+1} - z_i$,

$$f(z) = \frac{1}{\sqrt{\pi}} \int_{-\infty}^{z} \exp(-l^2/2)\,dl,$$

where *l* is an integration variable.

The number of periodic repetitions of the unit cell is specified in the model. Periodicity of unit-cells packing in the film can be determined directly from the Bragg peaks present on the reflectivity curve; the distance between these peaks determines the period value. The model was assumed to be ideal, and the simulated scattering curve played the role of the experimental data. We made an attempt to restore the "ideal" model from the "experimental" scattering curve using various initial models.

The initial model of the structure was chosen at random but it should meet a number of conditions. The deviations of d_i and $\mathrm{Re}\rho_i$ for any layers should not exceed 50% of the respective values of the "true" model, with the total thickness of the film (or of the periodically repeated unit cell) being presented. The models selected could have both symmetric and asymmetric unit cells. For all the structures considered, the substrate parameter was $\mathrm{Re}\rho_i = 0.71$, which corresponded to the scattering density of silicon. Scattering intensity curves from the models were calculated for CuK_α radiation ($\lambda = 1.5420$ Å) in the range of scattering angles $0° < \theta < 8°$ conventionally used in the real reflectometry measurements.

The calculated intensity curves were distorted either by addition of the Gaussian noise or of constant relative deviation within the whole angular range or, in order to imitate the real experiment, by deviations dependent on an angular range: 5% for the grazing angles $0° < \theta < 2°$ in the initial part of the curve, 10–20% in the middle range ($2° < \theta < 5°$), and up to 50% for the end part of the reflectogram ($5° < \theta < 8°$).

Usually, we managed to restore the density profile using the above software packages in an automatic mode up to a four-layer model (from both the exact and "noisy" curves); therefore, the focus was on five-layer models.

The d_i and $\mathrm{Re}\rho_i$ values were selected in accordance with the characteristic parameters of the fatty acids often used for synthesizing organic films. We analyzed the restored structures of a five-layer film with the parameters $d_1 = d_5 = 1.0$, $d_2 = d_4 = 26.0$, $d_3 = 6.0$ Å and $\mathrm{Re}\rho_1 = \mathrm{Re}\rho_2 = 0.14$, $\mathrm{Re}\rho_1 = \mathrm{Re}\rho_2 = 0.47$, $\mathrm{Re}\rho_3 = 0.84$ (one unit cell) and a film with tenfold periodic repetition of the same set of layers (10 unit cells) using the arbitrary approximations selected in a way to cover the most typical variants of deviations from the true model (Fig. 1).

The β_i values in the given experiment were not varied because it was established earlier that the values of these parameters are one order of magnitude lower than

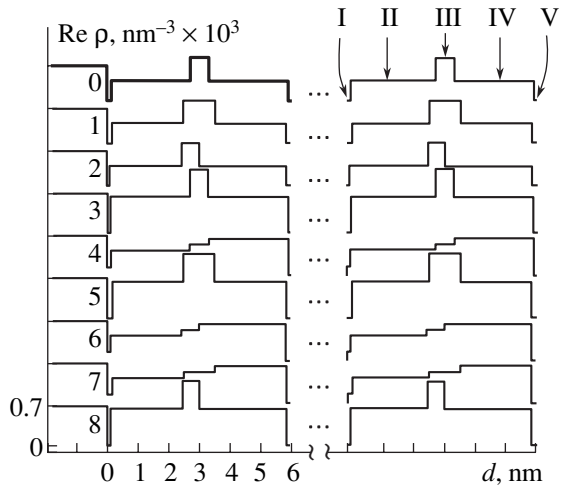

Fig. 1. Variants of scattering-density profiles of the unit cells of the model structure assumed to be (0) "ideal" and (1–8) starting models. The structures consisting of one and ten cells on a silicon substrate were considered. The substrate corresponds to negative *d* values. Discontinuity along the *d* axis signifies unit-cells repetition. Numbers of layers in the unit cell are indicated by Roman numerals. For more clear presentation, the structures are displaced by 0.7×10^3 along the vertical axis.

$\mathrm{Re}\rho_i$, and, therefore, their influence on the restoration is negligible, whereas the repeated local minimization with the preliminary $\mathrm{Re}\rho_i$ values results rather fast in good estimates of β_i. The results obtained at the variation of the parameters σ_i are considered below.

Choice of Weights of the Object Function

The essential feature of refleclometry is a fast fall of the scattering intensity with an increase in the grazing angle of the incident beam. In practice, the range of change can reach six to eight orders of magnitude, which, without the introduction of the weight coefficients w_i, results in the loss of a considerable part of the information contained in the objective function described by Eq. (1), because the differences between the experimental and calculated model intensities $I_{\mathrm{exp}} - I_{\mathrm{mod}}$ at pronounced grazing angles become negligible in comparison with the differences in the vicinity of the zero angle. Thus, the information on fine details of the sample structure is lost. The influence of these details is seen on the scattered-intensity curve only with an increase in the grazing angle.

The optimum method of leveling of the contributions of the $I_{\mathrm{exp}} - I_{\mathrm{mod}}$ differences in Eq. (1) was suggested in [6], where the weight function is determined by the Fresnel law.

We used the dependence $w_i = I_i^{-2}$ that also levels the contributions of the differences but is independent of the violation of the Fresnel law in the case of nonzero absorption. Therefore, hereafter, we describe the results obtained with these weight coefficients.

Computational Experiment

The ideal structure of the film was restored by refining the initial model using the local minimization of functional (1) and the programs mentioned above.

Two types of models (consisting of one and ten unit cells) were used. Density profiles of eight cells used in the experiment are shown in Fig. 1. We studied the possible model restoration based on both exact reflectivity curves and the curves with random deviations from the estimated values, which imitated the measurement errors in the real experiment.

The minimum of the objective function was sought in the restricted range ($p_{\min}$, $p_{\max}$) of each physical parameter of the model p_i. The limiting values of the range were used in the corresponding packages to normalize the parameter values, with their working values in the FITRXN program being obtained by dividing $(p_{\max} + p_{\min})/2$ into two, and in REFLAN, by the transition from the physical values of p_i to the conditional ones t_i according to the formula

$$p_i = (p_{\max} + p_{\min})/2 + \sin(t_i)(p_{\max} - p_{\min})/2. \qquad (3)$$

Thus, in the first software package, the conditional minimization was made, whereas, in the second one, unconditional minimization was made.

For the majority of the initial models with the five-layer unit cell, all the variants of the computations resulted in the solution after one local minimization using the REFLAN program. An interesting fact was observed: the noisy curve gave a solution with a better convergence than the noise-free curve. Of all the model computations, only two variants (model 1 with 10% noise and model 2 with 25% noise) required two-stage local minimization.

If the local minimization with use of all the points of the intensity curve gave no satisfactory solution, then the range of curve definition, in which the calculated curve is fitted to the experimental curve, was decreased in such a way that considerable divergence of the curves in the remaining range could be observed within only one subrange.

After fitting the calculated and experimental intensity curves within the reduced range, this range was gradually increased up to covering the whole range; at each step of this procedure, the curves were fitted again. For the eight starting models considered in the article, the refinement using the FITRXN software package was made within three steps of increasing the range for models 1 and 4; within four steps for models 5, 6, 7 and 8; and only one step of the local minimization within the whole angular range for model 2. It should be noted that the search for a model using the REFLAN program was faster, which seems to be associated with a better NL2SOL algorithm of the local minimization. This

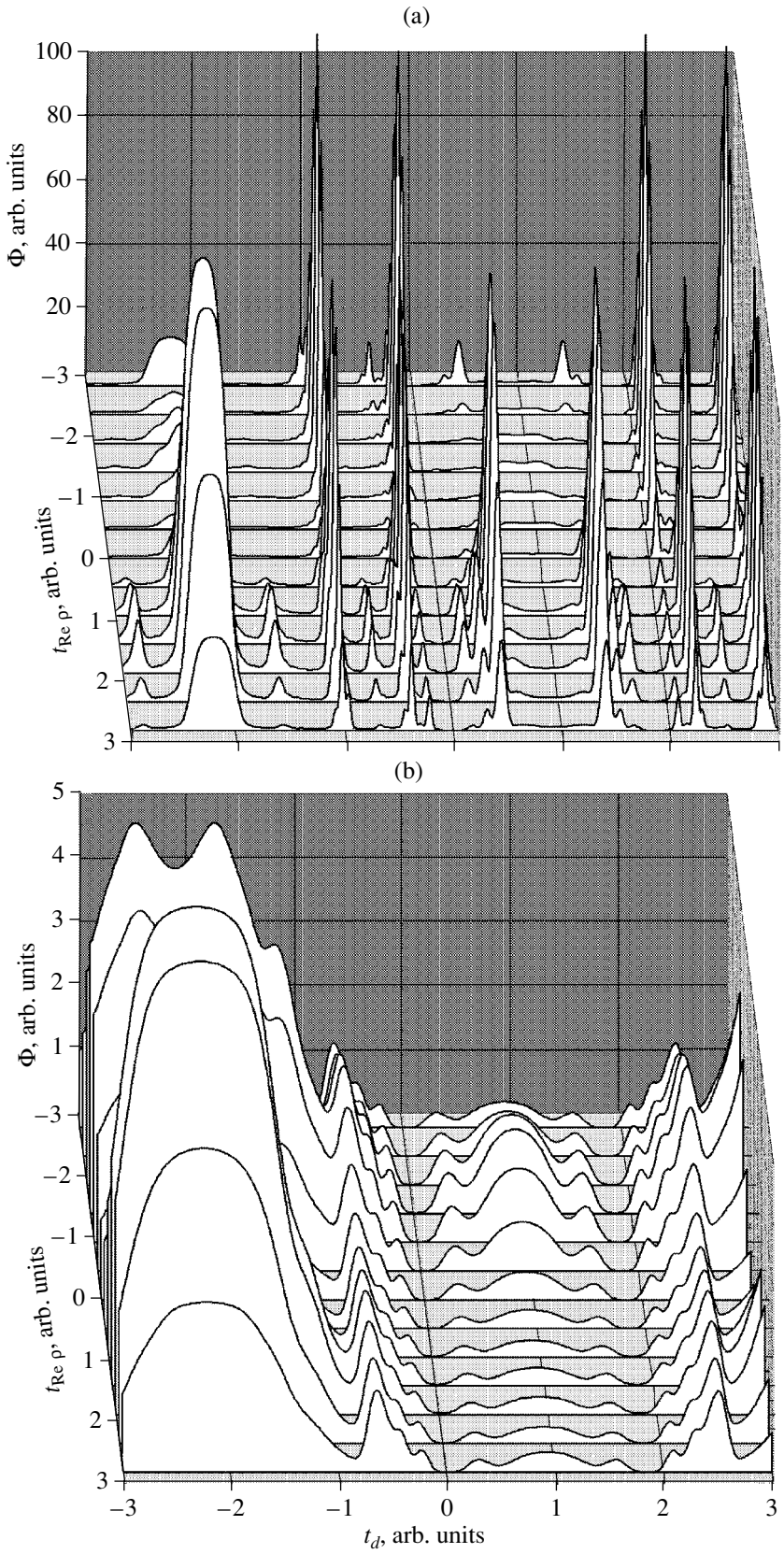

Fig. 2. Two-dimensional sections of the surface of the discrepancy functional Φ described by Eq. (1) with respect to the parameters t_d and $t_{Re\rho}$ corresponding to the thickness and density of unit-cell layer II according to recalculation formula (3) in the vicinity of the global-minimum point for model 5 (Fig. 1): (a) section for calculation of Φ using all the points of the curve ($0 < q_z < 10.6\ nm^{-1}$) and for the reduced range ($0 < q_z < 3.5\ nm^{-1}$) (b).

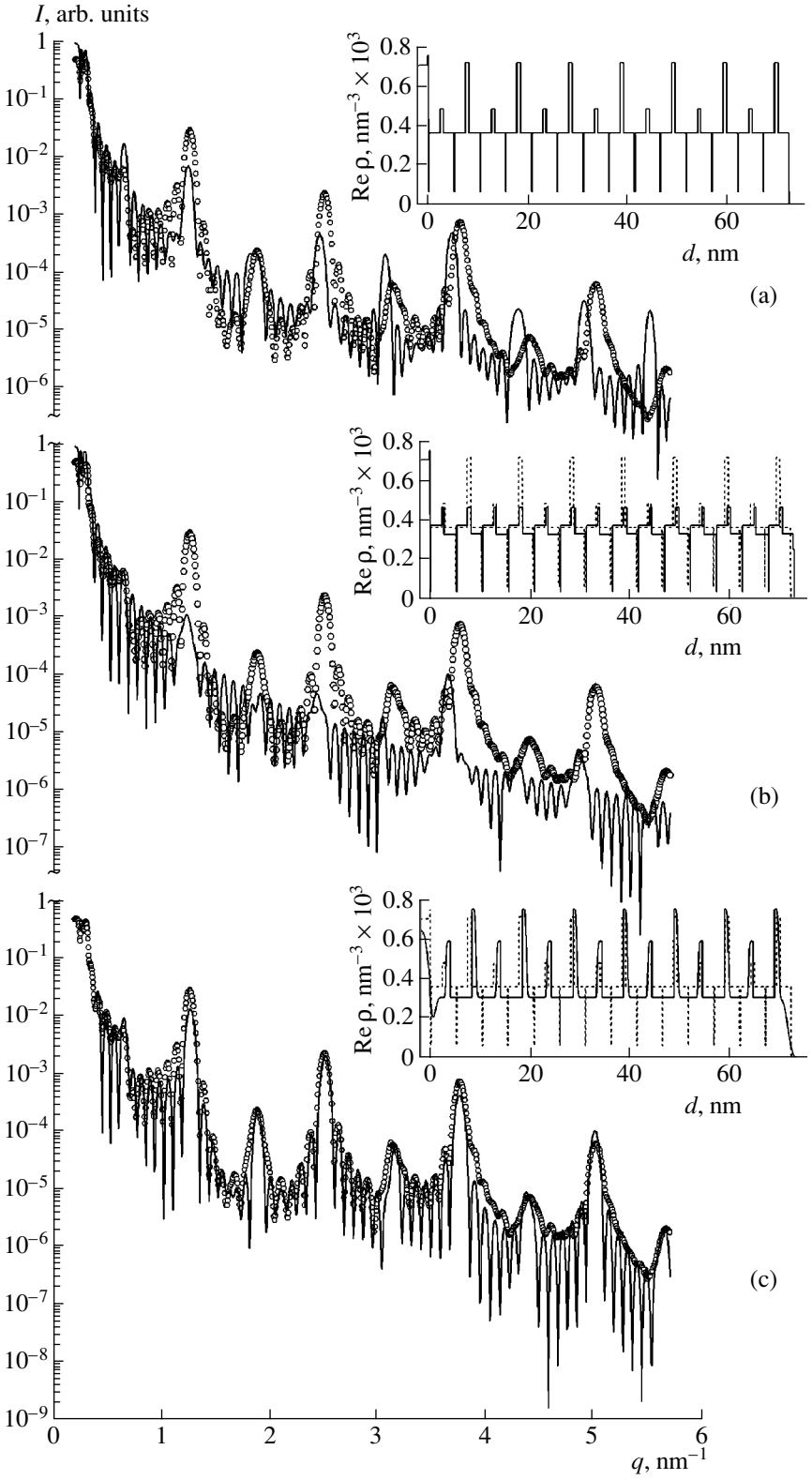

Fig. 3. Comparison of the experimental (dots) and calculated (solid lines) reflectivity curves: (a) for the electron-density profile of starting model with expected values of the d_i and $\mathrm{Re}\,\rho_i$ parameters (solid line in the inset (a) and dashed lines on the (b and c) insets) and for the calculated profiles (solid lines on the corresponding insets); (b) for the model obtained after local minimization over the whole range of measurements; (c) for the final model obtained by the stepwise minimization. At this stage, the curve was restored without taking into account roughness and absorption.

method allowed us to obtain the solutions for all eight starting models shown in Fig. 1 (the FITRXN package) and for another similar series of 15 models (REFLAN and FITRXN packages).

In all the cases, yet another method was very useful: the model structure was refined for each type of parameters separately. Thus, we refined first d_i, then $\mathrm{Re}\rho_i$, then both d_i and $\mathrm{Re}\rho_i$, and only then the roughness parameter σ_i. It was noticed that simultaneous refinement of the d_i and σ_i parameters may considerably change their real relationships because of their statistical dependence. A pair of physically independent d_i and $\mathrm{Re}\rho_i$ parameters can be refined simultaneously. However, one has to bear in mind that too large an error in the ratio of d_i and d_j for the starting model at $d_i \gg d_j$ can deteriorate the found values of $\mathrm{Re}\rho_i$ and $\mathrm{Re}\rho_j$ during the refinement of the pair d_i and $\mathrm{Re}\rho_i$. A similar situation can also arise in the refinement of the pair β_i and $\mathrm{Re}\rho_i$ (usually, the $\beta_i = \mathrm{Re}\rho_i/10$ values were used as the initial ones).

As the position of the Bragg peaks on the scattered intensity curve defines the repetition period of the unit cell in a multilayer film, and the fixation of the period is of great importance for the successful search for the model parameters, the refinement of the period is the most important stage of the restoration of a film structure. It is necessary to note that the range of Bragg reflexes contains the characteristic information on the density ratio of the layers. This fact confirms the possibility of using one more procedure: the refinement at the first stage not of the whole curve but only on a set of the segments containing individual Bragg peaks, including the initial small-angle segment of the curve before the first Bragg reflection. It is in this small-angle range that the Kiessig oscillations containing the information on the total thickness of the film are usually most pronounced. This justifies the necessity of including this range in the data set at the initial refinement of the layer periods and the related parameter of the total thickness of the film. Moreover, in the vicinity of the angle of total external reflection, both the substrate density and the ratio of the substrate density to the effective average density of the film are essential. This fact enables one to refine the above parameters of the density and the total thickness of the film on the segment before the first Bragg maximum using the primitive model of a homogeneous film on a substrate described by these three parameters. The computational experiments showed that, if a good approximation to the "experimental" curve is obtained on the small segment, the further refinement can be made based on the found approximation as a new starting model with the simultaneous gradual increase in the data in the sequence described above. The attempts of the structure refinement of films with interface roughness allowed us to record some specific features.

If rather narrow ranges of the values of the parameter d_i and $\mathrm{Re}\rho_i$ are unknown and no preliminary refinement of these parameters was made, then the refinement of the roughness parameters σ_i at unknown d_i can yield paradoxical results. The individual Bragg maxima on the intensity curve can disappear because of certain combinations of the parameters, and the curve thus found can considerably differ from the experimental one, to which it should have tended, whereas the values of roughness σ_i obtained during minimization may exceed the thicknesses d_i of the corresponding layers.

If the parameters d_i and $\mathrm{Re}\rho_i$ are determined correctly in the preliminary refinement, then σ_i values are refined fast and correctly. On the contrary, if during minimization the parameters of the layers of small thicknesses and densities are found incorrectly (the presence of such layers was assumed in the required model), then one may obtain better results by excluding these layers from the model (model simplification).

To estimate the accuracy of finding the minimum of noisy intensity curves, we constructed histograms of errors. It was found that the discrepancy of the curves in all the cases was proportional to the noise level introduced into the "experimental" curves. Thus, it was concluded that, within the given error, the found models are consistent with the sought models in full accordance with the accepted estimates of the accuracy of the curve restoration [1].

The computational experiments were directed at the establishment of the topographical features of the surface in the vicinity of the functional minima used in the refinement of the film model. Computational experiment confirmed the hypothesis of the ravine structure of the surface of the discrepancy functional. It was established that the FITRXN software package yielded worse refinement because the minimization program used in the package (Nelder–Mead downhill simplex method [9]) often stopped operating without reaching a local minimum. This is also confirmed by the fact that a new start from the same point determined as the local minimum gave a new solution displaced with respect to the first solution. In the REFLAN software package, another minimization program is used (Levenberg–Marquardt nonlinear least squares method combined with the variable metrics method [8]). This program is rather useful in work with ravine surfaces, which seems to explain better results in model restoration. However, the application of this package also did not allow one to solve the problem of minimization started at a point remote from the position of the global minimum of the complicated surface in all the cases. The maximum admissible size of the interval of constraints can be estimated by simulating a typical structure and analyzing the shape of one-dimensional sections of the surface of the objective function with respect to a certain parameter. The surface section along the thickness parameters is a curve with periodic maxima and minima. This periodicity is caused by the displacement of the positions of

the groups of Kiessig oscillations with the variation of the thickness parameters. With the variation of the density, absorption, and roughness parameters, these oscillations cannot arise, and the relative size of the admissible interval of these parameters can exceed the thickness parameters. This signifies that, when constructing the initial model, the layer thickness should be known *a priori* and with a higher relative accuracy than the values of other parameters for solving the problem by methods of the local minimization alone. Some idea on the character of the corrugation of the surface of the functional Φ (1) was obtained by constructing its two-dimensional sections, i.e., the plots of Φ as a function of *t*–parameters corresponding to two physical parameters of the model and related to *t* by formula (3). Figure 2 shows an example of such a section with respect to the parameters t_d and $t_{\mathrm{Re}\rho}$ in the vicinity of the point of the global minimum corresponding to the true model (Fig. 1, model 5, parameters *d* and $\mathrm{Re}\rho$ of layers II of the unit cell). The sections were constructed for calculation of Φ using all the points of the reflectivity curve (Fig. 2a) and the points corresponding to the initial part of the curve (30% of the whole interval) (Fig. 2b). Smoothing of the objective-function surface with the reduction of the angular range of the data explains the efficiency of the methods of the search for solutions suggested here. One can see that even the use of two free parameters does not allow one to obtain the global minimum if the minimization is started at a remote point. The program of local minimization, bypassing the "hills," can change the direction of the search and can lead to the local minimum with the parameters inconsistent with the physical ideas *n* the film structure. The surface of the discrepancy functional can be approximated by the squared function for which the mathematically justified methods of the local minimization are developed only in the rather narrow vicinity of the global minimum.

The results obtained show the importance of the preliminary choice of the adequate initial approximation. One has to take into account not only indirect data on the nature of the object and conditions of the film formation (which, as a rule, does not allow one to narrow the range of the search for the parameters) but also the data of the preliminary analysis of the experimental intensity curve, and the application of the step-by-step correction of the starting model during minimization.

To confirm the efficiency of the methods considered above, they were tested on the refinement of the scattering-density profile of a multilayer film using the experimental intensity curve from a real object (Fig. 3a). The sample was a silicon substrate containing an oxide layer and a layer of a water repellant (dimethyldichlorsilane) coated with a film of seven unit cells consisting of pairs of bilayers of fatty acid salts of two metals—lead stearate and yttrium stearate. Only the sequence of the layer deposition and the electron densities of each of the substances in the crystalline state were known *a priori*. It was assumed that ions of different metals penetrate the film differently and that some mixing of the layers takes place in the water subphase during film deposition; therefore, it was necessary to set a rather wide range for the search for layer parameters. The structure was described by a rather complex model (Fig. 3a) with the nine-layer unit cell sevenfold multiplied on the silicon substrate and surrounded with additional sublayers and overlayers. The attempt of the local minimization beginning with this model did not allow us to fit the model experimental curves (Fig. 3b) and gave physically unjustified distortions of the resulting model of the film structure (Fig. 3b). To search for the film model, we used the following methods of the successive refinement of the starting model:

—an initial restoration of the structure using the simplified model with a five-layer unit cell (from nine earlier assumed layers, four thinnest ones with the lowest densities were rejected);

—the initial search for the basic d_i and $\mathrm{Re}\rho_i$ parameters was made using the segments containing Bragg reflections (the β_i and σ_i parameters were not varied);

—the refinement was first made in the reduced angular range ($0° < \theta \le 1.5°$) with its successive gradual increase;

—in order to check the efficiency of the stepwise refinement, minimization was performed simultaneously in the same angular ranges with the rejection of the segments with the most pronounced discrepancy of the logarithms of the experimental and calculated intensity curves, i.e., ignoring the periodic "dips" on the calculated curve usually not fixed during the experiment. As was assumed, the presence of such dips did not considerably affect the model refinement.

As a result of such a sequence of steps, we obtained the model shown in Fig. 3c. This model made it possible (even without the refinement of the roughness parameters) to reduce to minimize the divergence between the experimental and calculated curves in the vicinities of the characteristic points—the Bragg and Kiessig maxima (which characterize the general thickness and periodicity parameters of the film), the angle of the total external reflection (which determines the ratio of the electron density of the substrate and the effective average density of the film), and the correlation in the alternation of the Bragg-peak intensities. The thickness and the electron-density parameters of the model layers lie within the limits that are allowed by physical conditions of the film formation even without the final step of roughness refinement.

CONCLUSIONS

The conclusions are based on the results obtained with the weight function $w = I^{-2}$. The procedure of the gradual search for the parameters of the structure model allowed us to restore the structure of the scattering density of thin films by local minimization of the squared discrepancy functional. The approach suggested con-

sists of the refinement of the thickness and density parameters first in some selected ranges of the reflectivity curve (the range close to the angle of total external reflection and the range of Bragg maxima), where the variation of these parameters most pronouncedly affects the character of the scattering curve. Then, the values obtained are used as the parameters of the starting models in the search for the solution in the extended (and, finally, in the whole) experimental range.

A stage that can possibly simplify the search for the optimum model is a preliminary reduction of the number of layers of the initial model and the approximation of the reflection curve by varying only the most significant structural parameters—those of thickness and density—at fixed values of the less important ones (absorption and roughness).

A gradual increase of the curve range used for computing the objective function often allows one to attain better fit between the calculated and experimental curves. Thus, in some instances, the gradual restoration of the structure allows one to overcome the difficulties associated with construction of a good initial model for finding solution along the whole experimental curve.

The methods suggested here for preliminary refinement of the parameters of the starting model and gradual (in several stages) restoration of the structure can be considered as the initial step of studying the relation between the characteristics of packing of layered films and the shape of the experimental scattering curve, which should facilitate the search for the final solution.

ACKNOWLEDGMENTS

The authors are grateful to L.A. Feigin for providing us with his experimental data and fruitful discussions and to I.I. Samoilenko for providing us with the adapted variant of the program for intensity calculations.

REFERENCES

1. Yu. V. Linnik, *Method of Least Squares and Principles of the Theory of Observations* (Fizmatgiz, Moscow, 1962; Pergamon Press, Oxford, 1961).
2. V. I. Mudrov and V. L. Kushko, *Methods of Processing of Measured Data* (Radio i Svyaz', Moscow, 1983).
3. B. M. Shchedrin and N. P. Zhidkov, *Program Library for Studying the Structures of Materials and Compounds by Diffraction Methods* (Mosk. Gos. Univ., Moscow, 1987).
4. I. M. Gel'fand, E. B. Vul, S. L. Ginzburg, and Yu. G. Fedorov, *Method of Ravines for Problems of X-Ray Diffraction Analysis* (Nauka, Moscow, 1966).
5. I. I. Samoĭlenko, O. V. Konovalov, L. A. Feĭgin, and B. M. Shchedrin, Kristallografiya **44** (2), 347 (1999) [Crystallogr. Rep. **44**, 310 (1999)].
6. O. V. Konovalov, I. I. Samoĭlenko, L. A. Feĭgin, and B. M. Shchedrin, Kristallografiya **41** (4), 635 (1996) [Crystallogr. Rep. **41**, 598 (1996)].
7. I. I. Samoĭlenko, L. A. Feĭgin, and B. M. Shchedrin, Kristallografiya **40** (5), 801 (1995) [Crystallogr. Rep. **40**, 739 (1995)].
8. J. E. Dennis, D. M. Gay, and R. E. Welsch, ACM Trans. Math. Softw. **7**, 348 (1983).
9. W. H. Press, S. A. Teukolsky, W. T. Vetterling, and B. P. Flannery, *Numerical Recipes in Fortran 77: The Art of Scientific Computing* (Cambridge Univ. Press, 1992), p. 402.

Translated by E. Shtykova

Crystallography Reports, Vol. 48, No. 5, 2003, pp. 868–871. Translated from Kristallografiya, Vol. 48, No. 5, 2003, pp. 930–933.

NANOMATERIALS

Dedicated to the 60th Anniversary of the Shubnikov Institute of Crystallography of the Russian Academy of Sciences

Refractive Indices of Laser Nanocrystalline Ceramics Based on $Y_3Al_5O_{12}$

A. A. Kaminskii*, K. Ueda, A. F. Konstantinova*, H. Yagi***, T. Yanagitani***, A. V. Butashin*, V. P. Orekhova*, J. Lu**, K. Takaichi**, T. Uematsu**, M. Musha**, and A. Shirokava****

** Shubnikov Institute of Crystallography, Russian Academy of Sciences, Leninskiĭ pr. 59, Moscow, 119333 Russia*

e-mail: afkonst@ns.crys.ras.ru

*** Institute for Laser Science, University of Electro-Communications, Chofu, Tokyo 182, Japan*

e-mail: lu@ils.uec.ac.jp

**** Takuma Works, Konoshima Chemical Co., Ltd., 80 Kouda, Takuma, Mitoyo, Konashima 769, Japan*

Received December 26, 2002

Abstract—Refractive indices of the nanocrystalline $Y_3Al_5O_{12}$ ceramic and a garnet single crystal of the same composition have been measured. In the visible and near IR range (0.4–1.064 μm), the prism method was used; in the medium IR range (2–6.2 μm), the interference method with the use of thin plates was applied. The refractive indices of these crystalline materials are practically the same over the entire spectral range studied and are described by the approximate formula proposed earlier for a single crystal. The parameters of the continuous-wave lasing in the nanocrystalline $Y_3Al_5O_{12}$ ceramic doped with Nd^{3+} and Yb^{3+} ions measured recently are presented. © *2003 MAIK "Nauka/Interperiodica".*

The technology of manufacturing highly transparent $Y_3Al_5O_{12} : Nd^{3+}$-based ceramic based on vacuum sintering without the application of external pressure [1, 2] was developed five years ago. This technology opened new vistas in production of continuous-wave solid-state lasers pumped by semiconductor lasers. Within a short time, $Y_3Al_5O_{12} : Nd^{3+}$-ceramic-based lasers with an output power of 1.47 kW (operating on the 1.064-μm transition of the main $^4F_{3/2} \longrightarrow {}^4I_{11/2}$ lasing channel) [3] and lasers with an output power of 36 W (operating on the 1.33-μm $^4F_{3/2} \longrightarrow {}^4I_{13/2}$ transition) [4] were produced. Comparative experiments showed that the laser potential of the $Y_3Al_5O_{12} : Nd^{3+}$ ceramic is close to that of single crystals of the same composition. The first recent experiments on lasing in the $Y_3Al_5O_{12} : Yb^{3+}$ ceramic showed that the power of one-micron emission ($^2F_{5/2} \longrightarrow {}^2F_{7/2}$) was 0.35 W [5]. The high optical quality of the $Y_3Al_5O_{12}$ ceramic was confirmed by excitation of a high-order stimulated Raman scattering [6]. Considering the practical characteristics of the $Y_3Al_5O_{12} : Nd^{3+}$ laser ceramic such as the largest possible dimensions and price, we can state that the ceramic offers certain advantages over the best commercial $Y_3Al_5O_{12} : Nd^{3+}$ lasing single crystals even at the present stage of its study.

This work continues our comprehensive investigation of the spectral, lasing, nonlinear, and mechanical properties of the nanocrystalline $Y_3Al_5O_{12}$ ceramic [3–8]; we measured its refractive indices over a wide wavelength range from 0.4 to 6.2 μm. For comparison, we also used $Y_3Al_5O_{12}$ single crystals in our experiments. The refractive indices of $Y_3Al_5O_{12}$ single crystals were measured in a number of studies (see, e.g., [9–12]); the most complete and reliable data were obtained in [12].

Refractive indices of the nanocrystalline $Y_3Al_5O_{12}$ ceramic were measured in the wavelength range 0.405–1.064 μm by the prism method [13] on a GS-5 goniometer at room temperature. The prism with the refracting angle $\alpha = 40.15074°$ and a 1 cm^2-aperture was made. The light sources were a PRK-4 mercury lamp, a helium–neon laser ($\lambda = 0.6328$ μm), and a crystalline $Y_3Al_5O_{12} : Nd^{3+}$ laser ($\lambda = 1.06415$ μm). The experimentally measured refractive indices are listed in the table. In the range 0.436–0.6328 μm, the refractive indices were measured with an accuracy of ±0.0002. At $\lambda =$ 0.405 and 1.06415 μm, the accuracy was somewhat lower (±0.001).

In the visible spectral range, the refractive indices n of the ceramic were approximated by the one-term Sellmeier formula

$$n^2 - 1 = K_0\lambda^2/((\lambda)^2 - \lambda_0^2), \quad (1)$$

where $K_0 = 2.274226$ and $\lambda_0 = 0.110716$ are the coefficient and the corresponding characteristic wavelength, respectively, and λ is the wavelength of the incident light. Figure 1 shows the dependence $1/(n^2 - 1) = f(\lambda^{-2})$. It is clearly seen that, in this spectral range, the dependence is linear and, therefore, can be well approximated by a straight line. The refractive indices of the $Y_3Al_5O_{12}$ ceramic obtained in the range up to 1.064 μm and the refractive indices of $Y_3Al_5O_{12}$ single crystals reported in [9–12] are practically equal.

At present, there are several methods of determining refractive indices in the IR spectral range, which include the measurements on prisms by the method of the minimum deviation recorded on goniometers with appropriate optics and IR detectors. Single crystals are also studied in reflected light on ellipsometers of various designs with appropriate optics. These devices are less available and used not as often as spectrophotometers which allow one to record absorption and reflection spectra of various materials over a wide spectral range. Spectrophotometers are also used to determine refractive indices of thin films by the interference method. However, spectrophotometers are rarely used to study single crystals because of the difficulties associated with the preparation of thin plane-parallel plates. We measured refractive indices of the ceramic by the interference method.

It is well known that, at the normal light incidence from air onto a transparent sample, the intensity of the transmitted light J_t with due regard for multiple reflection is written in the form [14]

$$I/I_0 = J_t = (1 - R)^2/[(1 - R)^2 + 4R\sin^2\Delta], \quad (2)$$

where $\Delta = (2\pi/\lambda)nd = (2\pi\nu)nd$ is the phase difference, n is the refractive index, d is the sample thickness, λ is the wavelength of the incident light, $\nu = 1/\lambda$, and $R = (n - 1)^2/(n + 1)^2$. With due regard for multiple reflection, the intensity of the transmitted (and, obviously, reflected) light changes periodically with the change in the wavelength. The intensity maxima J_t are observed if the phase difference is $\Delta = m\pi$ and, correspondingly,

$$2dn = m\lambda, \quad (3)$$

and the intensity minima, if the phase difference equals $\Delta = (m + 0.5)\pi$. If the change in the incident-light wavelength $\delta\lambda$ gives rise to the change in the refractive index, δn, the next maxima is observed at

$$2d(n - \delta n) = (m - 1)(\lambda + \delta\lambda). \quad (4)$$

Obviously, the determination of the refractive indices requires the knowledge of the sample thickness and the interference order m. In fact, this is the key problem in the determination of refractive indices by the interference method. If the dependence of the refractive index on wavelength is ignored or if n = const in a certain spectral range, the interference order m is

$$m = \lambda/\delta\lambda + 1. \quad (5)$$

Once the interference order m is determined, one can calculate the refractive-index dispersion. The accuracy of the measurements of the refractive indices by the

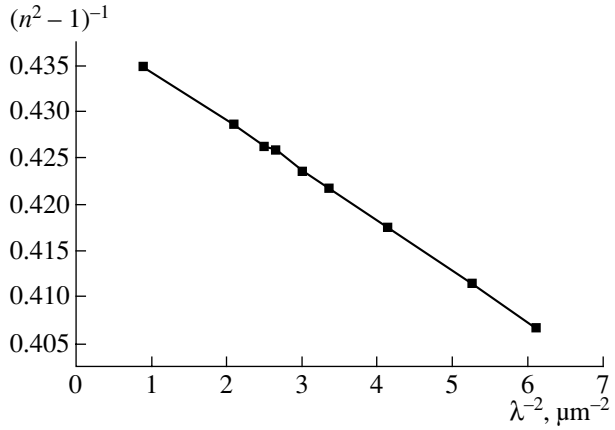

Fig. 1. $1/(n^2 - 1)$ as a function of $1/\lambda^2$ for the $Y_3Al_5O_{12}$ ceramic.

Refractive indices n of the $Y_3Al_5O_{12}$ ceramic

λ, μm	n
0.405	1.8599
0.436	1.8522
0.491	1.8428
0.546	1.8361
0.579	1.8333
0.615	1.8300
0.6328	1.8293
0.691	1.8259
1.06415	1.8165
1.9965	1.8005
2.5072	1.7923
3.0148	1.7824
3.5108	1.7705
4.0151	1.7567
4.4944	1.7409
5.0064	1.7218
5.4800	1.7019
6.0349	1.6726
6.1549	1.6659

Note: In the range 0.405–1.064 μm, refractive indices were measured by the prism method; in the range 1.9965–6.2 μm, by the interference method (the wavelengths correspond to some of the maxima of the transmission curve).

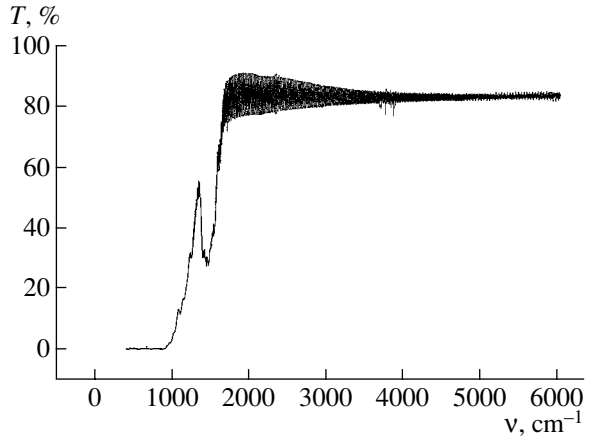

Fig. 2. Transmission spectrum of the $Y_3Al_5O_{12}$ ceramic in the IR range (d = 150.4 μm).

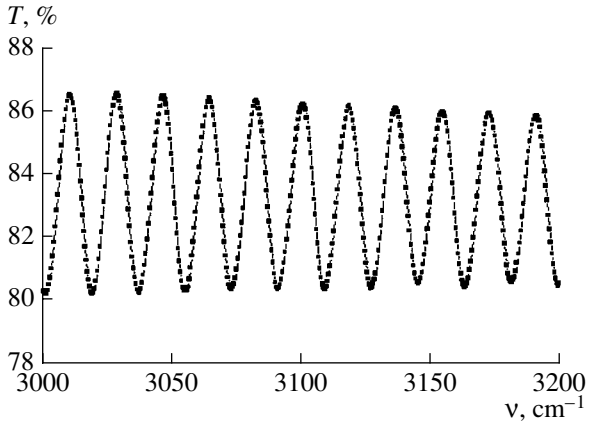

Fig. 3. Experimental oscillating transmission curve for the $Y_3Al_5O_{12}$ ceramic in the 3000–3200 cm^{-1} range (d = 150.4 μm).

above method is discussed in [15]. The situation becomes much more complex if the refractive index depends on the wavelength in the whole spectral range studied. Then, one has to invoke some additional data.

The refractive indices of the ceramic and single crystal were measured as follows. The samples in the shape of polished plane-parallel plates were prepared from a single crystal (with the thickness d = 95 and 150.9 μm) and a ceramic (d = 150.4 μm). The samples were plane parallel within an accuracy no worse than 10″. The transmission spectra from the samples were measured on a Perkin–Elmer (Spectrum RXIFT-IR System) and a Brooker (IFS-25) spectrometer in the 7000–500 cm^{-1} range at a resolution of 1 cm^{-1}. Since the most distinct interference patterns with a high resolution are obtained on thin samples, the first measurements were made on a single-crystal sample with the thickness d = 95 μm. In order to calculate the refractive indices, the positions of the maxima and minima on the oscillating curves were determined for the transmission spectra. Since the data measured did not allow us to determine the interference order m with sufficient accuracy, we determined the interference order by formula (3) using the value $n(\lambda)$ at λ = 3.33 μm from [12] and then calculated the dependence $n(\lambda)$ in the whole transparency range of the single crystal in the IR range. The thus calculated refractive indices of a garnet single crystal in the range of optical transparency proved to be the same (within the accuracy 5×10^{-4}) as the values reported in [12]:

$$n^2 - 1 = A\lambda^2/(\lambda^2 - B) + C\lambda^2/(\lambda^2 - D), \qquad (6)$$

where A = 2.282, $B = (0.108858)^2$, C = 3.27644, and $D = (16.81470)^2$; and λ is measured in micrometers.

In order to determine refractive indices, we also recorded the transmission spectra of the samples with the thickness ~150 μm prepared from single crystals and ceramics in the spectral range from 500 to 7000 cm^{-1} (20–1.429 μm). The transmission spectrum of the ceramics is shown in Fig. 2. The positions and the structure of the absorption bands of the ceramic and single crystal coincide in the whole range studied. For example, Fig. 3 shows the transmission spectra of the ceramic in the range 3000–3200 cm^{-1}. We also calculated the transmission curves by formula (2) using the Mathematica-4.1 package [16] and the dispersion dependence of the refractive indices given by formula (6). The positions of the maxima and minima in the experimental and calculated curves are in good agreement.

The positions of the maxima and minima in the transmission curves were determined for the single crystal and ceramic in the range 1600–5000 cm^{-1}. Since, according to our experiments, the refractive indices of the single crystal and ceramic are the same in the visible range of the spectrum and formula (6) is assumed to be valid, we used formula (3) to determine the interference order of one of the maxima at $\nu \sim$ 5000 cm^{-1} and then attributed the corresponding interference orders to all the other maxima and minima. Then, using Eq. (3), we calculated refractive indices of the ceramic and single crystal in the range 1600–5000 cm^{-1}. The refractive indices obtained for the ceramic and single crystal and those calculated using Eq. (6) are shown in Fig. 4. The refractive indices measured for the $Y_3Al_5O_{12}$ ceramic are also indicated in the table. Comparing the refractive indices measured for the ceramic and single crystal, we see that they are equal and coincide (within the accuracy up to 0.0005) with the refractive indices calculated by Eq. (6).

Thus, the refractive indices of the nanocrystalline $Y_3Al_5O_{12}$ ceramic and the $Y_3Al_5O_{12}$ single crystal practically coincide in the spectral range from 0.4 to 6.2 μm. The lasing characteristics of the $Y_3Al_5O_{12}$ ceramic doped with Nd^{3+} and Yb^{3+} ions can be competitive with

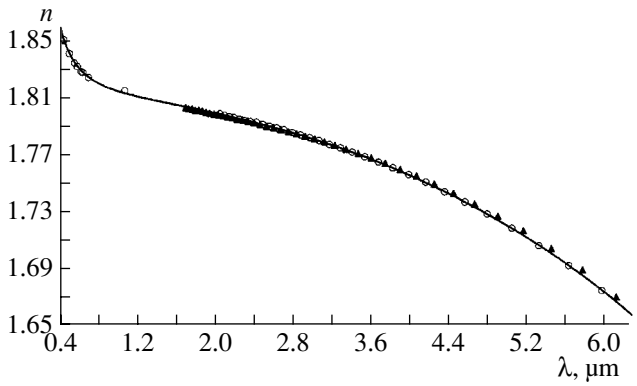

Fig. 4. Dispersion of the refractive indices for (○) $Y_3Al_5O_{12}$ ceramics, (▲) $Y_3Al_5O_{12}$ single crystal, and (—) calculation by formula (6).

the lasing characteristics of single crystals of the same composition.

ACKNOWLEDGMENTS

This study was supported by the Russian Foundation for Basic Research (project no. 01-02-16074), the Ministry of Industry, Science, and Technology of the Russian Federation, and the Ministry of Education, Science, Sport, and Culture of Japan. The study was performed within the framework of the scientific agreement between the Shubnikov Institute of Crystallography of the Russian Academy of Sciences and the Institute for Laser Science of the Tokyo University of Electro-Communications, and with the participation of the Joint Open Laboratory "Laser Crystals and Precision Laser Systems." The authors are grateful to A.I. Efimova and B.V. Lokshin for their help in measurements.

REFERENCES

1. T. Yanagitani, H. Yagi, and M. Ichikawa, Jpn. Patent No. 10-101333 (1998).
2. T. Yanagitani, H. Yagi, and Y. Hiro, Jpn. Patent No. 10-101,411 (1998).
3. J. Lu, K. Ueda, H. Yagi, *et al.*, J. Alloys Compd. **341** (2), 220 (2002).
4. Ju. Lu, J. Lu, T. Murai, *et al.*, Opt. Lett. **27** (13), 1120 (2002).
5. Ju. Lu, K. Takaichi, K. Ueda, *et al.*, Appl. Phys. Lett. (in press).
6. A. A. Kaminskiĭ, G. I. Eichler, K. Ueda, *et al.*, Pis'ma Zh. Éksp. Teor. Fiz. **72** (10), 717 (2000) [JETP Lett. **72**, 499 (2000)].
7. J. Lu, M. Prabhu, J. Song, *et al.*, Appl. Phys. B **71** (10), 469 (2000).
8. A. A. Kaminskiĭ, M. Sh. Akchurin, V. I. Alshits, *et al.*, Kristallografiya **48** (3), 562 (2003) [Crystallogr. Rep. **48**, 515 (2003)].
9. W. L. Bond, Appl. Phys. **36** (5), 1674 (1965).
10. K. L. Ovanesyan, A. G. Petrosyan, G. O. Shirinyan, and A. A. Avetisyan, Izv. Akad. Nauk SSSR, Neorg. Mater. **17** (3), 459 (1981).
11. E. V. Zharikov, Yu. S. Privis, P. A. Studenikin, *et al.*, Kristallografiya **34** (5), 1181 (1989) [Sov. Phys. Crystallogr. **34**, 712 (1989)].
12. D. E. Zelmon, D. L. Small, and R. Page, Appl. Opt. **37** (21), 4933 (1998).
13. N. M. Melankholin, *Methods of Studying Optical Properties of Crystals* (Nauka, Moscow, 1970).
14. M. Born and E. Wolf, *Principles of Optics: Electromagnetic Theory of Propagation, Interference, and Diffraction of Light*, 4th ed. (Pergamon Press, Oxford, 1969; Nauka, Moscow, 1970).
15. M. I. Strashnikova, Opt. Spektrosk. **93** (1), 142 (2002) [Opt. Spectrosc. **93**, 132 (2002)].
16. A. F. Konstantinova, K. K. Konstantinov, B. V. Nabatov, and E. A. Evdishchenko, Kristallografiya **47** (4), 702 (2002) [Crystallogr. Rep. **47**, 645 (2002)].

Translated by A. Zolot'ko

Crystallography Reports, Vol. 48, No. 5, 2003, pp. 872–877. Translated from Kristallografiya, Vol. 48, No. 5, 2003, pp. 934–939.

NANOMATERIALS

Dedicated to the 60th Anniversary of the Shubnikov Institute of Crystallography of the Russian Academy of Sciences

Nanostructure of Plasma-Sprayed Hydroxyapatite Coating

E. I. Suvorova*, V. V. Klechkovskaya*, V. V. Bobrovsky, Yu. D. Khamchukov**, and V. V. Klubovich****

** Shubnikov Institute of Crystallography, Russian Academy of Sciences, Leninskiĭ pr. 59, Moscow, 119333 Russia*

e-mail: suvorova@ns.crys.ras.ru

*** Institute of Technical Acoustic, Belarussian Academy of Sciences, pr. Ludnikova 13, Vitebsk, 210717 Belarus*

Received April 8, 2003

Abstract—Calcium phosphate coatings were studied by high-resolution transmission microscopy, microdiffraction, and X-ray energy-dispersive spectroscopy. Coatings were prepared by spraying hydroxyapatite targets onto copper, nickel, and chromium substrates and onto NaCl and BaF_2 single crystals in an argon plasma at a gas pressure of ~1 Pa; the sputter power was about 200 W; and the RF-generator frequency was 13.56 MHz. Under the conditions used, thin layers of nanocrystalline hydroxyapatite were formed regardless of the nature of the substrate. © *2003 MAIK "Nauka/Interperiodica".*

INTRODUCTION

A hydroxyapatite layer on the surface of materials (metals, metal alloys, and ceramics) implanted into living organisms is considered as a connection link between an implant and bone tissues [1–3]. This coating promotes integration of an artificial material with the bone surface and facilitates the regeneration of bone tissue around the implant [4, 5]. Materials providing conditions for the formation of interfacial bonds due to the affinity of their structures for living tissues are called bioactive. In addition, prostheses coated with such materials can be fixed without the use of cementing materials, for example, of poly(methyl methacrylate). Several methods have been developed for the preparation of hydroxyapatite coatings on different substrates; the structure of these coatings directly depends on the conditions of their formation [6–14]. Various knee and hip prostheses and other implants with plasma-sprayed hydroxyapatite coatings are manufactured and sold on the world market, for example, under the BIOLOX®osprovit and Integral® (Calcitec Inc.) trademarks. The standards for calcium phosphate coatings, which can be used for implantation, [5–17] required them to contain at least 95% of hydroxyapatite. However, it is known [18] that bioimplants can cause inflammation and be rejected. The microstructure of a hydroxyapatite layer plays key role in successful implantation and biocompatibility.

Therefore, information on the micro- and nanostructures of materials is, presumably, of decisive importance for preventing the above-mentioned phenomena and for determining of the conditions for the production of efficient bioimplants. It should be noted that optical microscopy, scanning electron microscopy, and X-ray diffraction analysis are the main methods used for studying the state of biosystems and their phase composition [14]. Transmission electron microscopy (TEM) is used much less frequently because of the difficulties associated with the preparation of samples, sensitivity of these samples to electron-beam exposure, and some other reasons. In these studies, only the images were interpreted, without using electron diffraction, which provides data on the structure. This methodology can lead (and often does) to misinterpretation of experimental data and, particularly, of images in the characterization of small-sized objects, such as hydroxyapatite crystals. It was demonstrated [19–21] that the appearance of diffuse scattering in X-ray and electron diffraction patterns depends on the crystal sizes. Data from high-resolution transmission electron microscopy (HRTEM) are required for a detailed phase analysis in a system of calcium phosphates with similar crystal structures. The present investigation was aimed at studying the morphology and nanostructure of coatings prepared by spraying plasma onto various substrates, establishing the structures of individual crystals comprising layers, examining their porosity, and revealing reasons for the formation of structurally disordered regions in the layers by TEM and diffraction analysis.

1063-7745/03/4805-0872$24.00

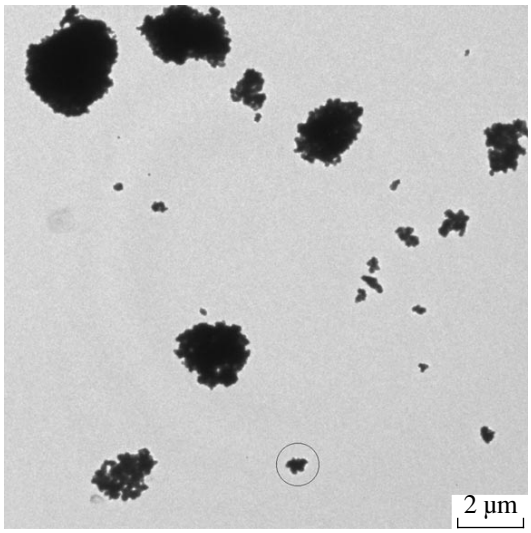

Fig. 1. Agglomerates of crystals in the initial powder, which was annealed at 950°C and used for the preparation of targets in plasma spraying.

MATERIALS AND METHODS

Hydroxyapatite for solid-state targets was prepared by deposition from aqueous solutions by the reaction

$$10Ca(NO_3)_2 + 6(NH_4)_2HPO_4 + 8NH_3 + 2H_2O$$

$$= Ca_{10}(OH)_2(PO_4)_6 + 20NH_4NO_3.$$

The powder thus synthesized was annealed for 2 h at 950°C. A mixture of the annealed powder and a plasticizing agent (polyvinyl alcohol) was pressed to form targets 58 mm in diameter, which were then annealed for 2 h at 500°C [22].

Targets were sprayed onto metal substrates (copper, nickel, chromium) and also onto NaCl and BaF_2 single crystals by RF-diode sputtering for 9.5 h at a power of about 200 W, with an RF-generator frequency of 13.56 MHz. A substrate was placed at the boundary between the near-electrode dark space and glow plasma. Argon at a pressure of ~1 Pa was used as the plasma-forming gas.

The substrate temperature close to the surface, which was measured by a chromel–alumel thermocouple, was about 100°C.

The morphology of the layers and cross sections were characterized in a Philips XL30 F and Philips XL30 S scanning electron microscopes. The chemical compositions of the samples were determined by energy-dispersive spectroscopy (EDS) using electron probes from 3.5 to 50 nm in diameter.

The electron diffraction patterns and images of the coatings, including high-resolution images, were obtained on a Philips CM 300 UT FEG transmission electron microscope operating at 300 kV with spherical aberration of 0.65 mm and resolution of 0.17 nm. The images were recorded on a Gatan 794 CCD camera. The image processing, including noise filtration and quantitative analysis of diffraction patterns, was carried out using the DigitalMicrograph program, version 3.6.1.

HRTEM images and electron diffraction patterns were calculated for the specified electron–optical parameters and the structural data of hydroxyapatite [23] (hexagonal space group $P6_3/m$, a = 0.942 and c = 0.688 nm) using the JAVA Electron Microscopy Simulation (JEMS) software package [24]. This simulation enabled us to perform unambiguous phase analysis and

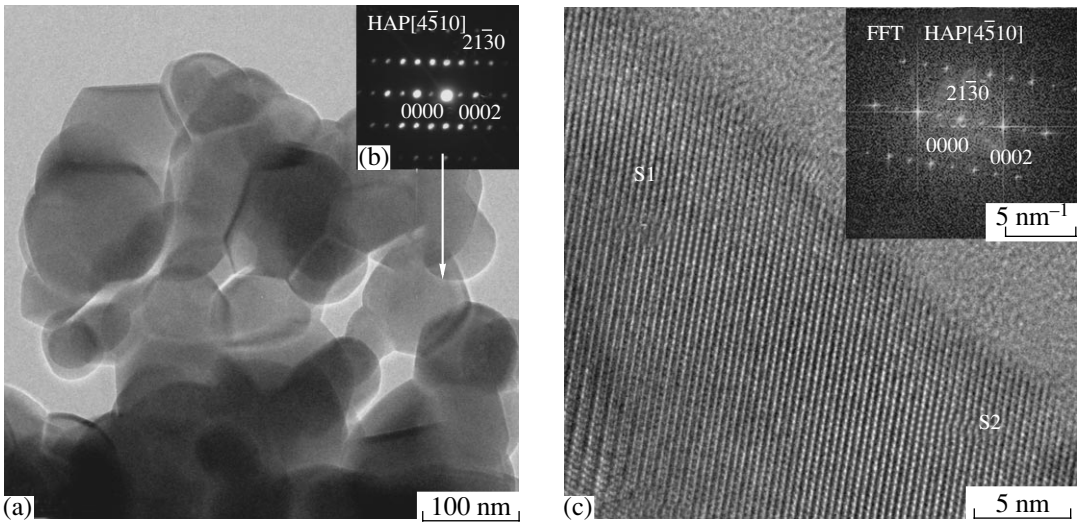

Fig. 2. (a) Hydroxyapatite crystals in agglomerates; (b) the electron diffraction pattern of a crystal (indicated by an arrow) with the [4$\bar{5}$10] zone axis; and (c) the HRTEM image of the same crystal and simulated images (insets *S*1 and *S*2) obtained for a crystal thickness of 3.2 nm, the [4$\bar{5}$10] zone axis and defocus values 21 or 23 nm, correspondingly.

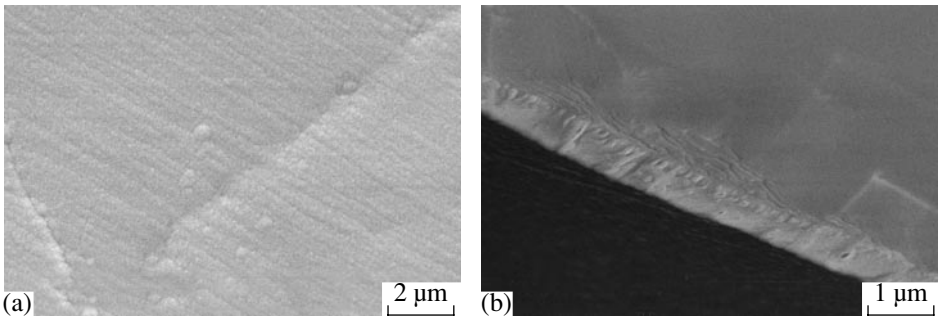

Fig. 3. (a) Surface of the coating on a copper substrate and (b) a cross section of the coating on a BaF_2 single crystal.

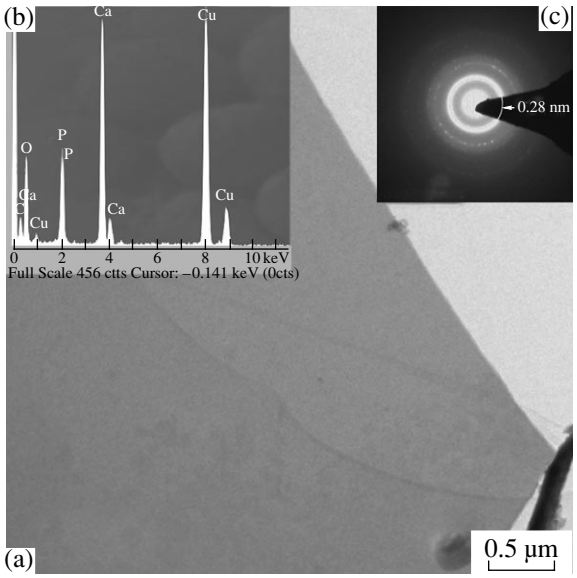

Fig. 4. (a) Plan view of a coating on BaF_2. (b) The elemental composition of the coating determined by EDS (the coating contains calcium, phosphorus, and oxygen; the peaks of copper and carbon were produced by a copper supporting grid and carbon film). (c) The electron diffraction pattern.

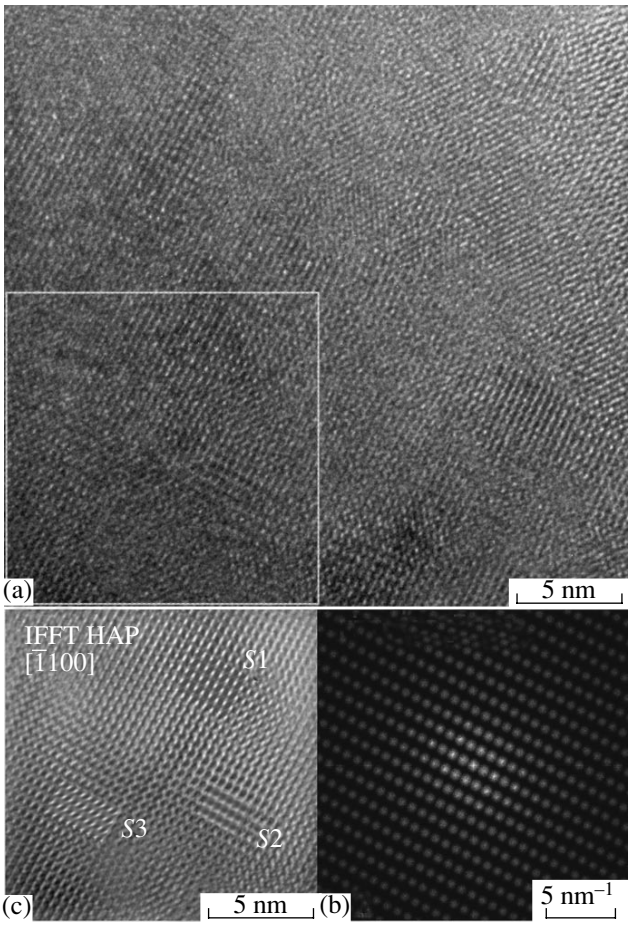

Fig. 5. (a) HRTEM image of a coating on BaF_2 and (b) a diffractogram taken from the selected area in the HRTEM image. (c) Inverse fast Fourier transform of the filtered image. The simulated images (in the insets *S*1, *S*2, and *S*3) were obtained at the defocus values of 40, 42, and 36 nm, respectively for a crystal thickness of 60, 72, and 72 nm and the crystal tilts to the $[1\bar{1}00]$ zone axis of 1.2° (in the $[\bar{1}\bar{1}20]$ direction), 1.3° (in the [0001] direction), and 1.1° (in the [2121] direction).

estimate the thickness of the crystals. For this purpose, the simulated and experimental images were compared to find the best match between them. We analyzed images obtained with the defocus varied from 0 to 60 nm (underfocus in the JEMS program) and the thickness of the samples ranged from 1 to 200 nm. The simulation was carried out also with an assumed tilt of the sample with respect to its exact zone axis.

RESULTS AND DISCUSSION

Granulometric analysis demonstrated that the size distribution of particles in the annealed hydroxyapatite powder has two maxima at 2.5 and 11.4 μm. TEM showed that such particles are agglomerates of crystals (Fig. 1). Correspondingly, the size of these agglomerates can vary up to the size of one crystal (to 200 nm). The hydroxyapatite phase was determined from electron diffraction patterns obtained from individual nanocrystals (Figs. 2a and 2b) and confirmed by comparing the experimental and simulated HRTEM images

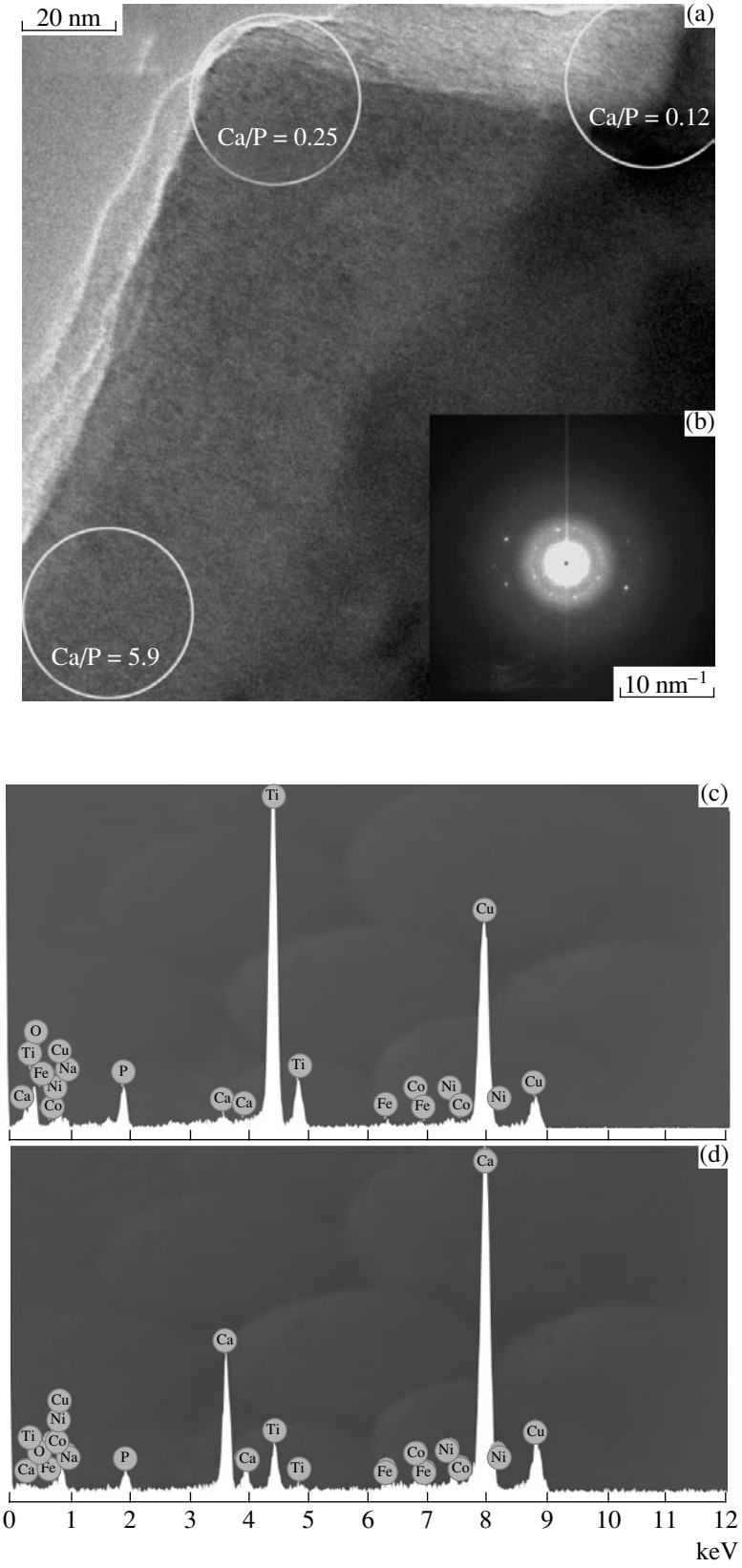

Fig. 6. Region of a calcium phosphate coating prepared on a titanium substrate by anodic spark deposition in an aqueous solution of the $Ca(H_2PO_4)_2$ electrolyte; (a) regions with substantially different Ca : P ratios; (b) the ring electron diffraction pattern corresponding to this region; (c, d) EDS spectra, from which the Ca : P ratios equal to (c) 0.12 and (d) 5.9 were determined.

(Fig. 2c). The orientation was determined from the fast Fourier transform (FFT). The HRTEM images were simulated for several thicknesses of the crystals, crystal tilts, and defocus values. The best match between the simulation (insets *S*1 and *S*2) and experiment was achieved for a hydroxyapatite crystal 3.2 nm thick with the $[4\bar{5}10]$ zone axis at defocus values of 21 or 23 nm. Therefore, the hydroxyapatite crystals in the initial annealed powder, which was used for pressing pellets, were very thin.

The micrographs obtained in a scanning electron microscope show the morphology of coatings deposited on metal substrates (Fig. 3a) and a BaF_2 single crystal (Fig. 3b). At this scale, coatings appear dense and homogeneous and are characterized by low surface roughness. The image of the cross section of the coating is shown in Fig. 3b. This image was obtained as follows. The surface of the BaF_2 substrate with a deposited coating was placed parallel to the incident electron beam of the microscope, which allowed us to determine the thickness of the coating and estimate its roughness and the rate of formation. The thickness of the layer ranged up to 400 nm; correspondingly, the rate of its formation was about 1 nm/min and the roughness was up to 10 nm.

Chemical analysis of different samples of the coatings (Fig. 4a) by EDS demonstrated that these samples contained calcium, phosphorus, and oxygen as the main elements (Fig. 4b). The peak of copper appeared due to the use of a copper supporting grid. Since the material of the coatings is sensitive to electron irradiation, the electron beam used in the spectroscopic measurements was not focused completely on the area under study (for example, when the spectrum was recorded for 40 s, the optimum diameter of an electron probe required for the signal to be measured with good statistics was smaller than 50 nm). However, the structural and phase composition of the compound cannot be determined based on the EDS data for the Ca : P ratio, because the relative phosphorus content decreased with respect to that of calcium as the irradiation time was increased. For example, the Ca : P ratio determined by quantitative EDS analysis within the first 40 s was 1.8. This value is higher than that typical of hydroxyapatite (1.67). The electron diffraction pattern (Fig. 4c) has broad diffuse reflections, and, hence, it cannot be used for phase analysis.

In this case, the structure of the coating was determined by the FFT (diffractogram) of the HRTEM image (Fig. 5). The phase composition of the sample was confirmed by image simulation of the area selected by a square in Fig. 5a. Since the sample was rather thick, the experimental and calculated images were compared using the inverse FFT (IFFT) of the filtered image, which was obtained by imposing a mask on the reflection maxima in the X-ray diffraction pattern. Insets *S*1, *S*2, and *S*3 show the calculated images at a defocus varying from 40 to 43 nm with the assumed thickness in the range of 60–72 nm and the crystal tilt to the $[1\bar{1}00]$ zone axis of about 1.2°. Thus, it was demonstrated that the coating consisted of hydroxyapatite nano- and subnanocrystals of about 5 nm in size, which are misoriented relative to each other.

In the experiment on plasma-sprayed coatings, we observed the formation of nanocrystalline hydroxyapatite. Regions with amorphous structure were not revealed. The effect of the substrate was limited only to the degree of surface roughness. The layers obtained on natural faces of BaF_2 and NaCl single crystals were smoother than coatings deposited on metal substrates.

Figure 6a shows the HRTEM image of a calcium phosphate coating prepared on a titanium substrate by anodic spark deposition in an aqueous solution of the $Ca(H_2PO_4)_2$ electrolyte [25] at a constant current of about 150 mA. In this case, the results of EDS analysis were important, because the electron diffraction pattern in Fig. 6b showing diffuse reflections is similar to the pattern shown in Fig. 4c, and no regular structures were observed in the HRTEM images. However, quantitative spectroscopic analysis (Figs. 6c and 6d) demonstrated that the phosphorus content in one part of the sample was much higher than that of calcium (under analogous conditions of measurements), whereas the calcium content was much higher than that of phosphorus in another part. In the micrographs, the regions for which quantitative EDS analysis was carried out are selected by the circles (the diameter of the electron probe). According to the results of XEDS analysis, nearby regions were characterized by different Ca : P ratios (0.12 and 5.9), which indicates that this coating contained several phases, including phosphorus and calcium oxides. At the atomic level, a mixture of these oxides forms a disordered structure.

CONCLUSIONS

In summary, our study demonstrated that a coating of nanocrystalline hydroxyapatite is formed in an argon plasma under specified conditions at a rate of approximately 1 nm/min. HRTEM study, which includes recording of experimental images, their processing, and simulation, is the most informative method for determining the phase composition of a material in microareas since their electron diffraction patterns have diffuse reflections due to small sizes of crystals and their different orientations with respect to the electron beam.

ACKNOWLEDGMENTS

We are grateful to Prof. Marcus Textor (ETHZ, Zurich, Switzerland) for providing us with samples and to Prof. Philippe Buffat (CIME EPFL Lausanne, Switzerland) for help in our study and kind permission to use the electron microscopes at the Center of Electron Microscopy.

This study was supported by the Russian Foundation for Basic Research (project no. 01-02-16176 and the Russian–Belarussian joint project no. 02-02-81009).

REFERENCES

1. L. L. Heych, J. Am. Ceram. Soc. **74**, 1482 (1991).
2. P. Ducheyne, P. Bianco, S. Radin, and E. Schepers, in *Bone-Bonding Biomaterials*, Ed. by P. Ducheyne, T. Kokubo, and C. A. van Blitterswijk (Reed Healthcare Communication, Netherlands, 1992), p. 13.
3. U. Sampathkumaran, M. R. De Guire, and R. Wang, Adv. Eng. Mater. **3** (6), 401 (2001).
4. W. J. A. Dhert, Med. Prog. Technol. **20**, 143 (1994).
5. M. T. Manley, in *Hedroxylapatite Coatings in Orthoppaedic Surgery*, Ed. by R. G. T. Geesink and M. T. Manley (Raven Press, New York, 1993), p. 1.
6. H. B. Wen, J. R. de Wijn, F. Z. Cui, and K. de Groot, J. Biomed. Mater. Res. **41**, 227 (1998).
7. T. Peltola, M. Pátsi, H. Rahiala, *et al.*, J. Biomed. Mater. Res. **41**, 504 (1998).
8. C. Mao, H. Li, F. Cui, *et al.*, J. Cryst. Growth **206**, 308 (1999).
9. J. P. Schreckenbach, G. Marx, F. Schlottig, *et al.*, J. Mater. Sci.: Mater. Med. **10** (8), 453 (1999).
10. J. L. Arias, M. B. Mayor, F. J. Garcia-Sanz, *et al.*, J. Mater. Sci.: Mater. Med. **8**, 873 (1997).
11. C. M. Cotell, D. B. Chrisey, K. S. Grabowski, and J. A. Spregue, J. Appl. Biomater. **3**, 87 (1992).
12. J. G. C. Wolke, K. de Groot, and J. A. Jansen, J. Biomed. Mater. Res. **39**, 524 (1998).
13. E. Park, R. A. Condrate, Sr., D. Lee, *et al.*, J. Mater. Sci.: Mater. Med. **13**, 211 (2002).
14. K. A. Gross, C. C. Berndt, and H. Herman, J. Biomed. Mater. Res. **39**, 407 (1998).
15. G. Willmann, Adv. Eng. Mater. **1** (2), 95 (1999).
16. *ASTM F 1609-95, Standard Specification for Calcium Phosphate Coatings for Inplanteable Materials* (1995).
17. *ASTM F 1185-88, Standard Specification for Composition of Ceramic Hydroxyapatic for Surgical Implants* (1988).
18. M. Ogiso, Y. Yamashita, and T. Matsumoto, J. Biomed. Mater. Res. **39**, 23 (1998).
19. E. I. Suvorova and P. A. Buffat, J. Microsc. (Oxford) **196**, 46 (1999).
20. E. I. Suvorova and P. A. Buffat, Kristallografiya **46** (5), 796 (2001) [Crystallogr. Rep. **46**, 722 (2001)].
21. E. I. Suvorova and P. A. Buffat, Eur. Cells Mater. **1**, 27 (2001); http://www.eurocelmat.org.uk.
22. Yu. D. Khamchukov, V. V. Klubovich, I. P. Potapenko, *et al.*, Fiz. Khim. Obrab. Mater., No. 1, 55 (1998).
23. M. I. Kay, R. A. Young, and A. S. Posner, Nature **204**, 1050 (1964).
24. P. Stadelmann, http://cimewww.epfl.ch/people/Stadelmann/jemsWebSite/jems.html.
25. P. Kurze, W. Krysmann, and H. G. Schneider, Cryst. Res. Technol. **21** (12), 1603 (1986).

Translated by T. Safonova

Crystallography Reports, Vol. 48, No. 5, 2003, pp. 878–882. Translated from Kristallografiya, Vol. 48, No. 5, 2003, pp. 940–944.

CRYSTAL GROWTH

Dedicated to the 60th Anniversary of the Shubnikov Institute of Crystallography of the Russian Academy of Sciences

Congruently Melting Compositions in the Series of Solid Solutions $R_{1-x}Sr_xF_{3-x}$ (R = La – Nd, $0 \le x \le 0.15$) with Tysonite Structure (Refinement by Directional Crystallization)

E. A. Krivandina*, Z. I. Zhmurova*, T. M. Glushkova, M. M. Firsova**, A. P. Shtyrkova**, and B. P. Sobolev***

** Shubnikov Institute of Crystallography, Russian Academy of Sciences, Leninskiĭ pr. 59, Moscow, 119333 Russia*

e-mail: sobolev@crossovers.com

*** Moscow State University, Faculty of Physics, Vorob'evy gory, Moscow, 119889 Russia*

Received April 21, 2003

Abstract—Congruently melting compositions in the series of solid solutions $R_{1-x}Sr_xF_{3-x}$ (R = La–Nd) with a defect structure of the tysonite type (LaF_3) were found by the comparing the densities (determined by hydrostatic weighing) of the top and bottom parts of the single crystals grown using the Bridgman method. Measurement errors are analyzed. © *2003 MAIK "Nauka/Interperiodica".*

INTRODUCTION

Demand for modern technology in new fluoride materials can be satisfied by the preparation of fluorides of complex chemical composition, because the assortment and technical possibilities of simple metal fluorides are insufficient [1–3]. This circumstance forces one to pass from one-component to multicomponent fluoride materials. Due to the controlled defect structure, such materials are characterized by properties that often differ dramatically from the properties of their components.

When the composition of a compound becomes more complex, several negative consequences can arise along with beneficial effects. In the general case, the most serious disadvantage is the incongruent behavior of multicomponent melts. The composition of the solid phase differs from that of the starting melt, due to which the growth of multicomponent crystals of solid solutions is accompanied by the inhomogeneous distribution of a dopant along the length and cross section of the crystal boule. Fluctuations of the composition (without distortion of the single-phase character) may attain values that would make these crystals inappropriate for practical use.

The preparation of homogeneous single crystals of solid solutions is a general problem. However, there are particular cases characterized by congruent-melting conditions, despite the multicomponent character of the melt. Such cases manifest themselves in anomalies in the melting curves (maxima). The maxima have been shown to be inherent in heterovalent solid solutions only [4]. The nonstoichiometric phases $R_{1-x}M_xF_{3-x}$ with the defect structure (of the tysonite type) formed in the MF_2–RF_3 systems (M = Ca, Sr; R are rare-earth elements) are examples of such solid solutions.

The compositions of solid solutions corresponding to the maxima in the melting curves are favorable for the growth of homogeneous crystals. For such crystals, the distribution coefficient of the second component $k = 1$ and the content of this component should not differ significantly along the crystal length.

The data on the coordinates of the maxima (composition and temperature) obtained by differential thermal analysis (DTA) [5, 6] are often insufficiently exact to be used in practice for growing $R_{1-x}M_xF_{3-x}$ crystals. One reason for this is the flat character of the maxima in the melting curves for the tysonite phases, which impedes the exact determination of congruently melting compositions.

We proposed using the method of directional crystallization from the melt [7] to refine the solid-solution composition at the maxima in the melting curves for the nonstoichiometric phases $La_{1-x}Sr_xF_{3-x}$. A similar approach was successfully used for the phases with the

1063-7745/03/4805-0878$24.00 © 2003 MAIK "Nauka/Interperiodica"

defect fluorite structure $Na_{0.5-x}R_{0.5+x}F_{2+2x}$ (R = Y, Yb) [8].

The purpose of this study is to continue our investigations aimed at refining congruently melting compositions for the $R_{1-x}Sr_xF_{3-x}$ tysonite phases in the systems with lanthanides of the cerium subgroup (R = La–Nd).

REFINEMENT OF THE COMPOSITION OF A SOLID SOLUTION AT THE MAXIMUM OF THE MELTING CURVE FOR TYSONITE PHASES IN THE SrF_2–LaF_3 SYSTEM

The $R_{1-x}Sr_xF_{3-x}$ solid solutions with the defect tysonite structure in the SrF_2–RF_3 systems (R = La–Nd) are characterized by wide regions of homogeneity, which extend to 17–19 mol % of SrF_2 at eutectic temperatures [5, 6]. In all systems, with an increase in the SrF_2 content, the distribution coefficient k passes through $k = 1$, corresponding to a maximum in the melting curve (the point of contact of the liquidus and solidus).

The differentiation in the content of components along the growth axis during directional crystallization was studied previously [7, 9] for the $La_{1-x}Sr_xF_{3-x}$ solid solutions. Let us briefly consider the results of these studies. Table 1 presents the data on k calculated from the phase diagram of the SrF_2–LaF_3 system (DTA method) [10] and the data from [9], where the values of k were determined by X-ray fluorescence analysis (XRFA) in studying the distribution of SrF_2 along the growth axis of an $La_{1-x}Sr_xF_{3-x}$ crystal (the directional crystallization in the Bridgman method).

It can be seen that these data are substantially different. The composition corresponding to the maximum with $x_0 = 0.10 \pm 0.02$ was determined using DTA. According to the experiment on crystal growth [9], the composition at the maximum ranges from 6.1 to 7.8 mol % of SrF_2 (Table 1). The analytical dependence of k on the content of SrF_2 (C, mol %) was obtained for the starting melt: $1/k = 0.088\ C \pm 0.38$. It was shown that $k = 1$ at $C = 7$ mol % of SrF_2. Since the experimental error in determining k is $\Delta k = \pm 0.02$ and the error in estimating C is $\Delta C = \pm 0.5$, $\Delta x = 0.005$, and $x_0 = 0.070 \pm 0.005$.

It can be seen from the phase diagram [6] in Fig. 1 that only four compositions were studied in the region of homogeneity of the tysonite phase, because the time-consuming problem of exact determination of the composition at the maximum was not stated. These data are insufficient for reliably plotting the liquidus and solidus curves in such a wide concentration range. It is also important that the conditions of crystal growth are closer to equilibrium than those in the case of fast (10–20 deg/min) cooling in the DTA regime.

The advantage of directional crystallization over DTA (in its conventional variant) for the refinement of the compositions of congruently melting solid solutions, seemingly undoubted, was demonstrated for the $La_{1-x}Sr_xF_{3-x}$ nonstoichiometric phase [7, 9].

Table 1. Dependence of the distribution coefficient of SrF_3 (k) on the content of SrF_3 in the starting melt according to the data of [6] and [9]

Content of SrF_2 in melt		Distribution coefficient, k	
C, mol %	x, molar fraction	phase diagram of SrF_2–LaF_3 [6]	experiment on crystal growth [9]
1.0	0.01	4.00	1.50
3.0	0.03	2.18	1.18
5.0	0.05	1.6	1.08
5.5	0.055	1.54	1.06
6.1	0.061	1.48	1.02
7	0.07	1.31	1.0
7.8	0.078	1.21	0.97
10.0	0.10	1.00	0.93
15.0	0.15	0.81	0.75

However, the method used in [9] for studying the distribution of the second component, in particular, SrF_2, along the crystal boule requires the destruction of crystalline samples under study. In this work, to refine the positions of maxima in the melting curves, we used the dependence of the density of the $La_{1-x}Sr_xF_{3-x}$ crystals on the content of SrF_2 [11]. The study of single crystals of $La_{1-x}Sr_xF_{3-x}$ solid solutions showed that the density ρ decreases linearly with an increase in the SrF_2 content [11]. For example, for pure LaF_3, $\rho = 5.936$ g/cm^3, and, for the compound $La_{0.85}Sr_{0.15}F_{2.85}$, $\rho = 5.663$ g/cm^3. At the same time, as can be seen from the data in Table 1, during crystallization in the chosen composition range $0.01 \le x \le 0.15$, the coefficient k varies from $k > 1$ to $k < 1$. At $k > 1$, the gradual depletion in the second component occurs along the crystal length and the density of the bottom part of the crystal

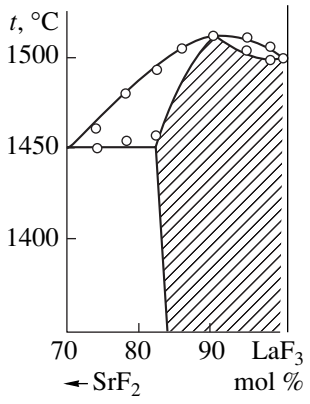

Fig. 1. Part of the phase diagram of SrF_2–LaF_3: the hatched area shows the region of homogeneity of the $La_{1-x}Sr_xF_{3-x}$ tysonite solid solutions.

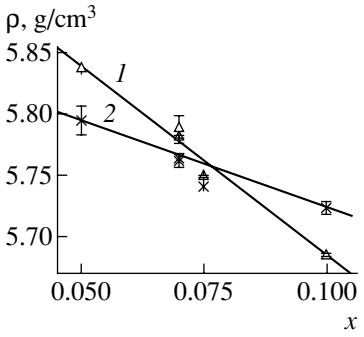

Fig. 2. Densities of the (*1*) top and (*2*) bottom parts of the $La_{1-x}Sr_xF_{3-x}$ crystal boule vs. x (molar fraction of SrF_2) for the starting melt.

ρ_b is lower than that of the top part ρ_t ($\rho_b < \rho_t$). On the contrary, at $k < 1$, the enrichment in the second component is observed [9] and $\rho_b > \rho_t$. Thus, by measuring and comparing the densities of the bottom and top parts of the crystal boule, one can determine the character of k (either $k > 1$ or $k < 1$) during crystal growth from melt with a specified composition. Evidently, the coincidence (within experimental error) of the densities of the top and bottom parts of the crystal would imply that the second component is uniformly distributed along the boule length and $k = 1$.

In order to verify the above concepts, we measured the densities of the bottom and top parts of $La_{1-x}Sr_xF_{3-x}$ crystals grown by directional crystallization. The position of the melting maximum in the phase diagram was refined for these crystals by XRFA [9].

The density was measured using the hydrostatic weighing method at a temperature of t = 18–20°C. The cylindrical samples used, 12 mm in diameter with a height of h = 6.5–12 mm, were cut from both ends of the crystals grown from the LaF_3 melt with a different initial content x (the molar fraction) of SrF_2: x = 0.05, 0.065, 0.07, 0.075, and 0.100.

The results listed in Table 2 show that the desired composition with the uniform distribution of SrF_2 along the crystal length (k = 1) corresponds to x_0 = 0.075. Plotting the variation in ρ_t and ρ_b with composition (Fig. 2) makes it possible to determine more exactly the value of x_0 at which $\rho_t = \rho_b$. It can be seen from Fig. 2 that the corresponding value $x_0 = 0.076 \pm 0.005$, which is close to $x_0 = 0.070 \pm 0.005$ obtained in [9].

Let us consider errors in determining the position of the melting maximum by comparing the densities of the top and bottom parts of the crystal. The error ($\Delta | x_0$) in the value of x_0 is the culmination of several factors. First, this is an error in the determination of ρ, which depends, in turn, on the accuracy of the method and on the sample weight. The accuracy of determining density by hydrostatic weighing is $\pm 1 \times 10^{-3}$ g/cm^3. This is characteristic of smooth samples with a small number of cleavages and cracks and with a weight of at least 5 g. These values correspond to cylindrical samples of tysonite crystals with a diameter of 12 mm and a height of $h \sim 8$ mm. The majority of the samples satisfied these requirements. If not, the error increased. For example, in the determination of ρ_b for the $La_{0.935}Sr_{0.065}F_{2.935}$ compound, the sample weight m was smaller than 1 g and the error in measurement was as high as 5×10^{-3} g/cm^3. The data for this crystal were excluded from the final analysis. The difference in the temperature of density measurements also increases the spread in the values of ρ.

Second, it should be kept in mind that, at $k \neq 1$, the second component is distributed nonlinearly along the crystal length [9]. Therefore, the variations in ρ along the crystal length are nonlinear. For large samples (>8 g), the value of ρ does not exactly correspond to the density of either the top or bottom end of the boule but includes partially the density of the regions forming the middle part of the crystal. As a result, the value of $|\Delta\rho| = \rho_b - \rho_t$ for this composition decreases, which introduces an additional error to the determination of x_0. A noticeable difference in the weights of the samples cut from the top and bottom of the boule results in the same effect. We should also take into account the error that occurs in weighing the starting components, when a mixture of reactants is prepared for the crystal growth. In this case, the error was $\pm 10^{-3}$ g.

As a result, the estimated error in determining the solid-solution composition at the maximum by measuring the density is Δx = 0.004–0.006.

REFINEMENT OF THE COMPOSITION OF SOLID SOLUTIONS AT THE MAXIMA OF MELTING CURVES FOR TYSONITE PHASES IN SrF_2–RF_3 SYSTEMS (R = Ce, Pr, Nd)

The procedure described was used for studying the $R_{1-x}Sr_xF_{3-x}$ crystals with R = Ce, Pr, and Nd. The results of [6], according to which the compositions with x_0 = 0.10 for Ce and Nd and 0.11 for Pr correspond to the melting maxima of these systems, were used as the initial data. In our experiments, the content of SrF_2 in the melt x varied from 0.07 to 0.16. Crystals with a diameter of 12 mm and a length of 40–45 mm were grown from melt by the Bridgman method [11] with the crucible lowered at a rate of $V = 5.0 \pm 1.5$ mm/h. The weight losses during crystallization were less than 5 wt %. The experimental conditions were the same as in [9].

The results of measurements of the densities of the bottom and top parts of the crystals grown are listed in Table 2. One can see that the value of the maximum for the tysonite solid solutions of the systems under study differs from that reported in [6]. The results obtained are plotted in Fig. 3 as $\Delta\rho = \Delta_t - \Delta_b = f(x)$. The value of x_0 derived from these plots for $La_{1-x}Sr_xF_{3-x}$ (at which $\Delta\rho = 0$) is 0.078 ± 0.006. The value of x_0 found from the

intersection of the curves $\rho_t(x)$ and $\rho_b(x)$ (Fig. 2) is 0.076 ± 0.005. The difference between these values lies within the experimental error. However, the plot in Fig. 3 is simpler for the estimation of the error. The calculation of the root-mean-square errors shows that the error in determining x_0 is $\Delta x = 0.006$.

Analysis of the data presented allows us to conclude the following. For crystals of $La_{1-x}Sr_xF_{3-x}$ solid solutions, we have the average of the two values presented above: $x_0 = 0.077 \pm 0.006$. For the $Pr_{1-x}Sr_xF_{3-x}$ crystals, the composition related to the melting maximum in the phase diagram corresponds to $x_0 = 0.122 \pm 0.006$, while for the $Nd_{1-x}Sr_xF_{3-x}$ crystals, $x_0 = 0.141 \pm 0.006$. For $Ce_{1-x}Sr_xF_{3-x}$ solid solutions, the samples of only two compositions were available: $x = 0.07$ and 0.10. This experimental set is insufficient for exact determination of the maximum. The estimate for this system is $x_0 = 0.093 \pm 0.007$.

The coordinates of the maxima (x_0) in the melting curves in the phase diagrams of the systems under study are listed in Table 3. The plot of x_0 vs. atomic number of the rare-earth element N_R is shown in Fig. 4. It can be seen that the coordinate of the maximum shifts to higher values of SrF_2 content with an increase in N_R. The approximation performed using the least-squares method yields the equation of a straight line in the form $x_0 = 2N_R - 105$.

Using the value of x_0 obtained, we calculated the molecular weights (M) of the grown crystals corresponding to the maxima in the melting curves. The weights calculated turned out to be almost the same for all four phases studied (Table 3).

Table 2. Densities of the bottom and top parts of the $R_{1-x}Sr_xF_{3-x}$ crystals (R = La, Ce, Pr, Nd) at t = 17–22°C vs. the composition of the starting melt and the character of the distribution coefficient ($k > 1$ and $k < 1$)

Composition of starting melt	Density of crystal, ρ, g/cm^3		$\rho_t - \rho_b$	k
	bottom, ρ_b	top, ρ_t		
$La_{0.95}Sr_{0.05}F_{2.95}$	5.795 ± 0.012	5.837 ± 0.002	0.042	>1
$La_{0.935}Sr_{0.065}F_{2.935}$	5.597 ± 0.05	5.817 ± 0.002	0.22	~1
$La_{0.930}Sr_{0.07}F_{2.930}$	5.764 ± 0.001	5.782 ± 0.001	0.018	~1
	5.762 ± 0.005	5.790 ± 0.010	0.026	~1
$La_{0.925}Sr_{0.075}F_{2.925}$	5.741 ± 0.001	5.750 ± 0.001	0.009	~1
$La_{0.9}Sr_{0.10}F_{2.9}$	5.724 ± 0.005	5.685 ± 0.005	–0.039	~1
$Ce_{0.93}Sr_{0.07}F_{2.93}$	5.883 ± 0.001	5.966 ± 0.005	0.083	>1
$Ce_{0.90}Sr_{0.10}F_{2.90}$	5.778 ± 0.008	5.760 ± 0.010	–0.019	<1
	5.781 ± 0.007	5.750 ± 0.003	–0.031	~1
		Sample with a crack		
$Pr_{0.90}Sr_{0.10}F_{2.90}$	5.994 ± 0.002	6.034 ± 0.005	0.04	>1
$Pr_{0.88}Sr_{0.12}F_{2.88}$	5.965 ± 0.010	5.969 ± 0.008	0.004	~1
$Pr_{0.85}Sr_{0.15}F_{2.85}$	5.925 ± 0.004	5.872 ± 0.003	–0.053	<1
$Nd_{0.90}Sr_{0.10}F_{2.90}$	6.172 ± 0.002	6.266 ± 0.005	0.094	>1
$Nd_{0.88}Sr_{0.12}F_{2.88}$	6.096 ± 0.013	6.159 ± 0.004	0.063	>1
	6.144 ± 0.003	6.188 ± 0.006	0.044	>1
$Nd_{0.87}Sr_{0.13}F_{2.87}$	6.094 ± 0.001	6.12 ± 0.001	0.026	>1
$Nd_{0.86}Sr_{0.14}F_{2.86}$	6.088 ± 0.005	6.080 ± 0.010	–0.005	~1
$Nd_{0.84}Sr_{0.16}F_{2.84}$	6.048 ± 0.003	6.009 ± 0.001	–0.039	<1

Table 3. Coordinates of maxima x_0 and molecular weights M (x_0) of the solid solutions $R_{1-x}Sr_xF_{3-x}$ (R = La–Nd)

R	N_R	$x_0 \pm \Delta x_0$	M (x_0)
La	57	0.077 ± 0.006	190.50
Ce	58	0.093 ± 0.007	190.47
Pr	59	0.122 ± 0.006	189.09
Nd	60	0.141 ± 0.006	190.54

RESULTS AND DISCUSSION

As shown in [8], the solid-solution compositions corresponding to the maxima in the melting curves for binary systems in the case of directional crystallization are usually refined by measuring the lattice parameters of the samples cut from both ends of grown crystals of specified composition. This method is appropriate in the case of strong dependence of the lattice parameters on the composition. For tysonite solid solutions, when the SrF_2 content x varies from 0 to 0.15, the error in determining the unit-cell parameters overlaps the change in the parameters [10]. Therefore, the method of refining the positions of maxima in melting curves by measuring the densities of the end parts of the crystal boule is preferential for tysonite solid solutions.

The above-mentioned discrepancy between the data obtained by DTA [6] and directional crystallization of $La_{1-x}Sr_xF_{3-x}$ [9] may be related to the supercooling of the melts in the course of determining the solidification temperature from the melting curves using DTA. It can be seen from the data in Table 1 that the difference in the values of k decreases with an increase in the SrF_2 content. Apparently, the lower the SrF_2 content, the stronger the supercooling of the melt. In addition, in the case of directional crystallization, due to a sufficiently low growth rate, the process is closer to equilibrium than in the case of DTA. The regular shift of the position of the melting maximum to higher SrF_2 concentrations observed in this work for the solid solutions with R = La–Nd does not contradict the general character of changes in this coordinate in the series of the $R_{1-x}Sr_xF_{3-x}$ tysonite phases [5].

There is some discrepancy between the values of the coordinate of the melting maximum x_0 for the $La_{1-x}Sr_xF_{3-x}$ crystals obtained in this work ($x_0 = 0.077 \pm 0.006$) and in [9] ($x_0 = 0.070 \pm 0.005$). However, the dif-

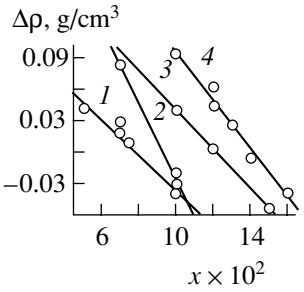

Fig. 3. Difference Δρ in the densities of the top and bottom parts of the $R_{1-x}Sr_xF_{3-x}$ crystals (R = La, Ce, Pr, Nd) vs. SrF_2 content (x) in the starting melt: R = (*1*) La, (*2*) Ce, (*3*) Pr, and (*4*) Nd.

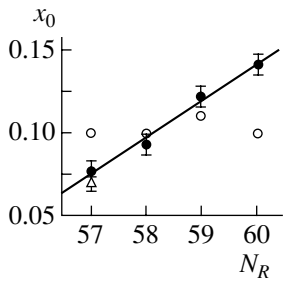

Fig. 4. Dependence of the coordinates of maxima x_0 for the tysonite solid solutions $R_{1-x}Sr_xF_{3-x}$ (R = La, Ce, Pr, Nd) on the atomic number of the rare-earth element N_R. The results of (○) [5], (△) [9], and (●) this study. The analytical dependence is shown by the solid line.

ference between these values lies within experimental error.

The method of determining density is simpler than XRFA; at the same time, the crystal need not be destroyed and may be used for other purposes. The accuracy of determining density may be increased substantially by eliminating some sources of errors. For example, if a grown crystal is fairly long and the samples cut from the top and bottom of the boule are 12 mm in diameter and ~8 mm in height with a weight of ~5 g and the number of compositions with different values of x at either side of the assumed value of x_0 is at least two (two compositions with $x < x_0$ and two with $x > x_0$), the error in determining x_0 can be reduced to 0.002. Such an accuracy exceeds that of DTA by an order of magnitude.

Thus, the data presented show that a comparison of the densities of the top and bottom parts of crystals grown by directional crystallization allows one to determine the composition at which $k = 1$ (the maximum in the melting curve for solid solutions) for the phases with tysonite structure in SrF_2–RF_3 systems. The accuracy of determination is not less than that of XRFA and is much higher than that of DTA.

CONCLUSIONS

A method is proposed for the refining the composition of congruently melting solid solutions of binary systems by comparing the densities of the top and upper parts of crystals grown by directional crystallization. The accuracy of the method is high, and the method does not require destruction of a sample.

The compositions of the solid solutions corresponding to the maxima in the melting curves of the phases with the tysonite structure formed in SrF_2–RF_3 systems (R = La, Ce, Pr, Nd) were refined. It was established that an increase in the atomic number of the rare-earth element R is accompanied by an increase in the content of this element in the maxima.

REFERENCES

1. B. P. Sobolev, *Rare Earth Trifluorides*, Part 1: *The High Temperature Chemistry of Rare Earth Trifluorides* (Inst. d'Estudis Catalans, Barcelona, 2000).
2. B. P. Sobolev, *Rare Earth Trifluorides*, Part 2: *Introduction to Materials Science of Multicomponent Metal Fluoride Crystals* (Inst. d'Estudis Catalans, Barcelona, 2001).
3. B. P. Sobolev, in *Crystals: Growth, Structure, and Properties* (Nauka, Moscow, 1993), p. 167.
4. P. P. Fedorov and B. P. Sobolev, Zh. Neorg. Khim. **24** (4), 1038 (1979).
5. B. P. Sobolev and K. B. Seĭranyan, Kristallografiya **20** (4), 763 (1975) [Sov. Phys. Crystallogr. **20**, 467 (1975)].
6. B. P. Sobolev and K. B. Seiranian, J. Solid State Chem. **39** (3), 337 (1981).
7. E. A. Krivandina, O. I. Lyamina, A. A. Samokhina, and B. P. Sobolev, *Expanded Abstracts of 7th All-Union Conference on Crystal Growth* (Moscow, 1988), Vol. 3, p. 132.
8. A. A. Bystrova, O. S. Bondareva, P. P. Fedorov, *et al.*, *Collected Abstracts of 11th International Conference on Crystal Growth* (The Hauge, 1995), p. 280.
9. E. A. Krivandina, Z. I. Zhmurova, O. I. Lyamina, *et al.*, Kristallografiya **41** (5), 958 (1996) [Crystallogr. Rep. **41**, 912 (1996)].
10. K. B. Seĭranyan, Candidate's Dissertation in Chemistry (Gos. Univ., Erevan, 1975).
11. E. A. Krivandina, Z. I. Zhmurova, G. V. Berezhkova, *et al.*, Kristallografiya **40** (4), 741 (1995) [Crystallogr. Rep. **40**, 686 (1995)].

Translated by E. Yablonskaya

Crystallography Reports, Vol. 48, No. 5, 2003, pp. 883–887. Translated from Kristallografiya, Vol. 48, No. 5, 2003, pp. 945–949.

CRYSTAL GROWTH

Dedicated to the 60th Anniversary of the Shubnikov Institute of Crystallography of the Russian Academy of Sciences

Y_2O_3–Al_2O_3–Nd_2O_3 Phase Diagram and the Growth of $(Y,Nd)_3Al_5O_{12}$ Single Crystals

L. V. Soboleva and A. P. Chirkin

Shubnikov Institute of Crystallography, Russian Academy of Sciences, Leninskiĭ pr. 59, Moscow, 119333 Russia

e-mail: labsol@ns.crys.ras.ru

Received April 24, 2002; in final form, January 20, 2003

Abstract—The optimum compositions of the melts used for the growth of yttrium–aluminum garnet (YAG) single crystals with different neodymium contents are determined using the phase diagram of the ternary system Y_2O_3–Al_2O_3–Nd_2O_3 with the binary sections $Y_3Al_5O_{12}$–Nd_2O_3 and $Y_3Al_5O_{12}$–$Nd_3Al_5O_{12}$. A number of melt compositions characterized by one garnet phase, namely, $(Y,Nd)_3Al_5O_{12}$, are established. Single crystals of yttrium–aluminum garnets with a high content of the activator (up to 2.6 wt % Nd) are grown by the Czochralski method. © *2003 MAIK "Nauka/Interperiodica".*

INTRODUCTION

Crystals of $(Y,Nd)_3Al_5O_{12}$ (Nd : YAG) are widely used as laser materials. The energy characteristics of active elements fabricated from these crystals depend on the degree of crystal perfection and the Nd^{3+} content. As was shown earlier in [1–3], the structural perfection of Nd : YAG crystals grown by the Czochralski method, in turn, substantially depends on a number of thermodynamic and kinetic factors.

The main thermodynamic factor in this case is associated with the phase diagram of the Y_2O_3–Al_2O_3–Nd_2O_3 ternary system, which determines the region of existence of yttrium–aluminum garnets with different Nd^{3+} contents, the optimum compositions of the melts used for growing Nd : YAG crystals, and the crystallization temperature. The controlling kinetic factor is the speed of pulling a crystal from a melt [1].

The growth of perfect YAG single crystals with a high Nd^{3+} content presents certain problems. One of the difficulties encountered in growing garnet crystals at high temperatures is associated with the deviation of the melt composition from stoichiometry of the $3(Y_2O_3 \cdot Nd_2O_3) : 5Al_2O_3$ garnet.

In the general case, the chemical interaction of the Y_2O_3 and Nd_2O_3 components with Al_2O_3 in the stoichiometric ratio $(Y_2O_3 \cdot Nd_2O_3) : Al_2O_3 = 3 : 5$ results in the formation of the garnet phase according to the following scheme:

$$3(Y_2O_3 \cdot Nd_2O_3) + 5Al_2O_3 \xrightarrow{>2000^\circ C} (Y,Nd)_3Al_5O_{12}.$$

However, during the crystal growth, the melt composition undergoes variations due to heating at a temperature slightly above 2000°C within a few days. The stoichiometry of the components in the melt is violated upon evaporation of the lower melting component Al_2O_3 with the melting temperature T_m = 2050°C, because the melting temperature of Y_2O_3 is higher than 2400°C and the melting temperature of Nd_2O_3 is approximately equal to 2300°C [4, 5]. This brings about a decrease in the Al_2O_3 content in the melt and, consequently, the formation of the aluminate phases $(Y,Nd)AlO_3$. The YAG crystals growing from these melts also have a nonstoichiometric composition and contain $YAlO_3$ and $NdAlO_3$ impurities. Note that the longer the time of high-temperature treatment of the melt, the greater the deviation of the composition of the melt and, hence, the crystal from stoichiometry.

Knowing the regularities of the phase formation in ternary melt systems [6], it is possible to determine the crystallization regions of newly formed three-component phases. In this respect, the possibility exists of establishing the concentration conditions of crystallization of the $(Y,Nd)_3Al_5O_{12}$ garnet phase in the Y_2O_3–Al_2O_3–Nd_2O_3 ternary system.

The purposes of the present work were as follows: (i) to investigate the physicochemical features of the Y_2O_3–Al_2O_3–Nd_2O_3 phase diagram based on the Y_2O_3–Al_2O_3, Nd_2O_3–Al_2O_3, and Y_2O_3–Nd_2O_3 binary systems; (ii) to determine the optimum compositions of the melts used for the growth of $Y_3Al_5O_{12}$ crystals with

1063-7745/03/4805-0883$24.00 © 2003 MAIK "Nauka/Interperiodica"

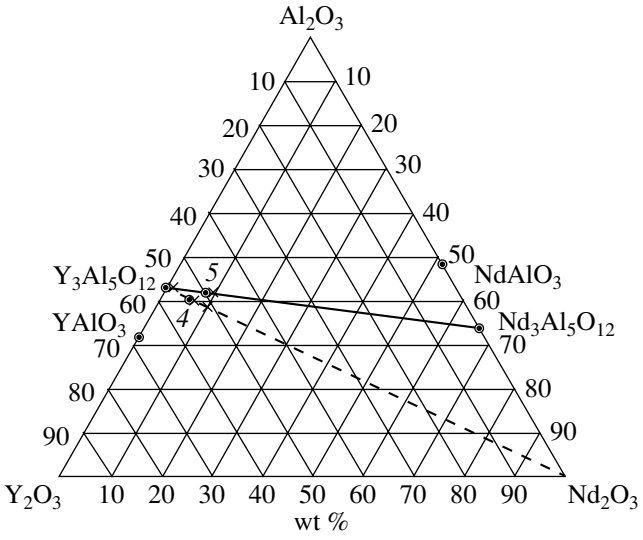

Fig. 1. Y_2O_3–Al_2O_3–Nd_2O_3 ternary system with the binary sections $Y_3Al_5O_{12}$–$Nd_3Al_5O_{12}$ (solid line) and $Y_3Al_5O_{12}$–Nd_2O_3 (dashed line). Open circles indicate the optimum compositions of the melts used for the growth of Nd : $Y_3Al_5O_{12}$ crystals.

different Nd^{3+} contents from analyzing the $Y_3Al_5O_{12}$–Nd_2O_3 and $Y_3Al_5O_{12}$–$Nd_3Al_5O_{12}$ binary sections; and (iii) to accomplish the Czochralski growth of perfect YAG single crystals with a high Nd^{3+} content.

PHYSICOCHEMICAL FEATURES OF THE PHASE DIAGRAM OF MELTING IN THE Y_2O_3–Al_2O_3–Nd_2O_3 TERNARY SYSTEM

Phase diagrams of binary and ternary systems can provide valuable information on the directivity of heterogeneous equilibria in the systems under investigation and make it possible to determine the optimum crystallization conditions for forming solid phases. Reasoning from the identity of the melting and solubility curves [6], which, in turn, represent the liquidus curves, the approach we previously used to determine the optimum crystallization conditions for solid phases in the solubility systems [7] was applied to analyze the melting diagrams of the binary systems studied in [8, 9].

In this work, the melting diagram of a ternary system was used to determine the optimum compositions of the melts for the growth of neodymium-containing YAG garnet crystals. For this purpose, we used the Gibbs triangular phase diagram [6] of the Y_2O_3–Al_2O_3–Nd_2O_3 ternary system with the $Y_3Al_5O_{12}$–Nd_2O_3 and $Y_3Al_5O_{12}$–$Nd_3Al_5O_{12}$ binary sections (Fig. 1).

To the best of our knowledge, reliable data on the Y_2O_3–Al_2O_3–Nd_2O_3 ternary system are not available in the literature; therefore, we consider this diagram from the standpoint of physicochemical features of the phase formation in its constituent binary systems.

The Y_2O_3–Al_2O_3 phase diagram [10] (Fig. 2a) is characterized by the formation of three new solid phases: (1) $2Y_2O_3 \cdot Al_2O_3$ (congruent melting), (2) $3Y_2O_3 \cdot 5Al_2O_3$ (congruent melting), and (3) $Y_2O_3 \cdot Al_2O_3$ (incongruent melting). According to Bondar' *et al.* [11], all solid phases undergo congruent melting. The Y_2O_3–Nd_2O_3 phase diagram [12] (Fig. 2b) contains extended regions of existence of solid solutions based on yttrium and neodymium oxides. The Nd_2O_3–Al_2O_3 phase diagram [11] (Fig. 2c) is characterized by the formation of only one new phase, namely, $NdAlO_3$.

SEARCH FOR OPTIMUM COMPOSITIONS OF THE MELTS USED FOR THE GROWTH OF Nd : YAG CRYSTALS

For the purpose of determining the optimum compositions of the melts used for the growth of YAG crystals with different Nd^{3+} contents from analyzing the Y_2O_3–Al_2O_3–Nd_2O_3 phase diagram, we performed an X-ray powder diffraction analysis of a number of compositions corresponding to points in the $Y_3Al_5O_{12}$–Nd_2O_3 and $Y_3Al_5O_{12}$–$Nd_3Al_5O_{12}$ binary sections of the ternary system under investigation (Fig. 1, Table 1).

The components Nd_2O_3 and $Nd_3Al_5O_{12}$ supply the melt with Nd^{3+} ions. We did not examine the $Nd_3Al_5O_{12}$–$NdAlO_3$ binary section, because $NdAlO_3$ has a perovskite structure. A comparison of the melt compositions in the binary sections $Y_3Al_5O_{12}$–Nd_2O_3 (**1**) and $Y_3Al_5O_{12}$–$Nd_3Al_5O_{12}$ (**2**) shows that, in these sections, the Nd_2O_3 content increases to the same extent; however, unlike the melt compositions in section **1**, the compositions in section **2** are characterized by a considerable decrease in the Y_2O_3 content, whereas the Al_2O_3 content remains nearly constant. It should be noted that, in both cases, the content of components in compositions *1–6* changes more monotonically as compared to compositions *7–10*.

The melts were prepared from the initial reactants Y_2O_3, Al_2O_3, and Nd_2O_3 (special-purity grade) in which the content of the main component was equal to 99.99%. The impurity content in all the initial reactants was as follows: Fe, Mg = 6×10^{-4} wt %; Cr, Pb = 5×10^{-4} wt %; and Si = 3×10^{-3} wt %. In order to prepare the melt compositions in the aforementioned sections, the weighed portions of Y_2O_3, Al_2O_3, and Nd_2O_3 (taken in the weight ratios given in Table 1) were separately precalcined in platinum crucibles in a muffle furnace at T = 1000°C for 2 h. After cooling in a desiccator over P_2O_5, the weighed portions were thoroughly mixed and ground to fine powder in a corundum mortar in a chamber filled with nitrogen. Then, the powders were pressed into pellets. The pellets were placed in molybdenum crucibles, which were preliminarily annealed under vacuum (2×10^{-5} mmHg) at a temperature of 2000°C for 3 h.

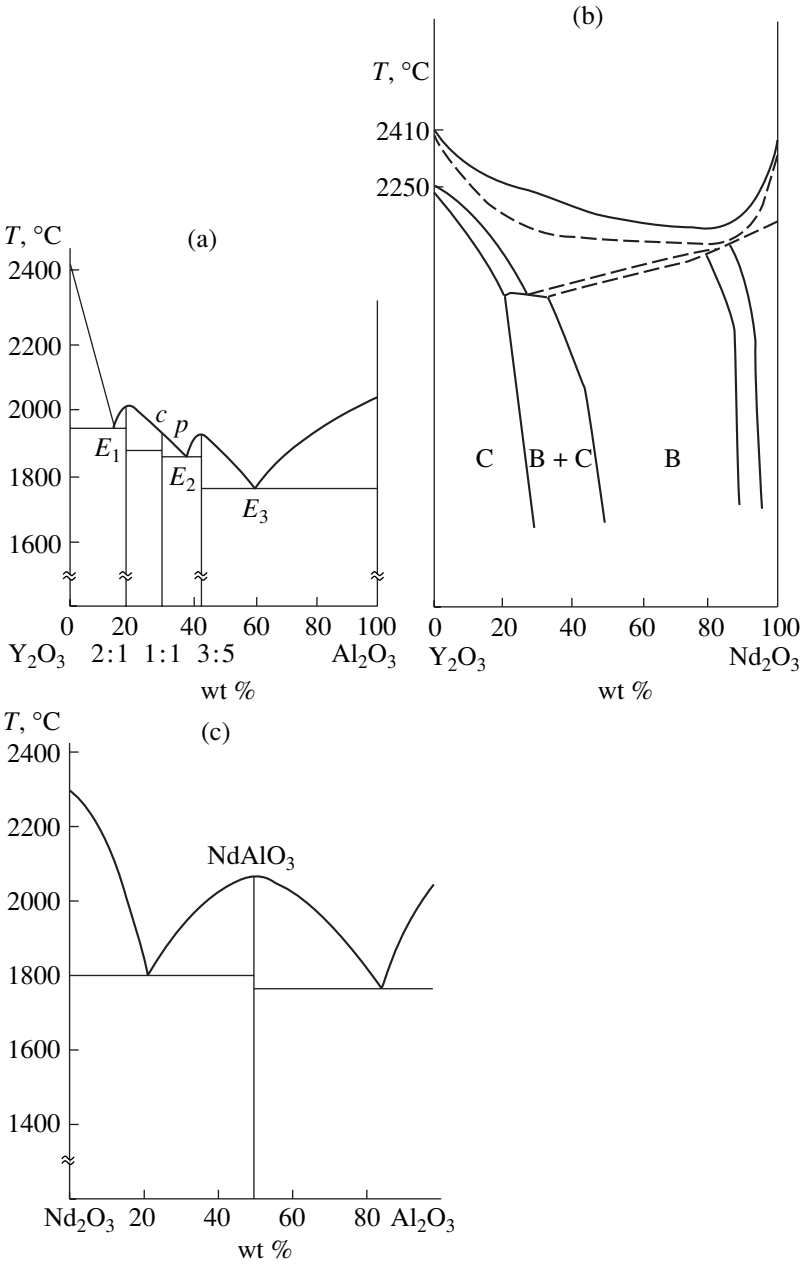

Fig. 2. Phase diagrams: (a) Y_2O_3–Al_2O_3, (b) Y_2O_3–Nd_2O_3, and (c) Nd_2O_3–Al_2O_3.

Then, crucibles with samples of different compositions were mounted on a holder and placed in a furnace in such a way that all the crucibles were heated to the same temperature, which was achieved with the use of a special set of shields arranged in the furnace. The furnace was evacuated to a residual pressure of 2×10^{-5} mmHg. The samples were heated for 2 h until their melting. Thereafter, the melts were held at $T = 2000$°C for 2 h and at a lower temperature for 5 h.

The cakes thus obtained were thoroughly ground in an agate mortar and were then subjected to X-ray powder diffraction analysis on a DRON-1.5 diffractometer. In order to make certain that the solid-phase reactions proceed to completion and to identify the solid phase formed, the samples were subjected to repeated melting and grinding and the X-ray powder diffraction analysis of these samples was performed again.

An examination of the X-ray diffraction diagrams of the cake samples whose compositions correspond to melts in sections **1** and **2** demonstrates that the chemical interaction proceeds to completion only upon a 5-h heat treatment of the melt at $T = 2000$°C. For example, X-ray diffraction diagrams of the cake samples containing 1–3 wt % Nd_2O_3 (section **1**) indicate that, in this

Table 1. Compositions of the melts corresponding to points in the $Y_3Al_5O_{12}$–Nd_2O_3 and $Y_3Al_5O_{12}$–$Nd_3Al_5O_{12}$ binary sections of the Y_2O_3–Al_2O_3–Nd_2O_3 phase diagram

Binary sections in the phase diagram						
Melt no.	$Y_3Al_5O_{12}$–Nd_2O_3, wt %			$Y_3Al_5O_{12}$–$Nd_3Al_5O_{12}$, wt %		
	Nd_2O_3	Al_2O_3	Y_2O_3	Nd_2O_3	Al_2O_3	Y_2O_3
1	1.00	42.70	56.30	1.09	42.70	56.13
2	2.00	42.10	55.90	2.17	42.64	55.20
3	3.00	41.70	55.30	4.20	42.35	53.56
4	4.00	41.30	54.70	6.10	42.08	51.82
5	5.00	40.90	54.10	7.89	41.82	50.82
6	6.00	40.40	53.60	8.39	40.83	50.78
7	7.00	40.00	53.00	8.74	41.71	49.55
8	8.00	39.50	52.50	9.58	41.59	48.83
9	9.00	39.00	52.00	10.00	41.80	48.20
10	10.00	38.80	51.20			

Table 2. Growth conditions and characteristics of the Nd : YAG crystals grown from melts

Experiment no.	Growth conditions		Characteristics of the crystal grown			
	pulling speed, mm/h	growth time, h	crystal size, mm		Nd^{3+} content	
			l	*d*	wt %	at. %
1	1.00	140	150	40	0.25	0.67
2	1.00	140	140	40	0.55	1.20
3	1.00	150	200	42	1.30	2.60
4	1.00	140	140	42	2.00	3.76
5	0.60	170	140	40	2.60	4.86
6	0.60	140	140	39		
7	0.60	140	140	40		
8	1.00	140	140	38		

case, the main phase is the $Y_3Al_5O_{12}$ garnet. However, the X-ray diffraction diagrams also exhibit sufficiently intense peaks that can be assigned to the $YAlO_3$ and $NdAlO_3$ phases. At a content of 4 wt % Nd_2O_3, the cake samples have a homogeneous composition and contain only one phase, namely, $(Y,Nd)_3Al_5O_{12}$. As the Nd_2O_3 content increases to 5 wt %, apart from the peaks associated with the garnet phase, there appear peaks attributed to $YAlO_3$ and $NdAlO_3$. Therefore, the melt composition optimum for the formation of the garnet phase in section **1** is as follows: Nd_2O_3, 4.00 wt %; Al_2O_3, 41.30 wt %; and Y_2O_3, 54.70 wt %.

Judging from the X-ray diffraction diagrams, the cake samples corresponding to the melt compositions in section **2**, unlike those in section **1**, are characterized by a greater degree of homogeneity with the garnet phase predominant. It was established that the melt composition optimum for the formation of the garnet phase in section **2** is as follows: Y_2O_3, 50.28 wt %; Al_2O_3, 41.82 wt %; and Nd_2O_3, 7.89 wt %. An increase in the Nd_2O_3 content above 8.5 wt % in the melts results in the formation of neodymium and yttrium aluminate phases.

GROWTH OF Nd : YAG SINGLE CRYSTALS

A comparison of the changes observed in the melt compositions along sections **1** and **2** (Table 1) revealed that an increase in the Nd_2O_3 content and a decrease in the Y_2O_3 content in the melts are more pronounced for the compositions of section **2** as compared to those of section **1**. It is worth noting that the Al_2O_3 content remains nearly constant in the melts of section **2** and decreases in the melts of section **1**.

Reasoning from these findings and the physicochemical features of the garnet formation at high temperatures, the compositions of the melts in section **2** are more preferable than those in section **1**. Consequently,

the melt compositions lying along section **2** were predominantly used for growing Nd : YAG single crystals.

Single crystals of Nd : YAG garnets were grown by the Czochralski method from melts according to the following procedure. A crucible rated at 1000 g of the melt was charged with the initial components in the chosen weight ratio and placed in a crystallization chamber. The chamber was evacuated to a residual pressure of 10^{-4} mmHg and was then filled with a mixture of an inert gas and hydrogen in the volume ratio 95 : 5. The gases involved in the mixture were preliminarily dried and purified. The starting material in the crystallization chamber was heated to the melting point and kept at this temperature for 10 h until the components were dissolved completely. Then, the rotating seed was immersed in the melt. After a time, the seed was slowly pulled from the melt. Upon completion of the growth process, the crystal was separated from the melt and cooled for 30 h.

The growth conditions and the main characteristics of the Nd : YAG crystals grown from the melts corresponding to points in section **2** (Table 1) are given in Table 2. The Nd^{3+} content in the crystals was determined using mass spectrometric analysis. As can be seen from Table 2, the higher the Nd_2O_3 content in the melt, the lower the speed of pulling of the crystal. In experiment nos. 1–4, the Nd_2O_3 content was equal to 1.09–6.10 wt % and the pulling speed was 1 mm/h. As the Nd_2O_3 content in the melt increased to 7.89 wt % (experiment no. 5), the pulling speed decreased to 0.6 mm/h. The Nd : YAG crystals grown from melts in experiment nos. 6–8 have an inhomogeneous composition.

The Nd : YAG crystals grown in experiment nos. 1–5 have a homogeneous composition. In this case, an increase in the Nd_2O_3 content in the initial melts leads to an increase in the Nd^{3+} content in the crystals from 0.25 to 2.60 wt % (0.67–4.86 at. %). It should be noted that, in [1–3, 13, 14], the Nd^{3+} content falls in the range from 1.0 to 1.5 at. %.

CONCLUSIONS

Thus, we analyzed the physicochemical features of the Y_2O_3–Al_2O_3–Nd_2O_3 phase diagram based on the $Y_3Al_5O_{12}$–Nd_2O_3 and $Y_3Al_5O_{12}$–$Nd_3Al_5O_{12}$ binary sections with the aim of determining the compositions of melts containing only one garnet phase, namely, $(Y,Nd)_3Al_5O_{12}$, with different Nd^{3+} contents. The X-ray powder diffraction analysis revealed a number of homogeneous compositions of the melts characterized by one garnet phase, $(Y,Nd)_3Al_5O_{12}$, with different Nd^{3+} contents. We devised a technique for growing Nd : YAG crystals from melts in an inert gas atmosphere. Homogeneous single crystals of Nd : YAG garnets with an activator content of 0.25–2.60 wt % Nd^{3+} were grown by the Czochralski method.

REFERENCES

1. C. Belouet, J. Cryst. Growth **15** (2), 188 (1972).
2. R. F. Belt, R. C. Puttbach, and D. A. Lepore, J. Cryst. Growth **13–14**, 268 (1972).
3. C. Janus, W. Jelenski, and A. Nikolas, J. Cryst. Growth **57** (3), 593 (1982).
4. G. V. Maksimova, V. O. Osiko, A. A. Sobol', *et al.*, Neorg. Mater. **9** (10), 1763 (1973).
5. A. A. Oganesyan and V. Ya. Khaimov-Mal'kov, Kristallografiya **25** (4), 886 (1980) [Sov. Phys. Crystallogr. **25**, 510 (1980)].
6. V. A. Anosov and S. A. Pogodin, *Fundamental Principles of Physicochemical Analysis* (Akad. Nauk SSSR, Moscow, 1974), p. 400.
7. L. V. Soboleva, Neorg. Mater. **31** (5), 614 (1995).
8. L. V. Soboleva, Neorg. Mater. **27** (4), 786 (1995).
9. L. V. Soboleva, Neorg. Mater. **27** (4), 874 (1995).
10. N. A. Toropov, I. A. Bondar', F. Ya. Galakhov, *et al.*, Izv. Akad. Nauk SSSR, Ser. Khim. **7**, 1158 (1964).
11. I. A. Bondar', L. N. Koroleva, and E. T. Bezruk, Neorg. Mater. **20** (2), 257 (1984).
12. P. A. Tikhonov, A. K. Kuznetsov, and É. F. Zhikhareva, Zh. Neorg. Khim. **22** (4), 1057 (1977).
13. N. S. Kovaleva, A. O. Ivanov, and É. P. Dubrovina, Kvantovaya Élektron. (Moscow) **8** (11), 2433 (1981).
14. N. G. Ryabtsev, *Materials for Quantum Electronics* (Sovetskoe Radio, Moscow, 1972), p. 136.

Translated by O. Borovik-Romanova

Crystallography Reports, Vol. 48, No. 5, 2003, pp. 888–896. Translated from Kristallografiya, Vol. 48, No. 5, 2003, pp. 950–958.

CRYSTAL GROWTH

Dedicated to the 60th Anniversary of the Shubnikov Institute of Crystallography of the Russian Academy of Sciences

Hydrothermal Crystallization in the $NaOH–GeO_2–H_2O$ System at 350°C: Mechanism of Self-Assembly of Subpolyhedral Clusters in $Na_4Ge_4^{[6]}Ge_5^{[4]}O_{20}$, $Na_3HGe_4^{[6]}Ge_3^{[4]}O_{16} \cdot 4H_2O$, and $NaHTi_2^{[6]}Si^{[4]}O_7 \cdot 2H_2O$

G. D. Ilyushin and L. N. Dem'yanets

Shubnikov Institute of Crystallography, Russian Academy of Sciences, Leninskiĭ pr. 59, Moscow, 119333 Russia

e-mail: ilyushin@ns.crys.ras.ru

Received November 22, 2002

Abstract—The Na,$Ge^{[6]}$-germanates of the compositions $Na_4Ge_4^{[6]}Ge_5^{[4]}O_{20}$ and $Na_3HGe_4^{[6]}Ge_3^{[4]}O_{16} \cdot 4H_2O$ are crystallized in the $NaOH–GeO_2–H_2O$ system under a pressure of 0.05 GPa and a temperature of 350°C. The structure of the germanates consists of open frameworks of *M* octahedra ($Ge^{[6]}$) and *T* tetrahedra ($Ge^{[4]}$). With an increase in the NaOH concentration, the crystallization fields change in the sequence *R*–GeO_2 (rutile structure type) $\Rightarrow$ *R*–GeO_2 + $Na_4Ge_4^{[6]}Ge_5^{[4]}O_{20}$ $\Rightarrow$ $Na_4Ge_4^{[6]}Ge_5^{[4]}O_{20}$ + $Na_3HGe_4^{[6]}Ge_3^{[4]}O_{16} \cdot 4H_2O$ $\Rightarrow$ $Na_3HGe_4^{[6]}Ge_3^{[4]}O_{16} \cdot 4H_2O$. The phase formation for Na,$Ge^{[6]}$ germanates and Na,Ti silicates ($Na_4Ti_4^{[6]}Si_3^{[4]}O_{16} \cdot 6H_2O$ and $NaHTi_2^{[6]}Si_3^{[4]}O_7 \cdot 2H_2O$) is considered based on the model of the matrix assembly of crystal structures from invariant $Ge^{[6]}$,$Ge^{[4]}$ subpolyhedral structural units. The homologous family of phases consisting of $Na_4Ge_4^{[6]}Ge_5^{[4]}O_{20}$ (M_4T_5 framework), $Na_3HGe_4^{[6]}Ge_3^{[4]}O_{16} \cdot 4H_2O$, $Na_4Ti_4^{[6]}Si_3^{[4]}O_{16} \cdot 6H_2O$ (M_4T_3 framework), and $NaHTi_2^{[6]}Si^{[4]}O_7 \cdot 2H_2O$ (M_4T_2 framework) phases with topologically equivalent one-dimensional *MT* structures is singled out. © *2003 MAIK "Nauka/Interperiodica".*

The crystallochemical family of Na germanates consists of eight phases [1, 2]. Four of these germanates, $Na_4Ge^{[4]}O_4$ [3], $Na_2Ge^{[4]}O_3$ [4], $Na_6Ge_2^{[4]}O_7$ [1], and $Na_2Ge_2^{[4]}O_5$ [1], are the representatives of the family of tetrahedral *T* structures. Three Na,$Ge^{[6]}$ germanates are built by two types of the simplest structural units—*T* tetrahedra [GeO_4] and *M* octahedra [GeO_6]. These phases have open three-dimensional *MT* frameworks and the compositions $Na_4Ge_9O_{20}$ = $Na_4Ge_4^{[6]}Ge_5^{[4]}O_{20}$ (M_4T_5 framework [5]), $Na_3HGe_7O_{16} \cdot 4H_2O$ = $Na_3HGe_4^{[6]}Ge_3^{[4]}O_{16} \cdot 4H_2O$ (M_4T_3 framework [6]), and $Na_2Ge_4O_9$ = $Na_2Ge^{[6]}Ge_3^{[4]}O_9$ (MT_3 framework [7]). The family of *MT* structures is complemented with the mixed Na,Li germanate of the composition $NaLiGe_4O_9$ = $NaLiGe^{[6]}Ge_3^{[4]}O_9$ [8] with the MT_3 framework topologically different from the framework of the $Na_2Ge^{[6]}Ge_3^{[4]}O_9$ structure.

The zeolite-like compounds $Na_3HGe_4^{[6]}Ge_3^{[4]}O_{16} \cdot 4H_2O$ [6], $Na_4Ti_4^{[6]}Si_3^{[4]}O_{16} \cdot 6H_2O$ [9] $A_3HTi_4^{[6]}Si_3^{[4]}O_{16} \cdot 4H_2O$, where *A* = K–Cs [10], possess *MT* frameworks of the type of pharmacosiderite $H_5Fe_4As_3O_{16} \cdot 5H_2O$ [11]. Like another zeolite-like silicate $NaHTi_2SiO_7 \cdot 2H_2O$ [12], these compounds are of great scientific and technological importance in connection with their possible use as efficient ion-exchange materials and molecular sieves and high ionic conductivity with respect to H^+ and Na^+ ions [10, 12–14].

1063-7745/03/4805-0888$24.00 © 2003 MAIK "Nauka/Interperiodica"

The present study was undertaken to identify the structure types of Ge phases formed in the NaOH–GeO_2(quartz)–H_2O system and determine the dependence of phase formation on the change in the GeO_2 content and NaOH concentration in the system. The experimental data are interpreted based on the crystallochemical analysis of Na germanates and the consideration of the specific features of their assembly from invariant $Ge^{[6]}$,$Ge^{[4]}$ subpolyhedral structural units. Earlier [15], we studied the LiOH–GeO_2 (quartz)–H_2O system and determined the dependence of hydrothermal crystallization of the Li,$Ge^{[6]}$ germanate on the weight content of GeO_2 and LiOH concentration and the temperature of the hydrothermal reactions (500 and 350°C). The data on hydrothermal crystallization in the NaOH–GeO_2–H_2O system in the temperature range 300–450°C [16, 17] indicate that, under these conditions, the only stable phase is $Na_4Ge_9O_{20}$.

This study is a continuation of the study [15, 18–23] of synthesis, analysis of the geometrical–topological characteristics of crystal phases, and simulation of the processes of self-organization in the AOH–MeO_2–TO_2–H_2O systems (A = Li, Na, K; Me = Zr, Ti, Hf, $Si^{[6]}$, $Ge^{[6]}$, Sn; T = $Si^{[4]}$, $Ge^{[4]}$).

EXPERIMENTAL

Hydrothermal synthesis was performed by the temperature-gradient method [15] based on the concept of creating continuous convective heat and mass exchange with the aid of a vertical temperature gradient.

Silver ampules 10 mm in diameter, 15 cm^3 in working volume were filled with the starting charge and solvent and then sealed. The filling coefficient was 0.7. The sealed ampules were placed into autoclaves with the cylindrical self-sealing closure. Autoclaves were heated in a furnace with a bottom heater.

Hydrothermal crystallization in the NaOH–GeO_2–H_2O system was studied under a temperature gradient along the vertical axis of the autoclave of 1.5–2.0 K/cm at a temperature in the dissolution zone of 350°C. The temperature at the external wall of the autoclave was maintained automatically within ±2 K. The initial charge consisted of GeO_2 (high purity grade, structure type of quartz) and NaOH (chemically pure grade). The duration of the experiment amounted to 240 h.

Solid insoluble products obtained as a result of high-temperature chemical interaction were washed with hot water, dried, and analyzed.

Structurally, the phases obtained were identified by X-ray phase analysis (DRON-2 and Rigaku D-Max 1500 diffractometers, Cu radiation) using the JCPDS [1] and ICSD [2] databases.

RESULTS

Depending on the NaOH concentration in the system and the weight of the introduced GeO_2 oxide, the products of hydrothermal crystallization were either colorless transparent 0.1- to 2.0-mm-large single crystals with regular faceting or fine crystalline powders. In some instances, we obtained nanocrystalline solids amorphous for X rays (hereafter called the XRA phase). The phase composition of the products of hydrothermal crystallization and the calculated molar ratio $\beta = n\mathrm{NaOH} : m\mathrm{GeO_2}$ (varied from 0.49 to 16.00) are listed in Table 1. The main crystallochemical data for germanates and silicates are listed in Table 2, where the phases with different chemical compositions, unit-cell parameters, and space groups are classified over the topological types of their *MT* frameworks.

In the hydrothermal NaOH–GeO_2–H_2O system, three compounds, which belong to two crystallochemically different groups, are crystallized—germanium dioxide GeO_2 (octahedral rutile-type structure R–TiO_2) and Na,$Ge^{[6]}$ germanates with the compositions $Na_4Ge_4^{[6]}Ge_5^{[4]}O_{20}$ and $Na_3HGe_4^{[6]}Ge_3^{[4]}O_{16} \cdot 4H_2O$ (*MT* structures).

The $Na_4Ge_4^{[6]}Ge_5^{[4]}O_{20}$ germanate has a crystallographically and topographically complex structure, since its *MT* framework consists of two types of T radicals—$[GeO_4]$ orthotetrahedra and infinite $[GeO_3]_\infty$ chains. The $Na_3HGe_4^{[6]}Ge_3^{[4]}O_{16} \cdot 4H_2O$ germanate is an example of an orthotetrahedral structure with isolated tetrahedra.

In the NaOH–GeO_2–H_2O system at 350°C, the formation of $Na_4Ge_4^{[6]}Ge_5^{[4]}O_{20}$ ($\beta = 2.1$) was revealed for series 1 (experiments 1–4, Table 1) with the minimum GeO_2 content (0.15 g) only at C_{NaOH} = 1 wt %. In all the remaining experiments, the solid phase was a nanocrystalline XRA phase ($\beta = 4.2$–18.0).

With the change in the concentration C_{NaOH}, we observed the following crystallization fields for the samples of series 2 (experiments 5–8, Table 1):

$$Na_4Ge_4^{[6]}Ge_5^{[4]}O_{20} \Rightarrow Na_3HGe_4^{[6]}Ge_3^{[4]}O_{16} \cdot 4H_2O + \text{XRA phase} \Rightarrow \text{XRA phase}.$$

With the change in concentration C_{NaOH}, the following crystallization fields were observed for the samples of series 3 (experiments 9–12, β = 0.49–2.28, Table 1):

$$Na_4Ge_4^{[6]}Ge_5^{[4]}O_{20} \Rightarrow Na_4Ge_4^{[6]}Ge_5^{[4]}O_{20} + Na_3HGe_4^{[6]}Ge_3^{[4]}O_{16} \cdot 4H_2O \Rightarrow Na_3HGe_4^{[6]}Ge_3^{[4]}O_{16} \cdot 4H_2O + \text{XRA phase}.$$

In the latter series of experiments characterized by high GeO_2 content in the system and high C_{NaOH} con-

Table 1. Phase composition of crystallization products in the NaOH–GeO_2(quartz)–H_2O system under a pressure of 0.05 GPa at a temperature of 350°C

	GeO_2, g	NaOH, wt %	β = NaOH : GeO_2	Phase composition			
				GeO_2	$Na_4Ge_4^{[6]}Ge_5^{[4]}O_{20}$	$Na_3HGe_4^{[6]}Ge_3^{[4]}O_{16} \cdot 4H_2O$	XRA phase
1	0.15	1.0	2.1	–	+	–	–
2		2.5	4.2	–	–	–	+
3		5.0	8.6	–	–	–	+
4		10.0	18.0	–	–	–	+
5	0.45	1.0	0.69	+	+	–	–
6		2.5	1.39	–	+	–	–
7		5.0	2.81	–	–	+	+
8		10.0	5.86	–	–	–	+
9	2.5	5.0	0.49	+	+	–	–
10		10.0	1.03	+	+	+	–
11		15.0	1.60	–	–	+	+
12		20.0	2.28	–	–	+	+

centrations (20%) (five time higher than the GeO_2 content in series 2), the $Na_3HGe_4^{[6]}Ge_3^{[4]}O_{16} \cdot 4H_2O$ germanate showed broadening of X-ray reflections corresponding to a crystallite size of ~150 Å.

The $Na_4Ge_4^{[6]}Ge_5^{[4]}O_{20}$ germanate synthesized at C_{NaOH} = 5 and 10% was obtained as well-faceted single crystals. The flattened tetragonal bipyramids were 1–2 mm long.

The change in the phase composition of Na,$Ge^{[6]}$ germanates observed with an increase of the C_{NaOH} concentration, $Na_4Ge_4^{[6]}Ge_5^{[4]}O_{20} \Rightarrow Na_3HGe_4^{[6]}Ge_3^{[4]}O_{16} \cdot 4H_2O \Rightarrow$ XRA phase (nanocrystalline phase), can be explained within the model of the matrix assembly of crystal structures and is considered below.

MODEL OF MATRIX ASSEMBLY OF CRYSTAL STRUCTURES

We note the following important characteristics of the structure (Table 2) and conditions of phase formation for the Na-germanate and N,Ti-silicate systems [10, 12]:

—the $Na_3HGe_4^{[6]}Ge_3^{[4]}O_{16} \cdot 4H_2O$ germanate and $Na_4Ti_4^{[6]}Si_3^{[4]}O_{16} \cdot 6H_2O$ silicate belong to the same family of framework structures of the pharmacosiderite $H_5Fe_4As_3O_{16} \cdot 5H_2O$ type;

—the $Na_3HGe_4^{[6]}Ge_3^{[4]}O_{16} \cdot 4H_2O$ germanate and $Na_4Ge_4^{[6]}Ge_5^{[4]}O_{20}$ are cocrystallized in the NaOH–GeO_2–H_2O system at 350°C;

—the $Na_4Ti_4^{[6]}Si_3^{[4]}O_{16} \cdot 6H_2O$ silicate, analogue of the $Na_3HGe_4^{[6]}Ge_3^{[4]}O_{16} \cdot 4H_2O$ germanate, and another zeolite-like $NaHTi_2^{[6]}Si^{[4]}O_7 \cdot 2H_2O$ silicate are crystallized in the NaOH–TiO_2–SiO_2–H_2O system at 170°C.

Taking into account the above data, we search for topologically equivalent fragments of the $Na_4Ge_4^{[6]}Ge_5^{[4]}O_{20}$, $Na_3HGe_4^{[6]}Ge_3^{[4]}O_{16} \cdot 4H_2O$ ($Na_4Ti_4^{[6]}Si_3^{[4]}O_{16} \cdot 4H_2O$), and $NaHTi_2^{[6]}Si^{[4]}O_7 \cdot 2H_2O$ structures at the suprapolyhedral *MT* level [19, 21, 22] and, thus, determine whether these three phases belong to the same homologous series.

As was already noted in [19], in the above chemically and crystallographically complex systems, the compounds are built not by simple polyhedral structural units (*T* tetrahedra or *M* octahedra) but by higher units of the hierarchical level of the structural organization. These are ready structural fragments or the so-called substructural units–precursors (SSUs–precursors) that, in the bound state, contain all the main types of structural units (SUs)—octahedra and tetrahedra. The topological types of SSUs–precursors were simulated in [19].

It is possible to identify the topological type of these SSUs–precursors in three-dimensional *closely related*

Table 2. Chemical composition and structural data for germanates and silicates with three different types of *MT* frameworks

Compound	Sp. gr.	Unit-cell parameters: *a*, *b*, *c*, Å; α, β, γ	*V*, Å^3	*Z*	*R*, %	Year of structure determination	ICSD code
		M_2TO_7 frameworks					
$NaHTi_2SiO_7 \cdot 2H_2O$	$P4_2/mcm$	7.832, 7.832, 11.945, 90.00, 90.00, 90.00	732.7	4	0.044	1996	82525
$Na_{1.64}H_{0.36}Ti_2SiO_7 \cdot 1.84H_2O$	$P4_2/mcm$	7.808, 7.808, 11.974, 90.00, 90.00, 90.00	730.0	4	0.055	1994	75343
$K_{1.38}H_{0.62}Ti_2SiO_7 \cdot H_2O$	$P4_2/mbc$	11.015, 11.015, 12.017, 90.00, 90.00, 90.00	1458.0	8	0.076	1996	82527
		$M_4T_3O_{16}$ frameworks					
$Na_3HGe_7O_{16}(H_2O)_4 = Na_3HGe_4^{[6]}Ge_3^{[4]}O_{16} \cdot 4H_2O$	$P\bar{4}3m$	7.690, 7.690, 7.690, 90.00, 90.00, 90.00	454.8	1		1954	33592
$Na_4Ti_4^{[6]}Si_3^{[4]}O_{16} \cdot 6H_2O$	$R3m$	7.812, 7.812, 7.812, 88.79, 88.79, 88.79	476.5	1	0.076	1997	85003
$K_3HTi_4^{[6]}Si_3^{[4]}O_{16} \cdot 4H_2O$	$P\bar{4}3m$	7.764, 7.764, 7.764, 90.00, 90.00, 90.00	468.1	1	0.023	1996	81366
$Cs_3HTi_4^{[6]}Si_3^{[4]}O_{16} \cdot 4H_2O$	$P\bar{4}3m$	7.821, 7.821, 7.821, 90.00, 90.00, 90.00	478.4	1	0.039	1996	81365
		$M_4T_5O_{20}$ frameworks					
$Na_4Ge_9O_{20} = Na_4Ge_4^{[6]}Ge_5^{[4]}O_{20}$	$I4_1/a$	15.026, 15.026, 7.397, 90.00, 90.00, 90.00	1670.2	4	0.026	1990	68507

structures by the methods of crystallochemical analysis of complex structures such as the method of local crystallostructural intersection of space groups [18, 23], two-color decomposition of structural graphs into primary and secondary contours [19], and the method of determining the equivalent coordination sequences [20–22].

The algorithm of the reconstruction of a three-dimensional structure from its SSUs–precursors (i.e., of the local region of the structure) based on the principle of the maximum connectedness of the SSUs–precursors in the transition to a higher level of the structural self-organization of the system allows one to reconstruct the mechanism of assembly of three-dimensional *MT* structures of germanates and silicates from invariant (local) regions of the *MT* framework.

Type of Invariant SSU–Precursor

At a suprapolyhedral *MT* level, the $Na_4Ge_4^{[6]}Ge_5^{[4]}O_{20}$ and $Na_3HGe_4^{[6]}Ge_3^{[4]}O_{16} \cdot 4H_2O$ germanates synthesized and the $NaHTi_2^{[6]}Si^{[4]}O_7 \cdot 2H_2O$ silicate are characterized by topologically equivalent (invariant) *MT* fragments of the structure. These fragments in the form of infinite *MT* chains S_3^1 of the composition M_4T indicate that the above three phases are the representatives of one homologous series of *MT*-condensed structures.

The mechanism of formation of invariant *MT* chains in the structures consists in the connection of links consisting of five polyhedra of the composition M_4T. In this case, two vertices of a *T* tetrahedron of one link are combined with two vertices of an *M* octahedron of the other link. The index of the complementary binding of links in the chain equals 2. Two repeating links of the *MT* chain in Fig. 1 are hatched differently. The numbers of germanium atoms correspond to the numbers of atoms in the ICSD database [2].

The stable chainlike *MT* fragments of the composition $2M_4T_1$ interpreted as SSUs–precursors of the three phases control all the processes of the subsequent development of a crystal-forming *MT* complex and provide the formation of an SSU of a higher level.

The SSU–precursor of crystal structures, which forms the primary chainlike *MT* structure, is fully determined by the mechanism of connection of two M_4T links. The distance between the M_4T links determines the close values of the modules of translation vectors for three types of structures equal to b = 7.832 Å for $NaHTi_2^{[6]}Si^{[4]}O_7 \cdot 2H_2O$, b = 7.812 Å for $Na_4Ti_4^{[6]}Si_3^{[4]}O_{16} \cdot 6H_2O$, b = 7.690 Å for

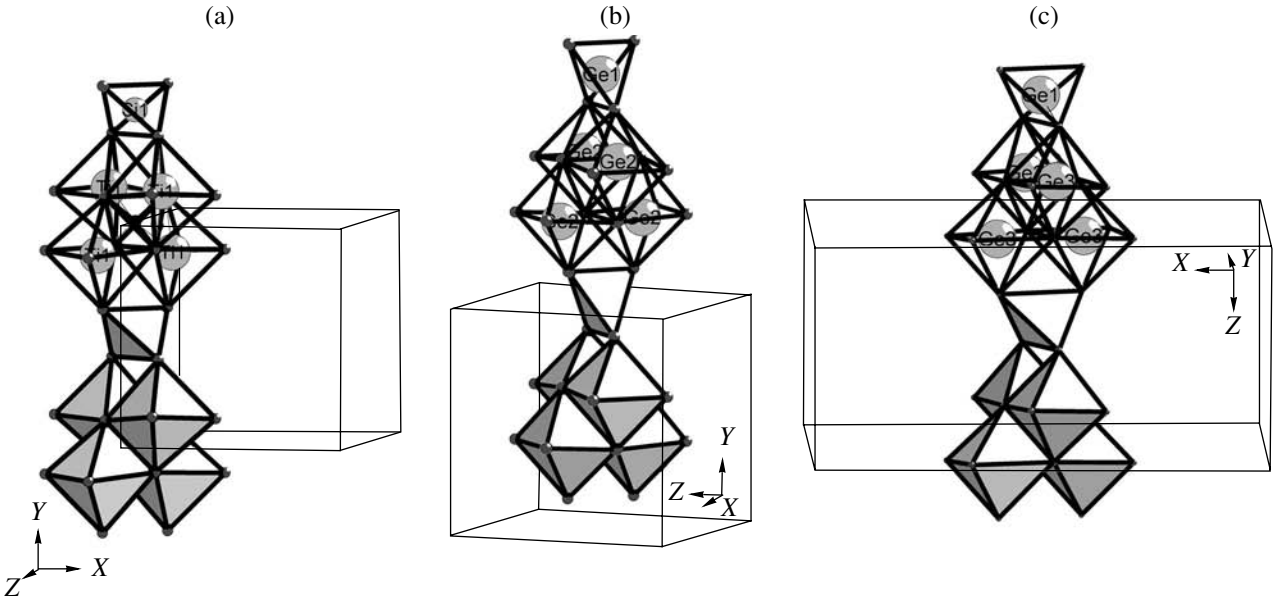

Fig. 1. Topologically equivalent fragments of *MT* frameworks in (a) $NaHTi_2^{[6]}Si^{[4]}O_7 \cdot 2H_2O$, (b) $Na_3HGe_4^{[6]}Ge_3^{[4]}O_{16} \cdot 4H_2O$, and (c) $Na_4Ge_4^{[6]}Ge_5^{[4]}O_{20}$ structures. The chain portions whose alternation determines the translation-vector modulus in the Bravais lattice are hatched in different ways. All the chains consist of two links of the M_4T_1 composition.

$Na_3HGe_4^{[6]}Ge_3^{[4]}O_{16} \cdot 4H_2O$, and c = 7.397 Å for $Na_4Ge_4^{[6]}Ge_5^{[4]}O_{20}$.

Types of Tetrahedrally (T) Modified SSUs–Precursors

The three-dimensional M_4T-frameworks of the structures considered here have the invariant *MT* chain of the composition M_4T and different polyhedral $M:T$ ratios equal to 4 : 5, 4 : 3, and 4 : 2. Therefore, the difference in the SSUs–precursors, which are changed with the formation of the *MT* structures with different chemical compositions, depend on the degree of *T* modification of the chain by orthotetrahedra. The number of tetrahedra that can modify the link of an SSU–precursor varies from one to four (maximum) (Fig. 2c), which is predetermined by the topology of a cluster consisting of four *M* octahedra.

Each *M* link of the chain is modified during the formation of the $NaHTi_2^{[6]}Si^{[4]}O_7 \cdot 2H_2O$ silicate by one *T* tetrahedron and, therefore, the *MT* composition of the SSU–precursor, $2M_4T_2$, corresponds to the *MT* composition of the three-dimensional framework. Packing of modified SSUs–precursors (mSSUs–precursors) according to the mechanism of complementary self-assembly would result in the fastest formation of the structure framework M_4T_2–$Ti_2^{[6]}Si^{[4]}O_7$.

During formation of the $Na_3HGe_4^{[6]}Ge_3^{[4]}O_{16} \cdot 4H_2O$ germanate, each 4*M* cluster in a link of the *MT* chain is modified by two *T* tetrahedra. Packing of mSSUs–precursors of the composition $2M_4T_3$ results in the formation of the structure framework M_4T_3–$Ge_4^{[6]}Ge_3^{[4]}O_{16}$.

During formation of $Na_4Ge_4^{[6]}Ge_5^{[4]}O_{20}$, the degree of *T* modification of the *MT* chain is maximal. Packing of the mSSUs–precursors of the composition $2M_4T_5$ results in the formation of the structure framework M_4T_5–$Ge_4^{[6]}Ge_5^{[4]}O_{20}$.

Consider in more detail the mechanism of condensation of mSSUs–precursors according to the principle of the maximum connectedness of the SSUs–precursors in the transition to a higher level of the structural self-organization of the system.

MATRIX (THREE-DIMENSIONAL) ASSEMBLY OF CRYSTAL STRUCTURES

$NaHTi_2^{[6]}Si^{[4]}O_7 \cdot 2H_2O$ *Silicate*

Assembly of an *MT* layer. The complementary interaction of two mSSUs–precursors along the *X* axis in the *XY* plane (Fig. 3a) according to the centrosymmetric mechanism results in the formation of a planar layer $S_3^2(g)$; the connectedness index of mSSU along this direction equals four. The modulus of the translation vector is $a = b$ = 7.832 Å.

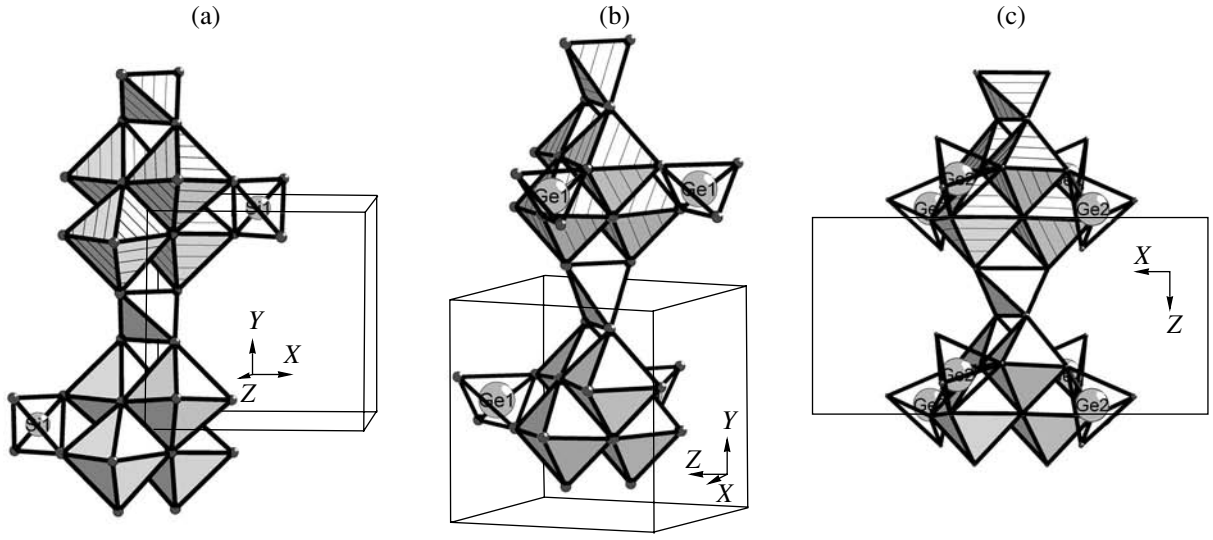

Fig. 2. *T* modification with TO_4 octahedra of the chain links in (a) $NaHTi_2^{[6]}Si^{[4]}O_7 \cdot 2H_2O$, (b) $Na_3HGe_4^{[6]}Ge_3^{[4]}O_{16} \cdot 4H_2O$, and (c) $Na_4Ge_4^{[6]}Ge_5^{[4]}O_{20}$ structures. The *MT* compositions of the SSUs-precursors, (a) M_8T_4, (b) M_8T_6, and (c) M_8T_{10}, correspond to the *MT* compositions of the three-dimensional frameworks.

Assembly of *MT* framework. The complementary interaction of two layers along the *Z* axis (Fig. 3a) according to the centrosymmetric mechanism results in the formation of the $S_3^3(g)$ framework; the connectedness index along this direction equals eight (Fig. 4a). The first and third layers of the *MT* framework are related by translations. The modulus of the translation vector equals $c = 11.945$ Å.

$Na_3HGe_4^{[6]}Ge_3^{[4]}O_{16} \cdot 4H_2O$ *Germanate–*

$Na_4Ti_4^{[6]}Si_3^{[4]}O_{16} \cdot 6H_2O$ *Silicate*

Assembly of an *MT* layer. Complementary interaction of two mSSUs–precursors in the direction of the *Z* axis in the *YZ* plane (Fig. 3b) according to the centrosymmetric mechanism results in the formation of the S_3^2 planar layer, the connectedness index of mSSU along this direction equals four. The modulus of the translation vector is $c = b = 7.690$ Å.

The mechanism of the layer assembly is topologically identical to the mechanism of the layer assembly in the $NaHTi_2^{[6]}Si^{[4]}O_7 \cdot 2H_2O$ silicate with the M_4T_2 framework.

Assembly of an *MT* framework. Complementary interaction of two layers along the *X* axis (Fig. 4b) according to the centrosymmetric mechanism results in the formation of the $S_3^3(g)$ framework; like in the $NaHTi_2^{[6]}Si^{[4]}O_7 \cdot 2H_2O$ silicate with the M_4T_2 framework, the connectedness index along this direction equals eight (Fig. 4b). All the S_3^2 layers in the *MT* framework are related by translations. The modulus of the translation vector is $a = 7.690$ Å.

The absence of two *T* tetrahedra on the surface of the S_3^2 layer results in the cessation of three-dimensional growth of germanate. The model of such an *MT* layer for the $NaHTi_2^{[6]}Si^{[4]}O_7 \cdot 2H_2O$ silicate with the M_4T_2 framework is shown in Fig. 3a. If the formed microparticles of the germanate with such surfaces interact complementary, a stacking fault is formed in the $Na_3Ge_4^{[6]}Ge_3^{[4]}O_{16} \cdot 4H_2O$ structure. The connectedness index of these particles is eight, as in the case of three-dimensional growth of the germanate structure. At the microlevel, particle stability remains to be equivalent, which results in the formation of the so-called polytypoid *MT* structures.

$Na_4Ge_4^{[6]}Ge_5^{[4]}O_{20}$ *Germanate*

Assembly of an *MT* layer. The formation of a planar S_3^2 layer from two mSSUs-precursors proceeds in accordance with the centrosymmetric mechanism along the *Y* axis (Fig. 3c). The sharing-vertex TO_4 orthotetrahedra form diorthogroups T_2O_7. During condensation, the chains are slightly displaced with respect to one another along the *Z* axis. The formation of diorthogroups dramatically changes the topology of the layer of this germanate from the *MT* layers of the above $Na_4Ti_4^{[6]}Si_3^{[4]}O_{16} \cdot 6H_2O$ silicate and $Na_3HGe_4^{[6]}Ge_3^{[4]}O_{16} \cdot 4H_2O$ germanate. The

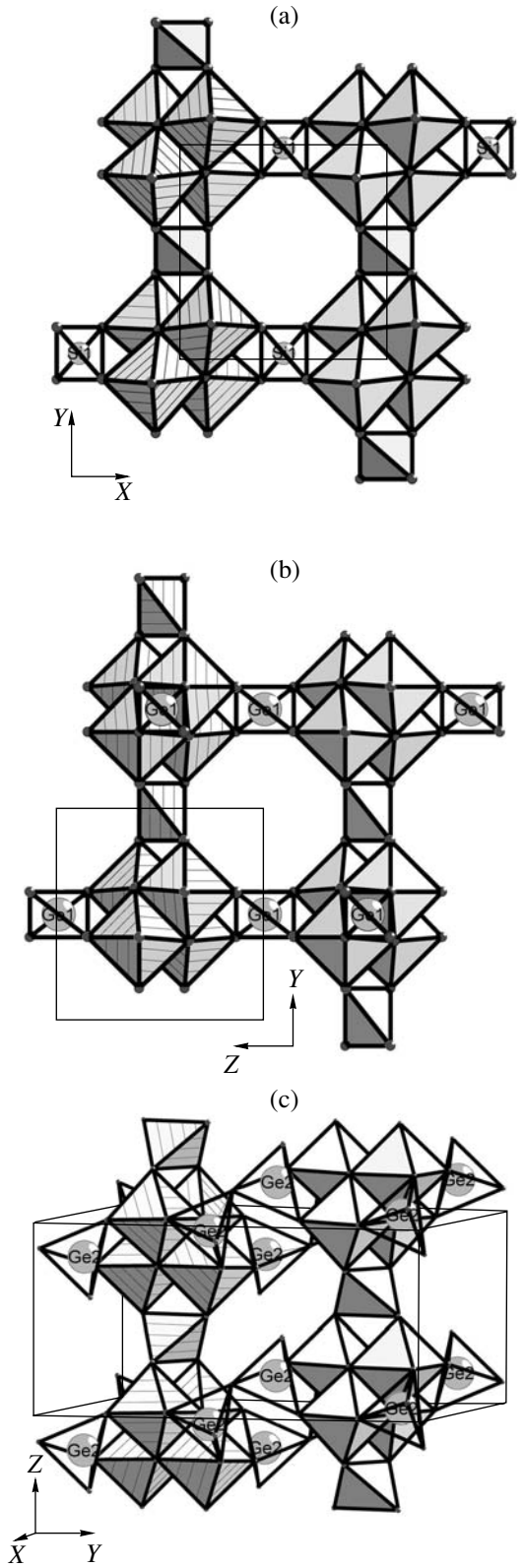

Fig. 3. Complementary layer assembly from two modified SSUs–precursors in (a) $NaHTi_2^{[6]}Si^{[4]}O_7 \cdot 2H_2O$, (b) $Na_3HGe_4^{[6]}Ge_3^{[4]}O_{16} \cdot 4H_2O$, and (c) $NaGe_4^{[6]}Ge_5^{[4]}O_{20}$.

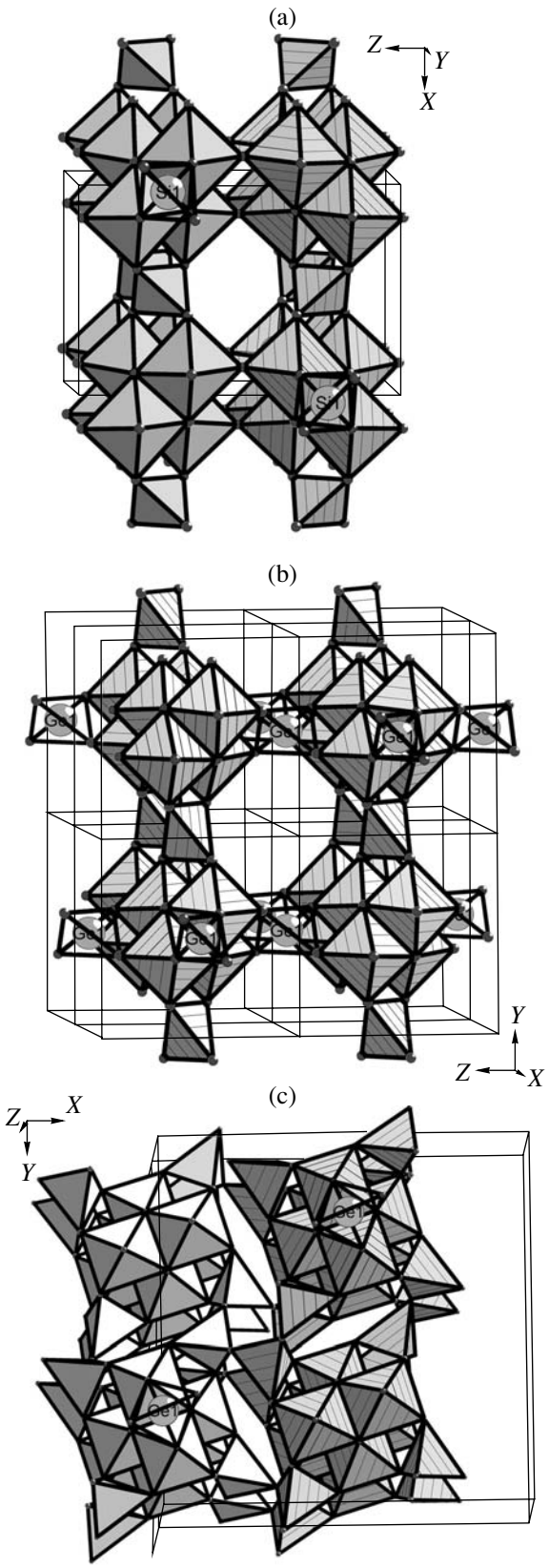

Fig. 4. Complementary assembly of the framework from four modified SSUs–precursors in (a) $NaHTi_2^{[6]}Si^{[4]}O_7 \cdot 2H_2O$, (b) $Na_3HGe_4^{[6]}Ge_3^{[4]}O_{16} \cdot 4H_2O$, and (c) $Na_4Ge_4^{[6]}Ge_5^{[4]}O_{20}$.

first and third chains in the structure are related by a translation. The modulus of the translation vector equals $c = 15.026$ Å.

Assembly of framework. A three-dimensional *MT*-condensed structure is formed due to connection of two *MT* layers along the *X* axis (Fig. 4c). The first and third layers in the *MT* framework are related by a translation. The modulus of the translation vector is $a = c = 15.026$ Å.

Now, consider the main consequences from the above modeling of the assembly of germanate and silicate crystal structures.

At all the states of the structure assembly, the *MT* composition of the *substructural units* of different levels—SSUs–precursors ($n \times M_8T_4$, $n \times M_8T_6$, $n \times M_8T_{10}$)—is constant and corresponds to the *MT* composition of *three-dimensional frameworks* in $NaHTi_2^{[6]}Si^{[4]}O_7 \cdot 2H_2O$, $Na_3HGe_4^{[6]}Ge_3^{[4]}O_{16} \cdot 4H_2O$, and $Na_4Ge_4^{[6]}Ge_5^{[4]}O_{20}$. The structure assembly proceeds according to the simplest (shortest) programs. In modeling, all the structures are formed as a result of SSU packing, i.e., are formed in the fastest way from interacting SSUs–precursors.

The maximum degree of the *T* modification of an invariant *MT* chain by four tetrahedra is established for $Na_4Ge_4^{[6]}Ge_5^{[4]}O_{20}$. This fact reflects the topology of the crystal-forming *MT* chain—the maximum number of free vertices of the octahedral 4*M* clusters (eight vertices sterically admissible for condensation) complementary interacting with two vertices of *T* tetrahedra. As a result of such a structure of crystal-forming *MT* chains, it is possible to predict the maximum and minimum SU ratio, *M*/*T*, for the three-dimensional *MT* frameworks in the homologous series of structures. It should be noted that the structures are built by an invariant *MT* chain with the degrees of additional *T* condensation 1, 2, and 4. The last value corresponds to an unusual stoichiometry of the *MT* structure as a whole, $M/T = 4 : 5$. Usually, the silicate and germanate structures with *MT* framework and isolated *M* octahedra are characterized by the *M*/*T* ratio changing from 1 : 1 to 1 : 6 at a step of 0.5 [21].

The experimental data show that the first structure type formed in the system with *R*–GeO_2 after the attainment of a certain threshold (minimum) value of NaOH concentration is the $Na_4Ge_4^{[6]}Ge_5^{[4]}O_{20}$ germanate. The formation of an SSUs–precursor of this germanate is provided by the maximum number of free $[Ge(OH)_4]^0$ tetrahedra modifying the *MT* chain whose maximum quantity is observed only in weak alkaline solutions.

With an increase of C_{NaOH}, the fraction of free $Ge(OH)_4$ gradually decreases and, after the formation of the $Na_4Ge_4^{[6]}Ge_5^{[4]}O_{20}$ phase, first, one observes the $Na_4Ge_4^{[6]}Ge_5^{[4]}O_{20}$ (with four modifying tetrahedra) and $Na_3HGe_4^{[6]}Ge_3^{[4]}O_{16} \cdot 4H_2O$ (with two modifying tetrahedra) cocrystallization and, later, only the formation of $Na_3HGe_4^{[6]}Ge_3^{[4]}O_{16} \cdot 4H_2O$ (with two modifying tetrahedra) accompanied by the appearance of the nanocrystalline XRA phase.

Fast topological differentiation of SSUs–precursors of two germanates occurs already at the stage of the layer assembly accompanied by the appearance of various *T* radicals in $Na_4Ge_4^{[6]}Ge_5^{[4]}O_{20}$ and preservation of one radical in $Na_3HGe_4^{[6]}Ge_3^{[4]}O_{16} \cdot 4H_2O$. It should be emphasized that two-dimensional layers of germanates are not complementary and cannot form polytypoid structures.

In strongly alkaline NaOH solutions at 350°C, no Ge analogue ($NaHGe_2^{[6]}Ge^{[4]}O_7 \cdot 2H_2O$) of the $NaHTi_2^{[6]}Si^{[4]}O_7 \cdot 2H_2O$ titanosilicate with one modifying tetrahedron can be formed. Moreover, in all the germanate systems with *A* = Li, Na, K, the formation of zeolite-like $A_3HGe_4^{[6]}Ge_3^{[4]}O_{16} \cdot 4H_2O$ compounds (with the crystallite size being the minimal in the strongest alkaline solutions) results in the cessation of macrocrystallization, and the solid phase formed is always a nanocrystalline phase. The appearance of this phase seems to be associated with stacking faults in microparticle packings in $Na_3HGe_4^{[6]}Ge_3^{[4]}O_{16} \cdot 4H_2O$ and $NaHGe_2^{[6]}Ge^{[4]}O_7 \cdot 2H_2O$ germanates (because of the topological similarity of their surfaces) and, as a result, the formation of aperiodic polytypoid structures.

CONCLUSIONS

In the NaOH–GeO_2–H_2O system at 350°C, the changes in the compositions of the cocrystallizing $Na_4Ge_4^{[6]}Ge_5^{[4]}O_{20}$ (M_4T_5 framework) and $Na_3HGe_4^{[6]}Ge_3^{[4]}O_{16} \cdot 4H_2O$ (M_4T_3 framework) phases are established, which are controlled by both m_{GeO_2} values and NaOH concentration.

An increase in the NaOH concentration results in the regular formation of germanates characterized by a decrease of the degree of *T* modifying of octahedral M_4 clusters of invariant *MT* chains.

The crystal structures of $Na_4Ge_4^{[6]}Ge_5^{[4]}O_{20}$ (M_4T_5 framework), $Na_3HGe_4^{[6]}Ge_3^{[4]}O_{16} \cdot 4H_2O$ (M_4T_3 framework), and $NaHTi_2^{[6]}Si^{[4]}O_7 \cdot 2H_2O$ (M_4T_2 framework) with topologically equivalent one-dimensional *MT* structures form a homologous series. The maximum content of the *T* component is characteristic of the $Na_4Ge_4^{[6]}Ge_5^{[4]}O_{20}$ germanate (M_4T_5 framework), the

intermediate content, for the $Na_3HGe_4^{[6]}Ge_3^{[4]}O_{16} \cdot 4H_2O$ germanate and $Na_4Ti_4^{[6]}Si_3^{[4]}O_{16} \cdot 4H_2O$ silicate (the M_4T_3 framework), and the minimum content, for the $NaHTi_2^{[6]}Si^{[4]}O_7 \cdot 2H_2O$ silicate (M_4T_2 framework).

ACKNOWLEDGMENTS

This study was supported by the Russian Foundation for Basic Research, project no. 02-02-16861.

REFERENCES

1. International Center for Diffraction Data (ICDD). 12 Campus Boulevard Newtown Square, PA 19073-3273, USA; S. N. Kabekkodu, J. Faber, and T. Fawcett, Acta Crystallogr., Sect. B: Struct. Sci. **58**, 333 (2002).
2. *Inorganic Crystal Structure Database (ICSD)* (Gmelin-Inst. fur Anorganische Chemie and FIC, Karlsruhe, 2002).
3. W. H. Baur, E. Halwax, and H. Voellenkle, Monatsch. Chem. **116**, 1367 (1985).
4. D. W. J. Cruickshank, A. Kalman, and J. S. Stephens, Acta Crystallogr. **34**, 1333 (1978).
5. M. E. Fleet and S. Muthupari, J. Solid State Chem. **140**, 175 (1998).
6. M. E. Fleet, Acta Crystallogr., Sect. C: Cryst. Struct. Commun. **46**, 1202 (1990).
7. H. Nowotny and A. Wittmann, Monatsch. Chem. **85**, 558 (1954).
8. H. Vollenkle, A. Wittmann, and H. Nowotny, Monatsch. Chem. **100**, 79 (1969).
9. M. S. Dadachov and W. T. A. Harrison, J. Solid State Chem. B **134**, 409 (1997).
10. E. A. Behrens, D. M. Poojary, and A. Clearfield, Chem. Mater. **8**, 1236 (1996).
11. M. J. Buerger, W. A. Dollase, and I. Garaycochea-Wittke, Z. Kristallogr. **125**, 92 (1967).
12. D. M. Poojary, A. I. Bortun, L. N. Bortun, *et al.*, Inorg. Chem. **35**, 6131 (1996).
13. S. Feng, M. Tsai, and M. Greenbladtt, Chem. Mater. **4**, 388 (1992).
14. S. Feng, M. Tsai, S.-P. Szu, and M. Greenbladtt, Chem. Mater. **4** (2), 468 (1992).
15. G. D. Ilyushin and L. N. Dem'yanets, Zh. Neorg. Khim. **47** (10), 1699 (2002).
16. I. P. Kuz'mina, Kristallografiya **13** (5), 854 (1968) [Sov. Phys. Crystallogr. **13**, 737 (1968)].
17. I. P. Kuz'mina, B. N. Litvin, and V. S. Kurazhkovskaya, *Study of Crystallization Processes under Hydrothermal Conditions* (Nauka, Moscow, 1970).
18. G. D. Ilyushin and L. N. Dem'yanets, *Germanates of Tetravalent Metals* (VINITI, Moscow, 1989).
19. G. D. Ilyushin and L. N. Dem'yanets, *Structural Studies of Crystals* (Nauka, Moscow, 2002), p. 96.
20. G. D. Ilyushin and L. N. Dem'yanets, Zh. Neorg. Khim. **47** (8), 1480 (2002).
21. G. D. Ilyushin and B. A. Blatov, Acta Crystallogr., Sect. B: Struct. Sci. **58** (2), 198 (2002).
22. G. D. Ilyushin, B. A. Blatov, and Yu. A. Zakutkin, Acta Crystallogr., Sect. B: Struct. Sci. **58** (6), 948 (2002).
23. G. D. Ilyushin and L. N. Dem'yanets, Kristallografiya **46** (5), 875 (2001) [Crystallogr. Rep. **46**, 801 (2001)].

Translated by L. Man

Crystallography Reports, Vol. 48, No. 5, 2003, pp. 897–898. Translated from Kristallografiya, Vol. 48, No. 5, 2003, pp. 959–960.

JUBILEES

Arkadiĭ Vladimirovich Shil'nikov (On the Occasion of His 70th Birthday)

Professor Arkadiĭ Vladimirovich Shil'nikov, a prominent figure of Russian higher education, a talented pedagogue, and one of the leading Russian scientists working in the field of ferroelectric physics and practical application of ferroelectrics, has turned seventy.

Shil'nikov was born on May 7, 1933, in Kazan, in a suburb of which his parents worked at a state farm: his father, as a chief agronomist, and his mother, as a agricultural-machines mechanic. Soon, the family moved to Stalingrad (at present, Volgograd), with which Shil'nikov's life has been closely connected to the present.

Shil'nikov lost his parents early and at the age of eleven started as a seasonal worker (a drover and herdsman). At the age of sixteen, he got a regular job as a municipal communication technician. In 1952, he finished a secondary school for working youths and entered the Physics and Mathematics Faculty of the Volgograd Pedagogical Institute. In 1956, he graduated with honors. During his student years, Shil'nikov continued working and began his research (he was one of the first Soviet researchers to investigate the problems of nonstationary electrolysis). In 1956, this research was confirmed by an author's certificate.

In 1954–1960, Shil'nikov taught physics at an experimental village secondary school. In 1961 he began working at the Department of Physics of the Volgograd State Academy of Architecture and Civil Engineering. Shil'nikov had passed through all stages of carrier growth to become the Head of the Department of Physics in 1975, and he has held this position ever since. In the periods of 1980–1985 and 1998–2001, he performed the duties of the prorector for education, and now he is an adviser to the rector of the academy.

From the very beginning of his work at the Department of Physics, Shil'nikov has been engaged in research. In 1972, he accomplished and successfully defended his candidate's dissertation in physics and mathematics entitled *Some Dielectric Properties of Polydomain Single Crystals of Seignette Salt, Triglycine Sulfate, and Potassium Dihydrogenphosphate*, which was done under the supervision of L.A. Shuvalov and S.L. Rapoport.

Shil'nikov founded a line of investigation of the properties of ferroelectrics, namely, investigation of the effect of domain and phase boundaries and other defects on the processes of low-frequency and infralow-frequency polarization and repolarization of ferroelectrics even in ultralow fields. He is one of the most authoritative Russian (or foreign) experts in this field.

Shil'nikov defended his doctoral dissertation on the above problem in 1989. He became a full professor in 1991.

Shil'nikov played an important role in organizing and carrying out pioneer works on the application of nematic liquid crystals to visualization of the statics and dynamics of domains in collinear ferroelectrics (triglycine sulfate and others), which became an important practical method of control.

Together with L.A. Shuvalov, Shil'nikov supervised the pioneering dissertation of A.G. Luchaninov entitled *The Piezoelectric Effect in Electrically Depolarized Polycrystalline Ferroelectrics*.

The team of scientists working under Shil'nikov's supervision gives much attention to applied research. Thus, a highly efficient conveyor polarization unit operating on the new principle of high-rate polarization was applied at the Avrora plant.

Shil'nikov is the author of more than 300 scientific publications and the editor of three issues of the series Dielectric and Semiconductor Physics, which have gained recognition in Russia and other countries. Shil'nikov was the head of organizing committees of all-Russia and international conferences held in Volgo-

1063-7745/03/4805-0897$24.00 © 2003 MAIK "Nauka/Interperiodica"

grad. He is a permanent member of organizing and program committees of different international and all-Russia forums on ferroelectricity. For many years, Shil'nikov has been a member of the Scientific Council "Ferroelectric and Dielectric Physics" (now a section of the Scientific Council "Solid-State Physics") of the Russian Academy of Sciences.

Shil'nikov is an Honored Scientist of the Russian Federation and a Corresponding Member of the Russian Academy of Natural Sciences.

Greeting his 70th birthday, Shil'nikov continues creative research work, supervises postgraduates and persons working for doctor's degree, and publishes his articles in leading scientific journals (*Fizika Tverdogo Tela* (Physics of the Solid State), *Kristallografiya* (Crystallography Reports), *Izvestiya Rossiĭskoĭ Akademii Nauk* (Herald of the Russian Academy of Sciences, Ferroelectrics, *et al.*).

Arkadiĭ Vladimirovich Shil'nikov won the respect of experts in the field of ferroelectricity and possesses authority with his students. All of them, together with the Editorial Board of *Kristallografiya* (Crystallography Reports), congratulate Professor Shil'nikov on his birthday and sincerely wish him health, many years of fruitful activity, and new achievements for the benefit of Russian science.

Translated by I. Polyakova